AD-A109 514 SEMICLASSICAL THEORY OF INJECTED LASERS WITH ARBITRARY STABLE AND UNSTABLE RESONATORS(U) AIR FORCE INST OF TECH WRIGHT-PATTERSON AFB OH SCHOOL OF ENGI.. 1/4

UNCLASSIFIED S M RINALDI DEC 87 AFIT/DS/PH/76-3 F/G 9/3 NL

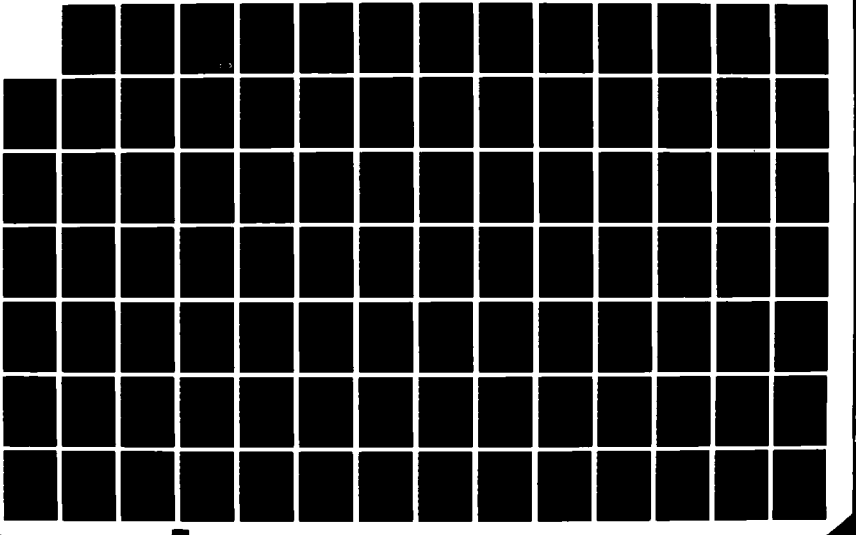

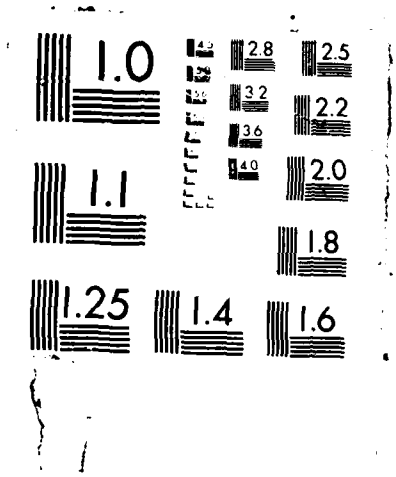
1.0
1.1
1.25
1.4
1.6
1.8
2.0
2.2
2.5
2.8
3.2
3.6
4.0

SEMICLASSICAL THEORY OF INJECTED LASERS
WITH
ARBITRARY STABLE AND UNSTABLE RESONATORS

DISSERTATION

Steven M. Rinaldi
Captain, USAF

AFIT/DS/PH/87-3

DEPARTMENT OF THE AIR FORCE
AIR UNIVERSITY
THE INSTITUTE OF TECHNOLOGY

Wright-Patterson Air Force Base, Ohio

1

AFIT/DS/PH/87-3

SEMICLASSICAL THEORY OF INJECTED LASERS WITH ARBITRARY STABLE AND UNSTABLE RESONATORS

DISSERTATION

Steven M. Rinaldi
Captain, USAF

AFIT/DS/PH/87-3

Approved for public release; distribution unlimited

DTIC
ELECTE
MAR 0 2 1988
S D
CH

AFIT/DS/PH/87-3

SEMICLASSICAL THEORY OF INJECTED LASERS WITH ARBITRARY STABLE AND UNSTABLE RESONATORS

DISSERTATION

Presented to the Faculty of the School of Engineering

of the Air Force Institute of Technology

Air University

In Partial Fulfillment of the

Requirements for the Degree of

Doctor of Philosophy

Steven M. Rinaldi, B.S., M.S.

Captain, USAF

December, 1987

Approved for public release; distribution unlimited

AFIT DS/PH/87-3

SEMICLASSICAL THEORY OF INJECTED LASERS WITH ARBITRARY STABLE AND UNSTABLE RESONATORS

Steven M. Rinaldi, B.S., M.S.
Captain, USAF

Approved

	Dec 8, 1987
	Dec 8, 1987
	Dec 8, 1987
	Dec 8, 1987
	Dec 8, 1987

Accepted

8 Dec. 1987

Dean, School of Engineering

Preface

Coupled laser devices are currently the subject of an intense research effort. Among the various coupling techniques, injection locking offers a relatively simple method of locking one or more lasers to a common source. This theoretical analysis evolved from perceived deficiencies in the previously developed models of injected lasers, in which the locking ranges of lasers with large outcouplings are incorrectly estimated. It is my hope that many of the shortcomings of the previous models have been eliminated in this project.

A large number of symbols are used throughout the derivations. A glossary of symbols and notation is included at the end of this dissertation.

As with any major undertaking, this project could not have been completed without the help, encouragement, and understanding of many people. My sincere appreciation goes to my advisor, Dr John Erkkila, for his insight and guidance throughout the past six years. The computer work would not have been possible without the help of several individuals. Specifically, I wish to thank Capt (Dr) Mark Rogers for providing funding for and assistance with the Air Force Weapons Laboratory Cray I computer; Capt Paul Sydney for obtaining and installing TEX on the ARVAX computer; and Mr Brian Kennedy, Capt Paul Sydney, and Lt Darryl Sanchez for answering innumerable questions about the ARVAX computer. Capt (Dr) John Glessner graciously provided the experimental excimer laser data analyzed in Chapter VII. Many enlighting technical discussions were held during the past three years with Dr Tom Ferguson. I wish to thank my wife Ginger and son Anthony for their understanding, love, and patience, especially during the particularly trying times. Finally, I offer my deepest thanks to the Lord, who patiently taught me the meaning of Matt. 7:7-11 during the course of my studies.

Steven M. Rinaldi

Accession For
NTIS GRA&I
DTIC TAB
Unannounced
Justification
By
Distribution/
Availability Codes
Avail and/or
Dist Special
A-1

DTIC COPY INSPECTED

Table of Contents

List of Figures

List of Tables

Abstract

A semiclassical analysis of injected lasers with stable and unstable resonators and arbitrary outcoupling fractions was performed. Homogeneously broadened lasers with Fabry-Perot and with positive branch, confocal unstable resonators were modeled. Both time-dependent and steady-state analyses of free-running and injected lasers were performed.

Because of deficiencies in the standing wave semiclassical and the simple saturable gain models, a new semiclassical theory of homogeneously broadened lasers was developed. The theory is predicated upon the following assumptions: the atoms are two-level, a single longitudinal mode exists in the cavity, the transverse mode structure can be adequately modeled by the geometric optics mode, and the laser electric fields can be described by a pair of counterpropagating planar, cylindrical, or spherical traveling waves with different amplitudes. A general semiclassical theory was first developed, and then specialized to the Fabry-Perot and positive branch, confocal unstable resonator cases. Both the Maxwell-Bloch and rate equation approximation forms of the theory were derived. The general theory is sufficiently broad to allow the modeling of the geometric optics mode of any standing wave resonator configuration. The theory was shown to reduce to the simple saturable gain and standing wave semiclassical models in the appropriate limits.

The analyses of the injected lasers were performed with the new semiclassical theory. Both time-dependent and steady-state analyses were performed. The parameter space explored allowed the outcoupling fractions to be varied and the injected signal frequencies to be detuned from the free-running laser frequencies. Observables of interest included the threshold injected intensities, the locking ranges, and the injected laser system gains. Comparisons to three alternate models of injected lasers were performed. In the appropriate limits, the present model was shown to reduce to the other models.

SEMICLASSICAL THEORY OF INJECTED LASERS WITH ARBITRARY STABLE AND UNSTABLE RESONATORS

I. Introduction

Coupling of laser devices has been performed over the past three decades in order to control various parameters of the output beam. A variety of schemes, each with advantages and disadvantages, have been used to couple lasers. These techniques include optically coupled resonators (1–19), master oscillator/power amplifiers or MOPAs (20–22), electronically coupled lasers (23–27), nonlinearly coupled lasers (28, 29), nonlinearly coupled MOPAs (30–32), and common mirror or shared optical element coupling (33, 34). A seventh technique, with which this research project is concerned, is injection locking.

The injection locking technique utilizes a low power master oscillator to control a higher power slave oscillator. The beam from the master oscillator is directly injected into the slave oscillator. This is illustrated in Figure 1.1. If the frequency of the injected field is relatively close to the free-running frequency of the slave oscillator and the injected intensity is above a minimum value, then the spatial and spectral properties of the slave laser beam will be the same as those of the master oscillator beam. Most importantly, the field emitted from the slave laser will have the same frequency as and a fixed phase relationship with the field from the master oscillator. This phenomenon is known as "locking". The range of frequencies over which the injected signal may vary from the free-running frequency of the slave oscillator while maintaining locking is known as the "locking range". The minimum or "threshold" value of injected intensity for which locking occurs is a function of the detuning of the injected field from the free-running field of the slave oscillator. As high power lasers often have poor spectral and spatial characteristics, a well-controlled beam from a low power master oscillator can cause a significant improvement in the output from the slave laser. For this reason, injection locking is a useful tool for providing high power, high quality laser radiation.

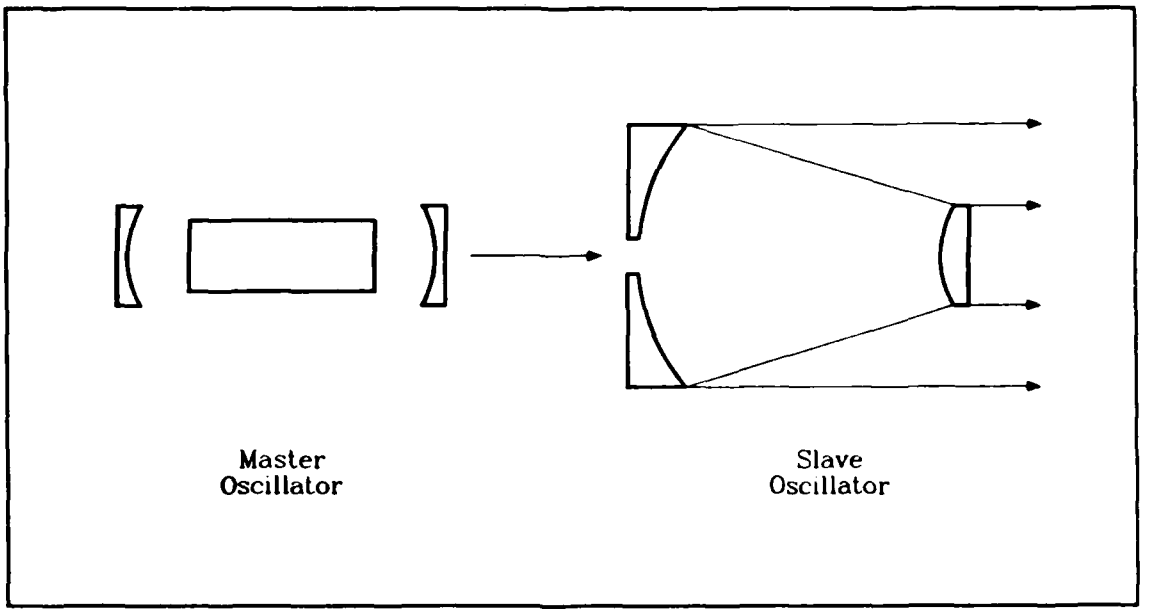

Figure 1.1. The basic concept of injection locking.

Injection locking is conceptually similar to the coupled resonator and MOPA coupling techniques. However, significant differences exist between these methods. In a coupled resonator device, each laser in the array is locked to the other lasers. Each laser is thus influenced by and influences all of the other lasers in the array. However, in an injected laser, the master oscillator is not affected by the slave oscillator. The master oscillator operates independently of the slave oscillator; it is essentially isolated from the slave. The MOPA differs in one fundamental aspect from the injected device. The power amplifier of the MOPA is below its lasing threshold. If the beam from the master oscillator is removed, the power amplifier will not lase by itself. However, the slave oscillator in an injected laser system is above its lasing threshold. If the injected signal is removed, the slave oscillator will lase.

Injection locking has been widely reported in the literature, in both experimental (35–76) and theoretical (77–106) studies. Several different coupling methods have been employed, the more common of which are illustrated in Figure 1.2. The experimental studies demonstrate a wide variety of output beam parameters that may be controlled by injection locking. The two most important

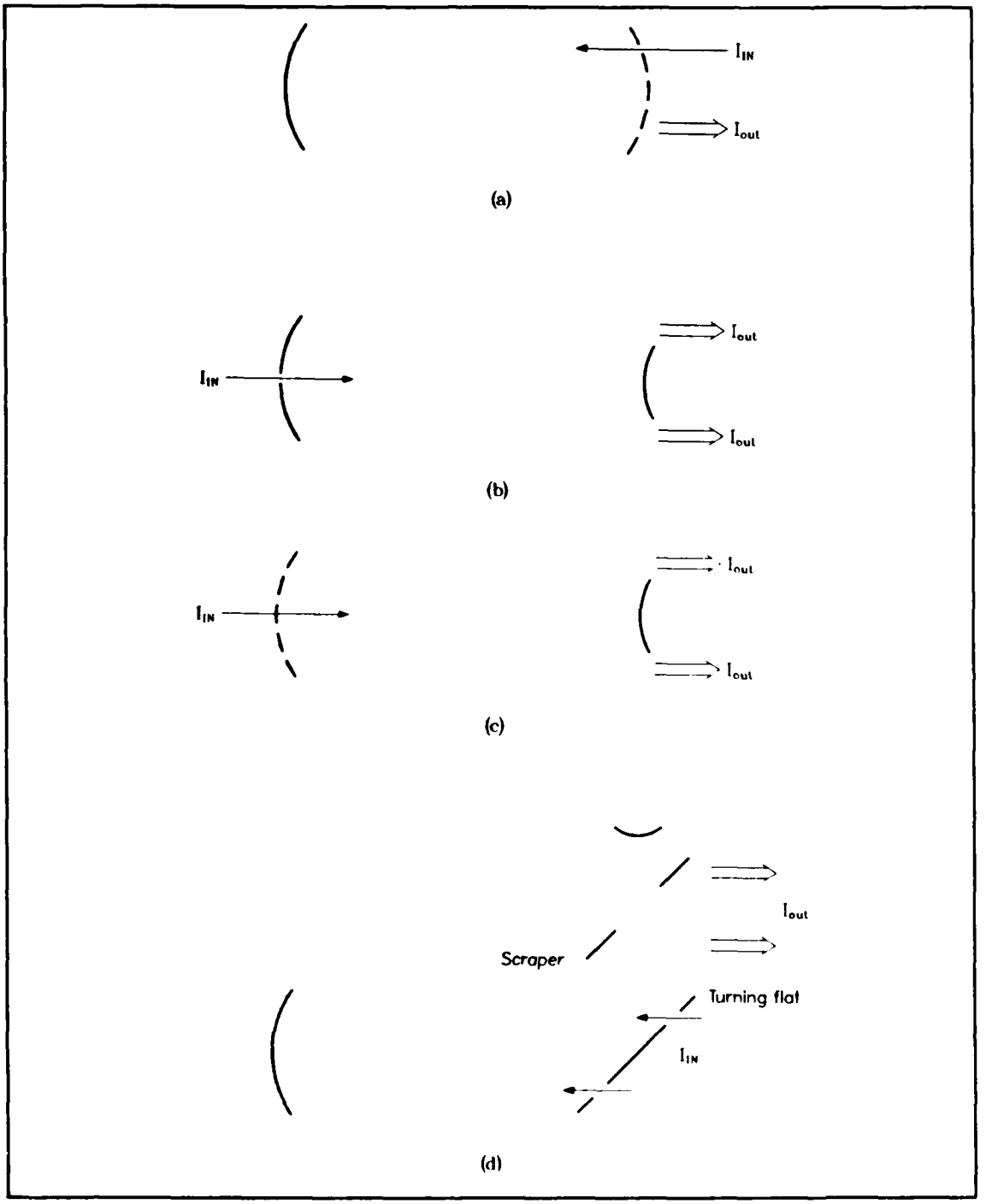

Figure 1.2. Various methods of injection locking. The dotted lines indicate partially transmissive mirrors. I_{IN} is the injected field; I_{out} is the output field from the slave laser. Adapted from (38).

parameters are the phase and frequency of the electric field of the slave laser. Subject to the locking range and threshold intensity constraints mentioned above, the phase and frequency of the slave field can be locked to those of the injected field. This provides an alternate method of tuning the frequency of the high power slave, as opposed to intracavity gratings or etalons. Spectral narrowing of the slave field is a third important effect of injection locking. Often, the output spectra of high power lasers are broad. The fields from dye and excimer lasers tend to be composed of many longitudinal modes and have considerable linewidth, for example. Injection locking has been used to significantly reduce the linewidth of the slave laser and force it to operate on only a few longitudinal modes. Additionally, by narrowing the spectrum, the power in the oscillating modes may increase significantly, as the gain is used by a narrower portion of the spectrum. Injection locking can be used to control the spatial properties of the output beams. The transverse modes and electric field polarizations of the slave laser output can be fixed by the injected fields, as well as the degree of output beam divergence. The master oscillator can thus control many of the temporal, spectral, and spatial properties of the slave laser.

This research effort is a theoretical analysis of injected lasers. Many theoretical studies have been performed in the past, but all suffer from one or more limitations. This project has been aimed at loosening some of the constraints of the previous works. The effort is composed of two parts. The first consists of developing a semiclassical theory of a laser with a general resonator and an arbitrary outcoupling. Most semiclassical theories assume small outcouplings from the laser; hence the fields are modeled as planar standing waves with amplitudes that do not vary spatially. This constraint is loosened by allowing the fields in the laser to be traveling waves with arbitrarily varying amplitudes. The resultant theory may be applied to free-running as well as injected lasers. In the second part of the research, the new semiclassical theory is applied to the injection locking problem. The injected field is modeled as a boundary condition. The effects of the injected field on the slave laser field are then explored. Of primary interest are the locking ranges and threshold injected intensities as functions of the outcoupling of the slave laser and the detuning of the injected signal from the

free-running slave laser fields. The assumptions and limitations of the research are discussed more fully later in this chapter.

Background

Injection locking of lasers is merely a specific case of the general locking phenomenon. Locking has been observed in a host of disciplines, including mechanics, electrical engineering, economics, and sociology (106). Perhaps the earliest recorded observation of locking was made by Christiaan Huygens, when he wrote in 1665:

> Being obliged to stay in my room for several days and also occupied in making observations on my two newly made clocks, I have noticed a remarkable effect which no one could have ever thought of. It is that these two clocks hanging next to one another separated by one or two feet keep an agreement so exact that the pendulums invariably oscillate together without variation. After admiring this for a while, I finally figured out that it occurs through a kind of sympathy: mixing up the swings of the pendulums, I have found that within a half hour they always return to consonance and remain so constantly afterwards as long as I let them go. I then separated them, hanging one at the end of the room and the other fifteen feet away, and noticed that in a day there was five seconds difference between them. Consequently, their earlier agreement must in my opinion have been caused by an imperceptible agitation of the air produced by the motion of the pendulums. The clocks are always shut in their boxes, each weighing a total of less than 100 pounds. When in consonance, the pendulums do not oscillate parallel to one another, but instead they approach and separate in opposite directions.

Huygens later deduced that the coupling was not caused by vibrations in the air, but rather by vibrations transmitted through the wall (106:52).

The coupling of two triode oscillators was discussed by Balth Van der Pol in 1920 (107). He analyzed a double tank circuit, and noted that cross coupling and cross saturation effects took place between the oscillating modes. He also examined a triode oscillator with a nonresonant sinusoidal forcing function. Under certain conditions, the signal from the oscillator would lock in frequency to the forcing function. He termed this "automatic synchronization". Robert Adler extended this work in 1946 with an analysis of tuned electronic oscillator circuits (108). He observed that the oscillator would lock to an impressed signal if the amplitude of the signal was above some threshold value. He was able to derive an expression for the threshold amplitude of the impressed signal. The threshold

depended upon the circuit design and component values. Additionally, he related the electronic locking phenomenon to a simple mechanical analogy.

Since the advent of the laser in 1960, many theoretical and experimental studies of injection locking have taken place. The earliest experimental study of injection locking was performed by Stover and Steier in 1966 (71). They coupled two HeNe lasers together, and observed that the locking thresholds and ranges qualitatively fit Adler's theory. Since that time, other experimental studies have been performed, using lasers with frequencies ranging from the far infrared to the ultraviolet. The experiments have verified that injection of radiation into the slave oscillator can force phase and frequency locking, single longitudinal mode selection, and spectral narrowing. Injection locked lasers are now commercially available, with improved output characteristics over the corresponding free-running lasers.

The theoretical studies have generally utilized one of two different analytic methods. The first employs the rate equations of the various atomic levels. Injection is modeled as a boundary condition. This technique may be extended to the steady-state, using the simple saturable gain model. The second method makes use of the semiclassical theory. The injected field is modeled as an additional source term in the wave equation.

The rate equation approach uses the gain medium rate equations to model the interaction between the electric fields and the medium, and incorporates the injected field via a boundary condition (87, 88, 90, 92, 95, 99). The analysis of a laser medium using the rate equations is well-developed (109–125). An energy level diagram of a typical lasing species is depicted in Figure 1.3. From this diagram, the rate equations may be written as:

$$\frac{dN_2}{dt} = R_2 - \left(\frac{1}{t_{sp}} + \frac{1}{t_{nr}} + \frac{1}{t_{20}}\right) N_2 - \left(N_2 - \frac{g_2}{g_1} N_1\right) B(\nu)\phi \tag{1.1a}$$

$$\frac{dN_1}{dt} = R_1 + \left(\frac{1}{t_{sp}} + \frac{1}{t_{nr}}\right) N_2 - \frac{N_1}{t_{10}} + \left(N_2 - \frac{g_2}{g_1} N_1\right) B(\nu)\phi \tag{1.1b}$$

$$\frac{d\phi}{dt} = \left(N_2 - \frac{g_2}{g_1} N_1\right) B(\nu)\phi - \frac{\phi}{t_c} \tag{1.1c}$$

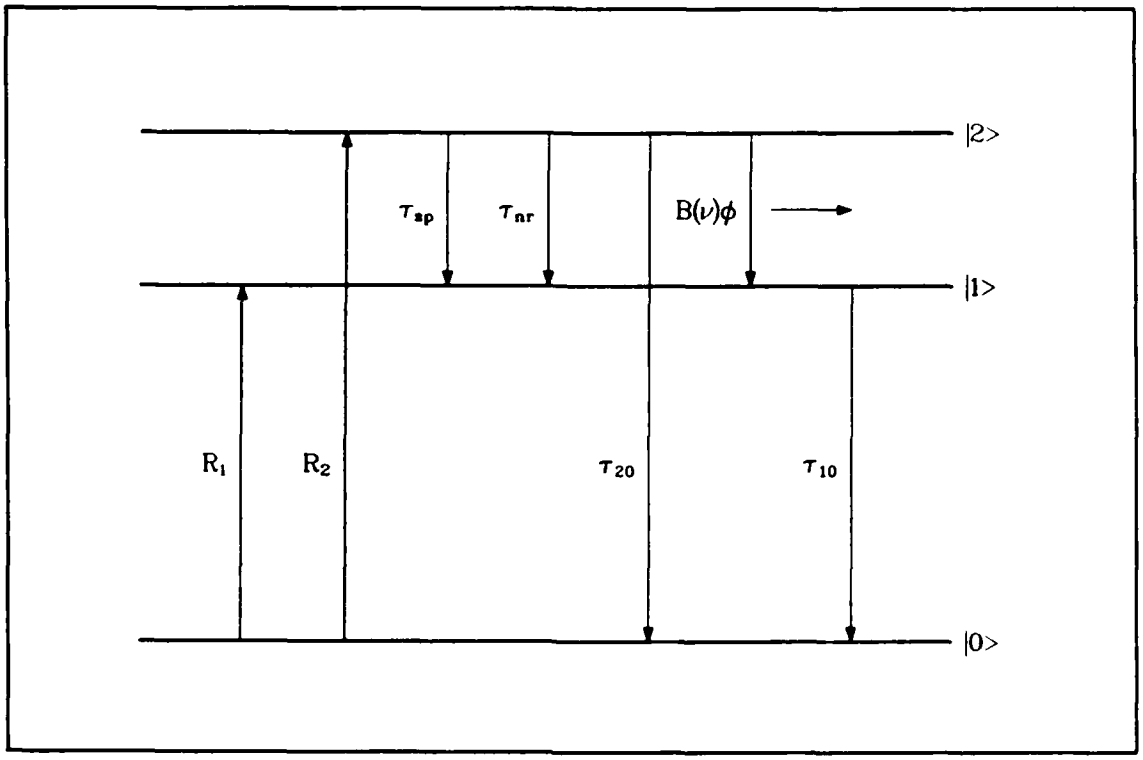

Figure 1.3. *Energy level diagram of a typical lasing atom.*

where N_i is the population density of the i^{th} level, ϕ is the photon flux density, R_i is the pumping rate to the i^{th} level, $B(\nu)$ is the stimulated emission coefficient as a function of frequency ν, g_i is the degeneracy of the i^{th} level, t_{sp} is the spontaneous decay rate, t_{nr} is the decay rate due to nonradiative processes, t_{ij} are the decay rates from level i to level j, and t_c is the photon lifetime. These equations can be expanded to include the effects of spatially dependent fields, amplified spontaneous emission, multiple longitudinal modes, additional atomic levels, etc.

Injection is incorporated into the rate equations via the boundary conditions at one of the mirrors. This is depicted in Figure 1.4, where the injection takes place at mirror B. The boundary conditions at mirror B can be expressed as:

$$I_L = \begin{cases} RI_R & \text{without injection} \\ RI_R + (1 - R - A)I_{IN} & \text{with injection} \end{cases} \tag{1.2}$$

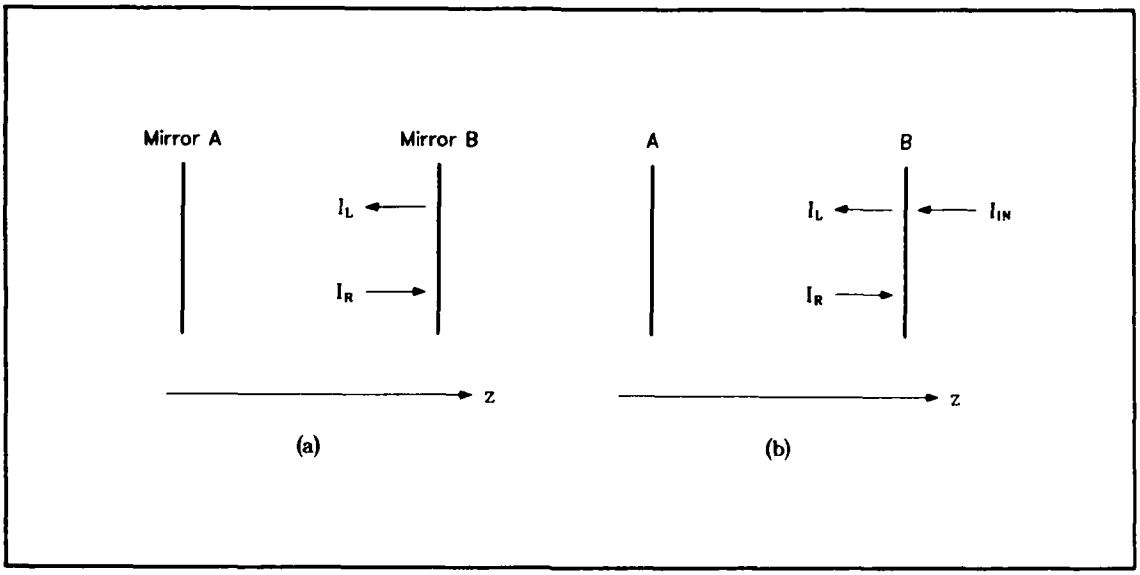

Figure 1.4. Fields at the injection mirror. (a) Without injection, (b) with injection.

where I_R and I_L are the intensities of the rightward and leftward traveling waves, I_{IN} is the intensity of the injected field, R is the intensity reflection coefficient of the mirror, and A is the absorption coefficient of the mirror.

A steady-state version of the rate equation approach is very simply developed, following the methods of Rigrod (121–123), Chernin (112), and Moore and McCarthy (119). At steady-state, the rate equations yield the following intensity equations along the optical axis z of the resonator:

$$\frac{dI_R}{dz} = (G_0 - \alpha_0)\, I_R \tag{1.3a}$$

$$\frac{dI_L}{dz} = -(G_0 - \alpha_0)\, I_L \tag{1.3b}$$

$$G_0 = \frac{g_0}{1 + \left(\frac{I_R + I_L}{I_{sat}}\right)} \tag{1.3c}$$

where g_0 is the small signal gain, α_0 is the nonsaturable loss of the medium, L is the length of the medium, z is the axial position in the resonator, and I_{sat} is the saturation intensity. g_0 and I_{sat} are obtained from the rate equations at steady-state. Eq (1.3) is the differential form of Beer's law,

and is alternately known as the simple saturable gain or g_0–I_{sat} model. The injected signal is again incorporated as a boundary condition. The equations can be solved by the methods of Moore and McCarthy.

There are several inherent problems with using the gain medium rate equations to model the injection process. The equations are based upon the intensities of the fields inside the laser. As such, no phase or frequency information is contained in the equations. Medium pushing and pulling effects are not modeled, so the actual oscillation frequency cannot be determined. Beating between the injected signal and the normal laser modes in the absence of locking will not appear in this formalism. Variations in the frequency of the output beam from the slave laser during the onset of locking will not be seen. Spatial hole burning effects due to the interference of the two traveling waves are not accounted for in the model. Despite these problems, the model can show the temporal changes in the mode intensities and competition for the gain by the various modes in the presence of an injected field. Temporally resolved spectra and some transient phenomena during the onset of locking can also be calculated with this method.

A more sophisticated treatment of the the injection locking problem uses the semiclassical theory (82, 83, 91, 100, 101). This theory models the lasing species quantum-mechanically and the electric fields classically. Generally, the fields in the laser are expanded as a series of plane, standing waves. The theory correctly accounts for frequency, phase, and spatial hole burning effects. In this sense, it more accurately models the operation of the laser. The injected signal is incorporated as an additional source term in the wave equation. This forces the injected field to be distributed throughout the laser, thus affecting all parts of the gain medium. In this manner, injection is modeled as a distributed process rather than as a boundary condition. Two of the prominent semiclassical theories of injection locking were developed by Spencer and Lamb (101) and Chow (82, 83). As these theories are discussed in detail in later chapters, the semiclassical equations will not be presented here.

The previous semiclassical theories of injection locking suffer from several main drawbacks. First, the injected field is distributed throughout the gain medium. This is only an approximation to the more accurate picture in which the injected field is incorporated in one of the mirror boundary conditions. Second, the use of uniform amplitude standing wave fields forces the outcouplings to be very small. As is shown in a later chapter, the standing wave theories break down for outcouplings of 10% or more. Nonetheless, these theories have been applied to lasers with very large outcouplings. Finally, the fields are modeled as plane waves. This precludes accurately applying the semiclassical model to arbitrary stable or unstable resonators, in which the fields are generally spherical or cylindrical waves.

Research Scope

The discussion above underscores the problems with the previous theoretical analyses of injected lasers. The purpose of the present research is to attempt to correct some of the deficiencies of the other works. This is accomplished by relaxing some of the constraints imposed in the other works. The extent, limitations, and some of the important assumptions of the current work are discussed in this section.

The first half of this project is the development of a semiclassical laser theory applicable to lasers with arbitrary outcoupling fractions. This is accomplished by decomposing the fields inside the laser into counterpropagating traveling waves, instead of the usual standing waves. Furthermore, the amplitudes and phases of the waves are allowed to vary slowly in time and space. From previous theoretical works (121–123), it is known that the amplitudes of the fields inside a general laser will vary spatially along the optic axis. The spatial variation of the waves is thus the key to modeling arbitrary outcouplings. Unlike the usual semiclassical theories, the traveling waves are allowed to be planar, cylindrical, or spherical. Consequently, unstable resonators as well as general stable resonators can be modeled with this theory, instead of just plane-parallel mirror cavities (Fabry-Perot interferometers). The theory is compared to the simple saturable gain model, the theory of Agrawal and Lax (142, 143), the Lamb semiclassical theory (134, 135), the theory of Spencer and

Lamb (101), Chow's model of the injected laser (82, 83), and Ferguson's injected laser model (87, 88). In the appropriate limits, the new theory is shown to reduce to all of these models.

Several simplifying assumptions are placed on the semiclassical model. First, the lasing atoms or molecules are assumed to be stationary. This forces the predominate broadening mechanism to be homogeneous. Second, the lasing species are modeled as two-level atoms. This is a typical assumption of the semiclassical theories. Third, only a single longitudinal mode is allowed to exist under the gain curve. This assumption is not unrealistic in homogeneously broadened lasers. If sufficient gain exists between the spatial holes burned in the medium by one mode, other longitudinal modes may oscillate. However, the usual situation is that only a single mode is above threshold, so the laser operates on only that mode. Fourth, the amplitudes and phases of the electric fields and the induced medium polarizations vary slowly in both space and time. The slow spatial variations can be justified by examining the works of Rigrod (121–123), Moore and McCarthy (119), and Agrawal and Lax (142, 143). The temporal variations are typically assumed to be slow in semiclassical theory. Finally, the modes are assumed to be the geometrical modes of the resonator. No transverse diffractive structure or higher order transverse modes are modeled. Again, the usual semiclassical approach ignores such transverse field variations.

The semiclassical equations of motion are derived via two methods. The first approach develops the Maxwell-Bloch equations for the medium polarizations, population inversion density, and electric field amplitudes and phases. Unfortunately, this set of equations is too complex to be solved numerically. Consequently, the equations of motion of the electric field are derived in the rate equation approximation (REA). Although also complicated, this set of spatially and temporally varying equations can be solved on a computer. The REA equations are easily solved numerically at steady-state. All of the numerical calculations performed as part of this research utilize the laser equations in the rate equation approximation.

The study of injected lasers comprises the second half of this research. As a wide variety of laser resonators exist, only two simple types of cavities are chosen for study: the Fabry-Perot plane-parallel

resonator, and the positive branch, confocal unstable resonator (PBCUR). The injected signal is incorporated as a boundary condition in both cases. The injected signal is assumed to have a fixed amplitude, phase, and frequency. This assumption does not affect the semiclassical theory discussed above; it affects only the numerical calculations through the boundary conditions. Although there are important cases in which the injected signal has a time-varying amplitude (such as in the locking of pulsed devices), these cases are not examined in this study. Finally, the parameter space examined allows for variable outcoupling from the slave laser and variable detunings of the injected signal from the free-running slave laser field. The locking ranges, threshold injected intensities, internal slave laser field intensities, and output powers are examined as functions of the slave laser outcoupling and injected field detuning.

Organization

The semiclassical theory of a laser with a general resonator is developed in detail in Chapter II. The theory is specialized to a laser with a Fabry-Perot resonator in Chapter III. Both the Maxwell-Bloch equations and the equations of motion in the REA are presented. The steady-state equations are developed, and the boundary conditions are given. Comparisons of the Fabry-Perot laser theory to alternate models of lasers with stable resonators are made in Chapter IV. The semiclassical theory of the PBCUR laser is developed in Chapter V. The Maxwell-Bloch equations and the equations of motion in the REA are presented, along with the steady-state theory and the appropriate boundary conditions. The PBCUR laser theory is compared to other models in Chapter VI. The numerical studies of the Fabry-Perot laser are discussed in Chapter VII. Included are studies of free-running and injected lasers, and comparisons of these results to the works of others. Chapter VIII examines the results of the numerical studies of the PBCUR laser. Again, both free-running and injected lasers are examined, and the results are compared to those in the literature where possible. The research is summarized in Chapter IX. Design criteria and recommendations for future studies are also presented in this chapter.

II. Semiclassical Theory of a Laser with a General Resonator

The semiclassical theory of the laser has existed for well over twenty years, since Lamb produced his pioneering work in 1964 (134). Since that time, the theory has been extended to include high intensity lasers, multimode lasers, traveling wave ring lasers, and laser amplifiers. Both homogeneous and inhomogeneous broadening mechanisms have been incorporated into the theory. However, with the exception of the amplifier theories, the models all assume that the outcoupling losses of the lasers are low, and thus do not allow the electric fields to vary spatially. The amplifier theories utilize plane, traveling waves that vary spatially. The amplifier models are single pass, so the internal fields are unidirectional. Unfortunately, none of these theories can be adequately applied to the case of a laser with a general stable or unstable resonator and high outcoupling losses. For these reasons, a modified version of the semiclassical theory was required for this research.

The semiclassical equations of motion of the complex electric fields inside a generalized, loaded laser resonator are derived in this chapter. From this case, the specific Fabry-Perot and positive branch, confocal unstable resonator (PBCUR) equation sets can be obtained. These cases are discussed more fully in Chapters III and V.

This chapter is designed to be tutorial in nature. For this reason, some of the material presented exists elsewhere in the literature (106, 126–141). This material is included for completeness, however.

This chapter is composed of eight sections. The first section discusses the philosophy of the semiclassical model of the laser. Next, the "general laser resonator" and other key definitions are presented. The population density matrix equations of motion are derived in the third section. The derivation of the Bloch equations follows. In the fifth section, the equations of motion of the electric fields are developed. The results of the fourth and fifth sections can be combined to yield the complete set of Maxwell-Bloch laser equations. This set of equations is normalized in the sixth section. The laser equations are next derived in the rate equation approximation. The important formulæ are summarized in the final section.

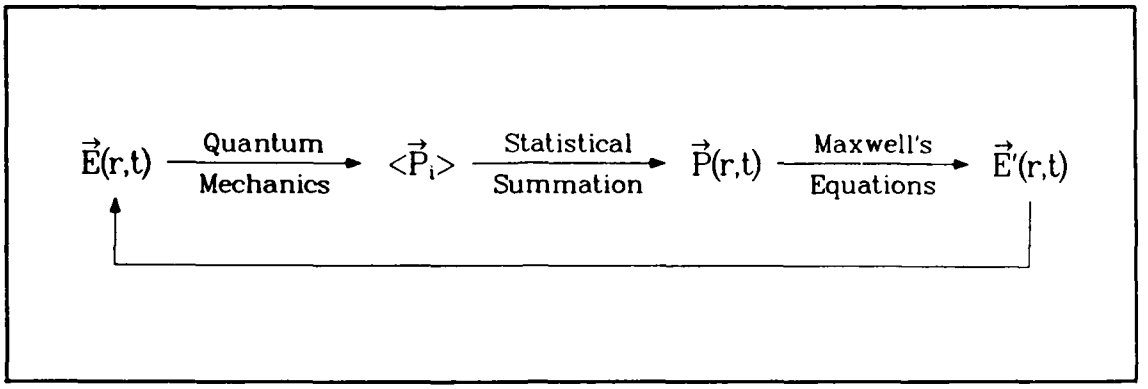

Figure 2.1. The self-consistent approach of the semiclassical theory. Adapted from (135:78).

The Semiclassical Laser Model

The semiclassical theory of the laser is a self-consistent model in which the electric fields are treated classically and the active lasing species are modeled quantum-mechanically. This is illustrated in Figure 2.1. The lasing species may be atoms or molecules; however, the species will simply be referred to as "atoms." The electric field $\vec{\mathbf{E}}(\vec{\mathbf{r}}, t)$ is first applied to a single atom, inducing a polarization $\langle\vec{\mathbf{P}}_i\rangle$ in the atom. A laser is composed of many such atoms, each of which interacts with the applied electric field. A statistical summation of the individual polarizations is performed, yielding an overall polarization $\vec{\mathbf{P}}(\vec{\mathbf{r}}, t)$ of the gain medium. This polarization is a driving term in Maxwell's equations, producing a reaction field $\vec{\mathbf{E}}'(\vec{\mathbf{r}}, t)$. When the reaction field is exactly the same as the initially applied field, the model becomes self-consistent. The fields and induced polarizations are then known.

For most laser devices, a semiclassical treatment is adequate. One might argue that the electric fields should be quantized as well as the atoms in order to properly treat the problem. In most lasers, however, the electric fields are quite intense, with very large photon numbers. By the correspondence principle of quantum mechanics, the quantized electric fields are more than adequately modeled by classical fields. Unless the laser is operating very close to threshold, the photon numbers are usually large enough to justify the use of classical fields.

The semiclassical theory can be applied to all laser problems that do not inherently depend upon the quantized nature of the electric fields. The temporal behavior and steady-state values of the laser electric fields, output powers, extraction efficiencies, and chaotic behavior are several examples of problems that have been successfully treated with the semiclassical theory. Problems dealing with photon statistics, threshold behavior, quantum fluctuations, noise, and spontaneous emission depend upon the quantized nature of the electric fields, and must be treated with a fully quantized (quantum-electrodynamic or QED) theory.

The General Laser Schematic

The general laser is pictured schematically in Figure 2.2. The resonator consists of two opposite mirrors of arbitrary radii of curvature with optic axis z. The mirrors have complex transmission and reflection coefficients given by:

$$\text{Mirror A:} \quad \begin{cases} \mathbf{r}_A = r_A e^{i\phi_{RA}} \\ \mathbf{t}_A = t_A e^{i\phi_{TA}} \end{cases} \tag{2.1a, b}$$

$$\text{Mirror B:} \quad \begin{cases} \mathbf{r}_B = r_B e^{i\phi_{RB}} \\ \mathbf{t}_B = t_B e^{i\phi_{TB}} \end{cases} \tag{2.1c, d}$$

As the resonator is of arbitrary design, outcoupling can be accomplished via mirror transmission and/or diffractive field spilling about either mirror. An active laser medium lies between the mirrors. The longitudinal extent of the medium is unimportant in the following derivations. The medium extends sufficiently in the transverse directions so that the resonator modes are not apertured by the gain cell boundaries.

The fields inside the resonator are depicted in Figure 2.3. The fields are generally two counter-propagating spherical or cylindrical traveling waves. As special cases, one or both of the waves may be planar, yielding the PBCUR and Fabry-Perot resonator cases, respectively. The fields emanate from focal points F_R and F_L on the z axis. The rightward and leftward traveling waves are given

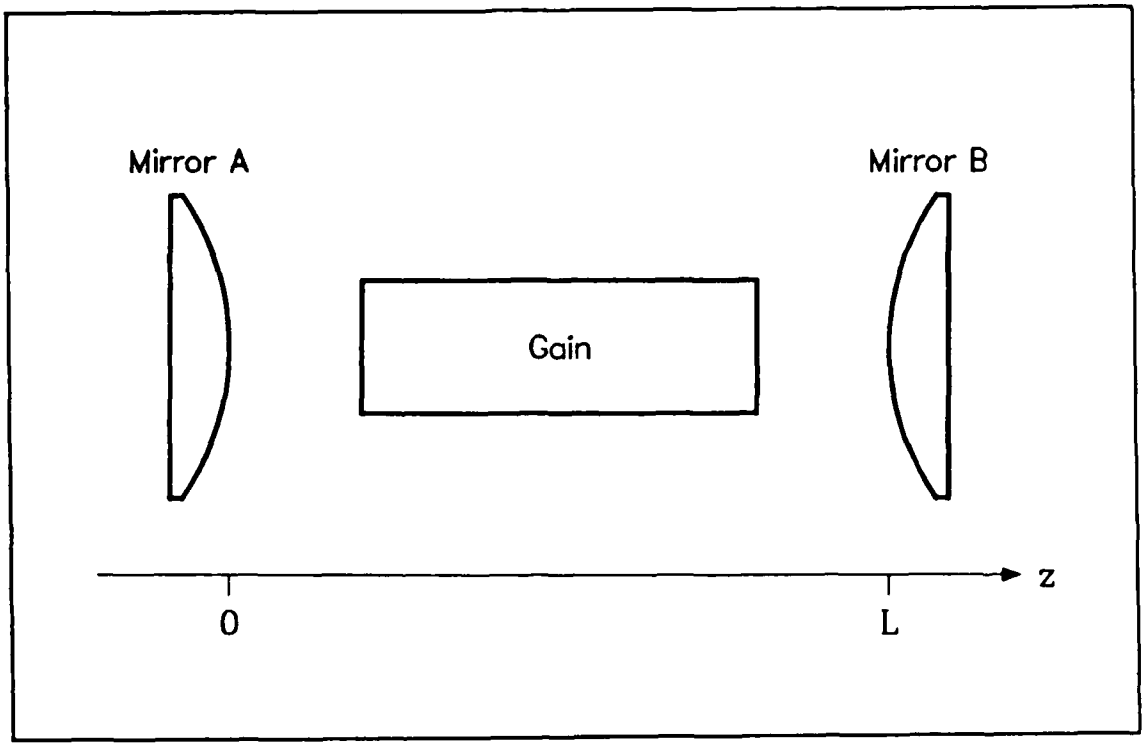

Figure 2.2. The general laser device.

by, respectively:

$$\mathbf{E}_R(z,t) = \frac{1}{2}\left\{\frac{1}{\rho_R^\alpha}E_R(z,t)\exp\left\{-i\left[\nu_I t - k\rho_R + \phi_R(z,t)\right]\right\} + \text{c.c.}\right\} \tag{2.2a}$$

$$\mathbf{E}_L(z,t) = \frac{1}{2}\left\{\frac{1}{\rho_L^\alpha}E_L(z,t)\exp\left\{-i\left[\nu_I t - k\rho_L + \phi_L(z,t)\right]\right\} + \text{c.c.}\right\} \tag{2.2b}$$

$$\alpha \equiv \begin{cases} \frac{1}{2}, & \text{cylindrical wave} \\ 1, & \text{spherical wave} \end{cases} \tag{2.3}$$

$$\rho_R \approx z + l_R \tag{2.4a}$$

$$\rho_L \approx L + l_L - z \tag{2.4b}$$

Here, $\rho_{R,L}$ are the radial distances from the focii $\mathrm{F_{R,L}}$, $E_{R,L}(z,t)$ are the field amplitudes, k is the wavenumber, and $\phi_{R,L}$ are the phases of the electric fields. ν_I is a reference frequency; when the laser has an injected signal, ν_I is the frequency of the injected field. Notice that $\nu_I + \dot{\phi}_R$

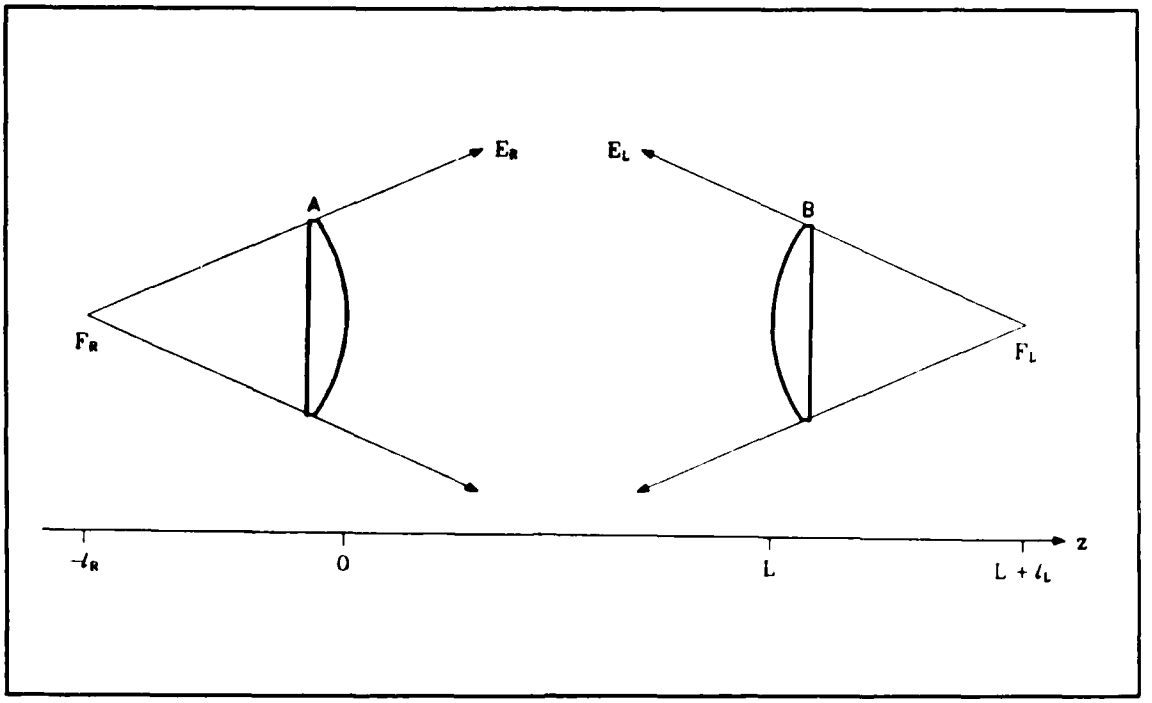

Figure 2.3. The general resonator fields. Adapted from (158:279).

and $\nu_I + \dot{\phi}_L$ are the instantaneous frequencies of $\mathbf{E}_R(z,t)$ and $\mathbf{E}_L(z,t)$, respectively. E_R, E_L, ϕ_R, and ϕ_L are real and assumed to vary slowly in time and space. α is a parameter describing the cylindrical/spherical nature of the waves. c.c. denotes the complex conjugate term. Finally, Eq (2.4) confines the ensuing derivations to the paraxial region.

The total electric field $\mathbf{E}(z,t)$ is given by the sum of the left and right traveling waves:

$$\mathbf{E}(z,t) = \mathbf{E}_R(z,t) + \mathbf{E}_L(z,t) \tag{2.5}$$

In a like manner, the total polarization $\mathbf{P}(z,t)$ is defined as the sum of two traveling wave parts:

$$\begin{aligned}\mathbf{P}(z,t) &= \mathbf{P}_R(z,t) + \mathbf{P}_L(z,t) \\ &= \frac{1}{2}\Big\{ P_R(z,t)\exp\left\{-i\left[\nu_I t - kz + \phi_R(z,t)\right]\right\} \\ &\quad + P_L(z,t)\exp\left\{-i\left[\nu_I t + kz + \phi_L(z,t)\right]\right\} + \text{c.c.}\Big\}\end{aligned}$$

$$= \frac{1}{2}\Big\{ P'_R(z,t)\exp\left\{-i\left[\nu_I t + \phi_R(z,t)\right]\right\}$$

$$+ P'_L(z,t)\exp\left\{-i\left[\nu_I t + \phi_L(z,t)\right]\right\} + \text{c.c.}\Big\} \tag{2.6}$$

P_R, P_L, P'_R, and P'_L are generally complex quantities. $P_{R,L}$ are slowly varying in both space and time, whereas $P'_{R,L}$ vary slowly in time only. Nothing is explicitly stated in Eq (2.6) about a spherical/cylindrical/planar nature of the polarization waves.

The Density Matrix Equations of Motion

The density matrix equations of motion are derived in this section. Although this material can be found elsewhere, it is included here for completeness.

The derivation commences with a general two-level atom, depicted in Figure 2.4. The eigenstates are $|a\rangle$ and $|b\rangle$, with energies $E_a = \hbar\omega_a$ and $E_b = \hbar\omega_b$, respectively. When the system transitions from $|a\rangle$ to $|b\rangle$, a photon of energy $\hbar\omega = E_a - E_b$ may be emitted. ω is the linecenter frequency of the atomic transition, and $\hbar$ is Planck's constant.

The atomic Hamiltonian is given by:

$$H_{atom} = -\frac{\hbar^2}{2m}\nabla^2 + V_{atom}(\vec{\mathbf{r}}) \tag{2.7}$$

A complete, orthonormal set of stationary states $\psi_a(\vec{\mathbf{r}})$, with energies E_a, is assumed to exist. With a phenomenologically introduced radiative damping term (106:82), the eigenstates are given by:

$$\Psi_a(\vec{\mathbf{r}},t) = e^{-\gamma_a t/2}e^{-iE_a t/\hbar}\psi_a(\vec{\mathbf{r}}) \tag{2.8}$$

γ_a is the mean lifetime of the state, as:

$$|\Psi_a|^2 = e^{-\gamma_a t}\,|\psi_a|^2 \tag{2.9}$$

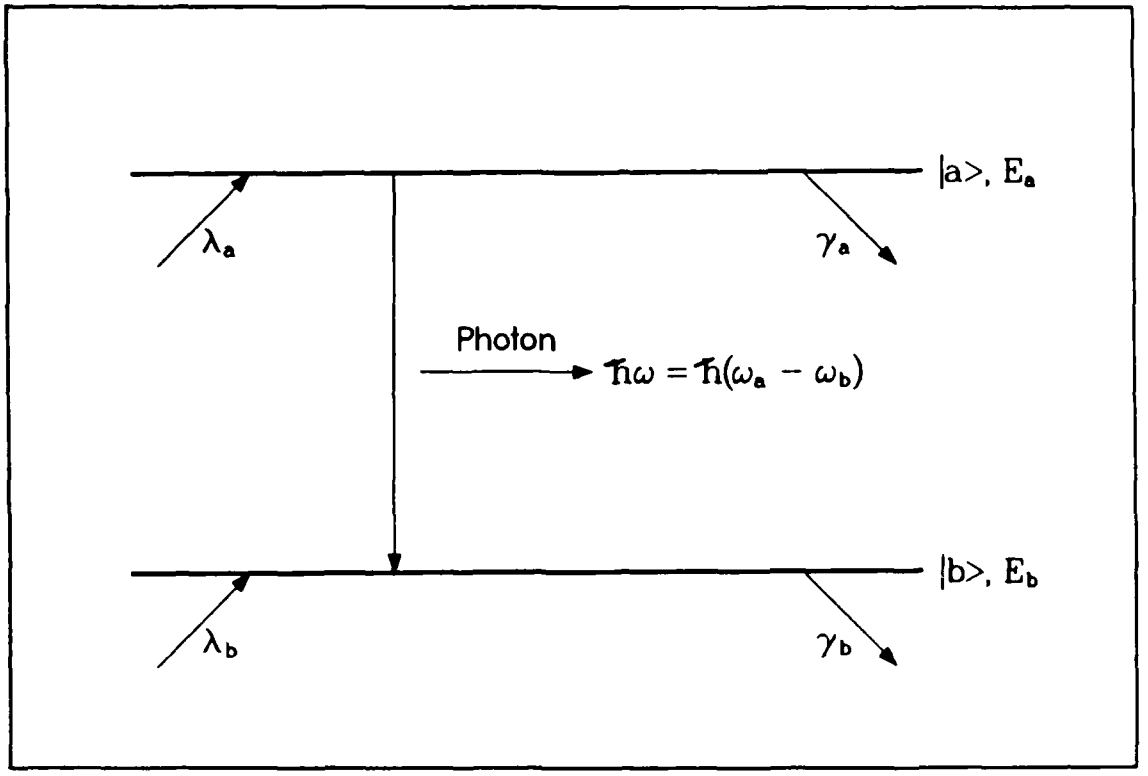

Figure 2.4. The two-level atomic system.

A small perturbing Hamiltonian V is applied to the atom, so that the total Hamiltonian H is given by:

$$H = H_{\text{atom}} + V \tag{2.10}$$

The perturbation of interest is an electric field, so the electric dipole interactions will be important. V is of the form:

$$V \equiv -\mathbf{e}\vec{\mathbf{r}} \cdot \vec{\mathbf{e}}\,\mathbf{E}(\vec{\mathbf{r}}, t) \tag{2.11}$$

where $\vec{\mathbf{e}}$ is the unit vector in the direction of the electric field, and e is the electron charge. The wavelengths of the electric fields of interest are much greater than the atomic system size, so the electric field can be regarded as spatially constant over the atomic volume. This is known as the "dipole approximation."

The perturbation will cause a mixing of atomic states, so that:

$$\Psi(\vec{\mathbf{r}},t) = a(t)\psi_a(\vec{\mathbf{r}}) + b(t)\psi_b(\vec{\mathbf{r}}) \tag{2.12}$$

where $a(t)$ and $b(t)$ are time-dependent coefficients. Following time-dependent perturbation theory, the equations of motion of $a(t)$ and $b(t)$ are:

$$i\hbar\dot{a} = a\hbar\omega_a + a\langle a|V|a\rangle + b\langle a|V|b\rangle \tag{2.13a}$$

$$i\hbar\dot{b} = b\hbar\omega_b + a\langle b|V|a\rangle + b\langle b|V|b\rangle \tag{2.13b}$$

Assuming that the atom has no static dipole moment, the integrations become:

$$\langle a|V|a\rangle = 0 \tag{2.14a}$$

$$\begin{aligned}\langle a|V|b\rangle &= -e\mathbf{E}\langle a|\vec{\mathbf{r}}\cdot\vec{\mathbf{e}}|b\rangle \\ &= -\mu\mathbf{E}\end{aligned} \tag{2.14b}$$

$$\begin{aligned}\langle b|V|a\rangle &= -e\mathbf{E}\langle b|\vec{\mathbf{r}}\cdot\vec{\mathbf{e}}|a\rangle \\ &= -\mu\mathbf{E}\end{aligned} \tag{2.14c}$$

$$\langle b|V|b\rangle = 0 \tag{2.14d}$$

where μ is the dipole moment matrix element. Suppressing the $\hbar$ terms and using Eq (2.14) in Eq (2.13) yields:

$$i\dot{a} = a\omega_a - \frac{\mu b}{\hbar}\mathbf{E} \tag{2.15a}$$

$$i\dot{b} = b\omega_b - \frac{\mu a}{\hbar}\mathbf{E} \tag{2.15b}$$

The effects of the damping terms remain to be included. With the decay introduced, Eq (2.15) becomes:

$$i\dot{a} = a\omega_a - \frac{\mu b}{\hbar}\mathbf{E} - i\frac{\gamma_a}{2}a \tag{2.16a}$$

$$i\dot{b} = b\omega_b - \frac{\mu a}{\hbar}\mathbf{E} - i\frac{\gamma_b}{2}b \tag{2.16b}$$

The dipole moment of the atom is given by:

$$\mathbf{e}\langle x \rangle = \mathbf{e} \int_{atom} (a\psi_a + b\psi_b)^* \, x \, (a\psi_a + b\psi_b) \, dx$$

$$= \mu (a^* b + b^* a) \tag{2.17}$$

The bilinear functions a^*b and b^*a are thus two quantities of importance. Further, a^*a and b^*b are the occupation probabilities of the upper and lower atomic states. This suggests using the density matrix formalism to determine the coefficients a and b, instead of solving Eq (2.16) directly. The density matrix ρ for a single atom is defined as:

$$\rho \equiv \begin{pmatrix} a^*a & b^*a \\ a^*b & b^*b \end{pmatrix} = \begin{pmatrix} \rho_{aa} & \rho_{ab} \\ \rho_{ba} & \rho_{bb} \end{pmatrix} \tag{2.18}$$

By further defining a "Hamiltonian matrix" $\mathfrak{H}$ and a "loss matrix" Γ,

$$\mathfrak{H} \equiv \begin{pmatrix} \omega_a & V/\hbar \\ V/\hbar & \omega_b \end{pmatrix} \tag{2.19a}$$

$$\Gamma \equiv \begin{pmatrix} \gamma_a & 0 \\ 0 & \gamma_b \end{pmatrix} \tag{2.19b}$$

Eq (2.16) can be recast as:

$$i\frac{d\rho}{dt} = \mathfrak{H}\rho - \rho\mathfrak{H} - \frac{i}{2}\left(\Gamma\rho + \rho\Gamma\right) \tag{2.20}$$

Eq (2.20) is the equation of motion of the density matrix of a single atom, with a phenomenologically introduced radiative damping term. However, the collection of atoms that forms the gain medium is of primary importance. Furthermore, the macroscopic polarization of the medium remains to be calculated. A statistical summation of the microscopic atomic polarizations is required.

The derivation requires several additional approximations. First, the atoms are assumed to be stationary. This causes the primary broadening mechanism to be homogeneous. The Hamiltonian matrix $\mathfrak{H}$ is assumed to be independent of time. Finally, some individual atom of interest is allowed to exist in a known eigenstate at an initial time t_0, represented by:

$$\rho(a) = \begin{pmatrix} 1 & 0 \\ 0 & 0 \end{pmatrix} \tag{2.21a}$$

or

$$\rho(b) = \begin{pmatrix} 0 & 0 \\ 0 & 1 \end{pmatrix} \tag{2.21b}$$

The system is in the state $\rho(\mathrm{a})$ when the perturbation V is applied at $t = t_0$. The general solution for $t > t_0$ is denoted as $\rho(\mathrm{a}, t_0, t)$, and it must satisfy Eq (2.20) with the initial condition:

$$\rho(\mathrm{a}, t_0, t_0) = \rho(\mathrm{a}) \tag{2.22}$$

In order to determine the macroscopic average of some property F, the expectation value of the corresponding operator must be calculated:

$$\begin{aligned} \langle\langle F \rangle\rangle &= \sum_i \mathrm{tr}\, F \rho(\mathrm{a}, t_{0i}, t) \\ &= \mathrm{tr}\, F \sum_i \rho(\mathrm{a}, t_{0i}, t) \end{aligned} \tag{2.23}$$

where the summation runs over all atoms in the medium. To this end, an average or "population" density matrix is introduced:

$$\varrho(\mathrm{a}, t) \equiv \sum_i \rho(\mathrm{a}, t_{0i}, t) \tag{2.24}$$

Letting $\lambda_{\mathrm{a}}(t_0)\, dt$ be defined as the average number of atoms excited to state $|\mathrm{a}\rangle$ during the time interval $t_0 \leq t \leq t_0 + dt$, with $\lambda_{\mathrm{a}}(t)$ independent of space (spatially uniform pumping), Eq (2.24) can be written as:

$$\varrho(\mathrm{a}, t) = \int_{-\infty}^{t} dt_0\, \lambda_{\mathrm{a}}(t_0) \rho(\mathrm{a}, t_0, t) \tag{2.25}$$

Differentiating with respect to t and assuming that λ_{a} is constant in time yields:

$$\begin{aligned} i \frac{d}{dt} \varrho(\mathrm{a}, t) &= i \left\{ \lambda_{\mathrm{a}} \rho(\mathrm{a}, t, t) - \lambda_{\mathrm{a}} \rho(\mathrm{a}, -\infty, t) + \int_{-\infty}^{t} dt_0\, \lambda_{\mathrm{a}} \frac{\partial}{\partial t} \rho(\mathrm{a}, t_0, t) \right\} \\ &= i \lambda_{\mathrm{a}} \rho(\mathrm{a}) + i \int_{-\infty}^{t} dt_0\, \lambda_{\mathrm{a}} \frac{\partial}{\partial t} \rho(\mathrm{a}, t_0, t) \end{aligned} \tag{2.26}$$

Using Eq (2.20) in Eq (2.26), the equation of motion of $\varrho(\mathrm{a},t)$ becomes:

$$i\frac{d}{dt}\varrho(\mathrm{a},t) = i\lambda_a\rho(\mathrm{a}) + \bar{\mathrm{H}}\varrho(\mathrm{a},t) - \varrho(\mathrm{a},t)\bar{\mathrm{H}} - \frac{i}{2}\left(\Gamma\varrho(\mathrm{a},t) + \varrho(\mathrm{a},t)\Gamma\right)$$

Finally, defining:

$$\bar{\Lambda} \equiv \begin{pmatrix} \lambda_a & 0 \\ 0 & \lambda_b \end{pmatrix} \tag{2.27}$$

$$\varrho(t) \equiv \sum_{\mathrm{a}=a,b} \varrho(\mathrm{a},t) \tag{2.28}$$

and summing over states $|a\rangle$ and $|b\rangle$, the equation of motion for the population density matrix becomes:

$$i\frac{d}{dt}\varrho(t) = \bar{\mathrm{H}}\varrho(t) - \varrho(t)\bar{\mathrm{H}} - \frac{i}{2}\left(\Gamma\varrho(t) + \varrho(t)\Gamma\right) + i\bar{\Lambda} \tag{2.29}$$

Eq (2.29) can be broken into several physically meaningful pieces. The first two terms of the right-hand side form the equation of motion of ϱ in the Schrödinger picture without the decay or pumping terms:

$$i\frac{d}{dt}\varrho = [\bar{\mathrm{H}}, \varrho]$$

The third and fourth terms on the right-hand side of Eq (2.29) can be written as an anticommutator bracket. This bracket physically represents the exponential decay of the populations of states $|\mathrm{a}\rangle$. Finally, the last term in the equation contains the linear pumping terms to states $|\mathrm{a}\rangle$.

The Bloch Equations

The Bloch equations for the gain medium are derived in this section. Since the polarization wave is composed of rightward and leftward traveling wave parts, five Bloch equations are obtained instead of three, as in a standing wave laser. The five equations describe the temporal behaviors of the real and imaginary parts of the two polarization waves and the population inversion density.

The equations of motion of the population density matrix elements can be obtained from Eq (2.29):

$$\dot{\varrho}_{ab} = -(i\omega + \gamma)\varrho_{ab} + \frac{i}{\hbar}V\left(\varrho_{aa} - \varrho_{bb}\right) \tag{2.30a}$$

$$\dot{\varrho}_{aa} = \lambda_a - \gamma_a\varrho_{aa} - \left(\frac{i}{\hbar}V\varrho_{ba} + \text{c.c.}\right) \tag{2.30b}$$

$$\dot{\varrho}_{bb} = \lambda_b - \gamma_b\varrho_{bb} + \left(\frac{i}{\hbar}V\varrho_{ba} + \text{c.c.}\right) \tag{2.30c}$$

where

$$\gamma \equiv \gamma_{ph} + \frac{\gamma_a + \gamma_b}{2} \tag{2.31}$$

γ_{ph} is a collisional dephasing time constant (106:84-89). Although the atoms are assumed to be stationary, γ_{ph} is added to the average of the decay constants of the states $|a\rangle$. This phenomenologically accounts for collisions that occur between "real" atoms. The addition of the term broadens the atomic line somewhat. Additionally, V can be expanded as:

$$V = -\frac{\mu}{2}\left\{\frac{1}{\rho_R^a}E_R e^{ikl_R}e^{-i(\nu_1 t - kz + \phi_R)}\right.$$

$$\left. + \frac{1}{\rho_L^a}E_L e^{ik(L+l_L)}e^{-i(\nu_1 t + kz + \phi_L)} + \text{c.c.}\right\} \tag{2.32}$$

where Eqs (2.2), (2.5), and (2.11) have been used.

The macroscopic polarization is given by (see Eq (2.23)):

$$\mathbf{P}(z,t) = \mu(\varrho_{ab} + \varrho_{ba}) \tag{2.33}$$

Substituting Eq (2.6) in Eq (2.33) yields:

$$\varrho_{ab} = \frac{1}{2\mu}\left\{P_R' e^{-i(\nu_1 t + \phi_R)} + P_L' e^{-i(\nu_1 t + \phi_L)}\right\} \tag{2.34}$$

Previously, E_R, E_L, ϕ_R, ϕ_L, P_R, and P_L were assumed to vary slowly in space. The spatial variations are so slow that locally (over a few wavelengths of the radiation), these six quantities can be taken as constants. For the field amplitudes, this approximation can be justified by considering

the results of (121–123, 142, 143). Over the length of a typical resonator, the intensities of the electric fields vary by a factor of about 10. For resonator lengths on the order of a few meters and optical frequency radiation, approximately 10^6 wavelengths are required to fill the cavity. Clearly, over a few wavelengths, E_R and E_L can be taken as constants. Similar arguments can be extended for P_R, P_L, ϕ_R, and ϕ_L.

With the assumption of local constancy, Eqs (2.6), (2.33), and (2.34) can be combined as:

$$P_R(z,t)\Big|_{z=z_0} = 2\mu e^{i(\nu_I t+\phi_R)}\left(\frac{2}{\lambda}\right)\int_{z_0}^{z_0+\lambda/2}\varrho_{ab}e^{-ikz}\,dz$$

$$= \frac{2}{\lambda}\int_{z_0}^{z_0+\lambda/2}\left[P'_R + P'_L e^{-i(\phi_L-\phi_R)}\right]e^{-ikz}\,dz \qquad (2.35a)$$

where z_0 is an arbitrary position on the optic axis in the gain medium, and λ is the wavelength of the optical radiation. Similarly:

$$P_L(z,t)\Big|_{z=z_0} = \frac{2}{\lambda}\int_{z_0}^{z_0+\lambda/2}\left[P'_R e^{i(\phi_L-\phi_R)} + P'_L\right]e^{ikz}\,dz \qquad (2.35b)$$

Notice that Eq (2.35) is similar to a Fourier transform. The z variations on the left-hand sides of the equations are quite slow; in the local region $[z, z_0+\lambda/2]$ there is essentially no z variation. The integrations over z effectively remove the rapidly varying parts of P'_R and P'_L.

Using Eqs (2.32) and (2.34), Eq (2.30a) can be expressed as:

$$\frac{\partial}{\partial t}\left\{P'_R e^{-i(\nu_I t+\phi_R)} + P'_L e^{-i(\nu_I t+\phi_L)}\right\} = -(i\omega+\gamma)\left\{P'_R e^{-i(\nu_I t+\phi_R)} + P'_L e^{-i(\nu_I t+\phi_L)}\right\}$$

$$-\frac{i\mu}{\hbar}\left\{\frac{1}{\rho''_R}E_R e^{ikl_R}e^{-i(\nu_I t-kz+\phi_R)} + \frac{1}{\rho''_L}E_L e^{ik(L+l_L)}e^{-(\nu_I t+kz+\phi_L)}\right\}w \qquad (2.36)$$

where

$$w = \mu(\varrho_{aa} - \varrho_{bb}) \qquad (2.37)$$

and the rotating wave approximation has been used. w is proportional to the population inversion density.

Eq (2.36) must now be separated into two equations, one describing the time evolution of P_R and the other describing P_L. The following identity from calculus will be required:

$$\frac{d}{da}\int_p^q f(x,a)\,dx = \int_p^q \frac{\partial}{\partial a} f(x,a)\,dx + f(q,a)\frac{\partial q}{\partial a} - f(p,a)\frac{\partial p}{\partial a} \tag{2.38}$$

The equation of motion of P_R is developed first. Multiplying both sides of Eq (2.36) by $e^{-ikz}\,dz$, integrating from z_0 to $z_0 + \lambda/2$, and using Eqs (2.35) and (2.38), the equation for P_R is obtained:

$$\dot{P}_R = -\left[i(\Delta\omega - \dot{\phi}_R) + \gamma\right] P_R$$

$$- \frac{2i\mu}{\lambda\hbar}\int_{z_0}^{z_0+\lambda/2} \left\{ \frac{1}{\rho_R^a} E_R e^{ikl_R} + \frac{1}{\rho_L^a} E_L e^{ik(L+l_L)} e^{-i(\phi_L - \phi_R + 2kz)} \right\} w\,dz \tag{2.39}$$

with

$$\Delta\omega \equiv \omega - \nu_I \tag{2.40}$$

Similarly, by multiplying Eq (2.36) by $e^{ikz}\,dz$, integrating from z_0 to $z_0 + \lambda/2$, and using Eqs (2.35) and (2.38), the equation for P_L is derived:

$$\dot{P}_L = -\left[i(\Delta\omega - \dot{\phi}_L) + \gamma\right] P_L$$

$$- \frac{2i\mu}{\lambda\hbar}\int_{z_0}^{z_0+\lambda/2} \left\{ \frac{1}{\rho_R^a} E_R e^{ikl_R} e^{i(\phi_L - \phi_R + 2kz)} + \frac{1}{\rho_L^a} E_L e^{ik(L+l_L)} \right\} w\,dz \tag{2.41}$$

Since P_R and P_L are complex quantities, they can be written as:

$$P_R = u_R(z,t) - iv_R(z,t) \tag{2.42a}$$

$$P_L = u_L(z,t) - iv_L(z,t) \tag{2.42b}$$

where $u_{R,L}$ and $v_{R,L}$ are the real and imaginary parts, respectively, of $P_{R,L}$. $u_{R,L}$ and $v_{R,L}$ vary slowly in time and space, and are real quantities. Substituting Eq (2.42) into Eqs (2.39) and (2.41)

and separating the real and imaginary parts, the first four Bloch equations are obtained:

$$\dot{u}_R = -\gamma u_R - (\Delta\omega - \dot{\phi}_R)v_R + \frac{2\mu}{\lambda\hbar}\int_{z_0}^{z_0+\lambda/2}\left\{\frac{1}{\rho_R^a}E_R\sin(kl_R)\right.$$

$$\left. - \frac{1}{\rho_L^a}E_L\sin\left[\phi_L - \phi_R + 2kz - k(L - l_L)\right]\right\}w\,dz \tag{2.43a}$$

$$\dot{v}_R = (\Delta\omega - \dot{\phi}_R)u_R - \gamma v_R + \frac{2\mu}{\lambda\hbar}\int_{z_0}^{z_0+\lambda/2}\left\{\frac{1}{\rho_R^a}E_R\cos(kl_R)\right.$$

$$\left. + \frac{1}{\rho_L^a}E_L\cos\left[\phi_L - \phi_R + 2kz - k(L + l_L)\right]\right\}w\,dz \tag{2.43b}$$

$$\dot{u}_L = -\gamma u_L - (\Delta\omega - \dot{\phi}_L)v_L + \frac{2\mu}{\lambda\hbar}\int_{z_0}^{z_0+\lambda/2}\left\{\frac{1}{\rho_R^a}E_R\sin(\phi_L - \phi_R + 2kz + kl_R)\right.$$

$$\left. + \frac{1}{\rho_L^a}E_L\sin\left[k(L + l_L)\right]\right\}w\,dz \tag{2.43c}$$

$$\dot{v}_L = (\Delta\omega - \dot{\phi}_L)u_L - \gamma v_L + \frac{2\mu}{\lambda\hbar}\int_{z_0}^{z_0+\lambda/2}\left\{\frac{1}{\rho_R^a}E_R\cos(\phi_L - \phi_R + 2kz + kl_R)\right.$$

$$\left. + \frac{1}{\rho_L^a}E_L\cos\left[k(L + l_L)\right]\right\}w\,dz \tag{2.43d}$$

Eq (2.43) describes the time behavior of the two polarization waves. The equation is dependent upon w, which does not vary slowly in space. The fifth Bloch equation describes the time evolution of w. From Eq (2.37), $\dot{w}$ is given by:

$$\dot{w} = \mu(\dot{\varrho}_{aa} - \dot{\varrho}_{bb})$$

$$= \mu(\lambda_a - \gamma_a\varrho_{aa} - \lambda_b + \gamma_b\varrho_{bb}) - 2\mu\left(\frac{i}{\hbar}V\varrho_{ba} + \text{c.c.}\right) \tag{2.44}$$

A "zero field inversion density" w_{eq} is defined as:

$$w_{eq} \equiv \mu\left[\frac{\lambda_a}{\gamma_a} - \frac{\lambda_b}{\gamma_b}\right] \tag{2.45}$$

w_{eq}/μ is the steady-state value of the population inversion density if the applied electric field **E** is zero. By further defining

$$\tau \equiv \frac{1}{2}\left(\frac{1}{\gamma_a}+\frac{1}{\gamma_b}\right) = \frac{\gamma_{ab}}{\gamma_a\gamma_b} \tag{2.46a}$$

$$\gamma_{ab} \equiv \frac{\gamma_a+\gamma_b}{2} \tag{2.46b}$$

one can write:

$$\mu(\lambda_a - \gamma_a\varrho_{aa} - \lambda_b + \gamma_b\varrho_{bb}) = -\frac{1}{\tau}(w - w_{eq}) \tag{2.47}$$

Using Eqs (2.30), (2.32), and (2.47) in Eq (2.44), the final Bloch is obtained:

$$\dot{w} = -\frac{1}{\tau}(w-w_{eq}) + \frac{\mu}{\hbar}\mathrm{Im}\left\{P'_R\left[\frac{1}{\rho_R^\alpha}E_R e^{-ik\rho_R} + \frac{1}{\rho_L^\alpha}E_L e^{i(\phi_L-\phi_R-k\rho_L)}\right]\right.$$

$$\left. + P'_L\left[\frac{1}{\rho_R^\alpha}E_R e^{-i(\phi_L-\phi_R+k\rho_R)} + \frac{1}{\rho_L^\alpha}E_L e^{-ik\rho_L}\right]\right\} \tag{2.48}$$

Eqs (2.43) and (2.48) comprise the Bloch equation set. Although rather complex, the equations can be understood if examined individually. The equations for u_R and v_R are essentially equivalent to the u_L and v_L equations. The first two terms on the right-hand side of these equations describe the coupling of the real and imaginary parts of the polarizations. The integrals contain the electric field terms that drive the polarizations. In the usual Bloch equations (see, for example, Section 7.5 of (106)), the integrations do not exist. They arise in Eq (2.43) as a result of the Fourier decompositions performed on Eq (2.36). The first term on the right-hand side of the w equation is a decay term. In the absence of the applied electric field **E**, the inversion density decays to its steady-state value $w = w_{eq}$. The coupling of **E** to the inversion density is contained in the final term of the Eq (2.48). Notice that this term depends upon $P'_{R,L}$, whereas Eqs (2.43) are the equations of motion of $P_{R,L}$. In order to solve the Bloch equations, an inverse transform pair related to Eq (2.35) is required.

The Electric Field Equations

The electric field equations of motion are obtained in this section. The derivations follow the standard approach used in semiclassical theory. The derivations culminate in four equations: an amplitude and phase equation for both $\mathbf{E}_R$ and $\mathbf{E}_L$.

The starting point for the derivation is Maxwell's equations (mks units):

$$\nabla \cdot \vec{\mathbf{D}} = 0 \tag{2.49a}$$

$$\nabla \cdot \vec{\mathbf{B}} = 0 \tag{2.49b}$$

$$\nabla \times \vec{\mathbf{E}} = -\frac{\partial}{\partial t}\vec{\mathbf{B}} \tag{2.49c}$$

$$\nabla \times \vec{\mathbf{H}} = \vec{\mathbf{J}} + \frac{\partial}{\partial t}\vec{\mathbf{D}} \tag{2.49d}$$

$$\vec{\mathbf{D}} = \epsilon_0 \vec{\mathbf{E}} + \vec{\mathbf{P}} \tag{2.49e}$$

$$\vec{\mathbf{B}} = \mu_0 \vec{\mathbf{H}} \tag{2.49f}$$

$$\vec{\mathbf{J}} = \sigma \vec{\mathbf{E}} \tag{2.49g}$$

Combining the equations and rearranging the terms yields the wave equation:

$$\nabla \times \nabla \times \vec{\mathbf{E}} + \mu_0 \sigma \frac{\partial}{\partial t}\vec{\mathbf{E}} + \mu_0 \epsilon_0 \frac{\partial^2}{\partial t^2}\vec{\mathbf{E}} = -\mu_0 \frac{\partial^2}{\partial t^2}\vec{\mathbf{P}} \tag{2.50}$$

Several simplifying approximations are in order. First, $\vec{\mathbf{E}}$ and $\vec{\mathbf{H}}$ are assumed to be linearly polarized in the $\hat{x}$ and $\hat{y}$ directions, respectively. This could be accomplished by placing Brewster windows at the ends of the gain medium, for example. Then,

$$\begin{aligned} \nabla \times \nabla \times \vec{\mathbf{E}} &= \nabla \times \nabla \times \mathbf{E}\hat{x} \\ &= \nabla(\nabla \cdot \mathbf{E}\hat{x}) - \nabla^2 \mathbf{E}\hat{x} \\ &= \frac{1}{\epsilon_0}\nabla(\nabla \cdot \mathbf{D}\hat{x} - \nabla \cdot \mathbf{P}\hat{x}) - \nabla^2 \mathbf{E}\hat{x} \\ &\approx -\nabla^2 \mathbf{E}\hat{x} \end{aligned} \tag{2.51}$$

The transverse field variations will be ignored. This can be justified over small distances (local areas), especially in low Fresnel number PBCURs or low order transverse modes of stable resonators. Confining the work to the paraxial region, Eq (2.4) can be expanded to:

$$\begin{aligned} \rho_R &\approx l_R + z & \rho_L &\approx L + l_L - z \\ \frac{\partial}{\partial x}\rho_R &= 0 & \frac{\partial}{\partial x}\rho_L &= 0 \\ \frac{\partial}{\partial y}\rho_R &= 0 & \frac{\partial}{\partial y}\rho_L &= 0 \\ \frac{\partial}{\partial z}\rho_R &= 1 & \frac{\partial}{\partial z}\rho_L &= -1 \end{aligned} \tag{2.52}$$

Consequently,

$$-\nabla^2 \mathbf{E}\hat{x} \approx -\frac{\partial^2}{\partial z^2}\mathbf{E}\hat{x} \tag{2.53}$$

Dropping the vector nature of the problem, Eq (2.50) can be written in scalar form as:

$$-\frac{\partial^2}{\partial z^2}\mathbf{E} + \mu_0\sigma\frac{\partial}{\partial t}\mathbf{E} + \mu_0\epsilon_0\frac{\partial^2}{\partial t^2}\mathbf{E} = -\mu_0\frac{\partial^2}{\partial t^2}\mathbf{P} \tag{2.54}$$

The damping term $\mu_0\sigma\frac{\partial \mathbf{E}}{\partial t}$ is retained to account for the various loss mechanisms in the medium: diffraction, scattering, absorption, etc. Unlike the standing wave theories, the damping term does not include the losses due to geometrical outcoupling or mirror transmission. These losses are accounted for in the boundary conditions of the problem. Since the fields are very highly monochromatic, the right-hand side of Eq (2.54) can be replaced with:

$$-\mu_0\frac{\partial^2}{\partial t^2}\mathbf{P} \approx \mu_0\nu^2\mathbf{P} \tag{2.55}$$

where ν is the actual laser frequency.

Utilizing Eqs (2.2), (2.5), (2.6), and (2.55) in Eq (2.54), and neglecting the small derivative terms on the order of:

$$\frac{\partial F}{\partial t} \ll \nu F$$

$$\frac{\partial F}{\partial z} \ll kF$$

$$\frac{\partial^2 F}{\partial t^2} \ll \nu \frac{\partial F}{\partial t}$$

$$\frac{\partial^2 F}{\partial z^2} \ll k \frac{\partial F}{\partial z}$$

$$\sigma \frac{\partial F}{\partial t}$$

$$F \in \{E_R, E_L, \phi_R, \phi_L, P'_R, P'_L\}$$

the wave equation becomes:

$$\left\{ -2i\Omega c \frac{\partial E_R}{\partial z} + \Omega^2 E_R - 2\Omega c E_R \frac{\partial \phi_R}{\partial z} - \frac{i\nu_I \sigma}{\epsilon_0} E_R - 2i\nu_I \frac{\partial E_R}{\partial t} \right.$$

$$\left. -(\nu_I + \dot{\phi}_R)^2 E_R \right\} \frac{1}{\rho_R^a} e^{ikl_R} e^{-i\phi_R} e^{ikz} + \left\{ 2i\Omega c \frac{\partial E_L}{\partial z} + \Omega^2 E_L \right.$$

$$\left. +2\Omega c E_L \frac{\partial \phi_L}{\partial z} - \frac{i\nu_I \sigma}{\epsilon_0} E_L - 2i\nu_I \frac{\partial E_L}{\partial t} - (\nu_I + \dot{\phi}_L)^2 E_L \right\}$$

$$\times \frac{1}{\rho_L^a} e^{ik(L+l_L)} e^{-i\phi_L} e^{-ikz} = \frac{\nu^2}{\epsilon_0} \left\{ P'_R e^{-i\phi_R} + P'_L e^{-i\phi_L} \right\} \tag{2.56}$$

where

$$\Omega \equiv \frac{k}{\sqrt{\mu_0 \epsilon_0}} \tag{2.57a}$$

$$c^2 = \frac{1}{\mu_0 \epsilon_0} \tag{2.57b}$$

Ω is the frequency of the barecavity mode. Over any interval $[z_0, z_0 + \lambda/2]$, $E_{R,L}$ and $\phi_{R,L}$, their partial derivatives with respect to space and time, and $\rho^{-a}_{R,L}$ vary so slowly that they can be approximated as constants. Multiplying Eq (2.56) by $e^{-ikz}\,dz$ and integrating from z_0 to $z_0 + \lambda/2$ gives:

$$-2i\Omega c\frac{\partial E_R}{\partial z} + \Omega^2 E_R - 2\Omega c E_R\frac{\partial \phi_R}{\partial z} - \frac{i\nu_I\sigma}{\epsilon_0}E_R - 2i\nu_I\frac{\partial E_R}{\partial t} - (\nu_I + \dot{\phi}_R)^2 E_R$$

$$= \frac{\nu^2}{\epsilon_0}\rho^a_R e^{-ikl_R}\left\{\frac{2}{\lambda}\int_{z_0}^{z_0+\lambda/2}\left[P'_R + P'_L e^{-i(\phi_L-\phi_R)}\right]e^{-ikz}\,dz\right\}$$

$$= \frac{\nu^2}{\epsilon_0}\rho^a_R e^{-ikl_R}P_R \tag{2.58}$$

Separating the real and imaginary parts of Eq (2.58) yields the first two electric field equations of motion:

$$\frac{\partial E_R}{\partial t} + c\frac{\partial E_R}{\partial z} = -\frac{\sigma}{2\epsilon_0}E_R + \frac{\nu}{2\epsilon_0}\rho^a_R\left[u_R\sin(kl_R) + v_R\cos(kl_R)\right] \tag{2.59a}$$

$$\frac{\partial \phi_R}{\partial t} + c\frac{\partial \phi_R}{\partial z} = \Omega - \nu_I - \frac{\nu}{2\epsilon_0}\frac{\rho^a_R}{E_R}\left[u_R\cos(kl_R) - v_R\sin(kl_R)\right] \tag{2.59b}$$

where

$$\frac{\Omega}{\nu_I} \approx \frac{\nu}{\nu_I} \approx 1 \tag{2.60a}$$

$$\Omega + \nu_I + \dot{\phi}_R \approx 2\nu \tag{2.60b}$$

In a similar manner, by multiplying Eq (2.56) by $e^{ikz}\,dz$, integrating from z_0 to $z_0 + \lambda/2$, and separating the real and imaginary parts of the resultant equation, the expressions for E_L and ϕ_L are obtained:

$$\frac{\partial E_L}{\partial t} - c\frac{\partial E_L}{\partial z} = -\frac{\sigma}{2\epsilon_0}E_L + \frac{\nu}{2\epsilon_0}\rho^a_L\Big\{u_L\sin\big[k(L+l_L)\big] + v_L\cos\big[k(L+l_L)\big]\Big\} \tag{2.61a}$$

$$\frac{\partial \phi_L}{\partial t} - c\frac{\partial \phi_L}{\partial z} = \Omega - \nu_I - \frac{\nu}{2\epsilon_0}\frac{\rho^a_L}{E_L}\Big\{u_L\cos\big[k(L+l_L)\big] - v_L\sin\big[k(L+l_L)\big]\Big\} \tag{2.61b}$$

Eqs (2.59) and (2.61) are the final field equations of motion. As with the Bloch equations, the two $\mathbf{E}_R$ expressions are analogous to the $\mathbf{E}_L$ expressions. The first term on the right-hand side of

each amplitude equation yields an exponential decay due to nonsaturable losses, such as medium absorption, scattering, diffraction effects, etc. The polarization drives the field amplitudes through the second term; hence, the second term is the atomic medium gain. The difference $\Omega - \nu_I$ in the phase equations is simply a frequency offset term. Notice that in the absence of a gain medium, the actual lasing frequency $\nu = \nu_I + \dot{\phi}$ is simply the barecavity mode frequency Ω. (At steady-state, $\dot{\phi}_R = \dot{\phi}_L \equiv \dot{\phi}$.) The polarization terms in the phase equations shift the actual laser frequency ν from Ω toward the linecenter frequency ω. The shift is due to the large change in the index of refraction of the medium near the linecenter. This frequency translation is commonly referred to as gain medium pushing and pulling. Finally, Eqs (2.43), (2.48), (2.59), and (2.61) form the complete Maxwell-Bloch equation set for a gain medium subjected to two counterpropagating electric fields.

The Equation Normalizations

The Maxwell-Bloch equations derived in the previous two sections are normalized below. There are four steps to the normalization process: a time normalization, a field normalization, a polarization normalization, and a series of miscellaneous normalizations. The four steps are described individually; the final equation set is then presented. The normalized variables are denoted with a "hat" accent (i.e., $\hat{E}_R$ is the normalized version of E_R).

The first normalization deals with time. Let:

$$\hat{t} \equiv \gamma t \tag{2.62a}$$

$$d\hat{t} = \gamma\, dt \tag{2.62b}$$

The time variable t is thus normalized by the inverse of the atomic linewidth. The following additional definitions are required:

$$\Delta\hat{\omega} \equiv \frac{\Delta\omega}{\gamma} \tag{2.62c}$$

$$\hat{\Omega} \equiv \frac{\Omega}{\gamma} \tag{2.62d}$$

$$\hat{\nu}_I \equiv \frac{\nu_I}{\gamma} \tag{2.62e}$$

$$\hat{\nu} \equiv \frac{\nu}{\gamma} \tag{2.62f}$$

$$\tau_{cav} \equiv \frac{2\epsilon_0}{\sigma} \tag{2.62g}$$

$$\hat{\tau}_1 \equiv \gamma\tau \tag{2.62h}$$

$$\hat{\tau}_2 \equiv \gamma\tau_{cav} \tag{2.62i}$$

All frequencies are normalized by the linewidth, and all time constants are normalized by the inverse of the linewidth. Note that τ_{cav} is not normalized; it is the lifetime of a photon in the cavity in the absence of outcoupling.

The second normalization pertains to the electric field amplitudes. First, $\rho_{R,L}$ are divided by the cavity length L:

$$\hat{\rho}_{R,L} \equiv \frac{\rho_{R,L}}{L} \tag{2.63a}$$

$\hat{\rho}_{R,L}$ are dimensionless distances. Next, $E_{R,L}$ are normalized:

$$\hat{E}_{R,L} \equiv \frac{\mu E_{R,L}}{\gamma\hbar L^a} \tag{2.63b}$$

Then,

$$\frac{\hat{E}_{R,L}}{\hat{\rho}^a_{R,L}} = \frac{\mu}{\gamma\hbar}\frac{E_{R,L}}{\rho^a_{R,L}} \tag{2.63c}$$

The polarization variables are normalized by defining:

$$\hat{F} \equiv \frac{\mu\hat{\nu}}{2\epsilon_0\gamma\hbar}F \tag{2.64a}$$

where

$$F \in \{u_R, v_R, u_L, v_L, w, w_{eq}, P'_R, P'_L\} \tag{2.64b}$$

Finally, a series of miscellaneous normalizations are performed. The spatial variable z in the electric field equations is normalized by the cavity length L:

$$\hat{z} \equiv \frac{z}{L} \tag{2.65a}$$

$$d\hat{z} \equiv \frac{dz}{L} \tag{2.65b}$$

$$\psi \equiv \frac{c}{\gamma L} \tag{2.65c}$$

ψ is the normalized speed of light. If a new angular variable θ is defined as:

$$\theta \equiv 2kz \tag{2.65d}$$

a change of variables can be performed on the integrals in the Bloch equations:

$$dz = \frac{1}{2k}\, d\theta = \frac{\lambda}{4\pi}\, d\theta \tag{2.65e}$$

$$z = z_0 \Rightarrow \theta = 2kz_0 \equiv \theta_0 \tag{2.65f}$$

$$z = z_0 + \lambda/2 \Rightarrow \theta = 2kz_0 + 2\pi = \theta_0 + 2\pi \tag{2.65g}$$

Finally, two additional angular variables $\xi_{R,L}$ are defined:

$$\xi_R \equiv kl_R \tag{2.65h}$$

$$\xi_L \equiv k(L + l_L) \tag{2.65i}$$

$\xi_{R,L}$ are merely fixed angular coordinates.

Using Eqs (2.62) through (2.65) in the Maxwell-Bloch equations results in:

$$\frac{\partial \hat{u}_R}{\partial \hat{t}} = -\hat{u}_R - \left(\Delta\hat{\omega} - \frac{\partial \phi_R}{\partial \hat{t}}\right)\hat{v}_R + \frac{1}{2\pi}\int_{\theta_0}^{\theta_0+2\pi}\left\{\frac{1}{\hat{\rho}_R''}\hat{E}_R \sin\xi_R - \frac{1}{\hat{\rho}_L''}\hat{E}_L \sin(\phi_L - \phi_R + \theta - \xi_L)\right\}\hat{w}\, d\theta \tag{2.66a}$$

$$\frac{\partial \hat{v}_R}{\partial \hat{t}} = \left(\Delta\hat{\omega} - \frac{\partial \phi_R}{\partial \hat{t}}\right)\hat{u}_R - \hat{v}_R + \frac{1}{2\pi}\int_{\theta_0}^{\theta_0+2\pi}\left\{\frac{1}{\hat{\rho}_R''}\hat{E}_R \cos\xi_R\right.$$

$$+ \frac{1}{\hat{\rho}_L^a} \hat{E}_L \cos\left(\phi_L - \phi_R + \theta - \xi_L\right) \Bigg\} \hat{w}\, d\theta \tag{2.66b}$$

$$\frac{\partial \hat{u}_L}{\partial \hat{t}} = -\hat{u}_L - \left(\Delta\hat{\omega} - \frac{\partial \phi_L}{\partial \hat{t}}\right) \hat{v}_L + \frac{1}{2\pi} \int_{\theta_0}^{\theta_0 + 2\pi} \Bigg\{ \frac{1}{\hat{\rho}_R^a} \hat{E}_R \sin\left(\phi_L - \phi_R + \theta + \xi_R\right)$$

$$+ \frac{1}{\hat{\rho}_L^a} \hat{E}_L \sin \xi_L \Bigg\} \hat{w}\, d\theta \tag{2.66c}$$

$$\frac{\partial \hat{v}_L}{\partial \hat{t}} = \left(\Delta\hat{\omega} - \frac{\partial \phi_L}{\partial \hat{t}}\right) \hat{u}_L - \hat{v}_L + \frac{1}{2\pi} \int_{\theta_0}^{\theta_0 + 2\pi} \Bigg\{ \frac{1}{\hat{\rho}_R^a} \hat{E}_R \cos\left(\phi_L - \phi_R + \theta + \xi_R\right)$$

$$+ \frac{1}{\hat{\rho}_L^a} \hat{E}_L \cos \xi_L \Bigg\} \hat{w}\, d\theta \tag{2.66d}$$

$$\frac{\partial \hat{w}}{\partial \hat{t}} = -\frac{\hat{w} - \hat{w}_{eq}}{\hat{\tau}_1} + \mathrm{Im}\Bigg\{ \hat{P}_R' \left[\frac{1}{\hat{\rho}_R^a} \hat{E}_R e^{-i(\xi_R + \theta/2)} + \frac{1}{\hat{\rho}_L^a} \hat{E}_L e^{i(\phi_L - \phi_R - \xi_L + \theta/2)} \right]$$

$$+ \hat{P}_L' \left[\frac{1}{\hat{\rho}_R^a} \hat{E}_R e^{-i(\phi_L - \phi_R + \xi_R + \theta/2)} + \frac{1}{\hat{\rho}_L^a} \hat{E}_L e^{-i(\xi_L - \theta/2)} \right] \Bigg\} \tag{2.66e}$$

$$\frac{\partial \hat{E}_R}{\partial \hat{t}} + \psi \frac{\partial \hat{E}_R}{\partial \hat{z}} = -\frac{\hat{E}_R}{\hat{\tau}_2} + \hat{\rho}_R^a \left(\hat{u}_R \sin \xi_R + \hat{v}_R \cos \xi_R\right) \tag{2.66f}$$

$$\frac{\partial \phi_R}{\partial \hat{t}} + \psi \frac{\partial \phi_R}{\partial \hat{z}} = \hat{\Omega} - \hat{\nu}_I - \frac{\hat{\rho}_R^a}{\hat{E}_R} \left(\hat{u}_R \cos \xi_R - \hat{v}_R \sin \xi_R\right) \tag{2.66g}$$

$$\frac{\partial \hat{E}_L}{\partial \hat{t}} - \psi \frac{\partial \hat{E}_L}{\partial \hat{z}} = -\frac{\hat{E}_L}{\hat{\tau}_2} + \hat{\rho}_L^a \left(\hat{u}_L \sin \xi_L + \hat{v}_L \cos \xi_L\right) \tag{2.66h}$$

$$\frac{\partial \phi_L}{\partial \hat{t}} - \psi \frac{\partial \phi_L}{\partial \hat{z}} = \hat{\Omega} - \hat{\nu}_I - \frac{\hat{\rho}_L^a}{\hat{E}_L} \left(\hat{u}_L \cos \xi_L - \hat{v}_L \sin \xi_L\right) \tag{2.66i}$$

Eq (2.66) is the Maxwell-Bloch equation set, in normalized form. Notice that although $\hat{u}_{R,L}$, $\hat{v}_{R,L}$, and $\hat{w}$ vary spatially, there are no $\hat{z}$ derivatives in the first five equations. For $\hat{u}_{R,L}$ and $\hat{v}_{R,L}$, this occurs because the equations of motion are defined over small, isolated regions of space, in which $\hat{u}_{R,L}$ and $\hat{v}_{R,L}$ are assumed spatially constant. The equation for $\hat{w}$ is likewise defined over a small spatial region. However, due to the $\hat{P}'_{R,L}$ terms, $\hat{w}$ will have a rapid $\hat{z}$ dependence of the form $e^{\pm ikz}$. This dependency is eliminated in the integrations in the first four equations. This $\hat{z}$

dependence is a manifestation of the spatial holes that are burned in the inversion density. The first five equations are thus consistent with each other, insofar as the $\hat{z}$ variations are concerned. The field equations, in contrast, are defined over the whole of the gain medium. Therefore, the partial derivatives with respect to $\hat{z}$ are incorporated into their equations of motion. These four equations are consistent with the Bloch equations in light of the following argument. At any given local region or "point" in space, the field amplitudes and phases are essentially constant in $\hat{z}$. The fields drive the atoms and create a locally constant polarization, which in turn drives the field equations. At an adjacent point in space, the same effect takes place. In moving to the adjacent point, though, the electric fields vary due to the $\frac{\partial}{\partial \hat{z}}$ terms in their equations of motion. This spatial change produces corresponding variations of the polarization and population inversion density terms in the "point" Bloch equations. Over the whole of the laser, there will be spatial variations in $\hat{u}_{R,L}$, $\hat{v}_{R,L}$, and $\hat{w}$, although these variations are not explicitly described by the Bloch equations. The Maxwell-Bloch equations are interesting, in that they consist of both "point" and "longitudinally varying" equations.

The Rate Equation Approximation

Eq (2.66) is an extremely complex set of nonlinearly coupled integro-differential equations. A numerical solution of the equations is impractical, if not virtually impossible. However, by using the "rate equation approximation" (106: Chapter 8), the equations can be reduced to a set of four coupled, nonlinear, partial differential equations. Although also complicated, the reduced equation set can be solved numerically. Additionally, the steady-state version of the reduced equation set can be solved very simply on a computer.

The rate equation approximation is based upon two main assumptions. First, the electric field amplitudes and phases vary only slightly in time $1/\gamma$. This fits well with the previous assumption of slowly varying amplitudes and phases of $\mathbf{E}_{R,L}$. Second, the population inversion density $\varrho_{aa} - \varrho_{bb}$ equilibrates so rapidly that the changing electric fields always experience a steady-state inversion density. That is, $\varrho_{aa} - \varrho_{bb}$ is continuously at steady-state for each instantaneous value of $\mathbf{E}_{R,L}$. The second assumption is also known as the "adiabatic approximation."

The derivation commences with the equation of motion for ϱ_{ab}:

$$\dot{\varrho}_{ab} = -(i\omega + \gamma)\varrho_{ab} + \frac{i}{\hbar}V(\varrho_{aa} - \varrho_{bb}) \tag{2.30a}$$

Formally integrating Eq (2.30a) yields:

$$\varrho_{ab}e^{(i\omega+\gamma)t} = -\frac{i\mu}{2\hbar}\int_{-\infty}^{t} dt'\,(\varrho_{aa} - \varrho_{bb})\left\{\frac{1}{\rho_R^a}E_R e^{ikl_R}e^{-i(\nu_I t' - kz + \phi_R)}\right.$$

$$\left. + \frac{1}{\rho_L^a}E_L e^{ik(L+l_L)}e^{-i(\nu_I t' + kz + \phi_L)}\right\}e^{(i\omega+\gamma)t'} \tag{2.67}$$

$\mathbf{E}_R$ and $\mathbf{E}_L$ may have slightly different frequencies, as ϕ_R and ϕ_L are temporally varying. Expanding $\phi_{R,L}$ to first order gives:

$$\phi_R = \phi_R' + \dot{\phi}_R t \tag{2.68a}$$

$$\phi_L = \phi_L' + \dot{\phi}_L t \tag{2.68b}$$

Since $\phi_{R,L}$ are slowly varying in time, $\dot{\phi}_{R,L}$ can be approximated as constants. Then,

$$\nu_I t - kz + \phi_R = \nu_R t - kz + \phi_R' \tag{2.69a}$$

$$\nu_I t + kz + \phi_L = \nu_L t + kz + \phi_L' \tag{2.69b}$$

where

$$\nu_R \equiv \nu_I + \dot{\phi}_R \tag{2.70a}$$

$$\nu_L \equiv \nu_I + \dot{\phi}_L \tag{2.70b}$$

Rewriting the frequencies in this manner is crucial. If the derivation were to proceed without the two frequencies explicitly separated, the final equation set would be incorrect. The set could not be reduced to the Lamb model (Chapter IV) in the limit of perfectly reflective planar mirrors. Continuing, Eq (2.67) can now be rewritten as:

$$\varrho_{ab} = -\frac{i\mu}{2\hbar}\int_{-\infty}^{t} dt'\,(\varrho_{aa} - \varrho_{bb})\left\{\frac{1}{\rho_R^a}E_R e^{ikl_R}e^{-i(\nu_R t' - kz + \phi_R')}\right.$$

$$\left. + \frac{1}{\rho_L^a}E_L e^{ik(L+l_L)}e^{-i(\nu_L t' + kz + \phi_L')}\right\}e^{-(i\omega+\gamma)(t-t')} \tag{2.71}$$

The terms containing $E_{R,L}$, $\phi'_{R,L}$, and $\varrho_{aa} - \varrho_{bb}$ can be factored outside the integral, provided they vary slowly in time $1/\gamma$ (the rate equation approximation). Then,

$$\varrho_{ab} = -\frac{i\mu}{2\hbar}(\varrho_{aa} - \varrho_{bb})\left\{ \left[\frac{1}{\rho_R^a} E_R e^{ikl_R} e^{-i(\nu_R t - kz + \phi'_R)} \right.\right.$$

$$\left. \times \int_{-\infty}^{t} dt'\, e^{-[i(\omega-\nu_R)+\gamma](t-t')} \right] + \left[\frac{1}{\rho_L^a} E_L e^{ik(L+l_L)} e^{-i(\nu_L t + kz + \phi'_L)} \right.$$

$$\left.\left. \times \int_{-\infty}^{t} dt'\, e^{-[i(\omega-\nu_L)+\gamma](t-t')} \right] \right\} \tag{2.72}$$

Since:

$$\int_{-\infty}^{t} dt'\, e^{-[i(\omega-\nu)+\gamma](t-t')} = \frac{1}{i(\omega-\nu)+\gamma} \tag{2.73}$$

Eq (2.72) reduces to

$$\varrho_{ab} = -\frac{i\mu}{2\hbar}(\varrho_{aa} - \varrho_{bb}) \left\{ \frac{e^{ikl_R}}{\rho_R^a} \frac{E_R e^{-i(\nu_l t - kz + \phi_R)}}{i\left(\Delta\omega - \dot{\phi}_R\right) + \gamma} \right.$$

$$\left. + \frac{e^{ik(L+l_L)}}{\rho_L^a} \frac{E_L e^{-i(\nu_l t + kz + \phi_L)}}{i\left(\Delta\omega - \dot{\phi}_L\right) + \gamma} \right\} \tag{2.74}$$

where Eqs (2.69) and (2.70) have again been used.

Eq (2.74) contains the expression $\varrho_{aa} - \varrho_{bb}$. The second assumption of the rate equation approximation states that $\varrho_{aa} - \varrho_{bb}$ is continuously at steady-state for each instantaneous value of $\mathbf{E}_{R,L}$. The steady-state expression for $\varrho_{aa} - \varrho_{bb}$ in terms of the electric fields is thus needed. Starting with the equations of motion for ϱ_{aa} and ϱ_{bb},

$$\dot{\varrho}_{aa} = \lambda_a - \gamma_a \varrho_{aa} - \left(\frac{i}{\hbar} V \varrho_{ba} + \text{c.c.}\right) \tag{2.30b}$$

$$\dot{\varrho}_{bb} = \lambda_b - \gamma_b \varrho_{bb} + \left(\frac{i}{\hbar} V \varrho_{ba} + \text{c.c.}\right) \tag{2.30c}$$

and using Eqs (2.32) and (2.74) and the rotating wave approximation, two "rate" equations are obtained:

$$\dot{\varrho}_{aa} = \lambda_a - \gamma_a \varrho_{aa} - R(\varrho_{aa} - \varrho_{bb}) \tag{2.75a}$$

$$\dot{\varrho}_{bb} = \lambda_b - \gamma_b \varrho_{bb} + R(\varrho_{aa} - \varrho_{bb}) \tag{2.75b}$$

where

$$R = \frac{\mu^2}{2\hbar^2} \left\{ \frac{\gamma E_R^2 \rho_R^{-2\alpha} + \gamma E_R E_L \rho_R^{-\alpha} \rho_L^{-\alpha} \cos\beta + \left(\Delta\omega - \dot{\phi}_R\right) E_R E_L \rho_R^{-\alpha} \rho_L^{-\alpha} \sin\beta}{\gamma^2 + \left(\Delta\omega - \dot{\phi}_R\right)^2} \right.$$

$$\left. + \frac{\gamma E_L^2 \rho_L^{-2\alpha} + \gamma E_R E_L \rho_R^{-\alpha} \rho_L^{-\alpha} \cos\beta - \left(\Delta\omega - \dot{\phi}_L\right) E_R E_L \rho_R^{-\alpha} \rho_L^{-\alpha} \sin\beta}{\gamma^2 + \left(\Delta\omega - \dot{\phi}_L\right)^2} \right\} \tag{2.76a}$$

$$\beta \equiv \phi_L - \phi_R + 2kz + kl_R - k(L + l_L)$$

$$= \phi_L - \phi_R + k(\rho_R - \rho_L) \tag{2.76b}$$

Assuming that ϱ_{aa} and ϱ_{bb} are at their steady-state values, Eq (2.75) becomes:

$$\varrho_{aa} - \varrho_{bb} = \frac{(\lambda_a/\gamma_a) - (\lambda_b/\gamma_b)}{1 + (R/R_s)} \tag{2.77}$$

where

$$R_s = \frac{\gamma_a \gamma_b}{2\gamma_{ab}} \tag{2.78}$$

Eq (2.77) corresponds directly to Eq (8.37) of (106). The expression for R is considerably more complex in this derivation, however. R contains the terms that describe the spatial hole burning (interference) effects of the counterpropagating electric fields.

Using Eq (2.77) in Eq (2.74), the off-diagonal component of the density matrix can now be written as:

$$\varrho_{ab} = -\frac{i}{2\hbar} \left\{ \frac{e^{ikl_R}}{\rho_R^{\alpha}} \frac{E_R e^{-i(\nu_l t - kz + \phi_R)}}{i\left(\Delta\omega - \dot{\phi}_R\right) + \gamma} \right.$$

$$\left. + \frac{e^{ik(L+l_L)}}{\rho_L^{\alpha}} \frac{E_L e^{-i(\nu_l t + kz + \phi_L)}}{i\left(\Delta\omega - \dot{\phi}_L\right) + \gamma} \right\} \frac{w_{eq}}{1 + (R/R_s)} \tag{2.79}$$

Using as many of the normalizations as possible, and collecting the $\sin\beta$ and $\cos\beta$ terms in the denominator of Eq (2.77), Eq (2.79) can be written as:

$$\varrho_{ab} = -\frac{i w_{eq}}{2\mu}\left\{\frac{e^{ikl_R}}{\hat{\rho}_R^{\alpha}}\frac{\hat{E}_R e^{-i(\nu_I t - kz + \phi_R)}}{1 + i\left(\Delta\hat{\omega} - \dot{\varphi}_R\right)}\right.$$

$$\left. + \frac{e^{ik(L+l_L)}}{\hat{\rho}_L^{\alpha}}\frac{\hat{E}_L e^{-i(\nu_I t + kz + \phi_L)}}{1 + i\left(\Delta\hat{\omega} - \dot{\varphi}_L\right)}\right\}\left\{\frac{1}{A + B\cos\beta + C\sin\beta}\right\} \tag{2.80}$$

where

$$A \equiv 1 + \hat{\tau}_1\left\{\frac{\hat{E}_R^2\hat{\rho}_R^{-2\alpha}}{1 + \left(\Delta\hat{\omega} - \dot{\varphi}_R\right)^2} + \frac{\hat{E}_L^2\hat{\rho}_L^{-2\alpha}}{1 + \left(\Delta\hat{\omega} - \dot{\varphi}_L\right)^2}\right\} \tag{2.81a}$$

$$B \equiv \frac{\hat{\tau}_1\hat{E}_R\hat{E}_L}{\hat{\rho}_R^{\alpha}\hat{\rho}_L^{\alpha}}\left\{\frac{1}{1 + \left(\Delta\hat{\omega} - \dot{\varphi}_R\right)^2} + \frac{1}{1 + \left(\Delta\hat{\omega} - \dot{\varphi}_L\right)^2}\right\} \tag{2.81b}$$

$$C \equiv \frac{\hat{\tau}_1\hat{E}_R\hat{E}_L}{\hat{\rho}_R^{\alpha}\hat{\rho}_L^{\alpha}}\left\{\frac{\left(\Delta\hat{\omega} - \dot{\varphi}_R\right)}{1 + \left(\Delta\hat{\omega} - \dot{\varphi}_R\right)^2} - \frac{\left(\Delta\hat{\omega} - \dot{\varphi}_L\right)}{1 + \left(\Delta\hat{\omega} - \dot{\varphi}_L\right)^2}\right\} \tag{2.81c}$$

$$\dot{\varphi}_{R,L} \equiv \frac{\partial\phi_{R,L}}{\partial\hat{t}} \tag{2.81d}$$

Eq (2.80) yields the steady-state value of ϱ_{ab}, for given fields $\mathbf{E}_R$ and $\mathbf{E}_L$ in the medium. Even though the electric fields can vary (slowly) in time, Eq (2.80) describes the steady-state value of the matrix element, per the adiabatic approximation discussed earlier.

ϱ_{ab} can be decomposed into P_R and P_L via Eq (2.35), rewritten slightly as:

$$P_R(z,t)\Big|_{z=z_0} = 2\mu e^{i(\nu_I t + \phi_R)}\left(\frac{2}{\lambda}\right)\int_{z_0}^{z_0+\lambda/2}\varrho_{ab}e^{-ikz}\,dz \tag{2.35a}$$

$$P_L(z,t)\Big|_{z=z_0} = 2\mu e^{i(\nu_I t + \phi_L)}\left(\frac{2}{\lambda}\right)\int_{z_0}^{z_0+\lambda/2}\varrho_{ab}e^{ikz}\,dz \tag{2.35b}$$

Eq (2.35a) is examined first. The integral on the right-hand side of the equation can be expanded with Eq (2.80) to give:

$$\int_{z_0}^{z_0+\lambda/2}\varrho_{ab}e^{-ikz}\,dz = -\frac{i w_{eq}}{2\mu}\int_{z_0}^{z_0+\lambda/2}\left\{\frac{e^{ikl_R}}{\hat{\rho}_R^{\alpha}}\frac{\hat{E}_R e^{-i(\nu_I t - kz + \phi_R)}}{1 + i\left(\Delta\hat{\omega} - \dot{\varphi}_R\right)}\right.$$

$$+\frac{e^{ik(L+l_L)}}{\hat{\rho}_L^{\alpha}}\frac{\hat{E}_L e^{-i(\nu_l t+kz+\phi_L)}}{1+i\left(\Delta\hat{\omega}-\dot{\varphi}_L\right)}\Bigg\}\frac{e^{-ikz}\,dz}{1+(R/R_s)}$$

$$=-\frac{iw_{eq}}{2\mu}\Bigg\{\frac{e^{ikl_R}}{\hat{\rho}_R^{\alpha}}\frac{\hat{E}_R e^{-i(\nu_l t+\phi_R)}}{1+i\left(\Delta\hat{\omega}-\dot{\varphi}_R\right)}\int_{z_0}^{z_0+\lambda/2}\frac{dz}{1+(R/R_s)}$$

$$+\frac{e^{ik(L+l_L)}}{\hat{\rho}_L^{\alpha}}\frac{\hat{E}_L e^{-i(\nu_l t+\phi_L)}}{1+i\left(\Delta\hat{\omega}-\dot{\varphi}_L\right)}\int_{z_0}^{z_0+\lambda/2}\frac{\cos(2kz)\,dz}{1+(R/R_s)}$$

$$-\frac{ie^{ik(L+l_L)}}{\hat{\rho}_L^{\alpha}}\frac{\hat{E}_L e^{-i(\nu_l t+\phi_L)}}{1+i\left(\Delta\hat{\omega}-\dot{\varphi}_L\right)}\int_{z_0}^{z_0+\lambda/2}\frac{\sin(2kz)\,dz}{1+(R/R_s)}\Bigg\} \tag{2.82}$$

The first integral in Eq (2.82) can be written as:

$$\int_{z_0}^{z_0+\lambda/2}\frac{dz}{1+(R/R_s)}=\int_{z_0}^{z_0+\lambda/2}\frac{dz}{A+B\cos\beta+C\sin\beta} \tag{2.83}$$

Eq (2.83) has an exact solution (159: Eq (2.558.4)). However, the form of the solution depends on whether $A^2-B^2-C^2$ is greater than, equal to, or less than 0. After some algebra, this discriminant becomes:

$$A^2-(B^2+C^2)=1+2\hat{\tau}_1\left\{\frac{\hat{E}_R^2\hat{\rho}_R^{-2\alpha}}{1+\left(\Delta\hat{\omega}-\dot{\varphi}_R\right)^2}+\frac{\hat{E}_L^2\hat{\rho}_L^{-2\alpha}}{1+\left(\Delta\hat{\omega}-\dot{\varphi}_L\right)^2}\right\}$$

$$+\hat{\tau}_1^2\left\{\frac{\hat{E}_R^2\hat{\rho}_R^{-2\alpha}}{1+\left(\Delta\hat{\omega}-\dot{\varphi}_R\right)^2}-\frac{\hat{E}_L^2\hat{\rho}_L^{-2\alpha}}{1+\left(\Delta\hat{\omega}-\dot{\varphi}_L\right)^2}\right\}^2$$

$$-\frac{\hat{\tau}_1^2\hat{E}_R^2\hat{E}_L^2\left(\dot{\varphi}_L-\dot{\varphi}_R\right)^2}{\hat{\rho}_R^{2\alpha}\hat{\rho}_L^{2\alpha}\left[1+\left(\Delta\hat{\omega}-\dot{\varphi}_R\right)^2\right]\left[1+\left(\Delta\hat{\omega}-\dot{\varphi}_L\right)^2\right]} \tag{2.84}$$

The first three terms on the right-hand side of Eq (2.84) are positive, while the last term is negative. $\left(\dot{\varphi}_L-\dot{\varphi}_R\right)^2$ should be very small; at steady-state, this term is identically zero. If the fourth term is assumed to be small compared to the previous three terms, then

$$A^2-\left(B^2+C^2\right)>0 \tag{2.85}$$

Eq (2.558.4) of (159) can now be applied to Eq (2.83):

$$\int_{z_0}^{z_0+\lambda/2} \frac{dz}{1+(R/R_s)} = \frac{\lambda}{2}\frac{1}{\sqrt{A^2-B^2-C^2}} \tag{2.86}$$

The second integral in Eq (2.82) is evaluated next. Using Eq (2.76) and performing a change of variables, the integral can be written as:

$$\int_{z_0}^{z_0+\lambda/2} \frac{\cos(2kz)\,dz}{1+(R/R_s)} = \frac{1}{2k}\int_{\beta_0}^{\beta_0+2\pi} \frac{\cos\beta\cos\beta_1+\sin\beta\sin\beta_1}{A+B\cos\beta+C\sin\beta}\,d\beta \tag{2.87}$$

where

$$\beta_0 \equiv \phi_L - \phi_R + 2kz_0 + kl_R - k(L+l_L) \tag{2.88a}$$

$$\beta_1 \equiv \phi_L - \phi_R + kl_R - k(L+l_L) \tag{2.88b}$$

Eq (2.558.2) of (159) can be used to integrate Eq (2.87), subject to the constraint of Eq (2.85):

$$\int_{z_0}^{z_0+\lambda/2} \frac{\cos(2kz)\,dz}{1+(R/R_s)} = \frac{\lambda}{2}\left[\frac{B\cos\beta_1+C\sin\beta_1}{B^2+C^2}\right]\left[1-\frac{A}{\sqrt{A^2-B^2-C^2}}\right] \tag{2.89}$$

Finally, the third integral in Eq (2.82) is evaluated in an identical manner, yielding:

$$\int_{z_0}^{z_0+\lambda/2} \frac{\sin(2kz)\,dz}{1+(R/R_s)} = \frac{\lambda}{2}\left[\frac{C\cos\beta_1-B\sin\beta_1}{B^2+C^2}\right]\left[1-\frac{A}{\sqrt{A^2-B^2-C^2}}\right] \tag{2.90}$$

Eqs (2.35a), (2.82), (2.86), (2.89), and (2.90) can now be combined, yielding an expression for $\hat{P}_R$:

$$\hat{P}_R(z,t) = -i\hat{w}_{eq}e^{ikl_R}\left\{\frac{\hat{E}_R\hat{\rho}_R^{-a}}{1+i\,(\Delta\hat{\omega}-\dot{\varphi}_R)}\frac{1}{\sqrt{A^2-B^2-C^2}}\right.$$

$$\left. + \frac{\hat{E}_L\hat{\rho}_L^{-a}}{1+i\,(\Delta\hat{\omega}-\dot{\varphi}_L)}\left[1-\frac{A}{\sqrt{A^2-B^2-C^2}}\right]\left[\frac{B-iC}{B^2+C^2}\right]\right\} \tag{2.91}$$

Using the same procedures, the corresponding expression for $\hat{P}_L$ can be derived:

$$\hat{P}_L(z,t) = -i\hat{w}_{eq}e^{ik(L+l_L)}\left\{\frac{\hat{E}_L\hat{\rho}_L^{-a}}{1+i\left(\Delta\hat{\omega}-\dot{\varphi}_L\right)}\frac{1}{\sqrt{A^2-B^2-C^2}}\right.$$

$$\left.+\frac{\hat{E}_R\hat{\rho}_R^{-a}}{1+i\left(\Delta\hat{\omega}-\dot{\varphi}_R\right)}\left[1-\frac{A}{\sqrt{A^2-B^2-C^2}}\right]\left[\frac{B+iC}{B^2+C^2}\right]\right\} \tag{2.92}$$

Eqs (2.91) and (2.92) describe the complex polarizations $\hat{P}_{R,L}$ at some axial location z and time t. These expressions are functions of the electric fields and the radial coordinates $\hat{\rho}_{R,L}$. This suggests substituting the two equations into the expressions for the electric fields, thus obtaining a self-consistent set of field equations. For convenience, Eq (2.58) is repeated, along with the analogous expression for $\mathbf{E}_L$:

$$-2i\Omega c\frac{\partial E_R}{\partial z}+\Omega^2E_R-2\Omega cE_R\frac{\partial\phi_R}{\partial z}-\frac{i\nu_I\sigma}{\epsilon_0}E_R-2i\nu_I\frac{\partial E_R}{\partial t}-(\nu_I+\dot{\phi}_R)^2E_R$$

$$=\frac{\nu^2}{\epsilon_0}\rho_R^a e^{-ikl_R}P_R \tag{2.58a}$$

and:

$$2i\Omega c\frac{\partial E_L}{\partial z}+\Omega^2E_L+2\Omega cE_L\frac{\partial\phi_L}{\partial z}-\frac{i\nu_I\sigma}{\epsilon_0}E_L-2i\nu_I\frac{\partial E_L}{\partial t}-(\nu_I+\dot{\phi}_L)^2E_L$$

$$=\frac{\nu^2}{\epsilon_0}\rho_L^a e^{-ik(L+l_L)}P_L \tag{2.58b}$$

Substituting Eqs (2.91) and (2.92) into Eq (2.58), separating the real and imaginary parts, and applying the normalizations, the final equations of motion in the rate equation approximation are derived:

$$\frac{\partial\hat{E}_R}{\partial\hat{t}}+\psi\frac{\partial\hat{E}_R}{\partial\hat{z}}=-\frac{\hat{E}_R}{\hat{\tau}_2}+\hat{w}_{eq}\hat{\rho}_R^a\left\{\frac{\hat{E}_R\hat{\rho}_R^{-a}}{1+\left(\Delta\hat{\omega}-\dot{\varphi}_R\right)^2}\frac{1}{\sqrt{A^2-B^2-C^2}}\right.$$

$$\left.+\frac{\hat{E}_L\hat{\rho}_L^{-a}}{1+\left(\Delta\hat{\omega}-\dot{\varphi}_L\right)^2}\left[1-\frac{A}{\sqrt{A^2-B^2-C^2}}\right]\left[\frac{B-C(\Delta\hat{\omega}-\dot{\varphi}_L)}{B^2+C^2}\right]\right\} \tag{2.93a}$$

$$\frac{\partial\phi_R}{\partial\hat{t}}+\psi\frac{\partial\phi_R}{\partial\hat{z}}=\hat{\Omega}-\hat{\nu}_I+\hat{w}_{eq}\frac{\hat{\rho}_R^a}{\hat{E}_R}\left\{\frac{\hat{E}_R\hat{\rho}_R^{-a}(\Delta\hat{\omega}-\dot{\varphi}_R)}{1+\left(\Delta\hat{\omega}-\dot{\varphi}_R\right)^2}\frac{1}{\sqrt{A^2-B^2-C^2}}\right.$$

$$+\frac{\hat{E}_L\hat{\rho}_L^{-a}}{1+(\Delta\hat{\omega}-\dot{\varphi}_L)^2}\left[1-\frac{A}{\sqrt{A^2-B^2-C^2}}\right]\left[\frac{B(\Delta\hat{\omega}-\dot{\varphi}_L)+C}{B^2+C^2}\right]\Bigg\} \tag{2.93b}$$

$$\frac{\partial\hat{E}_L}{\partial\hat{t}}-\psi\frac{\partial\hat{E}_L}{\partial\hat{z}}=-\frac{\hat{E}_L}{\hat{\tau}_2}+\hat{w}_{eq}\hat{\rho}_L^a\left\{\frac{\hat{E}_L\hat{\rho}_L^{-a}}{1+(\Delta\hat{\omega}-\dot{\varphi}_L)^2}\frac{1}{\sqrt{A^2-B^2-C^2}}\right.$$

$$+\frac{\hat{E}_R\hat{\rho}_R^{-a}}{1+(\Delta\hat{\omega}-\dot{\varphi}_R)^2}\left[1-\frac{A}{\sqrt{A^2-B^2-C^2}}\right]\left[\frac{B+C(\Delta\hat{\omega}-\dot{\varphi}_R)}{B^2+C^2}\right]\Bigg\} \tag{2.93c}$$

$$\frac{\partial\phi_L}{\partial\hat{t}}-\psi\frac{\partial\phi_L}{\partial\hat{z}}=\hat{\Omega}-\hat{\nu}_I+\hat{w}_{eq}\frac{\hat{\rho}_L^a}{\hat{E}_L}\left\{\frac{\hat{E}_L\hat{\rho}_L^{-a}(\Delta\hat{\omega}-\dot{\varphi}_L)}{1+(\Delta\hat{\omega}-\dot{\varphi}_L)^2}\frac{1}{\sqrt{A^2-B^2-C^2}}\right.$$

$$+\frac{\hat{E}_R\hat{\rho}_R^{-a}}{1+(\Delta\hat{\omega}-\dot{\varphi}_R)^2}\left[1-\frac{A}{\sqrt{A^2-B^2-C^2}}\right]\left[\frac{B(\Delta\hat{\omega}-\dot{\varphi}_R)-C}{B^2+C^2}\right]\Bigg\} \tag{2.93d}$$

Several observations should be made. First, the equations have the same form as Eqs (2.59) and (2.61). However, the polarization terms $\hat{u}_{R,L}$ and $\hat{v}_{R,L}$ have been replaced by the corresponding functions of $\hat{E}_{R,L}$ and $\phi_{R,L}$. The equations are thus functions only of the electric fields, and not of the polarizations. Second, Eq (2.93) is a set of coupled, nonlinear partial differential equations. Note that time derivatives of both ϕ_R and ϕ_L exist on the right-hand sides of all four equations. Unfortunately, these derivatives cannot be separated out and collected on the left-hand sides of Eqs (2.93b) and (2.93d). (This was the source of some of the stability problems of the time-dependent computer code for the Fabry-Perot laser.) Third, the equations reduce to a simple set of coupled, nonlinear ordinary differential equations at steady-state. These equations are easily solved on a computer, using a Runge-Kutta or similar numerical method. Finally, a high degree of symmetry exists between Eqs (2.93a) and (2.93c) and between Eqs (2.93b) and (2.93d), as one would expect. This symmetry is similar to that existing between the intensity equations of the simple saturable gain (g_0-I_{sat}) model.

Equation Summary

The main equation sets derived in this chapter are repeated here for reference. All quantities are in the normalized units.

The Bloch Equations

$$\frac{\partial \hat{u}_R}{\partial \hat{t}} = -\hat{u}_R - (\Delta\hat{\omega} - \dot{\varphi}_R)\hat{v}_R + \frac{1}{2\pi}\int_{\theta_0}^{\theta_0+2\pi}\left\{\frac{1}{\hat{\rho}_R^{\alpha}}\hat{E}_R \sin\xi_R - \frac{1}{\hat{\rho}_L^{\alpha}}\hat{E}_L \sin(\phi_L - \phi_R + \theta - \xi_L)\right\}\hat{w}\, d\theta \tag{2.66a}$$

$$\frac{\partial \hat{v}_R}{\partial \hat{t}} = (\Delta\hat{\omega} - \dot{\varphi}_R)\hat{u}_R - \hat{v}_R + \frac{1}{2\pi}\int_{\theta_0}^{\theta_0+2\pi}\left\{\frac{1}{\hat{\rho}_R^{\alpha}}\hat{E}_R \cos\xi_R + \frac{1}{\hat{\rho}_L^{\alpha}}\hat{E}_L \cos(\phi_L - \phi_R + \theta - \xi_L)\right\}\hat{w}\, d\theta \tag{2.66b}$$

$$\frac{\partial \hat{u}_L}{\partial \hat{t}} = -\hat{u}_L - (\Delta\hat{\omega} - \dot{\varphi}_L)\hat{v}_L + \frac{1}{2\pi}\int_{\theta_0}^{\theta_0+2\pi}\left\{\frac{1}{\hat{\rho}_R^{\alpha}}\hat{E}_R \sin(\phi_L - \phi_R + \theta + \xi_R) + \frac{1}{\hat{\rho}_L^{\alpha}}\hat{E}_L \sin\xi_L\right\}\hat{w}\, d\theta \tag{2.66c}$$

$$\frac{\partial \hat{v}_L}{\partial \hat{t}} = (\Delta\hat{\omega} - \dot{\varphi}_L)\hat{u}_L - \hat{v}_L + \frac{1}{2\pi}\int_{\theta_0}^{\theta_0+2\pi}\left\{\frac{1}{\hat{\rho}_R^{\alpha}}\hat{E}_R \cos(\phi_L - \phi_R + \theta + \xi_R) + \frac{1}{\hat{\rho}_L^{\alpha}}\hat{E}_L \cos\xi_L\right\}\hat{w}\, d\theta \tag{2.66d}$$

$$\frac{\partial \hat{w}}{\partial \hat{t}} = -\frac{\hat{w} - \hat{w}_{eq}}{\hat{\tau}_1} + \mathrm{Im}\left\{\hat{P}_R'\left[\frac{1}{\hat{\rho}_R^{\alpha}}\hat{E}_R e^{-i(\xi_R+\theta/2)} + \frac{1}{\hat{\rho}_L^{\alpha}}\hat{E}_L e^{i(\phi_L-\phi_R-\xi_L+\theta/2)}\right] + \hat{P}_L'\left[\frac{1}{\hat{\rho}_R^{\alpha}}\hat{E}_R e^{-i(\phi_L-\phi_R+\xi_R+\theta/2)} + \frac{1}{\hat{\rho}_L^{\alpha}}\hat{E}_L e^{-i(\xi_L-\theta/2)}\right]\right\} \tag{2.66e}$$

The Field (Maxwell) Equations

$$\frac{\partial \hat{E}_R}{\partial \hat{t}} + \psi\frac{\partial \hat{E}_R}{\partial \hat{z}} = -\frac{\hat{E}_R}{\hat{\tau}_2} + \hat{\rho}_R^{\alpha}(\hat{u}_R \sin\xi_R + \hat{v}_R \cos\xi_R) \tag{2.66f}$$

$$\frac{\partial \phi_R}{\partial \hat{t}} + \psi\frac{\partial \phi_R}{\partial \hat{z}} = \hat{\Omega} - \hat{\nu}_I - \frac{\hat{\rho}_R^{\alpha}}{\hat{E}_R}(\hat{u}_R \cos\xi_R - \hat{v}_R \sin\xi_R) \tag{2.66g}$$

$$\frac{\partial \hat{E}_L}{\partial \hat{t}} - \psi \frac{\partial \hat{E}_L}{\partial \hat{z}} = -\frac{\hat{E}_L}{\hat{\tau}_2} + \hat{\rho}_L^{\alpha} \left(\hat{u}_L \sin \xi_L + \hat{v}_L \cos \xi_L \right) \tag{2.66h}$$

$$\frac{\partial \phi_L}{\partial \hat{t}} - \psi \frac{\partial \phi_L}{\partial \hat{z}} = \hat{\Omega} - \hat{\nu}_I - \frac{\hat{\rho}_L^{\alpha}}{\hat{E}_L} \left(\hat{u}_L \cos \xi_L - \hat{v}_L \sin \xi_L \right) \tag{2.66i}$$

The Field Equations (in the Rate Equation Approximation)

$$\frac{\partial \hat{E}_R}{\partial \hat{t}} + \psi \frac{\partial \hat{E}_R}{\partial \hat{z}} = -\frac{\hat{E}_R}{\hat{\tau}_2} + \hat{w}_{eq} \hat{\rho}_R^{\alpha} \left\{ \frac{\hat{E}_R \hat{\rho}_R^{-\alpha}}{1 + (\Delta\hat{\omega} - \dot{\varphi}_R)^2} \frac{1}{\sqrt{A^2 - B^2 - C^2}} \right.$$

$$\left. + \frac{\hat{E}_L \hat{\rho}_L^{-\alpha}}{1 + (\Delta\hat{\omega} - \dot{\varphi}_L)^2} \left[1 - \frac{A}{\sqrt{A^2 - B^2 - C^2}} \right] \left[\frac{B - C(\Delta\hat{\omega} - \dot{\varphi}_L)}{B^2 + C^2} \right] \right\} \tag{2.93a}$$

$$\frac{\partial \phi_R}{\partial \hat{t}} + \psi \frac{\partial \phi_R}{\partial \hat{z}} = \hat{\Omega} - \hat{\nu}_I + \hat{w}_{eq} \frac{\hat{\rho}_R^{\alpha}}{\hat{E}_R} \left\{ \frac{\hat{E}_R \hat{\rho}_R^{-\alpha} (\Delta\hat{\omega} - \dot{\varphi}_R)}{1 + (\Delta\hat{\omega} - \dot{\varphi}_R)^2} \frac{1}{\sqrt{A^2 - B^2 - C^2}} \right.$$

$$\left. + \frac{\hat{E}_L \hat{\rho}_L^{-\alpha}}{1 + (\Delta\hat{\omega} - \dot{\varphi}_L)^2} \left[1 - \frac{A}{\sqrt{A^2 - B^2 - C^2}} \right] \left[\frac{B(\Delta\hat{\omega} - \dot{\varphi}_L) + C}{B^2 + C^2} \right] \right\} \tag{2.93b}$$

$$\frac{\partial \hat{E}_L}{\partial \hat{t}} - \psi \frac{\partial \hat{E}_L}{\partial \hat{z}} = -\frac{\hat{E}_L}{\hat{\tau}_2} + \hat{w}_{eq} \hat{\rho}_L^{\alpha} \left\{ \frac{\hat{E}_L \hat{\rho}_L^{-\alpha}}{1 + (\Delta\hat{\omega} - \dot{\varphi}_L)^2} \frac{1}{\sqrt{A^2 - B^2 - C^2}} \right.$$

$$\left. + \frac{\hat{E}_R \hat{\rho}_R^{-\alpha}}{1 + (\Delta\hat{\omega} - \dot{\varphi}_R)^2} \left[1 - \frac{A}{\sqrt{A^2 - B^2 - C^2}} \right] \left[\frac{B + C(\Delta\hat{\omega} - \dot{\varphi}_R)}{B^2 + C^2} \right] \right\} \tag{2.93c}$$

$$\frac{\partial \phi_L}{\partial \hat{t}} - \psi \frac{\partial \phi_L}{\partial \hat{z}} = \hat{\Omega} - \hat{\nu}_I + \hat{w}_{eq} \frac{\hat{\rho}_L^{\alpha}}{\hat{E}_L} \left\{ \frac{\hat{E}_L \hat{\rho}_L^{-\alpha} (\Delta\hat{\omega} - \dot{\varphi}_L)}{1 + (\Delta\hat{\omega} - \dot{\varphi}_L)^2} \frac{1}{\sqrt{A^2 - B^2 - C^2}} \right.$$

$$\left. + \frac{\hat{E}_R \hat{\rho}_R^{-\alpha}}{1 + (\Delta\hat{\omega} - \dot{\varphi}_R)^2} \left[1 - \frac{A}{\sqrt{A^2 - B^2 - C^2}} \right] \left[\frac{B(\Delta\hat{\omega} - \dot{\varphi}_R) - C}{B^2 + C^2} \right] \right\} \tag{2.93d}$$

$$A \equiv 1 + \hat{\tau}_1 \left\{ \frac{\hat{E}_R^2 \hat{\rho}_R^{-2\alpha}}{1 + (\Delta\hat{\omega} - \dot{\varphi}_R)^2} + \frac{\hat{E}_L^2 \hat{\rho}_L^{-2\alpha}}{1 + (\Delta\hat{\omega} - \dot{\varphi}_L)^2} \right\} \tag{2.81a}$$

$$B \equiv \frac{\hat{\tau}_1 \hat{E}_R \hat{E}_L}{\hat{\rho}_R^{\alpha} \hat{\rho}_L^{\alpha}} \left\{ \frac{1}{1 + (\Delta\hat{\omega} - \dot{\varphi}_R)^2} + \frac{1}{1 + (\Delta\hat{\omega} - \dot{\varphi}_L)^2} \right\} \tag{2.81b}$$

$$C \equiv \frac{\hat{\tau}_1 \hat{E}_R \hat{E}_L}{\hat{\rho}_R^{\alpha} \hat{\rho}_L^{\alpha}} \left\{ \frac{(\Delta\hat{\omega} - \dot{\varphi}_R)}{1 + (\Delta\hat{\omega} - \dot{\varphi}_R)^2} - \frac{(\Delta\hat{\omega} - \dot{\varphi}_L)}{1 + (\Delta\hat{\omega} - \dot{\varphi}_L)^2} \right\} \tag{2.81c}$$

III. Semiclassical Theory of the Fabry-Perot Laser

The semiclassical theory of a Fabry-Perot laser with arbitrary outcoupling is presented in this chapter. As a detailed derivation of the semiclassical theory of a general laser is presented in Chapter II, only the main results of a parallel derivation for the Fabry-Perot laser are presented here. The laser device and several main definitions are presented in the first section of this chapter. The Bloch equations are presented in the second section. The field equations are given next, followed by the equations of motion in the REA. The free-running laser at steady-state is discussed in the fifth section. The equations of motion for the laser and the appropriate boundary conditions are given. The injected laser at steady-state is discussed in a similar manner in the next section. The chapter is summarized in the final section.

The Fabry-Perot Laser

The Fabry-Perot laser consists of an active laser medium placed between two plane-parallel mirrors. The mirrors form the cavity, with an optic axis z. The cavity is essentially a Fabry-Perot interferometer. The Fabry-Perot cavity lies on the boundary between the stable and unstable resonators on a stability diagram (144). The resonator is therefore neither stable nor unstable. Light rays will walk out of the cavity, unless they are parallel to the optic axis. However, the rays will not walk out at an increasing rate, as in an unstable resonator, nor will they be refocused toward the optic axis, as in a stable resonator. Outcoupling from the laser occurs primarily via mirror transmission. Nonetheless, some diffractive spilling about the edges of the mirrors may occur. For the purposes of this work, the diffractive spilling will be ignored. This can be easily justified: for large enough mirrors, the amount of diffractive leakage is very small. The laser is illustrated schematically in Figure 3.1.

The mirrors forming the cavity have complex reflection and transmission coefficients given by:

$$\text{Mirror A:} \quad \begin{cases} r_A = r_A e^{i\phi_{rA}} \\ t_A = t_A e^{i\phi_{tA}} \end{cases} \tag{3.1a, b}$$

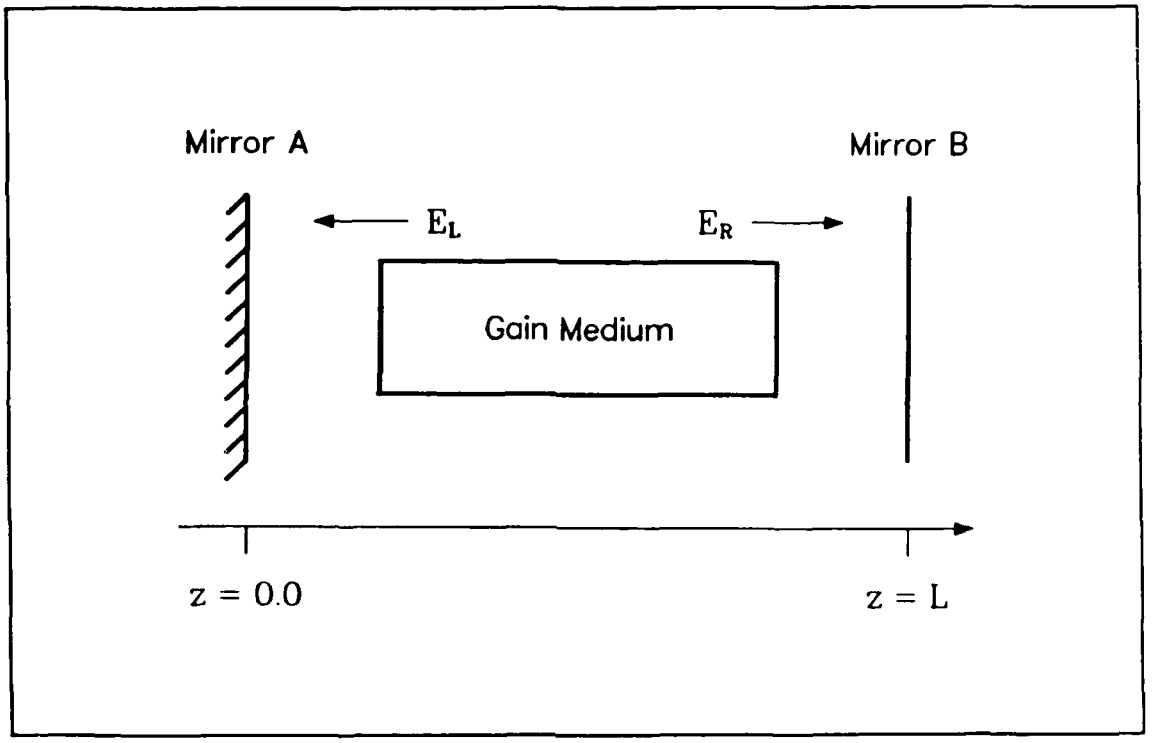

Figure 3.1. The Fabry-Perot laser.

$$\text{Mirror B:} \quad \begin{cases} r_B = r_B e^{i\phi_{RB}} \\ t_B = t_B e^{i\phi_{TB}} \end{cases} \tag{3.1c, d}$$

Although outcoupling can occur through both mirrors, in most practical cases one of the mirrors is perfectly reflective. Outcoupling then occurs only at one end of the laser. The gain medium extends far enough in the transverse directions so that it is not a limiting aperture for the laser fields. The longitudinal extent of the medium is unimportant in the derivation of the semiclassical equations.

The electric fields inside the resonator are assumed to be plane, traveling waves. This is the geometric optics mode for a Fabry-Perot interferometer. The total electric field is given by:

$$\mathbf{E}(z,t) = \mathbf{E}_R(z,t) + \mathbf{E}_L(z,t) \tag{3.2}$$

where the individual traveling waves are modeled by:

$$\mathbf{E}_R(z,t) = \frac{1}{2}\left\{ E_R(z,t) \exp\{-i[\nu_l t - kz + \phi_R(z,t)]\} + \text{c.c.} \right\} \tag{3.3a}$$

$$\mathbf{E}_L(z,t) = \frac{1}{2}\left\{ E_L(z,t)\exp\{-i[\nu_I t + kz + \phi_L(z,t)]\} + \text{c.c.} \right\} \tag{3.3b}$$

$E_{R,L}$ are the amplitudes of the rightward and leftward traveling waves, ν_I is the frequency of the waves, k is the wavenumber, and $\phi_{R,L}$ are the phases of the waves. In the absence of an injected signal, ν_I is simply a reference frequency; otherwise, it is the frequency of the injected wave. $\nu_I + \dot{\phi}_R$ and $\nu_I + \dot{\phi}_L$ are the instantaneous frequencies of the traveling waves. Note that only a single longitudinal mode is allowed to exist in the model. $E_{R,L}$ and $\phi_{R,L}$ are real and assumed to vary slowly in both time and space. "c.c." denotes the complex conjugate term.

The total polarization $\mathbf{P}(z,t)$ of the medium is defined in a similar manner:

$$\begin{aligned}
\mathbf{P}(z,t) &= \mathbf{P}_R(z,t) + \mathbf{P}_L(z,t) \\
&= \frac{1}{2}\Big\{ P_R(z,t)\exp\{-i[\nu_I t - kz + \phi_R(z,t)]\} \\
&\qquad + P_L(z,t)\exp\{-i[\nu_I t + kz + \phi_L(z,t)]\} + \text{c.c.} \Big\} \\
&= \frac{1}{2}\Big\{ P'_R(z,t)\exp\{-i[\nu_I t + \phi_R(z,t)]\} \\
&\qquad + P'_L(z,t)\exp\{-i[\nu_I t + \phi_L(z,t)]\} + \text{c.c.} \Big\}
\end{aligned} \tag{3.4}$$

The polarization wave amplitudes, $P_{R,L}$ and $P'_{R,L}$, are generally complex quantities. All four amplitudes vary slowly in time, whereas only $P_{R,L}$ vary slowly in space. $P'_{R,L}$ have rapidly varying z dependencies on the order of $e^{\pm ikz}$, in addition to slowly varying envelopes in z.

The Bloch Equations

The Bloch equations for the Fabry-Perot laser can be obtained in an identical manner as those for the general laser (Chapter II). Since there are no $\rho_{R,L}$ terms in the amplitudes of the electric fields, the Fabry-Perot derivation is slightly simpler than the general laser derivation. One subtle

difference in the two derivations lies in the normalization of the electric fields. Here, the fields are normalized as:

$$\hat{E}_{R,L} = \frac{\mu}{\gamma\hbar} E_{R,L} \tag{3.5}$$

Obviously, no normalizations of the radial coordinates $\rho_{R,L}$ are necessary.

In normalized form, the Bloch equations for the Fabry-Perot laser are:

$$\frac{\partial \hat{u}_R}{\partial \hat{t}} = -\hat{u}_R - \left(\Delta\hat{\omega} - \frac{\partial \phi_R}{\partial \hat{t}}\right)\hat{v}_R - \frac{1}{2\pi}\int_{\theta_0}^{\theta_0+2\pi} \hat{E}_L \sin(\phi_L - \phi_R + \theta)\hat{w}\, d\theta \tag{3.6a}$$

$$\frac{\partial \hat{v}_R}{\partial \hat{t}} = \left(\Delta\hat{\omega} - \frac{\partial \phi_R}{\partial \hat{t}}\right)\hat{u}_R - \hat{v}_R + \frac{1}{2\pi}\int_{\theta_0}^{\theta_0+2\pi} \left[\hat{E}_R + \hat{E}_L \cos(\phi_L - \phi_R + \theta)\right]\hat{w}\, d\theta \tag{3.6b}$$

$$\frac{\partial \hat{u}_L}{\partial \hat{t}} = -\hat{u}_L - \left(\Delta\hat{\omega} - \frac{\partial \phi_L}{\partial \hat{t}}\right)\hat{v}_L + \frac{1}{2\pi}\int_{\theta_0}^{\theta_0+2\pi} \hat{E}_R \sin(\phi_L - \phi_R + \theta)\hat{w}\, d\theta \tag{3.6c}$$

$$\frac{\partial \hat{v}_L}{\partial \hat{t}} = \left(\Delta\hat{\omega} - \frac{\partial \phi_L}{\partial \hat{t}}\right)\hat{u}_L - \hat{v}_L + \frac{1}{2\pi}\int_{\theta_0}^{\theta_0+2\pi} \left[\hat{E}_R \cos(\phi_L - \phi_R + \theta) + \hat{E}_L\right]\hat{w}\, d\theta \tag{3.6d}$$

$$\begin{aligned}\frac{\partial \hat{w}}{\partial \hat{t}} = &-\left(\frac{\hat{w} - \hat{w}_{eq}}{\hat{\tau}_1}\right) + \mathrm{Im}\Big\{\hat{P}'_R\left[\hat{E}_R e^{-i\theta/2} + \hat{E}_L e^{i(\phi_L - \phi_R + \theta/2)}\right] \\ &+ \hat{P}'_L\left[\hat{E}_R e^{-i(\phi_L - \phi_R + \theta/2)} + \hat{E}_L e^{i\theta/2}\right]\Big\}\end{aligned} \tag{3.6e}$$

These equations are similar in form to the Bloch equations of the general laser (Eq (2.66)), with only two main differences. The first difference is the absence of the $\hat{\rho}^{\alpha}_{R,L}$ terms. These terms do not appear as they are not part of the mathematical representation of the plane waves. The second important difference is the simpler integrands in the first four equations. The cylindrical/spherical nature of the waves in the general laser adds the phase terms $e^{i\xi_{R,L}}$ to the electric fields. This additional phase term creates the mixing of the fields in the integrands of Eq (2.66). Since the plane waves in the Fabry-Perot laser do not have these phase terms, there is no mixing in the integrands of the $\hat{u}_{R,L}$ equations. Additionally, these phase terms do not appear in the $\hat{w}$ equation for the Fabry-Perot laser.

The Electric Field (Maxwell) Equations

The derivation of the field equations for the Fabry-Perot laser parallels the derivation given in Chapter II. The main difference is again due to the $\hat{\rho}_{R,L}$ terms. In the general laser case, partial derivatives of these terms arise. They can generally be discarded in comparison to other larger terms in the equations. In the Fabry-Perot case, no such terms arise as the fields are modeled as plane waves.

In normalized form, the equations of motion of the electric fields in the Fabry-Perot laser are:

$$\frac{\partial \hat{E}_R}{\partial \hat{t}} + \psi \frac{\partial \hat{E}_R}{\partial \hat{z}} = -\frac{\hat{E}_R}{\hat{\tau}_2} + \hat{v}_R \tag{3.7a}$$

$$\frac{\partial \phi_R}{\partial \hat{t}} + \psi \frac{\partial \phi_R}{\partial \hat{z}} = \hat{\Omega} - \hat{\nu}_I - \frac{\hat{u}_R}{\hat{E}_R} \tag{3.7b}$$

$$\frac{\partial \hat{E}_L}{\partial \hat{t}} - \psi \frac{\partial \hat{E}_L}{\partial \hat{z}} = -\frac{\hat{E}_L}{\hat{\tau}_2} + \hat{v}_L \tag{3.7c}$$

$$\frac{\partial \phi_L}{\partial \hat{t}} - \psi \frac{\partial \phi_L}{\partial \hat{z}} = \hat{\Omega} - \hat{\nu}_I - \frac{\hat{u}_L}{\hat{E}_L} \tag{3.7d}$$

Eq (3.7) is considerably simpler than the corresponding equation for the general laser. The field amplitudes are driven by the quadrature component of the polarization wave, while the phases are driven by the in-phase term. This is in contrast to the general laser case, in which both the amplitudes and phases of the electric fields are driven by the in-phase and quadrature components of the polarization wave. The mixing of the driving terms $\hat{u}_{R,L}$ and $\hat{v}_{R,L}$ in Eq (2.66) is caused by the phase factors $e^{i\xi_{R,L}}$ of the cylindrical/spherical waves.

Eqs (3.6) and (3.7) form the Maxwell-Bloch equations for the Fabry-Perot laser. As in the general laser case, the set of equations is composed of both "point" and "longitudinally varying" equations. Nonetheless, the equation set is self-consistent. In order to solve the equations numerically, expressions relating $\hat{P}'_{R,L}$ to $\hat{P}_{R,L}$ are required in Eq (3.6e).

The Equations of Motion in the REA

The Maxwell-Bloch equation set is quite complex. Solving the equations numerically would be prohibitive, both in terms of the numerical methods required and the computer costs. If the REA can be justified for the particular laser of interest, the equations of motion become much more manageable. For many practical applications, the REA equation set can be used with excellent results.

As with the Maxwell-Bloch equations, the derivation of the equations of motion in the REA follows that given in Chapter II almost exactly. The final set of normalized equations is:

$$\frac{\partial \hat{E}_R}{\partial \hat{t}} + \psi \frac{\partial \hat{E}_R}{\partial \hat{z}} = -\frac{\hat{E}_R}{\hat{\tau}_2} + \hat{w}_{eq}\left\{ \frac{\hat{E}_R}{1+(\Delta\hat{\omega}-\dot{\varphi}_R)^2} \frac{1}{\sqrt{A^2-B^2-C^2}} + \frac{\hat{E}_L}{1+(\Delta\hat{\omega}-\dot{\varphi}_L)^2}\left[1-\frac{A}{\sqrt{A^2-B^2-C^2}}\right]\left[\frac{B-C(\Delta\hat{\omega}-\dot{\varphi}_L)}{B^2+C^2}\right]\right\} \tag{3.8a}$$

$$\frac{\partial \phi_R}{\partial \hat{t}} + \psi \frac{\partial \phi_R}{\partial \hat{z}} = \hat{\Omega} - \hat{\nu}_I + \frac{\hat{w}_{eq}}{\hat{E}_R}\left\{ \frac{\hat{E}_R(\Delta\hat{\omega}-\dot{\varphi}_R)}{1+(\Delta\hat{\omega}-\dot{\varphi}_R)^2} \frac{1}{\sqrt{A^2-B^2-C^2}} + \frac{\hat{E}_L}{1+(\Delta\hat{\omega}-\dot{\varphi}_L)^2}\left[1-\frac{A}{\sqrt{A^2-B^2-C^2}}\right]\left[\frac{B(\Delta\hat{\omega}-\dot{\varphi}_L)+C}{B^2+C^2}\right]\right\} \tag{3.8b}$$

$$\frac{\partial \hat{E}_L}{\partial \hat{t}} - \psi \frac{\partial \hat{E}_L}{\partial \hat{z}} = -\frac{\hat{E}_L}{\hat{\tau}_2} + \hat{w}_{eq}\left\{ \frac{\hat{E}_L}{1+(\Delta\hat{\omega}-\dot{\varphi}_L)^2} \frac{1}{\sqrt{A^2-B^2-C^2}} + \frac{\hat{E}_R}{1+(\Delta\hat{\omega}-\dot{\varphi}_R)^2}\left[1-\frac{A}{\sqrt{A^2-B^2-C^2}}\right]\left[\frac{B+C(\Delta\hat{\omega}-\dot{\varphi}_R)}{B^2+C^2}\right]\right\} \tag{3.8c}$$

$$\frac{\partial \phi_L}{\partial \hat{t}} - \psi \frac{\partial \phi_L}{\partial \hat{z}} = \hat{\Omega} - \hat{\nu}_I + \frac{\hat{w}_{eq}}{\hat{E}_L}\left\{ \frac{\hat{E}_L(\Delta\hat{\omega}-\dot{\varphi}_L)}{1+(\Delta\hat{\omega}-\dot{\varphi}_L)^2} \frac{1}{\sqrt{A^2-B^2-C^2}} + \frac{\hat{E}_R}{1+(\Delta\hat{\omega}-\dot{\varphi}_R)^2}\left[1-\frac{A}{\sqrt{A^2-B^2-C^2}}\right]\left[\frac{B(\Delta\hat{\omega}-\dot{\varphi}_R)-C}{B^2+C^2}\right]\right\} \tag{3.8d}$$

$$A = 1 + \hat{\tau}_1\left\{ \frac{\hat{E}_R^2}{1+(\Delta\hat{\omega}-\dot{\varphi}_R)^2} + \frac{\hat{E}_L^2}{1+(\Delta\hat{\omega}-\dot{\varphi}_L)^2} \right\} \tag{3.9a}$$

$$B = \hat{\tau}_1 \hat{E}_R \hat{E}_L\left\{ \frac{1}{1+(\Delta\hat{\omega}-\dot{\varphi}_R)^2} + \frac{1}{1+(\Delta\hat{\omega}-\dot{\varphi}_L)^2} \right\} \tag{3.9b}$$

$$C = \hat{\tau}_1 \hat{E}_R \hat{E}_L \left\{ \frac{(\Delta\hat{\omega} - \dot{\varphi}_R)}{1 + (\Delta\hat{\omega} - \dot{\varphi}_R)^2} - \frac{(\Delta\hat{\omega} - \dot{\varphi}_L)}{1 + (\Delta\hat{\omega} - \dot{\varphi}_L)^2} \right\} \tag{3.9c}$$

Eqs (3.8) and (3.9) will be referred to as the traveling wave laser (TWL) model. This model is a considerable simplification over the full Maxwell-Bloch equation set. As with the general laser equations in the REA, Eq (3.8) has time derivatives of $\phi_{R,L}$ on the right-hand sides of all four equations. This created considerable stability problems when the equations were solved on the computer. However, under the appropriate boundary and initial conditions, numerically stable solutions of the equations can be calculated. This is discussed in Appendix B.

The Free-Running Laser at Steady-State

The TWL equations can be used to calculate the laser fields in a free-running laser (i.e., a laser without an injected signal). Often, only the steady-state values of the fields and frequencies are required. The TWL equations reduce to a simple form in this limit. The reduced equations and the appropriate boundary conditions are derived in this section.

The frequencies of the barecavity modes are given by Eq (2.57a), rewritten somewhat as:

$$\hat{\Omega} = \frac{nc}{2\gamma L} \tag{3.10}$$

where n is some large integer. The spacing between the barecavity modes is given in normalized units by $c/2\gamma L$. In a loaded cavity, the actual lasing frequency $\hat{\nu}$ is "pulled" closer to linecenter. This occurs because of the large index of refraction changes in a medium near an atomic resonance. The laser frequency $\hat{\nu}$ will only equal $\hat{\Omega}$ when the barecavity mode lies exactly at linecenter ($\hat{\Omega} = \hat{\omega}$). Figure 3.2 shows the relative locations of $\hat{\Omega}$, $\hat{\nu}$, $\hat{\omega}$, and the reference frequency $\hat{\nu}_I$.

Several frequency differences are required in the ensuing derivations:

$$\Delta\hat{m} \equiv \hat{\omega} - \hat{\Omega} \tag{3.11a}$$

$$\Delta\hat{t} \equiv \hat{\omega} - \hat{\nu} \tag{3.11b}$$

$$\Delta\hat{\omega} \equiv \hat{\omega} - \hat{\nu}_I \tag{3.11c}$$

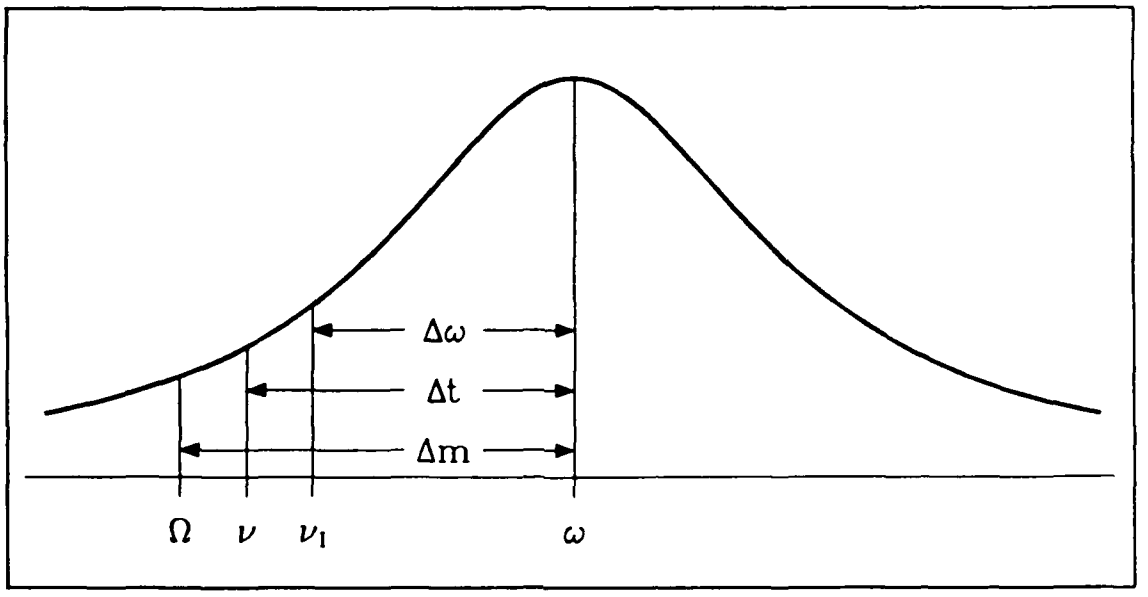

Figure 3.2. The atomic lineshape curve. Typical positions of the important frequencies are indicated.

These differences are positive if $\hat{\Omega}$, $\hat{\nu}$, and $\hat{\nu}_I$ lie to the left (low frequency side) of the atomic line center, and negative if the frequencies lie on the right or high frequency side of $\hat{\omega}$.

At steady-state, the laser frequency $\hat{\nu}$ is constant throughout the resonator. As a result:

$$\dot{\varphi}_R = \dot{\varphi}_L \equiv \dot{\varphi} \tag{3.12}$$

and:

$$\hat{\nu} = \hat{\nu}_I + \dot{\varphi}_R \tag{3.13a}$$

$$= \hat{\nu}_I + \dot{\varphi}_L \tag{3.13b}$$

$$= \hat{\nu}_I + \dot{\varphi} \tag{3.13c}$$

Notice that the time derivatives of $\phi_{R,L}$ do not go to zero at steady-state. They are merely constants, as $\hat{\nu}$ is fixed. Consequently, $\phi_{R,L}$ can vary linearly in time. The field amplitudes do not vary in time at steady-state, so that:

$$\frac{\partial \hat{E}_R}{\partial \hat{t}} = \frac{\partial \hat{E}_L}{\partial \hat{t}} = 0 \tag{3.14}$$

The TWL equations at steady-state can now be obtained. First, Eq (3.9) simplifies to:

$$A = 1 + \frac{\hat{\tau}_1(\hat{E}_R^2 + \hat{E}_L^2)}{1 + \Delta\hat{t}^2} \tag{3.15a}$$

$$B = \frac{2\hat{\tau}_1 \hat{E}_R \hat{E}_L}{1 + \Delta\hat{t}^2} \tag{3.15b}$$

$$C = 0 \tag{3.15c}$$

With a little algebra, Eqs (3.8a,c) can be written as:

$$\frac{\partial \hat{E}_R}{\partial \hat{z}} = \frac{1}{\psi}\left\{-\frac{\hat{E}_R}{\hat{\tau}_2} + \hat{w}_{eq}\left[\frac{\hat{E}_R}{(1+\Delta\hat{t}^2)\sqrt{A^2-B^2}} + \frac{1}{2\hat{\tau}_1\hat{E}_R}\left(1 - \frac{A}{\sqrt{A^2-B^2}}\right)\right]\right\} \tag{3.16a}$$

$$\frac{\partial \hat{E}_L}{\partial \hat{z}} = -\frac{1}{\psi}\left\{-\frac{\hat{E}_L}{\hat{\tau}_2} + \hat{w}_{eq}\left[\frac{\hat{E}_L}{(1+\Delta\hat{t}^2)\sqrt{A^2-B^2}} + \frac{1}{2\hat{\tau}_1\hat{E}_L}\left(1 - \frac{A}{\sqrt{A^2-B^2}}\right)\right]\right\} \tag{3.16b}$$

Eqs (3.8b,d) can be recast as:

$$\begin{aligned}\frac{\partial \phi_R}{\partial \hat{z}} &= \frac{1}{\psi}\Bigg\{\hat{\Omega} - (\hat{\nu}_I + \dot{\varphi}) \\ &\quad + \frac{\hat{w}_{eq}\Delta\hat{t}}{\hat{E}_R}\left[\frac{\hat{E}_R}{(1+\Delta\hat{t}^2)\sqrt{A^2-B^2}} + \frac{1}{2\hat{\tau}_1\hat{E}_R}\left(1 - \frac{A}{\sqrt{A^2-B^2}}\right)\right]\Bigg\} \\ &= \frac{1}{\psi}\left\{\Delta\hat{t} - \Delta\hat{m} + \frac{\hat{w}_{eq}\Delta\hat{t}}{\hat{E}_R}\left[\frac{\hat{E}_R}{(1+\Delta\hat{t}^2)\sqrt{A^2-B^2}} + \frac{1}{2\hat{\tau}_1\hat{E}_R}\left(1 - \frac{A}{\sqrt{A^2-B^2}}\right)\right]\right\}\end{aligned} \tag{3.16c}$$

$$\frac{\partial \phi_L}{\partial \hat{z}} = -\frac{1}{\psi}\left\{\Delta\hat{t} - \Delta\hat{m} + \frac{\hat{w}_{eq}\Delta\hat{t}}{\hat{E}_L}\left[\frac{\hat{E}_L}{(1+\Delta\hat{t}^2)\sqrt{A^2-B^2}} + \frac{1}{2\hat{\tau}_1\hat{E}_L}\left(1 - \frac{A}{\sqrt{A^2-B^2}}\right)\right]\right\} \tag{3.16d}$$

If the lasing frequency $\hat{\nu}$, and thus $\Delta\hat{t}$, is known *a priori*, Eqs (3.16a,b) can be used immediately to calculate the electric fields inside the laser. However, if $\hat{\nu}$ is unknown, all four equations are required in a calculation. Notice that the medium can cause the phases of the fields to vary spatially. These variations produce small frequency shifts in the output beam.

The boundary conditions can be obtained by considering Figure 3.3. Eqs (3.1) and (3.3) can be combined at mirror A to yield:

$$E_R(0)e^{-i\left[\nu_I t - kz + \phi_R(0)\right]} = r_A e^{i\phi_{RA}} E_L(0)e^{-i\left[\nu_I t + kz + \phi_L(0)\right]}$$

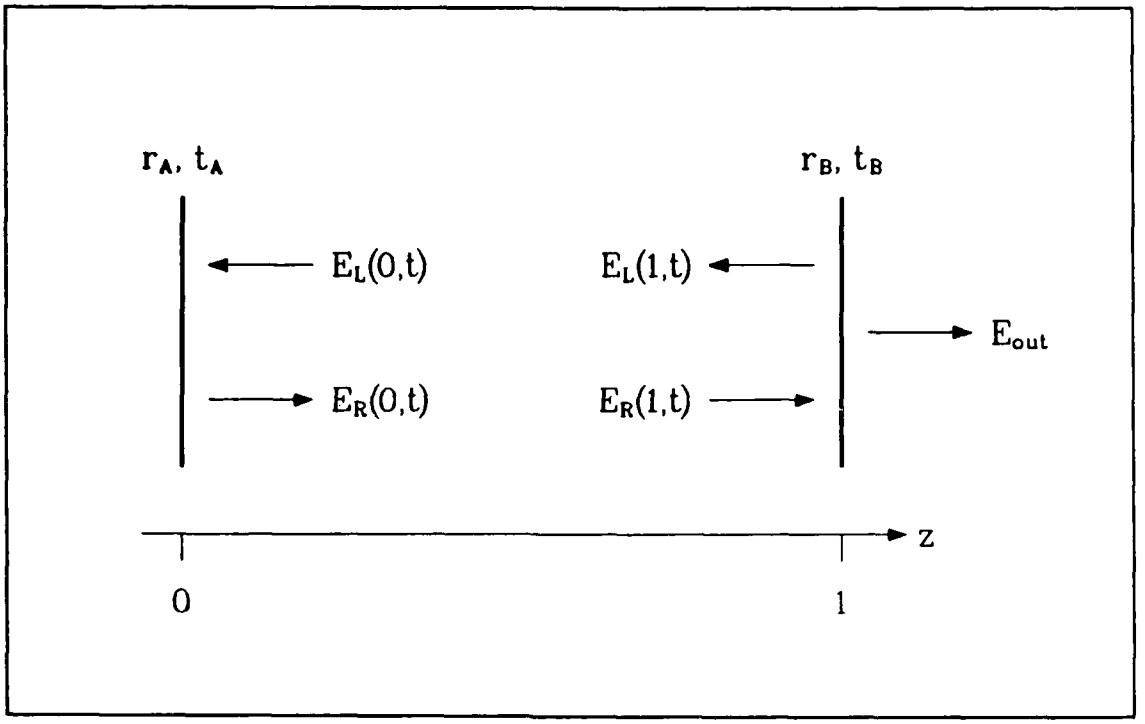

Figure 3.3. The boundary conditions for the free-running laser.

or, after simplifying and normalizing:

$$\hat{E}_R(0)e^{-i\phi_R(0)} = r_A\hat{E}_L(0)e^{-i\left[\phi_L(0)-\phi_{RA}\right]}$$

The time dependencies of $\hat{E}_{R,L}$ and $\phi_{R,L}$ are not explicitly indicated, as the laser is at steady-state. After separating the amplitudes and phases, the boundary condition at mirror A is given by:

$$\hat{E}_R(0) = r_A\hat{E}_L(0) \tag{3.17a}$$

$$\phi_R(0) = \phi_L(0) - \phi_{RA} \tag{3.17b}$$

In a typical laser, one of the mirrors is perfectly reflective so that energy is extracted from only one end of the resonator. This convention was adopted for this research. Mirror A is assumed to be perfectly reflective ($r_A = -1$), which results in the following boundary condition:

$$\hat{E}_R(0) = \hat{E}_L(0) \tag{3.18a}$$

$$\phi_R(0) = \phi_L(0) \quad \pi \tag{3.18b}$$

The boundary condition at mirror B is found in a similar manner. After some simple algebra:

$$\hat{E}_L(1) = r_B \hat{E}_R(1) \tag{3.19a}$$

$$\phi_L(1) = \phi_R(1) - 2kL - \phi_{RB} \tag{3.19b}$$

If the reference frequency $\hat{\nu}_I$ is equal to the actual lasing frequency $\hat{\nu}$, then $2kL$ is equal to $2m\pi$, where m is some integer. Then, in a round trip, the total change in phase due to $\phi_{R,L}$ will exactly equal the phase added in by the mirrors. If $\phi_{RA} + \phi_{RB} = 2\pi$, then the additional phase due to ϕ_R will exactly cancel that added in by ϕ_L across the whole of the resonator. On the other hand, if $\hat{\nu}_I$ is not equal to $\hat{\nu}$, then $2kL$ will not be an integral multiple of 2π. The total phase change in a round trip will not be an integral multiple of 2π, indicating that the reference frequency $\hat{\nu}_I$ is not the actual lasing frequency.

The phase equations and the boundary conditions thus describe a phase "error", due to operation away from the actual laser frequency $\hat{\nu}$. If the phase error at $\hat{\nu}_I$ is calculated, then $\hat{\nu}$ can be determined. A numerical algorithm for calculating $\hat{\nu}$ is described in Appendix B, based on the above discussion.

Mirror B is assumed to be partially transmissive, so the outcoupling occurs through this mirror. The radiated field is given by:

$$\hat{\mathbf{E}}_{out} = t_B e^{i\phi_{TB}} \hat{E}_R(1) e^{-i\left[\hat{\nu}_I t - kL + \phi_R(1)\right]} \tag{3.20}$$

The relationship between the transmission and reflection coefficients is discussed more fully in Appendix A.

The Injected Laser at Steady-State

The TWL equations reduce to a very simple form in the injected laser case. This set of equations is quite similar to the free-running laser equations. The injected field is incorporated as one of the boundary conditions. Before deriving the equations of motion and the boundary conditions, the underlying physical processes involved in injection locking must be discussed.

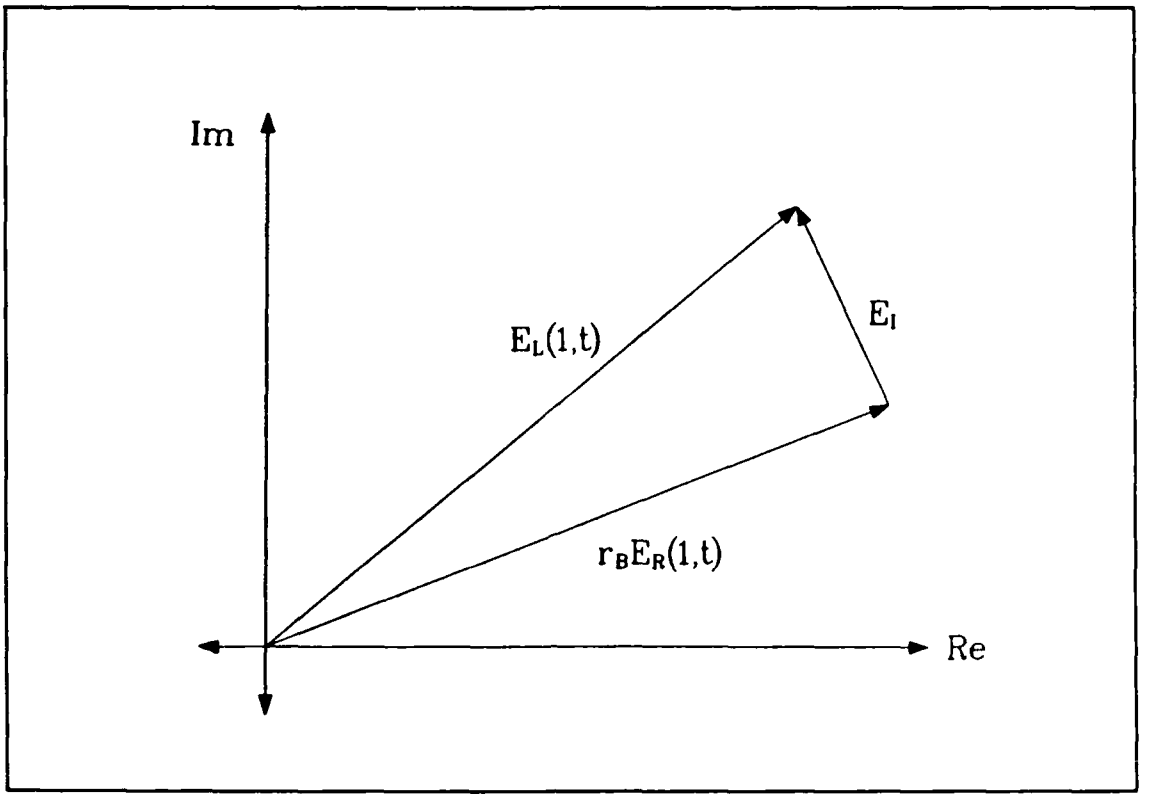

Figure 3.4. The phasor relationship at mirror B with an injected field.

For the purposes of this research project, the injected Fabry-Perot laser is assumed to have one perfectly reflective mirror (mirror A) and one partially transmissive mirror (mirror B). Injection is accomplished through the partially transmissive mirror, as is the outcoupling. The general schematic of the laser is given in Figure 1.2a.

Injection locking can be very easily understood if the electric fields are thought of as phasors. In the free-running case, a phasor ($\hat{\mathbf{E}}_L$) is launched from mirror B in the $-\hat{z}$ direction. After a round trip, the resultant phasor must be exactly the same as the initially launched field. This round trip condition fixes the frequency $\hat{\nu}$ of the free-running laser. The situation is somewhat different in the injected case. The laser is forced to operate at the nonresonant frequency $\hat{\nu}_I$ of the injected signal. Consequently, the initially launched phasor will not return upon itself in a round trip. However, if the vector sum of the field after the round trip plus the injected field exactly equals the initial phasor,

the round trip condition is once again satisfied. This is illustrated in Figure 3.4. The injected field required to lock the laser is the field that "closes" the vector triangle. In this manner, the laser can operate at a nonresonant frequency, yet still satisfy the round trip condition.

The injected field just inside mirror B is given by:

$$\hat{\mathbf{E}}_I(1,\hat{t}) = \hat{E}_I e^{-i(\hat{\nu}_I \hat{t} + kL + \phi_I)} \tag{3.21}$$

The phase of one of the three electric fields is arbitrary and can be set to any desired value. For simplicity, ϕ_I is selected and set equal to zero. If $\hat{\mathbf{E}}_{IN}$ denotes the injected field external to the slave laser, then clearly:

$$\hat{\mathbf{E}}_{IN} = \frac{\hat{E}_I e^{-i(\hat{\nu}_I \hat{t} + kz)}}{t_B e^{i\phi_{TB}}} \tag{3.22}$$

Notice that the amplitude of the injected field does not vary spatially or temporally.

Since $\hat{\nu}_I$ is the frequency of the fields inside the laser, the time derivatives of $\hat{E}_{R,L}$ and $\phi_{R,L}$ are identically zero at steady-state. This creates a significant reduction in complexity in the TWL equations. First, Eq (3.9) reduces to:

$$A = 1 + \frac{\hat{\tau}_1(\hat{E}_R^2 + \hat{E}_L^2)}{1 + \Delta\hat{\omega}^2} \tag{3.23a}$$

$$B = \frac{2\hat{\tau}_1 \hat{E}_R \hat{E}_L}{1 + \Delta\hat{\omega}^2} \tag{3.23b}$$

$$C = 0 \tag{3.23c}$$

Then, Eq (3.8) becomes:

$$\frac{\partial \hat{E}_R}{\partial \hat{z}} = \frac{1}{\psi}\left\{-\frac{\hat{E}_R}{\hat{\tau}_2} + \hat{w}_{eq}\left[\frac{\hat{E}_R}{(1+\Delta\hat{\omega}^2)\sqrt{A^2 - B^2}} + \frac{1}{2\hat{\tau}_1 \hat{E}_R}\left(1 - \frac{A}{\sqrt{A^2 - B^2}}\right)\right]\right\} \tag{3.24a}$$

$$\frac{\partial \hat{E}_L}{\partial \hat{z}} = -\frac{1}{\psi}\left\{-\frac{\hat{E}_L}{\hat{\tau}_2} + \hat{w}_{eq}\left[\frac{\hat{E}_L}{(1+\Delta\hat{\omega}^2)\sqrt{A^2 - B^2}} + \frac{1}{2\hat{\tau}_1 \hat{E}_L}\left(1 - \frac{A}{\sqrt{A^2 - B^2}}\right)\right]\right\} \tag{3.24b}$$

$$\frac{\partial \phi_R}{\partial \hat{z}} = \frac{1}{\psi}\left\{\hat{\Omega} - \hat{\nu}_I + \frac{\hat{w}_{eq}\Delta\hat{\omega}}{\hat{E}_R}\left[\frac{\hat{E}_R}{(1+\Delta\hat{\omega}^2)\sqrt{A^2 - B^2}} + \frac{1}{2\hat{\tau}_1 \hat{E}_R}\left(1 - \frac{A}{\sqrt{A^2 - B^2}}\right)\right]\right\} \tag{3.24c}$$

$$\frac{\partial \phi_L}{\partial \hat{z}} = -\frac{1}{\psi}\left\{\hat{\Omega} - \hat{\nu}_I + \frac{\hat{w}_{eq}\Delta\hat{\omega}}{\hat{E}_L}\left[\frac{\hat{E}_L}{(1+\Delta\hat{\omega}^2)\sqrt{A^2 - B^2}} + \frac{1}{2\hat{\tau}_1 \hat{E}_L}\left(1 - \frac{A}{\sqrt{A^2 - B^2}}\right)\right]\right\} \tag{3.24d}$$

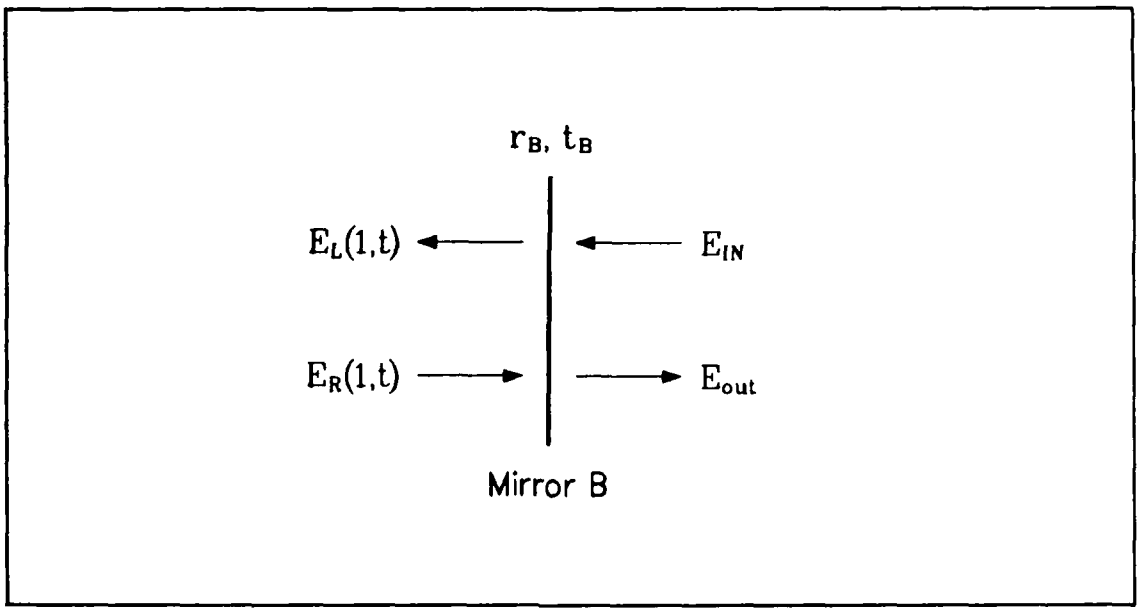

Figure 3.5. The boundary condition at mirror B.

Eqs (3.23) and (3.24) are quite similar in form to Eqs (3.15) and (3.16). The main difference lies in the frequency terms. Notice that $\hat{\Omega} - \hat{\nu}_I = \Delta\hat{\omega} - \Delta\hat{m}$.

Since mirror A is totally reflective, its boundary condition is given by Eq (3.18):

$$\hat{E}_R(0) = \hat{E}_L(0) \tag{3.18a}$$

$$\phi_R(0) = \phi_L(0) - \pi \tag{3.18b}$$

Referring to Figure 3.5, the boundary condition at mirror B can be written as:

$$r_B e^{i\phi_{RB}} E_R(L) e^{-i\left[\nu_I t - kL + \phi_R(L)\right]} + E_I e^{-i(\nu_I t + kL)} = E_L(L) e^{-i\left[\nu_I t + kL + \phi_L(L)\right]}$$

or, after canceling some of the exponential terms and normalizing:

$$r_B \hat{E}_R(1) e^{-i\left[\phi_R(1) - 2kL - \phi_{RB}\right]} + \hat{E}_I = \hat{E}_L(1) e^{-i\phi_L(1)} \tag{3.25}$$

Eq (3.25) cannot be separated into a pair of amplitude and phase equations. It must be solved as a vector equation.

The $2kL$ term must be accounted for in the boundary condition. Generally, the injected signal $\hat{\nu}_I$ will not coincide with $\hat{\nu}$. $2kL$ will be of the form:

$$2kL = 2m\pi + \hat{\vartheta}, \qquad m = 0, 1, 2, \ldots \tag{3.26}$$

where $\hat{\vartheta}$ is some fractional term in the range $(-\pi, \pi]$. As the frequency of the laser changes from one longitudinal mode to the next, $2kL$ changes by 2π. Referring to Figure 3.2, the phase offset $\hat{\vartheta}$ is approximately:

$$\frac{\hat{\vartheta}}{2\pi} \approx \frac{\hat{\nu}_I - \hat{\nu}}{(c/2\gamma L)}$$

so that:

$$\hat{\vartheta} \approx 2\pi\hat{\tau}_3(\hat{\nu}_I - \hat{\nu}) \tag{3.27a}$$

where $\hat{\tau}_3 = 2\gamma L/c$ is the normalized round trip time inside the cavity (inverse of the barecavity longitudinal mode spacing). Notice that Eq (3.27a) is only an approximation, as the actual longitudinal mode spacing will not equal $c/2\gamma L$ if the mode pushing and pulling effects are taken into account. Using the loaded cavity longitudinal mode separation expression, Eq (7.5c), the phase offset can be written exactly as:

$$\hat{\vartheta} \equiv 2\pi\hat{\tau}_3(\Delta\hat{t} - \Delta\hat{\omega})\left[1 + \frac{1}{\hat{\tau}_2} - \frac{1}{\hat{\tau}_3\hat{L}_g}\ln r_A r_B\right] \tag{3.27b}$$

The boundary condition at mirror B can now be written in its final form:

$$r_B\hat{E}_R(1)e^{-i\left[\phi_R(1) - \hat{\vartheta} - \phi_{RB}\right]} + \hat{E}_I = \hat{E}_L(1)e^{-i\phi_L(1)} \tag{3.28}$$

An overall "system" gain can be defined by examining Figure 3.5. This gain is the total field radiated from the laser divided by the injected field:

$$g_1 = \frac{\mathbf{t}_B\hat{\mathbf{E}}_R(1) + \mathbf{r}_B\hat{\mathbf{E}}_{IN}(1)}{\hat{\mathbf{E}}_{IN}(1)}$$

$$= \frac{t_B^2\hat{E}_R e^{-i(\phi_R - \hat{\vartheta} + \phi_{RB} - 2\phi_{TB})} + r_B\hat{E}_I}{\hat{E}_I} \tag{3.29}$$

The intensity gain is a somewhat more useful quantity; it is given by:

$$G_1 = g_1^* g_1$$

$$= \frac{1}{\hat{E}_I^2}\left[(1-r_B^2)^2\hat{E}_R^2 + r_B^2\hat{E}_I^2 + 2r_B(1-r_B^2)\hat{E}_I\hat{E}_R\cos(\phi_R - \hat{\vartheta} + \phi_{RB} - 2\phi_{TB})\right] \quad (3.30)$$

If the injected intensity is much smaller than the outcoupled radiation from the slave laser, G_1 will indicate the relative power required for locking. Experimentally measured system gains of up to 10^8 have been reported in the literature (40).

A second gain G_2 can be defined as:

$$G_2 = \frac{\hat{E}_L^2(1)}{\hat{E}_I^2} \quad (3.31)$$

G_2 is the ratio of the intensity of the phasor launched from mirror B and the internal injected intensity required for locking. It is indicative of the relative sizes of the internal laser intensities and the required injected intensities. G_2 is always greater than or equal to unity.

Summary

The semiclassical equations for the Fabry-Perot laser were described in this chapter. Both the Maxwell-Bloch set and the TWL equations were given. The derivations of these sets parallel the detailed derivations given in Chapter II. The TWL equations were reduced in two special cases: the free-running laser at steady-state and the injection locked laser at steady-state. The appropriate boundary conditions for each case were given. A system gain G_1 and an internal intensity gain G_2 were defined.

IV. Comparisons of the TWL Model to Other Theories

Many models have been developed to describe the operation of a laser. Among the theories published in the literature are the simple saturable gain model and the semiclassical model, described briefly in the first chapter. Both formalisms have been used to model free-running and injected lasers.

The semiclassical theory of the Fabry-Perot laser developed in the previous chapter is compared to six different models in this chapter. In the appropriate limits, the theory is shown to reduce to the other models. The lasing thresholds, free-running frequencies, and system gains of the various models are given, where appropriate. The first three sections compare the TWL theory to three different free-running laser models: the simple saturable gain model, the model of Agrawal and Lax (142, 143), and Lamb's semiclassical theory (134, 135). The TWL theory is then compared to the free-running and injected laser theories of Spencer and Lamb (101), the injected laser model of Chow (82, 83), and Ferguson's model of the injected laser (87, 88). The final section summarizes the chapter.

The Simple Saturable Gain Model

The simple saturable gain model, also referred to as the g_0-I_{sat} model, was introduced in Chapter I. A slightly expanded form of the theory can be written as (123):

$$\frac{dI_R}{d\hat{z}} = (G_0 - \alpha_0 L) I_R \tag{4.1a}$$

$$\frac{dI_L}{d\hat{z}} = -(G_0 - \alpha_0 L) I_L \tag{4.1b}$$

$$G_0 = \frac{g_0 L}{\left[1 + \frac{I_R + I_L}{I_{sat}}\right]^{\epsilon}} \tag{4.1c}$$

where

$$\epsilon = \begin{cases} \frac{1}{2} & \text{inhomogeneous broadening} \\ 1 & \text{homogeneous broadening} \end{cases} \tag{4.1d}$$

As only homogeneous broadening is of interest, ϵ will be set equal to unity in the following. The intensity terms in the denominator of Eq (4.1c) account for the saturation of the gain in the presence of an electric field. The L terms on the right-hand sides of Eq (4.1) are due to the length normalizations.

At very low pumping levels, $I_{R,L} \ll 1$. The first term in the denominator of Eq (4.1c) is the dominant term. The simple saturable gain model reduces to:

$$\frac{dI_R}{d\hat{z}} = (g_0 L - \alpha_0 L) I_R \tag{4.2a}$$

$$\frac{dI_L}{d\hat{z}} = -(g_0 L - \alpha_0 L) I_L \tag{4.2b}$$

The gain is exponential in this case. This limit can be applied to the region near the lasing threshold. In the opposite extreme of hard pumping, the intensity terms dominate the denominator. The gain is linear in this limit.

Despite its widespread use to calculate internal laser fields, output powers, and extraction efficiencies, the simple saturable gain model suffers from a serious deficiency: spatial hole burning is not accounted for. Spatial hole burning is an effect due to the interference of the leftward and rightward traveling waves in the gain medium. It is most easily understood in the context of a standing wave laser.

In the general laser device, there are two counterpropagating electric fields. If the outcoupling is very low (the standing wave laser limit), the two waves interfere with each other and form a standing wave inside the cavity. Over a half wavelength of the radiation, the standing wave changes from a null to a peak value to second null. In the peak intensity regions, the fields saturate the gain and depress the population inversion density. In the region about the nulls in the standing wave pattern, the inversion density is not depressed and the gain remains at its unsaturated value g_0. A series of "spatial holes" are thus "burned" into the population inversion density. This is illustrated in Figure 4.1. These holes, when spatially averaged, cause the overall gain of the device to be lower than the small signal gain g_0. The simple saturable gain model does not include the interference

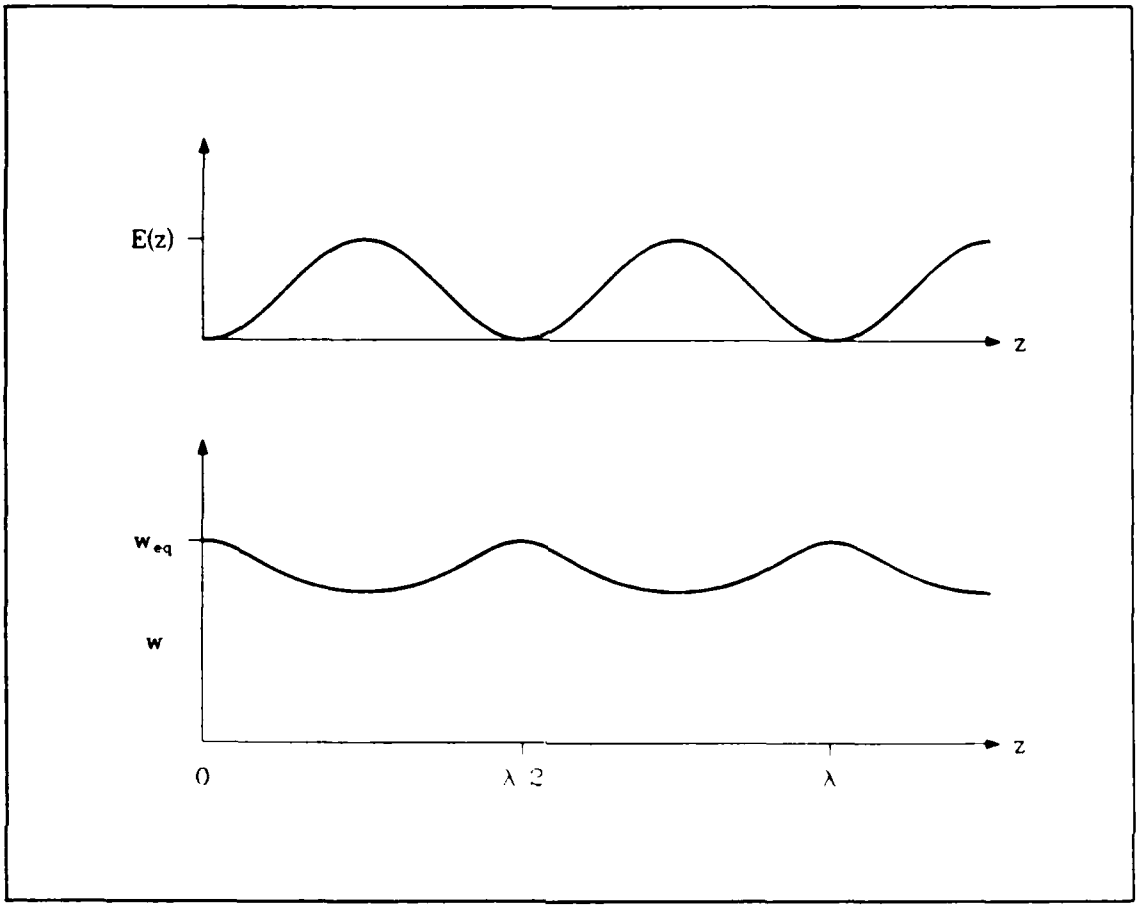

Figure 4.1. Spatial hole burning. The upper plot illustrates the standing wave electric field; the lower plot is the population inversion density.

effects of the traveling waves on the gain medium. The spatial holes are not burned into the inversion density, and the gain remains fixed at the small signal value g_0. As a result, the simple saturable gain model overestimates the gain and predicts higher field levels inside the laser than those that actually exist.

The TWL theory of Chapter III correctly accounts for spatial hole burning. In the derivation of the general laser theory (Chapter II), the interference of the two traveling waves can be clearly seen in Eq (2.76). The explicit $\hat{z}$ dependencies are averaged out in the integrations of Eq (2.35)

However, the overall effect of lowering the gain due to the interference of the traveling waves is properly incorporated into the semiclassical theory.

Near the lasing threshold, the intensities of the traveling waves are very small. The peak field amplitude of the interference pattern created by the waves is correspondingly small. The lowering of the gain due to spatial hole burning is minimized in this operating region. The TWL model should therefore reduce to the simple saturable gain theory in near threshold operation. This hypothesis can be tested by simplifying Eqs (3.8) and (3.9) under the assumption that $\hat{E}_{R,L}$ are very small.

Examining the TWL equation for $\hat{E}_R$ (Eq (3.8a)), the medium gain is given by the term:

$$\text{gain term} \propto \hat{w}_{eq}\left\{\frac{\hat{E}_R}{1+(\Delta\hat{\omega}-\dot{\phi}_R)^2}\frac{1}{\sqrt{A^2-B^2-C^2}}\right.$$
$$\left.+\frac{\hat{E}_L}{1+(\Delta\hat{\omega}-\dot{\phi}_L)^2}\left[1-\frac{A}{\sqrt{A^2-B^2-C^2}}\right]\left[\frac{B-C(\Delta\hat{\omega}-\dot{\phi}_L)}{B^2+C^2}\right]\right\} \tag{4.3}$$

The argument of the square roots can be expanded as (cf. Eq (2.84)):

$$A^2+B^2+C^2 = 1+2\hat{r}_1\left\{\frac{\hat{E}_R^2}{1+(\Delta\hat{\omega}-\dot{\phi}_R)^2}+\frac{\hat{E}_L^2}{1+(\Delta\hat{\omega}-\dot{\phi}_L)^2}\right\}$$
$$+\hat{r}_1^2\left\{\frac{\hat{E}_R^2}{1+(\Delta\hat{\omega}-\dot{\phi}_R)^2}+\frac{\hat{E}_L^2}{1+(\Delta\hat{\omega}-\dot{\phi}_L)^2}\right\}^2$$
$$+\frac{\hat{r}_1^2\hat{E}_R^2\hat{E}_L^2(\dot{\phi}_L-\dot{\phi}_R)^2}{\left[1+(\Delta\hat{\omega}-\dot{\phi}_R)^2\right]\left[1+(\Delta\hat{\omega}-\dot{\phi}_L)^2\right]} \tag{4.4}$$

If the fields are so small that $\hat{E}_{R,L}\ll 1$, then the terms of greater than second order in the fields can be neglected in Eq (4.4). The equation then reduces to:

$$A^2+B^2+C^2 \approx 1+2\hat{r}_1\left\{\frac{\hat{E}_R^2}{1+(\Delta\hat{\omega}-\dot{\phi}_R)^2}+\frac{\hat{E}_L^2}{1+(\Delta\hat{\omega}-\dot{\phi}_L)^2}\right\}$$
$$\equiv 1+\zeta \tag{4.5}$$

where $\zeta\ll 1$. Using the binomial series expansion, the square root term can be written as:

$$(A^2+B^2+C^2)^{1/2} = 1+\frac{1}{2}\zeta+\frac{3}{8}\zeta^2+\cdots$$
$$\approx 1+\hat{r}_1\left\{\frac{\hat{E}_R^2}{1+(\Delta\hat{\omega}-\dot{\phi}_R)^2}+\frac{\hat{E}_L^2}{1+(\Delta\hat{\omega}-\dot{\phi}_L)^2}\right\} \tag{4.6}$$

Using Eq (4.6) in (4.3) and again neglecting the terms of greater than second order in the electric fields, the gain term can be expressed as:

$$\text{gain term} \approx \frac{\hat{w}_{eq}\hat{E}_R}{1+\left(\Delta\hat{\omega}-\dot{\varphi}_R\right)^2} \tag{4.7}$$

This expression for the gain can be combined with Eq (3.8a) to yield the near threshold equation for $\hat{E}_R$:

$$\frac{\partial\hat{E}_R}{\partial\hat{t}}+\psi\frac{\partial\hat{E}_R}{\partial\hat{z}}=\left\{-\frac{1}{\hat{\tau}_2}+\frac{\hat{w}_{eq}}{1+\left(\Delta\hat{\omega}-\dot{\varphi}_R\right)^2}\right\}\hat{E}_R \tag{4.8}$$

Finally, taking Eq (4.8) to the steady-state, and multiplying both sides by $\hat{E}_R$, the intensity equation for the rightward traveling wave is obtained:

$$\frac{\partial I_R}{\partial\hat{z}}=\left\{-\frac{\hat{\tau}_3}{\hat{\tau}_2}+\frac{\hat{\tau}_3\hat{w}_{eq}}{1+\Delta\hat{t}^2}\right\}I_R \tag{4.9a}$$

where $I_R=\hat{E}_R^2$.

In a similar manner, the equation for I_L can be obtained from Eq (3.8c):

$$\frac{\partial I_L}{\partial\hat{z}}=-\left\{-\frac{\hat{\tau}_3}{\hat{\tau}_2}+\frac{\hat{\tau}_3\hat{w}_{eq}}{1+\Delta\hat{t}^2}\right\}I_L \tag{4.9b}$$

where $I_L=\hat{E}_L^2$.

Eq (4.9) has exactly the same form as Eq (4.2), if the following identifications are made:

$$g_0L=\frac{\hat{\tau}_3\hat{w}_{eq}}{1+\Delta\hat{t}^2} \tag{4.10a}$$

$$\alpha_0L=\frac{\hat{\tau}_3}{\hat{\tau}_2} \tag{4.10b}$$

Consequently, the TWL theory reduces to the simple saturable gain model in the limit of operation very close to the lasing threshold.

In order to complete the comparison between the two models, an expression for I_{sat} must be derived. This expression can be obtained by considering the limiting case in which $\hat{E}_L \rightarrow 0$ (the single pass amplifier). Considering Eq (3.9) of the TWL theory:

$$A\Big|_{\hat{E}_L \rightarrow 0} \rightarrow 1 + \frac{\hat{\tau}_1 \hat{E}_R^2}{1 + (\Delta\hat{\omega} - \dot{\varphi}_R)} \tag{4.11a}$$

$$B\Big|_{\hat{E}_L \rightarrow 0} \rightarrow 0 \tag{4.11b}$$

$$C\Big|_{\hat{E}_L \rightarrow 0} \rightarrow 0 \tag{4.11c}$$

Using Eq (4.11) in (3.8a), taking the resultant expression to steady-state and converting it the corresponding intensity equation yields:

$$\frac{\partial I_R}{\partial \hat{z}} = -\frac{\hat{\tau}_3}{\hat{\tau}_2} I_R + \left(\frac{\hat{\tau}_3 \hat{w}_{eq}}{1 + \Delta\hat{t}^2}\right)\left(1 + \frac{\hat{\tau}_1 I_R}{1 + \Delta\hat{t}^2}\right)^{-1} I_R$$

$$= \left\{ \frac{g_0 L}{1 + \left(\frac{\hat{\tau}_1 I_R}{1 + \Delta\hat{t}^2}\right)} - \alpha_0 L \right\} I_R \tag{4.12}$$

A similar relationship can be obtained from Eq (4.1a), if $I_L \rightarrow 0$:

$$\frac{dI_R}{d\hat{z}} = \left\{ \frac{g_0 L}{1 + \frac{I_R}{I_{sat}}} - \alpha_0 L \right\} I_R \tag{4.13}$$

Comparing Eqs (4.12) and (4.13) shows that:

$$I_{sat} = \frac{1 + \Delta\hat{t}^2}{\hat{\tau}_1} \tag{4.14}$$

I_{sat} increases as the frequency $\hat{\nu}$ of the laser moves away from linecenter. This makes sense physically, in light of the following argument. As the frequency $\hat{\nu}$ moves off linecenter, the stimulated emission cross section of the atom decreases, making it less probable that a given atom will undergo a

stimulated transition. The intensity required to saturate the medium should therefore increase as $\hat{\nu}$ moves away from $\hat{\omega}$. Additionally, Eq (2.134) of (145) shows that:

$$I_{sat} \propto \frac{1}{\sigma_a} \tag{4.15}$$

where σ_a is the stimulated emission cross section. Consequently, I_{sat} will increase as $\hat{\nu}$ departs from linecenter.

Since the TWL theory reduces to the simple saturable gain model near threshold, both models will exhibit the same threshold laser gain. An expression that describes the threshold inversion density required for the laser to operate can easily be derived. Eq (6.1-8) of (146) defines the threshold gain as:

$$g_0 L_g\Big|_{th} = \alpha_0 L_g - \ln r_A r_B \tag{4.16}$$

where L_g is the length of the gain medium (unnormalized units). Using Eqs (4.10) and letting $r_A = 1$ yields the threshold inversion density:

$$\hat{w}_{eq}\Big|_{th} = (1 + \Delta\hat{t}^2)\left[\frac{1}{\hat{\tau}_2} - \frac{1}{\hat{\tau}_3 \hat{L}_g} \ln r_B\right] \tag{4.17a}$$

where:

$$\hat{L}_g \equiv \frac{L_g}{L} \tag{4.17b}$$

Since $\hat{w}_{eq}$ is proportional to the zero field inversion density, $\hat{w}_{eq}\Big|_{th}$ is proportional to the threshold inversion required for lasing. A second useful quantity is the value of r_B for which the laser is at threshold for a fixed pump rate ($\hat{w}_{eq}$). This quantity can be found by inverting Eq (4.17a):

$$r_B\Big|_{th} = \exp\left[\hat{\tau}_3 \hat{L}_g \left(\frac{1}{\hat{\tau}_2} - \frac{\hat{w}_{eq}}{1 + \Delta\hat{t}^2}\right)\right] \tag{4.17c}$$

The Agrawal-Lax Theory

A limitation of the simple saturable gain model is that spatial hole burning is not modeled. Agrawal and Lax (142, 143) recognized this problem, and derived a steady-state theory of the laser that does incorporate the interference effects of the two traveling waves. In their theory, the electric field inside the laser is assumed to be composed of an infinite series of plane, traveling waves:

$$E = \sum_{n\ odd} E_n e^{inkz} \tag{4.18}$$

Substituting this expression for the field and a quantum-mechanically derived gain expression into the Helmholtz equation yields an infinite set of coupled equations describing the spatial evolution of the coefficients E_n. By neglecting the transverse field variations, selecting only the lowest order pair of traveling waves, and converting the field amplitude expressions into intensity expressions, a final pair of equations is obtained:

$$\frac{dI'_R}{d\tilde{z}} = \frac{g_3 L}{\sqrt{a^2 - b^2}} \left(1 - \frac{a - \sqrt{a^2 - b^2}}{2I'_R}\right) I'_R \tag{4.19a}$$

$$\frac{dI'_L}{d\tilde{z}} = -\frac{g_3 L}{\sqrt{a^2 - b^2}} \left(1 - \frac{a - \sqrt{a^2 - b^2}}{2I'_L}\right) I'_L \tag{4.19b}$$

where:

$$a = 1 + \Delta\tilde{t}^2 + I'_R + I'_L \tag{4.20a}$$

$$b = 2\sqrt{I'_R I'_L} \tag{4.20b}$$

$$g_3 = \frac{n\mu^2\nu}{\sqrt{k_l}\hbar\gamma\epsilon_0 c} \left(\frac{\lambda_a}{\gamma_a} - \frac{\lambda_b}{\gamma_b}\right) \tag{4.20c}$$

n is the atomic density and $k_l = k^2c^2/\nu^2$ is the linear dielectric constant. The nonsaturable medium losses are ignored in Eqs (4.19), but can be easily introduced.

The Agrawal-Lax equation set is identically the same as the TWL equation set at steady-state. This is easily demonstrated. Starting with Eq (3.16a) and ignoring the losses of the medium yields:

$$\frac{\partial \hat{E}_R}{\partial \hat{z}} = \frac{\hat{w}_{eq}}{\psi}\left\{\frac{\hat{E}_R}{(1+\Delta\hat{t}^2)\sqrt{A^2-B^2}} + \frac{1}{2\hat{\tau}_1\hat{E}_R}\left(1-\frac{A}{\sqrt{A^2-B^2}}\right)\right\}$$

$$= \frac{\hat{w}_{eq}}{\psi\sqrt{(1+\Delta\hat{t}^2)^2(A^2-B^2)}}\left\{1-\frac{A(1-\Delta\hat{t}^2)-\sqrt{(1-\Delta\hat{t}^2)^2(A^2-B^2)}}{2\hat{\tau}_1\hat{E}_R^2}\right\}\hat{E}_R \qquad (4.21)$$

With the definitions:

$$I'_R \equiv \hat{\tau}_1\hat{E}_R^2 \qquad (4.22a)$$

$$I'_L \equiv \hat{\tau}_1\hat{E}_L^2 \qquad (4.22b)$$

and Eq (3.15), the following identifications can be made:

$$a = A(1+\Delta\hat{t}^2) \qquad (4.23a)$$

$$b = B(1+\Delta\hat{t}^2) \qquad (4.23b)$$

The definitions in Chapter II can be used to demonstrate that:

$$g_3 L = \frac{2\hat{w}_{eq}}{\psi} \qquad (4.24)$$

Finally, converting Eq (4.21) into its intensity form and using Eqs (4.22) and (4.23), an expression for I'_R is obtained:

$$\frac{\partial I'_R}{\partial \hat{z}} = \frac{g_3 L}{\sqrt{a^2-b^2}}\left\{1-\frac{a-\sqrt{a^2-b^2}}{2I'_R}\right\}I'_R \qquad (4.25)$$

This is exactly the same expression as Eq (4.19a). In an identical manner, Eq (3.16b) can be shown to be equivalent to Eq (4.19b).

The intensity form of the TWL equation set at steady-state is thus the same as the Agrawal-Lax equations. The Agrawal-Lax set cannot be used to determine the lasing frequency ν, unlike the TWL equations in steady-state. It is interesting to note that once the gain g_3 is obtained from quantum mechanics, the Agrawal-Lax derivation is somewhat similar to the TWL equation set derivation.

Agrawal and Lax point out that the interference effects are contained in the term b (B in the TWL equation set). By setting B to zero, the effects of the spatial hole burning disappear, and the TWL equation set reduces to the simple saturable gain equations. In this limit, Eq (3.16a) becomes:

$$\frac{\partial \hat{E}_R}{\partial \hat{z}} = \frac{1}{\psi}\left\{ -\frac{\hat{E}_R}{\hat{\tau}_2} + \hat{w}_{eq}\left[\frac{\hat{E}_R}{A(1+\Delta\hat{t}^2)} + \frac{1}{2\hat{\tau}_1 \hat{E}_R}\left(1 - \frac{A}{A}\right)\right]\right\}$$

$$= \frac{1}{\psi}\left\{ -\frac{1}{\hat{\tau}_2} + \frac{\hat{w}_{eq}/(1+\Delta\hat{t}^2)}{1 + \frac{\hat{\tau}_1}{1+\Delta\hat{t}^2}(I_R + I_L)}\right\}\hat{E}_R$$

Converting this equation to the intensity form and using Eqs (4.10) and (4.14) finally gives:

$$\frac{\partial I_R}{\partial \hat{z}} = \left\{ \frac{g_0 L}{1 + \frac{I_R + I_L}{I_{sat}}} - \alpha_0 L \right\} I_R \tag{4.26}$$

Eq (4.26) is exactly the simple saturable gain model expression for I_R. The expression for I_L can be reduced in an identical manner; it also yields the simple saturable gain model expression. As a result, it is clear that the term B contains the interference information about the two traveling waves in the laser.

Since the Agrawal-Lax theory and the steady-state TWL theory are the same, both models will have the same threshold population inversion densities and threshold reflectivities. The expressions for the thresholds are given in Eq (4.17).

The Semiclassical Theory of the Standing Wave Laser

The semiclassical theory of the standing wave laser was first published by Lamb (135). The theory is quite similar to the traveling wave theory of this research. The derivations of Chapter II follow loosely the methods used by Lamb.

Several major differences exist between the TWL theory of Chapter III and Lamb theory, however. Lamb theory assumes that the outcoupling from the resonator is so small that the electric fields can be adequately expanded as a summation of plane, standing waves:

$$\mathbf{E}(z,t) = \frac{1}{2}\sum_n E_n(t) e^{-i\left[\nu_n t + \phi_n(t)\right]} \sin(k_n z) + \text{c.c.} \tag{4.27}$$

If only a single mode is oscillating, Eq (4.27) can be written as:

$$\mathbf{E}(z,t) = \frac{1}{2}E_n(t)e^{-i\left[\nu_I t + \phi_n(t)\right]}\sin(k_n z) + \text{c.c.} \tag{4.28}$$

Since the outcoupling is very low, the amplitudes $E_n(t)$ do not vary spatially. The leftward and rightward traveling waves that comprise the standing wave are assumed to be identical. The phases $\phi_n(t)$ of the standing waves do not vary spatially. Finally, boundary conditions such as those in the TWL theory are not required. The outcoupling losses are simply added to the medium loss term $1/\hat{\tau}_2$.

Under the REA, the Lamb equations of motion for a single longitudinal mode electric field can be written as (106):

$$\frac{d\hat{E}_n}{d\hat{t}} = -\left(\frac{1}{\hat{\tau}_2} - \frac{1}{\hat{\tau}_3\hat{L}_g}\ln r_B\right)\hat{E}_n + \frac{2\hat{w}_{eq}}{\hat{\tau}_1\hat{E}_n}\left\{1 - \left[1 + \frac{\hat{\tau}_1\hat{E}_n^2}{1 + (\Delta\hat{\omega} - \dot{\varphi}_n)^2}\right]^{-1/2}\right\} \tag{4.29a}$$

$$\frac{d\phi_n}{d\hat{t}} = \hat{\Omega} - \hat{\nu}_I + \frac{2\hat{w}_{eq}(\Delta\hat{\omega} - \dot{\varphi}_n)}{\hat{\tau}_1\hat{E}_n^2}\left\{1 - \left[1 + \frac{\hat{\tau}_1\hat{E}_n^2}{1 + (\Delta\hat{\omega} - \dot{\varphi}_n)^2}\right]^{-1/2}\right\} \tag{4.29b}$$

Eq (4.29) is in normalized form. Note that $\hat{\nu}_I$ is used as the reference frequency, instead of $\hat{\nu}_n$. Since only one longitudinal mode is present, the usual subscript n on $\hat{\Omega}$ is omitted. Also, the losses due to outcoupling are explicitly shown in Eq (4.29a), instead of being lumped into a loss constant $1/\hat{\tau}_n$. The outcoupling is assumed to only occur through mirror B. The gain medium does not necessarily fill the entire cavity, as is seen by the $\hat{L}_g$ factor in the field amplitude loss term.

When the outcoupling approaches zero, the TWL theory reduces to Lamb's standing wave theory. This is easily demonstrated. In the limit of no outcoupling, the left and right traveling waves are identical, except for the propagation direction. Consequently:

$$\hat{E}_R = \hat{E}_L = \frac{1}{2}\hat{E}_n \tag{4.30a}$$

$$\phi_R = \phi_L = \phi_n \tag{4.30b}$$

The spatial derivatives of the amplitudes and phases of the traveling waves go to zero. Under these constraints, Eq (3.9) becomes:

$$A = 1 + \frac{1}{2}\left[\frac{\hat{\tau}_1 \hat{E}_n^2}{1 + (\Delta\hat{\omega} - \dot{\varphi}_n)^2}\right] \tag{4.31a}$$

$$B = \frac{1}{2}\left[\frac{\hat{\tau}_1 \hat{E}_n^2}{1 + (\Delta\hat{\omega} - \dot{\varphi}_n)^2}\right] \tag{4.31b}$$

$$C = 0 \tag{4.31c}$$

Using Eqs (4.30) and (4.31) in Eq (3.8a) and dropping the spatial derivative gives:

$$\frac{1}{2}\frac{\partial \hat{E}_n}{\partial \hat{t}} = -\frac{\hat{E}_n}{2\hat{\tau}_2} + \hat{w}_{eq}\left[\frac{\hat{E}_n/2}{1 + (\Delta\hat{\omega} - \dot{\varphi}_n)^2}\frac{1}{\sqrt{A^2 - B^2}} + \frac{1}{\hat{\tau}_1 \hat{E}_n}\left(1 - \frac{A}{\sqrt{A^2 - B^2}}\right)\right]$$

or, after some simple algebra:

$$\frac{\partial \hat{E}_n}{\partial \hat{t}} = -\frac{\hat{E}_n}{\hat{\tau}_2} + \frac{2\hat{w}_{eq}}{\hat{\tau}_1 \hat{E}_n}\left\{1 - \left[1 + \frac{\hat{\tau}_1 \hat{E}_n^2}{1 + (\Delta\hat{\omega} - \dot{\varphi}_n)^2}\right]^{-1/2}\right\} \tag{4.32a}$$

In an identical manner, Eq (3.8b) transforms into:

$$\begin{aligned}\frac{\partial \phi_n}{\partial \hat{t}} &= \hat{\Omega} - \hat{\nu}_I + \frac{2\hat{w}_{eq}(\Delta\hat{\omega} - \dot{\varphi}_n)}{\hat{E}_n}\left[\frac{\hat{E}_n/2}{1 + (\Delta\hat{\omega} - \dot{\varphi}_n)^2}\frac{1}{\sqrt{A^2 - B^2}}\right. \\ &\quad \left. + \frac{1}{\hat{\tau}_1 \hat{E}_n}\left(1 - \frac{A}{\sqrt{A^2 - B^2}}\right)\right] \\ &= \hat{\Omega} - \hat{\nu}_I + \frac{2\hat{w}_{eq}(\Delta\hat{\omega} - \dot{\varphi}_n)}{\hat{\tau}_1 \hat{E}_n^2}\left\{1 - \left[1 + \frac{\hat{\tau}_1 \hat{E}_n^2}{1 + (\Delta\hat{\omega} - \dot{\varphi}_n)^2}\right]^{-1/2}\right\}\end{aligned} \tag{4.32b}$$

Eq (4.32) is exactly the same as Eq (4.29) in the limit $r_B \rightarrow 1$. The same procedures can be applied to Eq (3.8c,d) with the same results. Clearly, the TWL theory reduces to the standing wave theory as the outcoupling approaches zero.

The steady-state lasing frequency $\hat{\nu}$ can be obtained from Eq (4.29). With the time derivative of $\hat{E}_n$ set equal to zero, Eq (4.29a) can be rearranged as:

$$1 - \left[1 + \frac{\hat{\tau}_1 \hat{E}_n^2}{1 + (\Delta\hat{\omega} - \dot{\varphi}_n)^2}\right]^{-1/2} = \frac{\hat{\tau}_1 \hat{E}_n^2}{2\hat{w}_{eq}}\left(\frac{1}{\hat{\tau}_2} - \frac{1}{\hat{\tau}_3 \hat{L}_g}\ln r_B\right)$$

This equation can be substituted into Eq (4.29b) to give the (constant) steady-state value of $\dot{\varphi}_n$:

$$\dot{\varphi}_n = \frac{\hat{\Omega} - \hat{\nu}_I + \Delta\hat{\omega}\left(\frac{1}{\hat{\tau}_2} - \frac{1}{\hat{\tau}_3\hat{L}_g}\ln r_B\right)}{1 + \frac{1}{\hat{\tau}_2} - \frac{1}{\hat{\tau}_3\hat{L}_g}\ln r_B} \tag{4.33}$$

Since $\hat{\nu} = \hat{\nu}_I + \dot{\varphi}_n$, Eq (4.33) can be used to obtain the free-running laser frequency at steady-state:

$$\hat{\nu} = \frac{\hat{\Omega} + \hat{\omega}\left(\frac{1}{\hat{\tau}_2} - \frac{1}{\hat{\tau}_3\hat{L}_g}\ln r_B\right)}{1 + \frac{1}{\hat{\tau}_2} - \frac{1}{\hat{\tau}_3\hat{L}_g}\ln r_B} \tag{4.34a}$$

The frequency offset term $\Delta\hat{t}$ is a somewhat more useful quantity:

$$\Delta\hat{t} = \frac{\Delta\hat{m}}{1 + \frac{1}{\hat{\tau}_2} - \frac{1}{\hat{\tau}_3\hat{L}_g}\ln r_B} \tag{4.34b}$$

Note that only the losses of the laser, the linecenter frequency $\hat{\omega}$, and the barecavity frequency $\hat{\Omega}$ appear in the formulæ for $\hat{\nu}$ and $\Delta\hat{t}$. The larger the outcoupling loss, the closer $\hat{\nu}$ will be pulled toward linecenter. Eq (4.34) is equivalent to Eq (8.58) of (106), which was obtained with the third-order Lamb theory.

The lasing threshold can be found by considering Eq (4.29a) at steady-state. A few rearrangements of the terms yields:

$$\hat{E}_n^2 = \frac{D_2}{D_1}\left\{1 - \left[1 + \frac{\hat{\tau}_1\hat{E}_n^2}{1 + (\Delta\hat{\omega} - \dot{\varphi}_n)^2}\right]^{-1/2}\right\} \tag{4.35}$$

where

$$D_1 = \frac{1}{\hat{\tau}_2} - \frac{1}{\hat{\tau}_3\hat{L}_g}\ln r_B \tag{4.36a}$$

$$D_2 = \frac{2\hat{w}_{rq}}{\hat{\tau}_1} \tag{4.36b}$$

If the laser is operating very close to threshold, then

$$\frac{\hat{\tau}_1 \hat{E}_n^2}{1 + (\Delta\hat{\omega} - \dot{\varphi}_n)^2} \ll 1$$

Using a binomial series expansion on the square root term in Eq (4.35), discarding the terms of order $\hat{E}_n^3$ or greater, and performing some simple algebra results in:

$$\hat{E}_n^2 = \frac{4\left[1 + (\Delta\hat{\omega} - \dot{\varphi}_n)^2\right]}{3\hat{\tau}_1}\left\{1 - \frac{D_1\left[1 + (\Delta\hat{\omega} - \dot{\varphi}_n)^2\right]}{\hat{w}_{eq}}\right\} \tag{4.37}$$

At the threshold, $\hat{E}_n \rightarrow 0$, so that:

$$1 - \frac{D_1\left[1 + (\Delta\hat{\omega} - \dot{\varphi}_n)^2\right]}{\hat{w}_{eq}} = 0$$

or,

$$\hat{w}_{eq}\Big|_{th} = (1 + \Delta\hat{t}^2)\left[\frac{1}{\hat{\tau}_2} - \frac{1}{\hat{\tau}_3 \hat{L}_g} \ln r_B\right] \tag{4.38}$$

This is exactly the same threshold condition as was found for the simple saturable gain model and the TWL model. The standing wave model thus has the same threshold value of r_B as the other two models:

$$r_B\Big|_{th} = \exp\left[\hat{\tau}_3 \hat{L}_g \left(\frac{1}{\hat{\tau}_2} - \frac{\hat{w}_{eq}}{1 + \Delta\hat{t}^2}\right)\right] \tag{4.17c}$$

The Spencer-Lamb Theory

The Spencer-Lamb theory (101) is a modified version of the semiclassical theory of the standing wave laser. The physics of the interaction between the gain medium and the electric fields is identical to that of the Lamb theory. However, the theory makes use of a different mirror model. The mirror affects both the phase and frequency equations. The injection of an external signal is modeled by considering the boundary conditions for the electromagnetic fields at the transmissive mirror. The

injected signal appears as an additional source term in the wave equation, and hence as a source term in the field amplitude and phase equations.

Mirror A is assumed to be perfectly reflective, whereas mirror B is modeled as an infinitesimally thin slab of dielectric material. Mirror B, or the "dielectric bump," has a permittivity given by:

$$\epsilon_{DB}(z) = \epsilon_0\big[1 + \Lambda\delta(z - L)\big] \tag{4.39}$$

where $\delta(z)$ is the Dirac delta function. By matching the boundary conditions for electric and magnetic fields across the dielectric bump, the reflection and transmission coefficients can be obtained (147):

$$\mathbf{r}_D = r_D e^{i\phi_{RD}} = \frac{i\eta}{2 - i\eta} \tag{4.40a}$$

$$\mathbf{t}_D = t_D e^{i\phi_{TD}} = \frac{2}{2 - i\eta} \tag{4.40b}$$

where $\eta = k\Lambda$ is a measure of the height of the dielectric bump. The amplitudes and phases of the coefficients are given in terms of η as:

$$r_D = \frac{\eta}{\sqrt{4 + \eta^2}} \tag{4.41a}$$

$$\phi_{RD} = \frac{\pi}{2} + \arctan\left(\frac{\eta}{2}\right) \tag{4.41b}$$

$$t_D = \frac{2}{\sqrt{4 + \eta^2}} \tag{4.41c}$$

$$\phi_{TD} = \arctan\left(\frac{\eta}{2}\right) \tag{4.41d}$$

Additionally, η can be expressed in terms of r_D as:

$$\eta = \frac{2r_D}{\sqrt{1 - r_D^2}} \tag{4.41e}$$

The dielectric bump has some interesting and aphysical properties that are dealt with extensively in Appendix A. These properties directly affect the lasing frequency and lasing threshold.

The Spencer-Lamb model without an injected signal can be written in the normalized system as:

$$\frac{d\hat{E}_n}{d\hat{t}} = -\left[\frac{1}{\hat{\tau}_2} + \frac{2}{\hat{\tau}_3}\left(\frac{1}{\eta^2+1}\right)\right]\hat{E}_n + \frac{2\hat{w}_{eq}}{\hat{\tau}_1\hat{E}_n}\left\{1 - \left[1 + \frac{\hat{\tau}_1\hat{E}_n^2}{1+(\Delta\hat{\omega}-\dot{\varphi}_n)^2}\right]^{-1/2}\right\} \tag{4.42a}$$

$$\frac{d\phi_n}{d\hat{t}} = \hat{\Omega} - \hat{\nu}_I + \frac{2}{\hat{\tau}_3}\left(\frac{\eta}{\eta^2+1}\right) + \frac{2\hat{w}_{eq}(\Delta\hat{\omega}-\dot{\varphi}_n)}{\hat{\tau}_1\hat{E}_n^2}\left\{1 - \left[1 + \frac{\hat{\tau}_1\hat{E}_n^2}{1+(\Delta\hat{\omega}-\dot{\varphi}_n)^2}\right]^{-1/2}\right\} \tag{4.42b}$$

Eq (4.42) is very similar in form to Eq (4.29). The dielectric bump introduces a different loss term in the field amplitude equation, compared to the loss of a conventional mirror. It also adds a phase term to the ϕ_n equation. This extra phase term shifts the barecavity mode $\hat{\Omega}$ to a different value. The interactions between the electric field and the medium remain the same as in the Lamb model. The gain medium is assumed to extend completely between the mirrors in this model ($\hat{L}_g = 1.0$).

In the limit of $r_D \rightarrow 1$, the Spencer-Lamb model becomes identical to the Lamb model. As r_D approaches unity, η becomes infinite. The dielectric bump loss term in Eq (4.42a) and the additional phase term in Eq (4.42b) both approach zero when η approaches infinity. Thus, the Spencer-Lamb model reduces to the Lamb model when no outcoupling is allowed. In this limit, the TWL theory also reduces to the Lamb theory. Consequently, all three models converge when the outcoupling becomes negligible.

The free-running frequency $\hat{\nu}$ of the Spencer-Lamb model can be derived in the same manner as Eq (4.34). Following the same steps, the expression for $\dot{\varphi}_n$ is found to be:

$$\dot{\varphi}_n = \frac{\hat{\Omega} - \hat{\nu}_I + \frac{2}{\hat{\tau}_3}\left(\frac{\eta}{\eta^2+1}\right) + \left[\frac{1}{\hat{\tau}_2} + \frac{2}{\hat{\tau}_3}\left(\frac{1}{\eta^2+1}\right)\right]\Delta\hat{\omega}}{1 + \frac{1}{\hat{\tau}_2} + \frac{2}{\hat{\tau}_3}\left(\frac{1}{\eta^2+1}\right)} \tag{4.43}$$

The free-running frequency is then given by:

$$\hat{\nu} = \frac{\hat{\Omega} + \frac{2}{\hat{\tau}_3}\left(\frac{\eta}{\eta^2+1}\right) + \hat{\omega}\left[\frac{1}{\hat{\tau}_2} + \frac{2}{\hat{\tau}_3}\left(\frac{1}{\eta^2+1}\right)\right]}{1 + \frac{1}{\hat{\tau}_2} + \frac{2}{\hat{\tau}_3}\left(\frac{1}{\eta^2+1}\right)} \tag{4.44a}$$

or:

$$\Delta\hat{t} = \frac{\Delta\hat{m} - \frac{2}{\hat{\tau}_3}\left(\frac{\eta}{\eta^2+1}\right)}{1 + \frac{1}{\hat{\tau}_2} + \frac{2}{\hat{\tau}_3}\left(\frac{1}{\eta^2+1}\right)} \tag{4.44b}$$

As with the Lamb model, $\hat{\nu}$ depends only on the (shifted) bare cavity mode frequency, the linecenter frequency, and the losses of the laser.

The lasing threshold conditions can be found by the same procedure that was used to derive Eq (4.38). The threshold population inversion density is given by:

$$\hat{w}_{eq}\big|_{th} = (1 + \Delta\hat{t}^2)\left[\frac{1}{\hat{\tau}_2} + \frac{2}{\hat{\tau}_3}\left(\frac{1}{\eta^2+1}\right)\right] \tag{4.45a}$$

Inverting this expression and using Eq (4.41e) yields the threshold reflectivity:

$$r_D\big|_{th} = \left\{\frac{1 - \frac{\hat{\tau}_3}{2}\left(\frac{\hat{w}_{eq}}{1+\Delta\hat{t}^2} - \frac{1}{\hat{\tau}_2}\right)}{1 + \frac{3\hat{\tau}_3}{2}\left(\frac{\hat{w}_{eq}}{1+\Delta\hat{t}^2} - \frac{1}{\hat{\tau}_2}\right)}\right\}^{1/2} \tag{4.45b}$$

Since $r_D\big|_{th}$ is a function of $\Delta\hat{t}$ and $\Delta\hat{t}$ is a function of r_D, an iterative technique using Eqs (4.44b) and (4.45b) is required in order to determine the threshold reflectivity.

The dielectric bump introduces an interesting effect on the lasing threshold. Due to the mathematical form of the losses of the dielectric bump, there exists a critical value of $\hat{w}_{eq}$ above which the laser will always oscillate, regardless of the magnitude of the reflection coefficient. This behavior is in contrast to that of the Lamb, simple saturable gain, Agrawal-Lax, and TWL models, where there always exists some threshold reflectivity below which the laser will not operate. This effect is discussed more thoroughly in Appendix A.

The Spencer-Lamb model of the injected laser uses an injected signal of the form:

$$\mathbf{E}_{IN} = E_{IN} e^{-i(\hat{\nu}_I \hat{t} + kz)} \tag{4.46}$$

The amplitude and frequency of the signal are constant in time. The model of the laser with an injected signal is given in the normalized units by:

$$\frac{d\hat{E}_n}{d\hat{t}} = -\left[\frac{1}{\hat{\tau}_2} + \frac{2}{\hat{\tau}_3}\left(\frac{1}{\eta^2+1}\right)\right]\hat{E}_n + \frac{2\hat{w}_{eq}}{\hat{\tau}_1\hat{E}_n}\left\{1 - \left[1 + \frac{\hat{\tau}_1\hat{E}_n^2}{1+(\Delta\hat{\omega}-\dot{\varphi}_n)^2}\right]^{-1/2}\right\}$$

$$+ \frac{4T\hat{E}_{IN}}{\hat{\tau}_3}\cos(\psi_{DB} - \phi_n) \tag{4.47a}$$

$$\frac{d\phi_n}{d\hat{t}} = \hat{\Omega} - \hat{\nu}_I + \frac{2}{\hat{\tau}_3}\left(\frac{\eta}{\eta^2+1}\right) + \frac{2\hat{w}_{eq}(\Delta\hat{\omega}-\dot{\varphi}_n)}{\hat{\tau}_1\hat{E}_n^2}\left\{1 - \left[1 + \frac{\hat{\tau}_1\hat{E}_n^2}{1+(\Delta\hat{\omega}-\dot{\varphi}_n)^2}\right]^{-1/2}\right\}$$

$$+ \frac{4T\hat{E}_{IN}}{\hat{\tau}_3\hat{E}_n}\sin(\psi_{DB} - \phi_n) \tag{4.47b}$$

where:

$$T \equiv \frac{1}{\sqrt{\eta^2+1}} \tag{4.48a}$$

$$\psi_{DB} \equiv \arctan\frac{1}{\eta} \tag{4.48b}$$

Although the injected signal is modeled as a boundary condition at the dielectric bump, it enters the amplitude and phase equations as a source term. In this respect, the injected field is distributed throughout the medium. This is in contrast to the TWL model, in which the injected field is incorporated strictly as a boundary condition. The significance of the source terms will be more apparent in the following section on the Chow model.

A significant problem with the Spencer-Lamb injected laser model is that the $2kL$ term in Eq (3.26) is not properly accounted for. The very nature of the standing wave model dictates that $2kL$ must exactly equal an integral multiple of 2π, and can subsequently be ignored. The fractional phase term $\hat{\vartheta}$ in the boundary condition could be made up for in the phases of the mirrors. However this is not the case in the Spencer-Lamb model. (The dielectric bump has a phase [illegible] the reflection coefficient. This phase is totally unrelated to the term [illegible] perfectly reflective with r_A 1 in the Spencer-Lamb [illegible]

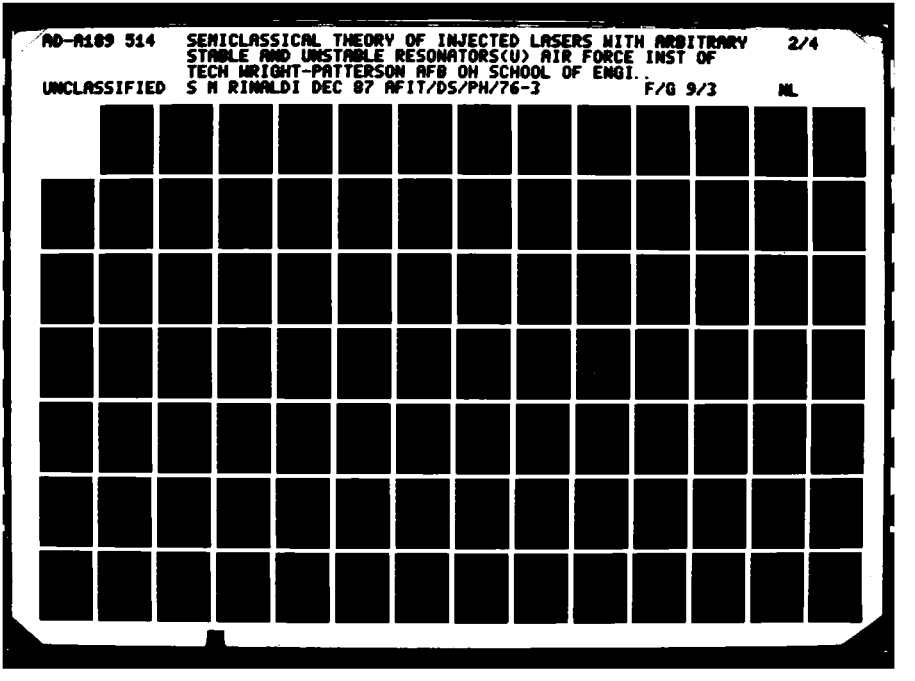
AD-A189 514 SEMICLASSICAL THEORY OF INJECTED LASERS WITH ARBITRARY STABLE AND UNSTABLE RESONATORS(U) AIR FORCE INST OF TECH WRIGHT-PATTERSON AFB OH SCHOOL OF ENGI. 2/4
UNCLASSIFIED S M RINALDI DEC 87 AFIT/DS/PH/76-3 F/G 9/3 NL

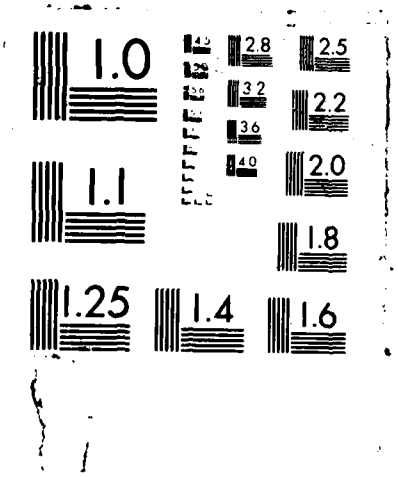
1.0
1.1
1.25
1.4
1.6
1.8
2.0
2.2
2.5
2.8
3.2
3.6
4.0

phase term that must be accounted for. The nonexistence of the $2kL$ term in the Spencer-Lamb theory is a major shortfall of the model.

A system gain, analogous to that given in Eq (3.30), is defined by Spencer and Lamb. In the normalized units, this gain is given by:

$$G_4 = 1 + \frac{\left[\frac{8}{\hat{\tau}_3(\eta^2+1)}\right]\left[-\frac{1}{\hat{\tau}_2} + f_1(\hat{E}_n)\right]}{\left[N_1 + f_1(\hat{E}_n)\right]^2 + \left[N_2 + \Delta\hat{\omega} f_1(\hat{E}_n)\right]^2} \tag{4.49}$$

where:

$$N_1 = -\left[\frac{1}{\hat{\tau}_2} + \frac{2}{\hat{\tau}_3}\left(\frac{1}{\eta^2+1}\right)\right] \tag{4.50a}$$

$$N_2 = \hat{\Omega} - \hat{\nu}_I + \frac{2}{\hat{\tau}_3}\left(\frac{\eta}{\eta^2+1}\right) \tag{4.50b}$$

$$f_1(\hat{E}_n) = \frac{2\hat{w}_{eq}}{\hat{\tau}_1 \hat{E}_n^2}\left\{1 - \left[1 + \frac{\hat{\tau}_1 \hat{E}_n^2}{1+\Delta\hat{\omega}^2}\right]^{-1/2}\right\} \tag{4.50c}$$

The internal field gain G_2 is given by:

$$G_2 = \frac{\hat{E}_n^2}{4\hat{E}_I^2} \tag{4.51}$$

This quantity corresponds to the gain defined in Eq (3.31).

The Chow Theory

The next laser model to be compared to the TWL theory is that developed by Chow (82, 83). The model is essentially the standing wave theory of Lamb, with the injected field incorporated as a pair of source terms in the amplitude and phase equations. The source terms are developed in a simple manner, and are merely added to the Lamb equations.

Since the Chow model reduces to the Lamb model in the limit of no injected field, the threshold population inversion density and threshold reflectivity are given by Eqs (4.38) and (4.17c). The steady-state lasing frequency $\hat{\nu}$ is given by Eq (4.34).

The injected signal source terms can be obtained by considering Figure 4.2. As discussed in Chapter III, under injected conditions, the phasor $\hat{E}_1$ launched into the laser from mirror B will generally not return upon itself in a round trip. Assuming that the mirror reflectivities are given by:

$$r_A = -1 \tag{4.52a}$$

$$r_B = -r_B \tag{4.52b}$$

where r_B is very close to unity, and that the injected frequency is very close to the free-running frequency, then the angle $\hat{\varepsilon}$ in Figure 4.2 will be very small. The additional source terms for the amplitude and phase equations can be given as:

$$\frac{d\hat{E}_n}{d\hat{t}} \approx \frac{\Delta \hat{E}_1}{\hat{\tau}_3} \tag{4.53a}$$

$$\frac{d\phi_n}{d\hat{t}} \approx \frac{\hat{\varepsilon}}{\hat{\tau}_3} \tag{4.53b}$$

These source terms represent the additional amplitude and phase that must be added to $\hat{E}_2$ in order to satisfy the round trip condition, divided by the round trip time.

The Chow model directly includes these source terms in the Lamb equations. With the gain medium filling the entire cavity ($\hat{L}_g = 1.0$) and the injected field given by Eq (4.46), the model can be written in normalized form as:

$$\frac{d\hat{E}_n}{d\hat{t}} = -\left(\frac{1}{\hat{\tau}_2} - \frac{1}{\hat{\tau}_3}\ln r_B\right)\hat{E}_n + \frac{2\hat{w}_{eq}}{\hat{\tau}_1 \hat{E}_n}\left\{1 - \left[1 + \frac{\hat{\tau}_1 \hat{E}_n^2}{1 + (\Delta\hat{\omega} - \dot{\varphi}_n)^2}\right]^{-1/2}\right\}$$

$$+ \frac{2t_B \hat{E}_{IN}}{\hat{\tau}_3}\cos\phi_n \tag{4.54a}$$

$$\frac{d\phi_n}{d\hat{t}} = \hat{\Omega} - \hat{\nu}_I + \frac{2\hat{w}_{eq}(\Delta\hat{\omega} - \dot{\varphi}_n)}{\hat{\tau}_1 \hat{E}_n^2}\left\{1 - \left[1 + \frac{\hat{\tau}_1 \hat{E}_n^2}{1 + (\Delta\hat{\omega} - \dot{\varphi}_n)^2}\right]^{-1/2}\right\}$$

$$+ \frac{2t_B \hat{E}_{IN}}{\hat{\tau}_3 \hat{E}_n}\sin\phi_n \tag{4.54b}$$

The internal field gain G_2 for the Chow model is defined in Eq (4.51).

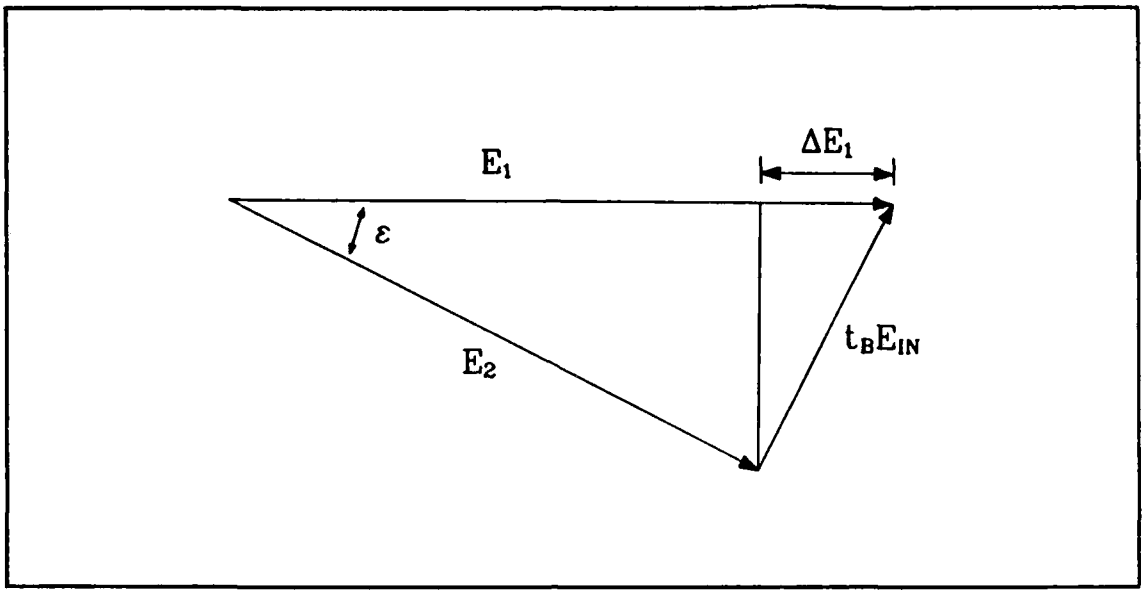

Figure 4.2. The round trip condition in the Chow model. $\hat{E}_1$ is the initially launched field, $\hat{E}_2$ is the field after a round trip, and $t_B \hat{E}_{IN}$ is the injected field inside the laser. Adapted from (82).

Comparing the injection source terms in Eqs (4.47) and (4.54) reveals a similarity between the Chow and Spencer-Lamb models. The injection process in the Spencer-Lamb model thus can be visualized as in Figure 4.2. Both models should be fairly accurate when the reflectivity of mirror B is very high and when the injected signal is detuned only slightly from the free-running laser frequency. Since both models are based on Lamb theory, the traveling wave theory of the Fabry-Perot laser with an injected signal will converge to these models in the limits $r_B \rightarrow 1$ and $\hat{\nu}_I \rightarrow \hat{\nu}$.

As the Chow equations are based upon a standing wave model of the internal laser fields, the $2kL$ term in Eq (3.25) is forced to be zero. This creates the same serious problems with the Chow theory as with the Spencer-Lamb theory. As the $2kL$ term is not accounted for in the phases of the mirrors, the Chow and Spencer-Lamb theories break down very rapidly as $\hat{\nu}_I$ departs from $\hat{\nu}$.

The Ferguson Model

The final model to be compared to the TWL model with an injected signal is that developed by Ferguson (87, 88). The model utilizes the simple saturable gain theory to describe the gain medium. Injection is incorporated as a boundary condition, as in the TWL model.

The laser model employed by Ferguson is given by Eq (4.1), with ϵ set equal to unity. Consequently, without an injected signal, the model yields the same threshold inversion density $\hat{w}_{eq}$ and reflectivity r_B as obtained by the TWL model.

The injected signal is incorporated as a boundary condition, in much the same manner as it is in the TWL model. The general phasor relationship existing at mirror B that is depicted in Figure 3.4 applies to the Ferguson model. If the injected signal frequency $\hat{\nu}_I$ is not equal to the free-running laser frequency $\hat{\nu}$, then the angle between $\hat{\mathbf{E}}_L$ and $\hat{\mathbf{E}}_R$ is given by $2kL$. In fact, the expression for $\hat{\vartheta}$ given in Eq (3.27) is used for the angle between the two phasors.

The boundary conditions are easily obtained. Since the simple saturable gain model is an intensity model and does not include phase information, a boundary condition for the field phases is not required at mirror A. Under the assumption that $\phi_{RA} = \pi$, the boundary condition at mirror A in the Ferguson model is:

$$I_R = r_A^2 I_L \tag{4.55a}$$

A slightly different situation exists at mirror B. Although the simple saturable gain model utilizes intensities, the phasor relationship described above exists at the mirror. In terms of the field amplitudes, the boundary condition is given by:

$$r_B \hat{E}_R e^{i\hat{\vartheta}} + \hat{E}_I e^{-i\phi_I} = \hat{E}_L \tag{4.55b}$$

Note that in this case, $\hat{\mathbf{E}}_I$ has a nonzero phase term, as the reference phasor in Eq (4.55b) is taken to be $\hat{\mathbf{E}}_L$. Additionally, ϕ_{RB} is assumed to be π. Since $\phi_{RA} + \phi_{RB} = 2\pi$, the reflection coefficient phase terms can be ignored in the boundary conditions. Once $\hat{E}_I$ is calculated from the boundary conditions, the injected intensity is immediately given by:

$$I_I = \hat{E}_I^2 \tag{4.56}$$

Although the Ferguson model is conceptually similar to the TWL model, it suffers from several shortcomings. First, spatial hole burning is not incorporated in the model. This will cause the calculated intensities inside the laser to be too high, and lead to erroneous values of the injected intensity. Second, the phases $\phi_{R,L}$ of the laser fields are not accounted for. The boundary condition at mirror B is thus only an approximation to the more accurate condition given in Eq (3.28). The boundary condition should be fairly accurate for small detunings of $\hat{\nu}_I$ from $\hat{\nu}$, though, as the additional phase due to ϕ_R will be approximately cancelled by that due to ϕ_L. Finally, although $g_0 L$ is a function of the detuning of $\hat{\nu}_I$ from the atomic linecenter frequency $\hat{\omega}$ as seen in Eq (4.10a), it is held fixed for all values of $\hat{\nu}_I$ in the Ferguson model. This will cause some inaccuracies in the calculated laser intensities and the injected intensity.

Summary

The TWL theory of the Fabry-Perot laser has been compared to six theories in this chapter. The key points of the comparisons are outlined below.

1. The simple saturable gain model.
   (a) The simple saturable gain model does not include the effects of spatial hole burning, whereas the TWL theory does.
   (b) The TWL theory reduces to the simple saturable gain model in the limit of near threshold operation.
   (c) Both models exhibit the same threshold population inversion densities and threshold reflectivities.
2. The Agrawal-Lax model.
   (a) The Agrawal-Lax model incorporates the effects of spatial hole burning.
   (b) The TWL model reduces to the Agrawal-Lax model in steady-state.
   (c) Both models have the same threshold population inversion densities and threshold reflectivities.

3. The Lamb model.

   (a) The TWL model reduces to the Lamb model in the limit of extremely low outcoupling.

   (b) The TWL model and the Lamb model have the same threshold inversion densities and threshold reflectivities.

   (c) A simple formula for the lasing frequency of the standing wave laser was derived. Comparisons to the TWL theory are not possible at this stage, as no analytic formula can be obtained for the frequency of the traveling wave laser.

4. The Spencer-Lamb model.

   (a) Without an injected signal, the TWL theory reduces to the Spencer-Lamb model in the limit of extremely low outcoupling.

   (b) The two laser models have different thresholds.

   (c) A formula for the lasing frequency $\hat{\nu}$ for the Spencer-Lamb model without an injected signal was derived. Again, no comparisons to the TWL theory can be made at this time.

   (d) With an injected signal, the TWL model reduces to the Spencer-Lamb model when the outcoupling approaches zero and when the injected frequency approaches the free-running frequency.

   (e) The Spencer-Lamb model does not account for the $2kL$ term in the boundary conditions, whereas the TWL model does.

5. The Chow model.

   (a) Without an injected signal, the TWL model reduces to the Chow model in the limit of very high reflectivities.

   (b) The two models have the same threshold population inversion densities and threshold reflectivities without an injected signal.

   (c) Since the Chow model without an injected signal is identical to the Lamb model, the free-running frequency $\hat{\nu}$ of the laser is given by the same formula derived for the Lamb model. No comparisons to the TWL theory can be made at this time.

(d) With an injected signal, the TWL laser reduces to the Chow model as $r_B \rightarrow 1$ and $\hat{\nu}_I \rightarrow \hat{\nu}$.

(e) The Chow model does not account for the $2kL$ term in the boundary conditions, whereas the TWL model does.

6. The Ferguson model.

(a) Without an injected signal, the TWL model reduces to the Ferguson model in the limit of near threshold operation.

(b) The TWL model and the Ferguson model have the same threshold population inversion densities and threshold reflectivities in the absence of an injected signal.

(c) The Ferguson model and the TWL model account for the injected signal in identical manners, i.e., through the boundary conditions.

(d) The Ferguson model does not include the effects of spatial holeburning, whereas the TWL model does.

(e) The Ferguson model does not account for the phase terms $\phi_{R,L}$, whereas the TWL model does.

(f) The Ferguson model incorporates the phase term $2kL$ in the same manner as the TWL model.

(g) The Ferguson model does not allow $g_0 L$ to vary as a function of the detuning of $\hat{\nu}_I$ from $\hat{\omega}$, whereas the TWL model does.

Each of the six models discussed in this chapter suffers from various limitations. For this reason, the traveling wave laser model was developed. In the applicable limits, the TWL model reduces to the six theories presented above. It extends the regions of validity of the other models, and corrects many of their deficiencies. The TWL model can be used for any outcoupling t_B and/or t_A and over a broad range of detunings of $\hat{\nu}_I$ from $\hat{\nu}$. As a result, the TWL model provides significantly improved representations of free-running and injected lasers.

V. Semiclassical Theory of the PBCUR Laser

The semiclassical theory developed in Chapter III does an excellent job of modeling the Fabry-Perot laser. However, the TWL model cannot be applied to a laser with a positive branch, confocal unstable resonator (PBCUR). This is due to the fact that one of the counterpropagating fields in the PBCUR laser is a spherical or cylindrical wave and the other field is a plane wave. The TWL model is predicated upon the assumption that both fields are planar. As a result, the TWL model must be modified before it can be applied to the PBCUR laser.

The semiclassical theory of the PBCUR laser with an arbitrary magnification (cavity loss) is presented in this chapter. Since the derivation of the model follows that presented in Chapter II almost exactly, only the main results are presented. The laser device is described in the first section, along with several key definitions. Next, the Bloch equations for the medium interactions with the electric fields are given. In the third section, the electric field equations are presented. As the Maxwell-Bloch equations are quite complex, the equations of motion in the REA are given in the fourth section. The equation set for the free-running laser at steady-state and the appropriate boundary conditions are presented next. In the sixth section, the equations and boundary conditions for the injected laser are derived. The chapter is summarized in the final section.

The PBCUR Laser

The laser with a PBCUR is shown schematically in Figure 5.1. The device consists of an active medium placed between the two curved mirrors. The mirrors form the unstable resonator, with an optic axis z. Since the resonator is confocal, the focii of both mirrors lie at the same point on the optic axis. The unstable nature of the resonator forces geometric rays to walk out of the resonator, rather than being continually refocused toward the optic axis as in a stable resonator. A given ray that is initially parallel to and displaced a distance x from the optic axis will again be parallel to the axis after a round trip through the cavity. However, the ray will be displaced a distance Mx from the axis after the round trip, where M is the geometric magnification of the resonator. In

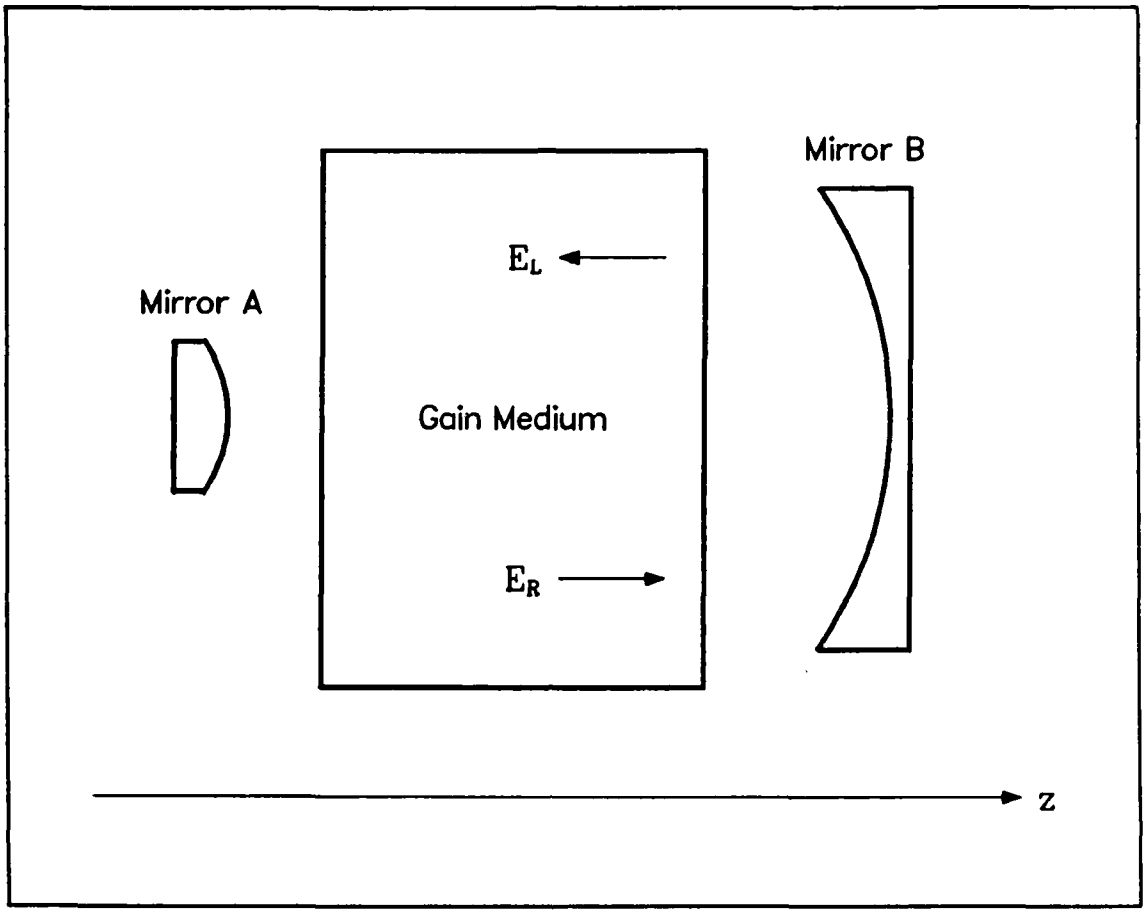

Figure 5.1. The PBCUR laser.

this manner, a ray will eventually walk out of the resonator after enough round trips. Conversely, if the propagation direction of the ray is reversed, the ray will walk down toward the optic axis on consecutive round trips. A bundle of such rays will never completely collapse to the optic axis; diffractive spreading will eventually overwhelm the geometric demagnification on each round trip. The rays will then begin to walk out of the resonator (148–152). The region in which diffractive spreading counteracts the geometric demagnification is known as the "Fresnel core", or alternately, the "diffractive core". It is in this region that the resonator mode is formed, and the interaction physics of the injection locking process take place. Finally, there is no internal focus of the laser fields

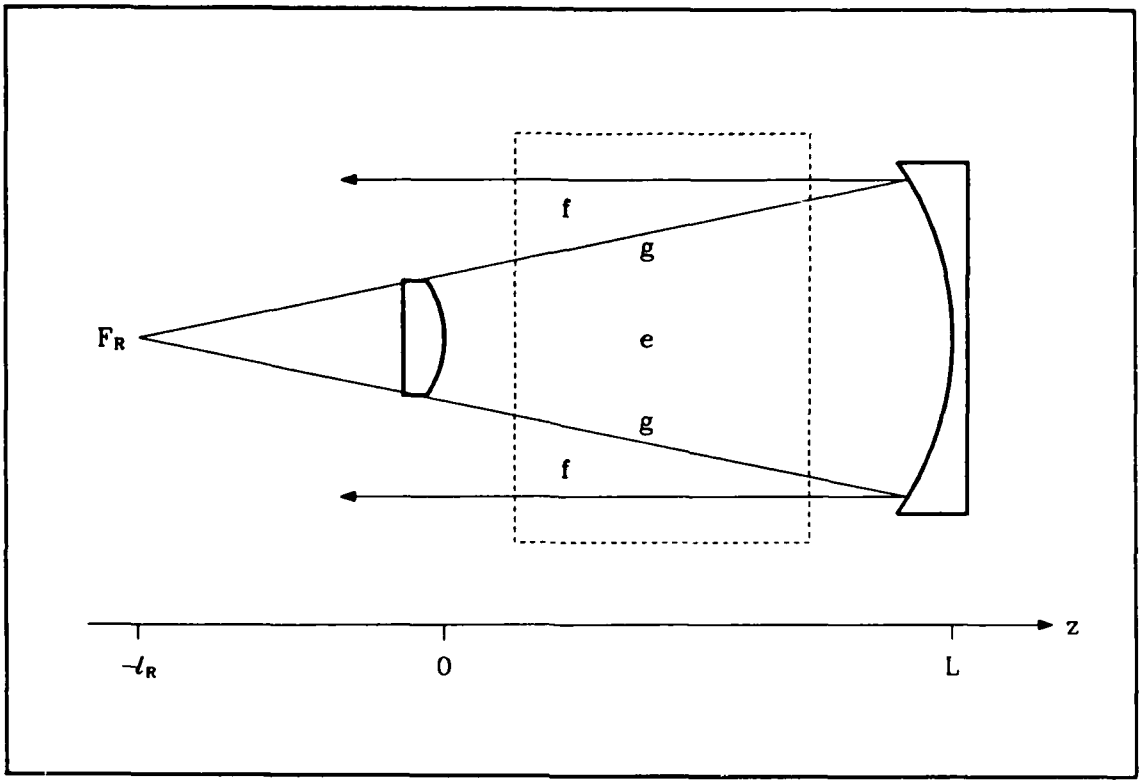

Figure 5.2. The fields in the PBCUR laser.

The fields in the laser are shown in greater detail in Figure 5.2. $\mathbf{E}_R$ is an expanding wave with focus F_R at $z = -l_R$, and $\mathbf{E}_L$ is a plane wave with focus F_L at $z = \infty$. $\mathbf{E}_R$ is either a cylindrical wave or a spherical wave, depending upon whether the resonator has strip or two-dimensional mirrors, respectively. The portion of $\mathbf{E}_L$ that geometrically spreads beyond the edges of mirror A forms the outcoupled beam. As $\mathbf{E}_L$ is a plane wave, the outcoupled field is collimated. Both $\mathbf{E}_R$ and $\mathbf{E}_L$ exist in the central conical region e of the gain medium. However, in the outer regions f, only $\mathbf{E}_L$ exists. This region acts as a single pass amplifier for $\mathbf{E}_L$. The cone of rays emanating from F_R and grazing the edges of mirror A form the boundary between the amplifier and central regions. This cone is designated g in the figure. The geometric mode of the laser is assumed to have a constant intensity in the transverse directions inside region e.

The resonator mirrors have complex reflection and transmission coefficients, given by:

$$\text{Mirror A:} \quad \begin{cases} r_A = r_A e^{i\phi_{RA}} \\ t_A = t_A e^{i\phi_{TA}} \end{cases} \tag{5.1a, b}$$

$$\text{Mirror B:} \quad \begin{cases} r_B = r_B e^{i\phi_{RB}} \\ t_B = t_B e^{i\phi_{TB}} \end{cases} \tag{5.1c, d}$$

Since outcoupling is performed geometrically around mirror A, the two mirrors are usually made perfectly reflective. This assumption will be used in this research. Mirror B and the gain medium are assumed to extend far enough in the transverse directions so as not to be limiting apertures for the mode. The longitudinal extent of the gain medium is unimportant in the derivation of the laser equations of motion.

Considering Figure 5.2, the magnification of the resonator can be expressed as:

$$M = \frac{l_R + L}{l_R} = 1 + \frac{L}{l_R} \tag{5.2}$$

The minimum magnification possible is $M = 1$. In this limit, the PBCUR becomes the Fabry-Perot interferometer or plane-parallel resonator modeled in Chapter III.

The total electric field $\mathbf{E}(z,t)$ inside the central core region of the laser is given by:

$$\mathbf{E}(z,t) = \mathbf{E}_R(z,t) + \mathbf{E}_L(z,t) \tag{5.3}$$

where the individual traveling waves are expressed as:

$$\mathbf{E}_R(z,t) = \frac{1}{2}\left\{ \frac{1}{\rho_R^{\alpha}} E_R(z,t) \exp\left\{-i\left[\nu_I t - k\rho_R + \phi_R(z,t)\right]\right\} + \text{c.c.} \right\} \tag{5.4a}$$

$$\mathbf{E}_L(z,t) = \frac{1}{2}\left\{ E_L(z,t) \exp\left\{-i\left[\nu_I t + kz + \phi_L(z,t)\right]\right\} + \text{c.c.} \right\} \tag{5.4b}$$

$$\alpha \equiv \begin{cases} \frac{1}{2}, & \text{cylindrical wave} \\ 1, & \text{spherical wave} \end{cases} \tag{5.5}$$

$$\rho_R \approx z + l_R \tag{5.6}$$

In these equations, ρ_R is the radial distance from the focus F_R, $E_{R,L}(z,t)$ are the amplitudes of the electric fields, k is the wavenumber, and $\phi_{R,L}(z,t)$ are the electric field phases. $\nu_I + \dot{\phi}_{R,L}$ are the instantaneous frequencies of the two traveling waves. In particular, ν_I is a reference frequency; when the laser has an injected field, ν_I is the frequency of the injected wave. The amplitudes $E_{R,L}$ and phases $\phi_{R,L}$ of the electric fields are real and assumed to vary slowly in both space and time. α is a parameter that describes the cylindrical/spherical nature of $\mathbf{E}_R$. Finally, the derivations are confined to the paraxial region, as noted in Eq (5.6).

The total polarization of the medium can be defined in a similar manner:

$$\begin{aligned}
\mathbf{P}(z,t) &= \mathbf{P}_R(z,t) + \mathbf{P}_L(z,t) \\
&= \frac{1}{2}\Big\{ P_R(z,t)\exp\{-i[\nu_I t - kz + \phi_R(z,t)]\} \\
&\qquad + P_L(z,t)\exp\{-i[\nu_I t + kz + \phi_L(z,t)]\} + \text{c.c.}\Big\} \\
&= \frac{1}{2}\Big\{ P'_R(z,t)\exp\{-i[\nu_I t + \phi_R(z,t)]\} \\
&\qquad + P'_L(z,t)\exp\{-i[\nu_I t + \phi_L(z,t)]\} + \text{c.c.}\Big\}
\end{aligned} \tag{5.7}$$

The total polarization is the sum of two traveling wave parts. In general, the amplitudes $P_{R,L}$ and $P'_{R,L}$ are complex quantities that vary slowly in time. $P_{R,L}$ vary slowly in space, whereas $P'_{R,L}$ have a rapidly varying spatial factor on the order of $e^{\pm ikz}$ and a slowly varying envelope term. Nothing is explicitly stated in Eq (5.7) about a cylindrical/spherical/planar nature of the polarization waves.

The Bloch Equations

The Bloch equations can be derived in a manner that closely parallels the derivation in Chapter II. Only minor differences exist. First, there is no ρ_L term, as $\mathbf{E}_L$ is a plane wave. Second, the

normalization of E_L is the same as that required in Chapter III:

$$\hat{E}_L = \frac{\mu}{\gamma\hbar} E_L \tag{5.8}$$

In normalized form, the Bloch equations for the PBCUR laser are:

$$\frac{\partial \hat{u}_R}{\partial \hat{t}} = -\hat{u}_R - \left(\Delta\hat{\omega} - \frac{\partial \phi_R}{\partial \hat{t}}\right)\hat{v}_R + \frac{1}{2\pi}\int_{\theta_0}^{\theta_0+2\pi}\left\{\frac{1}{\hat{\rho}_R^{\alpha}}\hat{E}_R \sin\xi_R - \hat{E}_L \sin\left(\phi_L - \phi_R + \theta\right)\right\}\hat{w}\, d\theta \tag{5.9a}$$

$$\frac{\partial \hat{v}_R}{\partial \hat{t}} = \left(\Delta\hat{\omega} - \frac{\partial \phi_R}{\partial \hat{t}}\right)\hat{u}_R - \hat{v}_R + \frac{1}{2\pi}\int_{\theta_0}^{\theta_0+2\pi}\left\{\frac{1}{\hat{\rho}_R^{\alpha}}\hat{E}_R \cos\xi_R + \hat{E}_L \cos\left(\phi_L - \phi_R + \theta\right)\right\}\hat{w}\, d\theta \tag{5.9b}$$

$$\frac{\partial \hat{u}_L}{\partial \hat{t}} = -\hat{u}_L - \left(\Delta\hat{\omega} - \frac{\partial \phi_L}{\partial \hat{t}}\right)\hat{v}_L + \frac{1}{2\pi}\int_{\theta_0}^{\theta_0+2\pi}\frac{1}{\hat{\rho}_R^{\alpha}}\hat{E}_R \sin\left(\phi_L - \phi_R + \theta + \xi_R\right)\hat{w}\, d\theta \tag{5.9c}$$

$$\frac{\partial \hat{v}_L}{\partial \hat{t}} = \left(\Delta\hat{\omega} - \frac{\partial \phi_L}{\partial \hat{t}}\right)\hat{u}_L - \hat{v}_L + \frac{1}{2\pi}\int_{\theta_0}^{\theta_0+2\pi}\left\{\frac{1}{\hat{\rho}_R^{\alpha}}\hat{E}_R \cos\left(\phi_L - \phi_R + \theta + \xi_R\right) + \hat{E}_L\right\}\hat{w}\, d\theta \tag{5.9d}$$

$$\frac{\partial \hat{w}}{\partial \hat{t}} = -\frac{\hat{w} - \hat{w}_{eq}}{\hat{\tau}_1} + \mathrm{Im}\left\{\hat{P}_R'\left[\frac{1}{\hat{\rho}_R^{\alpha}}\hat{E}_R e^{-i(\theta/2+\xi_R)} + \hat{E}_L e^{i(\phi_L-\phi_R+\theta/2)}\right] + \hat{P}_L'\left[\frac{1}{\hat{\rho}_R^{\alpha}}\hat{E}_R e^{-i(\phi_L-\phi_R+\theta/2+\xi_R)} + \hat{E}_L e^{i\theta/2}\right]\right\} \tag{5.9e}$$

Notice that the equations for the PBCUR laser are a "blending" of the corresponding equations for the Fabry-Perot laser (Chapter III) and the general laser (Chapter II). A comparison of Eq (5.9) to the corresponding set for the Fabry-Perot laser yields three minor differences. These differences

are all due to the spherical or cylindrical nature of $\hat{\mathbf{E}}_R$. First, the mixing of the electric field terms in the integrals is different. The mixing is due to the ξ_R phase term in the expression for $\hat{\mathbf{E}}_R$. Second, the phase term ξ_R appears in the expression for $\hat{w}$. The final difference is the appearance of $\hat{\rho}_R^{-\alpha}$ in conjunction with $\hat{E}_R$. These differences are all minor; functionally, Eq (5.9) is identical to Eqs (3.6) and (2.66).

The Electric Field (Maxwell) Equations

The derivation of the electric field equations for the PBCUR laser is virtually identical to the derivation given in Chapter II. The only difference lies in the fact that $\mathbf{E}_L$ is a plane wave in the PBCUR laser. Hence, no $\hat{\rho}_L$ term exists that must be dealt with.

In normalized form, the electric field equations of motion are:

$$\frac{\partial \hat{E}_R}{\partial \hat{t}} + \psi \frac{\partial \hat{E}_R}{\partial \hat{z}} = -\frac{\hat{E}_R}{\hat{\tau}_2} + \hat{\rho}_R^{\alpha} \left(\hat{u}_R \sin \xi_R + \hat{v}_R \cos \xi_R \right) \tag{5.10a}$$

$$\frac{\partial \phi_R}{\partial \hat{t}} + \psi \frac{\partial \phi_R}{\partial \hat{z}} = \hat{\Omega} - \hat{\nu}_I - \frac{\hat{\rho}_R^{\alpha}}{\hat{E}_R} \left(\hat{u}_R \cos \xi_R - \hat{v}_R \sin \xi_R \right) \tag{5.10b}$$

$$\frac{\partial \hat{E}_L}{\partial \hat{t}} - \psi \frac{\partial \hat{E}_L}{\partial \hat{z}} = -\frac{\hat{E}_L}{\hat{\tau}_2} + \hat{v}_L \tag{5.10c}$$

$$\frac{\partial \phi_L}{\partial \hat{t}} - \psi \frac{\partial \phi_L}{\partial \hat{z}} = \hat{\Omega} - \hat{\nu}_I - \frac{\hat{u}_L}{\hat{E}_L} \tag{5.10d}$$

As with the Bloch equations, the field equations appear to be a mixture of the corresponding equations from the Fabry-Perot and the general laser equation sets. The additional phase term ξ_R forces the mixing of the in-phase and quadrature components of the polarization in the $\hat{E}_R$ and ϕ_R equations, as in the general laser case. $\hat{E}_R$ is also modified by $\hat{\rho}_R^{\alpha}$, as expected. Note particularly that Eq (5.10a) is dimensionally correct, since $\hat{\rho}_R^{\alpha}$ premultiplies the polarization terms. Finally, the $\hat{E}_L$ and ϕ_L equations are identical to those in the Fabry-Perot laser case.

Eqs (5.9) and (5.10) form the Maxwell-Bloch equation set for the PBCUR laser. As with the Fabry-Perot and general laser cases, this model is a self-consistent set of "point" and "longitudinally

varying" equations. In order to solve the set, an expression relating $\hat{P}'_{R,L}$ to $\hat{P}_{R,L}$ similar to the inverse of Eq (2.35) is required in Eq (5.9e).

The Equations of Motion in the REA

Once again, the Maxwell-Bloch equations are too complex to solve. An analytic solution of the equations is virtually out of the question; a numerical solution would be prohibitive in terms of computer costs. Under the REA, however, the equations simplify to a very manageable set. If the REA can be justified, the following set of equations can be used relatively easily with excellent results.

The derivation of the equations of motion in the REA follow the approach presented in Chapter II. The final set of equations in normalized form is:

$$\frac{\partial \hat{E}_R}{\partial \hat{t}} + \psi \frac{\partial \hat{E}_R}{\partial \hat{z}} = -\frac{\hat{E}_R}{\hat{\tau}_2} + \hat{w}_{eq}\hat{\rho}_R^{\alpha}\left\{ \frac{\hat{E}_R \hat{\rho}_R^{-\alpha}}{1+(\Delta\hat{\omega}-\dot{\varphi}_R)^2} \frac{1}{\sqrt{A^2-B^2-C^2}} \right.$$

$$\left. + \frac{\hat{E}_L}{1+(\Delta\hat{\omega}-\dot{\varphi}_L)^2}\left[1-\frac{A}{\sqrt{A^2-B^2-C^2}}\right]\left[\frac{B-C(\Delta\hat{\omega}-\dot{\varphi}_L)}{B^2+C^2}\right]\right\} \qquad (5.11a)$$

$$\frac{\partial \phi_R}{\partial \hat{t}} + \psi \frac{\partial \phi_R}{\partial \hat{z}} = \hat{\Omega} - \hat{\nu}_I + \hat{w}_{eq}\frac{\hat{\rho}_R^{\alpha}}{\hat{E}_R}\left\{ \frac{\hat{E}_R \hat{\rho}_R^{-\alpha}(\Delta\hat{\omega}-\dot{\varphi}_R)}{1+(\Delta\hat{\omega}-\dot{\varphi}_R)^2} \frac{1}{\sqrt{A^2-B^2-C^2}} \right.$$

$$\left. + \frac{\hat{E}_L}{1+(\Delta\hat{\omega}-\dot{\varphi}_L)^2}\left[1-\frac{A}{\sqrt{A^2-B^2-C^2}}\right]\left[\frac{B(\Delta\hat{\omega}-\dot{\varphi}_L)+C}{B^2+C^2}\right]\right\} \qquad (5.11b)$$

$$\frac{\partial \hat{E}_L}{\partial \hat{t}} - \psi \frac{\partial \hat{E}_L}{\partial \hat{z}} = -\frac{\hat{E}_L}{\hat{\tau}_2} + \hat{w}_{eq}\left\{ \frac{\hat{E}_L}{1+(\Delta\hat{\omega}-\dot{\varphi}_L)^2} \frac{1}{\sqrt{A^2-B^2-C^2}} \right.$$

$$\left. + \frac{\hat{E}_R \hat{\rho}_R^{-\alpha}}{1+(\Delta\hat{\omega}-\dot{\varphi}_R)^2}\left[1-\frac{A}{\sqrt{A^2-B^2-C^2}}\right]\left[\frac{B+C(\Delta\hat{\omega}-\dot{\varphi}_R)}{B^2+C^2}\right]\right\} \qquad (5.11c)$$

$$\frac{\partial \phi_L}{\partial \hat{t}} - \psi \frac{\partial \phi_L}{\partial \hat{z}} = \hat{\Omega} - \hat{\nu}_I + \frac{\hat{w}_{eq}}{\hat{E}_L}\left\{ \frac{\hat{E}_L(\Delta\hat{\omega}-\dot{\varphi}_L)}{1+(\Delta\hat{\omega}-\dot{\varphi}_L)^2} \frac{1}{\sqrt{A^2-B^2-C^2}} \right.$$

$$\left. + \frac{\hat{E}_R \hat{\rho}_R^{-\alpha}}{1+(\Delta\hat{\omega}-\dot{\varphi}_R)^2}\left[1-\frac{A}{\sqrt{A^2-B^2-C^2}}\right]\left[\frac{B(\Delta\hat{\omega}-\dot{\varphi}_R)-C}{B^2+C^2}\right]\right\} \qquad (5.11d)$$

$$A \equiv 1 + \hat{\tau}_1 \left\{ \frac{\hat{E}_R^2 \hat{\rho}_R^{-2a}}{1 + (\Delta\hat{\omega} - \dot{\varphi}_R)^2} + \frac{\hat{E}_L^2}{1 + (\Delta\hat{\omega} - \dot{\varphi}_L)^2} \right\} \tag{5.12a}$$

$$B \equiv \frac{\hat{\tau}_1 \hat{E}_R \hat{E}_L}{\hat{\rho}_R^a} \left\{ \frac{1}{1 + (\Delta\hat{\omega} - \dot{\varphi}_R)^2} + \frac{1}{1 + (\Delta\hat{\omega} - \dot{\varphi}_L)^2} \right\} \tag{5.12b}$$

$$C \equiv \frac{\hat{\tau}_1 \hat{E}_R \hat{E}_L}{\hat{\rho}_R^a} \left\{ \frac{(\Delta\hat{\omega} - \dot{\varphi}_R)}{1 + (\Delta\hat{\omega} - \dot{\varphi}_R)^2} - \frac{(\Delta\hat{\omega} - \dot{\varphi}_L)}{1 + (\Delta\hat{\omega} - \dot{\varphi}_L)^2} \right\} \tag{5.12c}$$

Notice that the equation for $\hat{E}_R$ is dimensionally correct, as the term $\hat{\rho}_R$ premultiplies the gain term.

Eqs (5.11) and (5.12) will be referred to as the traveling wave unstable resonator laser (TWURL) model. This model, like the TWL model, is a considerable simplification over the Maxwell-Bloch equations. The model suffers from a problem that also affects the TWL and general laser models: time derivatives of both ϕ_R and ϕ_L exist on the right-hand sides of Eq (5.8). These derivative terms cannot be factored out and collected on the left-hand sides of the $\phi_{R,L}$ equations only. This potentially could lead to stability problems similar to those experienced in the time-dependent numerical solutions of the TWL model. (The numerical methods discussed in Appendix B could be used to obtain time-dependent solutions of the TWURL equations. However, no attempt was made to do this, as the primary data of interest were steady-state values.)

The Free-Running Laser at Steady-State

The TWURL equations describe the interaction of the counterpropagating electric fields with the atomic medium. As such, they can be employed to model the free-running laser. The steady-state version of the equations form a particularly simple subset of the TWURL model. The reduced equations and the appropriate boundary conditions are derived in this section.

The frequencies of the barecavity modes are given by the same expression as for the TWL model, Eq (3.10):

$$\hat{\Omega} = \frac{nc}{2\gamma L} \tag{5.13a}$$

where n is some large integer. The barecavity intermode frequency separation is given by:

$$\Delta\hat{\Omega} = \frac{c}{2\gamma L} \tag{5.13b}$$

Notice that both of these equations are given in the normalized units. The actual lasing frequency $\hat{\nu}$ will be pulled closer to linecenter, due to the large index of refraction changes near the atomic linecenter.

The following frequency differences, defined in Chapter III, will be required in the ensuing derivations and are repeated for convenience:

$$\Delta\hat{m} \equiv \hat{\omega} - \hat{\Omega} \tag{5.14a}$$

$$\Delta\hat{t} \equiv \hat{\omega} - \hat{\nu} \tag{5.14b}$$

$$\Delta\hat{\omega} \equiv \hat{\omega} - \hat{\nu}_I \tag{5.14c}$$

At steady-state, the lasing frequency $\hat{\nu}$ is constant throughout the laser. Since:

$$\hat{\nu} = \hat{\nu}_I + \dot{\varphi}_R = \hat{\nu}_I + \dot{\varphi}_L$$

the time derivatives of the phases must be constant and equal at steady-state. That is:

$$\dot{\varphi}_R = \dot{\varphi}_L = \dot{\varphi} \tag{5.15}$$

A nonzero but constant value of $\dot{\varphi}$ simply indicates that the reference frequency $\hat{\nu}_I$ was not chosen to equal $\hat{\nu}$. It does not imply that the laser is not at steady-state. The field amplitudes are constant at steady-state, so that:

$$\frac{\partial\hat{E}_R}{\partial\hat{t}} = \frac{\partial\hat{E}_L}{\partial\hat{t}} = 0 \tag{5.16}$$

The TWURL equations in the core region e of Figure 5.2 can now be simply derived. First, Eq (5.12) reduces to:

$$A = 1 + \frac{\hat{\tau}_1}{1 + \Delta\hat{t}^2}\left(\frac{\hat{E}_R^2}{\hat{\rho}_R^{2a}} + \hat{E}_L^2\right) \tag{5.17a}$$

$$B = \frac{2\hat{\tau}_1\hat{E}_R\hat{E}_L}{(1 + \Delta\hat{t}^2)\hat{\rho}_R} \tag{5.17b}$$

$$C = 0 \tag{5.17c}$$

Using Eq (5.17), the field amplitude equations simplify to:

$$\frac{\partial \hat{E}_R}{\partial \hat{z}} = \frac{1}{\psi}\left\{-\frac{\hat{E}_R}{\hat{\tau}_2} + \hat{w}_{eq}\hat{\rho}_R^a\left[\frac{\hat{E}_R\hat{\rho}_R^{-a}}{(1+\Delta\hat{t}^2)\sqrt{A^2-B^2}} + \frac{\hat{\rho}_R^a}{2\hat{\tau}_1\hat{E}_R}\left(1-\frac{A}{\sqrt{A^2-B^2}}\right)\right]\right\} \quad (5.18a)$$

$$\frac{\partial \hat{E}_L}{\partial \hat{z}} = -\frac{1}{\psi}\left\{-\frac{\hat{E}_L}{\hat{\tau}_2} + \hat{w}_{eq}\left[\frac{\hat{E}_L}{(1+\Delta\hat{t}^2)\sqrt{A^2-B^2}} + \frac{1}{2\hat{\tau}_1\hat{E}_L}\left(1-\frac{A}{\sqrt{A^2-B^2}}\right)\right]\right\} \quad (5.18b)$$

Eqs (5.11b,d) can be rewritten as:

$$\begin{aligned}\frac{\partial \phi_R}{\partial \hat{z}} &= \frac{1}{\psi}\Bigg\{\hat{\Omega} - (\hat{\nu}_I + \dot{\varphi}) \\ &\quad + \frac{\hat{w}_{eq}\Delta\hat{t}}{\hat{E}_R\hat{\rho}_R^{-a}}\left[\frac{\hat{E}_R\hat{\rho}_R^{-a}}{(1+\Delta\hat{t}^2)\sqrt{A^2-B^2}} + \frac{\hat{\rho}_R^a}{2\hat{\tau}_1\hat{E}_R}\left(1-\frac{A}{\sqrt{A^2-B^2}}\right)\right]\Bigg\} \\ &= \frac{1}{\psi}\left\{\Delta\hat{t} - \Delta\hat{m} + \frac{\hat{w}_{eq}\Delta\hat{t}}{\hat{E}_R\hat{\rho}_R^{-a}}\left[\frac{\hat{E}_R\hat{\rho}_R^{-a}}{(1+\Delta\hat{t}^2)\sqrt{A^2-B^2}} + \frac{\hat{\rho}_R^a}{2\hat{\tau}_1\hat{E}_R}\left(1-\frac{A}{\sqrt{A^2-B^2}}\right)\right]\right\} \quad (5.18c)\end{aligned}$$

$$\frac{\partial \phi_L}{\partial \hat{z}} = -\frac{1}{\psi}\left\{\Delta\hat{t} - \Delta\hat{m} + \frac{\hat{w}_{eq}\Delta\hat{t}}{\hat{E}_L}\left[\frac{\hat{E}_L}{(1+\Delta\hat{t}^2)\sqrt{A^2-B^2}} + \frac{1}{2\hat{\tau}_1\hat{E}_L}\left(1-\frac{A}{\sqrt{A^2-B^2}}\right)\right]\right\} \quad (5.18d)$$

Eq (5.18) is equivalent to Eq (3.16); the forms of the two equation sets are virtually identical. The medium creates small shifts in $\phi_{R,L}$, which in turn show up in the frequency pulling and pushing effects. As with the TWL equations, if the actual lasing frequency $\hat{\nu}$ is known *a priori*, then Eqs (5.18a) and (5.18b) can be solved directly with the boundary conditions to yield the steady-state field amplitudes. The phase equations are not required in this case. If $\hat{\nu}$ is unknown, then all four equations must be used in the manner described in Appendix B in order to calculate the free-running frequency and field amplitudes.

The equations of motion for $\hat{E}_L$ and ϕ_L are required for the amplifier regions f in the gain medium (Figure 5.2). This set is obtained by setting $\mathbf{E}_R$ equal to 0 in Eqs (5.11) and (5.12). Eq (5.12) reduces to:

$$A_f = 1 + \frac{\hat{\tau}_1\hat{E}_L^2}{1+\Delta\hat{t}^2} \quad (5.19a)$$

$$B_f = 0 \quad (5.19b)$$

$$C_f = 0 \quad (5.19c)$$

Substituting Eqs (5.15), (5.16), and (5.19) in Eq (5.11) gives the equations for $\mathbf{E}_L$ in the amplifier regions:

$$\frac{\partial \hat{E}_L}{\partial \hat{z}} = -\frac{1}{\psi}\left[-\frac{1}{\hat{r}_2} + \frac{\hat{w}_{eq}}{A_f(1+\Delta\hat{t}^2)}\right]\hat{E}_L \tag{5.20a}$$

$$\frac{\partial \phi_L}{\partial \hat{z}} = -\frac{1}{\psi}\left[\Delta\hat{t} - \Delta\hat{m} + \frac{\hat{w}_{eq}\Delta\hat{t}}{A_f(1+\Delta\hat{t}^2)}\right] \tag{5.20b}$$

The specific numerical algorithm through which Eq (5.20) can be applied to the amplifier region is given in Appendix B.

The boundary conditions can be derived in a manner similar to that used in Chapter III. Matching the fields at mirror A yields:

$$\frac{1}{\rho_R^{\alpha}} E_R(0) e^{-i\left[\nu_I t - k\rho_R + \phi_R(0)\right]} = r_A e^{i\phi_{RA}} E_L(0) e^{-i\left[\nu_I t + kz + \phi_L(0)\right]}$$

After simplifying and normalizing the expression and separating it into the real and imaginary parts, the boundary condition at mirror A becomes:

$$\hat{E}_R(0) = \hat{\rho}_R^{\alpha} r_A \hat{E}_L(0)$$

$$\phi_R(0) = \phi_L(0) - \phi_{RA} + kl_R$$

An additional simplification can be effected. Using Eq (5.2), $\hat{\rho}_R^{\alpha}$ can be written as:

$$\begin{aligned}\hat{\rho}_R^{\alpha} &= \left(\frac{l_R + z}{L}\right)^{\alpha} \\ &= \left(\frac{l_R}{L}\right)^{\alpha} \\ &= \left(\frac{1}{M-1}\right)^{\alpha}\end{aligned} \tag{5.21}$$

Substituting Eq (5.21) into the boundary condition expression yields:

$$\hat{E}_R(0) = \frac{r_A \hat{E}_L(0)}{(M-1)^{\alpha}} \tag{5.22a}$$

$$\phi_R(0) = \phi_L(0) - \phi_{RA} + kl_R \tag{5.22b}$$

In a similar manner, the boundary condition at mirror B can be obtained. Matching the fields across the mirror gives:

$$\frac{r_B e^{i\phi_{RB}}}{\rho_R^{\alpha}} E_R(L) e^{-i\left[\nu_I t - k\rho_R + \phi_R(L)\right]} = E_L(L) e^{-i\left[\nu_I t + kL + \phi_L(L)\right]}$$

After simplifying and using an expression analogous to Eq (5.21), the boundary condition can be written as:

$$\hat{E}_L(1) = \left(1 - \frac{1}{M}\right)^{\alpha} r_B \hat{E}_R(1) \tag{5.23a}$$

$$\phi_L(1) + kl_R = \phi_R(1) - \phi_{RB} - 2kL \tag{5.23b}$$

Notice that the kl_R term is added to ϕ_L in Eqs (5.22b) and (5.23b). Since the absolute phase of the fields is unnecessary, the kl_R term can be absorbed into ϕ_L and ignored in the above equations. It therefore is unnecessary to know the exact value of l_R in a calculation.

As mentioned at the beginning of this chapter, the mirrors are usually perfectly reflective, as the outcoupling is performed via geometric extraction of $\mathbf{E}_L$. This was assumed to be the case in all the numerical work performed in this research. The reflection coefficients for this case are:

$$r_A = e^{i\pi} \tag{5.24a}$$

$$r_B = e^{i\pi} \tag{5.24b}$$

Using Eq (5.24) in Eqs (5.22) and (5.23) yields the final set of boundary conditions:

$$\hat{E}_R(0) = \frac{\hat{E}_L(0)}{(M-1)^{\alpha}} \tag{5.25a}$$

$$\phi_R(0) = \phi_L(0) - \pi \tag{5.25b}$$

$$\hat{E}_L(1) = \left(1 - \frac{1}{M}\right)^{\alpha} \hat{E}_R(1) \tag{5.25c}$$

$$\phi_L(1) = \phi_R(1) - \pi - 2kL \tag{5.25d}$$

At steady-state, $2kL$ is equal to $2m\pi$, where m is some integer. The $2kL$ term can therefore be dropped from Eq (5.25d).

The output power, under the assumption of perfectly reflective mirrors, can be found by integrating the output intensity across the output aperture. This aperture is located in the plane of mirror A, i.e., at $\hat{z} = 0$. The particular expression for the output intensity will depend upon whether the resonator mirrors are strip or two-dimensional. The intensity in the output aperture is defined as:

$$I_{ap}(x, y, t) \equiv \hat{E}_L^2(x, y, \hat{z} = 0, \hat{t}) \tag{5.26}$$

where x and y are the transverse coordinates. Then, for strip mirrors, the output power P_{out} is given by:

$$P_{out} = \int_{ap} I_{ap}\, dx\, dy$$

$$= 2\Delta y \int_{d}^{Md} I_{ap}\, dx \tag{5.27a}$$

where x is the transverse coordinate, $2d$ is the width of mirror A in the x direction, and Δy is the depth of the mirror in the y or strip direction. If the mirrors are square and mirror A has sides of length $2d$, then the output power is given by:

$$P_{out} = 8 \int_{d}^{Md} x I_{ap}\, dx \tag{5.27b}$$

Finally, if the mirrors are round and mirror A has a diameter of $2d$, the output power is given by:

$$P_{out} = 2\pi \int_{d}^{Md} x I_{ap}\, dx \tag{5.27c}$$

where x is a radial coordinate perpendicular to the optic axis. Note that three implicit assumptions are used in Eq (5.27): the gain medium is uniformly pumped, the resonator mirrors are each symmetric about the optic axis, and the magnification is uniform and constant in all radial directions from the optic axis. Under these assumptions, I_{ap} is symmetric about the optic axis. If any of these

assumptions is not true, I_{ap} will in general not be symmetric about the optic axis. The integrations in Eq (5.27) must then be performed over the whole of the output aperture.

The extraction efficiency η_L of the laser is defined as the output power divided by the total available power in the gain medium:

$$\eta_L = \frac{P_{out}}{g_0 \hat{V}_g I_{sat}} \tag{5.28}$$

where $\hat{V}_g$ is the volume of the gain medium. Using the above expressions for P_{out}, the efficiency can be written as:

$$\eta_L = \begin{cases} \dfrac{\hat{\tau}_1}{g_0 \hat{L}_g M d (1+\Delta\tilde{t}^2)} \displaystyle\int_d^{Md} I_{ap}\, dx & \text{Strip mirrors} \\ \dfrac{2\hat{\tau}_1}{g_0 \hat{L}_g M^2 d^2 (1+\Delta\tilde{t}^2)} \displaystyle\int_d^{Md} x I_{ap}\, dx & \text{Square mirrors} \\ \dfrac{2\hat{\tau}_1}{g_0 \hat{L}_g M^2 d^2 (1+\Delta\tilde{t}^2)} \displaystyle\int_d^{Md} x I_{ap}\, dx & \text{Circular mirrors} \end{cases} \tag{5.29}$$

The Injected Laser at Steady-State

As in the TWL model, the TWURL equations reduce to a simple form when the PBCUR laser has an injected signal. The physics of the injection locking process is conceptually the same as in the Fabry-Perot laser, with only a few minor differences. Before developing the injected laser equations, the locking process will be examined in more detail.

The underlying concepts of injection locking can again be understood if the electric fields are thought of as phasors. As discussed in Chapter III, some phasor $\hat{\mathbf{E}}_L$ is initially launched from mirror B, undergoes a reflection at mirror A, returns to mirror B, and undergoes a second reflection. If the vector sum of the phasor that has completed the round trip and the injected phasor is exactly equal to the initially launched phasor, then a steady-state injection locked condition has been reached. This is depicted in Figure 3.4.

A few subtle differences exist between the injection locked Fabry-Perot laser and the injection locked PBCUR laser. The first difference involves the manner in which the injected signals enter the slave laser. In the Fabry-Perot laser, injection is performed through the partially transmissive mirror B. In the PBCUR laser, both mirrors are perfectly reflective. For the purposes of this research, injection is performed by directing the beam from the master oscillator into the output aperture of the slave laser, as depicted in Figure 5.3. The injected signal walks down toward the optic axis, until diffractive spreading causes the beam to fill the Fresnel core. The locking physics occurs in the Fresnel core. This differs from the Fabry-Perot laser, where locking occurs over the whole of the outcoupling aperture. In the PBCUR, the injected signal is mathematically modeled as an electromagnetic field source located at mirror B. This field is vectorally added to $\mathbf{r}_D \hat{\mathbf{E}}_R(1, \hat{t})$. The injected field thus enters into the boundary condition at mirror B. The injected signal could be added vectorally to the circulating fields at any given plane in the resonator. However, mirror B was chosen for simplicity and so that the injected field could be modeled as a plane wave.

The second difference in the injection processes is that the injected signal in the PBCUR may undergo an increase in intensity as it walks down to the optic axis (153). This increase is due to two factors. First, the beam footprint is geometrically demagnified as it walks down to the Fresnel core. Second, the injected signal is amplified by the gain medium with each pass through the resonator. As a result, the injected signal in the Fresnel core can potentially be more intense than the injected beam external to the slave laser. In the Fabry-Perot case, however, the injected intensity I_I inside the laser is less than the injected intensity external to the laser, due to the transmission coefficient of mirror B. The amplification during the walkdown is ignored in the present research for several reasons. The amount of amplification of the injected beam is highly dependent upon the physical layout and parameters of the laser. In order to keep the research scope broad, only "generic" resonators rather than specific devices were used. Finally, as the injected signal is modeled as a field source in the Fresnel core, the degree of amplification due to the walkdown is not required.

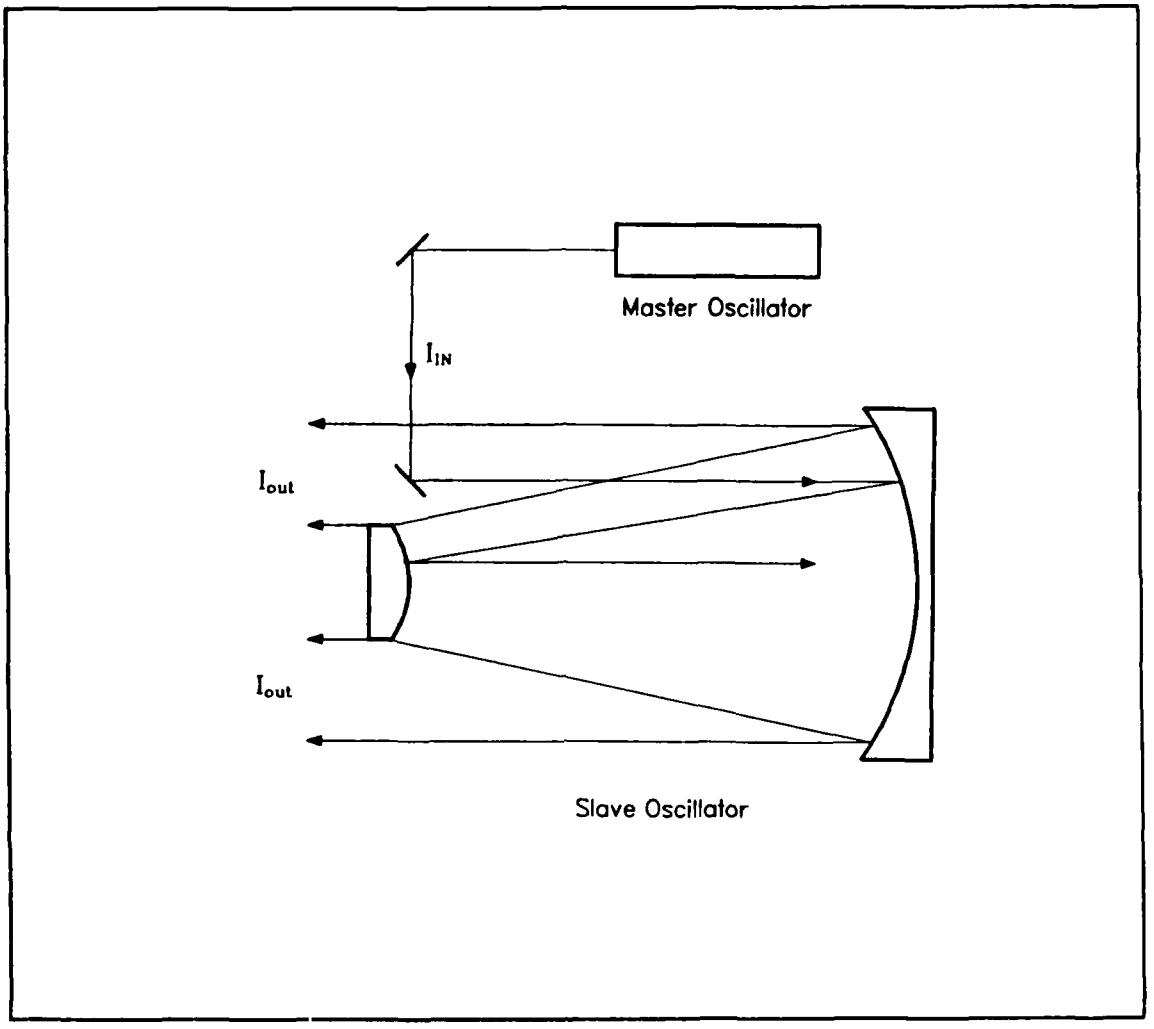

Figure 5.3. The injection technique used in the PBCUR laser. I_{IN} is the injected signal from the master oscillator; I_{out} is the beam radiated from the slave laser.

The injected signal at mirror B is given by:

$$\hat{\mathbf{E}}_I(1,\hat{t}) = \hat{E}_I e^{-i(\hat{\nu}_I \hat{t} + kz + \phi_I)} \tag{5.30}$$

The amplitude and phase of the injected signal are constant in both space and time. Since the phase of one of the three electric fields is arbitrary, it can be set to any desired reference value. For convenience, ϕ_I is chosen and set equal to zero.

In the injection locked laser, the oscillation frequency is by definition equal to $\hat{\nu}_I$. Therefore, the time derivatives of ϕ_R and ϕ_L are equal to zero. The time derivatives of the electric field amplitudes $\hat{E}_{R,L}$ are also equal to zero. With this in mind, Eq (5.12) reduces to:

$$A = 1 + \frac{\hat{\tau}_1}{1+\Delta\hat{\omega}^2}\left(\frac{\hat{E}_R^2}{\hat{\rho}_R^{2\alpha}} + \hat{E}_L^2\right) \tag{5.31a}$$

$$B = \frac{2\hat{\tau}_1 \hat{E}_R \hat{E}_L}{(1+\Delta\hat{\omega}^2)\hat{\rho}_R} \tag{5.31b}$$

$$C = 0 \tag{5.31c}$$

Combining Eqs (5.31) and (5.11), the electric field equations of motion are obtained:

$$\frac{\partial \hat{E}_R}{\partial \hat{z}} = \frac{1}{\hat{\psi}}\left\{-\frac{\hat{E}_R}{\hat{\tau}_2} + \hat{w}_{eq}\hat{\rho}_R^{\alpha}\left[\frac{\hat{E}_R\hat{\rho}_R^{-\alpha}}{(1+\Delta\hat{\omega}^2)\sqrt{A^2-B^2}} + \frac{\hat{\rho}_R^{\alpha}}{2\hat{\tau}_1\hat{E}_R}\left(1-\frac{A}{\sqrt{A^2-B^2}}\right)\right]\right\} \tag{5.32a}$$

$$\frac{\partial \hat{E}_L}{\partial \hat{z}} = -\frac{1}{\hat{\psi}}\left\{-\frac{\hat{E}_L}{\hat{\tau}_2} + \hat{w}_{eq}\left[\frac{\hat{E}_L}{(1+\Delta\hat{\omega}^2)\sqrt{A^2-B^2}} + \frac{1}{2\hat{\tau}_1\hat{E}_L}\left(1-\frac{A}{\sqrt{A^2-B^2}}\right)\right]\right\} \tag{5.32b}$$

$$\begin{aligned}\frac{\partial \phi_R}{\partial \hat{z}} &= \frac{1}{\hat{\psi}}\left\{\hat{\Omega} - \hat{\nu}_I + \frac{\hat{w}_{eq}\Delta\hat{\omega}}{\hat{E}_R\hat{\rho}_R^{-\alpha}}\left[\frac{\hat{E}_R\hat{\rho}_R^{-\alpha}}{(1+\Delta\hat{\omega}^2)\sqrt{A^2-B^2}} + \frac{\hat{\rho}_R^{\alpha}}{2\hat{\tau}_1\hat{E}_R}\left(1-\frac{A}{\sqrt{A^2-B^2}}\right)\right]\right\} \\ &= \frac{1}{\hat{\psi}}\left\{\Delta\hat{\omega} - \Delta\hat{m} + \frac{\hat{w}_{eq}\Delta\hat{\omega}}{\hat{E}_R\hat{\rho}_R^{-\alpha}}\left[\frac{\hat{E}_R\hat{\rho}_R^{-\alpha}}{(1+\Delta\hat{\omega}^2)\sqrt{A^2-B^2}} + \frac{\hat{\rho}_R^{\alpha}}{2\hat{\tau}_1\hat{E}_R}\left(1-\frac{A}{\sqrt{A^2-B^2}}\right)\right]\right\}\end{aligned} \tag{5.32c}$$

$$\frac{\partial \phi_L}{\partial \hat{z}} = -\frac{1}{\hat{\psi}}\left\{\Delta\hat{\omega} - \Delta\hat{m} + \frac{\hat{w}_{eq}\Delta\hat{\omega}}{\hat{E}_L}\left[\frac{\hat{E}_L}{(1+\Delta\hat{\omega}^2)\sqrt{A^2-B^2}} + \frac{1}{2\hat{\tau}_1\hat{E}_L}\left(1-\frac{A}{\sqrt{A^2-B^2}}\right)\right]\right\} \tag{5.32d}$$

Eqs (5.31) and (5.32) are identical to Eqs (5.17) and (5.18), except that the $\Delta\hat{t}$ terms have been replaced by $\Delta\hat{\omega}$.

The equations for $\hat{E}_L$ and ϕ_L in the amplifier region of the gain medium are similarly obtained. First, Eq (5.12) reduces to:

$$A_f = 1 + \frac{\hat{\tau}_1\hat{E}_L^2}{1+\Delta\hat{\omega}^2} \tag{5.33a}$$

$$B_f = 0 \tag{5.33b}$$

$$C_f = 0 \tag{5.33c}$$

Then, the equations for $\hat{E}_L$ and ϕ_L can be written as:

$$\frac{\partial \hat{E}_L}{\partial \hat{z}} = -\frac{1}{\hat{\psi}}\left[-\frac{1}{\hat{\tau}_2} + \frac{\hat{w}_{eq}}{A_f(1+\Delta\hat{\omega}^2)}\right]\hat{E}_L \tag{5.34a}$$

$$\frac{\partial \phi_L}{\partial \hat{z}} = -\frac{1}{\hat{\psi}}\left[\Delta\hat{\omega} - \Delta\hat{m} + \frac{\hat{w}_{eq}\Delta\hat{\omega}}{A_f(1+\Delta\hat{\omega}^2)}\right] \tag{5.34b}$$

The boundary conditions are readily derived. At mirror A, the boundary conditions are identical to those for the free-running laser:

$$\hat{E}_R(0) = \frac{r_A}{(M-1)^\alpha}\hat{E}_L(0) \tag{5.35a}$$

$$\phi_R(0) = \phi_L(0) - \phi_{RA} + kl_R \tag{5.35b}$$

At mirror B, the vector boundary condition is:

$$r_B\left(\frac{M-1}{M}\right)^\alpha \hat{E}_R(1)e^{-i\left[\phi_R(1)-\phi_{RB}-kl_R-2kL\right]} + \hat{E}_I = \hat{E}_L(1)e^{-i\phi_L(1)} \tag{5.36}$$

As in the free-running laser case, the phase term kl_R can be absorbed into ϕ_R, and thus eliminated from the boundary conditions. The mirrors are also perfectly reflective, so that:

$$\mathbf{r}_A = \mathbf{r}_B = e^{i\pi}$$

Finally, the $2kL$ term can be accounted for in exactly the same manner as in the injection locked Fabry-Perot laser, namely:

$$2kL = 2m\pi + \hat{\vartheta}, \qquad m = 0, 1, 2, \ldots$$

where:

$$\hat{\vartheta} \equiv 2\pi\hat{\tau}_3(\Delta\hat{\iota} - \Delta\hat{\omega})\left[1 + \frac{1}{\hat{\tau}_2} - \frac{1}{\hat{\tau}_3\hat{L}_g}\ln\left(\frac{r_A r_B}{M^\alpha}\right)\right]$$

Incorporating these facts into Eqs (5.35) and (5.36) yields the final set of boundary conditions:

$$\hat{E}_R(0) = \frac{\hat{E}_L(0)}{(M-1)^\alpha} \tag{5.37a}$$

$$\phi_R(0) = \phi_L(0) - \pi \tag{5.37b}$$

$$\left(\frac{M-1}{M}\right)^{\alpha} \hat{E}_R(1)e^{-i\left[\phi_R(1)-\pi-\hat{\vartheta}\right]} + \hat{E}_I = \hat{E}_L(1)e^{-i\phi_L(1)} \tag{5.37c}$$

Finally, an internal field gain G_2, identical to that given in Eq (3.31), can be defined:

$$G_2 = \frac{\hat{E}_L^2(1)}{\hat{E}_I^2} \tag{5.38}$$

G_2 is indicative of the ratio of the intensities of the circulating fields to the intensity of the injected field.

Summary

The Maxwell-Bloch and TWURL equation sets for the PBCUR laser were presented in this chapter. The equations were seen to be very similar to the corresponding equations for the Fabry-Perot laser. The steady-state equations of motion in the REA were derived for the free-running laser. The injection locked laser was described physically, and the equations of motion governing its behavior were given. The appropriate boundary conditions for both the free-running and injection locked lasers were derived.

VI. Comparisons of the TWURL Model to other Theories

Several theories have been developed that describe the operation of the PBCUR laser. However, these models all suffer from one or more deficiencies. For this reason, the TWURL model of the previous chapter was developed.

In this chapter, the TWURL model is compared to two free-running laser theories that have been published in the literature. In the appropriate limits, the TWURL model is shown to reduce to the other models. The TWURL model is first compared to a modified version of the g_0–I_{sat} model. Similar threshold behavior of the two models is demonstrated. A comparison of the TWURL model and the Agrawal-Lax model of the PBCUR laser is presented in the second section. As in the Fabry-Perot laser case, the Agrawal-Lax model is shown to be the steady-state version version of the TWURL model. A summary of the comparisons is given in the final section.

The Simple Saturable Gain Model

The simple saturable gain model developed by Rigrod (121–123) can be readily extended to model the PBCUR laser (154). The general form of the model is:

$$\frac{d\hat{E}_R}{d\hat{z}} = \frac{1}{2}(G_0 - \alpha_0 L)\hat{E}_R \tag{6.1a}$$

$$\frac{d\hat{E}_L}{d\hat{z}} = -\frac{1}{2}(G_0 - \alpha_0 L)\hat{E}_L \tag{6.1b}$$

$$G_0 = \frac{g_0 L}{\left[1 + \frac{I_R + I_L}{I_{sat}}\right]^{\epsilon}} \tag{6.1c}$$

where:

$$\epsilon = \begin{cases} \frac{1}{2} & \text{inhomogeneous broadening} \\ 1 & \text{homogeneous broadening} \end{cases} \tag{6.1d}$$

and:

$$I_R \equiv \frac{\hat{E}_R^2}{\hat{\rho}_R^{2\alpha}} \tag{6.1e}$$

$$I_L \equiv \hat{E}_L^2 \tag{6.1f}$$

Since the TWURL model employs homogeneous broadening, ϵ will be set equal to 1 in the following discussion.

The simple saturable gain model has two serious shortcomings. First, the model does not account for spatial hole burning. This causes the gain used in the model to be artificially higher than the actual value. As a result, the intensities calculated by the model are too high. Second, phase and frequency effects are not taken into account. Frequency pulling and pushing effects and the lasing frequency $\hat{\nu}$ cannot be calculated with the simple saturable gain model. Although injection locking could be modeled in a manner similar to Ferguson's method, the results would suffer due to the lack of spatial hole burning, phase, and frequency information. Both of these deficiencies are corrected in the TWURL model.

Both the simple saturable gain model and the TWURL model reduce to the same form at the lasing threshold. As in the Fabry-Perot laser, this is due to the negligible effects of spatial hole burning in this regime. In the TWURL model, the peaks of the interference pattern of the traveling waves are quite small. As a result, the population inversion is affected negligibly by the the interference of the traveling waves. The gain becomes approximately equal to, but slightly less than, $g_0 L$. The equivalence of the two models at the threshold can be shown by letting the field intensities be arbitrarily small. The simple saturable gain model reduces to:

$$\frac{d\hat{E}_R}{d\hat{z}} = \frac{1}{2}(g_0 L - \alpha L)\hat{E}_R \tag{6.2a}$$

$$\frac{d\hat{E}_L}{d\hat{z}} = -\frac{1}{2}(g_0 L - \alpha L)\hat{E}_L \tag{6.2b}$$

Following the same procedures used in Chapter IV for the TWL model, Eqs (5.18a,b) become:

$$\frac{\partial\hat{E}_R}{\partial\hat{z}} = \left(-\frac{\hat{\tau}_3}{2\hat{\tau}_2} + \frac{\hat{\tau}_3\hat{w}_{eq}}{2(1+\Delta\hat{t}^2)}\right)\hat{E}_R \tag{6.3a}$$

$$\frac{\partial\hat{E}_L}{\partial\hat{z}} = -\left(-\frac{\hat{\tau}_3}{2\hat{\tau}_2} + \frac{\hat{\tau}_3\hat{w}_{eq}}{2(1+\Delta\hat{t}^2)}\right)\hat{E}_L \tag{6.3b}$$

Eq (6.3) is identical to Eq (6.2), if the following identifications are made:

$$g_0 L = \frac{\hat{\tau}_3 \hat{w}_{eq}}{1 + \Delta\hat{t}^2} \tag{6.4a}$$

$$\alpha_0 L = \frac{\hat{\tau}_3}{\hat{\tau}_2} \tag{6.4b}$$

Notice that the definitions of $g_0 L$ and $\alpha_0 L$ are the same as those given in Eq (4.10) for the Fabry-Perot laser.

The value for I_{sat} must be derived in order to complete the comparison of the two models. I_{sat} can be obtained by considering the single pass amplifier case, i.e., the limiting case in which $\hat{E}_R \rightarrow 0$ or $\hat{E}_L \rightarrow 0$. The later case has already been derived for the amplifier region of the gain medium in the PBCUR laser. The equations of motion for $\hat{\mathbf{E}}_L$ are given in Eq (6.20). The amplitude equation can be rewritten slightly as:

$$\begin{aligned} \frac{\partial \hat{E}_L}{\partial \hat{z}} &= -\frac{1}{\psi}\left[-\frac{1}{\hat{\tau}_2} + \left(\frac{\hat{w}_{eq}}{1+\Delta\hat{t}^2}\right)\left(1 + \frac{\hat{\tau}_1 \hat{E}_L^2}{1+\Delta\hat{t}^2}\right)^{-1}\right]\hat{E}_L \\ &= -\frac{1}{2}\left\{\frac{g_0 L}{1 + \left(\frac{\hat{\tau}_1 I_L}{1+\Delta\hat{t}^2}\right)} - \alpha_0 L\right\}\hat{E}_L \end{aligned} \tag{6.5}$$

Similarly, the amplifier expression for $\hat{E}_L$ can be obtained for the simple saturable gain model by letting $\hat{E}_R \rightarrow 0$ in Eq (6.1b):

$$\frac{d\hat{E}_L}{d\hat{z}} = -\frac{1}{2}\left\{\frac{g_0 L}{1 + \frac{I_L}{I_{sat}}} - \alpha_0 L\right\}\hat{E}_L \tag{6.6}$$

Comparing the two equations yields the expression for I_{sat}:

$$I_{sat} = \frac{1 + \Delta\hat{t}^2}{\hat{\tau}_1} \tag{6.7}$$

Notice that this equation is identical to Eq (4.14). The fact that $g_0 L$, $\alpha_0 L$, and I_{sat} are the same for both the TWL and TWURL models is not unexpected. These parameters are characteristics of the

gain medium only, and have nothing to do with the nature of the electromagnetic fields propagating inside the laser.

Since the TWURL model reduces to the simple saturable gain model near threshold, both models have the same values of threshold gain and resonator magnification. The threshold gain for the simple saturable gain model is given by (154):

$$g_0 L_g\Big|_{th} = \alpha_0 L_g - \ln\left(\frac{r_A r_B}{M^\alpha}\right) \tag{6.7}$$

Using the values for $g_0 L$ and $\alpha_0 L$ and letting $r_{A,B} = 1$, the expression for the threshold population inversion density is obtained:

$$\hat{w}_{eq}\Big|_{th} = (1 + \Delta\hat{t}^2)\left[\frac{1}{\hat{\tau}_2} + \frac{1}{\hat{\tau}_3 \hat{L}_g} \ln M^\alpha\right] \tag{6.8a}$$

Inverting Eq (6.8a) yields the maximum value of M^α for which the laser will operating with a fixed pumping rate ($\hat{w}_{eq}$):

$$M^\alpha\Big|_{th} = \exp\left[\hat{\tau}_3 \hat{L}_g \left(\frac{\hat{w}_{eq}}{1 + \Delta\hat{t}^2} - \frac{1}{\hat{\tau}_2}\right)\right] \tag{6.8b}$$

Note that the value of M^α in Eq (6.8b) is just the inverse of the threshold reflectivity given in Eq (4.17b).

The Agrawal-Lax Model

In addition to the Fabry-Perot laser equations, Agrawal and Lax also present a set of expressions for the intensities inside a general unstable resonator (142, 143). The particular resonators modeled have two-dimensional mirrors, such that $\mathbf{E}_R$ is a spherical wave ($\alpha = 1$). Specifically examining the PBCUR case, their equations are:

$$\frac{dI'_R}{d\hat{z}} + \frac{2(M-1)}{1 + (M-1)\hat{z}} I'_R = \frac{g_3 L}{\sqrt{a^2 - b^2}}\left(1 - \frac{a - \sqrt{a^2 - b^2}}{2I'_R}\right) I'_R \tag{6.9a}$$

$$\frac{dI'_L}{d\hat{z}} = -\frac{g_3 L}{\sqrt{a^2-b^2}}\left(1-\frac{a-\sqrt{a^2-b^2}}{2I'_L}\right)I'_L \tag{6.9b}$$

where a, b, and g_3 are defined in Eq (4.20). As in their Fabry-Perot laser equations, this set models the effects of spatial hole burning. b is the interference term between the two traveling waves; if $b = 0$, Eq (6.9) reduces to the simple saturable gain model of the previous section.

The Agrawal-Lax model is identical to the TWURL model at steady-state. The model can be used to calculate the intensities of the fields in a free-running laser for a given lasing frequency $\hat{\nu}$. The main deficiency of the model is that phase and frequency effects are not addressed. The model does not have a pair of phase expressions analogous to Eqs (5.18c,d). Consequently, frequency pulling and pushing effects and the lasing frequency $\hat{\nu}$ cannot be determined with this model. For the same reason, injection locking cannot be adequately addressed with the Agrawal-Lax equations. The angle between the phasors in the boundary condition for mirror B can not be accurately determined, except for very small detunings of the injected signal from the free-running frequency. As a result, the injected signals calculated by the model would only be accurate in a very narrow range of detunings about the free-running frequency.

The equivalence of Eqs (6.9) and (5.18a,b) can be demonstrated with a little effort. Eq (5.18a) can be rewritten as:

$$\frac{\partial \hat{E}_R}{\partial \hat{z}} = \frac{\hat{w}_{eq}}{\psi\sqrt{(1+\Delta\tilde{t}^2)^2(A^2-B^2)}}\left\{1-\frac{A(1+\Delta\tilde{t}^2)-\sqrt{(1+\Delta\tilde{t}^2)^2(A^2-B^2)}}{2\hat{\tau}_1\hat{E}_R^2\hat{\rho}_R^{-2}}\right\}\hat{E}_R \tag{6.10}$$

Notice that $\alpha = 1$ in the above equation. By defining:

$$I'_R \equiv \frac{\hat{\tau}_1\hat{E}_R^2}{\hat{\rho}_R^2} \tag{6.11a}$$

$$I'_L \equiv \hat{\tau}_1\hat{E}_L^2 \tag{6.11b}$$

$$a \equiv A(1+\Delta\tilde{t}^2) \tag{6.11c}$$

$$b \equiv B(1+\Delta\tilde{t}^2) \tag{6.11d}$$

and using Eq (4.24), Eq (6.10) can be cast as:

$$\frac{2\hat{\tau}_1 \hat{E}_R}{\hat{\rho}_R^2} \frac{\partial \hat{E}_R}{\partial \hat{z}} = \frac{g_3 L}{\sqrt{a^2 - b^2}} \left(1 - \frac{a - \sqrt{a^2 - b^2}}{2I'_R}\right) I'_R \tag{6.12}$$

Next, expanding the left-hand side of Eq (6.9a) yields:

$$\frac{\partial I'_R}{\partial \hat{z}} + \frac{2(M-1)}{1 + (M-1)\hat{z}} I'_R = \frac{\partial}{\partial \hat{z}} \left(\frac{\hat{\tau}_1 \hat{E}_R^2}{\hat{\rho}_R^2}\right) + \frac{2(M-1)}{1 + (M-1)\hat{z}} I'_R$$

$$= \frac{2\hat{\tau}_1 \hat{E}_R}{\hat{\rho}_R^2} \frac{\partial \hat{E}_R}{\partial \hat{z}} - \frac{2I'_R}{\hat{\rho}_R} + \frac{2(M-1)}{1 + (M-1)\hat{z}} I'_R \tag{6.13}$$

However, since:

$$M = \frac{l_R + L}{l_R} = 1 + \frac{L}{l_R}$$

Eq (6.13) can be reduced to:

$$\frac{\partial I'_R}{\partial \hat{z}} + \frac{2(M-1)}{1 + (M-1)\hat{z}} I'_R = \frac{2\hat{\tau}_1 \hat{E}_R}{\hat{\rho}_R^2} \frac{\partial \hat{E}_R}{\partial \hat{z}} - \frac{2I'_R}{\hat{\rho}_R} + \frac{2I'_R}{\hat{\rho}_R}$$

$$= \frac{2\hat{\tau}_1 \hat{E}_R}{\hat{\rho}_R^2} \frac{\partial \hat{E}_R}{\partial \hat{z}} \tag{6.14}$$

Finally, substituting Eq (6.14) into (6.12) yields:

$$\frac{\partial I'_R}{\partial \hat{z}} + \frac{2(M-1)}{1 + (M-1)\hat{z}} I'_R = \frac{g_3 L}{\sqrt{a^2 - b^2}} \left(1 - \frac{a - \sqrt{a^2 - b^2}}{2I'_R}\right) I'_R \tag{6.15}$$

Eq (6.15) is identical to Eq (6.9a). In a similar manner, Eq (5.18b) can be transformed into Eq (6.9b). Clearly, then, the Agrawal-Lax equations are equivalent to the TWURL field amplitude equations at steady-state.

A consequence of the equivalence is that both models have the same threshold population inversion densities and resonator magnifications. The threshold expressions are given in Eq (6.8).

Summary

The TWURL model was compared to two free-running laser models in this chapter. A list of the key points from the comparisons is given below.

1. The simple saturable gain model.
   (a) The simple saturable gain model does not include the effects of spatial hole burning, whereas the TWURL model does.
   (b) The TWURL model reduces to the simple saturable gain model in the limit of threshold operation.
   (c) Both models have the same values of threshold population inversion density and resonator magnification.
   (d) The simple saturable gain model does not include the phase and frequency information (equations), unlike the TWURL model.
2. The Agrawal-Lax model.
   (a) The Agrawal-Lax model accounts for the effects of spatial hole burning, as does the TWURL model.
   (b) The Agrawal-Lax model is identical to the steady-state field amplitude equations of the TWURL model.
   (c) The Agrawal-Lax model is a steady-state model, whereas the TWURL model can be used for time-dependent calculations.
   (d) The Agrawal-Lax and (TWURL) models both have the same values of threshold population inversion density and resonator magnification.
   (e) The Agrawal-Lax model does not include the phase and frequency information (equations) that are included in the TWURL model.

The TWURL model was developed to correct the deficiencies in the existing PBCUR models. The TWURL model extends the range of possible calculations, including time-dependent and in-

jection locking studies, beyond those of the other models. In the appropriate limits, the TWURL reduces to the two models presented in this chapter.

VII. TWL Model Numerical Results

A variety of numerical studies of the Fabry-Perot laser were performed as part of the research. Three generic lasers were modeled; each was examined at four different barecavity frequencies $\Delta\hat{m}$. Time-dependent and steady-state runs of both free-running and injected lasers were performed. The parameter space explored had two free variables: the outcoupling (reflectivity r_B) and the detuning of the injected signal from the free-running frequency $(\hat{\nu} - \hat{\nu}_I)$.

The results of the numerical studies are discussed in detail below. The twelve data sets used are listed first; the rational for selecting the given parameters is discussed. The cubic curves are examined next. The time-dependent results for both free-running and injected lasers are explored in the following two sections. The final sections discuss the results of the steady-state studies for the free-running and injected lasers. Detailed comparisons to the alternate laser models presented in Chapter IV are made throughout the chapter. To avoid an excessive number of figures, a complete set of plots for data sets 27 and 36 are given in Appendix C.

Data Sets

Three general lasers are examined in the numerical studies. The laser parameters are not tied to any specific laser or lasing medium. Some of the parameters are taken from the examples in Chapter 8 of Sargent, Scully, and Lamb's text (106) and from Spencer and Lamb's paper (101). Each laser is "operated" at four separate barecavity frequencies, for a total of twelve different data sets. In all cases, mirror A is assumed to be perfectly reflective and mirror B is partially transmissive:

$$r_A = e^{i\pi}$$

$$r_B = r_B e^{i\pi}$$

The gain medium completely fills the region between the two mirrors, i.e., $\hat{L}_g = 1.0$. A complete list of the parameters is given in Table I.

TABLE I

Fabry-Perot Laser Numerical Studies: Laser Parameters†

Data Set	$\hat{\tau}_1$	$\hat{\tau}_2$	$\hat{\tau}_3$	$\hat{w}_{eq}$	$\Delta\hat{m}$	g_0/α_0	$r_B\|_{th}$
27	6.05	21.04145	$1.\bar{3}$	0.567	0.0	11.93	0.5003
28	6.05	36.54837	$1.\bar{3}$	0.54722	0.0	20.00	0.5000
29	6.05	21.04145	$1.\bar{3}$	1.0872	0.0	22.88	0.2500
30	6.05	21.04145	$1.\bar{3}$	0.567	0.03	11.92	0.5006
31	6.05	36.54837	$1.\bar{3}$	0.54722	0.03	19.98	0.5003
32	6.05	21.04145	$1.\bar{3}$	1.0872	0.03	22.86	0.2503
33	6.05	21.04145	$1.\bar{3}$	0.567	0.15	11.67	0.5086
34	6.05	36.54837	$1.\bar{3}$	0.54722	0.15	19.56	0.5081
35	6.05	21.04145	$1.\bar{3}$	1.0872	0.15	22.37	0.2581
36	6.05	21.04145	$1.\bar{3}$	0.567	0.375	10.46	0.5491
37	6.05	36.54837	$1.\bar{3}$	0.54722	0.375	17.53	0.5471
38	6.05	21.04145	$1.\bar{3}$	1.0872	0.375	20.06	0.2989

†Note: g_0/α_0 and $r_B|_{th}$ are calculated at $\Delta\hat{m}$, not at the more correct value of $\Delta\hat{t}$. Consequently, the tabulated g_0/α_0 values are slightly lower than the actual values, and the $r_B|_{th}$ values are somewhat high.

The following parameters are obtained from Figures 8.4 through 8.7 of (106):

$$\gamma = 2\pi \times 10^8 \text{ rads/sec}$$

$$\gamma_{ab} = \frac{\gamma}{2}$$

$$= \pi \times 10^8 \text{ rads/sec}$$

The lifetime of the upper atomic state is arbitrarily assumed to be 10 times that of the lower state: $\gamma_a = 10\gamma_b$. This is not unrealistic; the lifetime of the upper lasing level must be greater than that of the lower level in order to maintain a population inversion. Using these parameters with the definitions of γ_{ab} and $\hat{r}_1$ leads to:

$$\hat{r}_1 = \frac{\gamma\gamma_{ab}}{\gamma_a\gamma_b}$$

$$= 6.05$$

The resonator length is assumed to be 2.0 meters. Then:

$$\hat{r}_3 = \frac{2}{\psi}$$

$$= \frac{2\gamma L}{c}$$

$$= 1.3333\ldots$$

The barecavity mode spacing is 0.75 (in units of the atomic linewidth).

Four barecavity frequency offsets $\Delta\hat{m}$ are used in the study. Each laser is examined at linecenter ($\Delta\hat{m} = 0.0$), the maximum possible detuning from linecenter ($\Delta\hat{m} = \frac{0.75}{2} = 0.375$), and two intermediate values of $\Delta\hat{m}$. Because of the symmetry of the laser equations about linecenter, only positive values of $\Delta\hat{m}$ are used.

The pumping rate $\hat{w}_{eq}$ and the loss term $\hat{r}_2$ are chosen to yield g_0/α_0 ratios in the range $(10, 25)$ at linecenter. The linecenter threshold reflectivities are $r_B = 0.50$ (two cases) and $r_B = 0.25$ (one case). The actual parameters used in the analyses are listed in the table.

One additional detuning variable is required:

$$\Delta\hat{o} \equiv \hat{\nu} - \hat{\nu}_I$$

$$= \Delta\hat{\omega} - \Delta\hat{t} \tag{7.1}$$

This frequency difference is the detuning of the injected signal from the free-running laser frequency. Since one of the assumptions of the rate equation approximation is that the phases vary slowly in time $1/\gamma$, $\Delta\hat{o}$ is restricted to the range $[-0.1, 0.1]$.

The Cubic Curves

Spencer and Lamb (101) discuss in some detail plots of the internal laser intensity I_n vs the injected intensity I_I at steady-state. At low intensities, I_I is a cubic function of I_n. Similar curves can be generated with the TWL equations. Since the fields in the Fabry-Perot laser vary longitudinally, plots of $I_{R,L}(\hat{z})$ vs I_I can be produced for any axial location $\hat{z} = \ell$. The curves depict the injected intensity required to produce a given intensity value $I_{R,L}$ at some longitudinal position in the laser. An sample "cubic curve" is shown in Figure 7.1.

The TWL equations reduce to a form quite similar to the Spencer-Lamb equations at mirror A, as $E_R(0) = E_L(0)$ and $\dot{\varphi}_R(0) = \dot{\varphi}_L(0)$. Consequently, most of the cubic curves examined in this project are plots of $I_R(0)$ vs I_I. The following sections discuss the stability of injected lasers in the context of the cubic curves, the general behavior of the curves, and the unusual behavior of the curves noted by Ferguson (87, 88).

Injected Laser Stability. Spencer and Lamb derive a series of stability criteria for the injected laser from a perturbative analysis of their equations of motion. Their analysis demonstrates that the laser will lock to an injected signal provided that I_I is greater than some threshold value $I_I\big|_{th}$. The threshold injected intensity corresponds to the value of I_I at the turning point C in Figure 7.1. The laser will not lock to injected signals with intensities less than this threshold value. Furthermore, the injected laser will almost always lock to the upper branch (I) of the cubic curve. The laser cannot operate on branch II, and will operate on branch III in extremely limited circumstances. The laser will never operate on branch IV, as it is unlocked in this region.

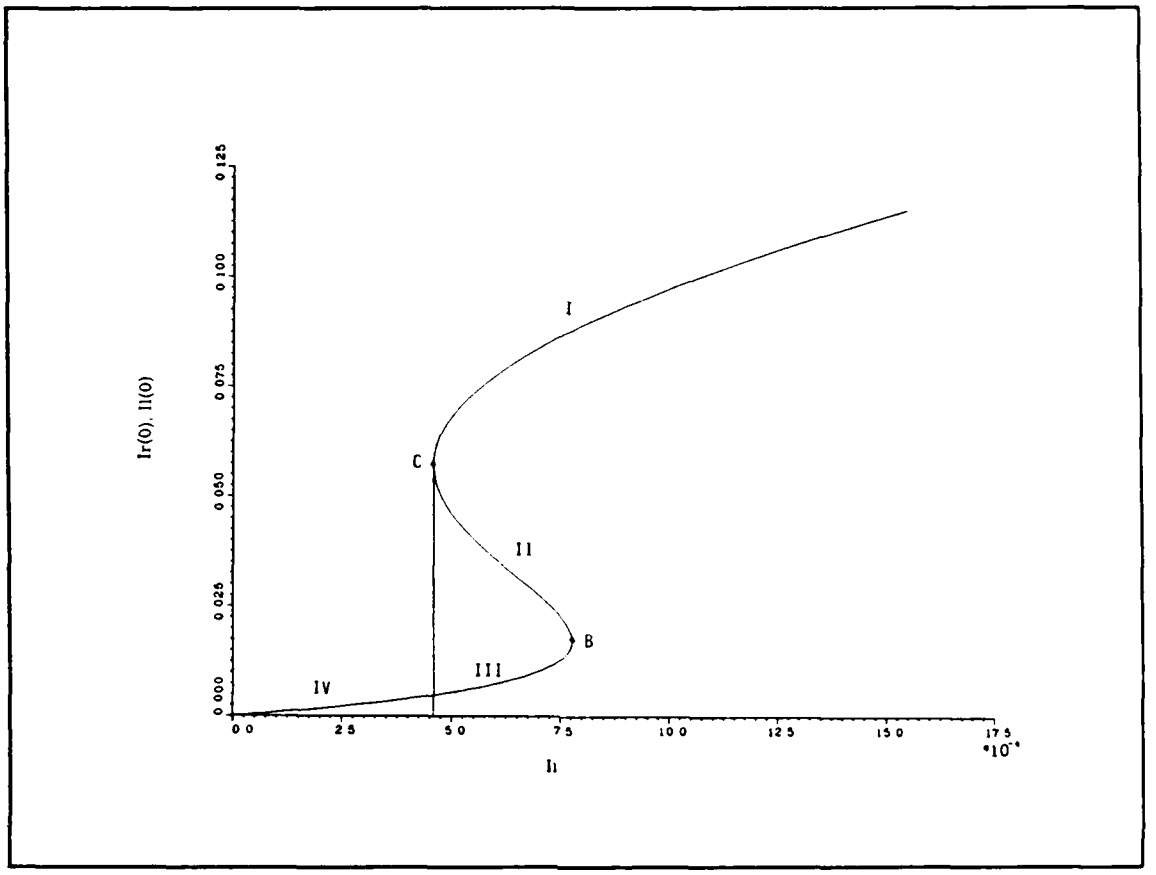

Figure 7.1. A sample cubic curve. $r_B = 0.75$, $\Delta\hat{o} = 0.008$. All other parameters are taken from data set 27.

Several heuristic arguments can be given to substantiate this behavior. In order to force the laser to operate at a nonresonant frequency, some minimum injected intensity must be applied to the device. Below this minimum, the laser will not lock to the injected signal. Rather, the laser field will beat against the injected signal. This region of operation corresponds to branch IV of the cubic curve. Above the minimum injected intensity, the laser will lock to the injected signal. On branches II or III, the fields inside the laser are not as intense as those on branch I. Consequently, the gain is not as depleted on the lower two branches as on branch I. From thermodynamics, the laser will tend to operate with the gain as depleted as possible (minimum stored energy condition), i.e., on branch I. Thus, the stability criteria derived for the Spencer-Lamb model make sense physically.

Lugiato *et al* (97) have performed numerical stability analyses of injected lasers. They are able to generate similar cubic curves using the Lorentz laser model. In certain operating regimes, chaos, period doubling, spiking and other unusual behavior can occur if $I_I < I_I\big|_{th}$. Under certain circumstances, the threshold injected intensity has a value greater than that corresponding to the turning point C. Their model always locks to branch I when operated above the threshold injected intensity point. Similar chaotic behavior was noted using the Maxwell-Bloch equations for the Lamb laser, derived as part of this research. Some work has indicated that chaos is not likely to occur when the rate equation approximations (adiabatic elimination of the polarization terms) are made (155).

An attempt was made to derive stability and locking conditions with a perturbative analysis of the TWL equations. The results of the analysis predicted unlocked behavior in regions where the time-dependent codes clearly showed locking. Attempts to locate the errors in the analysis failed. Consequently, this approach was dropped.

A series of time-dependent computer runs were performed to numerically examine the stability of injected lasers. The variables are listed in Table II. In only one case (run 15) did the numerical results indicate locking below the turning point C. In this run, it is likely that the laser was *not* locked, but rather in an extremely long-period oscillation (see the section on time-dependent results for injected lasers). A similar phenomenon was observed in run 14. Dramatically extending the number of time steps in run 14 showed that the laser was indeed unlocked and in a very long-period oscillation. In all the cases in which $I_I > I_I\Big|_{th}$, the laser locked to branch I of the cubic curve.

In light of the limited numerical results listed in Table II, the stability and locking criteria obtained by Spencer and Lamb were adopted for this research: the minimum injected intensity for locking is that corresponding to turning point C, and the laser will always lock to branch I of the cubic curve. It must be noted that the Spencer-Lamb locking criteria may not be directly applicable to this problem, as their equations are only an approximation to the TWL set. The analyses by Lugiato *et al* also may not be directly applicable, as the rate equation approximations are used in the derivation of the TWL equations. One alternative is to perform a time-dependent analysis

TABLE II

Injected Laser Stability Analysis†

Run Number	$\Delta\hat{m}$	$\Delta\hat{o}$	$I_{IN}^{\ddagger}$	$I_{IN}\|_{th}$	Laser Behavior
1	0.0	0.005	2.50×10^{-5}	1.661×10^{-4}	Unlocked
2	0.0	0.005	3.61×10^{-4}	1.661×10^{-4}	Locked
3	0.0	0.005	1.00×10^{-3}	1.661×10^{-4}	Locked
4	0.0	0.010	4.00×10^{-4}	6.224×10^{-4}	Unlocked
5	0.0	0.010	7.00×10^{-4}	6.224×10^{-4}	Locked
6	0.0	0.010	9.00×10^{-4}	6.224×10^{-4}	Locked
7	0.0	-0.010	4.00×10^{-4}	6.224×10^{-4}	Unlocked
8	0.0	-0.010	7.00×10^{-4}	6.224×10^{-4}	Locked
9	0.0	-0.010	9.00×10^{-4}	6.224×10^{-4}	Locked
10	0.10	0.00796	1.00×10^{-4}	3.986×10^{-4}	Unlocked
11	0.10	0.00796	3.00×10^{-4}	3.986×10^{-4}	Unlocked
12	0.10	0.00796	3.30×10^{-4}	3.986×10^{-4}	Unlocked
13	0.10	0.00796	3.60×10^{-4}	3.986×10^{-4}	Unlocked
14	0.10	0.00796	3.90×10^{-4}	3.986×10^{-4}	Unlocked
15	0.10	0.00796	3.98×10^{-4}	3.986×10^{-4}	Locked
16	0.10	0.00796	4.00×10^{-4}	3.986×10^{-4}	Locked
17	0.10	0.00796	4.10×10^{-4}	3.986×10^{-4}	Locked
18	0.10	0.00796	4.20×10^{-4}	3.986×10^{-4}	Locked
19	0.10	0.00796	4.50×10^{-4}	3.986×10^{-4}	Locked
20	0.10	0.00796	4.80×10^{-4}	3.986×10^{-4}	Locked
21	0.10	0.00796	5.10×10^{-4}	3.986×10^{-4}	Locked
22	0.10	0.00796	5.40×10^{-4}	3.986×10^{-4}	Locked
23	0.10	0.00796	5.70×10^{-4}	3.986×10^{-4}	Locked
24	0.10	0.00796	6.00×10^{-4}	3.986×10^{-4}	Locked
25	0.10	0.00796	6.30×10^{-4}	3.986×10^{-4}	Locked
26	0.10	0.00796	6.60×10^{-4}	3.986×10^{-4}	Locked
27	0.10	0.00796	6.90×10^{-4}	3.986×10^{-4}	Locked
28	0.10	0.00796	7.20×10^{-4}	3.986×10^{-4}	Locked
29	0.10	0.00796	7.50×10^{-4}	3.986×10^{-4}	Locked
30	0.10	0.00796	7.80×10^{-4}	3.986×10^{-4}	Locked
31	0.10	0.00796	8.10×10^{-4}	3.986×10^{-4}	Locked
32	0.10	0.00796	9.00×10^{-4}	3.986×10^{-4}	Locked

† $r_B = 0.70$. All other laser parameters are taken from data set 27.

‡ From Eq (3.22), $I_{IN} = I_I/t_B^2$.

to determine the locking point for each laser operating condition. This is not feasible due to the computer run costs and the sensitivity of the numerical routines (see Appendix B).

Cubic Curve Behavior. The cubic curves display a regular behavior as a function of $|\Delta\hat{o}|$. A sequence of the curves, with $\Delta\hat{o}$ as the parameter, are shown in Figure 7.2. In this example, $\Delta\hat{m} = 0.0$. When the injected signal frequency $\hat{\nu}_I$ is the same as the free-running laser frequency $\hat{\nu}$, turning point C lies on the vertical axis. This is the free-running laser operating point; the laser will oscillate at this point in the absence of an injected field. As the injected signal is detuned from $\hat{\nu}$, the "s-shaped" region of the curves shift outward, progressively becoming narrower. In the linecenter case ($\Delta\hat{m} = 0.0$), $I_R(0)$ at point C decreases while the value at turning point B increases as $\Delta\hat{o}$ increases from 0.0. Eventually, at a large enough value of $\Delta\hat{o}$, the two turning points coalesce into a single point with infinite slope. For larger values of $\Delta\hat{o}$, the cubic curves are monotonically increasing functions of I_I. The same behavior is exhibited if $\Delta\hat{o}$ is made increasingly negative, due to symmetry about linecenter. Ferguson has noted similar behavior of the cubic curves. Physically, the behavior indicates that increasingly larger injected signals are required to lock the laser as the detuning increases. $I_R(0)$ decreases at the locking threshold point C when $|\Delta\hat{o}|$ rises since the laser is forced to operate under increasingly nonresonant conditions.

The trajectory of point C as a function of $\Delta\hat{o}$ is altered somewhat if $\Delta\hat{m} \neq 0.0$, due to the asymmetry of the gain curve about $\hat{\nu}$. As $\Delta\hat{o}$ becomes increasingly positive for positive $\Delta\hat{t}$ ($\Delta\hat{m}$), $I_R(0)$ at point C first increases then decreases until the two turning points merge. Note that the gain decreases as $\Delta\hat{o}$ rises. In the $I_R(0)$–I_I plane, the trajectory of point C first rises and then falls. If $\Delta\hat{o}$ becomes increasingly negative for positive $\Delta\hat{t}$, $I_R(0)$ at point C monotonically decreases until the two turning points merge. In this case, the gain increases as $\Delta\hat{o}$ decreases. The trajectory of point C monotonically decreases in the $I_R(0)$–I_I plane. Ferguson did not observe these effects as his gain g_0 is not a function of $\hat{\nu}$. Although not examined, similar effects should hold on the opposite side of the gain curve due to symmetry.

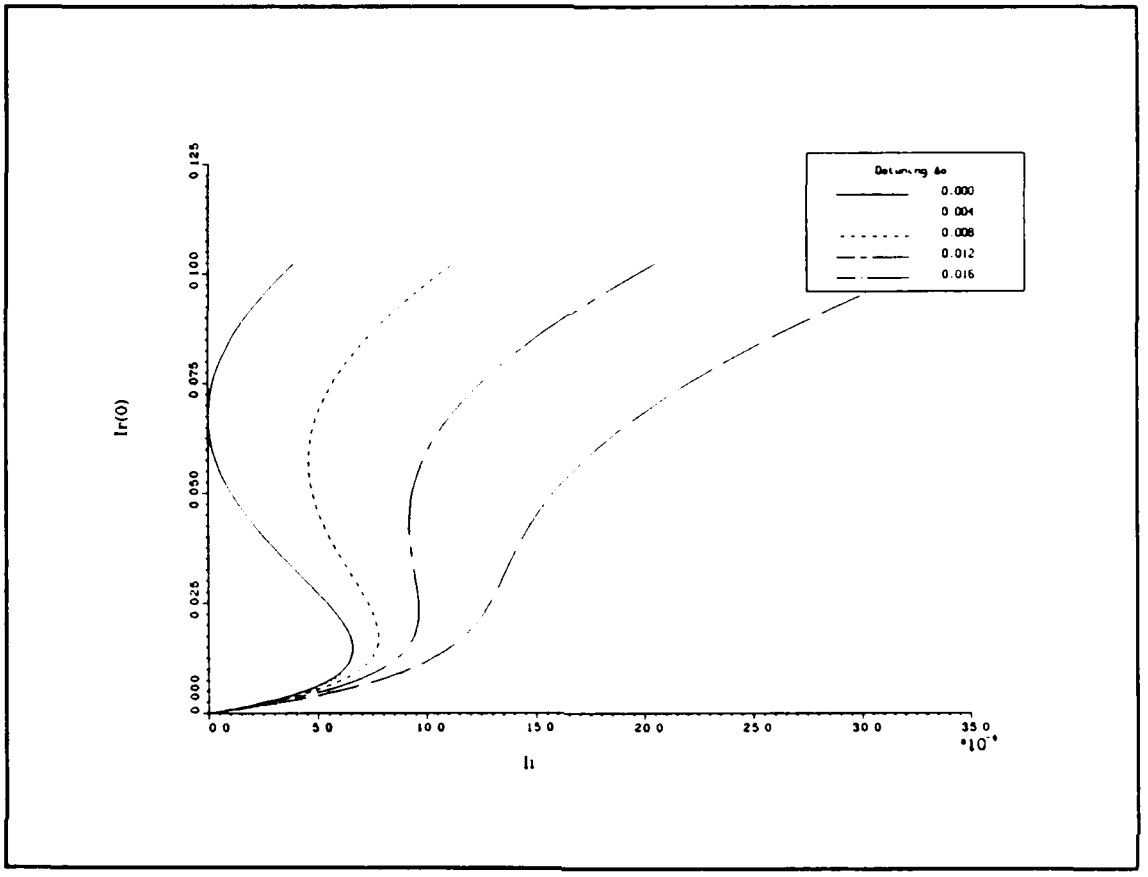

Figure 7.2. The cubic curves as functions of $\Delta\hat{o}$. $r_B = 0.75$ and $\Delta\hat{m} = 0.0$. All other parameters are taken from data set 27.

The detunings $\pm\Delta\hat{o}_{max}$ at which points C and B merge are functions of the reflectivity r_B. Here, the $\pm$ sign denotes the positive and negative $\Delta\hat{o}$ values at which the turning points coalesce. $|\pm\Delta\hat{o}_{max}|$ increase as r_B rises from $r_B|_{th}$, reach a maximum value, then decrease as $r_B \rightarrow 1.0$. The decrease at the higher reflectivity values is much more pronounced at high $\Delta\hat{m}$ values than near linecenter. Only at linecenter ($\Delta\hat{m} = 0.0$) does $+\Delta\hat{o}_{max} = -\Delta\hat{o}_{max}$ for all reflectivities r_B.

Anomalous Behavior of the Cubic Curves. Ferguson has performed an extensive analytic examination of the cubic curves. If $r_A = 1.0$, then the cubic curves obtained from his model at any location in the resonator have the characteristic s-shape and display the behavior noted above. Regardless of the axial location $\hat{z}$, the turning points B and C occur at the same respective values of I_I. However,

if $r_A < 1.0$, the cubic curve representing $I_R(1)$ vs I_I can take on a variety of anomalous shapes. Extrema in $I_R(1)$ (defined as points at which the slope $\frac{\partial I_R(1)}{\partial I_I}$ is zero) can be obtained. Cusps and loops can exist in the curves. To a large degree, the location and orientation of the cusps and loops can be set by the appropriate choice of laser gains, reflectivities, and detunings $\Delta\hat{o}$. Ferguson has analytically shown that the anomalous behavior only occurs in plots of $I_R(1)$ vs I_I; at any other location in the resonator, the curves are always s-shaped or monotonically increasing. Additionally, the extrema can only exist if the laser model allows for longitudinal growth of the electric fields, as in the TWL and simple saturable gain models. Such behavior will not occur in a standing wave model, such as the Spencer-Lamb and Chow theories.

Despite the differences between Ferguson's laser model and the current theory, similar "cubic curves" can be obtained with the TWL model. Representative curves are shown in Figures 7.3–7.4. The first figure shows the transition from the usual s-shape to a near-horizontal cusp to a loop, as the value of $\hat{w}_{eq}$ is increased. The second plot is a near-vertical cusp. After reaching the cusp, the value of $I_R(1)$ decreases rapidly, reaches a second extreme value, then rises again. Note the very large value of $\Delta\hat{o}$ required in this plot. This value is clearly outside of the range imposed in Section 1.

The behavior of the curves raises questions about the stability criteria derived by Spencer and Lamb. Regions of branch I on the above curves exist where the slopes are negative. Moreover, the slopes are positive in these regions for *all* other cubic curves at every other axial location in the resonator. According to the stability criteria, the regions with negative slope should be unstable. However, since the Spencer-Lamb model does not allow for longitudinal growth of the electric fields, it is doubtful that their criteria can be applied to the present case. Clearly, there is a need for stability criteria beyond those derived by Spencer and Lamb to treat lasers with longitudinal electric field growth.

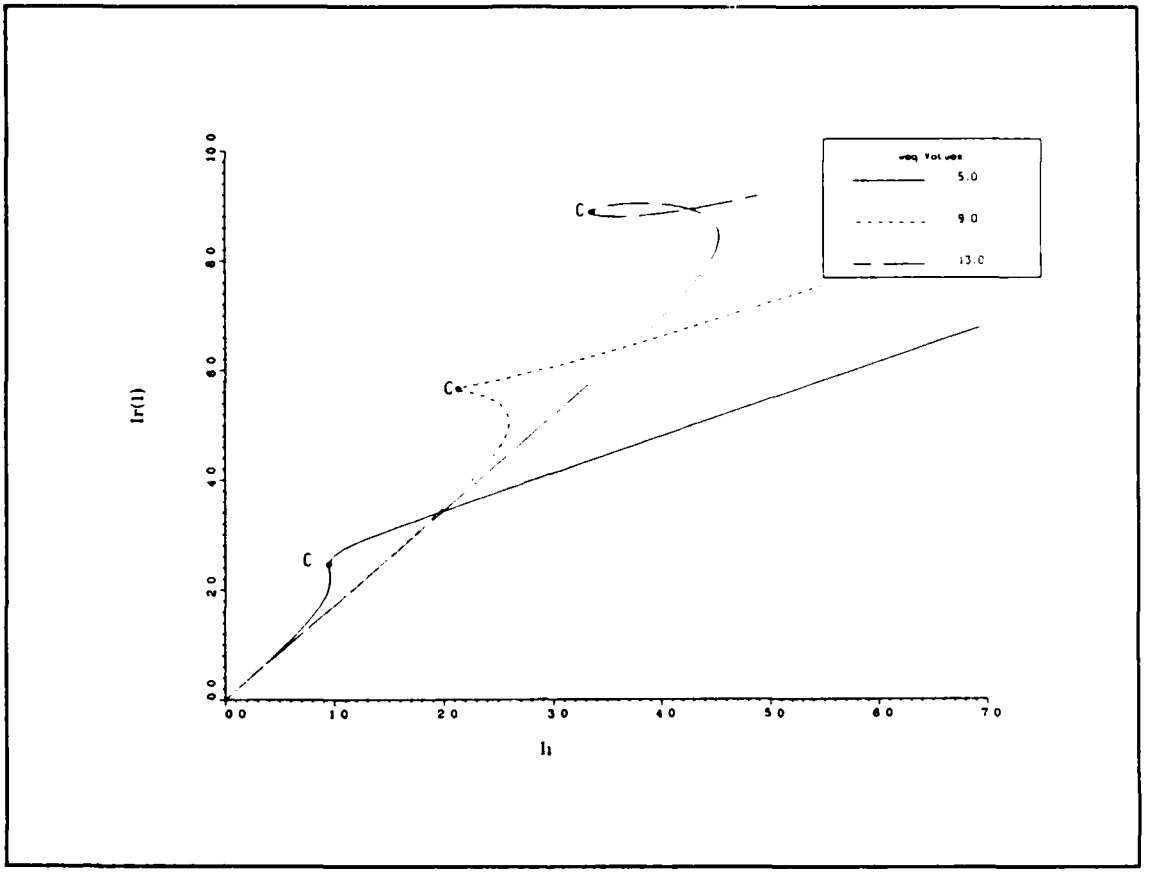

Figure 7.3. Near-horizontal cusps and loops. In these plots, $\hat{r}_1 = 1.0$, $\hat{r}_2 = 10^{10}$, $\hat{r}_3 = 1.0$, $\Delta\hat{m} = 0.0$, $\Delta\hat{o} = 0.0717$, $r_A = 0.632$, and $r_B = 0.763$. Turning point C is denoted on the curves.

Time-Dependent Laser Behavior

A series of time-dependent runs with and without injected signals were performed. In general, the results compare quite favorably to those published in the literature (101, 106). Due to numerical stability problems and the high computer run costs, the amount of analysis with the time dependent codes was limited.

Free-Running Lasers. A typical run without injection is shown in Figure 7.5. The general shape of the electric field amplitudes is quite similar to those shown (106). At high and low values of r_B, a rippled or sawtooth behavior occurs in the field amplitudes (Figure 7.6). The ripples usually

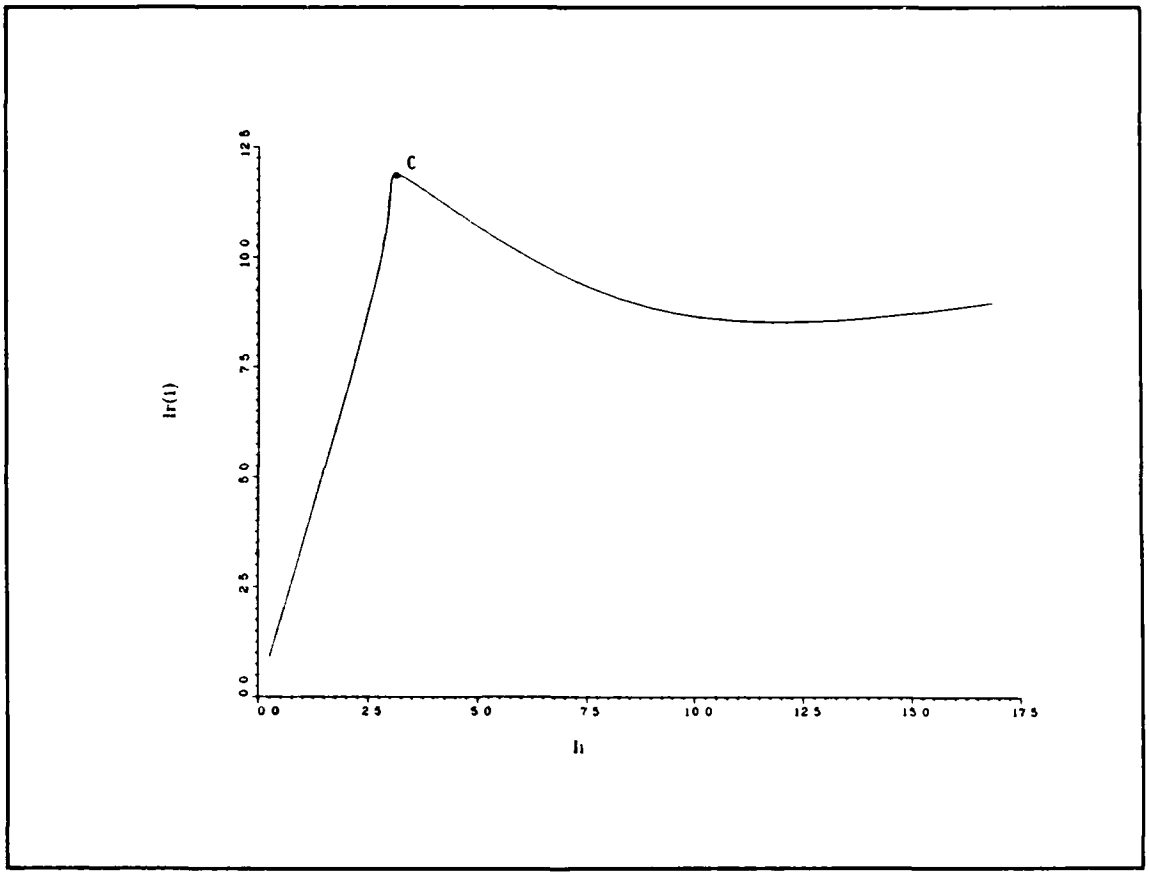

Figure 7.4. Near-vertical cusp. In this plot, $\hat{r}_1 = 1.0$, $\hat{r}_2 = 10^{10}$, $\hat{r}_3 = 1.0$, $\Delta\hat{m} = 0.0$, $\Delta\hat{\sigma} = 0.285$, $r_A = 0.548$, $r_B = 0.536$, and $\hat{w}_{eq} = 17.0$. Turning point C is denoted on the plot.

damp out; however, when $r_B \approx 1.0$ or $r_B \approx r_B|_{th}$, the ripples grow exponentially in time until the numerical routine becomes unstable. Analysis demonstrated that the ripples are due solely to the initial conditions and are not a laser phenomenon. (See Appendix B for a detailed explanation of the effect.) At intermediate values of r_B, the ripples sometimes existed, but usually damped out rapidly. The steady-state amplitudes agreed excellently with those calculated from the steady-state codes.

Relaxation oscillations (141, 146) were not noted in any of the runs. In all cases, the fields rose smoothly to the steady-state values, without overshooting and ringing. This could be due to

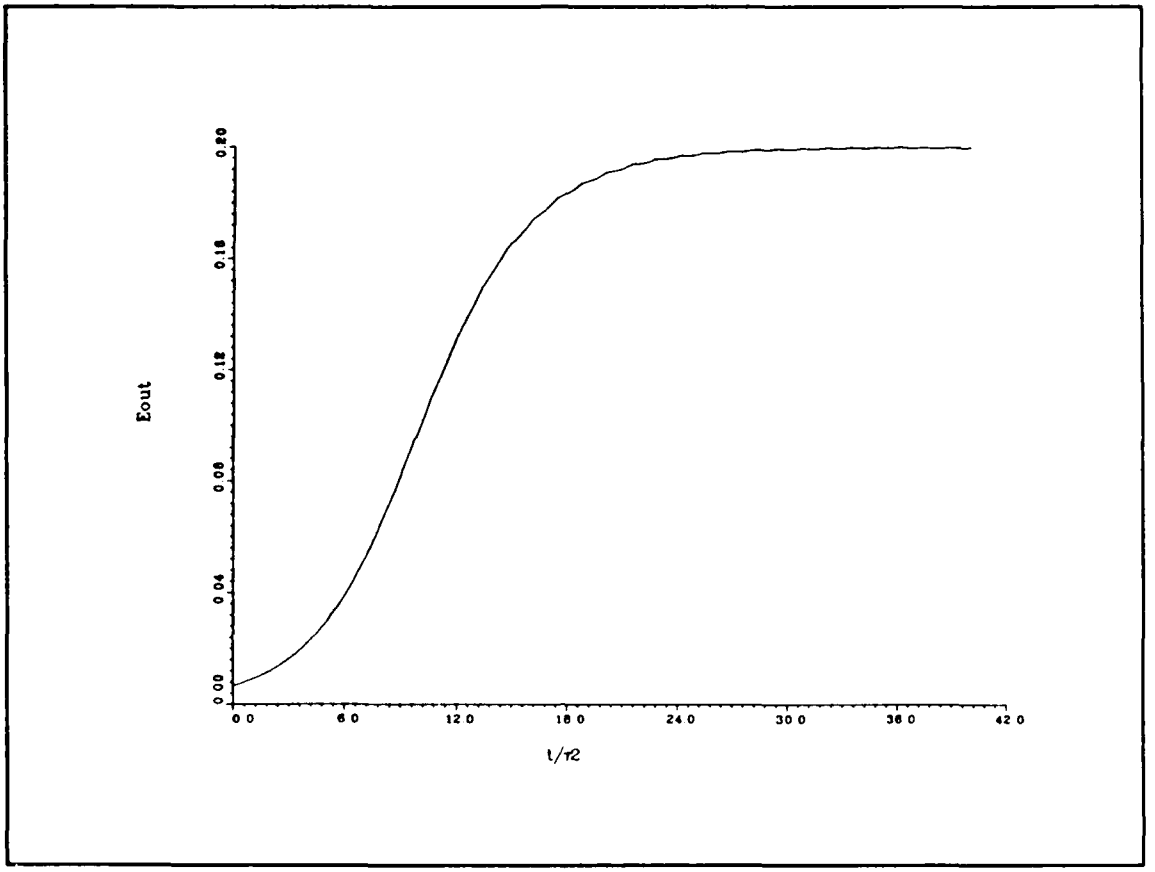

Figure 7.5. Typical time-dependent laser run. $\hat{E}_{out}$ vs $\hat{t}$, for $r_B = 0.75$. All other parameters are taken from data set 27.

the limited parameter space explored. In other regions of the space (i.e., very strong pumping), relaxation oscillations might occur.

Plots of the phase time derivatives $\dot{\varphi}_{R,L}$ vs $\hat{t}$ generally display a shift from some initial value to a final, constant value. This final value is the offset of input reference frequency $\hat{\nu}_I$ from the actual lasing frequency $\hat{\nu}$. (Recall that $\hat{\nu} \equiv \hat{\nu}_I + \dot{\varphi}_{R,L}$.) Transients, often severe, exist in the plots of $\dot{\varphi}_{R,L}$ vs $\hat{t}$. They are principally due to the initial conditions for $\dot{\varphi}_{R,L}$. The computer code sets the initial value of the phase time derivatives equal to zero. This will generally force an immediate shift in frequency to some finite value that eventually decays to the final constant value. The frequency shift couples through the gain into the field amplitudes and the explicit values of $\dot{\varphi}_{R,L}$. More realistic

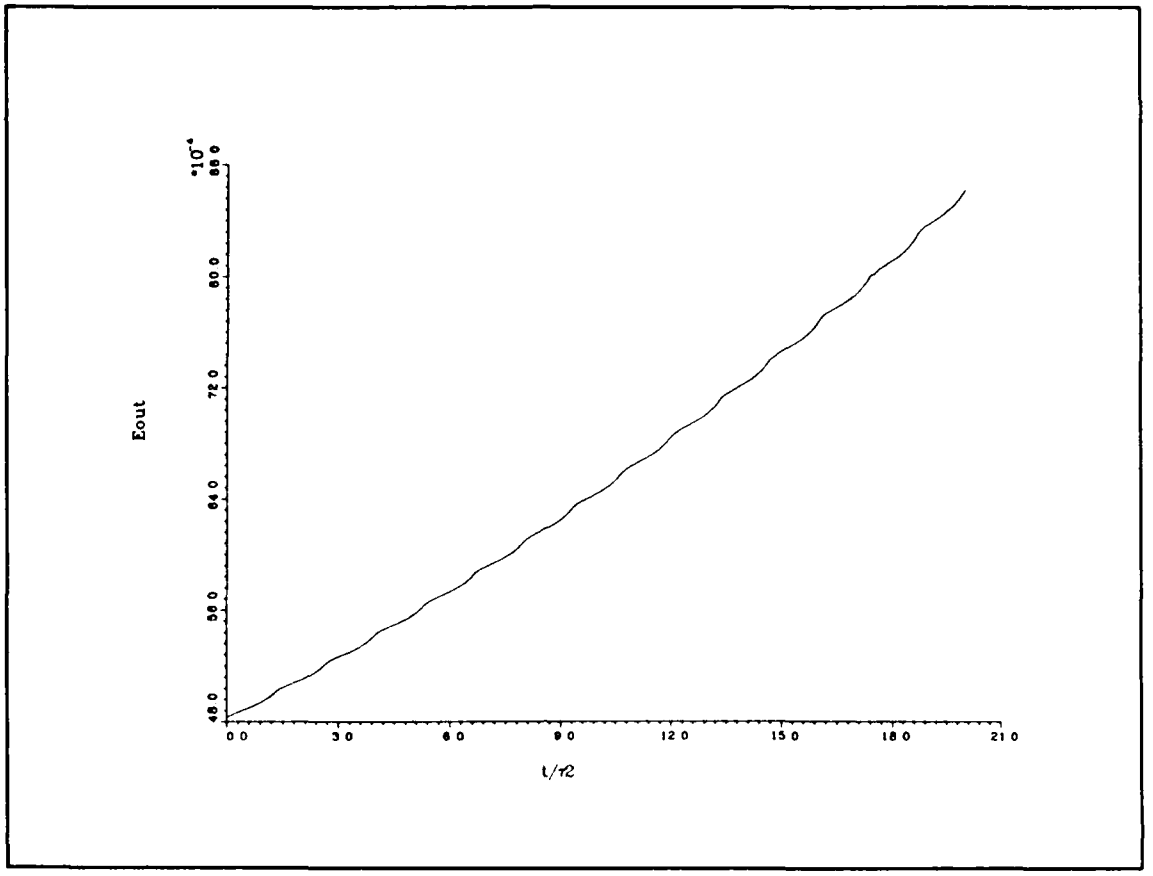

Figure 7.6. $\hat{E}_{out}$ vs $\hat{t}$, for $r_B = 0.26$. All other parameters are taken from data set 29. Note the ripples in the output field amplitude. Only the initial field rise is plotted.

initial conditions for $\dot{\varphi}_{R,L}$ might preclude or diminish such transient behavior. In all the runs examined, $\dot{\varphi}_R$ and $\dot{\varphi}_L$ were equal and constant in $\hat{z}$ at steady-state. This implies that the frequency of $\hat{\mathbf{E}}_R$ is equal to that of $\hat{\mathbf{E}}_L$, and that the frequency is constant spatially.

Injected Lasers. The behavior of the injected laser depends upon whether the injected signal amplitude is above or below the locking threshold. If the signal is greater than the threshold value, the field amplitudes approach some constant, steady-state value and the phase time derivatives are driven to zero. If the injected signal strength is less than the threshold value, the output laser field displays amplitude and frequency modulation. Example plots are shown in Figures 7.7–7.9.

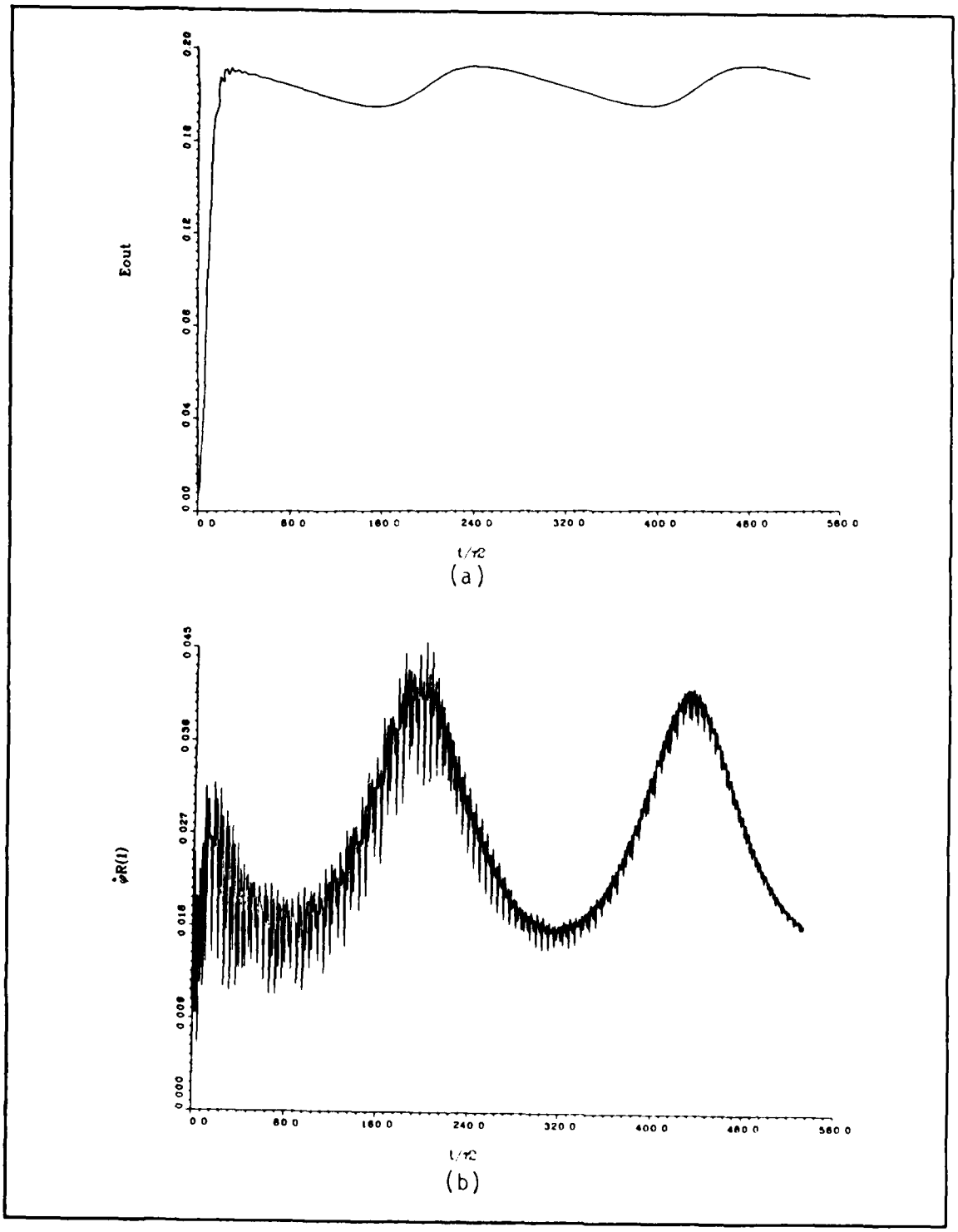

Figure 7.7. Injected laser output field with the injected signal strength below the locking threshold. $r_B = 0.70$, $I_{IN} = 2.50 \times 10^{-5}$, $\Delta\hat{m} = 0.0$, and $\Delta\hat{\delta} = 0.005$. All other parameters are taken from data set 27. $I_{IN}|_{th} = 1.661 \times 10^{-4}$. (a) $\hat{E}_{out}$ vs $\hat{t}$. (b) $\dot{\varphi}_B(1)$ vs $\hat{t}$.

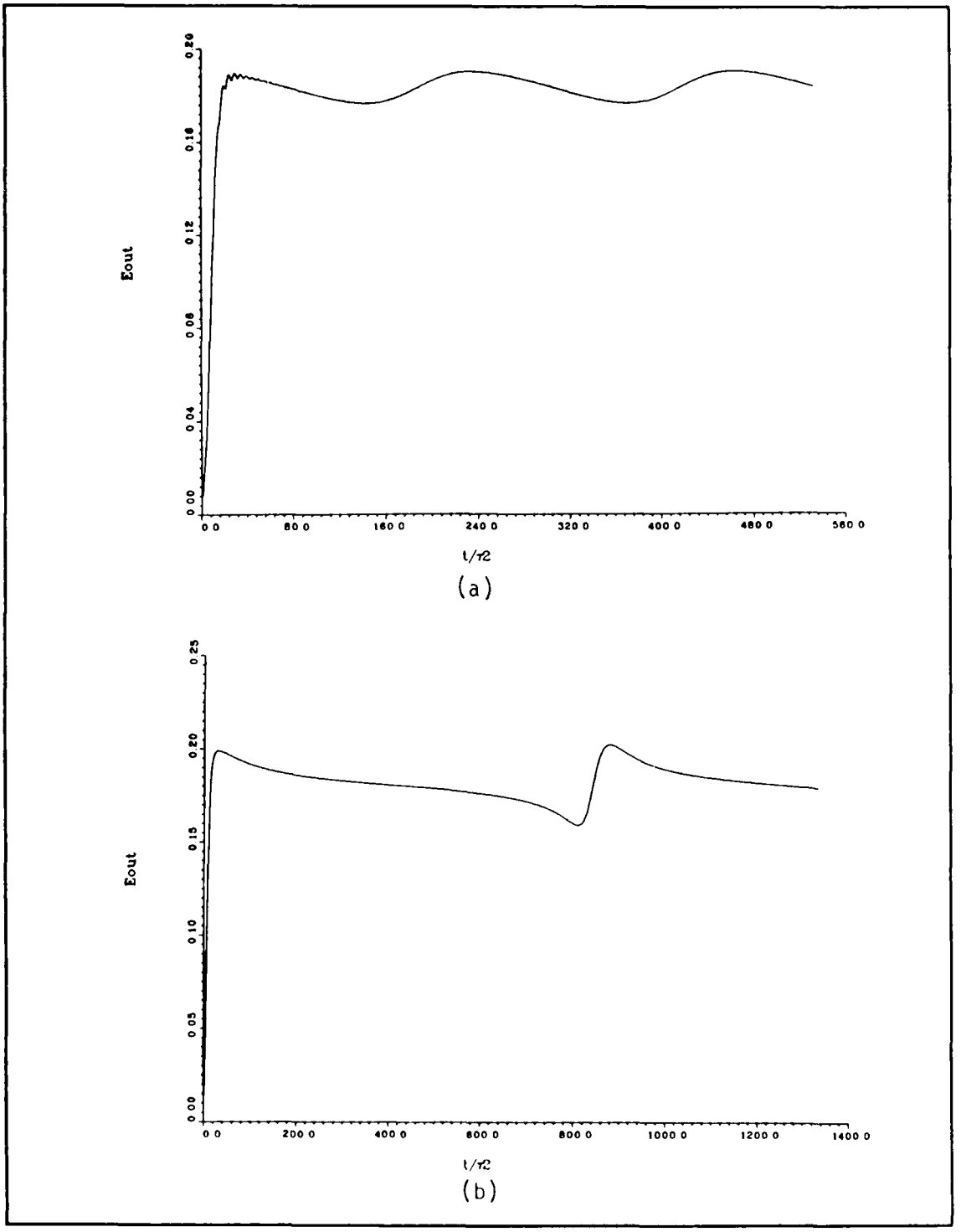

Figure 7.8. Injected laser output field amplitudes as a function of injected signal strength. (a) $I_{IN} = 1.5 \times 10^{-5}$. (b) $I_{IN} = 1.5 \times 10^{-4}$. All other parameters are taken from Figure 7.7.

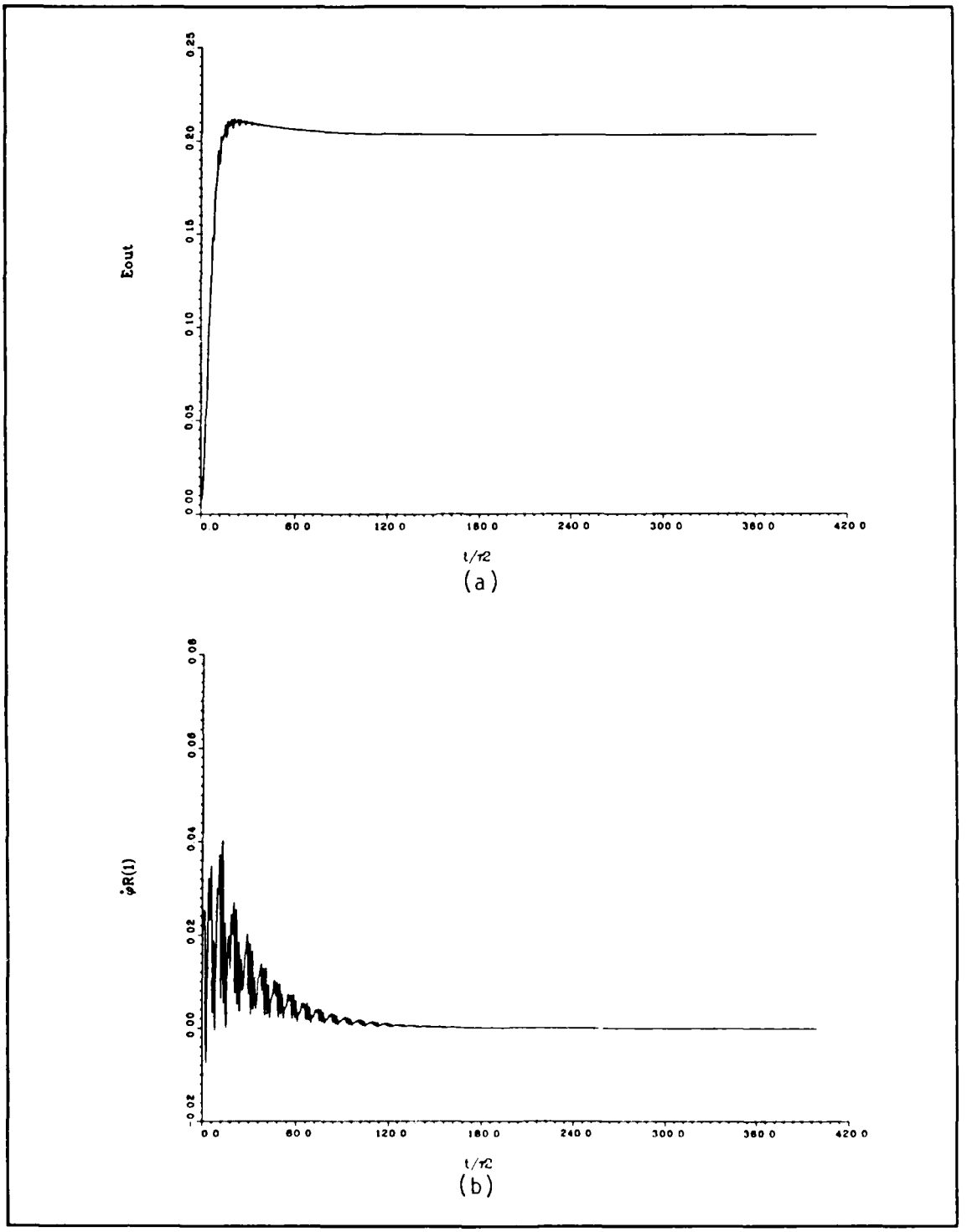

Figure 7.9. Injected laser output field with the injected signal strength above the locking threshold. $I_{IN} = 3.61 \times 10^{-4}$. All other parameters are taken from Figure 7.7. (a) $\hat{E}_{out}$ vs $\hat{t}$. (b) $\dot{\varphi}_R(1)$ vs $\hat{t}$.

When I_{IN} is less than the minimum signal strength required for locking, the injected field beats against the free-running laser field. This results in amplitude and phase modulations of $\hat{\mathbf{E}}_{out}$, as seen in Figure 7.7. (Note the large amount of numerical noise present in the figures. In many runs, the noise did not damp out, even after several hundred thousand time steps. The phase noise always required much longer to damp out than the field amplitude noise. This is due primarily to the phase time derivatives present on the right-hand sides of the TWL equations.) The plots are qualitatively similar to those in Figures 3 and 4 of (101). In general, the periods of the oscillations are governed by the strength of the injected signal. The oscillation periods are relatively short when the injected signals are very weak. As I_{IN} approaches the locking threshold, the periods of the oscillations become extremely long. This effect occurs for *fixed* detuning $\Delta\hat{o}$ of the injected signal from the free-running frequency. This behavior is depicted in Figure 7.8. Similar behavior has been noted experimentally in injected semiconductor lasers (51). The modulation depth remains roughly constant, regardless of the amplitude of the injected signal. This is counterintuitive; the expected behavior is that the beat frequency remains fixed as I_I varies but the modulation depth changes. In all cases tested, the threshold injected intensity for locking corresponded to the turning point C on the cubic curves.

Figure 7.9 displays the behavior of the outcoupled field when I_{IN} is above the locking threshold value. Note that the electric field amplitude overshoots the steady-state value after the initial rise. After some ringing, the amplitude decays to the steady-state value. The phase time derivatives suffer an initial transient that decays to zero at steady-state. The final value of zero implies that $\hat{\nu} = \hat{\nu}_I$, as expected. This behavior was observed in all of the runs that were performed. No runs were performed with $\Delta\hat{o}$ so large that the cubic curves were monotonically increasing functions of I_{IN}.

Steady-State Behavior: Free-Running Lasers

The free-running laser at steady-state was examined extensively. Comparisons of the TWL model and the simple saturable gain, Lamb, and Spencer-Lamb models were performed. Additionally, experimental data from an XeF laser were reduced using the TWL and simple saturable gain models. These comparisons and XeF data are discussed in the following sections.

The Simple Saturable Gain and TWL Models. Comparisons of the TWL and simple saturable gain models were made for the twelve data sets listed in Table I. For convenience and to expedite the comparisons, the free-running frequencies were forcibly set equal to the barecavity frequencies ($\hat{\nu} = \hat{\Omega}$). Consequently, $\Delta\hat{t} = \Delta\hat{m}$. (Note that this does *not* ignore the effects of medium pushing and pulling. As discussed below, $\hat{\nu}$ is a function of the mirror reflectivities. In order to simplify the comparisons of the two models, $\hat{\nu}$ was fixed for all r_B values. For consistency with the data set values, $\Delta\hat{t}$ was set equal to $\Delta\hat{m}$. An alternate way to view this is that the values of $\Delta\hat{m}$ were tuned for each r_B value such that the $\Delta\hat{t}$ values were constant for all r_B. This was only done in the comparisons of the simple saturable gain and TWL models.)

A typical plot of $I_R(0)$ vs r_B is depicted in Figure 7.10. The fields rise monotonically as r_B increases, due to the decreasing losses of the resonator. The simple saturable gain model predicts higher field amplitudes as the model does not include the effects of spatial holeburning. The differences in the intensities from the two models are typically in the range 20-30%. The spatial holeburning effects are thus quite significant. The energy extraction efficiencies calculated with the simple saturable gain model are correspondingly higher than the correct values calculated with the TWL model. Increasing $|\Delta\hat{t}|$ causes a decrease in the field amplitudes in both models. This can be understood by examining Eq (4.10a). As the frequency shifts off linecenter, the small signal gain $g_0 L$ decreases. Consequently, the fields supported by the laser decrease in amplitude.

Both models produce the same lasing threshold reflectivity $r_B|_{th}$. This is expected, as explained in Chapter IV. The threshold reflectivity values agreed excellently with the values calculated from

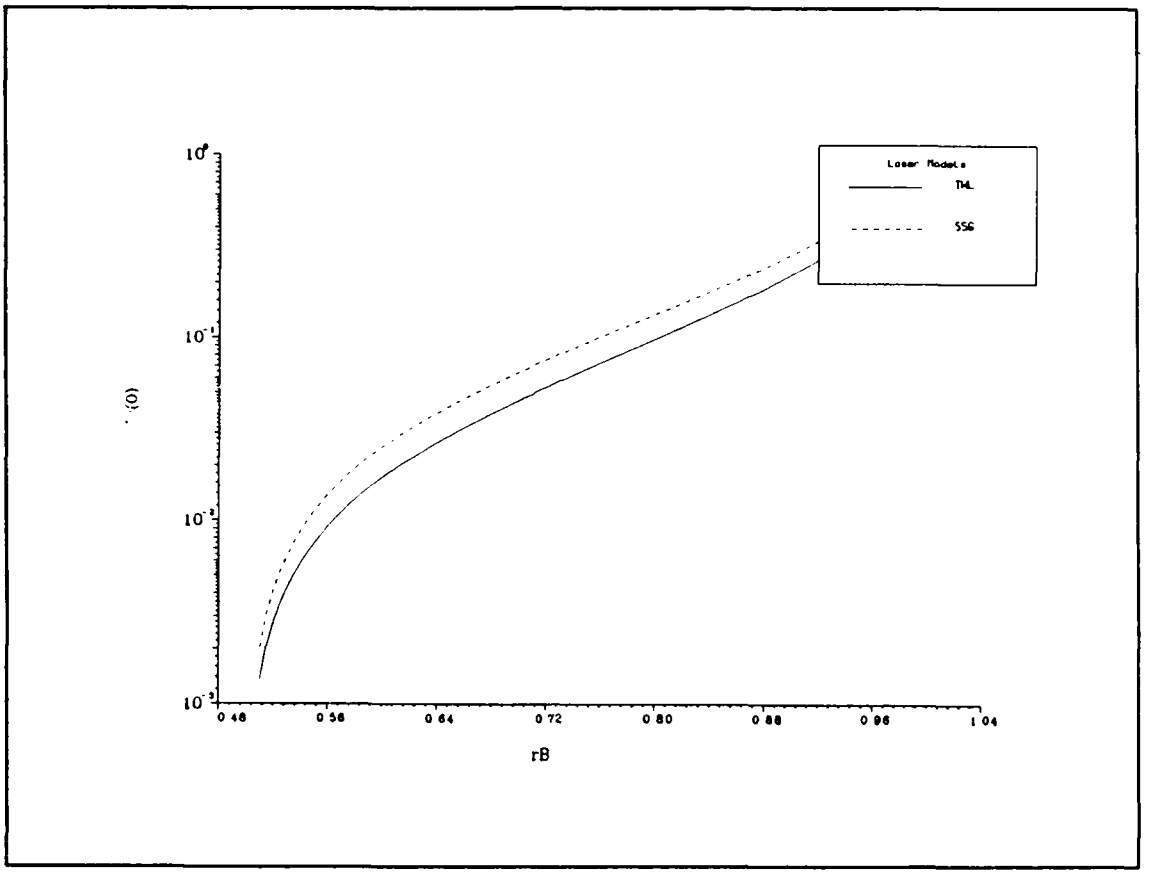

Figure 7.10. $I_R(0)$ vs r_B for the simple saturable gain (SSG) model and the TWL model. All parameters are taken from data set 27.

Eq (4.17c). A slightly expanded version of the threshold equation, verified numerically, is:

$$(r_A r_B)\Big|_{th} = \exp\left[\hat{r}_3 \hat{L}_g \left(\frac{1}{\hat{r}_2} - \frac{\hat{w}_{eq}}{1+\Delta\hat{t}^2}\right)\right] \tag{7.2}$$

A close examination of the intensity values near threshold reveals an anomalous behavior. Both models predict that the intensity approaches zero as $r_B \rightarrow r_B\big|_{th}$. The percentage difference in the intensities of the two models increases, however, as $r_B \rightarrow r_B\big|_{th}$. Physically, the intensities are approaching zero, but at different rates in the two models. A careful reduction of the TWL equations

of motion to the threshold regime yields:

$$\frac{\partial \tilde{I}_R}{\partial \hat{z}} \approx \{-\alpha_0 L + g_0 L[1 - \tilde{I}_R - 2\tilde{I}_L + \tilde{I}_R^2 + 6\tilde{I}_R\tilde{I}_L + 3\tilde{I}_L^2 - \tilde{I}_R^3 - 12\tilde{I}_R^2\tilde{I}_L - 18\tilde{I}_R\tilde{I}_L^2 - 4\tilde{I}_L^3|\}\tilde{I}_R \tag{7.3a}$$

$$\frac{\partial \tilde{I}_L}{\partial \hat{z}} \approx -\{-\alpha_0 L + g_0 L[1 - 2\tilde{I}_R - \tilde{I}_L + 3\tilde{I}_R^2 + 6\tilde{I}_R\tilde{I}_L + \tilde{I}_L^2 - 4\tilde{I}_R^3 - 18\tilde{I}_R^2\tilde{I}_L - 12\tilde{I}_R\tilde{I}_L^2 - \tilde{I}_L^3|\}\tilde{I}_L \tag{7.3b}$$

The simple saturable gain model reduces to:

$$\frac{d\tilde{I}_R}{d\hat{z}} \approx \{-\alpha_0 L + g_0 L[1 - \tilde{I}_R - \tilde{I}_L + \tilde{I}_R^2 + 2\tilde{I}_R\tilde{I}_L + \tilde{I}_L^2 - \tilde{I}_R^3 - 3\tilde{I}_R^2\tilde{I}_L - 3\tilde{I}_R\tilde{I}_L^2 - \tilde{I}_L^3|\}\tilde{I}_R \tag{7.3c}$$

$$\frac{d\tilde{I}_L}{d\hat{z}} \approx -\{-\alpha_0 L + g_0 L[1 - \tilde{I}_R - \tilde{I}_L + \tilde{I}_R^2 + 2\tilde{I}_R\tilde{I}_L + \tilde{I}_L^2 - \tilde{I}_R^3 - 3\tilde{I}_R^2\tilde{I}_L - 3\tilde{I}_R\tilde{I}_L^2 - \tilde{I}_L^3|\}\tilde{I}_R \tag{7.3d}$$

where:

$$\tilde{I}_{R,L} \equiv \frac{I_{R,L}}{I_{sat}} \tag{7.3e}$$

To second order in the intensities, the models are significantly different. Only in the zero field limit (exactly at threshold) are the two models identical. Consequently, the two models approach the same threshold, but at different rates.

Figure 7.11 is a plot of the output intensities vs the reflectivity of mirror B. Both models generate the usual peaked plots. The output fields are zero as $r_B = 1.0$ since the mirror transmission is zero. As the reflectivity drops, $\hat{E}_{out}$ rises to a peak. The peak occurs when the increase in transmissivity is overcome by the decrease in $\hat{E}_R(1)$. The peak output field occurs at a slightly lower value of r_B in the simple saturable gain model than in the TWL model. This is of some significance, as lasers are often designed to operate at the peak output power. Use of the simple saturable gain model

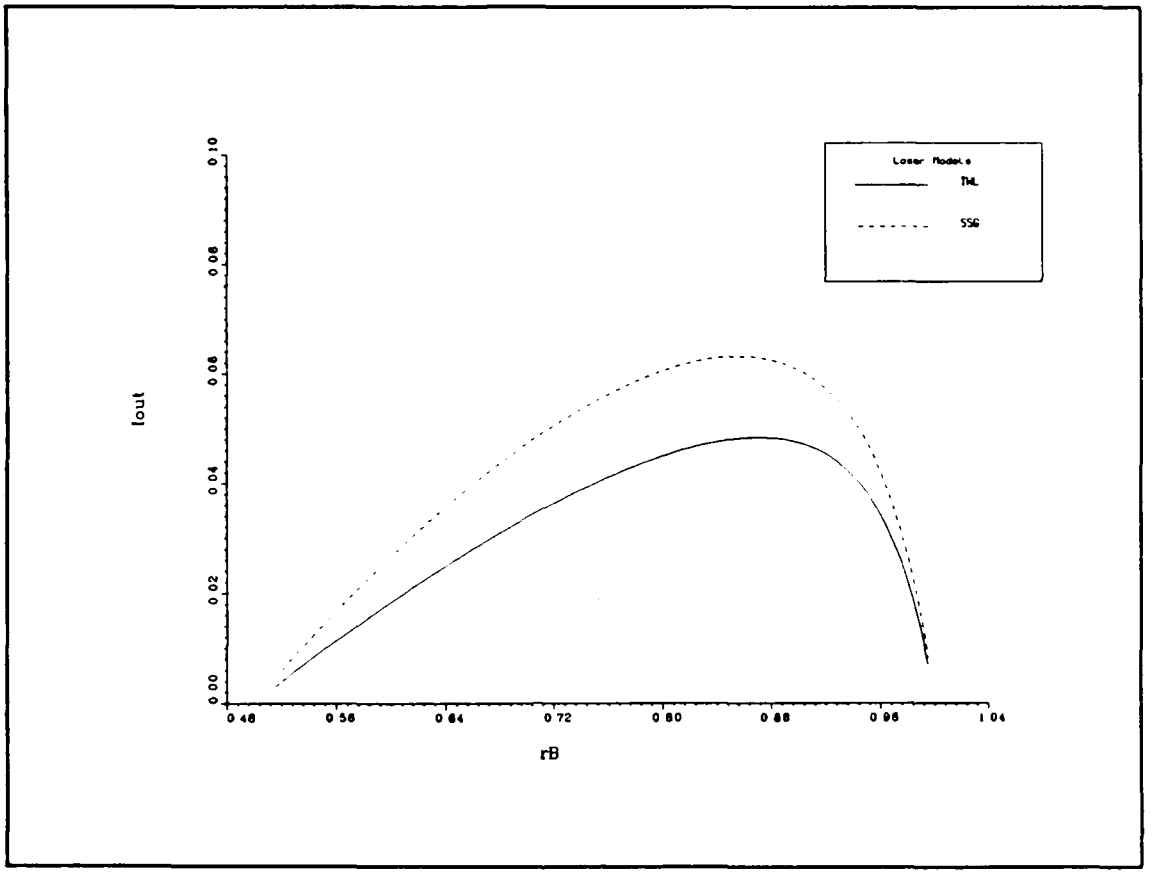

Figure 7.11. I_{out} vs r_B for the SSG and the TWL models. All parameters are the same as in Figure 7.10.

to optimize the output power will result in extracting slightly less than the peak power. These observations are similar to those noted by Agrawal and Lax (142, 143).

The Standing Wave and TWL Models. The TWL model was compared to three standing-wave laser models (Lamb, Spencer-Lamb, and a modified version of the Spencer-Lamb model). The standing-wave models are often used for laser design and analysis. However, as is shown below, these models are only valid for very high mirror reflectivities.

For convenience, the Lamb model is repeated below:

$$\frac{d\hat{E}_n}{d\hat{t}} = -\left(\frac{1}{\hat{\tau}_2} - \frac{1}{\hat{\tau}_3 \hat{L}_g} \ln r_B\right) \hat{E}_n + \frac{2\hat{w}_{eq}}{\hat{\tau}_1 \hat{E}_n} \left\{1 - \left[1 + \frac{\hat{\tau}_1 \hat{E}_n^2}{1 + (\Delta\hat{\omega} - \dot{\varphi}_n)^2}\right]^{-1/2}\right\} \qquad (7.4a)$$

$$\frac{d\phi_n}{d\hat{t}} = \hat{\Omega} - \hat{\nu}_I + \frac{2\hat{w}_{eq}(\Delta\hat{\omega} - \dot{\varphi}_n)}{\hat{\tau}_1 \hat{E}_n^2}\left\{1 - \left[1 + \frac{\hat{\tau}_1 \hat{E}_n^2}{1 + (\Delta\hat{\omega} - \dot{\varphi}_n)^2}\right]^{-1/2}\right\} \tag{7.4b}$$

The Spencer-Lamb model is:

$$\frac{d\hat{E}_n}{d\hat{t}} = -\left[\frac{1}{\hat{\tau}_2} + \frac{2}{\hat{\tau}_3}\left(\frac{1}{\eta^2 + 1}\right)\right]\hat{E}_n + \frac{2\hat{w}_{eq}}{\hat{\tau}_1 \hat{E}_n}\left\{1 - \left[1 + \frac{\hat{\tau}_1 \hat{E}_n^2}{1 + (\Delta\hat{\omega} - \dot{\varphi}_n)^2}\right]^{-1/2}\right\} \tag{7.4c}$$

$$\frac{d\phi_n}{d\hat{t}} = \hat{\Omega} - \hat{\nu}_I + \frac{2}{\hat{\tau}_3}\left(\frac{\eta}{\eta^2 + 1}\right) + \frac{2\hat{w}_{eq}(\Delta\hat{\omega} - \dot{\varphi}_n)}{\hat{\tau}_1 \hat{E}_n^2}\left\{1 - \left[1 + \frac{\hat{\tau}_1 \hat{E}_n^2}{1 + (\Delta\hat{\omega} - \dot{\varphi}_n)^2}\right]^{-1/2}\right\} \tag{7.4d}$$

A modified version of the Spencer-Lamb model was also used in the comparisons. The dielectric bump introduces a large frequency shift, as discussed in Appendix A. In the modified model, the phase effects of the dielectric bump are ignored, but the losses are retained. The model is given by:

$$\frac{d\hat{E}_n}{d\hat{t}} = -\left[\frac{1}{\hat{\tau}_2} + \frac{2}{\hat{\tau}_3}\left(\frac{1}{\eta^2 + 1}\right)\right]\hat{E}_n + \frac{2\hat{w}_{eq}}{\hat{\tau}_1 \hat{E}_n}\left\{1 - \left[1 + \frac{\hat{\tau}_1 \hat{E}_n^2}{1 + (\Delta\hat{\omega} - \dot{\varphi}_n)^2}\right]^{-1/2}\right\} \tag{7.4e}$$

$$\frac{d\phi_n}{d\hat{t}} = \hat{\Omega} - \hat{\nu}_I + \frac{2\hat{w}_{eq}(\Delta\hat{\omega} - \dot{\varphi}_n)}{\hat{\tau}_1 \hat{E}_n^2}\left\{1 - \left[1 + \frac{\hat{\tau}_1 \hat{E}_n^2}{1 + (\Delta\hat{\omega} - \dot{\varphi}_n)^2}\right]^{-1/2}\right\} \tag{7.4f}$$

The Lamb, Spencer-Lamb, and modified Spencer-Lamb models will be referred to as the SWL, SL1, and SL2 models, respectively.

The models were compared using the parameters from data sets 27–29. The output intensities, threshold reflectivities, peak output powers, and ranges of validity of the standing-wave models were explored.

Figure 7.12 is a comparison of I_{out} vs r_B for the four models. The four models show the usual peaked behavior. In all runs, the TWL model predicted the highest output fields, followed (in order) by the SWL, SL2, and SL1 models. A set of simple arguments can explain the ordering. At mirror A, the TWL equations reduce to a form almost identical to the SWL model, except for the presence of the spatial derivatives. The field amplitudes at mirror A should be quite close to, but slightly lower than, those calculated with the SWL model. Comparisons of the amplitudes reveal this to be the case. However, in the propagation from mirror A to mirror B, $\hat{E}_R(\hat{z})$ grows in the TWL model but

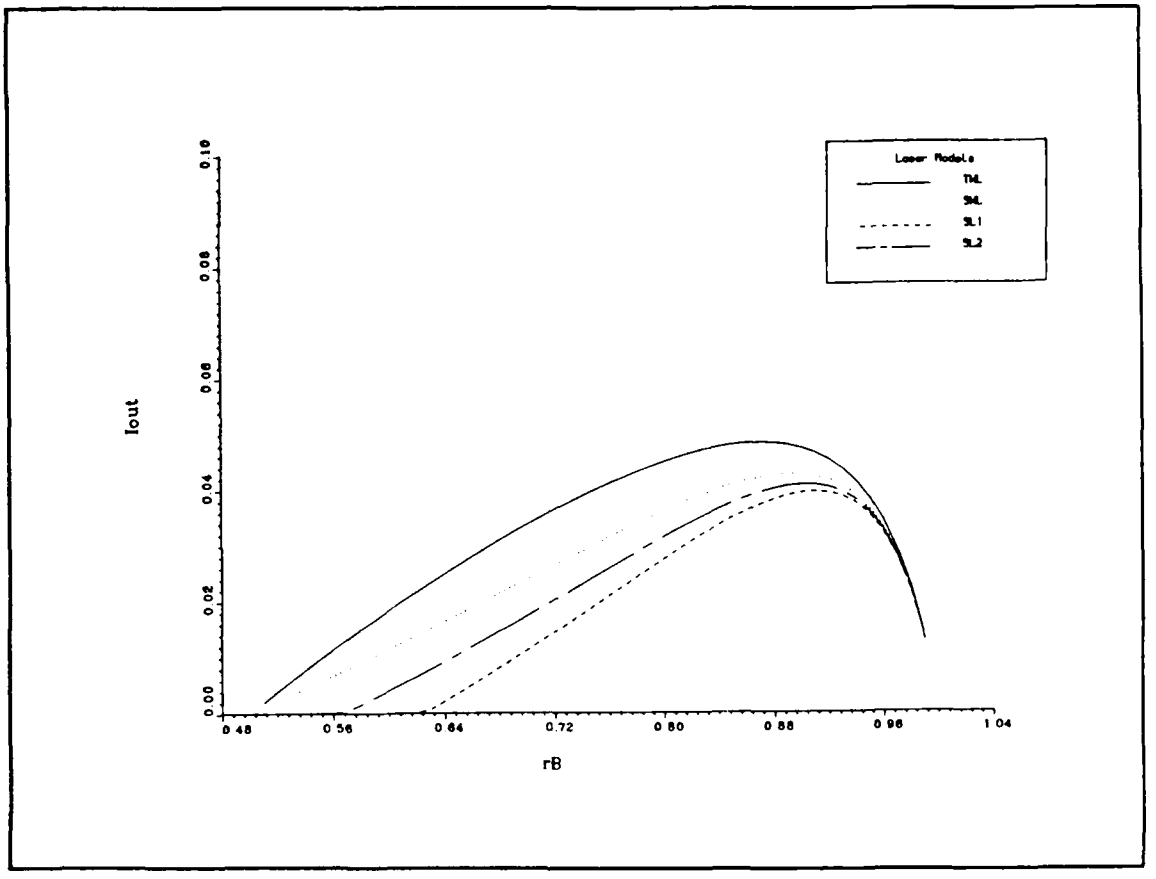

Figure 7.12. I_{out} vs r_B for the TWL, SWL, SL1, and SL2 models. All parameters are from data set 27.

stays constant in the SWL model. The field amplitudes at mirror B, and consequently I_{out}, will be greater in the TWL model than in the SWL model except possibly when $r_B \approx 1.0$. As discussed in Appendix A, the losses due to the dielectric bump are greater than those due to mirror B for $r_D > 0.166$. With greater losses, the Spencer-Lamb models yield lower field values than the SWL model. Since the SL1 model incurs a large frequency shift due to the dielectric bump, its gain (off linecenter) is lower than that of the SL2 model. The SL1 model thus predicts lower field values than the SL2 model. These arguments explain physically the ordering of the the output field intensities.

The values of $r_B\big|_{th}$ are ordered in a similar manner. The TWL and SWL models have the same value of lasing threshold, as discussed in Chapter IV. The Spencer-Lamb models have higher

thresholds due to the larger losses of the dielectric bump. The SL1 model has the highest lasing threshold, as the frequency shift of the dielectric bump lowers the effective laser gain. The threshold values for the TWL, SWL, and SL2 models agree excellently with the values from Eqs (4.17c) and (4.45b). No attempt was made to calculate the threshold reflectivities for the SL1 model.

The output intensities peak at different values of r_B in the four models. The TWL model has its peak at the lowest value of r_B, followed by the the SWL, SL2, and SL1 models. The peak value is the highest for the TWL model. Note the relevance this has on laser design: the standing-wave laser models underpredict the peak output fields (and therefore, extraction efficiencies), and give incorrect reflectivities r_B at which the peaks occur.

Figure 7.13 is an expanded version of Figure 7.12. At very high reflectivities, the amplitudes $\hat{E}_R(\hat{z})$ and $\hat{E}_L(\hat{z})$ are approximately constant in $\hat{z}$ and equal. In this limit, the fields in the TWL model can be approximated as plane, standing waves. The losses of the dielectric bump are roughly equal to those of mirror B. Additionally, the frequency shift due to the dielectric bump is small. Consequently, the four models yield approximately the same output field amplitudes. For $r_B > 0.95$, the TWL model can be replaced by any of the standing wave models with reasonably accurate results. However, for $r_B < 0.90$, the standing wave models are no longer valid, due to the breakdown of the standing wave approximation. Considering that the steady-state codes for the TWL model are extremely fast (less than one second is required to calculate the fields for a single value of r_B on a VAX 8700 computer), there is little justification for using the standing wave models except when $r_B > 0.95$.

The Steady-State Lasing Frequency. A shortcoming of the TWL model is that the equations of motion cannot be solved for the steady-state lasing frequency $\hat{\nu}$. This frequency can be calculated numerically, using the procedure described in Appendix B.

$\hat{\nu}$ was calculated at over 3000 operating points in a wide parameter space. The twelve data sets (Table I) were used as the basis of the space. The gain length $\hat{L}_g$ was varied, as was the location of the gain medium inside the resonator. Both mirror reflectivities were allowed to be less than unity.

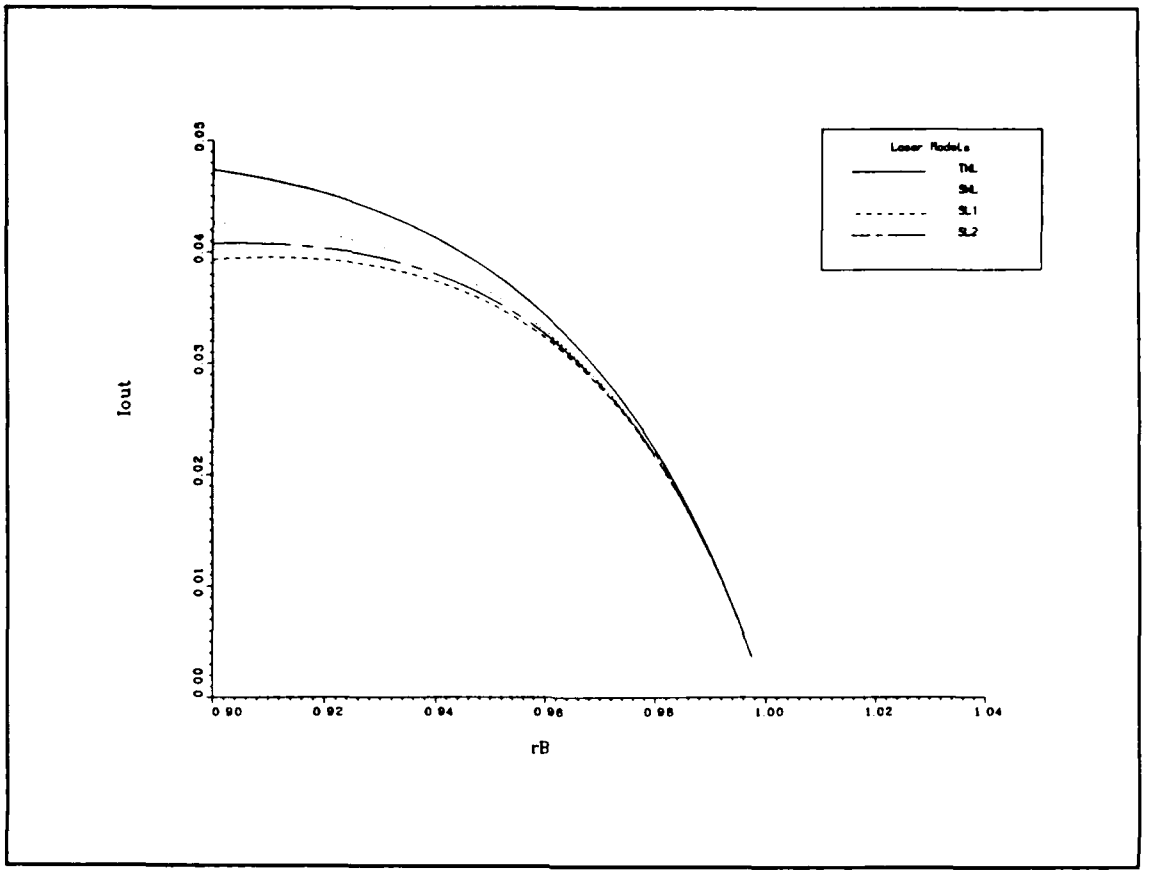

Figure 7.13. I_{out} vs r_B for the TWL, SWL, SL1, and SL2 models at high mirror reflectivities. All parameters are from data set 27.

The calculated frequencies were compared to those obtained at the same operating points from the Lamb model; i.e., Eq (4.34a). In all cases, the numerically calculated frequencies for the TWL model agreed with those obtained from the Lamb model to within the numerical error given by Eq (B.15). It may be inferred, then, that the formula for $\hat{\nu}$ obtained from the Lamb model is valid for the TWL model. A slightly expanded version of the formula that allows for variable reflectivities at either mirror is:

$$\hat{\nu} = \frac{\hat{\Omega} + \hat{\omega}\left(\frac{1}{\hat{r}_2} - \frac{1}{\hat{r}_3\hat{L}_g}\ln r_A r_B\right)}{1 + \frac{1}{\hat{r}_2} - \frac{1}{\hat{r}_3\hat{L}_g}\ln r_A r_B} \tag{7.5a}$$

or:

$$\Delta\hat{t} = \frac{\Delta\hat{m}}{1 + \frac{1}{\hat{\tau}_2} - \frac{1}{\hat{\tau}_3\hat{L}_g}\ln r_A r_B} \tag{7.5b}$$

The longitudinal mode spacing, including the effects of the gain medium, can be obtained by combining Eqs (7.5a) and (B.8):

$$\begin{aligned}\delta\hat{\nu} &= \hat{\nu}_{n+1} - \hat{\nu}_n \\ &= \frac{c/2\gamma L}{1 + \frac{1}{\hat{\tau}_2} - \frac{1}{\hat{\tau}_3\hat{L}_g}\ln r_A r_B} \\ &= \frac{1}{\hat{\tau}_3\left[1 + \frac{1}{\hat{\tau}_2} - \frac{1}{\hat{\tau}_3\hat{L}_g}\ln r_A r_B\right]}\end{aligned} \tag{7.5c}$$

Eq (7.5) can be interpreted in the following light. A Fabry-Perot resonator has a Lorentzian response curve (146:79), with a full width at half-maximum given by (unnormalized units):

$$\Delta f_{1/2} \equiv \frac{c}{2\pi n}\left(\alpha_0 - \frac{1}{L_g}\ln r_A r_B\right) \tag{7.6}$$

where n is the index of refraction inside the resonator. Assuming that $n \approx 1$ and using Eq (4.10b) in the above expression, the full width at half-maximum (in radian frequency and normalized units) can be written as:

$$\Delta\hat{\omega}_{1/2} = 2\left(\frac{1}{\hat{\tau}_2} - \frac{1}{\hat{\tau}_3\hat{L}_g}\ln r_A r_B\right) \tag{7.7}$$

Substituting Eq (7.7) into Eq (7.5b) yields:

$$\Delta\hat{t} = \frac{\Delta\hat{m}}{1 + \frac{\Delta\hat{\omega}_{1/2}}{2}} \tag{7.8}$$

The amount of frequency pulling is dependent only upon the halfwidth of the resonator response curve. Figure 7.14 displays the underlying physics of frequency pulling. The resonator response curve is centered about the barecavity mode frequency $\hat{\Omega}$. Due to the finite width of the cavity

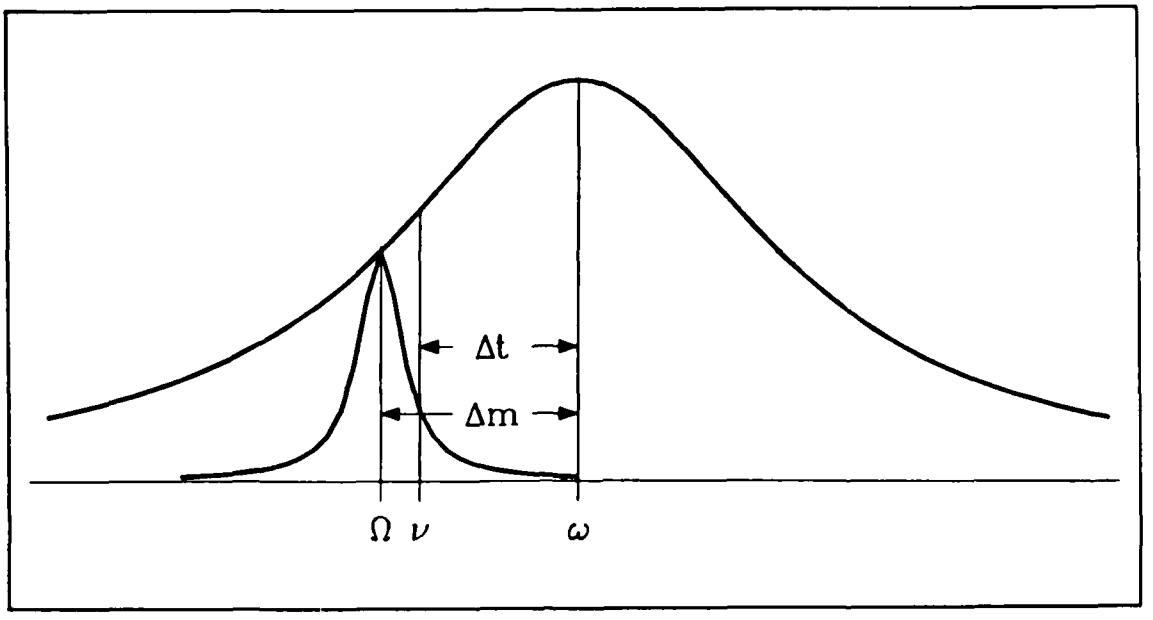

Figure 7.14. The physical mechanism underlying frequency pulling and pushing. $\hat{\nu}$ is pulled toward linecenter, but still remains under the resonator response curve.

resonance, the actual lasing frequency $\hat{\nu}$ shifts slightly toward linecenter, where the laser gain is higher. For lossy resonators, the response curve is broad and $\hat{\nu}$ can shift a considerable distance toward linecenter. The effects of frequency pulling and pushing are minimized in very high Q resonators. Finally, the longitudinal mode separation is reduced by the factor:

$$\frac{1}{1+\frac{\Delta\hat{\omega}_{1/2}}{2}}$$

from the barecavity mode separation when the cavity and medium losses are taken into account.

Experimental Excimer Laser Results. A series of experimental XeF laser data were reduced using both the TWL and simple saturable gain models (156). The excimer laser is depicted schematically in Figure 7.15. The cavity was essentially a Fabry-Perot resonator. The central section of the gain region was pumped with an electron gun. The absorption of the unpumped region of the gain cell was ignored in the following analysis, as were any effects from the window at $z = 131\,\text{cm}$. The objective of the experiment was to determine the small signal gain g_0 and absorption α_0. The

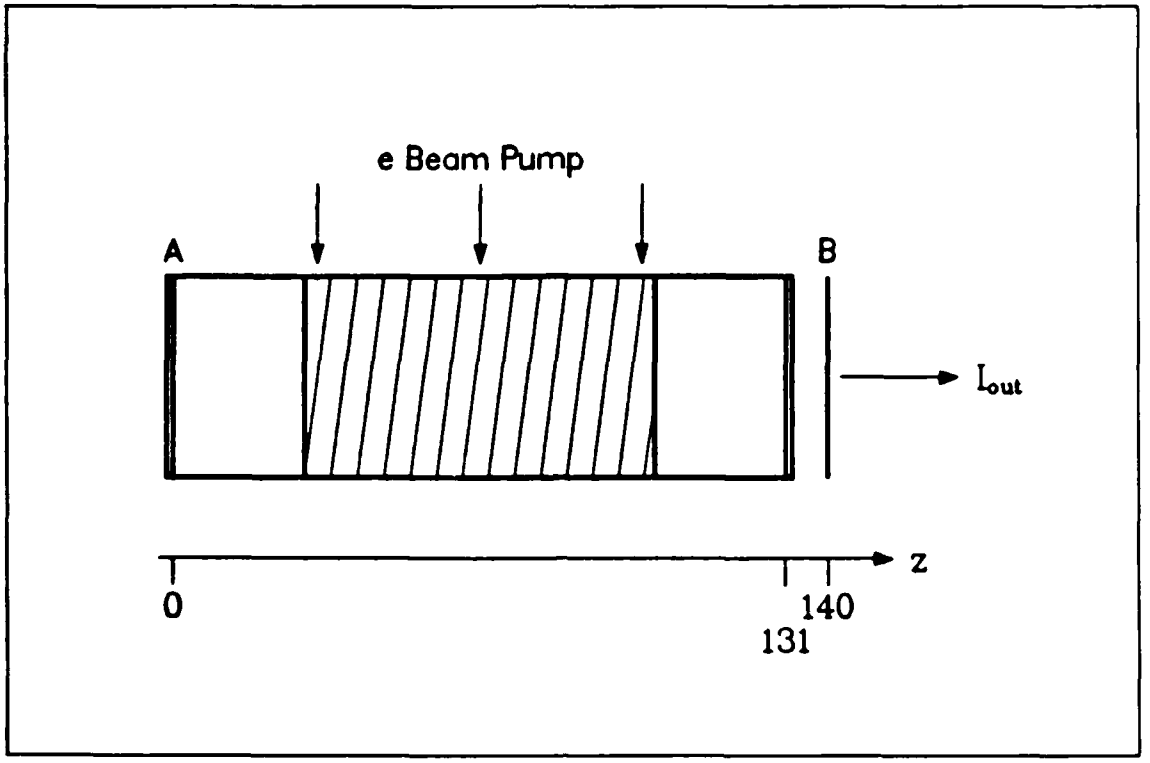

Figure 7.15. The XeF laser. Mirror A has a radius of curvature of 917 cm, whereas mirror B is a flat. Only the central portion (crosshatched) is pumped. All dimensions are in centimeters.

output powers of the device were measured for a series of different output coupler reflectivities. The reflectivity of mirror A was held constant at $r_A = -1.0$, while that of mirror B was allowed to vary. Five series of runs were performed. The output intensities and reflectivities r_B^2 are listed in Table III. No error bars were given for the data.

The laser was assumed to be homogeneously broadened and operating on a single longitudinal mode at linecenter ($\Delta\hat{t} = 0.0$). The saturation intensity was arbitrarily set equal to unity ($\hat{\tau}_1 = 1.0$). The common factor $\hat{\tau}_3$ in the g_0 and α_0 expressions (Eq (4.10)) was set equal to unity for simplicity. The problem then reduced to obtaining pairs of $(\hat{w}_{eq}, \hat{\tau}_2)$ that would best fit an I_{out} vs r_B^2 curve to the experimental data. The $\hat{w}_{eq}$ and $\hat{\tau}_2$ values were then converted to g_0 and α_0, respectively, with Eq (4.10). Both the TWL and simple saturable gain models were used to compute the small signal

TABLE III

XeF Laser Data: I_{out} as a Function of r_B^2 †

r_B^2	Series 1	Series 2	Series 3	Series 4	Series 5
0.95	73.76	68.32	63.83	59.03	57.88
0.90	110.33	95.83	90.15	85.91	84.59
0.80	117.49	112.50	104.00	103.56	99.91
0.70	143.12	142.86	134.03	125.42	126.93
0.60	141.90	136.09	131.22	128.21	125.98
0.50	126.19	118.94	113.68	109.43	102.40

† All I_{out} values are in units of kW/cm^2.

TABLE IV

XeF Laser Data: Small Signal Gains and Losses

Run No.	Model	$\hat{w}_{eq}$	$\hat{\tau}_2$	$g_0(\%\,cm^{-1})$	$\alpha_0(\%\,cm^{-1})$
1	TWL	17.0	1.1	1.51	0.081
1	SSG	21.0	1.03	1.41	0.065
2	TWL	9.1	0.87	1.19	0.151
2	SSG	10.6	0.82	1.12	0.129
3	TWL	9.5	0.91	1.25	0.144
3	SSG	10.9	0.86	1.18	0.126
4	TWL	10.8	0.92	1.34	0.127
4	SSG	12.3	0.91	1.25	0.111
5	TWL	10.6	1.08	1.48	0.129
5	SSG	12.1	1.01	1.38	0.113

gains and losses. The curvefitting results are listed in Table IV. In all cases, the TWL model predicts slightly higher g_0 and α_0 values. The values compare reasonably well with the expected values of $g_0 = 1.1\,\%\,cm^{-1}$ and $\alpha_0 = 0.1\,\%\,cm^{-1}$. The data and fitted curves for Series 2 are displayed in Figure 7.16.

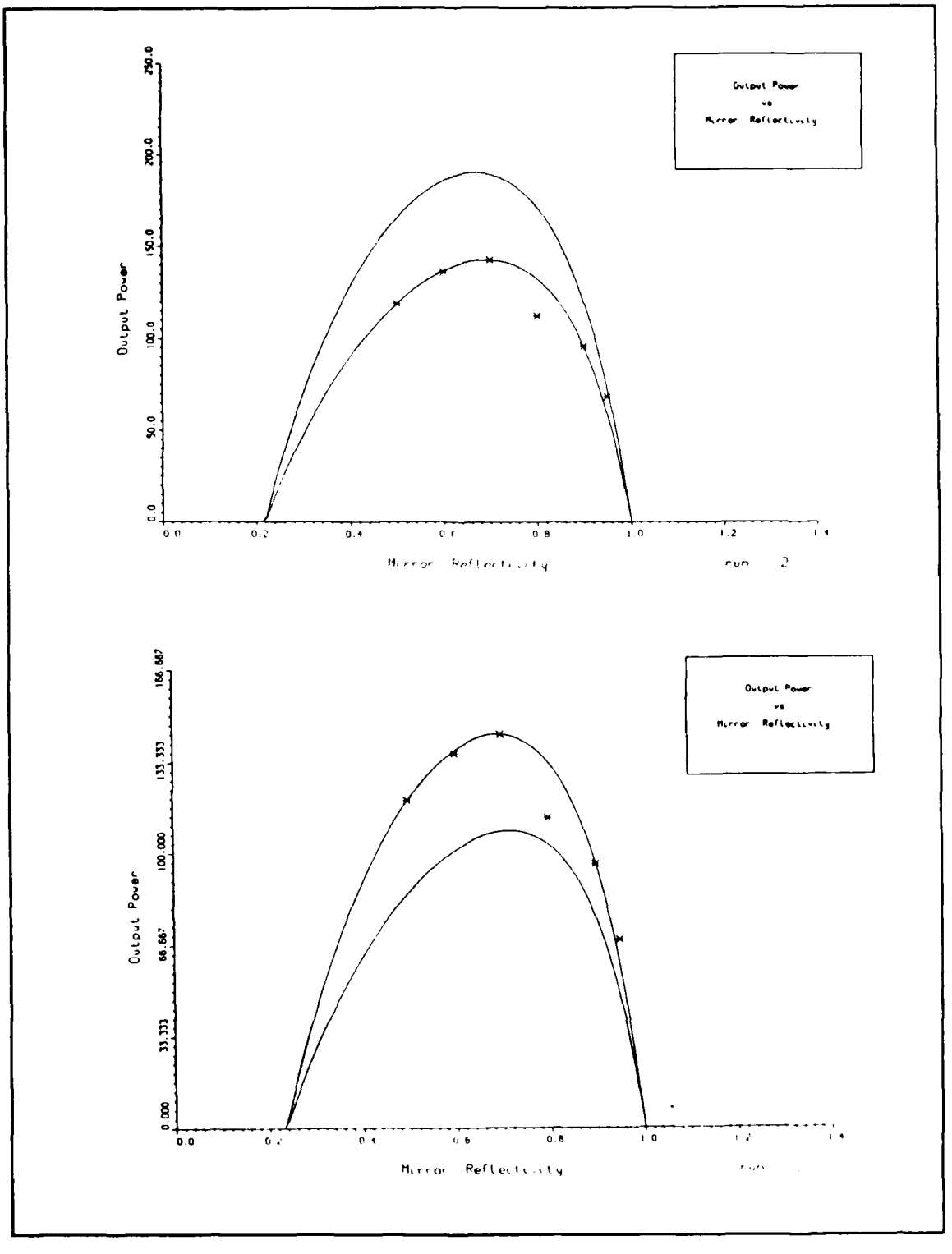

Figure 7.16. XeF laser data. Theoretical curves for both models are plotted. (a) Data fit to the TWL model. (b) Data fit to the simple saturable gain model.

Steady-State Behavior: Injected Lasers

The majority of the numerical analyses performed dealt with injected lasers at steady-state. The behaviors of the lasers were examined at three operating points: the minimum injected intensity point (MII point, corresponding to turning point C on the cubic curves), the point at which G_1 reaches its maximum (MG1 point), and the point at which G_2 is maximized (MG2 point). The MII point is the locking threshold point, according to the Spencer-Lamb criteria. The MG1 point yields the maximum system gain obtainable from the laser. Finally, the MG2 point indicates the maximum ratio of internal laser fields to injected fields that can be achieved.

The positions of the MG1 and MG2 points on the cubic curves are functions of $|\Delta\hat{o}|$ and r_B. The MG2 point in all cases examined lies on branch I of the cubic curve. At high r_B and low $|\Delta\hat{o}|$ values, the MG1 point lies on branch II of the cubic curve. These operating points cannot be achieved in practice as they lie on an unstable branch. As $|\Delta\hat{o}|$ rises or r_B decreases, the MG1 point shifts through the MII point, and thereafter lies on branch I. These regions are indicated in Figure 7.17. Since only branch I of the cubic curve is stable, the maximum G_1 point was constrained to lie on this branch only. That is, even when the actual (global) maximum occurred on branch II, only the maximum point on branch I was located. (When the global maximum existed on branch II, the maximum on branch I coincided with the MII point.) The behavior of the MII point (turning point C) as a function of $|\Delta\hat{o}|$ has been discussed previously. All told, the operating points can exist in one of three different relative positions on branch I. First, all three points coincide when $\Delta\hat{o} = 0.0$. This is the free-running laser point; gains G_1 and G_2 are infinite under this operating condition. Second, the MG2 point can lie on branch I away from the MII point, with the MG1 point between them. Finally, the MII and MG2 points can coincide, with the MG2 point shifted out along branch I.

At each operating point, four physical quantities (observables) were calculated: $I_R(0)$, I_I, G_1, and G_2. The parameter space examined had $\Delta\hat{o}$ and r_B as variables. $\Delta\hat{m}$ was held fixed in each data set, so $\Delta\hat{t}$ varied as a function of r_B. However, the frequency variable of interest was $\Delta\hat{o}$; it was

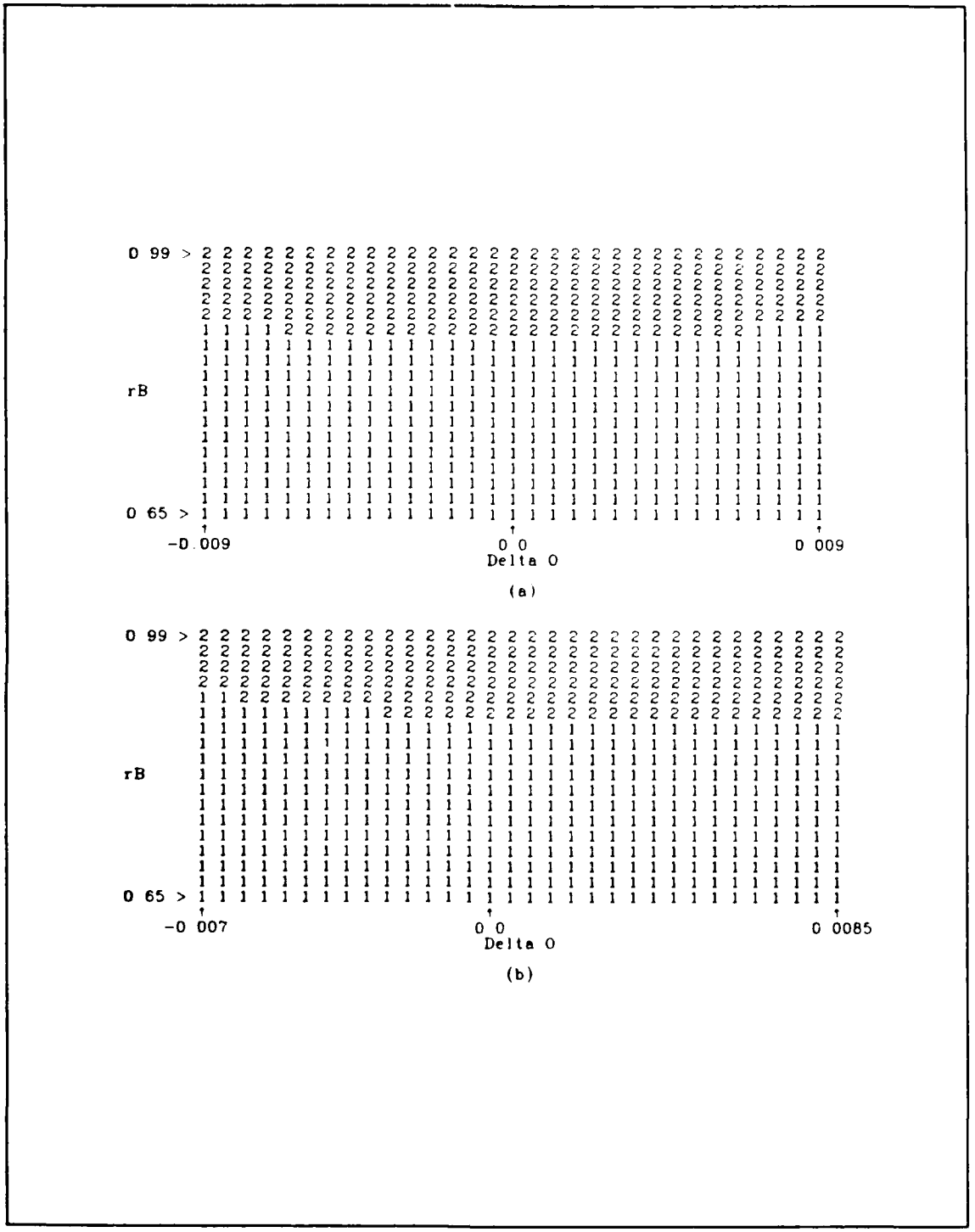

Figure 7.17. Locations of the MG1 point on the cubic curves. The numbers denote the particular branch of the cubic curve on which the MG1 point lies. (a) From data set 27, (b) from data set 36.

measured relative to the (varying) $\Delta\hat{\ell}$. Physically, this corresponds to maintaining a fixed cavity length, but varying the reflectivity of mirror B and the detuning of the injected signal.

Two series of calculations were performed. First, the observables were computed at the three operating points in the region of the $(\Delta\hat{o}, r_B)$ plane where the cubic curves exhibit the s-shape. Second, the observables were calculated at the MG2 point in as wide a region of the $(\Delta\hat{o}, r_B)$ plane as possible. In this case, the parameter space was bounded by the constraints $r_b|_{th} \leq r_B \leq 1.0$ and $|\Delta\hat{o}| \leq 0.1$. (As will be seen, $I_R(0)$ often became infinite at the MG2 point for $|\Delta\hat{o}| < 0.1$. This condition became the actual constraint on $\Delta\hat{o}$.) The second set of calculations requires the assumption that the MG2 point is always a locked and stable operating point. As noted above, the MG2 point always lies on branch I of the s-shaped cubic curves and is therefore (presumably) a stable, locked operating point. As $|\Delta\hat{o}| \rightarrow |\pm\Delta\hat{o}_{max}|$, the MG2 point moves away from the MII point at an increasing rate. When $|\Delta\hat{o}| > |\pm\Delta\hat{o}_{max}|$, nothing can be stated about stability or locking. However, since the MG2 point continuously moves away from the MII point, it is assumed that the MG2 point is always locked and stable.

The numerical studies were performed with the approximate formula for $\hat{\vartheta}$, Eq (3.27a), used in the boundary condition for mirror B. The loaded cavity mode spacing, and hence the exact expression for $\hat{\vartheta}$, were obtained after the analyses were completed. Four cases (data sets 27, 29, 36, and 38) were repeated with the exact equation for $\hat{\vartheta}$ employed in the boundary condition. The impact of using the approximate expression in the boundary condition was observed to be minimal: the curves shifted somewhat and the contour levels changed slightly, but the general shapes of all of the plots remained the same. As a result, the physical interpretations of the locking process remain unchanged.

The following sections examine the behavior of the four observables at the three operating points. Due to the large number of figures, contour and slice plots of the data are relegated to Appendix C. For simplicity, only data from sets 27 and 36 are presented. The lasers parameters are identical in these sets except that $\Delta\hat{m} = 0.0$ in set 27 and $\Delta\hat{m} = 0.375$ in set 36. These sets are

representative of linecenter and off linecenter operation of the injected lasers. All of the following plots and those in Appendix C were generated with the exact expression for $\hat{\vartheta}$. One additional definition is required: $F|_{\text{Mxx}}$ denotes the observable F at the Mxx operating point. For example, $I_R(0)|_{\text{MII}}$ denotes $I_R(0)$ at the MII point.

Behavior of $I_R(0)$. Contour plots of $I_R(0)$ in the $(\Delta\hat{o}, r_B)$ plane are given in Figures C.1–C.8. Slice diagrams through these contours are shown in Figures C.9–C.17. All plots are symmetric about the line $\Delta\hat{o} = 0.0$ in data set 27, as the gain profile is symmetric about linecenter. In data set 36, the gain is no longer symmetric about the free-running point; this asymmetry is reflected in the plots.

The contour plots are a series of smooth, concoidal curves. At high r_B and low $|\Delta\hat{o}|$ values, the contours overlap in the MG1 and MII cases. This occurs where the global maximum G_1 point lies on branch II of the cubic curve, and the local maximum on branch I coincides with the MII point. The MII, MG1, and MG2 contours are tangential to each other along the $\Delta\hat{o} = 0.0$ line. The MG2 and MG1 (MII) contours separate in opposite directions from this line.

Generally, $I_R(0)$ increases monotonically as r_B increases, for fixed $\Delta\hat{o}$. This is exhibited at the three operating points. As the losses of the laser decrease (r_B increases), the circulating fields in the injected laser should also rise. A notable exception arises at very high $|-\Delta\hat{o}|$ values for the MG2 points. $I_R(0)$ first decreases then increases as r_B rises. This can be observed in the contour plots.

Plots of $I_R(0)$ vs $\Delta\hat{o}$ at the MII and MG1 points are concave downward. If $\Delta\hat{m} = 0.0$, the maximum point on each curve occurs at $\Delta\hat{o} = 0.0$. If $\Delta\hat{m} \neq 0.0$, the maximum always occurs at some $\Delta\hat{o} > 0.0$. A possible explanation for the behavior at the MII points can be advanced. As $|\Delta\hat{o}|$ increases, the cavity becomes increasingly nonresonant. The minimum stable, locked field configuration should therefore decrease in amplitude as $|\Delta\hat{o}|$ increases. This would account for a general decrease in $I_R(0)$ with rising $|\Delta\hat{o}|$. However, the shift of the maximum to a positive $\Delta\hat{o}$ value when $\Delta\hat{m} \neq 0.0$ runs contrary to this explanation. The unsaturated gain g_0 is lower at the peak than at $\Delta\hat{o} = 0.0$; this further confuses the issue.

In the discussion of the cubic curves, the trajectory of turning point C as a function of $|\Delta\hat{o}|$ in the $(I_I, I_R(0))$ plane was examined. The trajectories can be correlated to the $I_R(0)$ vs $\Delta\hat{o}$ plots. When $\Delta\hat{m} \neq 0.0$, $I_R(0)$ first rises then falls as $\Delta\hat{o}$ increases in the MII plots. This corresponds to the rising and falling trajectory of turning point C with increasing $\Delta\hat{o}$. Note that $I_R(0)$ decreases monotonically as $-\Delta\hat{o}$ decreases. This creates a similar monotonic drop in the trajectory of the turning point when $\Delta\hat{o} < 0.0$.

At the MG2 point, the $I_R(0)$ vs $\Delta\hat{o}$ plots are concave upward. For large enough values of $|\Delta\hat{o}|$, $I_R(0)$ becomes infinite. If $\Delta\hat{m} = 0.0$, the minimum $I_R(0)$ value occurs at $\Delta\hat{o} = 0.0$. For $\Delta\hat{m} \neq 0.0$, the minimum shifts to some negative value of $\Delta\hat{o}$. In all runs examined, $I_R(0)|_{\mathrm{MG2}} > I_R(0)|_{\mathrm{MG1}} \geq I_R(0)|_{\mathrm{MII}}$. The only exception to this inequality occurs if $\Delta\hat{o} = 0.0$, when the three $I_R(0)$ values are equal.

As a general rule, $I_R(0)$ values at some point $(\Delta\hat{o}, r_B)$ are greater than the corresponding values at the reflected point $(-\Delta\hat{o}, r_B)$. This was observed for the three operating points. This is intriguing, as the gain is higher for $\Delta\hat{o} < 0.0$ than for $\Delta\hat{o} > 0.0$. These effects were not observed in data sets 27–29, due to the gain symmetry.

Behavior of I_I. Contour plots of I_I in the $(\Delta\hat{o}, r_B)$ plane are given in Figures C.18–C.25. Slice diagrams are shown in Figures C.26–C.34. At $\Delta\hat{o} = 0.0$, $I_I = 0.0$ at the three operating points. The asymmetries due to operation off linecenter are clearly visible in the plots from data set 36.

In all data sets, the contour plots exhibit a characteristic flaired shape. In order to avoid an infinite number of contours about the $\Delta\hat{o} = 0.0$ line, I_I was set equal to 0.05 times the smallest calculated value in the plane instead of the correct value of 0.0. As a result, the contour density is artifically low about this line. The contours for the MII and MG1 operating points are the same at high r_B, low $\Delta\hat{o}$ values, as expected.

A physical argument can be advanced to explain the flaired shape of the contour plots. At some high reflectivity r_B, the cavity losses are low and the quality factor Q is high. The linewidth due to the cavity is relatively small. At a second, lower reflectivity r'_B, the losses are greater and Q is

lower. The cavity linewidth is correspondingly broader. It should therefore be easier to support a field detuned by some $\Delta\hat{o}$ at r_B' than at r_B. A given injected intensity I_I should be able to lock the laser over a broader range of $\Delta\hat{o}$ values at low reflectivities than at high reflectivities. Consequently, the contour lines for I_I should flair as r_B decreases.

I_I is always largest at the MG2 point when $\Delta\hat{o} \neq 0.0$: $I_I|_{\mathrm{MG2}} > I_I|_{\mathrm{MG1}} \geq I_I|_{\mathrm{MII}}$. $I_I|_{\mathrm{MG1}}$ is equal to $I_I|_{\mathrm{MII}}$ only when the two points coincide.

$I_I|_{\mathrm{MII}}$ increases monotonically as r_B rises. As r_B increases and the laser losses decreases, the free-running fields that can be sustained by the laser rise. In order to capture the gain from the free-running field, the minimum injected intensity required to lock the laser must undergo a corresponding increase. The I_I values at the MG1 point display identical behavior. In general, similar behavior is exhibited at the MG2 point. However, for very large negative detunings $-\Delta\hat{o}$, I_I decrease then increase with rising r_B. This is similar to the behavior of $I_R(0)$ at the MG2 point.

$I_I|_{\mathrm{MII}}$ also increases monotonically with $|\Delta\hat{o}|$. In order to force the laser to operate away from $\hat{\nu}$, some minimum value of injected intensity is required. As $|\Delta\hat{o}|$ rises and the cavity becomes increasingly nonresonant, the injected intensity required to capture the gain from the free-running mode must increase. Similar behavior is observed with $I_I|_{\mathrm{MG1}}$ and $I_I|_{\mathrm{MG2}}$. The monotonic increases of I_I with r_B and $|\Delta\hat{o}|$ give the contours the flaired shape.

When $\Delta\hat{m} \neq 0.0$, the injected intensities are greater at every point $(\Delta\hat{o}, r_B)$ than at the corresponding point $(-\Delta\hat{o}, r_B)$. This occurs at all three operating points. The medium gain is slightly lower at positive $\Delta\hat{o}$ values than at negative detunings. The injected intensity required to capture the gain from the free-running mode will consequently be somewhat higher at point $(\Delta\hat{o}, r_B)$ than at $(-\Delta\hat{o}, r_B)$.

The contours at the MII point have an important physical interpretation. The contour line for some given I_I represents the locus of points at which the laser is just locked. Two contours exist in the $(\Delta\hat{o}, r_B)$ plane for each value of I_I. The laser will lock to the injected signal at every point between the two contours. The width of the region parallel to the $\Delta\hat{o}$ axis defines the "locking

range" of the laser for the given injected signal strength. The locking range is clearly a function of the injected intensity and r_B. Of particular importance is that the locking range broadens as the reflectivity r_B decreases or I_I increases.

Behavior of G_1. The G_1 contour plots are given in Figures C.35–C.42. Slice plots through the contours are displayed in Figures C.43–C.51. Once again, the asymmetries in the plots from data set 36 are due to the asymmetric gain about the line $\Delta\hat{o} = 0.0$.

In all data sets, the contour plots for the three operating points have a flaired shape. On the line $\Delta\hat{o} = 0.0$, the gain G_1 is infinite. The actual contours approach the $\Delta\hat{o} = 0.0$ line asymptotically. The contour density becomes infinite as $\Delta\hat{o} \rightarrow 0.0$. In order to avoid an infinite number of contour lines in this region, the G_1 values at $\Delta\hat{o} = 0.0$ are set equal to 20.0 times the higher system gain at the two adjacent $\Delta\hat{o}$ mesh points. This has three effects: the plotted contours cross the $\Delta\hat{o} = 0.0$ line instead of approaching it asymptotically, the contour density is reduced in the vicinity of the asymptote, and the maximum contour value is finite instead of infinite.

At high $|\Delta\hat{o}|$ and r_B values, the system gain G_1 is less than 1.0. This indicates that the injected signal $\mathbf{I}_{IN}$ has a greater magnitude than the total output signal $\mathbf{t}_B\mathbf{E}_R(1) + \mathbf{r}_B\mathbf{I}_{IN}$. In these regions, one of the primary advantages of injection locking is lost: control of a high-power beam with a weaker beam.

By definition, G_1 has the highest value at the MG1 point. At low r_B values, $G_1|_{\mathrm{MG2}} > G_1|_{\mathrm{MII}}$. At intermediate to high reflectivities, the inequality reverses: $G_1|_{\mathrm{MG2}} < G_1|_{\mathrm{MII}}$. In the region where the MII and MG1 points are the same, $G_1|_{\mathrm{MII}} = G_1|_{\mathrm{MG1}}$.

G_1 decreases monotonically as r_B increases at the three operating points. This is due primarily to the decreased transmission of mirror B. As the reflectivity increases, I_I increases. I_{IN} will therefore increase, but at a faster rate than I_I, as $I_{IN} = \frac{I_I}{1 - r_B^2}$. In an analogy with the free-running laser, at high reflectivities the outcoupled fields decrease as r_B rises. These factors cause the numerator to decrease relative to the rapidly increasing denominator in the system gain definition, Eq (3.30). As a result, G_1 decreases monotonical as r_B approaches unity.

G_1 is a monotonically decreasing function of $|\Delta\hat{o}|$ at the three operating points. From the definition of G_1, this implies that the ratio $\frac{I_R(1)}{I_I}$ decreases as $|\Delta\hat{o}|$ increases. This can be observed in the slice diagrams for the MII and MG1 cases. For small detunings, this effect can also be seen in the MG2 slice diagrams. At moderately high values of $\Delta\hat{o}$, G_1 decreases to the order of unity. In these regions, the injected signal has approximately the same magnitude as the outcoupled field.

In general, the system gain is higher for some point $(-\Delta\hat{o}, r_B)$ than for the corresponding point $(\Delta\hat{o}, r_B)$. This was observed at the three operating points. The relative difference between the two values of G_1 becomes more pronounced as the barecavity mode $\hat{\Omega}$ is increasingly detuned from linecenter.

The G_1 contours for the MG1 operating point have a useful physical interpretation. A given system gain G_1 has two associated contours. Between these contours, the maximum system gain that can be achieved is higher. If a given gain is required for a specific application, the laser must be operated at some point between the two corresponding contours. Notice that the $\Delta\hat{o}$ range between the contours widens as r_B decreases. The injected signal can be detuned over a wider range and still meet the G_1 requirements at the lower r_B values than at the higher values.

Behavior of G_2. The G_2 contour plots are given in Figures C.52–C.59. Slice diagrams through the contours are presented in Figures C.60–C.70. Although present, the asymmetries in the plots from data set 36 are not as pronounced as in the previous contour plots.

The contours for the MII and MG1 operating points are bowed outward from the $\Delta\hat{o} = 0.0$ line. The bulging is slightly more pronounced in the MII contour plots. The MG2 contours are slightly flaired. Along the line $\Delta\hat{o} = 0.0$, G_2 is infinite at the three operating points. As a result, an infinite number of contour lines exist in the neighborhood of the $\Delta\hat{o} = 0.0$ line. Similar to the G_1 contour plots, the G_2 values on the $\Delta\hat{o} = 0.0$ line are set equal to 20.0 times the highest G_2 value calculated elsewhere in the $(\Delta\hat{o}, r_B)$ plane. This has two main effects: the contours near $\Delta\hat{o} = 0.0$ are somewhat low, and the number of contours in this neighborhood is reasonable.

At low r_B values, the MG1 and MG2 contours virtually coincide. At intermediate reflectivities, the MG1 contours bend inward toward the $\Delta\hat{o} = 0.0$ line. At high reflectivities, the MG1 contours overlap the MII contour lines. In the region where the MII and MG1 points are the same, the contours are identical.

By definition, G_2 is largest at the MG2 point. As best as can be observed from the plots, G_2 is smallest at the MII point. Thus, $G_2|_{\mathrm{MG2}} > G_2|_{\mathrm{MG1}} \geq G_2|_{\mathrm{MII}}$. Equality occurs at the MII and MG1 points only when the two operating points are identical.

G_2 is a relatively weak function of r_B. The observable increases monotonically with r_B at the MG2 point. The increases are relatively small; G_2 never varies by more than 25% from the lowest reflectivity to the highest. This results in relatively parallel contours for the MG2 operating point. Plots of G_2 vs r_B for fixed $\Delta\hat{o}$ at the MII and MG1 operating points are concave downward. The curvature is more pronounced at low r_B values at the MII point. At high values, especially where the MII and MG1 points are coincident, the curvatures are approximately equal. This results in the bowed nature of the contour plots.

G_2 decreases monotonically with rising $|\Delta\hat{o}|$ at the three operating points. The decrease is quite rapid in the vicinity of the $\Delta\hat{o} = 0.0$ line. In the MII and MG1 cases, the circulating laser fields generally decrease whereas the injected intensity increases with rising $|\Delta\hat{o}|$. This forces G_2 to decrease as $|\Delta\hat{o}|$ rises. The increase of I_I is most rapid when $|\Delta\hat{o}|$ is small; hence G_2 decreases most rapidly in the neighborhood of the $\Delta\hat{o} = 0.0$ line. At the MG2 operating point, the circulating fields generally increase with increasing $|\Delta\hat{o}|$. Near the $\Delta\hat{o} = 0.0$ line, the laser fields increase at a much slower rate than the injected field, leading to the rapid decrease of G_2. At high $|\Delta\hat{o}|$ values, the increase in the circulating fields is still less rapid than that of I_I. Thus, G_2 is a monotonically decreasing function of $|\Delta\hat{o}|$ at this operating point. At relatively high detunings of the injected signal, G_2 is on the order of unity at the three operating points. This implies that I_I is of the same order as the circulating fields inside the laser.

When $\Delta\hat{m} \neq 0.0$, the asymmetry of the gain profile forces G_2 to have different values on opposite sides of the $\Delta\hat{o} = 0.0$ line. At the MII and MG1 points, G_2 is larger at some point $(\Delta\hat{o}, r_B)$ than at the corresponding location $(-\Delta\hat{o}, r_B)$ if r_B is low. At high reflectivities, the opposite is true. At the MG2 point, G_2 is always greater at the point $(\Delta\hat{o}, r_B)$ than at $(-\Delta\hat{o}, r_B)$, regardless of the outcoupling.

Comparisons to the Spencer-Lamb Model. A series of comparisons of the TWL and Spencer-Lamb models was performed. The laser parameters were taken from data set 27. r_B and $\Delta\hat{o}$ values were elements of the sets:

$$r_B \in (0.75, 0.80, 0.85, 0.90, 0.95, 0.9999) \tag{7.8a}$$

$$\Delta\hat{o} \in (0.0, \pm 0.005, \pm 0.01, \ldots, \pm 0.05) \tag{7.8b}$$

ϕ_{RB} and ϕ_{TB} in the TWL model were set equal to the corresponding values ϕ_{RD} and ϕ_{TD} from the dielectric bump. The phases were calculated from Eq (A.6). For all of the reflectivity values, the cubic curves exhibited the s-shape. The four observables from each model ($I_R(0)$ and I_n, I_I, G_1, and G_2) were compared at the MII point.

A serious shortcoming of the Spencer-Lamb model noted in Chapter IV is that the $2kL$ term ($\hat{\vartheta}$) in Eq (3.27) is not accounted for. Regardless of the value of $\Delta\hat{o}$, the standing wave approximation in the Spencer-Lamb model forces this term to equal 0.0. The effects of ignoring this phase term can be significant, as shown in Figure 7.18. The first figure is a plot of the two cubic curves with $\hat{\vartheta}$ calculated according to Eq (3.27b) for the TWL model. The curves differ dramatically. The second plot displays the two cubic curves for the same case, but with $\hat{\vartheta}$ forcibly set equal to 0.0 in the TWL model. The two curves have reasonably close shapes. Neglect of the $\hat{\vartheta}$ term is clearly a serious flaw of the Spencer-Lamb model. It results in an extremely rapid breakdown of the Spencer-Lamb model as $|\Delta\hat{o}|$ increases from 0.0. In order to facilitate the comparisons of the two models, $\hat{\vartheta}$ was set equal to 0.0 in the TWL model.

A second major difference between the two models is that the formula for $\hat{\nu}$ for the Spencer-Lamb model, Eq (4.44), does not apply to the TWL model. This is true even if $\mathbf{r}_B = \mathbf{r}_D$ and

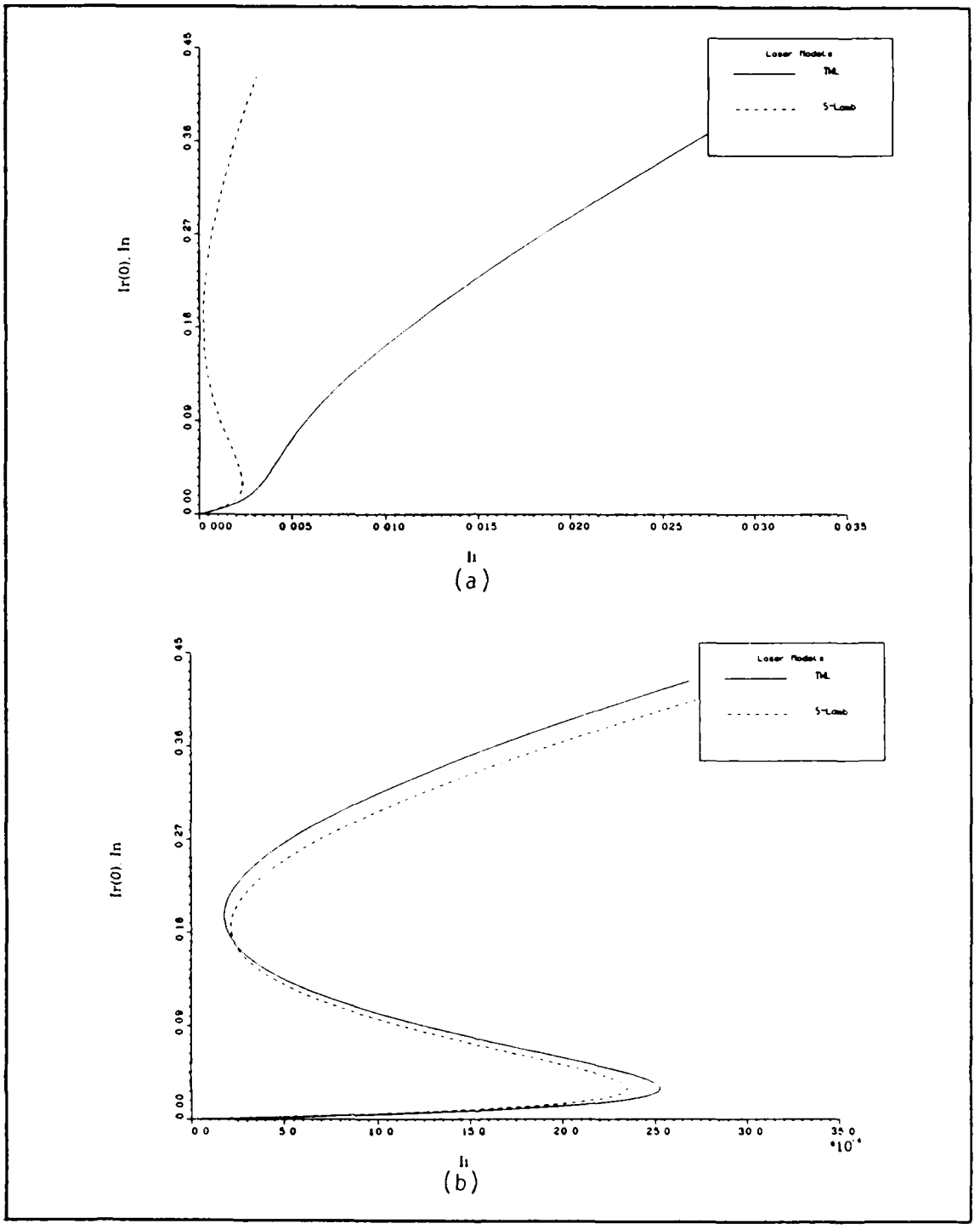

Figure 7.18. Cubic curve comparisons between the Spencer-Lamb and TWL models. $r_B = 0.90$ and $\Delta\hat{o} = 0.025$. All other parameters are taken from data set 27. (a) $\hat{\vartheta}$ calculated from Eq (3.27b) in the TWL model. (b) $\hat{\vartheta} = 0.0$ in the TWL model. Note that the two curves are similar in shape.

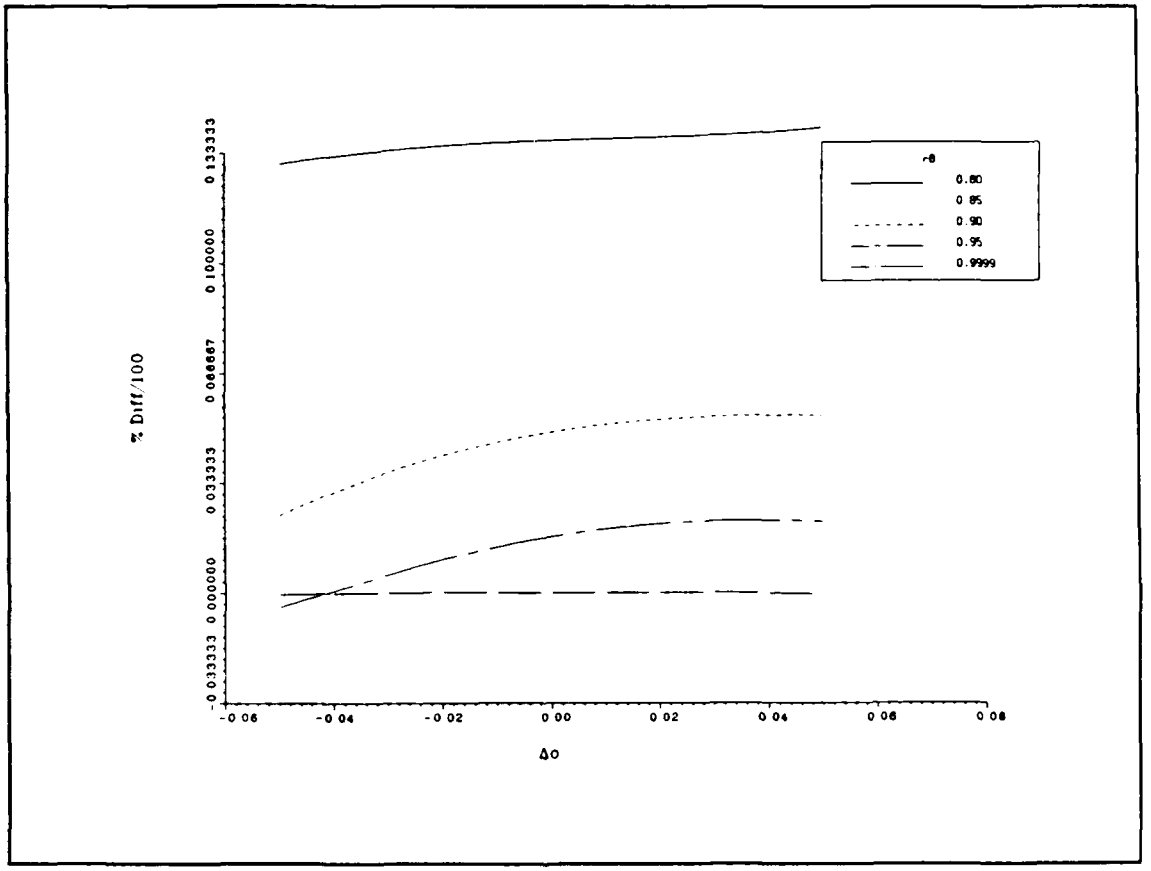

Figure 7.19. Percentage differences in $I_R(0)$ and I_n, TWL and Spencer-Lamb models. Note that the differences increase as r_B decreases. Effects of varying $|\Delta\hat{o}|$ are not clear. The parameters are from data set 27.

$t_B = t_D$. Eq (4.44) was used with the TWL model for the sake of comparison. Examination of the data from the TWL model show the formula to be incorrect: for $\Delta\hat{o} = 0.0$, I_I is equal to some small, nonzero value. Plots of I_I vs $\Delta\hat{o}$ go to zero at some small $\Delta\hat{o} \neq 0.0$. Similarly, plots of G_1 and G_2 vs $\Delta\hat{o}$ become infinite at small, nonzero values of $\Delta\hat{o}$. This complicates the comparisons of the two models. In the vicinity of $\Delta\hat{o} = 0.0$, the values of I_I, G_1, and G_2 are significantly different between the two models.

Direct comparisons of the cubic curves of the models show that the Spencer-Lamb theory breaks down as r_B decreases. The breakdown is due to the decreasing validity of the standing-

wave approximation in the Spencer-Lamb model. For $r_B = 0.9999$, the cubic curves of the two models overlap almost exactly. For $r_B < 0.90$, significant differences in the cubic curves exist. The percentage difference between $I_R(0)$ and I_n at the MII point increase as r_B decreases. This is shown in Figure 7.19. The differences become significant for $r_B < 0.90$, especially at high $\Delta\hat{o}$ values. Because of the problems mentioned in the previous paragraph, comparisons of I_I, G_1, and G_2 are of almost no value.

No conclusions can be drawn about the validity of the Spencer-Lamb model as $\Delta\hat{o}$ varies. This is due to the frequency problem discussed above. If $\Delta\hat{t}$ had been properly calculated for the TWL model, it is likely that the Spencer-Lamb model would have broken down as $|\Delta\hat{o}|$ increases. This conjecture is based upon the small angle approximations used to obtain the injection source terms in the model.

Comparisons to the Chow Model. A similar series of comparisons between the TWL and Chow models were performed. The laser parameters were taken from data set 27. r_B and $\Delta\hat{o}$ were elements of the sets listed in Eq (7.8). $\phi_{RB} = \pi$ and $\phi_{TB} = \frac{\pi}{2}$. As with the Spencer-Lamb model, $\hat{v} = 0.0$ in all calculations with the TWL model, regardless of the value of $\Delta\hat{o}$. Without this approximation, the cubic curves differed dramatically between the TWL and Chow models. Consequently, the Chow model has the same serious flaw due to the standing wave approximation as the Spencer-Lamb model. This causes the Chow model to break down extremely rapidly as $|\Delta\hat{o}|$ increases.

Over the parameter space explored, the cubic curves for both models retain the s-shape. Consequently, comparisons of the observables were made at the MII point. The free-running frequencies for the TWL and Chow models were identical, so comparisons of I_I and G_2 were possible. No comparisons of G_1 were performed.

Plots of the percentage differences for the three observables are given in Figure 7.20. As r_B decreases, the differences in $I_R(0)$ and I_n and I_I grow, indicating the breakdown of the standing wave approximation inherent in the Chow model. This breakdown is not observed in the G_2 plot. Also apparent is that the percentage differences increase for all three observables as $|\Delta\hat{o}|$ increases.

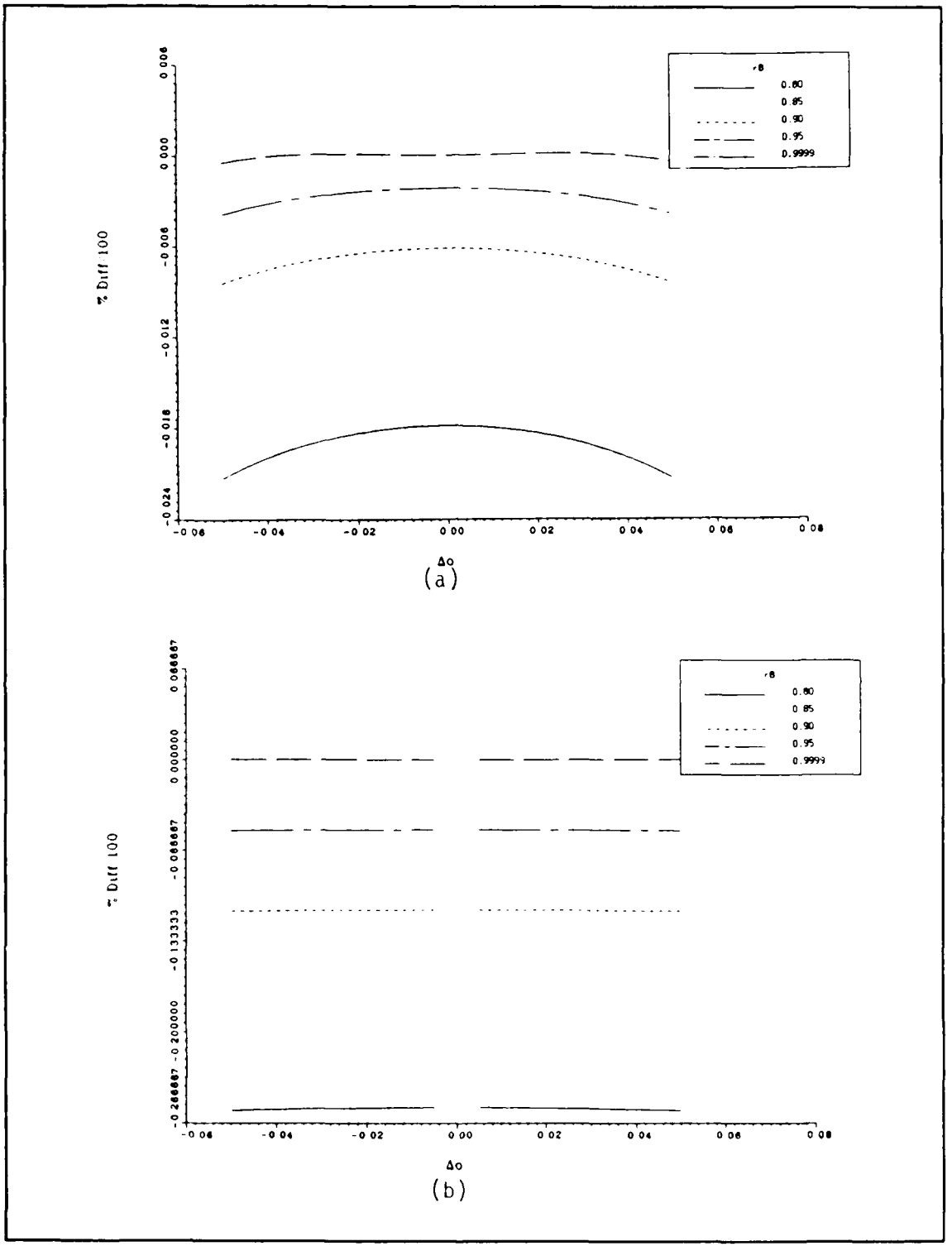

Figure 7.20. Percentage differences in the observables, TWL and Chow models. The laser parameters are from data set 27. (a) $I_R(0)$ and I_{n_1}, (b) I_I, and (c) G_2.

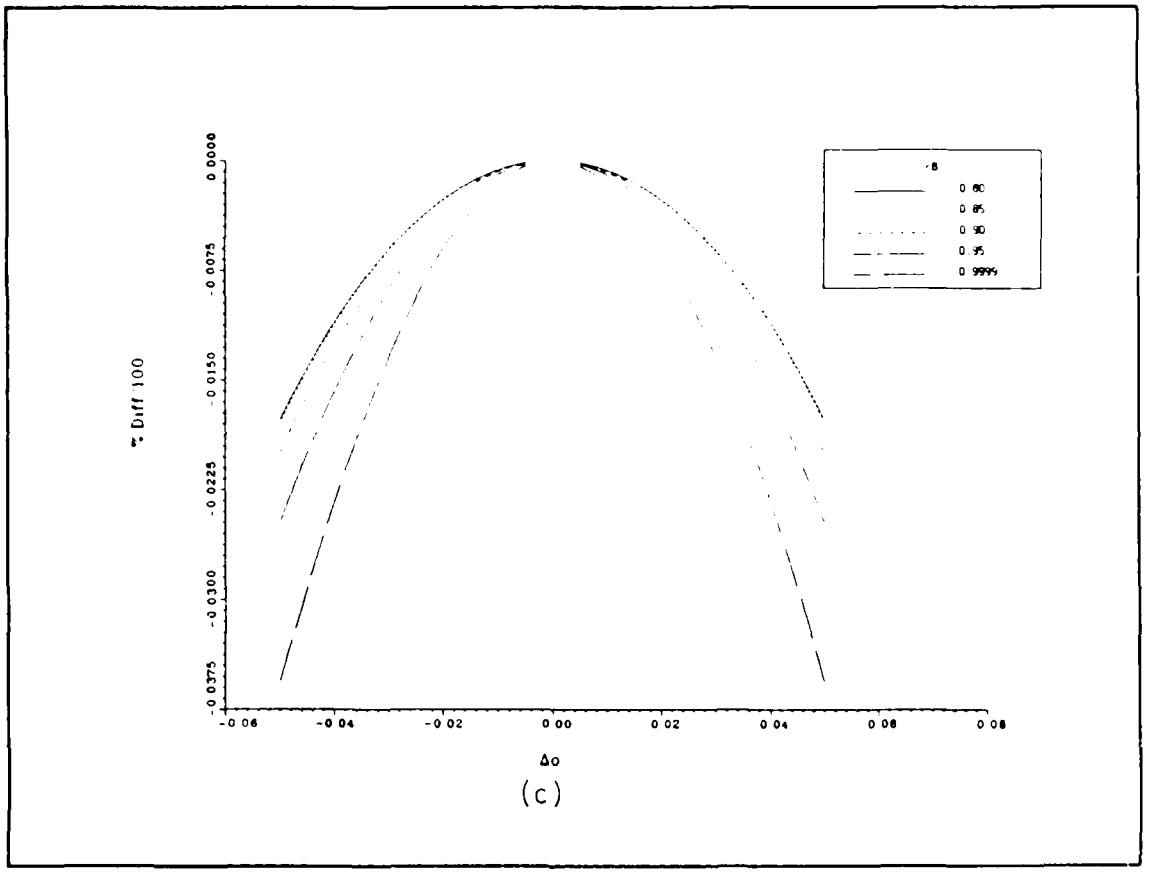

Figure 7.20, con't.

This is due failure of the small angle approximation used to derive the injection source terms in the Chow model. The MII point in the Chow model thus shifts away from that in the TWL model as $(\Delta\hat{\sigma}, r_B)$ departs from $(0.0, 1.0)$. Based upon the plots, the Chow model should not be used if $r_B < 0.90$.

Comparisons of the cubic curves reveal the same breakdowns. At high r_B, low $\Delta\hat{\sigma}$ values, the cubic curves are nearly overlapping. For $(\Delta\hat{\sigma}, r_B) = (0.0, 0.9999)$, the two cubic curves are indistinguishable. However, as r_B decreases or $|\Delta\hat{\sigma}|$ rises, the curves depart from one another. When $r_B = 0.75$, the curves are significantly different.

Locking Range Comparisons. The locking range is an often-used figure of merit for coupled lasers, including injection-locked devices. The broadest locking ranges possible are usually desired

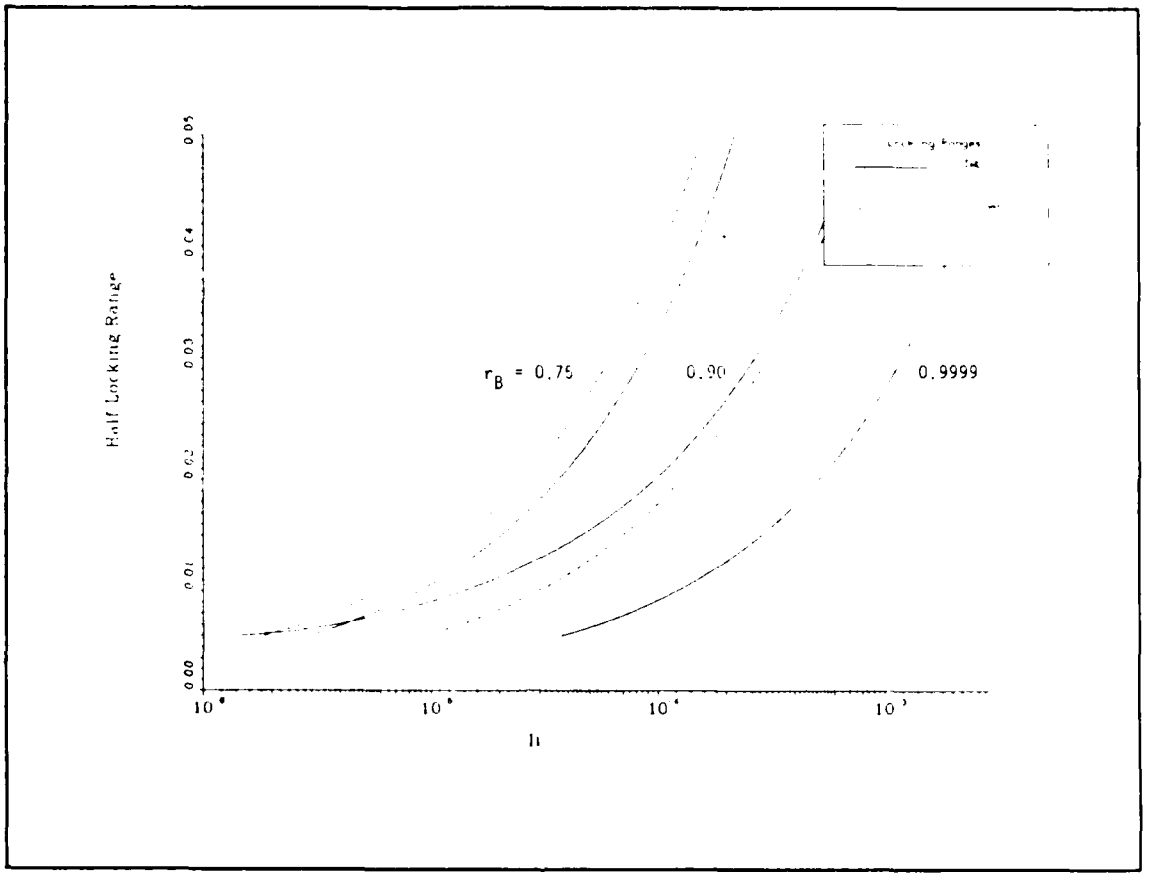

Figure 7.21. Half-locking range comparisons between the TWL and Spencer-Lamb models. The laser parameters are from data set 27.

from a coupled laser system. As noted in previous paragraphs, the locking range is the range of detunings $\Delta\hat{o}$ over which the slave laser remains locked in phase and frequency to the master oscillator for some fixed injected intensity I_I. The contour plots of I_I were seen to contain locking range information.

Figure 7.21 is a comparison of the locking ranges as functions of I_I with r_B as a parameter for the TWL and Spencer-Lamb models. The laser parameters are from data set 27. The $2kL$ term in the mirror B boundary condition of the TWL model was set equal to 0.0 in order facilitate the comparisons. Due to the frequency shifting effects of the dielectric bump, plots of I_I vs $\Delta\hat{o}$ are not symmetric about $\Delta\hat{o} = 0.0$. As a result, only the half-locking range is plotted. This range is

defined as the maximum positive $\Delta\hat{o}$ value of detuning that can occur before locking is lost for some fixed I_I. (A similar half-locking range for negative detunings can also be defined.) For $r_B = 0.9999$, the locking ranges are virtually indistinguishable. As the reflectivity decreases, the locking ranges start to differ between the two models. For $r_B = 0.75$, the ranges are significantly different. The difference is due to the breakdown of the standing wave approximation inherent in the Spencer-Lamb model.

Comparisons of the full locking ranges from the TWL and Chow models are presented in Figure 7.22. The laser parameters are from data set 27. $2kL$ was once again set equal to 0.0 to facilitate the comparisons. The full locking range is the difference between the maximum positive and negative detunings $\Delta\hat{o}$ over which the slave oscillator remains locked to a injected signal. When r_B is very high, the locking ranges from the two models are almost identical. As the reflectivity of mirror B decreases, the locking ranges become significantly different. The difference once again arises because of the breakdown of the standing wave approximation used in the Chow model.

Summary

The results of the numerical studies of the TWL model were presented. The cubic curves were discussed; comparisons were made to the curves from the Spencer-Lamb, Chow, and Ferguson models. Time-dependent results for both free-running and injected lasers were given. The free-running laser at steady-state was explored; comparisons to the simple saturable gain, Agrawal-Lax, Lamb, and Spencer-Lamb models were made. The steady-state injected laser results were discussed extensively. Comparisons to the Spencer-Lamb and Chow models with injected signals were performed.

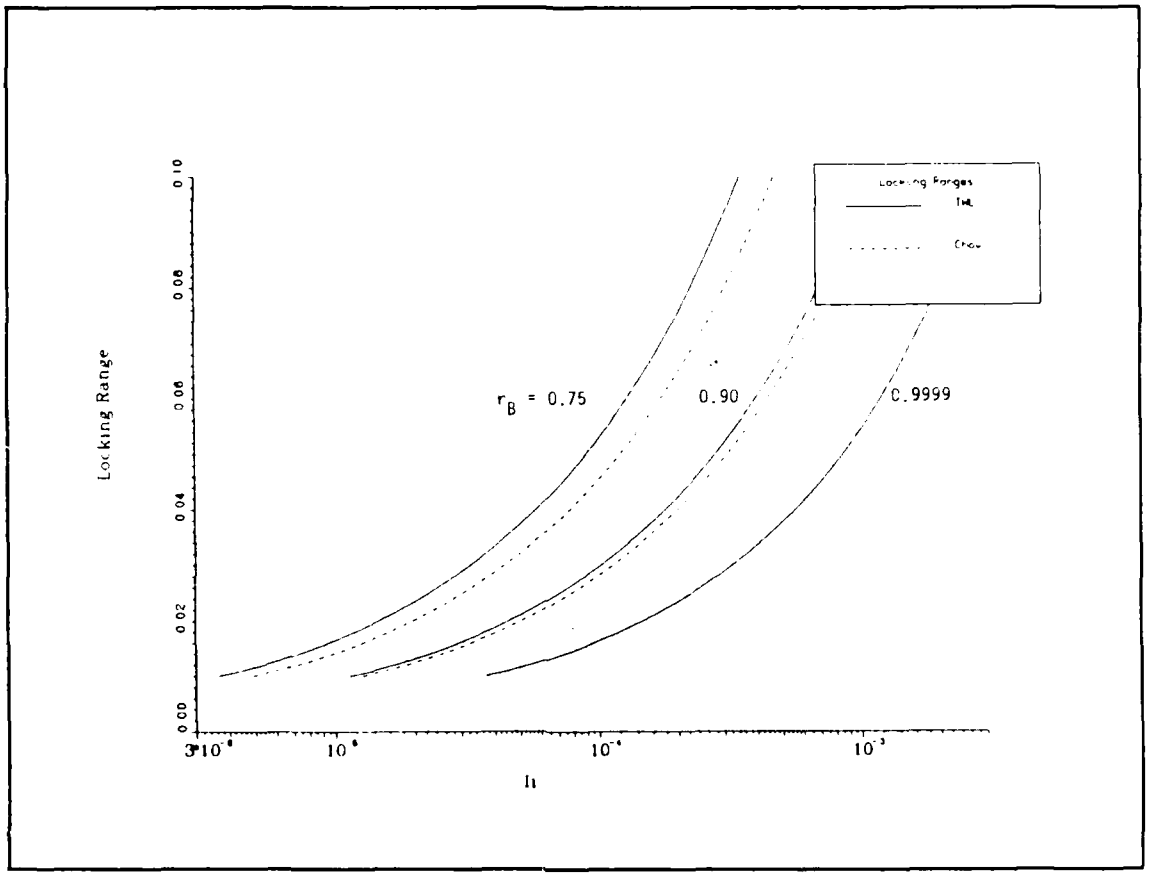

Figure 7.22. Full locking range comparisons between the TWL and Chow models. The laser parameters are from data set 27.

VIII. TWURL Model Numerical Results

The PBCUR laser was studied extensively through numerical simulations. Both free-running and injected lasers were modeled. Only steady-state analyses were performed, due to the numerical stability and cost problems experienced with the time-dependent analyses of the TWL model. The results of the simulations were virtually identical to those of the TWL model, with only a few minor differences.

This chapter examines the results of the numerical studies of the TWURL model. The first section lists the data sets that were used. The cubic curves are discussed next. The free-running laser results are presented in the third section. The injected laser is examined in the final section. Comparisons to the TWL and simple saturable gain models are made throughout the chapter.

Data Sets

The three generic lasers modeled in Chapter VII are employed in the TWURL numerical studies. The twelve data sets examined in Chapter VII are used in the following analyses. The laser parameters are listed in Table V. The resonator magnification is assumed to be variable. Mirrors A and B are perfectly reflective:

$$\mathbf{r}_A = \mathbf{r}_B = e^{i\pi}$$

The mirrors are two-dimensional and square. As a result, $\hat{\mathbf{E}}_R$ is an expanding spherical wave ($\alpha = 1$). The gain medium completely fills the region between the two mirrors:

$$\hat{L}_g = 1.0$$

The gain medium extends sufficiently in the transverse directions so that it is not a limiting aperture.

An inverse relationship exists between M (TWURL model) and r_B (TWL model). This can be observed in the threshold formulæ, Eqs (4.17c) and (6.8b). The laser losses increase as r_B or $\frac{1}{M}$ decrease. As a result, almost all of the phenomena associated with increasing (decreasing) r_B in the TWL model are observed by decreasing (increasing) M in the TWURL model.

TABLE V

PBCUR Laser Numerical Studies: Laser Parameters†

Data Set	$\hat{r}_1$	$\hat{r}_2$	$\hat{r}_3$	$\hat{w}_{eq}$	$\Delta\hat{m}$	g_0/α_0	$M\|_{th}$
15	6.05	21.04145	$1.\bar{3}$	0.567	0.0	11.93	1.9990
16	6.05	36.54837	$1.\bar{3}$	0.54722	0.0	20.00	2.0000
17	6.05	21.04145	$1.\bar{3}$	1.0872	0.0	22.88	3.9998
18	6.05	21.04145	$1.\bar{3}$	0.567	0.03	11.92	1.9976
19	6.05	36.54837	$1.\bar{3}$	0.54722	0.03	19.98	1.9987
20	6.05	21.04145	$1.\bar{3}$	1.0872	0.03	22.86	3.9945
21	6.05	21.04145	$1.\bar{3}$	0.567	0.15	11.67	1.9660
22	6.05	36.54837	$1.\bar{3}$	0.54722	0.15	19.56	1.9681
23	6.05	21.04145	$1.\bar{3}$	1.0872	0.15	22.37	3.8742
24	6.05	21.04145	$1.\bar{3}$	0.567	0.375	10.46	1.8211
25	6.05	36.54837	$1.\bar{3}$	0.54722	0.375	17.53	1.8279
26	6.05	21.04145	$1.\bar{3}$	1.0872	0.375	20.06	3.3452

†Note: g_0/α_0 and $M|_{th}$ are calculated at $\Delta\hat{m}$, not at the more correct value of $\Delta\hat{t}$. Consequently, the tabulated g_0/α_0 and $M|_{th}$ values are slightly lower than the actual values.

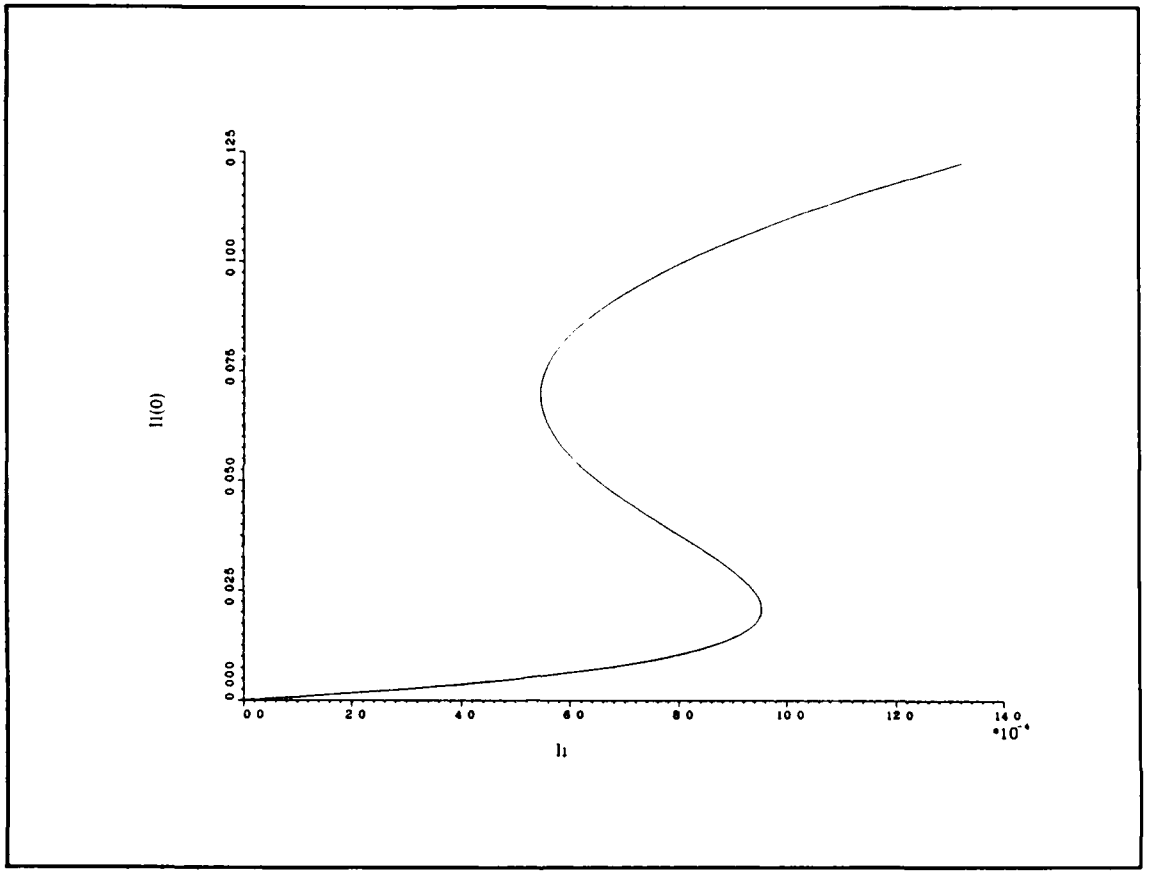

Figure 8.1. A sample cubic curve. $M = 1.33$, $\Delta\hat{o} = 0.008$. All other parameters are taken from data set 15.

The Cubic Curves

Cubic curves can be generated for the TWURL model as well as the TWL model. A curve can be plotted for $I_R(\hat{z})$ or $I_L(\hat{z})$ at any axial location $\hat{z} = \ell$. For consistency with the TWL model, the only cubic curves examined were plots of $I_R(0)$ vs I_I. A sample cubic curve is shown in Figure 8.1. Note that it is quite similar in shape to the curve in Figure 7.1.

The TWURL model cubic curves behave in the same manner as the TWL model cubic curves. At low values of $|\Delta\hat{o}|$, the curves display an s-shaped section. As $|\Delta\hat{o}|$ rises, the s-shaped section narrows and shifts outward along the I_I axis. At some value of $|\pm\Delta\hat{o}_{max}|$, turning points B and C merge into a single point with infinite slope. Above $|\pm\Delta\hat{o}_{max}|$, the cubic curves are monotonically

increasing functions of I_I. The trajectories of turning point C in the $I_R(0)$-I_I plane as functions of $\Delta\hat{o}$ are similar in the two models. The curves were not examined for the anomalous behavior noted in the Ferguson model.

The TWL model cubic curves yielded considerable insight into the stability and locking properties of the injected Fabry-Perot laser. Time-dependent stability and locking analyses of the TWURL model with injected fields were not performed. Nothing can therefore be explicitly stated about the stability or locking properties of the PBCUR laser in the context of the cubic curves. However, based on the heuristic arguments presented in Chapter VII and the similar behavior of the TWL and TWURL cubic curves, the Spencer-Lamb stability and locking criteria were used in the analyses of the TWURL model. Clearly, stability conditions derived from the TWURL equations are required. However, no attempt was made to analytically obtain stability conditions due to the failure of the derivation for the TWL model.

Steady-State Behavior: Free-Running Lasers

A detailed examination of the free-running laser at steady-state was performed. Comparisons of the TWURL and simple saturable gain models were made. A formula for the free-running frequency $\hat{\nu}$ was obtained empirically. The comparisons and the frequency formula are discussed below.

The Simple Saturable Gain and TWURL Models. The simple saturable gain and TWURL models were compared for the twelve data sets listed in Table V. The threshold behavior, $I_R(0)$, P_{out}, and η_L were examined. In general, the results were identical to those from the TWL-simple saturable gain model comparisons.

Eq (6.8b) was numerically verified to be the threshold expression. A slightly expanded version of the formula, allowing for variable mirror reflectivities, was also verified numerically. The expanded equation is:

$$M^a\Big|_{th} = r_A r_B \exp\left[\hat{\tau}_3 \hat{L}_g \left(\frac{\hat{w}_{eq}}{1+\Delta\hat{\iota}^2} - \frac{1}{\hat{\tau}_2}\right)\right] \tag{8.1}$$

The output power P_{out} is somewhat different for the PBCUR laser than for the Fabry-Perot device. Since I_{ap} varies across the output aperture, the geometrical output power must be obtained via integration (see Eq (5.27)). P_{out} for the Fabry-Perot laser is simply given by:

$$P_{out} = I_{out} A_{ap} \qquad \text{(Fabry-Perot laser)} \tag{8.2}$$

where A_{ap} is the output aperture area. Nonetheless, the observations from Chapter VII apply to the PBCUR case. The simple saturable gain model yields higher output powers, as spatial holeburning is not incorporated in the model (Figure 8.2). The differences in output power can be significant: 25-30% differences were commonly observed. The output power is a peaked function of M. The peak P_{out} value occurs at a lower magnification in the TWURL model than in the simple saturable gain model. This has relevance in laser design—optimizing a laser with respect to output power requires a lower magnification than that calculated with the simple saturable gain model. The output powers decrease as $|\Delta\hat{t}|$ rises in both models, as the unsaturated gain decreases. The above observations are similar to those noted by Agrawal and Lax (142, 143).

The extraction efficiency η_L is also a peaked function of M. Plots of η_L vs M for the TWURL and simple saturable gain models are shown in Figure 8.3. The peak efficiency occurs at a slightly lower value of M in the TWURL model than in the simple saturable gain model. The efficiencies for the simple saturable gain model are always higher than those for the TWURL model, due again to spatial holeburning effects. The differences are typically on the order of 25%. This has two impacts on laser design. First, if the laser is designed to operate at the peak efficiency, the magnification will be slightly lower than that calculated with the simple saturable gain model. Second, if the laser is required to operate above some given minimum efficiency, the range of magnification values that yield the required η_L is smaller than that calculated with the simple saturable gain model.

The Steady-State Lasing Frequency. As with the TWL model, the TWURL equations of motion cannot be solved for the steady-state free-running frequency $\hat{\nu}$. The methods of Appendix B can be used to calculate $\hat{\nu}$, however.

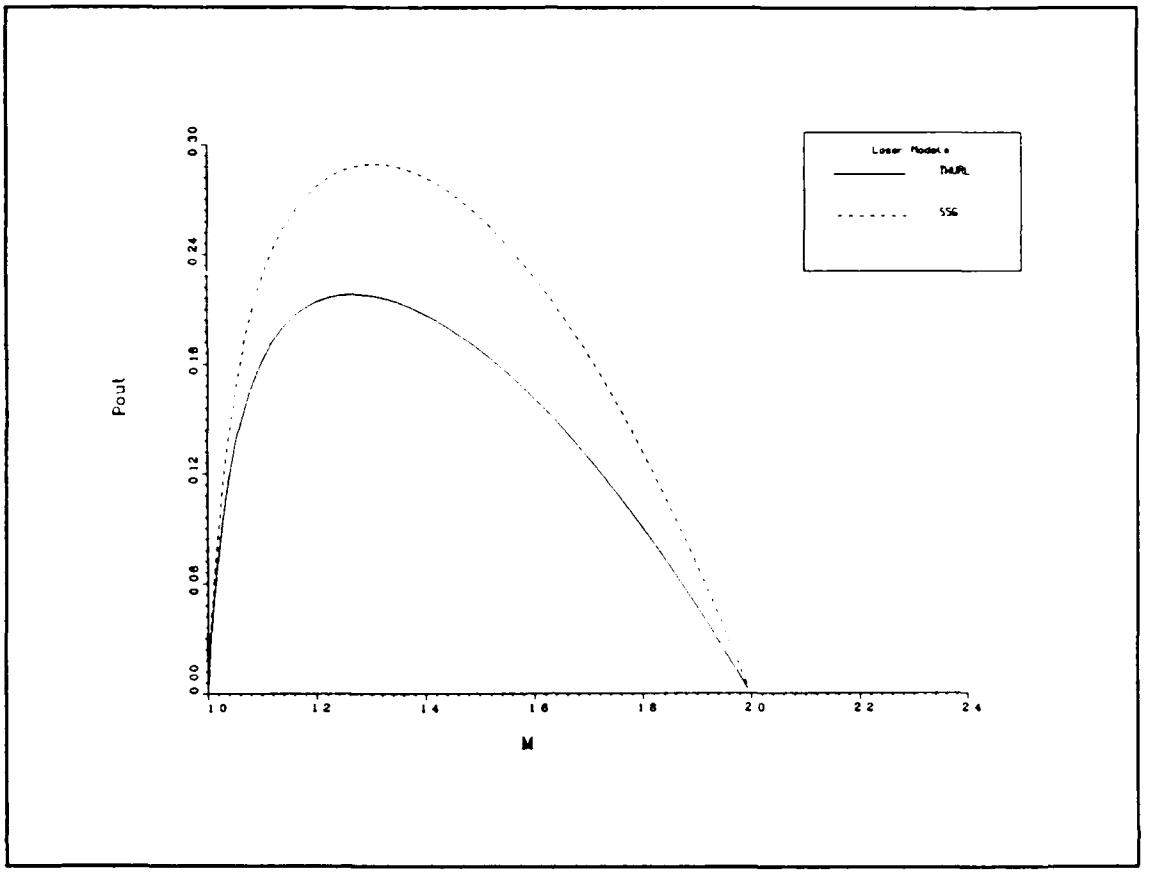

Figure 8.2. P_{out} vs M for the TWURL and simple saturable gain models. All parameters are from data set 15.

The free-running frequency was calculated at over 3000 operating points, using a variety of mirror reflectivities, magnifications, gain lengths, and bare cavity frequencies. Both strip and three-dimensional mirrors were employed. The twelve data sets listed in Table V were used as the basis set. The calculated frequencies were compared to a modified version of the Lamb model frequency formula, Eq (4.34a). In all cases, the numerically calculated frequencies agreed with Eq (4.34a) to within the error given in Eq (B.15). The modified Lamb model formula can be inferred to be the proper frequency equation:

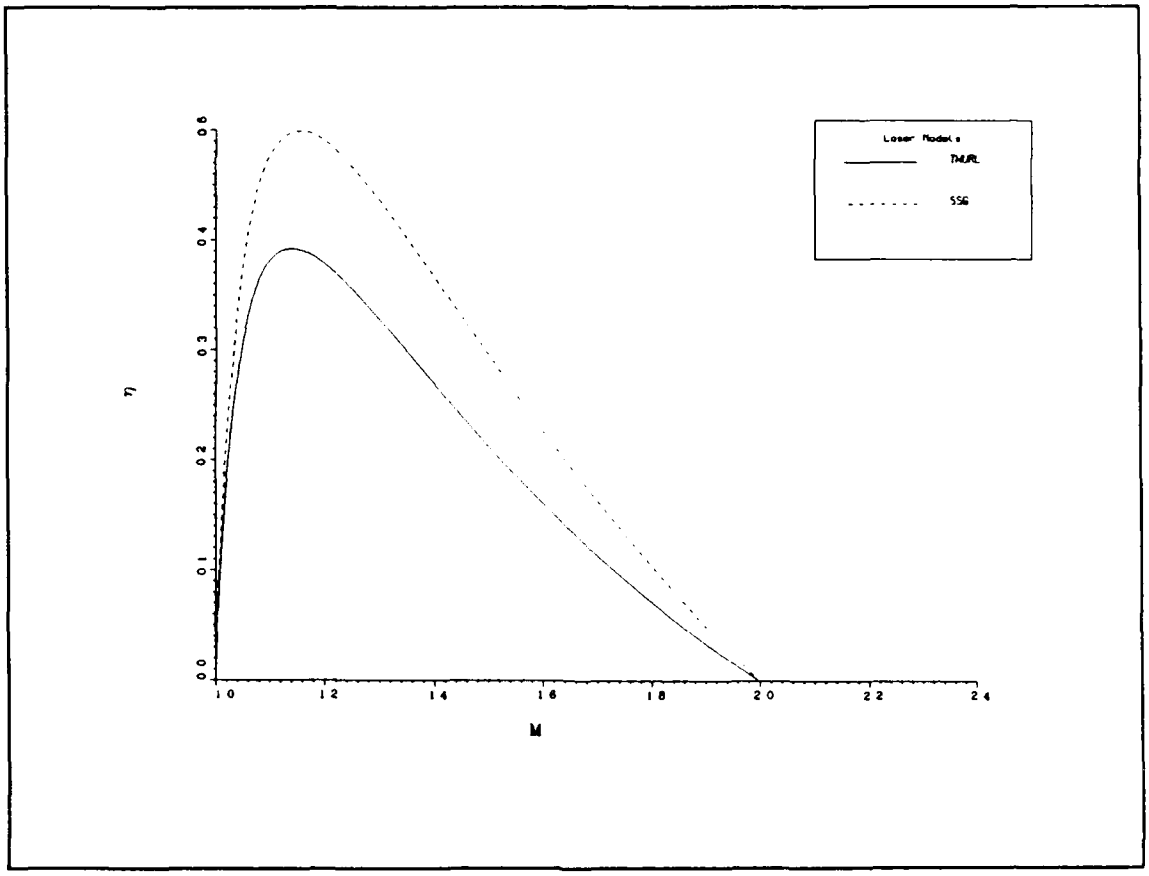

Figure 8.3. η_L vs M for the TWURL and simple saturable gain models. All parameters are the same as in Figure 8.2.

$$\hat{\nu} = \frac{\hat{\Omega} + \hat{\omega}\left[\frac{1}{\hat{\tau}_2} - \frac{1}{\hat{\tau}_3 \hat{L}_g} \ln\left(\frac{r_A r_B}{M^4}\right)\right]}{1 + \frac{1}{\hat{\tau}_2} - \frac{1}{\hat{\tau}_3 \hat{L}_g} \ln\left(\frac{r_A r_B}{M^4}\right)} \tag{8.3a}$$

or:

$$\Delta\hat{t} = \frac{\Delta\hat{m}}{1 + \frac{1}{\hat{\tau}_2} - \frac{1}{\hat{\tau}_3 \hat{L}_g} \ln\left(\frac{r_A r_B}{M^4}\right)} \tag{8.3b}$$

The longitudinal mode spacing, including the medium effects and cavity losses, is given by:

$$\delta\hat{\nu} = \frac{1}{\hat{\tau}_3\left[1 + \frac{1}{\hat{\tau}_2} - \frac{1}{\hat{\tau}_3 \hat{L}_g} \ln\left(\frac{r_A r_B}{M^4}\right)\right]} \tag{8.3c}$$

Eq (8.3) has the same interpretation as its counterpart for the Fabry-Perot laser, Eq (7.5). $\hat{\nu}$ is pulled toward linecenter, but still remains under the bare cavity resonance curve. If the cavity losses increase, then the width of the bare cavity resonance increases. $\hat{\nu}$ is consequently pulled closer toward linecenter. The opposite effect occurs if the cavity losses are decreased: $\hat{\nu}$ is shifted away from linecenter and toward $\hat{\Omega}$. In all cases, $\hat{\nu}$ lies between $\hat{\Omega}$ and linecenter. The longitudinal mode separation in the presence of medium and resonator losses is reduced from the barecavity mode separation by the constant factor:

$$\frac{1}{1+\frac{1}{\hat{\tau}_2}-\frac{1}{\hat{\tau}_3\hat{L}_g}\ln\left(\frac{r_A r_B}{M^4}\right)}$$

Steady-State Behavior: Injected Lasers

The majority of the calculations performed were steady-state simulations of injected lasers. Since there is no system gain equivalent to G_1, only $I_R(0)$, I_I, and G_2 were calculated. The observables were computed at the MII and MG2 points. The parameter space explored was the $(\Delta\hat{o}, M)$ plane, analogous to the $(\Delta\hat{o}, r_B)$ plane examined with the TWL model. Two series of runs were performed. The first was in the region of the $(\Delta\hat{o}, M)$ plane where the cubic curves retain the s-shape. The three observables were calculated at the MII and MG2 points in this region. The second series of runs explored as large a region in the $(\Delta\hat{o}, M)$ plane as possible, subject to the constraints that $1.0 \leq M \leq M|_{th}$ and $-0.1 \leq \Delta\hat{o} \leq 0.1$. The observables were computed at the MG2 point in the second series.

As with the TWL model, the calculations required the implicit assumption that the MG2 point always lies on a locked and stable section of the cubic curves. In the first run series, the MG2 point lay on branch I of the cubic curves for all points examined. Because of the similar behavior of the TWL and TWURL models, the MG2 point was therefore assumed to be a locked and stable operating point.

The observables were originally calculated with the approximate formula for $\hat{\vartheta}$, Eq (3.27a). After the completion of the analyses, the correct formula for $\hat{\vartheta}$ was derived using Eq (8.3c). Data sets 17 and 26 were determined to be affected the most by the approximation. The analyses were repeated for these two sets using the exact expression for $\hat{\vartheta}$. The impact of the approximation was observed to be negligible. The contour levels and the exact values of the observables shifted slightly. However, the overall shapes and behavior of the contour and slice plots remained unchanged.

The observables behaved in identical manners as their TWL model counterparts in the twelve data sets. The contour and slice plots had the same basic characteristics in the two laser models. The shapes of the curves varied only slightly, and any differences were minor and isolated. The interpretations of the locking physics for the PBCUR laser are consequently the same as for the Fabry-Perot laser.

Summary

Detailed analyses of the TWURL were performed at steady-state. Both free-running and injected lasers were examined. In general, the TWURL model behaved in the same manner as the TWL model. Only in isolated, individual circumstances did the two models differ in their behavior. The general conclusions in Chapter VII can therefore be applied to the TWURL model.

IX. Summary and Recommendations

Many theoretical and numerical results were presented in the previous chapters. Several design guidelines for free-running and injected lasers emerged from this research. The main results and design guidelines are summarized in this chapter.

The first section briefly lists the main results of the numerical studies. Both free-running and injected lasers are discussed. Several general rules for the design of free-running and injected lasers are described in the second section. A simplified coupled laser-phased array system is presented. Four follow-on research topics are recommended in the final section.

Results Summary

The principle results of this research are outlined in the following paragraphs.

1. Steady-state analyses, free-running lasers.

   (a) The simple saturable gain models predict higher intensities than the TWL or TWURL models. This is due to the lack of spatial holeburning effects in the simple saturable gain models. Except when $r_B \approx 1.0$, lower values of I_{out} are calculated with the SWL, SL1, and SL2 models than with the TWL model.

   (b) P_{out} peaks at higher outcouplings in the simple saturable gain models than in the TWL or TWURL models. The peak occurs at lower outcouplings in the SWL, SL1, and SL2 models than in the TWL model.

   (c) The extraction efficiencies calculated with the simple saturable gain models are higher than those produced by the TWL or TWURL models. Except when $r_B \approx 1.0$, the extraction efficiencies calculated with the SWL, SL1, and SL2 models are lower than those calculated with the TWL model.

   (d) The extraction efficiency peaks at higher outcouplings in the simple saturable gain model than in the TWL or TWURL models. The peak occurs at lower outcouplings in the SWL, SL1, and SL2 models than in the TWL model.

(e) The TWL and TWURL models reduce to the simple saturable gain models near the lasing threshold.

(f) The TWL model reduces to the Lamb model when $r_B \approx 1.0$.

(g) The simple saturable gain, TWL (TWURL), and Lamb models have the same threshold outcoupling values.

(h) The frequency formula for the TWL and TWURL models is the same as that for the Lamb model. The frequency pulling depends only on the cavity resonance width. The longitudinal mode spacing in the presence of gain is independent of frequency and less than the barecavity longitudinal mode spacing.

2. Time-dependent analyses, injected lasers.

(a) The minimum injected intensity I_I required for locking is that corresponding to turning point C on the cubic curves. For injected intensities greater than this value, the laser locks to branch I of the cubic curves.

(b) If I_I is less than the minimum required to lock, the free-running laser field will beat against the injected signal. Amplitude and frequency modulation of the laser fields occur.

(c) When unlocked, the period of the beat note of the laser field depends primarily on the strength of I_I. As I_I increases, the period of the note lengthens.

(d) The modulation depth of the beat note depends only slightly on I_I.

3. Steady-state analyses, injected lasers.

(a) In general, the injected Fabry-Perot and PBCUR lasers behave in similar manners.

(b) The locking range can be defined as the range of detunings $\Delta\hat{o}$ over which the laser remains locked for fixed I_I. The I_I contour plots for the MII point are essentially plots of the locking ranges.

(c) The locking range increases as the outcoupling increases for fixed I_I.

(d) For a fixed detuning $\Delta\hat{o}$, the minimum injected intensity required to lock the laser increases as the outcoupling decreases.

(e) Generally, $I_R(0)$ increases as the outcoupling decreases for fixed $\Delta\hat{o}$ at the three operating points. An exception occurs at the MG2 point if $\Delta\hat{o}$ is large and negative. In these cases, $I_R(0)$ first decreases then increases as the outcoupling decreases.

(f) Plots of $I_R(0)$ vs $\Delta\hat{o}$ are concave upward at the MG2 point and concave downward at the MII and MG1 points.

(g) The range of $\Delta\hat{o}$ values over which a specific system gain G_1 can be achieved increases as the outcoupling increases.

(h) Gains G_1 and G_2 decrease as the detuning $|\Delta\hat{o}|$ increases at the three operating points.

(i) The MG2 point always lies on a locked and stable section of the cubic curves. At high r_D and low $|\Delta\hat{o}|$ values, the global MG1 point lies on an unstable branch of the cubic curves. Elsewhere, the MG1 point lies on a locked and stable section of the cubic curves. By definition, the MII point always lies at the edge of the locked region.

Design Guidelines

Several general guidelines for laser design can be drawn from the results of the numerical studies. The guidelines are discussed below, along with a proposed design for a coupled laser-phased array device based on injected lasers.

The simple saturable gain models are frequently used to design free-running lasers. The models are used to calculate the outcouplings required for peak output power and extraction efficiency. However, as noted in Chapters VII and VIII, the actual outcouplings at which P_{out} [illegible] are shifted slightly from the values obtained with the simple saturable gain models. TWL or TWURL models should be used to calculate the required outcouplings when peak output power or efficiency is required from the laser. The simple models predict an erroneously wide range of outcouplings over which the specified [illegible] TWL or TWURL models should be used to calculate the [illegible] the fields, powers, and efficiencies calculated with the [illegible]

AD-A109 514 SEMICLASSICAL THEORY OF INJECTED LASERS WITH ARBITRARY STABLE AND UNSTABLE RESONATORS(U) AIR FORCE INST OF TECH WRIGHT-PATTERSON AFB OH SCHOOL OF ENGI.. 3/4

UNCLASSIFIED S M RINALDI DEC 87 AFIT/DS/PH/76-3 F/G 9/3 NL

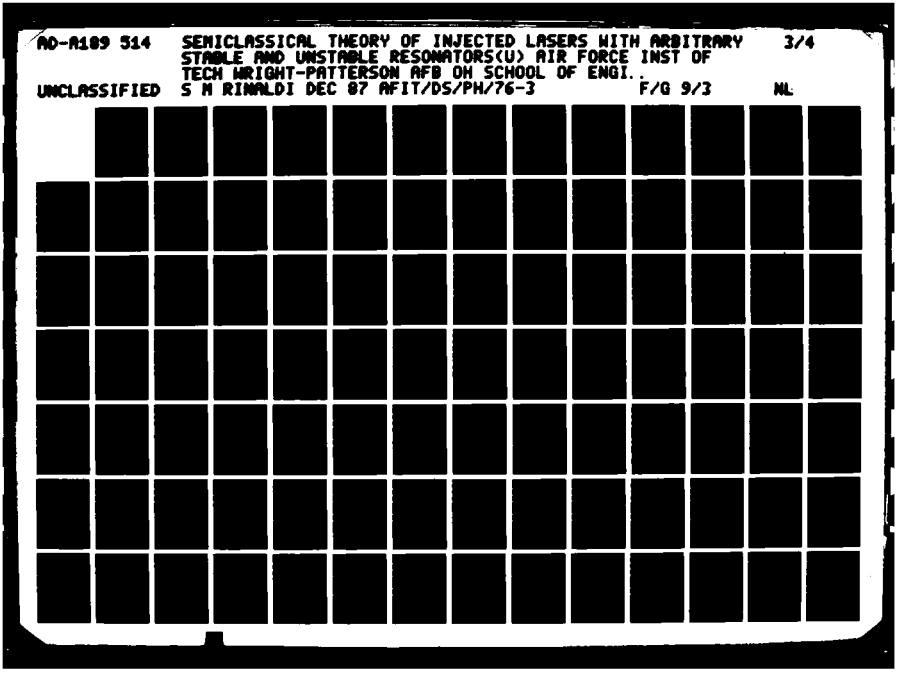

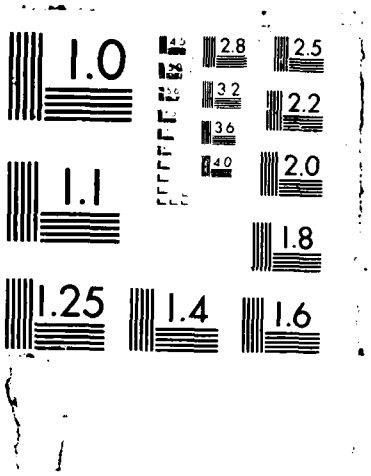
1.0
2.8
2.5
3.2
2.2
3.6
4.0
2.0
1.1
1.8
1.25
1.4
1.6

to spatial holeburning effects. The TWL or TWURL models should be used to more accurately predict the performance of the laser.

A figure of merit for an injected laser is the locking range. Generally, a broad locking range is desired. This allows greater tolerance to variations in $\Delta\hat{o}$ induced by mechanical vibrations, gain medium inhomogeneities, amplified spontaneous emission, etc. Since the locking range broadens as the outcoupling increases, an injected laser should be designed with as large an outcoupling as is consistent with energy extraction considerations. The I_I contours for the MII point can be used to determine the locking ranges. The injected laser should never be designed to operate at the MII point, as any perturbations have the potential to break the lock.

A second figure of merit for injected lasers is the range of $\Delta\hat{o}$ values over which a given system gain G_1 can be attained. This range can be obtained directly from the G_1 contour plots for the MG1 point. The range broadens as the outcoupling increases. Again, the laser should be designed to have as broad a range as possible, consistent with the energy extraction requirements. Broader ranges provide greater tolerances to fluctuations of $\Delta\hat{o}$. This requires designing the slave oscillator to have as large an outcoupling as possible.

Examination of the boundary conditions for mirror B (Eqs (3.28) and (5.37c)) shows that the absolute phases of $\hat{\mathbf{E}}_R$, $\hat{\mathbf{E}}_L$, and $\hat{\mathbf{E}}_{out}$ can be controlled by varying the phase of $\hat{\mathbf{E}}_{IN}$. This observation can be used to advantage in the design of a coupled laser-phased array system. An example of a system is depicted in Figure 9.1. Fine piston tuning (phasing) can be achieved with the nonlinear optical (NLO) media in the injected beam trains (157). If the nonlinear material exhibits the linear electrooptic effect, the index of refraction of the material can be changed by varying an applied electric field (146: Chapter 9). This will force variations in the absolute phases of the injected signals applied to the slave oscillators. In this manner, fine piston tuning can be achieved in the low power injected beam trains without mechanical devices (optical trombones). To some degree, injected pathlength equalization can be accomplished with the nonlinear material. With a

properly designed system, only the gross external pathlength differences would require equalization with optical trombones. This function could be performed by the phased array.

Suggested Follow-on Research Topics

Several research topics follow naturally from this work. The following suggestions are not meant to an all-inclusive list, but rather a starting point for future efforts.

Locking Criteria. As noted in Chapter VII, an attempt was made to derive the locking and stability criteria for the Fabry-Perot laser. A perturbative approach similar to that used by Spencer and Lamb was employed. The attempt clearly failed. No effort was made to derive locking and stability expressions for the PBCUR laser.

A definite requirement for the criteria exists. Other approaches, such as that employed by Walsh for coupled lasers (19), might be utilized. Until the locking and stability criteria are known, the true MII point can only be determined from time-dependent analyses. This is undesirable due to the stability problems encountered with the time-dependent codes.

Inhomogeneously Broadened Lasers. The laser models developed in this project apply to homogeneously broadened media. An extension of the TWL and TWURL models to inhomogeneously broadened lasers should be straightforward. Brown's methodology could be employed: the density matrix equations of motion could be modified to include the effects of atomic motion. The derivations should then be similar to those presented in Chapter II. Comparisons to other laser models, particularly the simple saturable gain model (near threshold) and Lamb's inhomogeneously broadened laser model (for $r_B \approx 1.0$), should be performed.

Transverse Field Structures. A primary shortcoming of the semiclassical models is that the transverse laser modes are ignored. The models are strictly one-dimensional (longitudinal). This downfall might be eliminated by expanding the fields in terms of basis sets other than planar, cylindrical, or spherical traveling waves. Two such basis sets are the Hermite-Gaussian and Laguerre-Gaussian functions. The resultant theory could be readily applied to lasers with stable resonators.

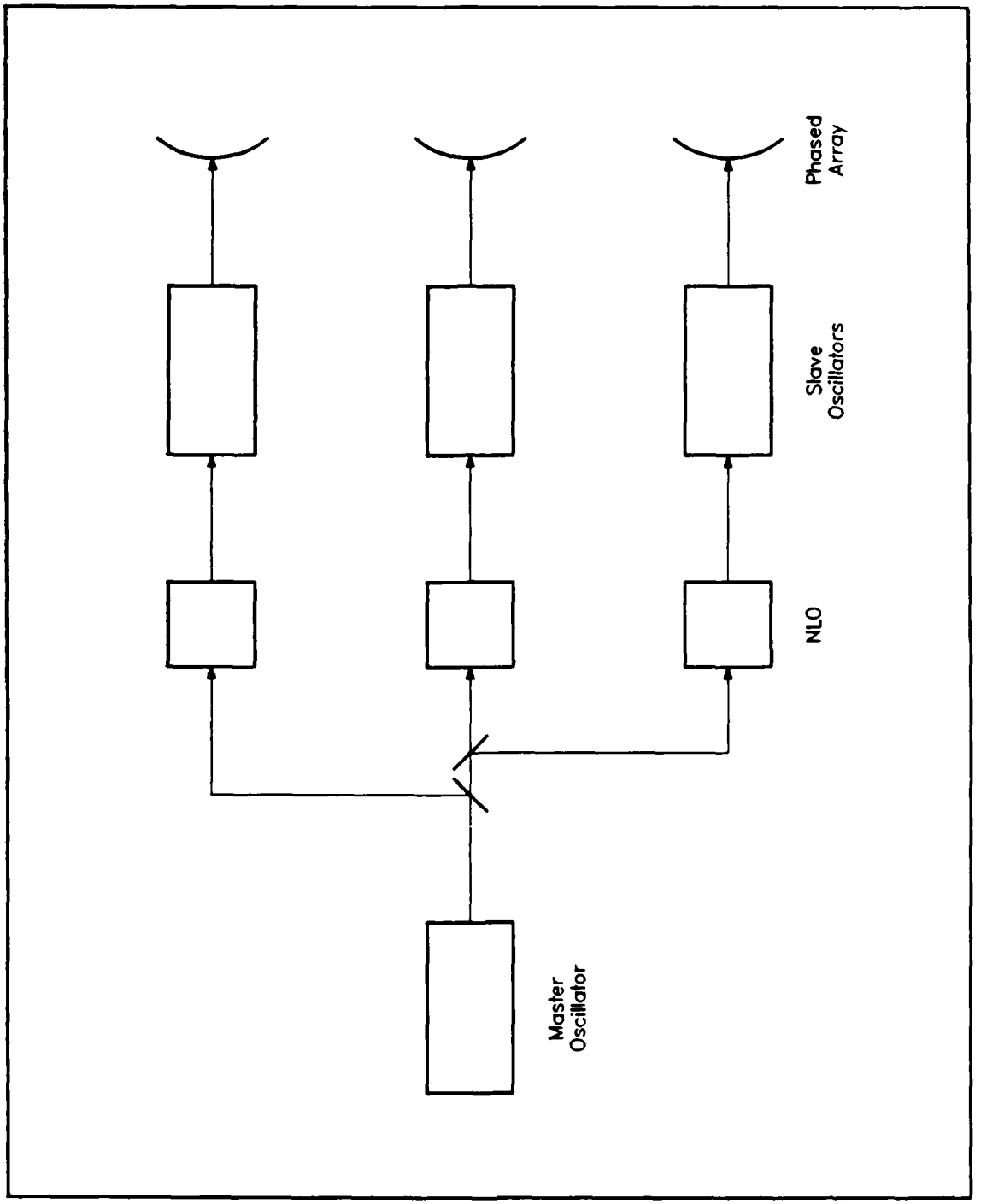

Figure 9.1. A coupled laser-phased array system. The nonlinear optical material is used to provide fine piston tuning and injected pathlength equalization.

The derivations would be fundamentally similar to those presented in Chapter II. The lowest order transverse field dependencies would be retained. The resultant partial differential equations would probably include derivative terms on the order of:

$$\frac{\partial \mathbf{E}}{\partial x}, \qquad \frac{\partial \mathbf{E}}{\partial y}, \qquad \frac{\partial \mathbf{E}}{\partial z}, \qquad \frac{\partial \mathbf{E}}{\partial t}$$

The final equation set will undoubtedly be extremely complex. Suitable approximations will probably be required in order to solve the system numerically.

Coupled Lasers. Coupled lasers are currently a topic of great research interest, both experimentally and theoretically. The theoretical analyses can be grouped in two main classes: diffractive models (with and without gain sheets), and one-dimensional models with gain. The gain models employed in the one-dimensional analyses are generally standing wave, semiclassical models or simple saturable gain models. As a result, the models suffer from the same problems that led to the current research.

Applying the TWL and TWURL models to the coupled laser problem is a simple extension of the injected laser problem. If the supermodes of the coupled system can be calculated, a variety of important phenomena can be explored. Among these are fine piston tuning via resonator length adjustments, locking ranges, farfield coherent intensities, and resonator tuning curves.

Summary

The principle conclusions and results of the research were outlined. Several general design guidelines were presented, along with a coupled laser-phased array system concept. In the final section, four follow-on research topics were presented.

APPENDIX A

Mirror Models

The resonator mirrors play an important role in determining the longitudinal modes of the laser. The phase shifts of the mirrors are required before the barecavity mode frequencies $\hat{\Omega}$, and thus the free running frequencies $\hat{\nu}$, can be calculated. Since the specific mirror model will determine the phase shifts incurred at the mirrors, the particular model employed must accurately describe the properties of the "real" mirror. It is therefore important to understand the properties and peculiarities of the mirror models used in a calculation.

The two mirror models used in this research are discussed below. The first section examines two general means by which a mirror may be modeled. The mirror model used with the traveling wave laser theory is examined in the second section. In the third section, the dielectric bump model used by Spencer and Lamb (101) is discussed. A summary is given in the final section.

Methods of Modeling Mirrors

Two main approaches exist for modeling the mirrors of a laser resonator. The first approach is a general technique. No particular physical mirror is modeled; the mirror is simply visualized as a passive two-port device with a specified set of reflection, transmission, and absorption coefficients. The coefficients are constrained by a few simple mathematical relationships. The second approach involves modeling an actual piece of hardware. The mathematics of the model must accurately describe the measurable properties of the physical mirror. Once the specific mirror or class of mirrors is selected, the model and its properties become fixed. Consequently, the second modeling philosophy is somewhat rigid and inflexible.

The first modeling approach is more flexible than the second. In this method, no specific physical device is modeled. Rather, a set of general reflection, transmission, and absorption coefficients are given that satisfy a few simple relationships. It is assumed that a mirror can be manufactured that has the given coefficients; however, the exact mirror type (dielectric stack, vapor-deposited metal

on a substrate, polished metal slab, etc.) is not specified. This philosophy is used in the Lamb model and the TWL/TWURL models of this research. The mirrors are simply specified as a set of transmission and reflection coefficients in Eqs (2.1), (3.1), and (5.1). This modeling approach is very general, and is not limited by specific mirror hardware.

The second approach involves modeling an existing mirror or mirror class. For example, the mirrors to be modeled may be quarter-wave dielectric stacks on some substrate. Each slab of dielectric material has its own value of permittivity ϵ, permeability μ, absorption σ, and thickness. By matching the boundary conditions of the electric and magnetic fields across the dielectric interfaces and incorporating the absorption σ, the total fields reflected, absorbed, and transmitted by the stack can be calculated. As the number of dielectric slabs, the thicknesses of the slabs, or the values of ϵ, μ, and σ vary, the reflection, absorption, and transmission coefficients change. However, the coefficients can always be calculated from explicit formulæ. A specific example of this approach is the lossless dielectric bump model used by Spencer and Lamb. The reflection and transmission coefficients of the dielectric bump are calculated by matching the boundary conditions of the electromagnetic fields across the bump. The "height" η of the dielectric bump may vary from problem to problem; however, the formulæ for the reflection and transmission coefficients remain fixed functions of η. This particular modeling philosophy is rather inflexible, as once the mirror is described physically, the reflection, transmission, and absorption coefficients become fixed functions of the physical parameters.

The Mirror Models of the TWL/TWURL Theories

The mirror models used in the TWL/TWURL theories of this research follow the more general philosophy described in the previous section. The mirrors are of unspecified type; they are assumed to be lossless, passive two-port devices with reflection and transmission coefficients given in Eqs (2.1), (3.1), and (5.1). A few simple relationships govern the complex reflection and transmission coefficients.

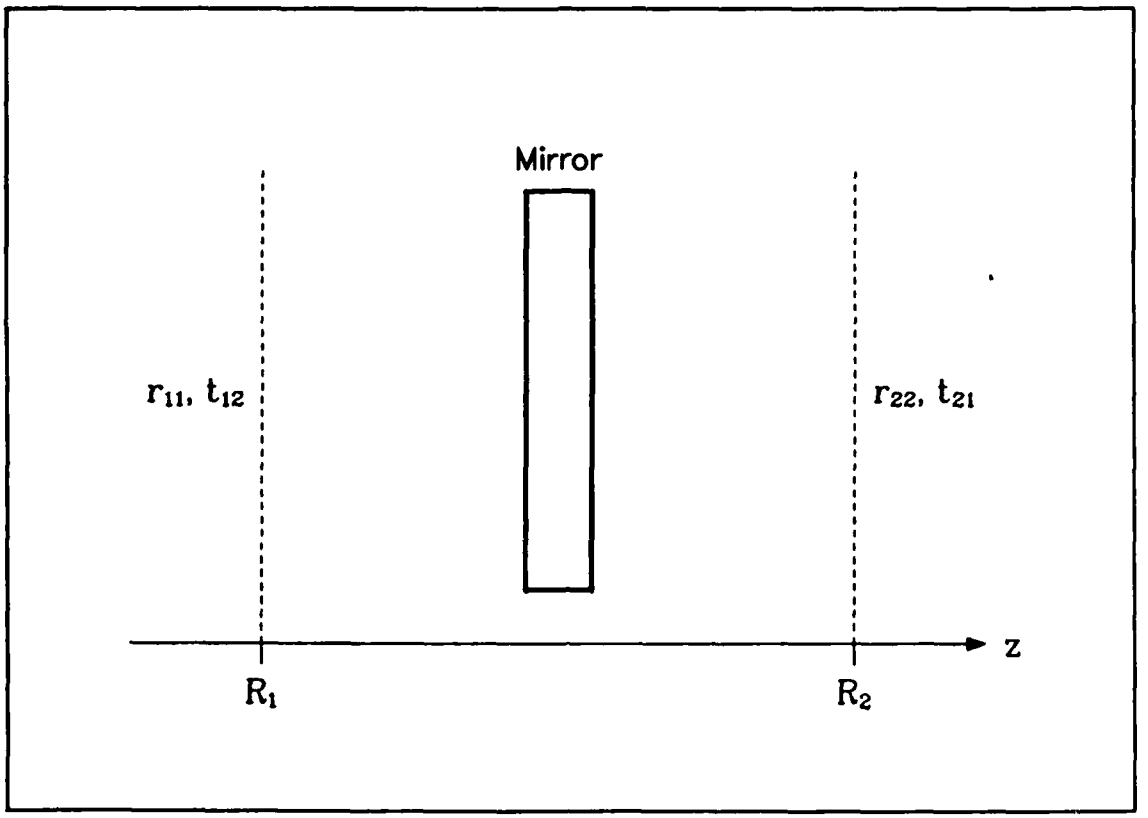

Figure A.1. Schematic diagram of a general mirror.

The general mirror is depicted in Figure A.1. The mirror is described by a set of four complex reflection and transmission coefficients, given by r_{11}, r_{22}, t_{12}, and t_{21}. The coefficients are calculated or measured at the pair of reference planes $R_{1,2}$ that lie on opposite sides of the mirror. The actual location of the reference planes is arbitrary; for a particular physical device, however, the locations may fall at obvious points. For example, for a dielectric stack deposited on some substrate, two obvious locations for the reference planes are at the air-dielectric and air-substrate interfaces. Notice that by shifting the location of the reference planes, the values of the coefficients will change. At a minimum, the phases of the coefficients will change if the reference planes are translated. This is due to the different optical path that the radiation must traverse.

Seigman (160:504–506) gives three simple relationships that govern the four coefficients for lossless, passive mirrors such as those used in this research. First, the two transmission coefficients are exactly equal; that is:

$$t_{12} = t_{21} \equiv t \tag{A.1}$$

t will be used for the remainder of the discussion to denote the transmission coefficient. The reflection and transmission coefficients are related as follows:

$$|r_{11}|^2 = |r_{22}|^2 = 1 - |t|^2 \tag{A.2}$$

$$r_{11}t^* + r_{22}^* t = 0 \tag{A.3}$$

These relationships follow by considering the conservation of power flow through the mirror.

By examining the relationships, it is clear that three free parameters completely specify the mirror. First, from Eq (A.2), only one of the amplitudes of the coefficients may be arbitrarily chosen. Once fixed, the magnitudes of the other two coefficients are determined. Second, only two of the three phases of the coefficients may be freely chosen. The third phase depends upon the other two, as seen in Eq (A.3). The exact values of the three parameters depend upon the particular choice of reference planes.

In the numerical analyses of the TWL/TWURL models (Chapters VII and VIII), the two reflection coefficients of a given mirror were set equal to each other. Additionally, they were both chosen to be purely real and negative, i.e., their phases were set equal to π. This is a typical convention used throughout laser texts. From Eq (A.3), the phase of the transmission coefficient was thus forced to be $\pi/2$. Once a specific reflection or transmission coefficient amplitude was chosen, the other amplitude was fixed by Eq (A.2). The mirror was then completely specified. These conventions for the coefficients were used in all the numerical work with the TWL/TWURL models in this project.

The Dielectric Bump Mirror Model

Spencer and Lamb use a standing wave laser model with a Fabry-Perot resonator in their analyses. Schematically, their laser is the same as that depicted in Figure 4.1. Mirror A is perfectly reflective, with a reflection coefficient given by $r_A = -1$. Mirror B, through which injection and outcoupling are performed, is assumed to be an infinitesimally thin slab of dielectric material. This mirror, or dielectric bump, has several interesting and aphysical properties that warrant further investigation.

The dielectric bump is modeled as an instantaneous change in the permittivity ϵ at the mirror position $z = L$. Mathematically, the bump is described by:

$$\epsilon_{DB}(z) = \epsilon_0[1 + \Lambda\delta(z - L)] \tag{A.4}$$

where $\delta(z)$ is the Dirac delta function and Λ is the "height" of the change in permittivity.

Matching the boundary conditions for the electric and magnetic fields across the dielectric bump yields its reflection and transmission coefficients:

$$r_D = r_D e^{i\phi_{RD}} = \frac{i\eta}{2 - i\eta} \tag{A.5a}$$

$$t_D = t_D e^{i\phi_{TD}} = \frac{2}{2 - i\eta} \tag{A.5b}$$

where $\eta = k\Lambda$ and k is the wavenumber. The reflection coefficient is the same on either side of the dielectric bump. It is a trivial exercise to show that r_D and t_D satisfy Eqs (A.2) and (A.3).

A bit of simple algebra yields the amplitudes and phases of the reflection and transmission coefficients in terms of η:

$$r_D = \frac{\eta}{\sqrt{4 + \eta^2}} \tag{A.6a}$$

$$\phi_{RD} = \frac{\pi}{2} + \arctan\left(\frac{\eta}{2}\right) \tag{A.6b}$$

$$t_D = \frac{2}{\sqrt{4 + \eta^2}} \tag{A.6c}$$

$$\phi_{TD} = \arctan\left(\frac{\eta}{2}\right) \tag{A.6d}$$

Note that any expression in Eq (A.6) can be inverted to yield a equation for η in terms of either the magnitude or phase of r_D or t_D. In particular, inverting Eq (A.6a) gives:

$$\eta = \frac{2r_D}{\sqrt{1 - r_D^2}} \tag{A.7}$$

This fact has an important ramification. The dielectric bump has only one free parameter that may be arbitrarily chosen. Once any one of the five parameters (η, r_D, ϕ_{RD}, t_D, or ϕ_{TD}) is arbitrarily chosen, the other four parameters are fixed. Of particular importance is that the phases of the mirror coefficients are fixed functions of r_D (or t_D). For a fixed value of r_D, there is one and only one corresponding value of ϕ_{RD}. Recall that the general mirror model used in the TWL/TWURL theories has three free parameters. The fact that the dielectric bump has only one free parameter makes the model much less flexible than the TWL/TWURL mirror models.

The dielectric bump parameter η can have any nonnegative, real value, i.e., $\eta \in [0, \infty]$. The corresponding ranges for the magnitudes and phases of the reflection and transmission coefficients are:

$$r_D \in [0, 1] \tag{A.8a}$$

$$\phi_{RD} \in \left[\frac{\pi}{2}, \pi\right] \tag{A.8b}$$

$$t_D \in [1, 0] \tag{A.8c}$$

$$\phi_{TD} \in \left[0, \frac{\pi}{2}\right] \tag{A.8d}$$

The dielectric bump introduces two significant effects into the laser model. First, the bump forces frequency shifts in the barecavity and free-running laser modes. Second, the bump causes the mirror losses to behave in an unusual manner. These important properties are discussed in the following two sections.

The Dielectric Bump Frequency Shifts. One of the significant properties of the dielectric bump is that the phase of the reflection coefficient is a function of r_D:

$$\phi_{RD} = \frac{\pi}{2} + \arctan\left(\frac{r_D}{\sqrt{1 - r_D^2}}\right) \tag{A.9}$$

The phase ϕ_{RD} displaces the barecavity mode frequencies from the usual values of $\hat{\Omega} = nc/2\gamma L$, where n is some (large) integer, to:

$$\hat{\Omega}' = \hat{\Omega} + \frac{2}{\hat{\tau}_3}\left(\frac{\eta}{\eta^2+1}\right) \tag{A.10}$$

The barecavity intermode spacing of $c/2\gamma L$ (normalized units) remains the same as in the TWL, TWURL, or Lamb models. The shift of the barecavity modes can be observed in the $\dot{\varphi}_n$ equation of the Spencer-Lamb model (Eq (4.42b)). Note in particular that since η is a function of r_D, then the shifted barecavity frequencies $\hat{\Omega}'$ are also functions of r_D.

The phase of the dielectric bump reflection coefficient also affects the frequency of the free-running laser mode. Eq (4.44) gives the free-running frequency:

$$\hat{\nu} = \frac{\hat{\Omega} + \frac{2}{\hat{\tau}_3}\left(\frac{\eta}{\eta^2+1}\right) + \hat{\omega}\left[\frac{1}{\hat{\tau}_2} + \frac{2}{\hat{\tau}_3}\left(\frac{1}{\eta^2+1}\right)\right]}{1 + \frac{1}{\hat{\tau}_2} + \frac{2}{\hat{\tau}_3}\left(\frac{1}{\eta^2+1}\right)} \tag{A.11}$$

Note that the shifted barecavity frequency $\hat{\Omega}'$ appears in the numerator of Eq (A.11). This forces a potentially large shift of $\hat{\nu}$ that is not seen in the TWL/TWURL or Lamb models. A more useful representation of $\hat{\nu}$, particularly in light of the numerical work discussed in Chapter VII, is $\Delta\hat{t}$:

$$\begin{aligned}\Delta\hat{t} &= \hat{\omega} - \hat{\nu} \\ &= \frac{\Delta\hat{m} - \frac{2}{\hat{\tau}_3}\left(\frac{\eta}{\eta^2+1}\right)}{1 + \frac{1}{\hat{\tau}_2} + \frac{2}{\hat{\tau}_3}\left(\frac{1}{\eta^2+1}\right)}\end{aligned} \tag{A.12}$$

The second term in the numerator of Eq (A.12) is the frequency offset due to ϕ_{RD}. This term can force significant shifts of $\Delta\hat{t}$, as shown in Figure A.2. The parameters used in the figure are taken from data set 27.

The peak shift that $\Delta\hat{t}$ undergoes and the corresponding value of r_D can be readily calculated. This is done by computing the value of r_D for which the derivative of $\Delta\hat{t}$ with respect to r_D is equal

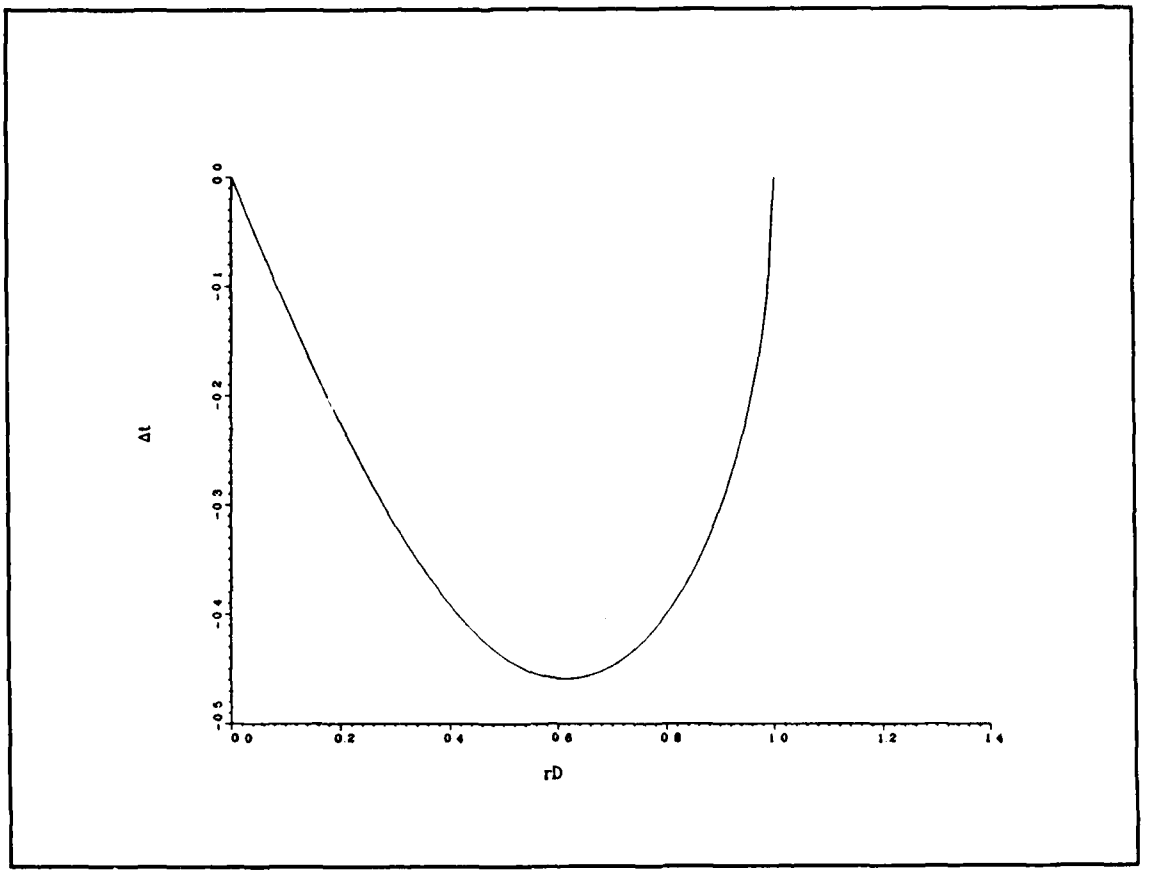

Figure A.2. The shift of $\Delta\hat{t}$ vs r_D. The parameters used in the calculation come from data set 27: $\Delta\hat{m} = 0.0$, $\hat{r}_2 = 21.04145$, and $\hat{r}_3 = 4/3$.

to zero. Using the chain rule from calculus, the derivative can be written as:

$$\frac{d\Delta\hat{t}}{dr_D} = \frac{d\Delta\hat{t}}{d\eta}\frac{d\eta}{dr_D} \tag{A.13}$$

But:

$$\frac{d\eta}{dr_D} = \frac{d}{dr_D}\left(\frac{2r_D}{\sqrt{1-r_D^2}}\right)$$

$$= \frac{2}{(1-r_D^2)^{3/2}}$$

Similarly:

$$\frac{d\Delta\hat{t}}{d\eta} = \frac{\left(\frac{2}{\hat{r}_3}\right)\left[\left(1+\frac{1}{\hat{r}_2}\right)\eta^2 + 2\eta\Delta\hat{m} - \left(1+\frac{1}{\hat{r}_2}+\frac{2}{\hat{r}_3}\right)\right]}{\left[\left(1+\frac{1}{\hat{r}_2}\right)\eta^2 + \left(1+\frac{1}{\hat{r}_2}+\frac{2}{\hat{r}_3}\right)\right]^2}$$

Incorporating the two derivatives into Eq (A.13) yields:

$$\frac{d\Delta\hat{t}}{dr_D} = \frac{\left(\frac{4}{\hat{r}_3}\right)\left[\left(1+\frac{1}{\hat{r}_2}\right)\eta^2 + 2\eta\Delta\hat{m} - \left(1+\frac{1}{\hat{r}_2}+\frac{2}{\hat{r}_3}\right)\right]}{(1-r_B^2)^{3/2}\left[\left(1+\frac{1}{\hat{r}_2}\right)\eta^2 + \left(1+\frac{1}{\hat{r}_2}+\frac{2}{\hat{r}_3}\right)\right]^2} \tag{A.14}$$

The denominator of Eq (A.14) is always greater than or equal to zero, so that the extreme value of $\Delta\hat{t}$ will only occur at a zero of the numerator. Solving the quadratic expression for η in the numerator and discarding the physically meaningless negative root yields:

$$\eta = \frac{\left[\Delta\hat{m}^2 + \left(1+\frac{1}{\hat{r}_2}\right)\left(1+\frac{1}{\hat{r}_2}+\frac{2}{\hat{r}_3}\right)\right]^{1/2} - \Delta\hat{m}}{1+\frac{1}{\hat{r}_2}} \tag{A.15}$$

Using Eq A.15, the value of η for which $\Delta\hat{t}$ undergoes the maximum shift can be determined. Eq (A.6a) can then be used to calculate the corresponding r_D value. Finally, Eq (A.12) can be used to calculate the amount of shifting that $\Delta\hat{t}$ undergoes. For the example given in Figure A.2, $\Delta\hat{t}$ shifts from the nominal value of 0.0 to a peak value of -0.459 at $r_D = 0.615$ and $\eta = 1.559$. This shift is a sizeable fraction of the atomic linewidth. It is important to recognize that these shifts in frequency are due solely to the effects of the dielectric bump, and not to gain medium pulling and pushing.

The medium gain that the lasing mode experiences is directly affected by the shift of $\Delta\hat{t}$. The small signal gain g_0L of the Spencer-Lamb model is the same as that of the TWL/TWURL models, given by Eq (4.10a). A sizeable change in $\Delta\hat{t}$ can lead to a large change in g_0L. Using the example of Figure A.2, the small signal gain changes from a maximum value of $g_0L = 0.756$ at $r_D = 1.0$ to a minimum value of $g_0L = 0.624$ at $r_D = 0.615$, a 17.5% change. In some cases, the free-running mode may be shifted to a portion of the gain curve in which the gain is below the lasing threshold.

Lasing on that mode would then cease. The dependency of $g_0 L$ on the reflectivity of the outcoupling mirror is not seen in the TWL/TWURL or Lamb models, as the phases of the reflection coefficients are not functions of the reflectivities in these models.

In summary, the phase of the reflection coefficient of the dielectric bump has two significant effects. First, ϕ_{RD} causes frequency shifts of the barecavity and free-running laser modes. These frequency shifts depend upon the magnitude of the reflection coefficient. Second, shifting $\hat{\nu}$ creates a change in the small signal gain of the laser. The frequency shifts and the gain changes due to variations in r_D have no counterparts in the TWL/TWURL or Lamb models.

The Dielectric Bump Losses. The second significant property of the dielectric bump is the losses that it induces on the laser. The loss L_D can be readily obtained from Eq (4.42a):

$$L_D = \frac{2}{\hat{\tau}_3}\left(\frac{1}{\eta^2 + 1}\right) \tag{A.16a}$$

The loss varies over a finite range, from $L_D = 0.0$ when $r_D = 1.0$ to a maximum of $L_D = 2/\hat{\tau}_3$ when $r_D = 0.0$.

L_D can be compared to the mirror loss L_L in the field equation for the Lamb model:

$$L_L = -\frac{1}{\hat{\tau}_3} \ln r_B \tag{A.16b}$$

Note the implicit assumption in Eq (A.16b) that the gain medium fills the entire cavity. The losses are plotted in Figure A.3. For very high $r_{B,D}$ values, the losses L_D and L_L are close. L_D is greater than L_L over most of the reflectivity range. However, as the mirror or dielectric bump reflectivities decrease, significant differences appear in the losses. The two loss curves cross at $r_{B,D} = 0.166$. L_L becomes infinite as r_B approaches zero, whereas L_D remains bounded. Although the losses appear to be relatively close, the percentage difference in the losses depicted in Figure A.4 can be substantial.

The most striking feature about the loss L_D is that it is bounded and finite. As a result, if the medium gain is high enough, the laser will oscillate regardless of the value of r_D. The threshold

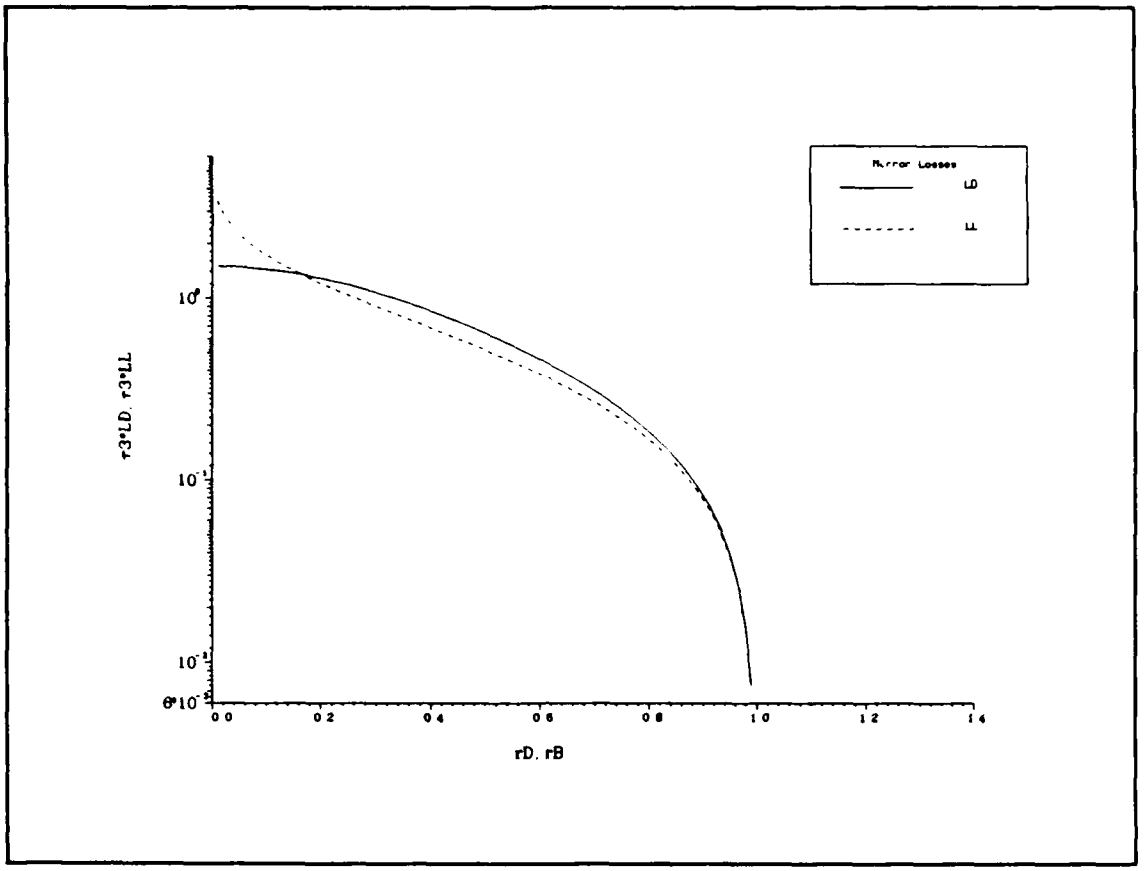

Figure A.3. Comparison of the laser losses $L_{D,L}$ vs mirror reflectivity. Note that the losses are parameterized in terms of $\hat{r}_3$.

inversion density for the Spencer-Lamb model is given in Eq (4.45):

$$\hat{w}_{eq}\Big|_{th} = (1 + \Delta\hat{t}^2)\left[\frac{1}{\hat{r}_2} + \frac{2}{\hat{r}_3}\left(\frac{1}{\eta^2 + 1}\right)\right] \tag{A.17}$$

$\Delta\hat{t}$ has a maximum value that can be calculated with the method described previously. Therefore, an upper bound exists for the right-hand side of Eq (A.17). If $\hat{w}_{eq}$ is greater than the bound, the laser will oscillate regardless of the outcoupling. This critical value of $\hat{w}_{eq}$ can be expressed as:

$$\hat{w}_{eq}\Big|_{cr} = \left[1 + \Delta\hat{t}^2\Big|_{max}\right]\left[\frac{1}{\hat{r}_2} + \frac{2}{\hat{r}_3}\right] \tag{A.18}$$

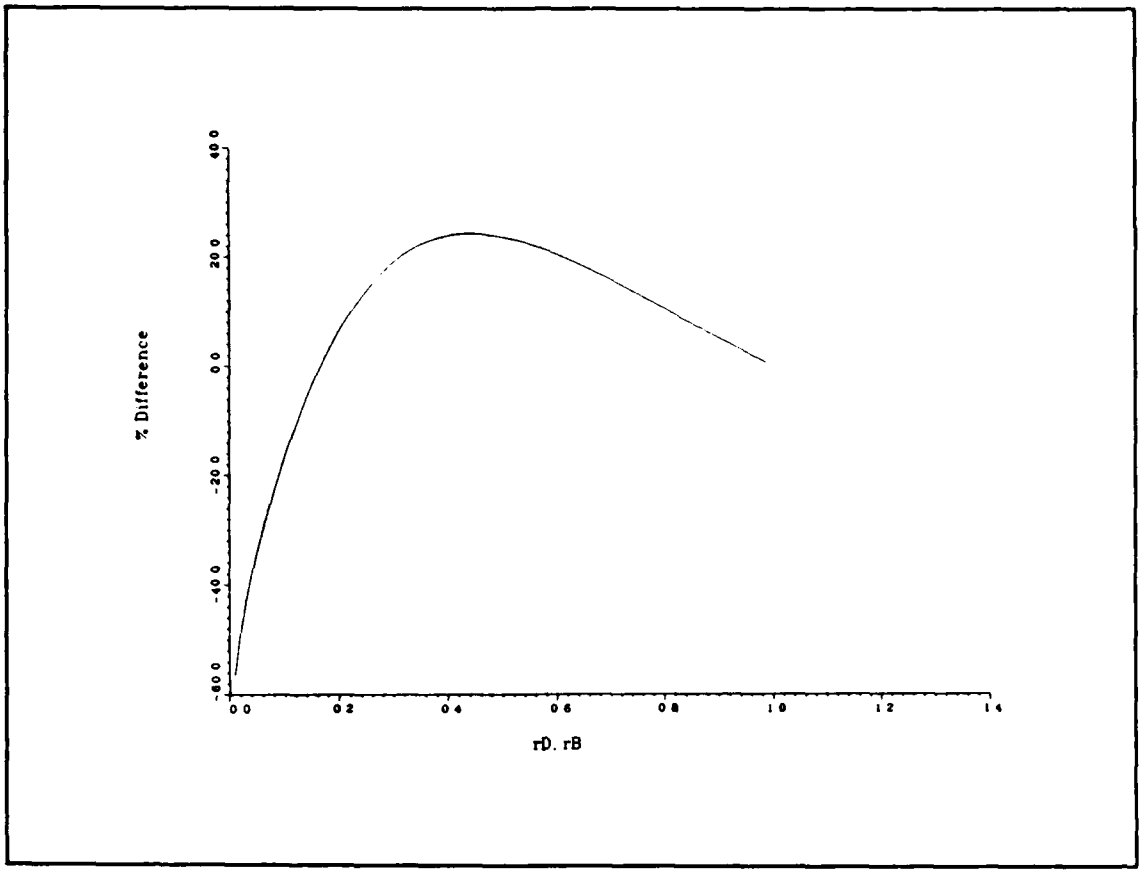

Figure A.4. Percentage difference in the losses L_D and L_L vs mirror reflectivity. The percentage difference is defined as $(L_D - L_L)/L_L$.

Consider again data set 27. Using the maximum value of $\Delta\hat{t}$ calculated in the previous section, the critical population inversion density is $\hat{w}_{eq}\Big|_{cr} = 1.874$. This value is only 75% greater than the value used in data set 29.

To summarize, the losses induced by the dielectric bump have a finite upper bound. This differs from the TWL/TWURL and Lamb models, in which the mirror losses become infinite as $r_B \rightarrow 0$. A direct consequence of the bounded losses is that a critical value of $\hat{w}_{eq}$ exists for which the laser will oscillate regardless of the value of r_D.

Summary

The different mirror models used in this research were examined in this appendix. A general philosophy of mirror modeling techniques was given initially. The mirrors used in the TWL/TWURL and Lamb models were discussed next. The relationships between the reflection and transmission coefficients derived by Seigman were presented. The dielectric bump mirror used by Spencer and Lamb was analyzed in detail in the third section. The frequency shifts and the losses induced by the dielectric bump were analyzed.

It must be noted that at very high reflectivities, the frequency shift and loss effects of the dielectric bump are minimized. The loss and frequency shift effects become significant in regions where the standing wave approximation critical to the Lamb and Spencer-Lamb gain models has already broken down. Technically, the dielectric bump model could be used as an approximation in the region where the standing wave model is valid. Its limitations and peculiarities must be understood in order to properly interpret the results of any calculations. Of course, this model should be used if the physical mirror it represents behaves like a dielectric bump.

APPENDIX B

Numerical Techniques

Several general types of problems were studied during the course of this research. The problems can be grouped into the following four classes: steady-state intensity calculations for free-running lasers, steady-state frequency calculations for free-running lasers, steady-state intensity and gain (G_1, G_2) calculations for injected lasers, and time-dependent studies of free-running and injected Fabry-Perot lasers. With the exception of the standing wave laser models (Lamb, Spencer-Lamb, and Chow models), no analytic solutions of the equations can be obtained. As a result, the problems involving the TWL, TWURL, and small signal gain models have to be solved numerically.

The computer codes developed to study the above four classes of problems are discussed in this appendix. Each class is separately examined in detail in the first four sections. The types of calculations performed, the particular numerical methods and computer code algorithms, and the boundary/initial conditions (as applicable) are explored for each class. Specifics of the codes, such as flowcharts, I/O files, libraries, required hardware environments, etc., are not discussed. As over twenty codes were written, no source code listings are given. The appendix is summarized in the final section.

Steady-State Intensity Calculations: Free-Running Lasers

The first class of problems to be examined is the calculation of the steady-state intensities $I_R(\hat{z})$ and $I_L(\hat{z})$ in the free-running laser. For the PBCUR laser, this includes the intensities $I_L(x, y, \hat{z})$ in the amplifier region and $I_{ap}(x, y, \hat{z} = 0)$ in the output aperture. Either the TWL, TWURL, or simple saturable gain models can be used in the calculations. The lasing frequency $\hat{\nu}$ and thus $\Delta\hat{t} = \hat{\omega} - \hat{\nu}$ are assumed to be time-independent and known *a priori*. Consequently, the phase equations in the TWL and TWURL models are not required. Only the field amplitude or intensity equations and the appropriate boundary conditions are necessary for the calculations.

The required differential equations for the calculations are listed in Table VI. Notice that each equation set is a pair of coupled, nonlinear ordinary differential equations. The calculation of the internal intensities is essentially a boundary value problem; however, a separate boundary condition must be satisfied at each mirror. Many techniques exist that can be used to numerically solve the equations for the intensities. In this project, a "shooting method" using fourth-order Runge-Kutta was employed to solve the differential equations.

Although the Runge-Kutta techniques are fairly common and are discussed in most numerical methods texts, the vector scheme is presented below for completeness. The shooting algorithm employed in the codes is explained next. Finally, some specifics about step sizes, initial intensity values, and accuracies of the results are discussed.

The Fourth-Order Runge-Kutta Method. The Runge-Kutta methods are based on truncated Taylor series expansions of the differential equations. A relatively easy to implement yet quite accurate method in the family is the fourth-order technique. This technique is briefly outlined below. A more complete presentation, including derivations and error and stability analyses, can be found in (161: Chapter 8, 162: Chapter 9). The following discussion uses the notation of (161).

Let the set of n differential equations to be solved be denoted by the following vector system:

$$\frac{\partial \vec{y}}{\partial x} = \vec{f}(x, \vec{y}) = \begin{pmatrix} f_1(x, \vec{y}) \\ f_2(x, \vec{y}) \\ \vdots \\ f_n(x, \vec{y}) \end{pmatrix} \tag{B.1}$$

The initial conditions for the problem are given by the vector $\vec{y}(x_0)$:

$$\vec{y}(x_0) = \vec{y}_0 = \begin{pmatrix} (y_1)_0 \\ (y_2)_0 \\ \vdots \\ (y_n)_0 \end{pmatrix} \tag{B.2}$$

TABLE VI

Required Equation Sets

Calculation	Laser Model	Operating Condition	Equations of Motion	Boundary Conditions
Steady-state Intensity	TWL	Free-running	Eq 3.16a 3.16b	Eq 3.18 3.19
	TWURL	Free-running	5.18a 5.18b 5.20a	5.25
Steady-state Frequency	TWL	Free-running	3.16	3.18 3.19
	TWURL	Free-running	5.18	5.25
Steady-state Intensity	TWL	Injected	3.24	3.18 3.28
	TWURL	Injected	5.30 5.32	5.37
Time-dependent Intensity, Phase	TWL	Free-running	3.8	3.18 3.19
	TWL	Injected	3.8	3.18 3.28

The step in x is given by h, that is:

$$x_{k+1} = x_k + h \tag{B.3}$$

h is the same for the n functions that comprise $\vec{y}$. If $\vec{y}_k$ denotes the vector function at the k^{th} step in x, then $\vec{y}_{k+1}$ is given by:

$$\vec{y}_{k+1} = \vec{y}_k + \vec{\Delta}_k \tag{B.4a}$$

where:

$$\vec{\Delta}_k = \frac{1}{6}\left(\vec{\Delta}_k^{(1)} + 2\vec{\Delta}_k^{(2)} + 2\vec{\Delta}_k^{(3)} + \vec{\Delta}_k^{(4)}\right) \tag{B.4b}$$

and:

$$\vec{\Delta}_k^{(1)} = h\vec{f}(x_k, \vec{y}_k) \tag{B.4c}$$

$$\vec{\Delta}_k^{(2)} = h\vec{f}\left(x_k + \frac{h}{2}, \vec{y}_k + \frac{1}{2}\vec{\Delta}_k^{(1)}\right) \tag{B.4d}$$

$$\vec{\Delta}_k^{(3)} = h\vec{f}\left(x_k + \frac{h}{2}, \vec{y}_k + \frac{1}{2}\vec{\Delta}_k^{(2)}\right) \tag{B.4e}$$

$$\vec{\Delta}_k^{(4)} = h\vec{f}\left(x_k + h, \vec{y}_k + \vec{\Delta}_k^{(3)}\right) \tag{B.4f}$$

Fourth-order Runge-Kutta has several advantages and disadvantages. The first positive feature is that the method is quite accurate. The single-step error is given by a very complex formula, but is $O(h^5)$. For small h values, the single-step errors are small. Notice that the single-step error is not the same as the accumulated error, i.e., the total error after propagating m steps in x. A second advantage is that the method is self-starting. Only the initial vector $\vec{y}_0$ is required to start the calculation. Other methods, such as the Adams-Moulton and Milne-Simpson methods, require the values of $\vec{y}$ at the first several x steps in order to start. Third, for many systems of ordinary differential equations, the fourth-order Runge-Kutta method is strongly stable. Finally, the method is quite simple to implement in a computer code. The primary disadvantage of the method is that four evaluations of $\vec{f}(x, \vec{y})$ are required for each propagation step. If the differential equations are quite complex, a considerable amount of computer time may be required to propagate

the equations. Because of its positive features, fourth-order Runge-Kutta was chosen to solve the differential equations in all of the steady-state calculations in this research.

The Numerical Algorithm. The algorithm used to determine the axial fields in the Fabry-Perot and PBCUR lasers is a shooting method. The method involves guessing the intensities at mirror A, propagating the guessed intensities through the resonator, and applying the boundary conditions at mirror B. A new guess of the intensities at mirror A is made based upon a comparison of the intensities at mirror B. The procedure is then iterated a preset number of times. The algorithm is outlined in detail below.

(1). A high and a low guess of $\hat{E}_L(0)$ is made. The guesses are denoted by $\hat{E}_{HI}$ and $\hat{E}_{LO}$, respectively. For the first iteration, $\hat{E}_L(0)$ is set equal to their average, that is:

$$\hat{E}_L(0) = \frac{\hat{E}_{HI} + \hat{E}_{LO}}{2} \tag{B.5}$$

The boundary conditions at mirror A are applied to the guess of $\hat{E}_L(0)$ to yield $\hat{E}_R(0)$. In all cases, the initial values of $\hat{E}_{HI}$ and $\hat{E}_{LO}$ were hardwired into the computer codes.

(2). Fourth-order Runge-Kutta is used to propagate the fields the length of the laser.

(3). The boundary conditions are applied to the fields at mirror B.

(4). A new pair of guesses $\hat{E}_{HI}$ and $\hat{E}_{LO}$ are made based on the results of a comparison of the fields at mirror B. If:

$$\hat{E}_L(1) > r_B \hat{E}_R(1)$$

then:

$$\hat{E}_{HI} = \hat{E}_L(0) \tag{B.6a}$$

$$\hat{E}_{LO} = \hat{E}_{LO} \tag{B.6b}$$

otherwise:

$$\hat{E}_{HI} = \hat{E}_{HI} \tag{B.6c}$$

$$\hat{E}_{LO} = \hat{E}_L(0) \tag{B.6d}$$

(5). The procedure is iterated by returning to step (2).

(6). After a preset number of iterations, the procedure is terminated. The final set of calculated axial fields is the numerical solution to the problem. The number of iterations was in all cases hardwired into the computer codes.

The above procedure is used to calculate the axial fields in both the Fabry-Perot and PBCUR lasers. Since the geometric mode of the Fabry-Perot laser has a constant intensity in the transverse directions, no further calculations are required for this device. The situation is somewhat different in the PBCUR. Refer to Figure 5.2. In the central core region e, the fields are assumed to be constant in any transverse direction. However, the field $\hat{E}_L(x, y, \hat{z})$ in the amplifier regions f has a transverse structure. This structure is due to the fact that rays displaced different distances from the optic axis traverse different path lengths through the amplifier and core regions. The geometry of the PBCUR must be taken into account when the field $\hat{E}_{ap}(x, y, 0)$ is calculated.

The procedure for calculating the field in the output aperture is quite simple. First, the axial fields are calculated as described above. The field $\hat{E}_L(\hat{z} = \ell)$ on cone g is simply the same as the axial field at $\hat{z} = \ell$. These fields are then propagated backwards from the amplifier/core region boundary to the output aperture via Eq (5.20). Various axial positions $z = \ell$ will require propagations of differing lengths through the amplifier region. The output aperture field $\hat{E}_L(x, y, 0)$ is then known.

Algorithm Specifics. As mentioned in the paragraphs above, certain values were preset or hardwired into the codes. In all codes, the step size h was set equal to 0.01. Consequently, 100 steps were required to propagate the fields from mirror A to mirror B. The initial high and low field guesses at mirror A were set to $\hat{E}_{HI} = 100.0$ and $\hat{E}_{LO} = 0.0$. Finally, the number of iterations n was set equal to 40.

Some conclusions about the error sizes and accuracies of the calculated intensities can be drawn. First, the single step error for the Runge-Kutta method is $O(h^5) \approx 10^{-10}$. The small value of h thus leads to quite small single step errors. A tradeoff exists for the step size, however: the smaller the step size, the smaller the single step error, and the more steps required to propagate the fields across the

laser. Thus, small single step errors are obtained at the expense of additional computational time. $h = 0.01$ was chosen since it produced a small single step error, yet had reasonable computational times.

A second conclusion can be made about the accuracies of the calculated values of $\hat{E}_L(0)$ and $\hat{E}_R(0)$. If no roundoff or numerical errors are made by the computer, then the maximum error in the values of $\hat{E}_R(0)$ and $\hat{E}_L(0)$ is given by:

$$\text{error} = \frac{\hat{E}_{HI} - \hat{E}_{LO}}{2 \times 2^{n-1}} \tag{B.7}$$

where n is the number of iterations performed. Using the values listed above, the error in the final field values is approximately 9×10^{-11}.

All calculations in this class were performed on a VAX 11-782 computer using double precision variables. Since double precision numbers on the VAX retain fourteen significant digits, the truncation and roundoff errors were less than the single step errors or the errors in calculating $\hat{E}_{R,L}(0)$.

Steady-State Frequency Calculations: Free-Running Lasers

The second class of problems studied involves the calculation of the free-running laser frequency $\hat{\nu}$. This frequency is a critical parameter in the injection locking studies, as it is required in the boundary conditions for mirror B (Eq (3.27)). Unfortunately, the TWL and TWURL equations cannot be solved to yield $\hat{\nu}$, as in the standing wave theories. Therefore, $\hat{\nu}$ must be determined numerically.

The technique used to calculate $\hat{\nu}$ for both the Fabry-Perot and PBCUR lasers is discussed below. First, some background information on the problem is given. The algorithm is presented next. The final subsection deals with specifics of the algorithm and an estimate of its accuracy.

Background. The frequency calculations were performed using the steady-state equations of motion. The specific equations used are given in Table VI. Since $\hat{\nu}$ is a function of the gain medium pulling and pushing effects, the phase equations are required in this calculation. $\hat{\nu}$ is calculated in

identical manners for both the TWL and TWURL models. By extension, $\hat{\nu}$ could also be calculated for the general laser analyzed in Chapter II, even though no attempt was made to do so.

The barecavity longitudinal mode frequencies are given by:

$$\hat{\Omega} = \frac{nc}{2\gamma L} \tag{B.8}$$

as discussed elsewhere. However, the actual lasing frequencies are "pulled" toward the linecenter from $\hat{\Omega}$. This is due to the large change in the index of refraction that exists about $\hat{\omega}$. If $\hat{\Omega} = \hat{\omega}$, the mode experiences no pulling or pushing. Using $\hat{\Omega}$ as the lasing frequency will generally produce inaccurate results, as the frequency pulling can be rather large.

At the free-running frequency, $2kL = 2n\pi$ provided that the phase changes due to the mirror reflection coefficients total some integral multiple of 2π. Since integral multiples of 2π do not effect the calculations, they can be ignored. Hence, at $\hat{\nu}$, the net round trip phase change is effectively equal to 0. Forced operation of the laser at a frequency $\hat{\nu}_I < \hat{\nu}$ will produce a negative phase change in a round trip. Operation at some $\hat{\nu}_I > \hat{\nu}$ will result in a net positive round trip phase change. This fact is critical to the operation of the numerical algorithm.

The Numerical Algorithm. A bisection technique is used to determine the frequency $\hat{\nu}$. The method searches for some frequency $\hat{\nu}'$ that has a round trip phase error bounded by some ϵ_ϕ, where ϵ_ϕ can be made arbitrarily small. The frequency $\hat{\nu}'$ is then defined as the free-running frequency $\hat{\nu}$.

The algorithm consists of the following steps:

(1). Two initial frequency guesses, $\hat{\nu}_{HI}$ and $\hat{\nu}_{LO}$, are made that bracket $\hat{\nu}$. The guesses are made so that the net round trip phase change is negative for one of the guesses and positive for the other. The barecavity mode frequencies on either side of $\hat{\nu}$ are an example of such a frequency pair.

(2). The axial intensities are calculated at $\hat{\nu}_{LO}$ in the manner discussed in the previous section. Only the field amplitude equations are required in this step. The field amplitudes are stored during the final iteration.

(3). Two initial phases $\phi_R(0)$ and $\phi_L(0)$ are chosen at mirror A. The exact values of the phases are arbitrary, but they must satisfy the boundary condition for mirror A. The phase equations are used

to propagate the phases the length of the resonator. The field amplitudes stored in step (2) are used in the phase propagation.

(4). The phase error ϕ_E at mirror B is calculated, where:

$$\phi_E \equiv \phi_R(1) - \phi_{RB} - \phi_L(1) \tag{B.9}$$

Notice that Eq (B.9) is equivalent to Eqs (3.19b) and (5.25d). The phase error ϕ_E is the error in $2kL$ after the round trip; that is:

$$2kL = 2n\pi + \phi_E \tag{B.10}$$

(5). Steps (2)-(4) are repeated for $\hat{\nu}_{HI}$. The phase errors for $\hat{\nu}_{HI}$ and $\hat{\nu}_{LO}$ must have opposite signs. If so, the run continues at step (6). If the phase errors have the same sign, then $\hat{\nu}_{HI}$ and $\hat{\nu}_{LO}$ lie on the same side of $\hat{\nu}$. In this situation, the run is terminated.

(6). A new average frequency $\hat{\nu}_{ave}$ is defined:

$$\hat{\nu}_{ave} = \frac{\hat{\nu}_{LO} + \hat{\nu}_{HI}}{2} \tag{B.11}$$

Steps (2)-(4) are repeated for $\hat{\nu}_{ave}$. Two new values of $\hat{\nu}_{HI}$ and $\hat{\nu}_{LO}$ are defined depending upon the sign of ϕ_E calculated for $\hat{\nu}_{ave}$. If ϕ_E has the same sign as the phase error for $\hat{\nu}_{LO}$, then:

$$\hat{\nu}_{LO} = \hat{\nu}_{ave} \tag{B.12a}$$

$$\hat{\nu}_{HI} = \hat{\nu}_{HI} \tag{B.12b}$$

Otherwise,

$$\hat{\nu}_{LO} = \hat{\nu}_{LO} \tag{B.12c}$$

$$\hat{\nu}_{HI} = \hat{\nu}_{ave} \tag{B.12d}$$

(7). Step (6) is iterated until the phase error for $\hat{\nu}_{ave}$ is bounded by a predefined limit ϵ_ϕ:

$$|\phi_E| < \epsilon_\phi \tag{B.13}$$

The calculation is terminated, and the current value of $\hat{\nu}_{ave}$ is taken to be the free-running frequency $\hat{\nu}$.

(8). If ϕ_E for the initially chosen values of $\hat{\nu}_{LO}$ or $\hat{\nu}_{HI}$ satisfies Eq (B.13), the calculation is terminated. $\hat{\nu}$ is set equal to the frequency value ($\hat{\nu}_{LO}$ or $\hat{\nu}_{HI}$) used in the calculation.

The method requires a significant number of calculations. Several steps can be taken to reduce the computational load. A numerical technique other than bisection can be used to increase the rate of convergence to $\hat{\nu}$. For example, the method of false position (*regula falsi*) could be used if ϕ_E is a fairly linear function of frequency in the region about $\hat{\nu}$. Since the behavior of ϕ_E was unknown when the codes were written, the bisection method was chosen to ensure a consistent rate of convergence. The number of iterations required to calculate $\hat{\nu}$ can be decreased by tightly bracketing the frequency with the initial guesses of $\hat{\nu}_{LO}$ and $\hat{\nu}_{HI}$. This requires some prior knowledge of the location of $\hat{\nu}$ on the gain curve. Finally, the error limit ϵ_ϕ can be increased, thus lowering the number of iterations required. Raising the error limit will decrease the accuracy of the calculated value of $\hat{\nu}$, however.

Algorithm Specifics. Some of the variables controlling the algorithm were hardwired into the computer codes. The field intensity calculations in step (2) used 40 iterations, with a step size of $h = 0.01$. The phase error bound used was $\epsilon_\phi = 10^{-6}$. Finally, the initial values of $\hat{\nu}_{LO}$ and $\hat{\nu}_{HI}$ were set equal to the barecavity mode frequency $\hat{\Omega}$ and the linecenter frequency $\hat{\omega}$. Since only the modes closest to linecenter were analyzed, this bracket is tighter than one composed of the barecavity frequencies on either side of $\hat{\nu}$.

A rough estimate of the maximum frequency error can be obtained. First, $\delta\hat{\nu}$ is defined as the frequency error:

$$\delta\hat{\nu} \equiv \hat{\nu} - \hat{\nu}' \tag{B.14}$$

where $\hat{\nu}'$ is the calculated value of the frequency. Then, the maximum value of $\delta\hat{\nu}$ is given by the phase error bound divided by the round trip time:

$$|\delta\hat{\nu}| < \frac{\epsilon_\phi}{\hat{\tau}_3 \hat{L}_g} \tag{B.15}$$

With $\epsilon_\phi = 10^{-6}$, $\hat{\tau}_3 = 4/3$, and $\hat{L}_g = 1.0$, the maximum frequency error is 7.5×10^{-7}.

Steady-State Intensity Calculations: Injected Lasers

The third class of problems studied is the calculation of the steady-state intensities in the injected laser. The calculation is similar to that for the free-running laser. The main difference is that the phases of the electric fields are required in order to calculate the injected phasor. As a result, both the amplitude and phase equations are used in the calculation. The numerical algorithm employed is given below, followed by a discussion of some specifics of the computer codes that were developed.

The Numerical Algorithm. The numerical algorithm employed is the same for both the Fabry-Perot and PBCUR lasers. The equations used in the calculations are listed in Table VI. The boundary condition at mirror B is depicted in Figure 3.4. In general, $\mathbf{r}_B\mathbf{E}_R(1)$ and $\mathbf{E}_L(1)$ are not collinear phasors. The effects of the gain medium on the electric field phases must be accounted for. For this reason, the phase equations are required in the calculation. Both $\hat{\nu}_I$ and $\hat{\nu}$ are assumed to be known *a priori*. Consequently, $\Delta\hat{\omega}$ is also known.

The algorithm is composed of the following steps:

(1). A value of $\hat{E}_L(0)$ at mirror A is chosen. $\phi_L(0)$ is arbitrarily set equal to 0.0. The mirror boundary conditions are applied to yield $\hat{E}_R(0)$ and $\phi_R(0)$.

(2). Fourth-order Runge-Kutta is used to propagate the field amplitudes and phases across the resonator.

(3). The boundary conditions at mirror B are applied to determine the injected phasor $\mathbf{E}_I$ required to lock the laser.

(4). Since the theory was developed under the assumption that ϕ_I is the reference phase, the three phasors at mirror B are rotated so that $\phi_I = 0.0$. (Note that the *actual* values of the phases are unnecessary; only the phasor relationship at the mirror is of importance.)

(5). The gains G_1 and G_2 are calculated, if desired.

The above steps are used to calculate the fields in the laser for a single value of intensity $I_L(0)$ at mirror A. In order to generate a cubic curve, the injected fields for a set of $I_L(0)$ values must be

computed. It is interesting to note that generating the cubic curves involves calculating the abscissæ I_I for a range of ordinates $I_L(0)$. This is contrary to the usual manner of generating a plot; i.e., calculating the ordinate corresponding to each abscissa. Ferguson (87, 88) has demonstrated for his model that one and only one value of I_I exists for each value of $I_L(\hat{z} = 0)$ if mirror A is perfectly reflective. I_I is thus a function in the mathematical sense of $I_L(0)$. It is likely that the same is true for the TWL and TWURL models. Consequently, the complete set of I_I values can be generated for the cubic curve with the above algorithm.

Algorithm Specifics. As with the other numerical methods, the Runge-Kutta step size h was hardwired equal to 0.01. Since only a single propagation is required to calculate I_I for a given $I_L(0)$ value, the routine is quite fast.

A precaution is required in the calculation of ϕ_I due to a peculiarity of the VAX FORTRAN compiler (version V4.0) intrinsic function DATAN2. The computer codes calculate the real and imaginary parts of $\hat{\mathbf{E}}_I$ from the boundary conditions at mirror B. The DATAN2 function is then used to calculate ϕ_I. Erroneous values of the phase can be returned if one of the arguments of the DATAN2 function is zero. An error is generated if both arguments are zero. Additional logic was written into the codes to handle situations in which of one or both of the arguments was equal to zero. The chance, however, of either argument being exactly equal to zero is extremely small. Numerical errors and noise will usually preclude either value from being identically zero, even if the laser is operated at the free-running point.

Time-Dependent Intensity Calculations

The final class of problems examined involves time-dependent calculations of the laser intensities, phases, and frequencies. The calculations can be performed for both free-running and injected lasers. The calculations can be used to demonstrate the buildup of laser intensity from noise, pulling of the laser frequency to the injected frequency, and beating of the injected signal with the free-running laser field.

Originally, all numerical analyses in this research project were to be performed with the time-dependent codes. However, problems with numerical stability and very high computer costs forced the analyses to be done with the steady-state codes. Only the stability of the cubic curves and the dynamics of locking were studied with the time-dependent codes. The Fabry-Perot laser alone was modeled numerically.

The numerical routines are discussed at length in this section. The reasons for the detail are twofold. First, considerable effort was required in order to make the codes function properly. Approximately six months were spent developing the codes. Second, obtaining numerically stable and converged results for partial differential equations is often quite difficult. As noted in (163):

> The methodology for numerical solution of partial differential equations tends to be much more subtle than solution of ordinary differential equations, and one finds that strong results concerning error bounds, convergence, and stability are dependent on the characteristics of the particular partial differential equation being studied. Especially lacking are general methods and convergence bounds in the nonlinear case. This weakness, diversity, and specificity of results parallels and, in part, stems from a similar condition in the analytic theory of partial differential equations ...

Several subtle "tricks" derived from general knowledge of the solution characteristics were necessary to make the codes numerically stable. Additional detail in this section is warranted to explain these tricks. Future attempts to solve similar partial differential equations may benefit from the lessons learned in the present research.

Background. The equations used in the time-dependent calculations are listed in Table VI. The equations of motion are a set of nonlinear, coupled partial differential equations (PDEs). The equations are similar in form to hyperbolic PDEs. The difference lies in the fact that the time derivatives $\dot{\varphi}_R$ and $\dot{\varphi}_L$ exist on the right-hand sides of Eq (3.8). These derivatives cannot be factored to the left-hand sides of the equations. The homogeneous form of Eq (3.8) is, however, a set of hyperbolic PDEs.

A wide variety of explicit and implicit numerical routines were examined for use with the PDEs. The various techniques were tested on the PDEs governing the propagation of a pulse through a

laser amplifier. Frantz and Nodvik (114) give these equations as:

$$\frac{\partial n}{\partial t} + c\frac{\partial n}{\partial z} = \sigma c n \Delta \tag{B.16a}$$

$$\frac{\partial \Delta}{\partial t} = -2\sigma c n \Delta \tag{B.16b}$$

where $n(z,t)$ is the photon density inside the amplifier, $\Delta(z,t)$ is the population inversion density, c is the speed of light, and σ is the resonance absorption cross section. The amplifier is assumed to have an optic axis z, where $0 \leq z \leq L$. For a given initial inversion density $\Delta_0(z,0)$ and input beam $n(0,t)$, the general solution of Eq (B.16) is given by:

$$n(z,t) = \frac{n_0(t - z/c)}{1 - \left\{1 - \exp\left[-\sigma \int_0^z \Delta_0(z')\,dz'\right]\right\} \exp\left[-2\sigma c \int_{-\infty}^{t-z/c} n_0(t')\,dt'\right]} \tag{B.17a}$$

$$\Delta(z,t) = \frac{\Delta_0(z) \exp\left[-\sigma \int_0^z \Delta_0(z')\,dz'\right]}{\exp\left[2\sigma c \int_{-\infty}^{t-z/c} n_0(t')\,dt'\right] + \exp\left[-\sigma \int_0^z \Delta_0(z')\,dz'\right] - 1} \tag{B.17b}$$

For the special cases of square, Lorentzian, or Gaussian input pulses and uniform initial inversion densities, the equations for $n(z,t)$ and $\Delta(z,t)$ reduce to simple expressions. These special cases were used in the tests of the various numerical methods.

The explicit techniques generally performed much better than the implicit methods. The numerical solutions from the implicit methods tended to be very noisy, especially at the edges of the pulses. Deviations of 10% or greater from the analytic solutions were often noted. The noise problem had a very interesting origin. In all cases, the initial photon density inside the amplifier was set equal to zero. However, after the first time step, $n(z,t)$ would be nonzero at every spatial point in the amplifier. The implicit methods were thus generating and propagating noise beyond the leading edge of the pulse. Examining the matrix equations of the implicit methods showed this to be a general characteristic. The noise could grow to the point where it would partially deplete the inversion in

front of the pulses. This would create large errors in the calculated solutions. The explicit methods were very accurate; the numerical solutions often were indistinguishable from the analytic solutions. The primary disadvantage of the explicit techniques was that they required considerably more time steps per run than the implicit methods. A pair of explicit methods was chosen for the Fabry-Perot laser calculations because of the numerical accuracy.

The Numerical Techniques. Two explicit methods are used in the numerical computations. A modified Heun technique described by Wendroff (164) is used to calculate the fields inside the laser. The method cannot be used at the laser mirrors, however. A less accurate technique developed by Courant, Isaacson, and Rees (165) is employed at the mirrors. This method will be referred to as the C-I-R technique.

The modified Heun method is an outgrowth of the Heun technique used with ordinary differential equations. The method is composed of four steps. The space-time plane is divided into a rectangular grid with mesh points $(\hat{z}_i, \hat{t}_j)$, as depicted in Figure B.1. The space and time steps are given by $\hat{h}$ and $\hat{k}$, respectively:

$$\hat{z}_{i+1} = \hat{z}_i + \hat{h} \tag{B.18a}$$

$$\hat{t}_{j+1} = \hat{t}_j + \hat{k} \tag{B.18b}$$

The laser equations of motion can be written in the following generic form:

$$\frac{\partial B}{\partial \hat{z}} \pm \psi \frac{\partial B}{\partial \hat{t}} = g(B) \tag{B.19}$$

where B is either a field amplitude or phase and $g(B)$ is a general representation of the driving functions. If B_i^j denotes B at the mesh point $(\hat{z}_i, \hat{t}_j)$, then the modified Heun method can be written as:

$$B_{i+1/2}^j = \frac{B_i^j + B_{i+1}^j}{2} \tag{B.20a}$$

$$B_i^{j+1/2} = B_i^j \mp \frac{\hat{k}\psi}{2\hat{h}} \left(B_{i+1/2}^j - B_{i-1/2}^j \right) + \frac{\hat{k}}{2} g(B_i^j) \tag{B.20b}$$

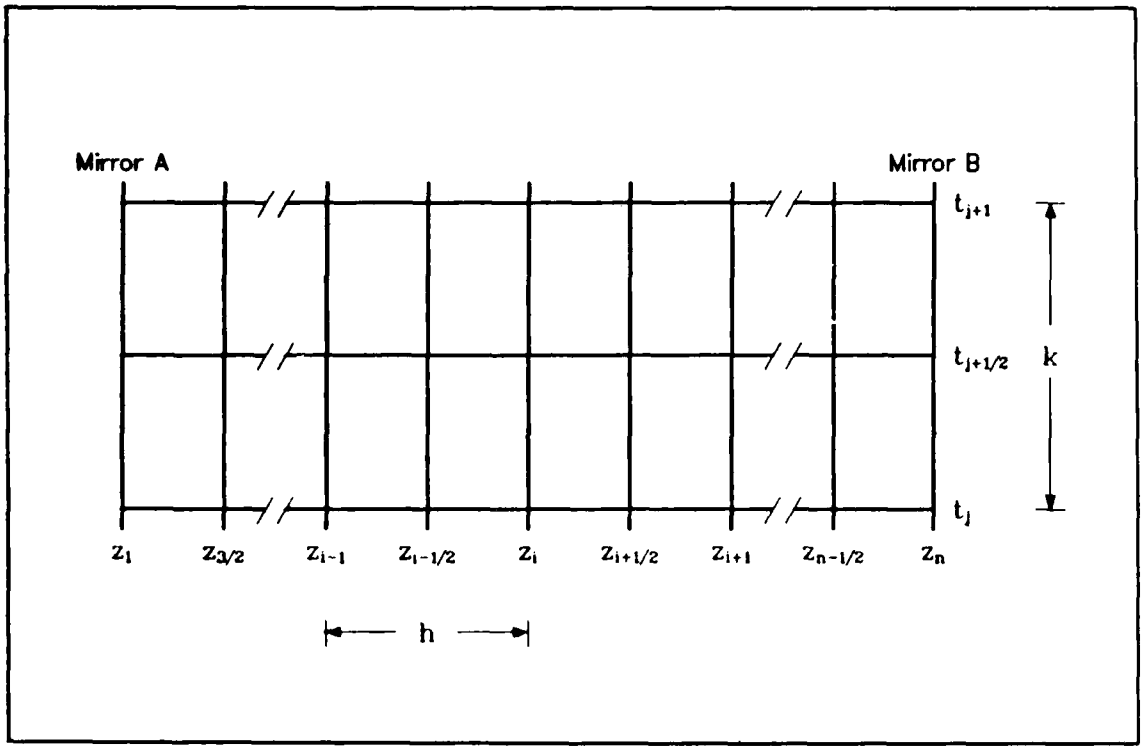

Figure B.1. The rectangular grid used with the modified Heun method.

$$B_{i+1/2}^{j+1/2} = B_{i+1/2}^{j} \mp \frac{\hat{k}\psi}{2\hat{h}}\left(B_{i+1}^{j} - B_{i}^{j}\right) + \frac{\hat{k}}{2} g(B_{i+1/2}^{j}) \tag{B.20c}$$

$$B_{i}^{j+1} = B_{i}^{j} \mp \frac{\hat{k}\psi}{\hat{h}}\left(B_{i+1/2}^{j+1/2} - B_{i-1/2}^{j+1/2}\right) + \hat{k} g(B_{i}^{j+1/2}) \tag{B.20d}$$

Following the equations listed above, the fields and phases at time $\hat{t}_{i+1}$ can be calculated from the values at time t_i. The method is self-starting: only the initial values at t_0 are required for the method to commence. Unfortunately, the fields at the mirrors cannot be calculated with this method. Some other technique is required to produce these functional values.

The derivatives $\dot{\varphi}_R$ and $\dot{\varphi}_L$ are required at each step of the calculation, as these terms are part of the right-hand sides of the equations. The backwards difference operator is used to obtain the

derivatives:

$$\frac{\partial \varphi^j_{R,L}}{\partial \hat{t}} \approx \frac{\phi^j_{R,L} - \phi^{j-1}_{R,L}}{\hat{k}} \quad \frac{\phi^j_{R,L} - \phi^{j-1/2}_{R,L}}{\hat{k}/2} \tag{B.21}$$

The backwards difference operators are first-order techniques, with truncation errors of $O(\hat{k})$. Central difference methods, with errors of $O(\hat{k}^2)$ are not practical for use with the modified Heun method.

The modified Heun method has a truncation error of $O(\hat{k}^3)$ for a set of PDEs of the general form:

$$\frac{\partial B}{\partial \hat{t}} + \frac{\partial}{\partial \hat{z}}\left(a(\hat{z},\hat{t})B\right) = g(\hat{z},\hat{t},B) \tag{B.22}$$

where $a(\hat{z},\hat{t})$ is a symmetric matrix. The TWL equations are similar in form, except that g is a function of $\dot{\varphi}_{R,L}$. The actual accuracy will be somewhat less than of $O(\hat{k}^3)$, since the backwards difference operators are used to approximate the phase time derivatives. For the hyperbolic system given in Eq (B.22), the modified Heun method converges in the mean square sense provided that:

$$\frac{\hat{k}}{\hat{h}}\left|a(\hat{z},\hat{t})\right|_{sp} \leq 1 \tag{B.23a}$$

where:

$$\left|a(\hat{z},\hat{t})\right|_{sp} = \max_{au=\tau u} |\tau| \tag{B.23b}$$

is the spectral radius of $a(\hat{z},\hat{t})$. Eq (B.23) implies that the step sizes must satisfy the relationship:

$$\frac{\hat{k}\psi}{\hat{h}} \leq 1 \tag{B.24}$$

in order for the modified Heun method to be convergent.

The method is computationally intense. To advance the fields in time from mesh point $(\hat{z}_i,\hat{t}_j)$ to $(\hat{z}_i,\hat{t}_{j+1})$, twelve evaluations of g must be performed (three separate evaluations of each of the four g functions). To lower the computational load, the grid spacing can be increased. This reduces

the accuracy of the numerical solution. A balance must be struck between the solution accuracy and the computational loading.

As mentioned above, the modified Heun method cannot be used to calculate the electric fields at the mirrors. The C-I-R method is used at these boundaries. The form of the equations is slightly different at each mirror. At mirror A, the equations are given by:

$$B_1^{j+1} = B_1^j + \frac{\hat{k}\psi}{\hat{h}}\left(B_2^j - B_1^j\right) + \hat{k}g(B_1^j), \qquad B_i^j \in (\hat{E}_L, \phi_L) \tag{B.25a}$$

The values of $\hat{E}_R$ and ϕ_R are calculated from the boundary conditions. At mirror B, the expressions are:

$$B_n^{j+1} = B_n^j - \frac{\hat{k}\psi}{\hat{h}}\left(B_n^j - B_{n-1}^j\right) + \hat{k}g(B_n^j), \qquad B_i^j \in (\hat{E}_R, \phi_R) \tag{B.25b}$$

$\hat{E}_L$ and ϕ_L are calculated from the boundary conditions at mirror B. As in the modified Heun method, backwards difference quotients are used to approximate the time derivatives $\dot{\varphi}_{R,L}$ on the right-hand sides of the TWL equations.

The C-I-R method has a truncation error of $O(\hat{k})$. This error is due to the first-order difference methods that replace the partial derivatives in the TWL equations. The method is convergent if the step sizes satisfy the condition given in Eq (B.24). The C-I-R technique is self-starting, so only the field values at time t_0 are required to begin a calculation.

Algorithm Specifics. The modified Heun and C-I-R methods tend to be numerically stable over very limited regions of the laser parameter space. The stability is quite sensitive to the initial and boundary conditions. The phase equations are particularly susceptible to numerical noise as a result of the $\dot{\varphi}_{R,L}$ terms on the right-hand sides of the equations. A set of "tricks" or fixes to the initial and boundary conditions and the phase equations were used to make the numerical methods stable over much wider regions of the parameter space. These fixes are described below.

The first trick involves the initial fields amplitudes $\hat{E}_R(\hat{z}_i, \hat{t}_0)$ and $\hat{E}_L(\hat{z}_i, \hat{t}_0)$. The first version of the code set the initial field amplitudes equal to some small constant value. Thus, the fields

were assumed to be spatially uniform. For low values of reflectivity at mirror B ($r_B \leq 0.70$), the calculations would "blow up". This instability can be understood by examining Figure B.2. During the initial several time steps, the field amplitudes rise uniformly throughout the left half of the laser. However, a discontinuity in $\hat{E}_L$ evolves in the right half of the device. The discontinuity is due to the boundary conditions at mirror B. At the first time step, $\hat{E}_L(\hat{z}_n, \hat{t}_1)$ is given by (without an injected field):

$$\hat{E}_L(\hat{z}_n, \hat{t}_1) = r_B \hat{E}_R(\hat{z}_n, \hat{t}_1) \tag{B.26}$$

The adjacent field amplitude, $\hat{E}_L(\hat{z}_{n-1}, \hat{t}_1)$, is approximately equal to $\hat{E}_R(\hat{z}_n, \hat{t}_1)$. The discontinuity propagates throughout the laser, as shown in the sequence of plots. Eventually, if r_B is high enough, the field amplitudes reach steady-state. However, if r_B is relatively low, $\hat{E}_L(\hat{z}_n, \hat{t}_j)$ can be driven negative. On the next time step, the algorithm blows up. The discontinuity manifests itself in the sawtooth behavior of the output laser intensity, as seen in Figure B.3.

The initial field amplitudes can be modified to resolve the stability problem. One such modification uses linearly varying initial field amplitudes. A small value of $\hat{E}_R(\hat{z}_n, \hat{t}_0)$ is chosen by the user, and the other field values at the mirror are set equal to:

$$\hat{E}_L(\hat{z}_n, \hat{t}_0) = r_B \hat{E}_R(\hat{z}_n, \hat{t}_0) \tag{B.27a}$$

$$\hat{E}_{R,L}(\hat{z}_1, \hat{t}_0) = \frac{\hat{E}_R(\hat{z}_n, \hat{t}_0) + \hat{E}_L(\hat{z}_n, \hat{t}_0)}{2} \tag{B.27b}$$

The initial amplitudes vary linearly between these values elsewhere in the laser. This initial condition provides numerically stable results except when r_B is within a few percent of its threshold value. The sawtooth nature of I_{out} is markedly reduced. For values of r_B approaching threshold, the numerical methods are again unstable.

A second form of the field amplitude initial conditions uses scaled steady-state fields. The steady-state fields for the laser are calculated as described in Section 1. The laser frequency is given by:

$$\Delta\hat{t} = \frac{\Delta\hat{m}}{1 + \frac{1}{\hat{\tau}_2}} \tag{B.28}$$

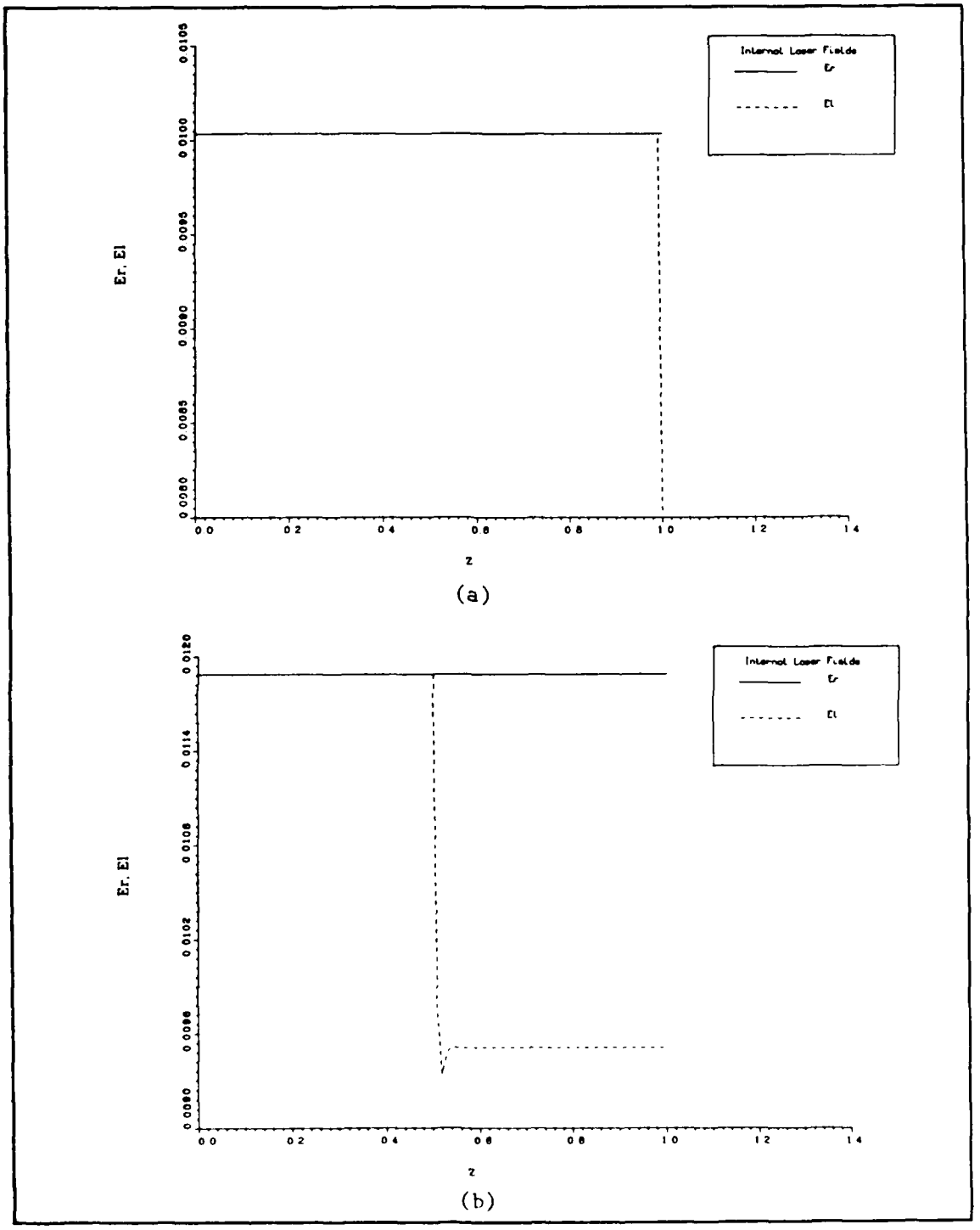

Figure B.2. The field amplitudes at various times in the laser. $r_B = 0.80$, and 101 mesh points are used in the $\hat{z}$ direction. All of the other input parameters are taken from data set 27. (a) $\hat{t} = \hat{t}_1$, (b) $\hat{t} = \hat{t}_{50}$, (c) $\hat{t} = \hat{t}_{150}$, (d) $\hat{t} = \hat{t}_{250}$.

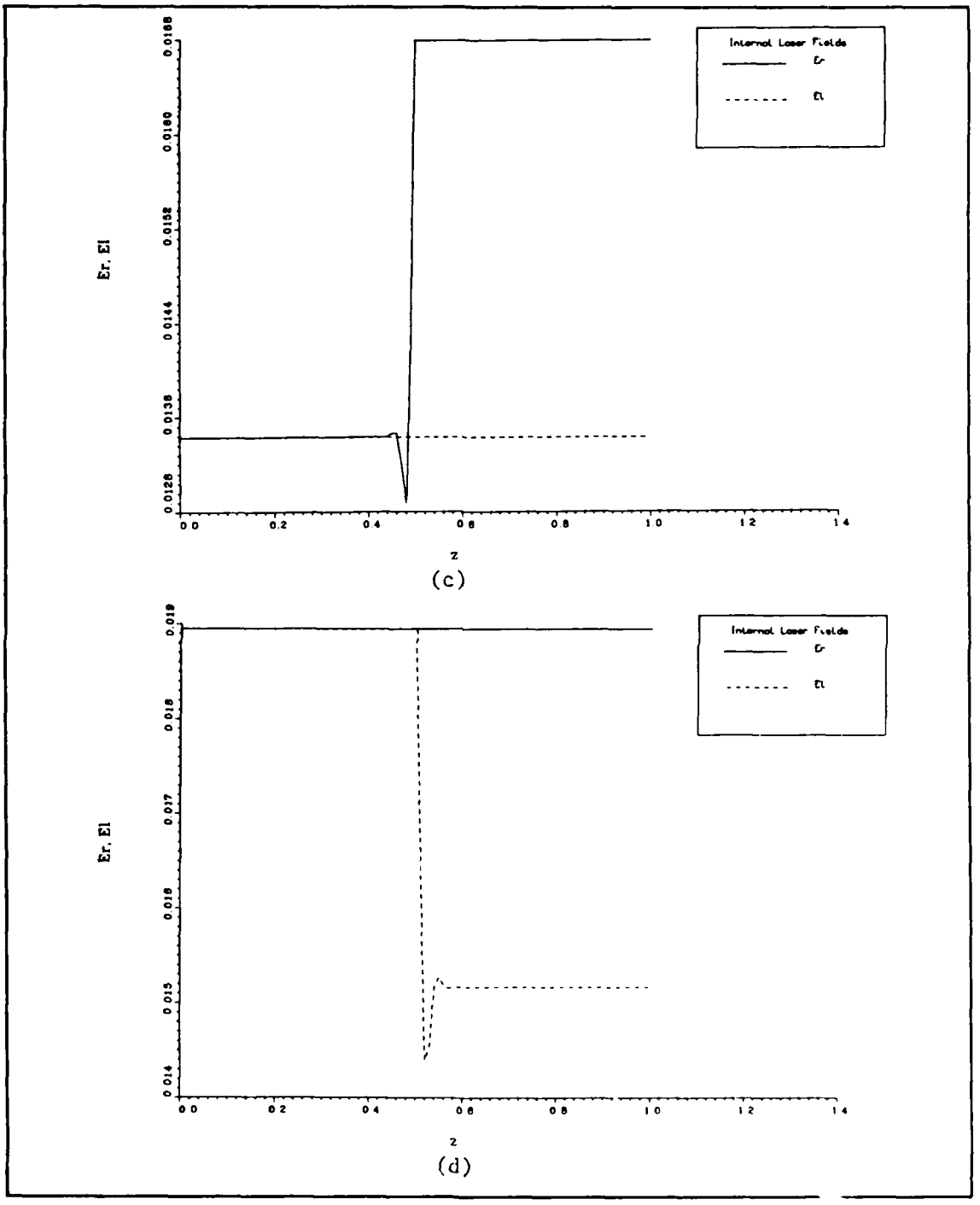

Figure B.2, continued.

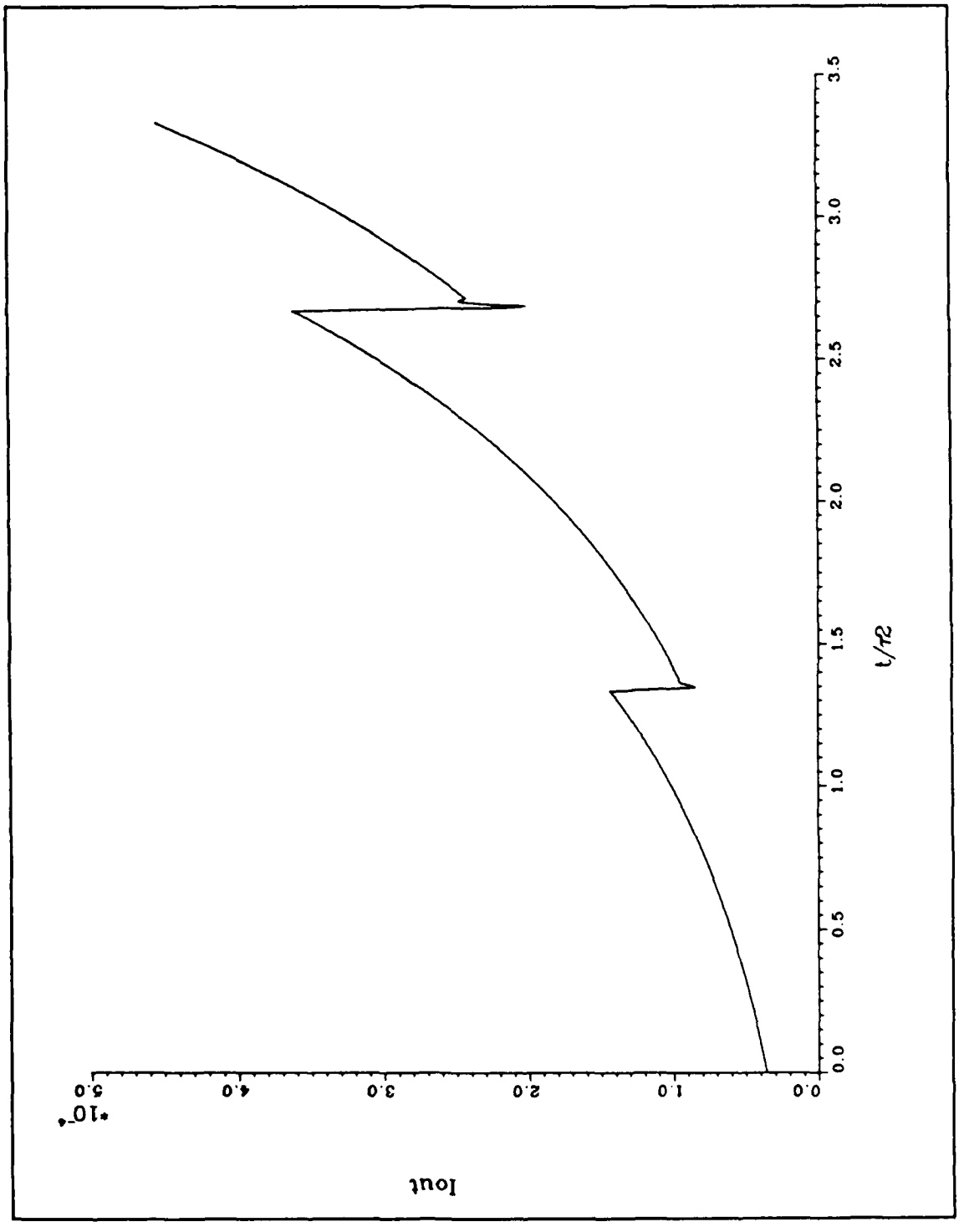

Figure B.3. I_{out} vs $\hat{t}$. All parameters are the same as in Figure B.2.

(The correct expression for the frequency is given in Eq (7.5). However, this expression had not been obtained when the time-dependent codes were written.) The steady-state field amplitudes are scaled by some factor, typically in the range $[0.01, 0.05]$. The scaled amplitudes are then used as the initial conditions. This technique works extremely well when the laser is free-running. The numerical routines are stable for values of r_B approaching threshold. The sawtooth ripples on I_{out} are virtually eliminated. The initial condition also works quite well when an injected signal is present. This initial condition was implemented in the computer codes.

The initial conditions for the field phases and phase time derivatives must be carefully chosen in order to obtain numerically stable results. The phase calculations are very sensitive to noise and prone to numerical instabilities. Small phase errors can lead to wild behavior in the calculations. For example, typical values of ψ and $\hat{h}$ are:

$$\psi \approx 1.5$$

$$\hat{h} \approx 0.01$$

For convergence, $\hat{k} \leq 6.67 \times 10^{-3}$. An error in phase on the order of the time step can create a frequency error approximately equal to the linewidth of the laser. Such an error will suppress the gain if the lasing frequency is shifted a significant distance from linecenter. The first set of initial conditions tested used constant phases across the laser. This set would often lead to the form of instability described above, especially at mirror B. Clearly, the initial conditions must be carefully chosen in order to avoid numerical problems.

The initial conditions finally implemented are based upon the frequency of the injected signal. In a round trip, the phase of the laser must change by $2m\pi$ radians, where m is some integer. When operating at a nonresonant injected frequency $\hat{\nu}_I$, the round trip condition is not satisfied, as:

$$2kL = 2n\pi + \hat{\vartheta} \tag{B.29}$$

where $\hat{\vartheta}$ is defined in Eq (3.27). The round trip condition is only preserved when the injected field is vectorally added to the laser field, as depicted in Figure 3.5. However, to avoid large frequency

shifts due to phase errors, the $\hat{\vartheta}$ term must be accounted for in the initial conditions. The excess phase $\Delta\phi$ in a round trip due to the mirror reflection coefficient phases and $\hat{\vartheta}$ can be approximated as:

$$\Delta\phi = 2\pi - \phi_{RA} - \phi_{RB} - \hat{\vartheta} \tag{B.30}$$

This phase error must be distributed uniformly across the resonator in the initial conditions in order to avoid frequency shift problems. By defining a fractional phase change as:

$$\delta\phi \equiv \frac{\Delta\phi}{2(n-1)}$$

$$= \frac{2\pi - \phi_{RA} - \phi_{RB} - \hat{\vartheta}}{2(n-1)} \tag{B.31}$$

where n is the number of grid points in the z direction, the initial conditions for the phases can be written as:

$$\phi_R(\hat{z}_1, \hat{t}_0) = -\phi_{RA} \tag{B.32a}$$

$$\phi_R(\hat{z}_{i+1}, \hat{t}_0) = \phi_R(\hat{z}_i, \hat{t}_0) - \delta\phi \tag{B.32b}$$

$$\phi_L(\hat{z}_1, \hat{t}_0) = 0 \tag{B.32c}$$

$$\phi_L(\hat{z}_{i+1}, \hat{t}_0) = \phi_L(\hat{z}_i, \hat{t}_0) + \delta\phi \tag{B.32d}$$

Again, the *actual* values of the phases are unimportant; only the phase differences between adjacent mesh points are of concern. Consequently, $\phi_L(\hat{z}_1, \hat{t}_0)$ is arbitrarily set equal to zero. Since the phase time derivatives $\dot{\varphi}_R$ and $\dot{\varphi}_L$ are unknown, they are initially set equal to zero. This condition undoubtedly causes some noise and transient behavior in the numerical solutions. If *a priori* knowledge of the phase time derivatives existed, the stability of the runs could be improved through a better initial condition. Overall, the pair of initial conditions worked well in the computer codes.

The third trick with the numerical routines involves the phase calculations from one time step to the next. Under certain circumstances, the values of $|\dot{\varphi}_{R,L}|$ can be extremely large, thus forcing the laser gain to be approximately zero. Suppressing the gain in one time step generally causes the numerics to become unstable and blow up. The problem stems from the fact that the phases are

constrained to lie in the range $(-\pi, \pi]$. Depending upon the progression of the calculations, the following situations can arise:

$$\phi_R(\hat{z}_i, \hat{t}_j) = \pi - \epsilon_1$$

$$\phi_R(\hat{z}_i, \hat{t}_{j+1}) = -\pi + \epsilon_2$$

or

$$\phi_R(\hat{z}_i, \hat{t}_j) = -\pi + \epsilon_3$$

$$\phi_R(\hat{z}_i, \hat{t}_{j+1}) = \pi - \epsilon_4$$

where the ϵ_i are some small constants. The time derivatives are given by.

$$\frac{\partial}{\partial \hat{t}} \phi_R(\hat{z}_i, \hat{t}_{j+1}) \approx \frac{2\pi}{\hat{k}}$$

For a value of $\hat{k} = 6.6 \times 10^{-3}$, $\dot{\varphi}_R \approx 950$. Similar situations can occur for $\phi_L(\hat{z}_i, \hat{t}_j)$. To prevent this from happening, additional logic is incorporated into the routines to check for single-step phase changes on the order of 2π. If such a change is detected, the actual values of the phases are used in the derivatives, not the values in the range $(-\pi, \pi]$. In this manner, large values of $\dot{\varphi}_{R,L}$ are avoided. A related problem with the spatial derivatives exists, but is much less likely to occur.

Even with the previous modifications, the numerical routines work poorly when the laser is operated off linecenter or when $\hat{\nu}_i \neq \hat{\nu}$. The problem is partially due to the phase time derivatives on the right-hand sides of the phase equations. The two equations can be rewritten in more stable forms. Consider the ϕ_R equation. Two of the $\dot{\varphi}_R$ terms on the right-hand side can be factored to the left-hand side of the equation:

$$\left[1 + \frac{\hat{w}_{eq}}{[1 + (\Delta\hat{\omega} - \dot{\varphi}_R)^2]\sqrt{A^2 - B^2 - C^2}} + \frac{\hat{w}_{eq}}{\hat{r}_1 \hat{E}_R^2 [4 + (\dot{\varphi}_L - \dot{\varphi}_R)^2]} \left(1 - \frac{A}{\sqrt{A^2 - B^2 - C^2}}\right)\right] \frac{\partial \phi_R}{\partial \hat{t}}$$

$$+\psi \frac{\partial \phi_R}{\partial \hat{z}} = \hat{\Omega} - \hat{\nu}_I + \frac{\hat{w}_{eq}}{\hat{E}_R} \left[\frac{\hat{E}_R \Delta\hat{\omega}}{[1 + (\Delta\hat{\omega} - \dot{\varphi}_R)^2]\sqrt{A^2 - B^2 - C^2}}\right.$$

$$\left. + \frac{2\Delta\hat{\omega} - \dot{\varphi}_L}{\hat{r}_1 \hat{E}_R [4 + (\dot{\varphi}_L - \dot{\varphi}_R)^2]} \left(1 - \frac{A}{\sqrt{A^2 - B^2 - C^2}}\right)\right]$$

Rewriting slightly yields:

$$\frac{\partial \phi_R}{\partial \hat{t}} + \psi_R \frac{\partial \phi_R}{\partial \hat{z}} = \left[1 + \frac{\hat{w}_{eq}}{[1 + (\Delta\hat{\omega} - \dot{\varphi}_R)^2]\sqrt{A^2 - B^2 - C^2}} \right.$$

$$\left. + \frac{\hat{w}_{eq}}{\hat{\tau}_1 \hat{E}_R^2 [4 + (\dot{\varphi}_L - \dot{\varphi}_R)^2]} \left(1 - \frac{A}{\sqrt{A^2 - B^2 - C^2}} \right) \right]^{-1}$$

$$\times \left\{ \hat{\Omega} - \hat{\nu}_I + \frac{\hat{w}_{eq}}{\hat{E}_R} \left[\frac{\hat{E}_R \Delta\hat{\omega}}{[1 + (\Delta\hat{\omega} - \dot{\varphi}_R)^2]\sqrt{A^2 - B^2 - C^2}} \right. \right.$$

$$\left. \left. + \frac{2\Delta\hat{\omega} - \dot{\varphi}_L}{\hat{\tau}_1 \hat{E}_R [4 + (\dot{\varphi}_L - \dot{\varphi}_R)^2]} \left(1 - \frac{A}{\sqrt{A^2 - B^2 - C^2}} \right) \right] \right\} \qquad \text{(B.33a)}$$

where:

$$\psi_R \equiv \psi \left[1 + \frac{\hat{w}_{eq}}{[1 + (\Delta\hat{\omega} - \dot{\varphi}_R)^2]\sqrt{A^2 - B^2 - C^2}} \right.$$

$$\left. + \frac{\hat{w}_{eq}}{\hat{\tau}_1 \hat{E}_R^2 [4 + (\dot{\varphi}_L - \dot{\varphi}_R)^2]} \left(1 - \frac{A}{\sqrt{A^2 - B^2 - C^2}} \right) \right]^{-1} \qquad \text{(B.33b)}$$

The analogous expressions for ϕ_L are:

$$\frac{\partial \phi_L}{\partial \hat{t}} - \psi_L \frac{\partial \phi_L}{\partial \hat{z}} = \left[1 + \frac{\hat{w}_{eq}}{[1 + (\Delta\hat{\omega} - \dot{\varphi}_L)^2]\sqrt{A^2 - B^2 - C^2}} \right.$$

$$\left. + \frac{\hat{w}_{eq}}{\hat{\tau}_1 \hat{E}_L^2 [4 + (\dot{\varphi}_L - \dot{\varphi}_R)^2]} \left(1 - \frac{A}{\sqrt{A^2 - B^2 - C^2}} \right) \right]^{-1}$$

$$\times \left\{ \hat{\Omega} - \hat{\nu}_I + \frac{\hat{w}_{eq}}{\hat{E}_L} \left[\frac{\hat{E}_L \Delta\hat{\omega}}{[1 + (\Delta\hat{\omega} - \dot{\varphi}_L)^2]\sqrt{A^2 - B^2 - C^2}} \right. \right.$$

$$\left. \left. + \frac{2\Delta\hat{\omega} - \dot{\varphi}_R}{\hat{\tau}_1 \hat{E}_L [4 + (\dot{\varphi}_L - \dot{\varphi}_R)^2]} \left(1 - \frac{A}{\sqrt{A^2 - B^2 - C^2}} \right) \right] \right\} \qquad \text{(B.33c)}$$

and:

$$\psi_L \equiv \psi \left[1 + \frac{\hat{w}_{eq}}{[1 + (\Delta\hat{\omega} - \dot{\varphi}_L)^2]\sqrt{A^2 - B^2 - C^2}} \right.$$

$$\left. + \frac{\hat{w}_{eq}}{\hat{\tau}_1 \hat{E}_L^2 [4 + (\dot{\varphi}_L - \dot{\varphi}_R)^2]} \left(1 - \frac{A}{\sqrt{A^2 - B^2 - C^2}} \right) \right]^{-1} \qquad \text{(B.33d)}$$

These forms of the phase equations dramatically improve the stability of the numerical methods, thus allowing exploration of a wider range of the parameter space.

A comment must be made about the convergence criterion given in Eq (B.23). Since $\psi_{R,L} < \psi$, then:

$$\hat{k} \leq \frac{\hat{h}}{\psi} < \frac{\hat{h}}{\psi_{R,L}} \tag{B.34}$$

Consequently, the convergence criterion given in Eq (B.24) is still valid.

Additional Modifications. Several other steps can be taken to increase the stability of the numerical routines. These modifications were not implemented; in retrospect, they could potentially improve the performance of the computer codes. Most of the ideas presented below came about after the time-dependent research was completed. Future work with the PDEs may benefit from the modifications listed below.

The first modifications involve solutions of the PDEs in the free-running laser case. As with the steady-state solutions for this case, only the electric field amplitude equations are required if the steady-state frequency is known exactly. From Chapter VII, the steady-state lasing frequency is given by:

$$\begin{aligned} \Delta\hat{t} &= \Delta\hat{\omega} - \dot{\varphi}_R \\ &= \Delta\hat{\omega} - \dot{\varphi}_L \\ &= \frac{\Delta\hat{m}}{1 + \frac{1}{\hat{\tau}_2} - \frac{1}{\hat{\tau}_3 \hat{L}_g} \ln r_B} \end{aligned} \tag{7.5b}$$

This frequency can be calculated *a priori*. Substituting $\Delta\hat{t}$ for the frequency terms $\Delta\hat{\omega} - \dot{\varphi}_{R,L}$ in the field amplitude equations gives:

$$\frac{\partial \hat{E}_R}{\partial \hat{t}} + \psi \frac{\partial \hat{E}_R}{\partial \hat{z}} = -\frac{\hat{E}_R}{\hat{\tau}_2} + \hat{w}_{eq} \left[\frac{\hat{E}_R}{(1 + \Delta\hat{t}^2)\sqrt{A^2 - B^2}} + \frac{1}{2\hat{\tau}_1 \hat{E}_R} \left(1 - \frac{A}{\sqrt{A^2 - B^2}} \right) \right] \tag{B.35a}$$

$$\frac{\partial \hat{E}_L}{\partial \hat{t}} - \psi \frac{\partial \hat{E}_L}{\partial \hat{z}} = -\frac{\hat{E}_L}{\hat{\tau}_2} + \hat{w}_{eq} \left[\frac{\hat{E}_L}{(1 + \Delta\hat{t}^2)\sqrt{A^2 - B^2}} + \frac{1}{2\hat{\tau}_1 \hat{E}_L} \left(1 - \frac{A}{\sqrt{A^2 - B^2}} \right) \right] \tag{B.35b}$$

where:

$$A = 1 + \frac{\hat{\tau}_1(\hat{E}_R^2 + \hat{E}_L^2)}{1 + \Delta\hat{t}^2} \tag{B.36a}$$

$$B = \frac{2\hat{\tau}_1 \hat{E}_R \hat{E}_L}{1 + \Delta\hat{t}^2} \tag{B.36b}$$

Eq (B.35) is not an approximation to the TWL equations–it is merely a simplification. Note that the right-hand sides of Eq (B.35) are not functions of $\phi_{R,L}$ or $\dot{\varphi}_{R,L}$. With only two PDEs to solve, Eq (B.35) represents a considerable decrease in complexity of the time-dependent TWL equations.

An improved set of initial conditions can be obtained following Brown's approach (28). The method entails solving Eq (B.35) in the limit of very weak fields. A derivation parallel to Brown's yields:

$$\hat{E}_R(\hat{z})|_{\hat{t}=0} = \begin{cases} \hat{E}_R(\hat{\ell}_L) & 0 \le \hat{z} \le \hat{\ell}_L \\ \hat{E}_0 r_A (r_A r_B)^{-\hat{\varsigma}/2} & \hat{\ell}_L \le \hat{z} \le \ell_R \\ \hat{E}_R(\hat{\ell}_R) & \hat{\ell}_R \le \hat{z} \le 1 \end{cases} \tag{B.37a}$$

and:

$$\hat{E}_L(\hat{z})|_{\hat{t}=0} = \begin{cases} \hat{E}_L(\hat{\ell}_L) & 0 \le \hat{z} \le \hat{\ell}_L \\ \hat{E}_0 (r_A r_B)^{\hat{\varsigma}/2} & \hat{\ell}_L \le \hat{z} \le \ell_R \\ \hat{E}_L(\hat{\ell}_R) & \hat{\ell}_R \le \hat{z} \le 1 \end{cases} \tag{B.37b}$$

with:

$$\hat{\varsigma} = \frac{\hat{z} - \hat{\ell}_L}{\hat{\ell}_R - \hat{\ell}_L} \tag{B.37c}$$

$\hat{\ell}_{R,L}$ are the right and left edges of the gain medium (normalized units) and $\hat{E}_0$ is some small initial field value. Eqs (B.35)-(B.37) should dramatically improve the stability of numerical routines for the free-running laser. Convergence is assured if the modified Heun method is used to solve the equations.

The second set of modifications involves the equations for the injected laser case. With some simple algebra, the $\phi_{R,L}$ equations can be recast as:

$$\frac{\partial \phi_R}{\partial \hat{t}} + \psi_{R1}\frac{\partial \phi_R}{\partial \hat{z}} + \psi_{R2}\frac{\partial \phi_L}{\partial \hat{t}} = \left[1 + \frac{\hat{w}_{eq}}{[1+(\Delta\hat{\omega}-\dot{\varphi}_R)^2]\sqrt{A^2-B^2-C^2}}\right.$$

$$\left. + \frac{\hat{w}_{eq}}{\hat{\tau}_1 \hat{E}_R^2[4+(\dot{\varphi}_L-\dot{\varphi}_R)^2]}\left(1 - \frac{A}{\sqrt{A^2-B^2-C^2}}\right)\right]^{-1}$$

$$\times \left\{\hat{\Omega} - \hat{\nu}_I + \frac{\hat{w}_{eq}}{\hat{E}_R}\left[\frac{\Delta\hat{\omega}\hat{E}_R}{[1+(\Delta\hat{\omega}-\dot{\varphi}_R)^2]\sqrt{A^2-B^2-C^2}}\right.\right.$$

$$\left.\left. + \frac{2\Delta\hat{\omega}}{\hat{\tau}_1\hat{E}_R[4+(\dot{\varphi}_L-\dot{\varphi}_R)^2)]}\left(1 - \frac{A}{\sqrt{A^2-B^2-C^2}}\right)\right]\right\} \qquad \text{(B.38a)}$$

$$\frac{\partial \phi_L}{\partial \hat{t}} - \psi_{L1}\frac{\partial \phi_L}{\partial \hat{z}} + \psi_{L2}\frac{\partial \phi_R}{\partial \hat{t}} = \left[1 + \frac{\hat{w}_{eq}}{[1+(\Delta\hat{\omega}-\dot{\varphi}_L)^2]\sqrt{A^2-B^2-C^2}}\right.$$

$$\left. + \frac{\hat{w}_{eq}}{\hat{\tau}_1 \hat{E}_L^2[4+(\dot{\varphi}_L-\dot{\varphi}_R)^2]}\left(1 - \frac{A}{\sqrt{A^2-B^2-C^2}}\right)\right]^{-1}$$

$$\times \left\{\hat{\Omega} - \hat{\nu}_I + \frac{\hat{w}_{eq}}{\hat{E}_L}\left[\frac{\Delta\hat{\omega}\hat{E}_L}{[1+(\Delta\hat{\omega}-\dot{\varphi}_L)^2]\sqrt{A^2-B^2-C^2}}\right.\right.$$

$$\left.\left. + \frac{2\Delta\hat{\omega}}{\hat{\tau}_1\hat{E}_L[4+(\dot{\varphi}_L-\dot{\varphi}_R)^2)]}\left(1 - \frac{A}{\sqrt{A^2-B^2-C^2}}\right)\right]\right\} \qquad \text{(B.38b)}$$

$$\psi_{R1} = \psi\left[1 + \frac{\hat{w}_{eq}}{[1+(\Delta\hat{\omega}-\dot{\varphi}_R)^2]\sqrt{A^2-B^2-C^2}}\right.$$

$$\left. + \frac{\hat{w}_{eq}}{\hat{\tau}_1 \hat{E}_R^2[4+(\dot{\varphi}_L-\dot{\varphi}_R)^2]}\left(1 - \frac{A}{\sqrt{A^2-B^2-C^2}}\right)\right]^{-1} \qquad \text{(B.38c)}$$

$$\psi_{R2} = \frac{\hat{w}_{eq}}{\hat{\tau}_1 \hat{E}_R^2[4+(\dot{\varphi}_L-\dot{\varphi}_R)^2]}\left(1 - \frac{A}{\sqrt{A^2-B^2-C^2}}\right)$$

$$\times \left[1 + \frac{\hat{w}_{eq}}{[1+(\Delta\hat{\omega}-\dot{\varphi}_R)^2]\sqrt{A^2-B^2-C^2}}\right.$$

$$\left. + \frac{\hat{w}_{eq}}{\hat{\tau}_1 \hat{E}_R^2[4+(\dot{\varphi}_L-\dot{\varphi}_R)^2]}\left(1 - \frac{A}{\sqrt{A^2-B^2-C^2}}\right)\right]^{-1} \qquad \text{(B.38d)}$$

$$\psi_{L1} = \psi\left[1 + \frac{\hat{w}_{eq}}{[1+(\Delta\hat{\omega}-\dot{\varphi}_L)^2]\sqrt{A^2-B^2-C^2}}\right.$$

$$\left. + \frac{\hat{w}_{eq}}{\hat{r}_1\hat{E}_L^2[4+(\dot{\varphi}_L-\dot{\varphi}_R)^2]}\left(1-\frac{A}{\sqrt{A^2-B^2-C^2}}\right)\right]^{-1} \tag{B.38e}$$

$$\psi_{L2} = \frac{\hat{w}_{eq}}{\hat{r}_1\hat{E}_L^2[4+(\dot{\varphi}_L-\dot{\varphi}_R)^2]}\left(1-\frac{A}{\sqrt{A^2-B^2-C^2}}\right)$$

$$\times\left[1 + \frac{\hat{w}_{eq}}{[1+(\Delta\hat{\omega}-\dot{\varphi}_L)^2]\sqrt{A^2-B^2-C^2}}\right.$$

$$\left. + \frac{\hat{w}_{eq}}{\hat{r}_1\hat{E}_L^2[4+(\dot{\varphi}_L-\dot{\varphi}_R)^2]}\left(1-\frac{A}{\sqrt{A^2-B^2-C^2}}\right)\right]^{-1} \tag{B.38f}$$

The derivatives that cause most of the numerical instabilities have been isolated on the left-hand sides of the equations. The remaining phase time derivatives occur in three terms:

$$\text{term 1} = \frac{1}{4+(\dot{\varphi}_L-\dot{\varphi}_R)^2}\left(1-\frac{A}{\sqrt{A^2-B^2-C^2}}\right)$$

$$\text{term 2} = \frac{1}{[1+(\Delta\hat{\omega}-\dot{\varphi}_R)^2]\sqrt{A^2-B^2-C^2}}$$

$$\text{term 3} = \frac{1}{[1+(\Delta\hat{\omega}-\dot{\varphi}_L)^2]\sqrt{A^2-B^2-C^2}}$$

If the effects of $\dot{\varphi}_{R,L}$ on terms 1–3 are small, then the derivatives can be dropped with possibly little impact on the numerical solutions of the PDEs. A worst-case analysis has indicated that neglecting the time derivatives in term 1 causes less than a 7% error for $\dot{\varphi}_{R,L} \leq 0.2$. In terms 2 and 3, the error is less than 3.5%. If the variations in $\dot{\varphi}_{R,L}$ are less than 0.1, then the errors for terms 1 and 2 (or 3) are 3.5% and 0.9%, respectively. It should be possible, to a good approximation, to suppress the time derivatives of the phases.

Suppressing the phase time derivatives leads to the following set of PDEs:

$$\frac{\partial\hat{E}_R}{\partial\hat{t}} + \psi\frac{\partial\hat{E}_R}{\partial\hat{z}} = -\frac{\hat{E}_R}{\hat{r}_2} + \hat{w}_{eq}\left[\frac{\hat{E}_R}{(1+\Delta\hat{\omega}^2)\sqrt{A^2-B^2}} + \frac{1}{2\hat{r}_1\hat{E}_R}\left(1-\frac{A}{\sqrt{A^2-B^2}}\right)\right] \tag{B.39a}$$

$$\frac{\partial\hat{E}_L}{\partial\hat{t}} - \psi\frac{\partial\hat{E}_L}{\partial\hat{z}} = -\frac{\hat{E}_L}{\hat{r}_2} + \hat{w}_{eq}\left[\frac{\hat{E}_L}{(1+\Delta\hat{\omega}^2)\sqrt{A^2-B^2}} + \frac{1}{2\hat{r}_1\hat{E}_L}\left(1-\frac{A}{\sqrt{A^2-B^2}}\right)\right] \tag{B.39b}$$

$$\frac{\partial \phi_R}{\partial \hat{t}} + \psi_{R1}\frac{\partial \phi_R}{\partial \hat{z}} + \psi_{R2}\frac{\partial \phi_L}{\partial \hat{t}} = \left[1 + \frac{\hat{w}_{eq}}{(1+\Delta\hat{\omega}^2)\sqrt{A^2-B^2}} + \frac{\hat{w}_{eq}}{4\hat{\tau}_1\hat{E}_R^2}\left(1 - \frac{A}{\sqrt{A^2-B^2}}\right)\right]^{-1} \times \left\{\hat{\Omega} - \hat{\nu}_I + \frac{\Delta\hat{\omega}\hat{w}_{eq}}{\hat{E}_R}\left[\frac{\hat{E}_R}{(1+\Delta\hat{\omega}^2)\sqrt{A^2-B^2}} + \frac{1}{2\hat{\tau}_1\hat{E}_R}\left(1 - \frac{A}{\sqrt{A^2-B^2}}\right)\right]\right\} \tag{B.39c}$$

$$\frac{\partial \phi_L}{\partial \hat{t}} - \psi_{L1}\frac{\partial \phi_L}{\partial \hat{z}} + \psi_{L2}\frac{\partial \phi_R}{\partial \hat{t}} = \left[1 + \frac{\hat{w}_{eq}}{(1+\Delta\hat{\omega}^2)\sqrt{A^2-B^2}} + \frac{\hat{w}_{eq}}{4\hat{\tau}_1\hat{E}_L^2}\left(1 - \frac{A}{\sqrt{A^2-B^2}}\right)\right]^{-1} \times \left\{\hat{\Omega} - \hat{\nu}_I + \frac{\Delta\hat{\omega}\hat{w}_{eq}}{\hat{E}_L}\left[\frac{\hat{E}_L}{(1+\Delta\hat{\omega}^2)\sqrt{A^2-B^2}} + \frac{1}{2\hat{\tau}_1\hat{E}_L}\left(1 - \frac{A}{\sqrt{A^2-B^2}}\right)\right]\right\} \tag{B.39d}$$

with:

$$\psi_{R1} = \psi\left[1 + \frac{\hat{w}_{eq}}{(1+\Delta\hat{\omega}^2)\sqrt{A^2-B^2}} + \frac{\hat{w}_{eq}}{4\hat{\tau}_1\hat{E}_R^2}\left(1 - \frac{A}{\sqrt{A^2-B^2}}\right)\right]^{-1} \tag{B.39e}$$

$$\psi_{R2} = \frac{\hat{w}_{eq}}{4\hat{\tau}_1\hat{E}_R^2}\left(1 - \frac{A}{\sqrt{A^2-B^2}}\right) \times \left[1 + \frac{\hat{w}_{eq}}{(1+\Delta\hat{\omega}^2)\sqrt{A^2-B^2}} + \frac{\hat{w}_{eq}}{4\hat{\tau}_1\hat{E}_R^2}\left(1 - \frac{A}{\sqrt{A^2-B^2}}\right)\right]^{-1} \tag{B.39f}$$

$$\psi_{L1} = \psi\left[1 + \frac{\hat{w}_{eq}}{(1+\Delta\hat{\omega}^2)\sqrt{A^2-B^2}} + \frac{\hat{w}_{eq}}{4\hat{\tau}_1\hat{E}_L^2}\left(1 - \frac{A}{\sqrt{A^2-B^2}}\right)\right]^{-1} \tag{B.39g}$$

$$\psi_{L2} = \frac{\hat{w}_{eq}}{4\hat{\tau}_1\hat{E}_L^2}\left(1 - \frac{A}{\sqrt{A^2-B^2}}\right)$$

$$\times \left[1 + \frac{\hat{w}_{eq}}{(1+\Delta\hat{\omega}^2)\sqrt{A^2-B^2}} + \frac{\hat{w}_{eq}}{4\hat{\tau}_1\hat{E}_L^2}\left(1 - \frac{A}{\sqrt{A^2-B^2}}\right)\right]^{-1} \tag{B.39h}$$

and:

$$A = 1 + \frac{\hat{\tau}_1(\hat{E}_R^2 + \hat{E}_L^2)}{1+\Delta\hat{\omega}^2} \tag{B.39i}$$

$$B = \frac{2\hat{\tau}_1\hat{E}_R\hat{E}_L}{1+\Delta\hat{\omega}^2} \tag{B.39j}$$

Following Brown's approach as before, the initial conditions in complex form can be derived:

$$\hat{E}_R(\hat{z})e^{-i\phi_R(\hat{z})}\big|_{\hat{t}=0} = \begin{cases} \hat{E}_R(\hat{\ell}_L)\exp\left[-i\phi_R(\hat{\ell}_L)\right] & 0 \le \hat{z} \le \hat{\ell}_L \\ \hat{E}_0 r_A\left(r_A r_B e^{i\hat{\vartheta}}\right)^{-\varsigma/2} + \dfrac{r_A E_I \exp\left[q\hat{\tau}_3(1+\varsigma)/2\right]}{1 - r_A r_B e^{i\hat{\vartheta}} e^{q\hat{\tau}_3}} & \hat{\ell}_L \le \hat{z} \le \hat{\ell}_R \\ \hat{E}_R(\hat{\ell}_R)\exp\left[-i\phi_R(\hat{\ell}_R)\right] & \hat{\ell}_R \le \hat{z} \le 1 \end{cases} \tag{B.40a}$$

and:

$$\hat{E}_L(\hat{z})e^{-i\phi_L(\hat{z})}\big|_{\hat{t}=0} = \begin{cases} \hat{E}_L(\hat{\ell}_L)\exp\left[-i\phi_L(\hat{\ell}_L)\right] & 0 \le \hat{z} \le \hat{\ell}_L \\ \hat{E}_0\left(r_A r_B e^{i\hat{\vartheta}}\right)^{\varsigma/2} + \dfrac{E_I \exp\left[q\hat{\tau}_3(1-\varsigma)/2\right]}{1 - r_A r_B e^{i\hat{\vartheta}} e^{q\hat{\tau}_3}} & \hat{\ell}_L \le \hat{z} \le \hat{\ell}_R \\ \hat{E}_L(\hat{\ell}_R)\exp\left[-i\phi_L(\hat{\ell}_R)\right] & \hat{\ell}_R \le \hat{z} \le 1 \end{cases} \tag{B.40b}$$

with:

$$q \equiv \frac{\hat{w}_{eq}}{1 + i\Delta\hat{\omega}} - i(\Delta\hat{\omega} - \Delta\hat{m}) - \frac{1}{\hat{\tau}_2} \tag{B.40c}$$

If $E_I = 0$ (the free-running condition), Eq (B.40) reduces to Eq (B.37). The initial conditions are based upon the exact TWL equations in the limit of small fields; they can be used with either Eqs (3.8)-(3.9) or Eq (B.39).

Eq (B.39) is a true hyperbolic set of PDEs. Unfortunately, the modified Heun method cannot be used to solve the equations. A linear transformation does not exist that will render the PDEs

into the form required by this technique. However, linear transformations exist that will convert the equations into the normal form. The C-I-R method can then be used to solve the set. If the loss of accuracy due to the suppression of the $\dot{\varphi}_{R,L}$ terms and the use of the C-I-R method is outweighed by an increase in stability of the solutions, then the use of Eq (B.39) with the C-I-R method is warranted.

Run Specifics and Characteristics. The computer codes based upon the above discussions had several interesting run characteristics. "Rules of thumb" that enhanced the numerical stability emerged as the codes were used. The run constants, rules of thumb, and run characteristics are described below.

In all runs, the number of spatial steps is set equal to 101. Thus, $\hat{h} = 0.01$. With $\psi = 1.5$, the convergence criteria dictate that $\hat{k} \leq 6.667 \times 10^{-3}$. Some experimentation is usually required to obtain values of $\hat{k}$ that produce numerically stable results. As a general rule, stability is enhanced as $\hat{k}$ approaches 6.667×10^{-3}.

A large number of time steps are usually required in order for the transients to die out. 40,000 to 200,000 time steps are often necessary. This leads to exorbitant computer costs. For 200,000 time steps, approximately 10 minutes of CPU time on a CRAY 1S computer is required. The costs are exasperated when experimentation is necessary to determine $\hat{k}$ values that produce stable numerics. The high costs exist despite vectorization of all possible loops and other code optimizations.

The magnitude of the initial field amplitudes impact the number of time steps required to reach steady-state. If the initial amplitudes are very low, the time required for the fields to rise can be quite long. On the other hand, if the initial field amplitudes are relatively high, the laser turn-on transients are lost. Generally, if the initial amplitudes are one-tenth to one-twentieth of the steady state amplitudes, the turn-on transients are not lost and the run times are limited to reasonable values.

The solutions of the TWL equations undergo initial numerical transients. These transients are due to the numerical techniques, initial conditions, and boundary conditions. They are distinct from

the transients due to the laser behavior described in the previous paragraph. The transients in the free-running laser case are relatively mild. The boundary conditions described above help minimize the transient behavior.

In the injected laser case, the transients can be severe enough to lead to numerical instabilities. The field amplitude transients arise due to a mismatch in the boundary conditions at mirror B, similar to that depicted in Figure B.2. The damping time can be decreased significantly by an appropriate choice of initial field amplitudes. If the initial field amplitudes are large compared to injected signal, the amplitude transients damp out quickly. If the injected signal is comparable to the initial amplitudes, the transients will linger for a longer time. The phase transients are more severe than the amplitude transients. This is due to two factors. First, the initial values of $\dot{\varphi}_{R,L}$ are set equal to zero. This introduces discontinuities that must decay. Second, since terms containing $\dot{\varphi}_{R,L}$ exist on the right-hand sides of both phase equations, the phases will necessarily be more sensitive to noise and transients. Using Eq (B.39) as the laser model may lessen the impact of the phase transients and decrease the damping times.

Summary

The numerical algorithms for the four problem classes were outlined in this appendix. The specific numerical methods and accuracies were given. Details about numerical constants, initial conditions, boundary conditions, and solution characteristics were discussed where appropriate. Finally, some suggestions to improve the performance of the time-dependent codes were given.

APPENDIX C

Injected Laser Data

A large volume of data was collected during the analyses of the injected lasers. Over fifty contour and slice plots were produced for each data set. In order to reduce the number of figures in Chapter VII, the injected laser plots for data sets 27 and 36 are included in this appendix. Only those representative plots required to display the main data trends are included herein. The plots from these two sets are typical of the results seen data sets 27–38 (injected Fabry-Perot lasers).

Figures C.1–C.17 display the behavior of $I_R(0)$, or equivalently $I_L(0)$, in the $(\Delta\hat{o}, r_B)$ plane. Figures C.18–C.34 are plots of the injected intensity I_I. The behavior of the system gain G_1 is depicted in Figures C.35–C.51. Finally, plots of the gain G_2 are displayed in Figures C.52–C.70. Since the four observables vary over several orders of magnitude in each contour plot, the observables are logarithmically scaled. That is, $\log_{10} F$ are depicted in the contour plots, where F is the observable of interest.

All plots from data set 27 are symmetric about the line $\Delta\hat{o} = 0.0$. This arises because the free-running mode is set at the atomic gain linecenter ($\Delta\hat{t} = 0.0$). The gain, and therefore the plots, are symmetric about the line $\Delta\hat{o} = 0.0$. Since $\Delta\hat{t} \neq 0.0$ in data set 36, the plots from this set are not symmetric about the line $\Delta\hat{o} = 0.0$. The data in the plots were obtained using the exact expression for $\hat{\vartheta}$, Eq (3.27b).

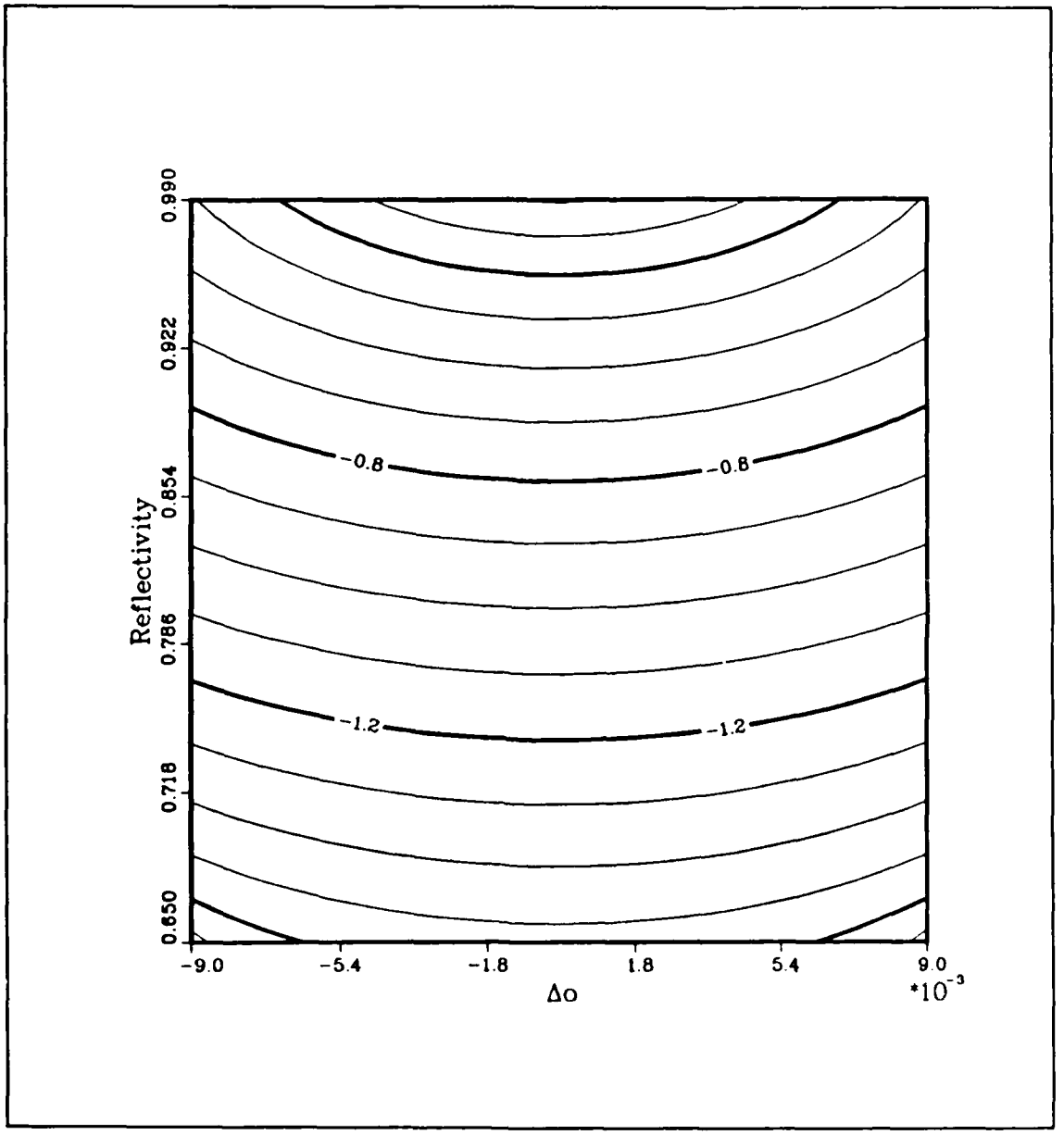

Figure C.1. $\log_{10} I_R(0)$ contours at the MII point (data set 27).

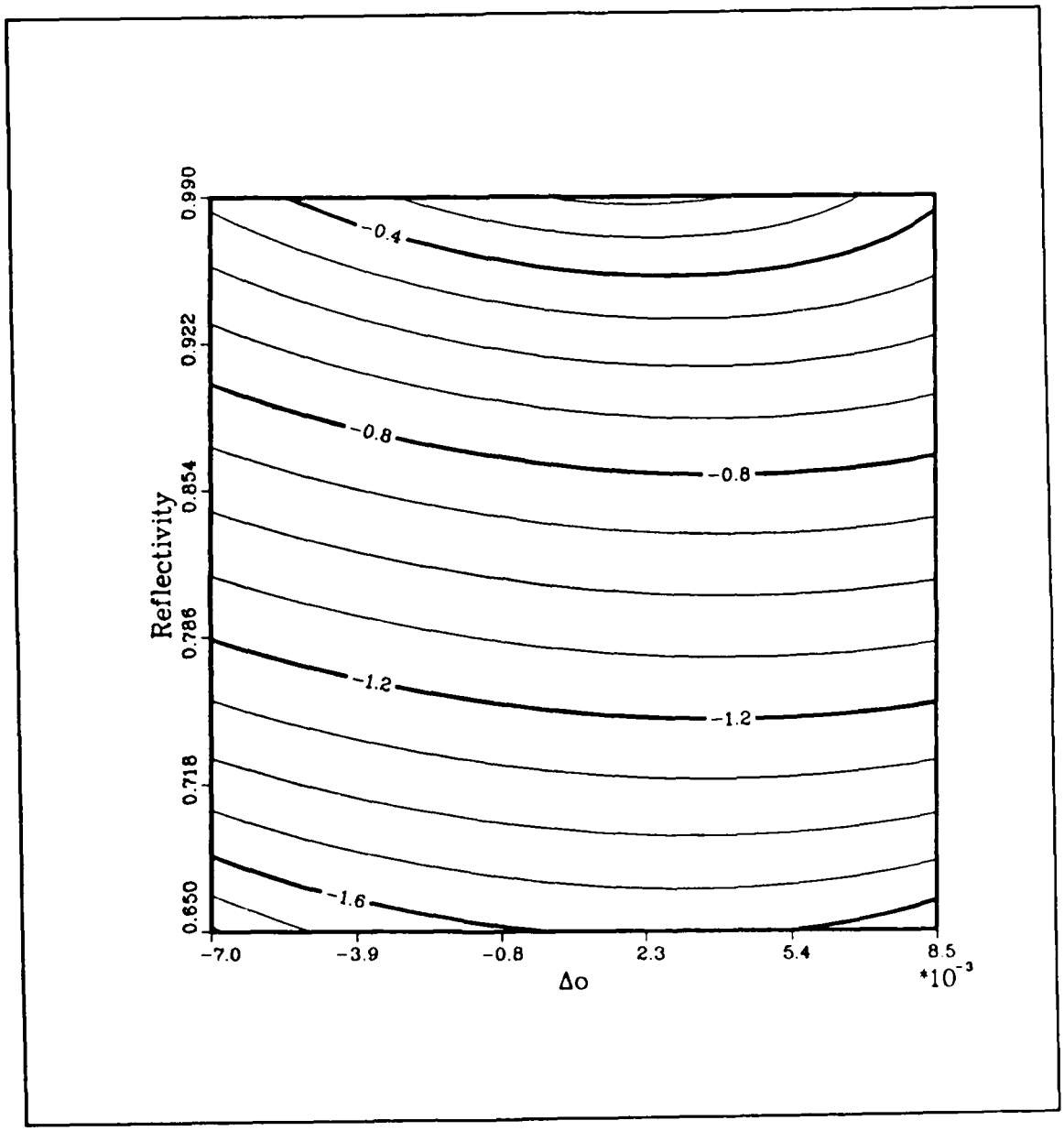

Figure C.2. $\log_{10} I_R(0)$ contours at the MII point (data set 36).

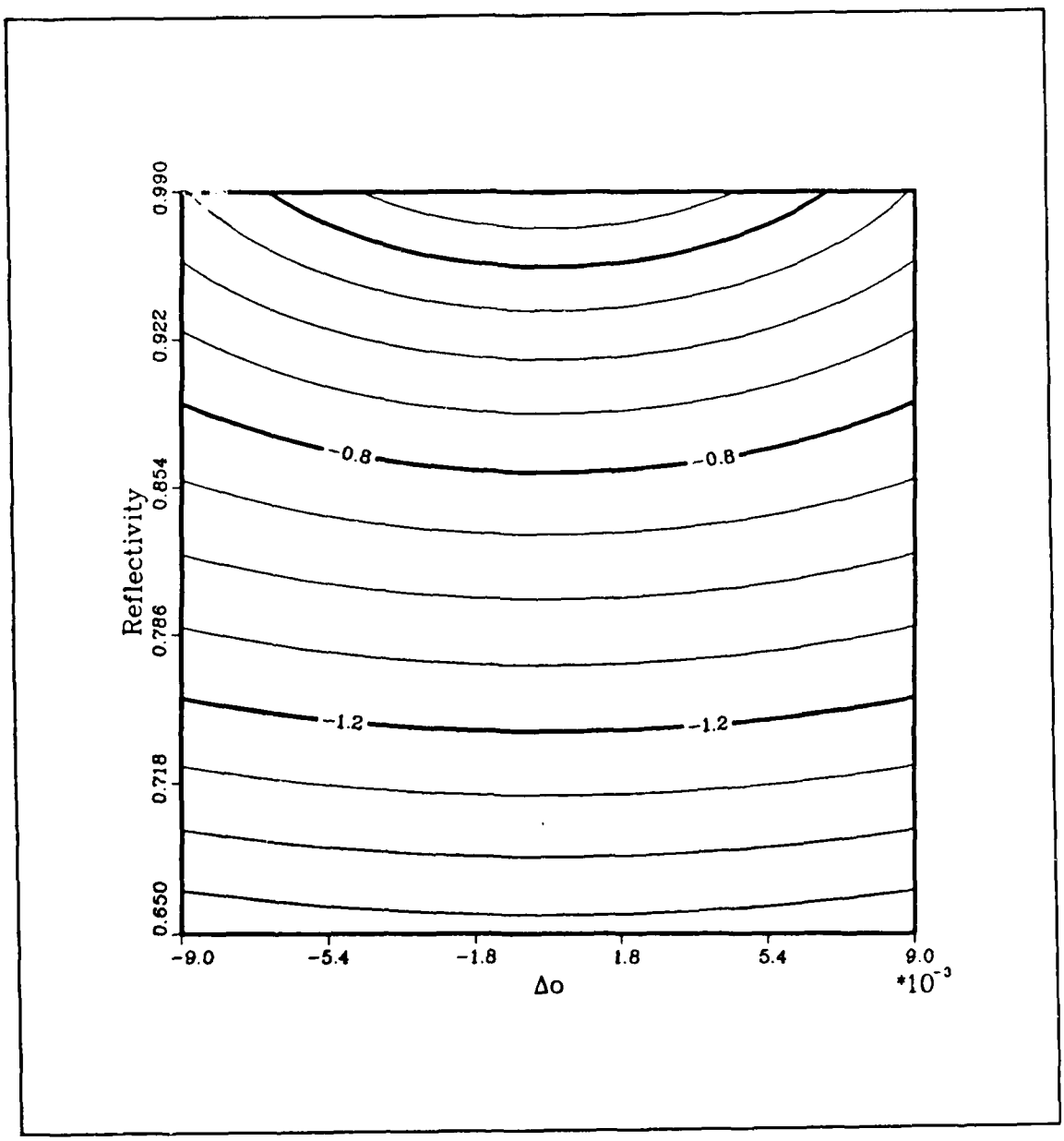

Figure C.3. $\log_{10} I_R(0)$ contours at the MG1 point (data set 27).

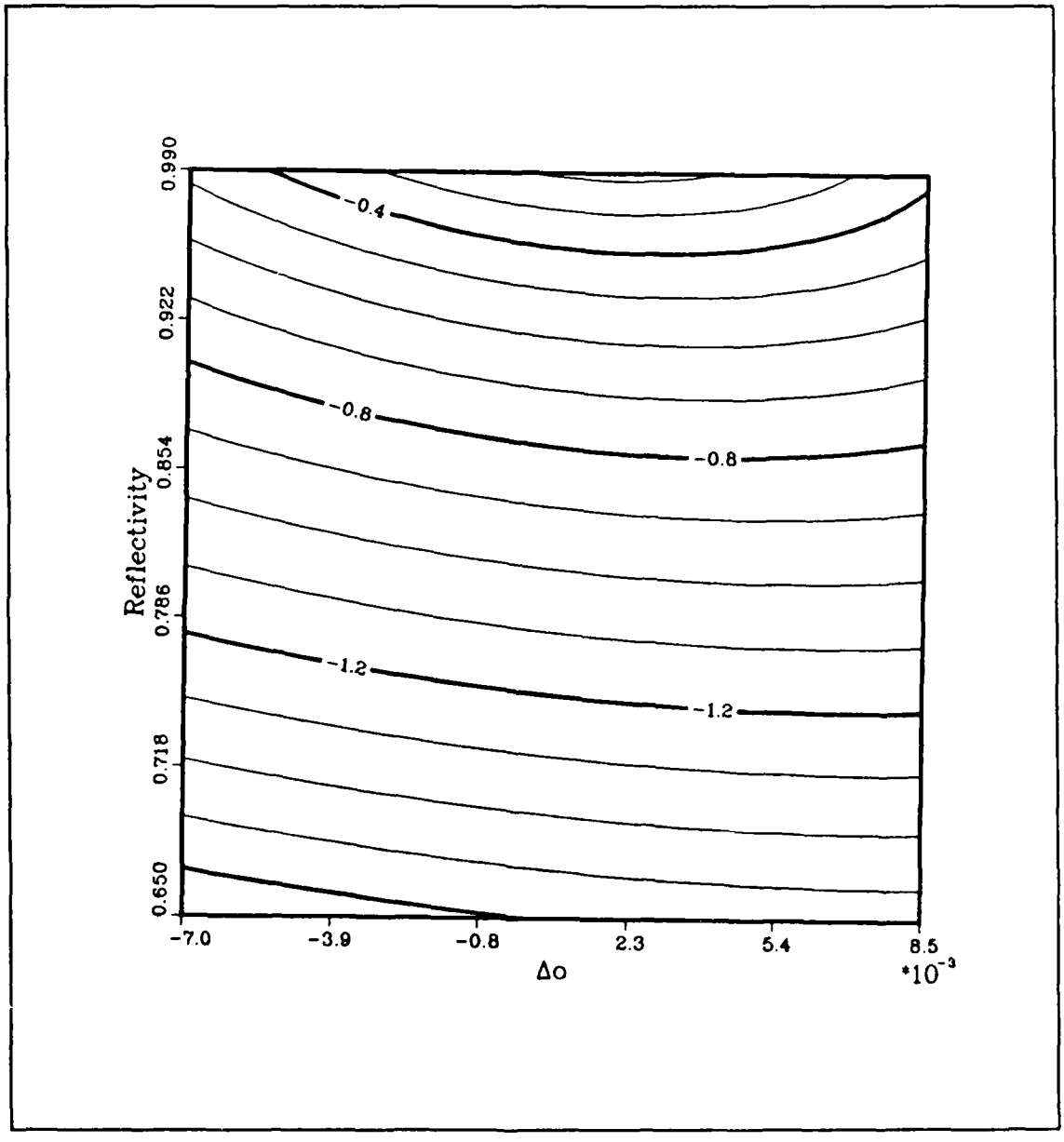

Figure C.4. $\log_{10} I_R(0)$ contours at the MG1 point (data set 36).

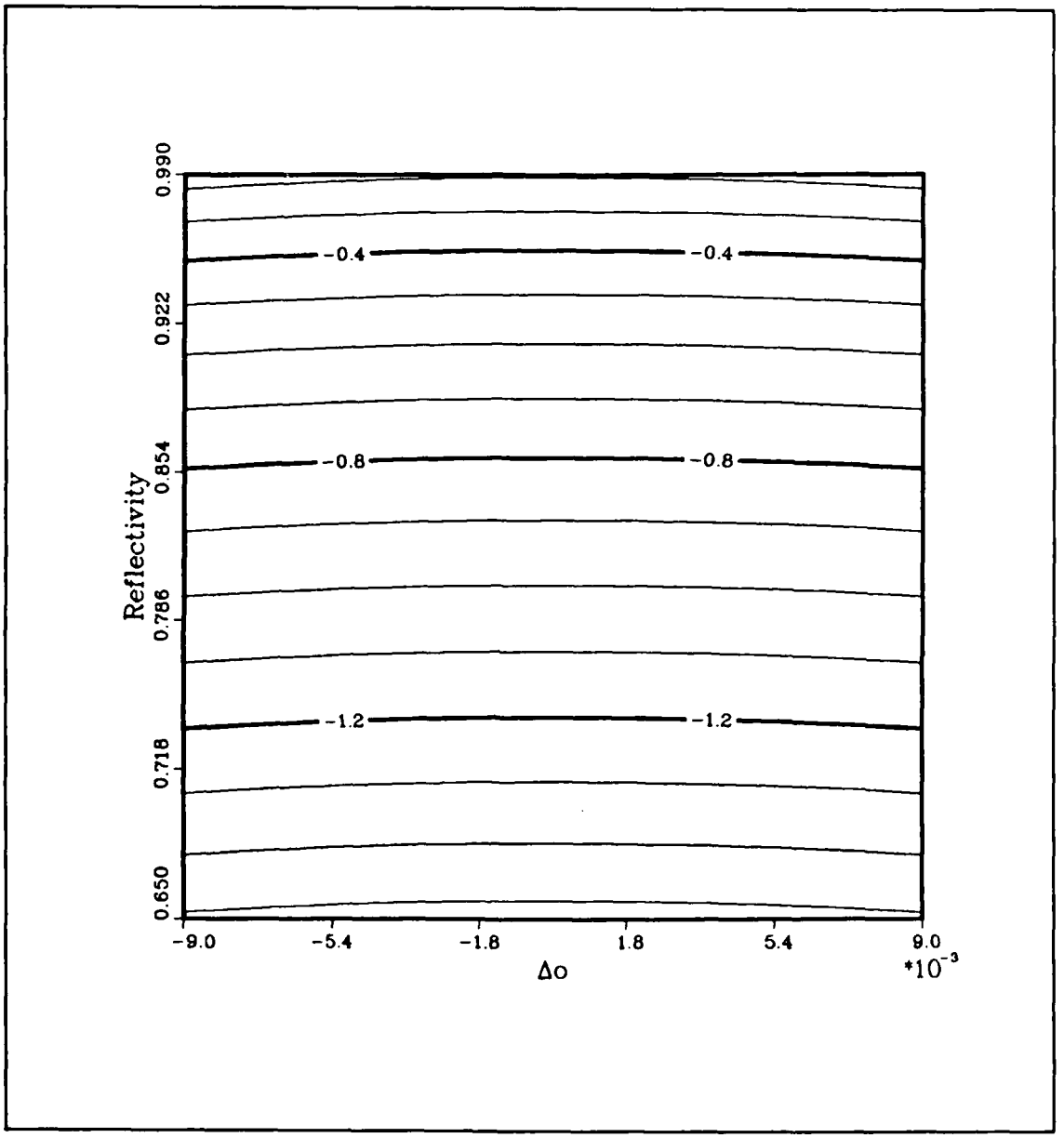

Figure C.5. $\log_{10} I_R(0)$ contours at the MG2 point (data set 27). The data is from the region in the $(\Delta\hat{o}, r_B)$ plane where the cubic curves retain the s-shape.

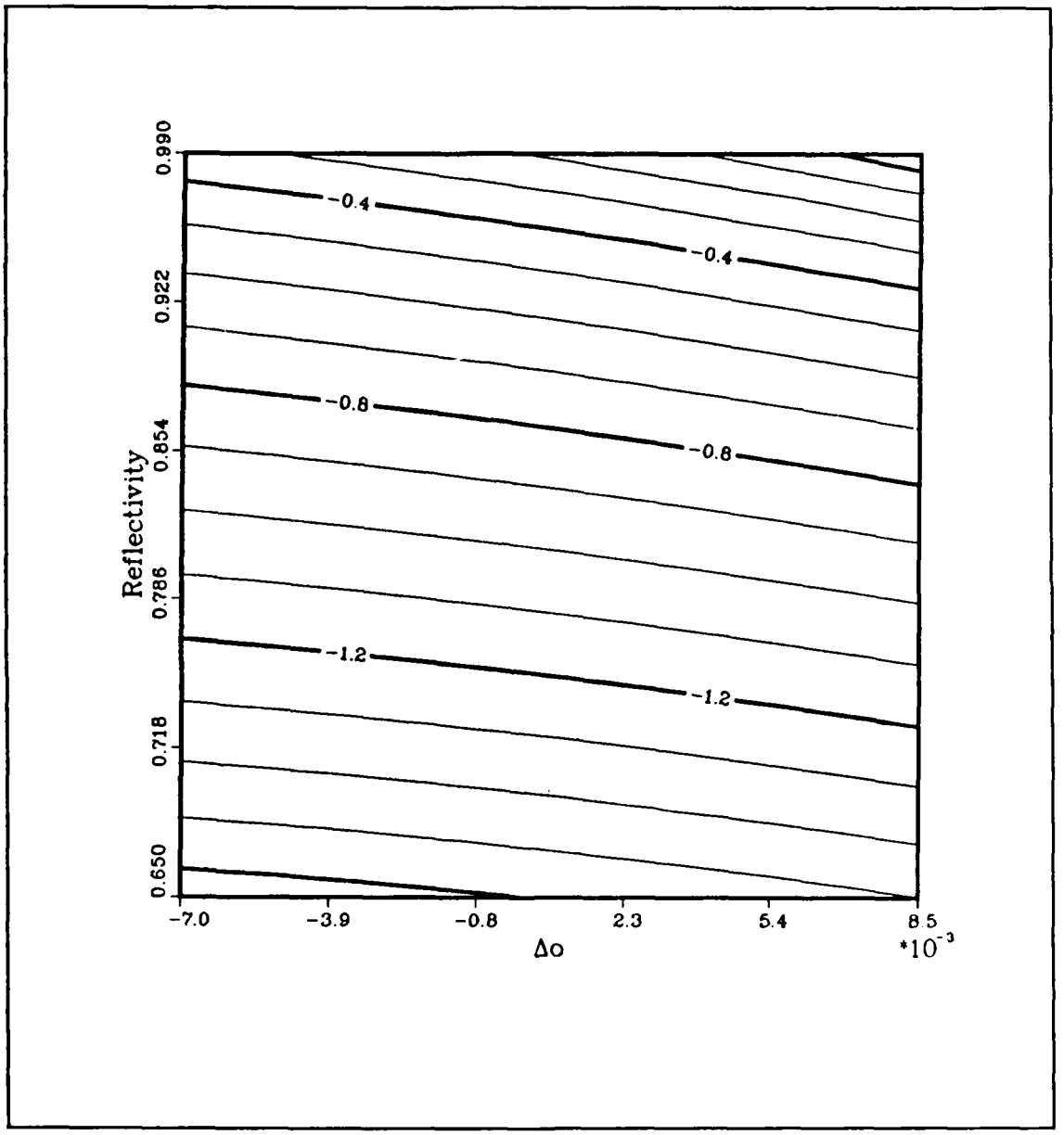

Figure C.6. $\log_{10} I_R(0)$ contours at the MG2 point (data set 36). The data is from the region in the $(\Delta\hat{o}, r_B)$ plane where the cubic curves retain the s-shape.

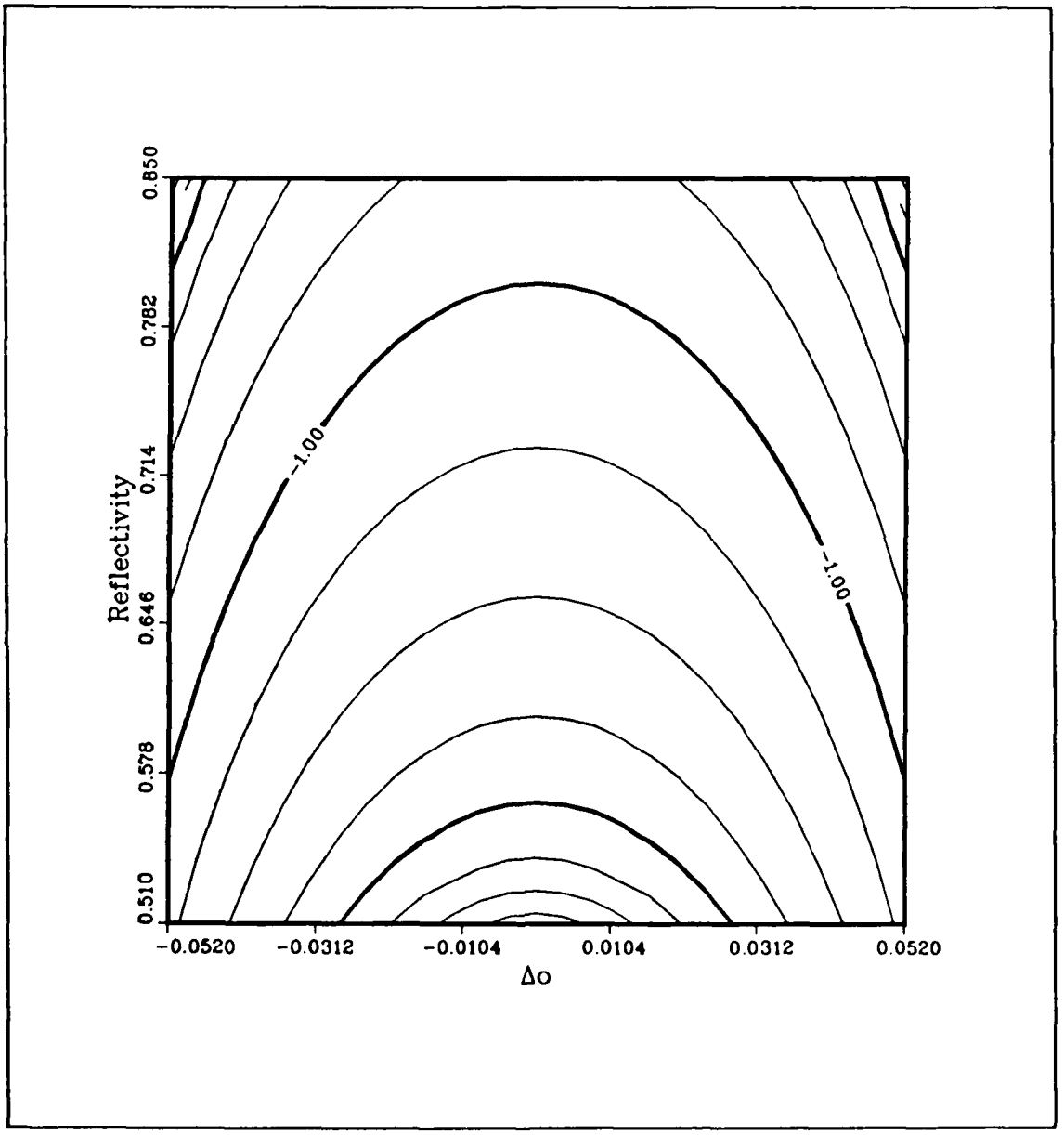

Figure C.7. $\log_{10} I_R(0)$ contours at the MG2 point (data set 27). The data is from as large a rectangular region in the $(\Delta\hat{o}, r_D)$ plane as possible.

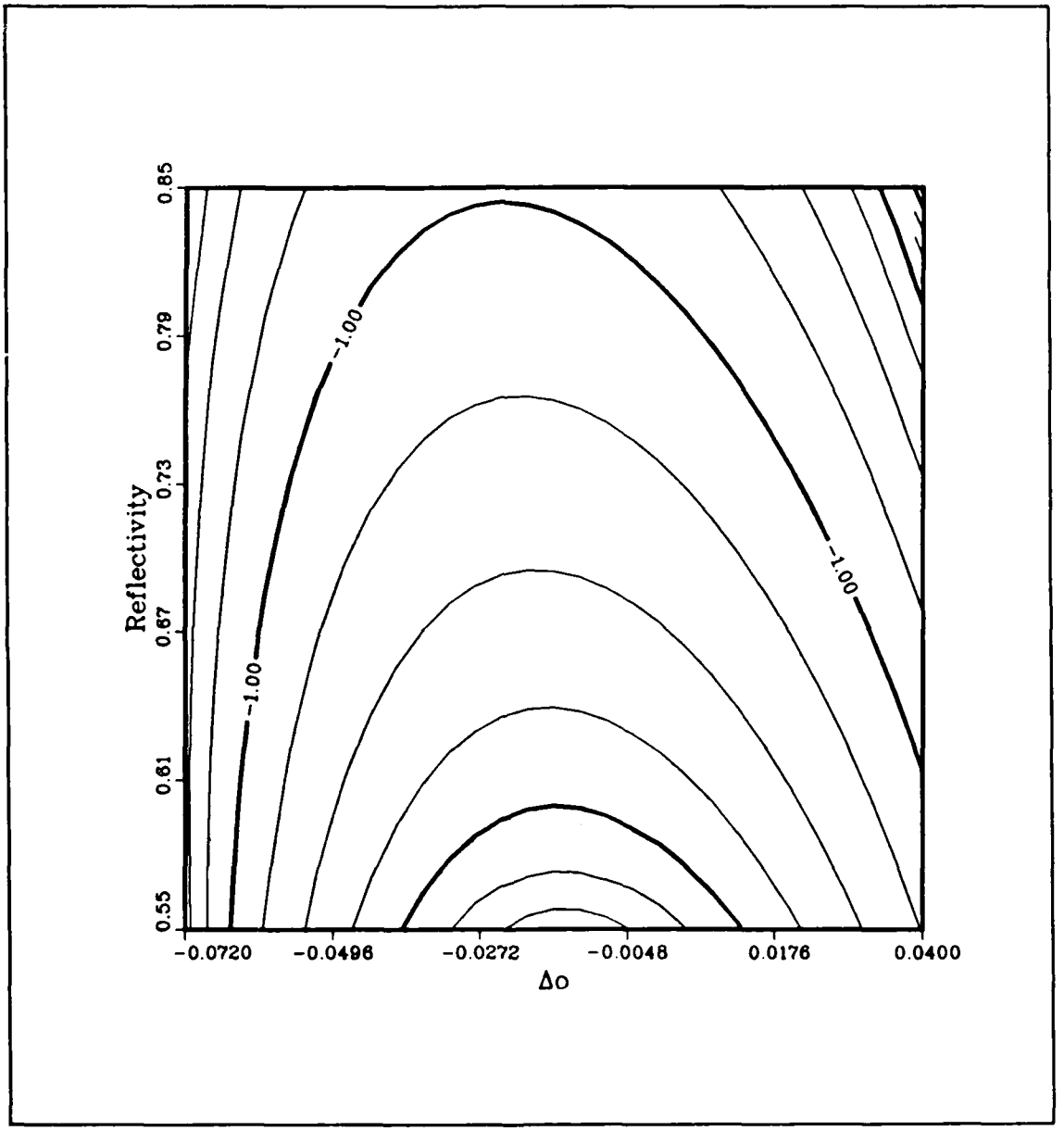

Figure C.8. $\log_{10} I_R(0)$ contours at the MG2 point (data set 36). The data is from as large a rectangular region in the $(\Delta\hat{o}, r_B)$ plane as possible.

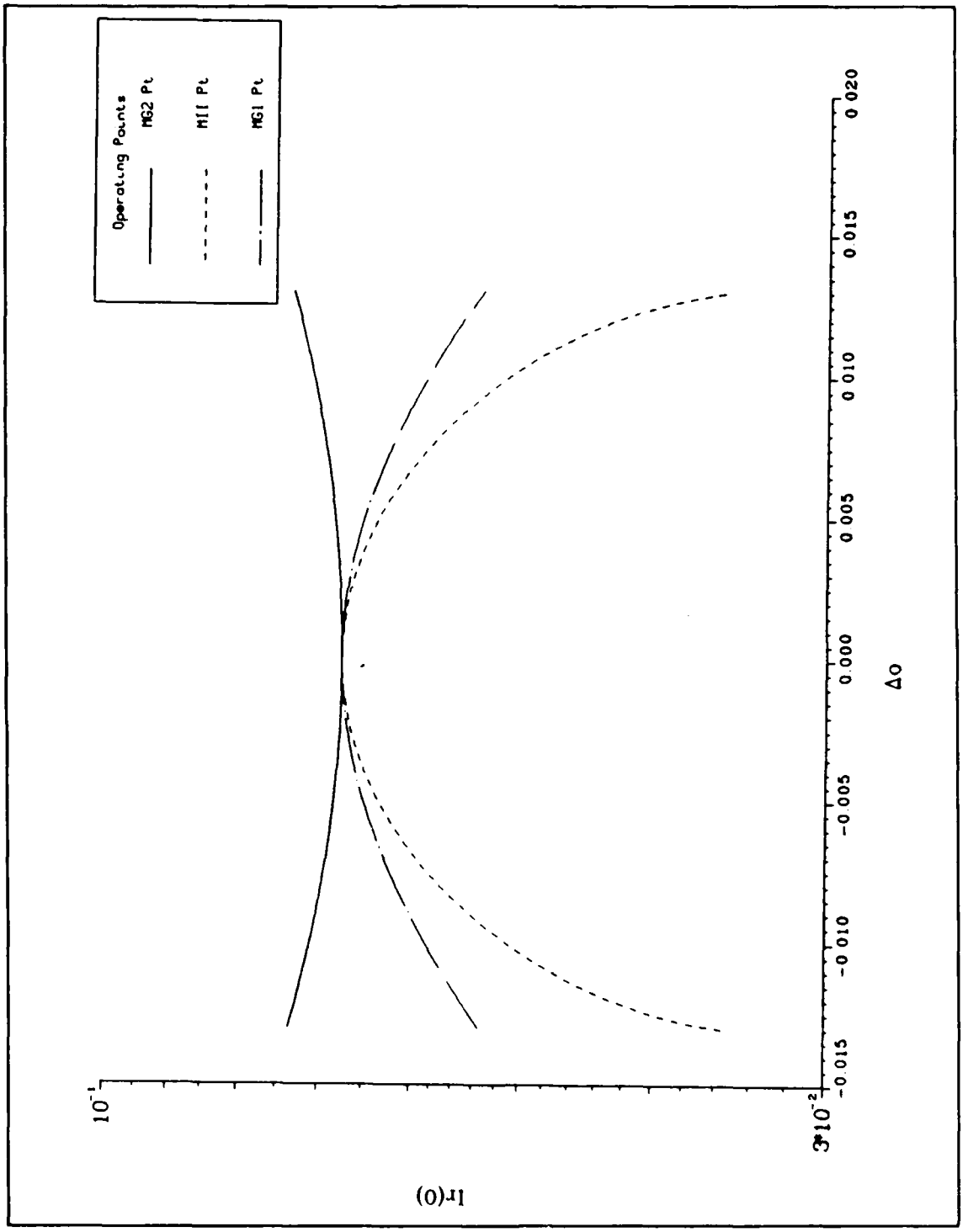

Figure C.9. $I_R(0)$ vs $\Delta\delta$ (data set 27). $r_B = 0.75$. Curves for the three operating points are displayed in the figure.

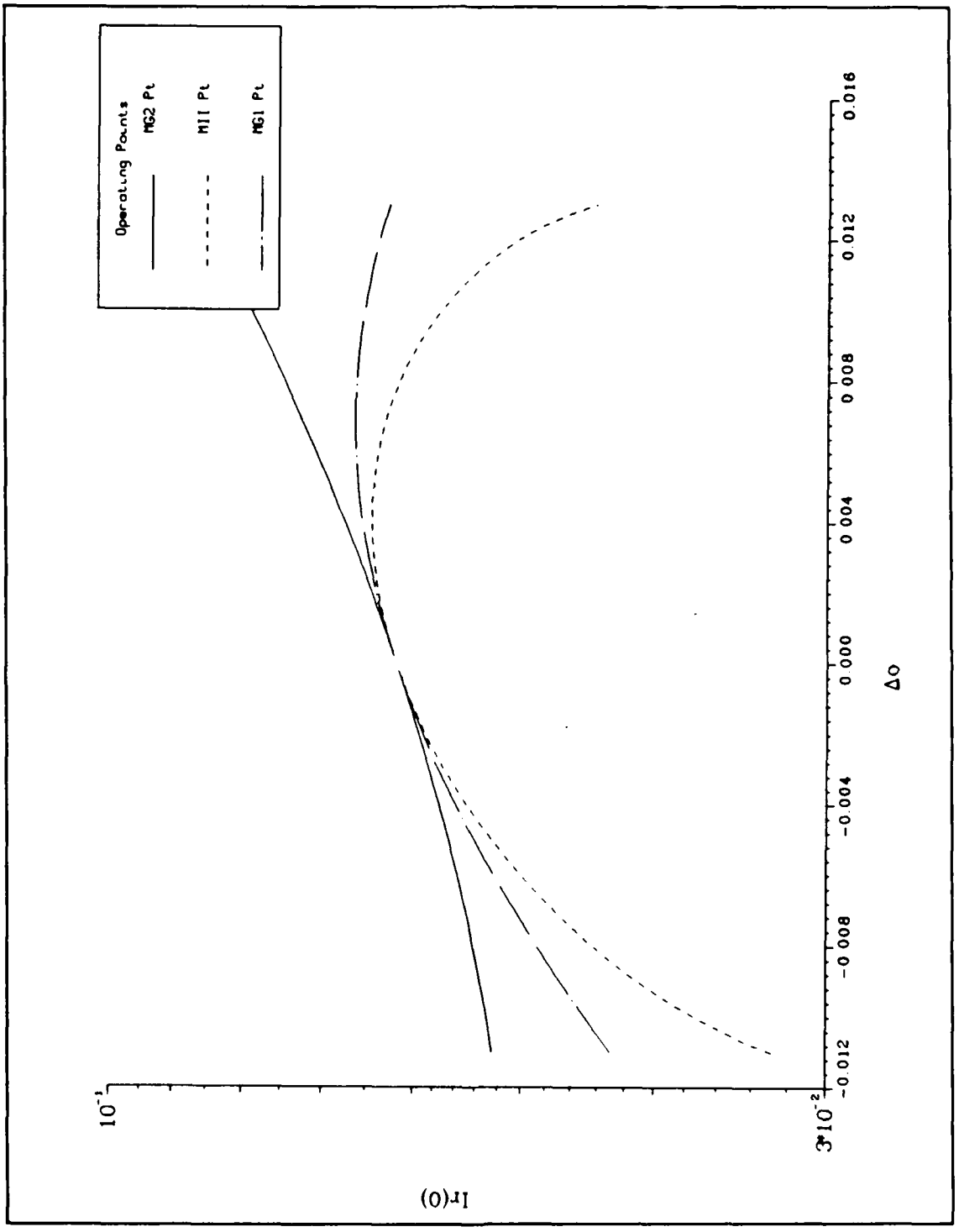

Figure C.10. $I_R(0)$ vs $\Delta\hat{o}$ (data set 36). $r_B = 0.75$. Curves for the three operating points are displayed in the figure.

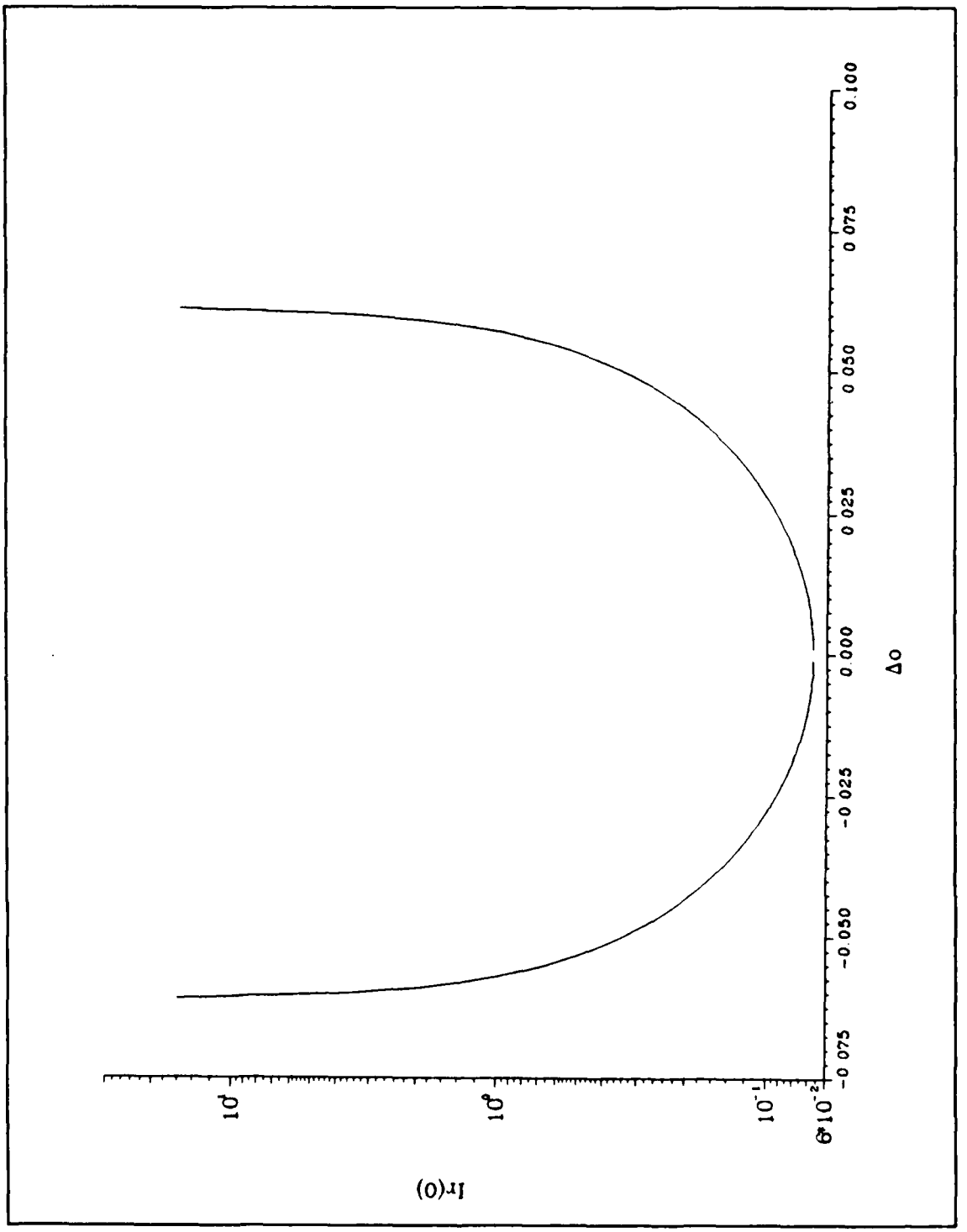

Figure C.11. $I_R(0)$ vs $\Delta\hat{\delta}$ (data set 27). $r_B = 0.75$. The curve is taken from the MG2 operating point data.

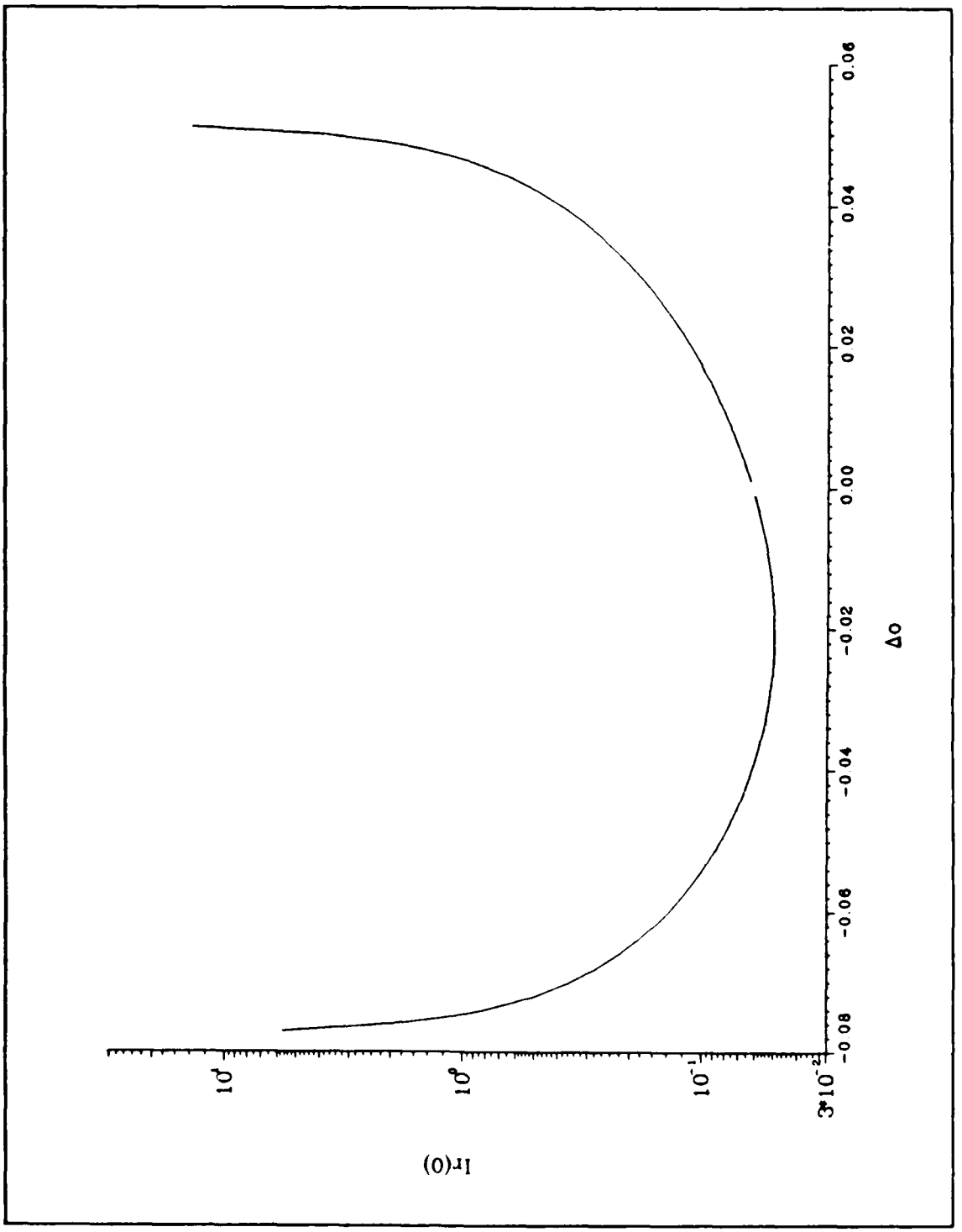

Figure C.12. $I_R(0)$ vs $\Delta\hat{o}$ (data set 36). $r_B = 0.75$. The curve is taken from the MG2 operating point data.

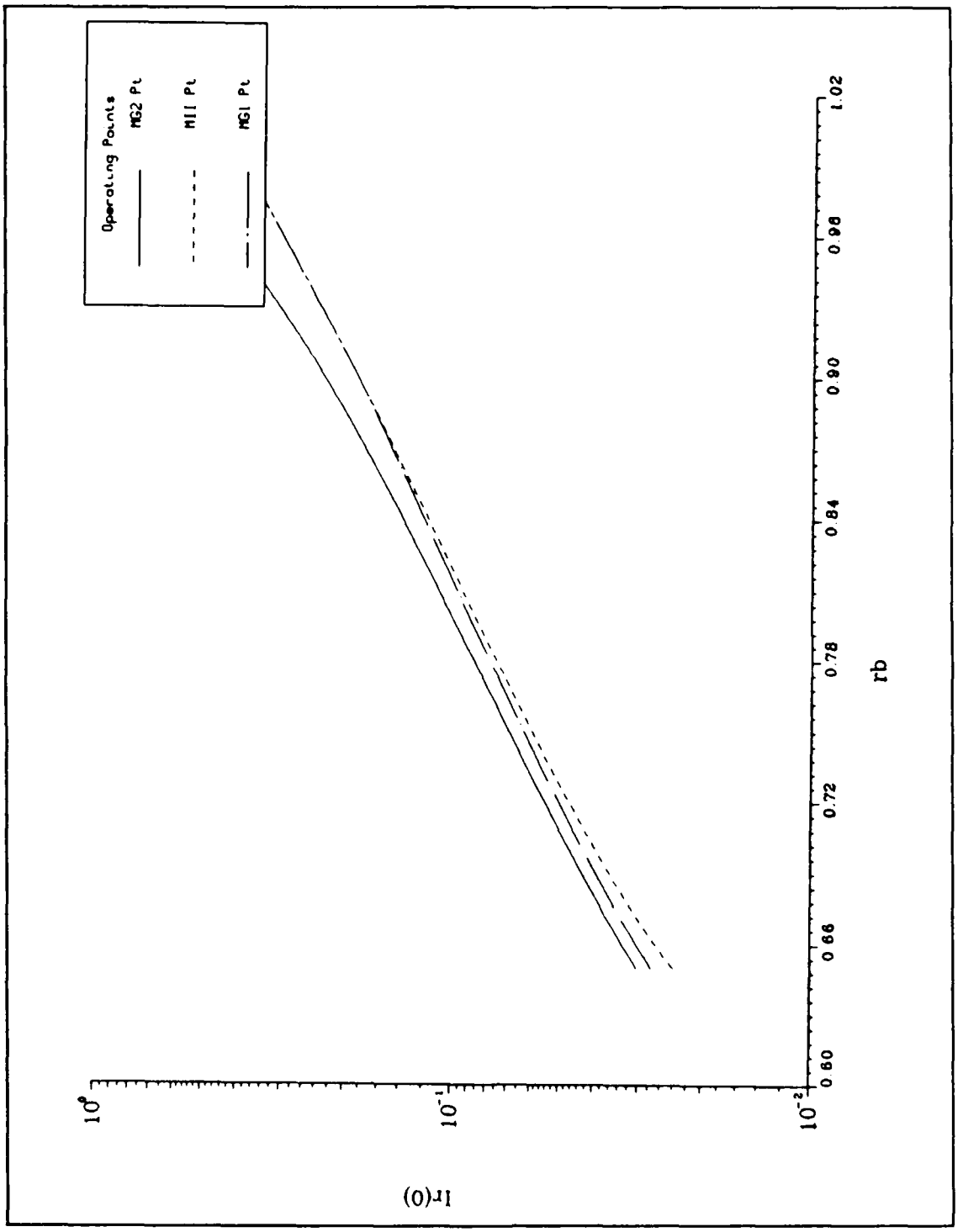

Figure C.13. $I_R(0)$ vs r_B (data set 27). $\Delta\delta = 0.007$. Curves for the three operating points are displayed in the figure.

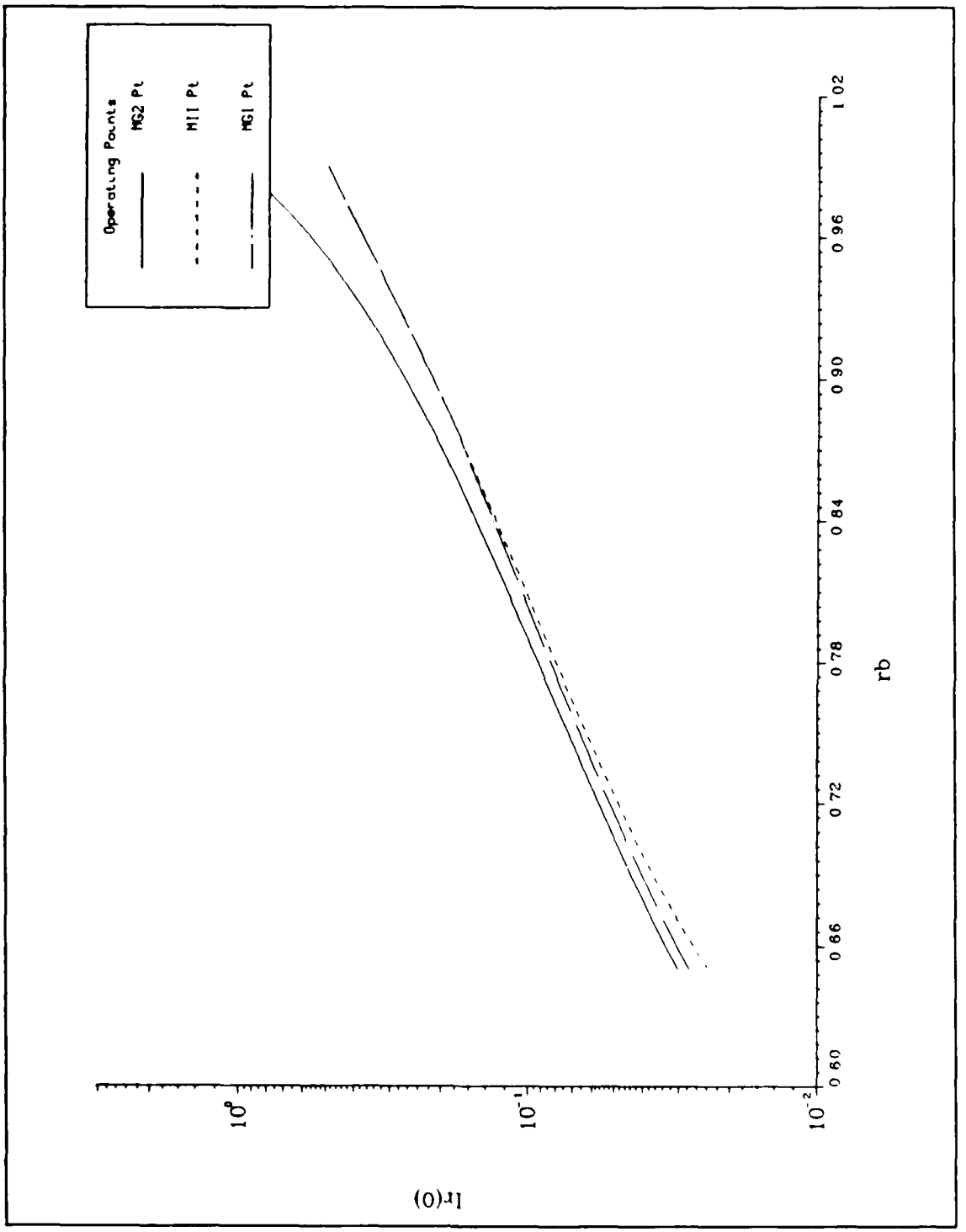

Figure C.14. $I_R(0)$ vs r_B (data set 36). $\Delta\hat{\sigma} = 0.007$. Curves for the three operating points are displayed in the figure.

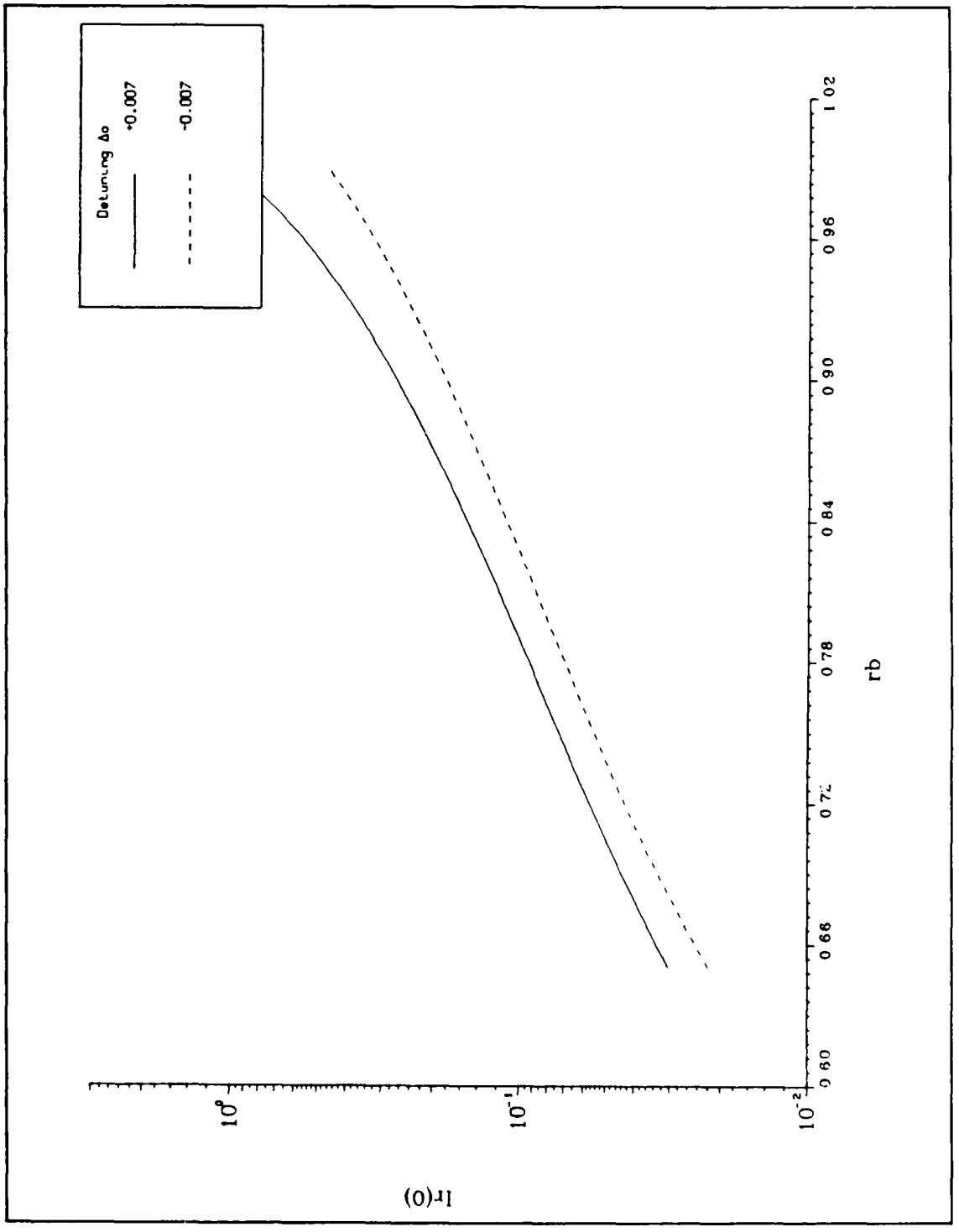

Figure C.15. $I_R(0)$ vs r_B (data set 36). $\Delta\hat{\sigma} = \pm 0.007$. The curves are taken from the MG2 operating point data.

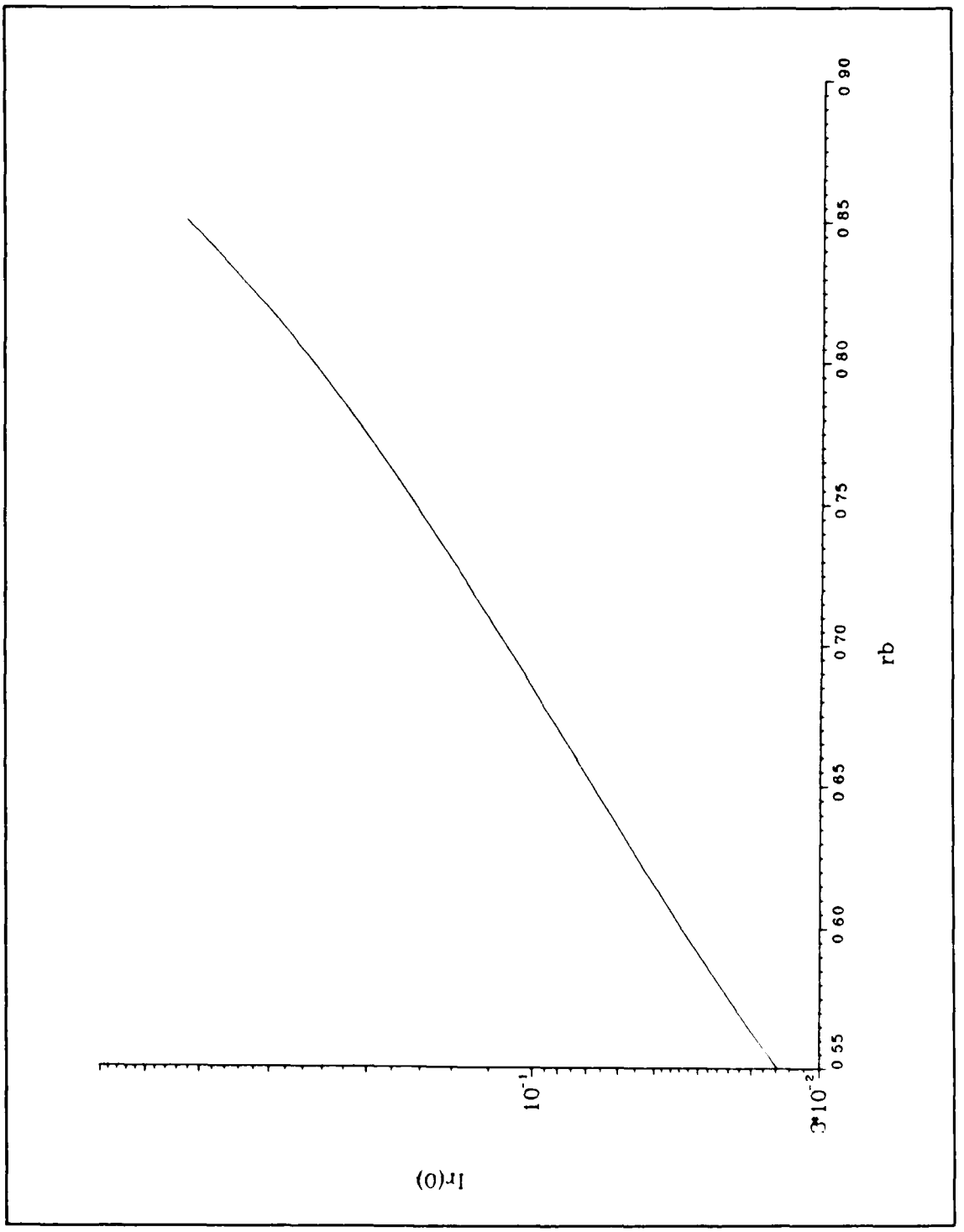

Figure C.16. $I_R(0)$ vs r_B (data set 27). $\Delta\hat{o} = 0.040$. The curve is taken from the MG2 operating point data.

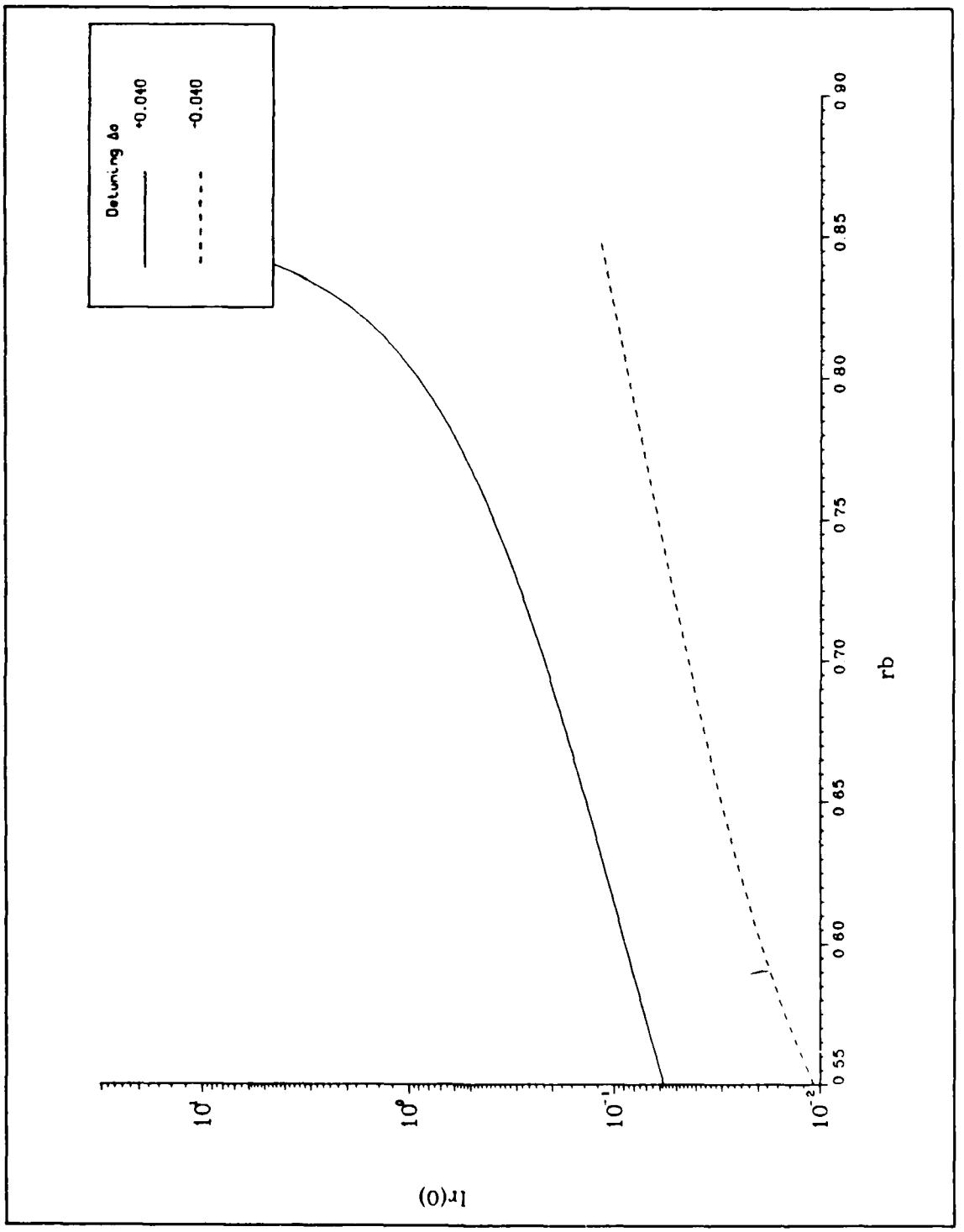

Figure C.17. $I_R(0)$ vs r_B (data set 36). $\Delta\delta = \pm 0.040$. The curves are taken from the MG2 *operating point* data.

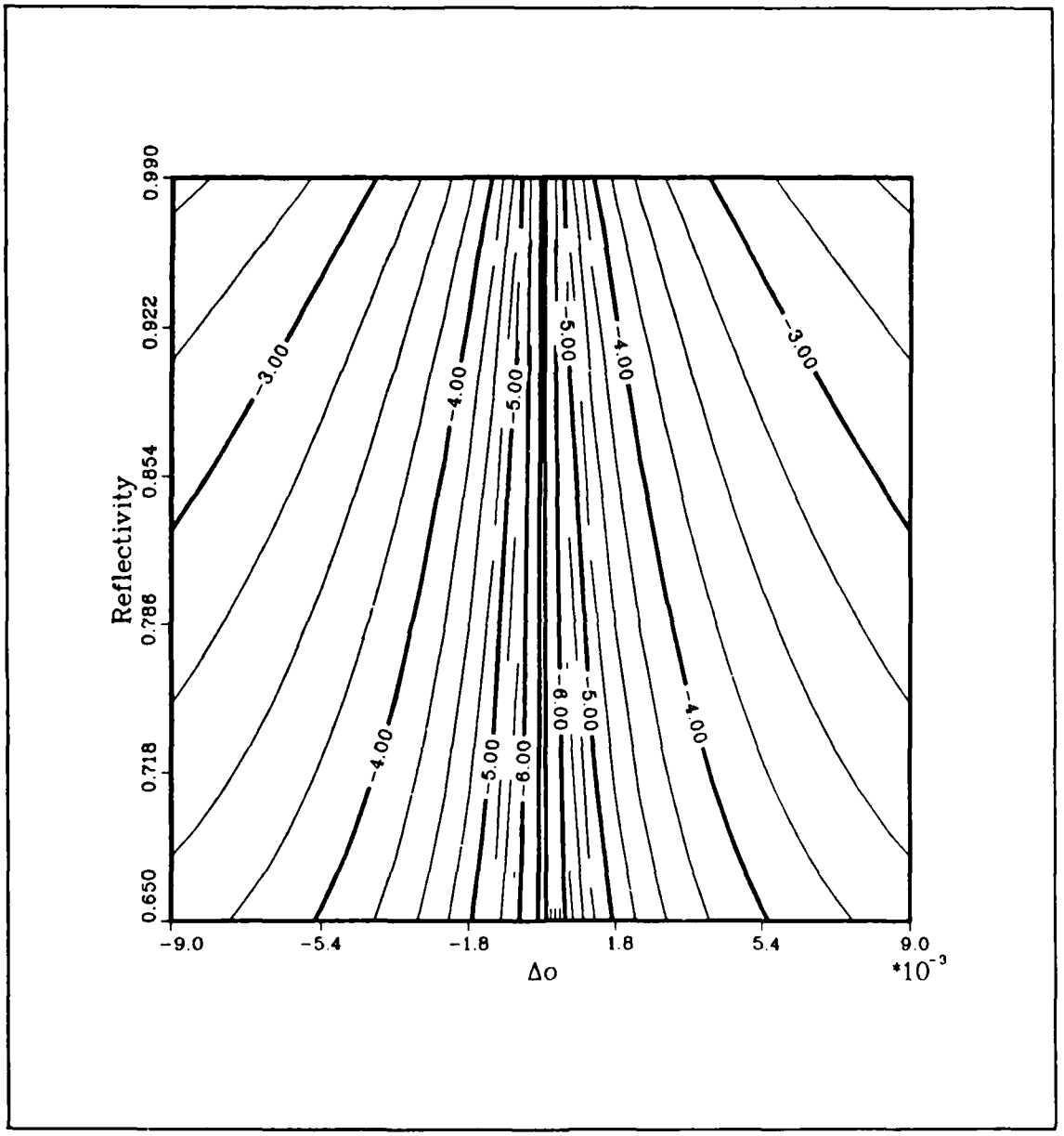

Figure C.18. $\log_{10} I_I$ contours at the MII point (data set 27).

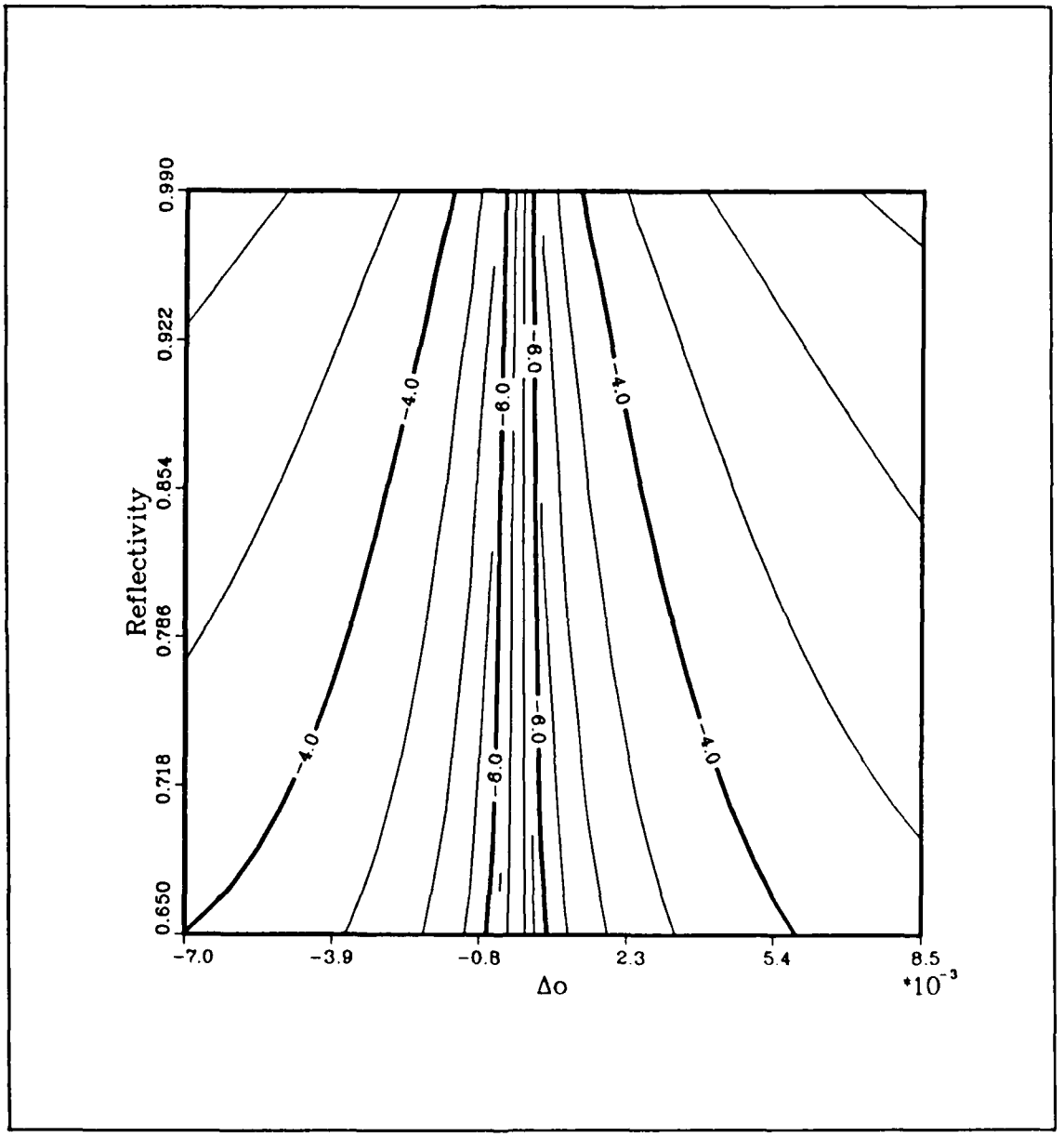

Figure C.19. $\log_{10} I_I$ contours at the MII point (data set 36).

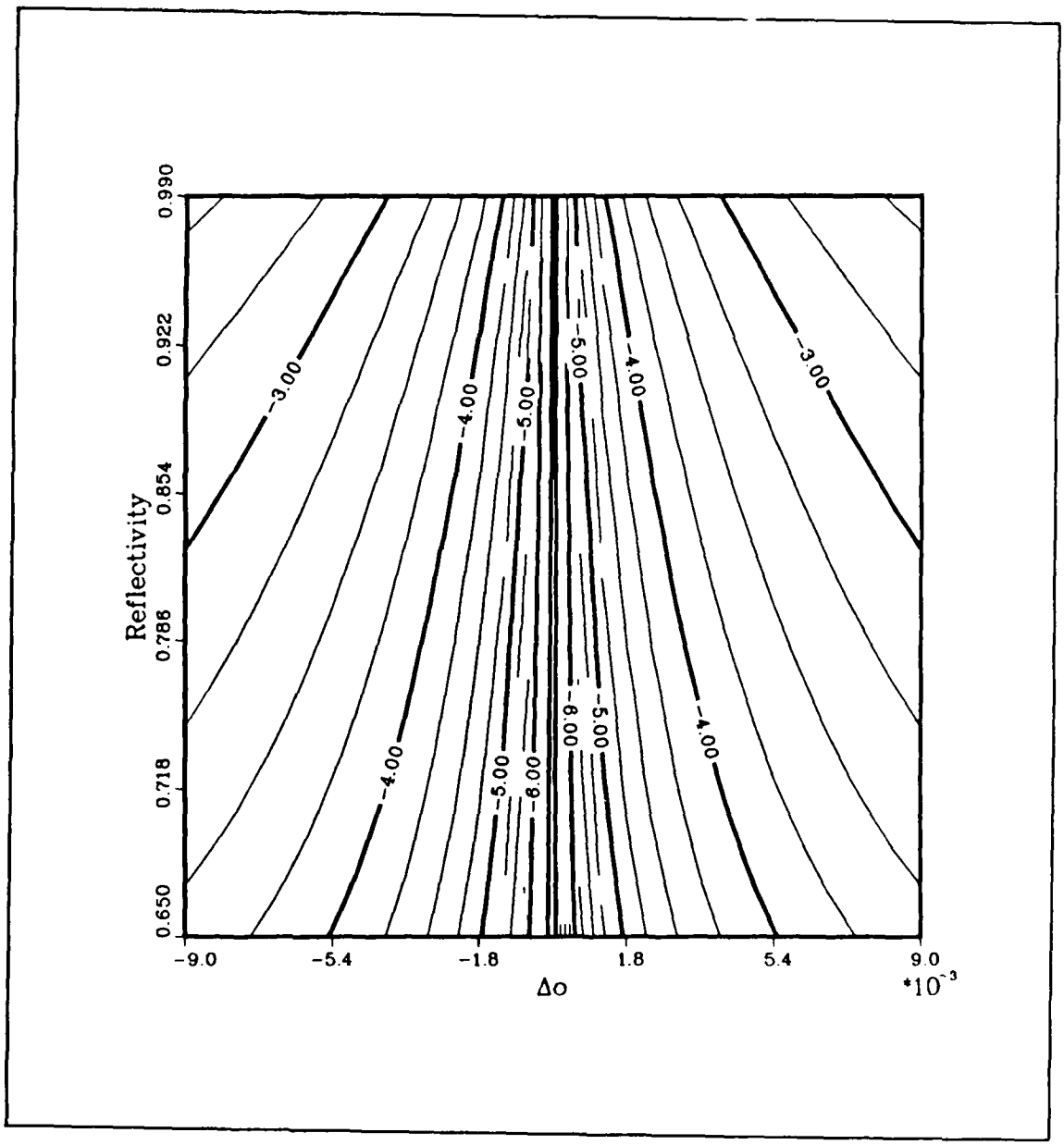

Figure C.20. $\log_{10} I_I$ contours at the MG1 point (data set 27).

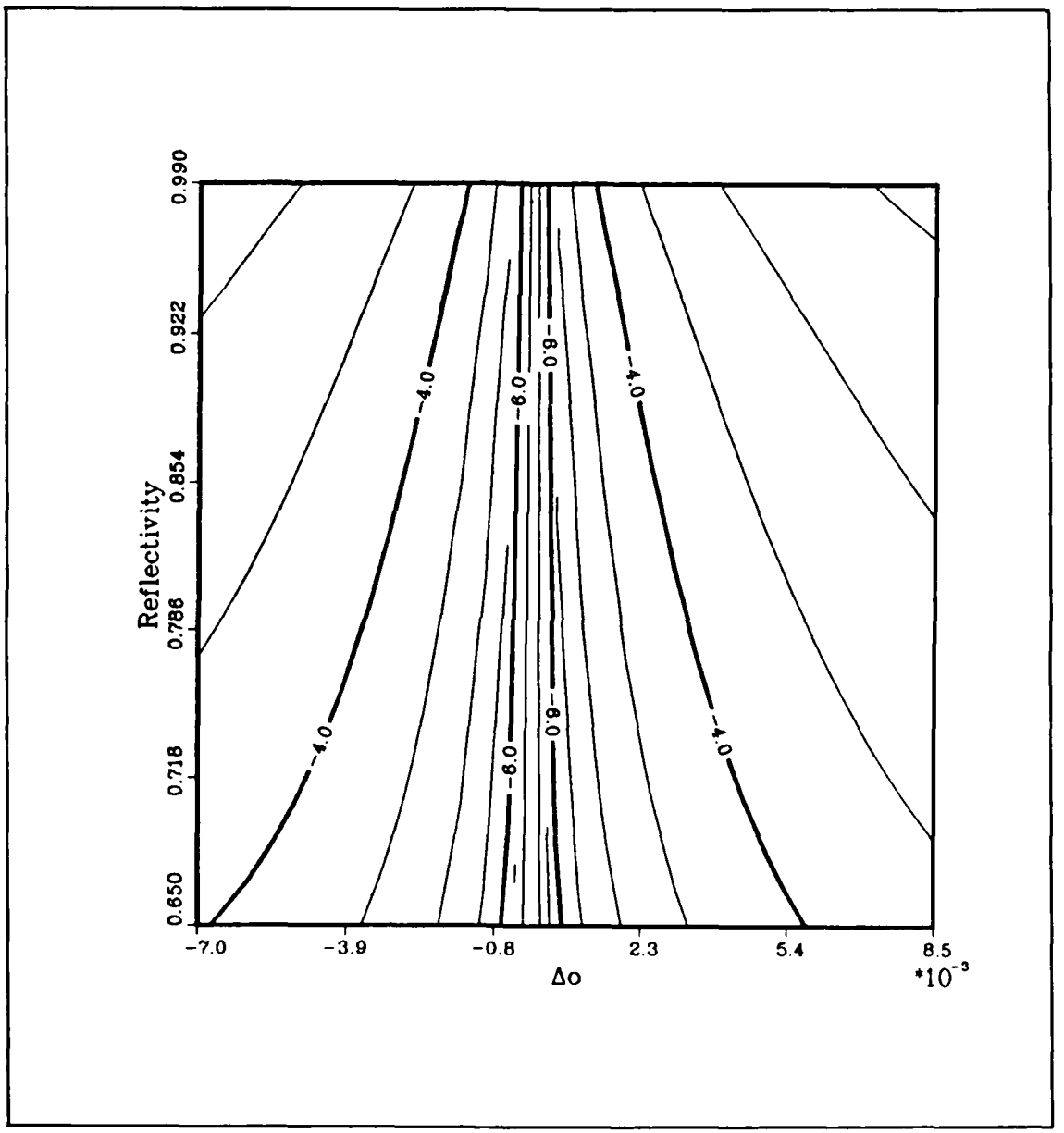

Figure C.21. $\log_{10} I_I$ contours at the MG1 point (data set 36).

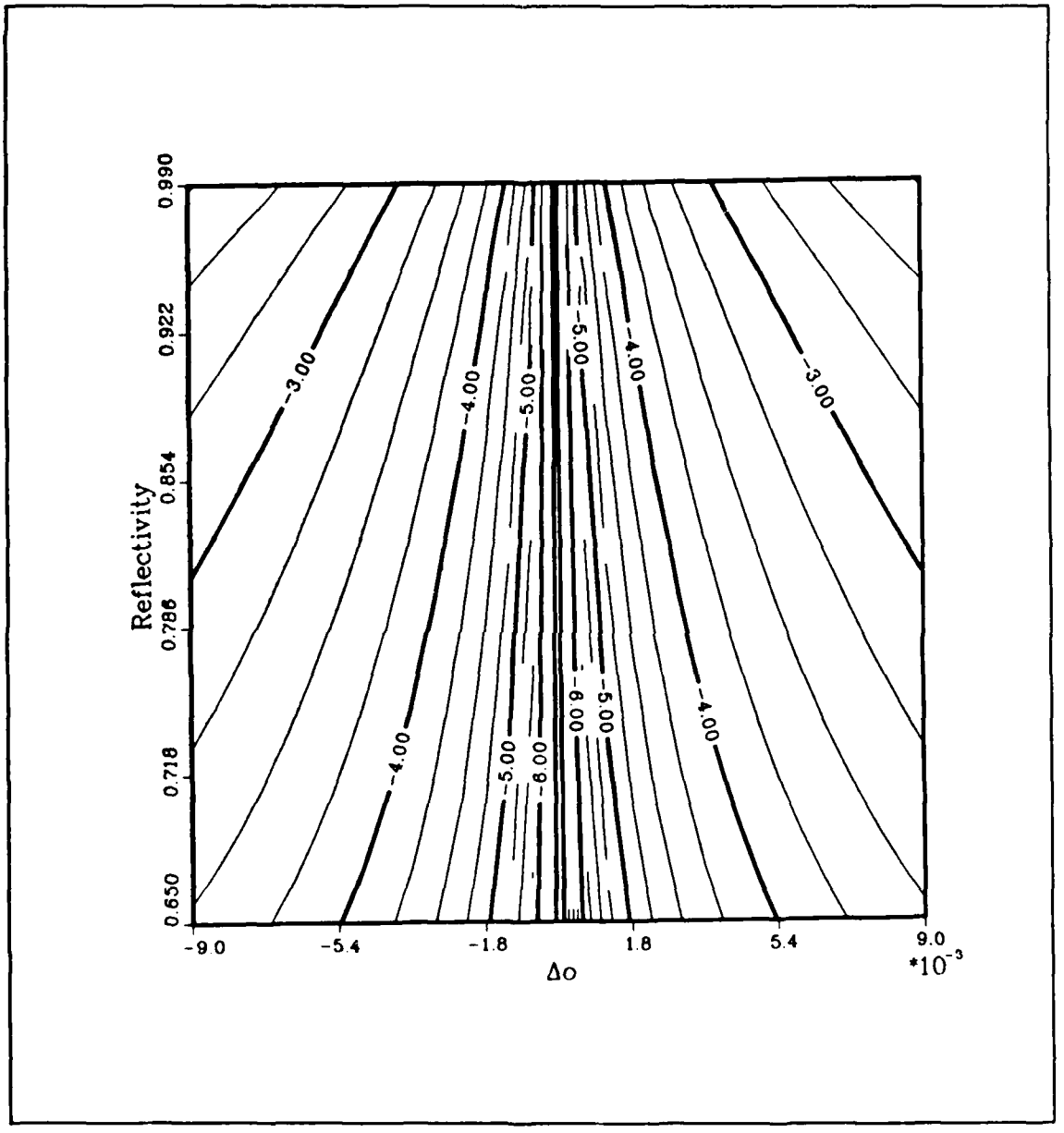

Figure C.22. $\log_{10} I_I$ contours at the MG2 point (data set 27). The data is from the region in the $(\Delta\hat{o}, r_D)$ plane where the cubic curves retain the s-shape.

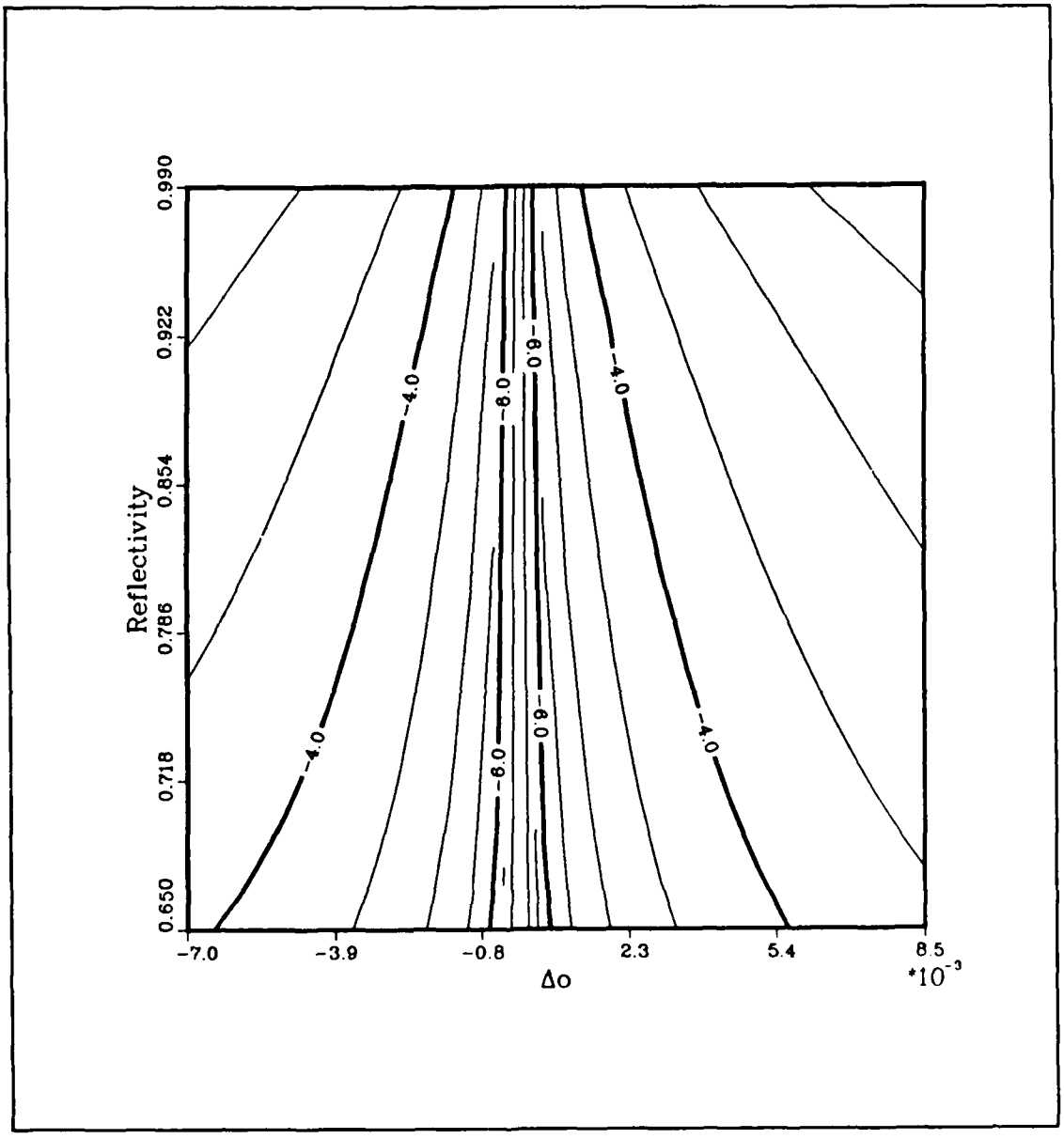

Figure C.23. $\log_{10} I_I$ contours at the MG2 point (data set 36). The data is from the region in the $(\Delta\hat{o}, r_B)$ plane where the cubic curves retain the s-shape.

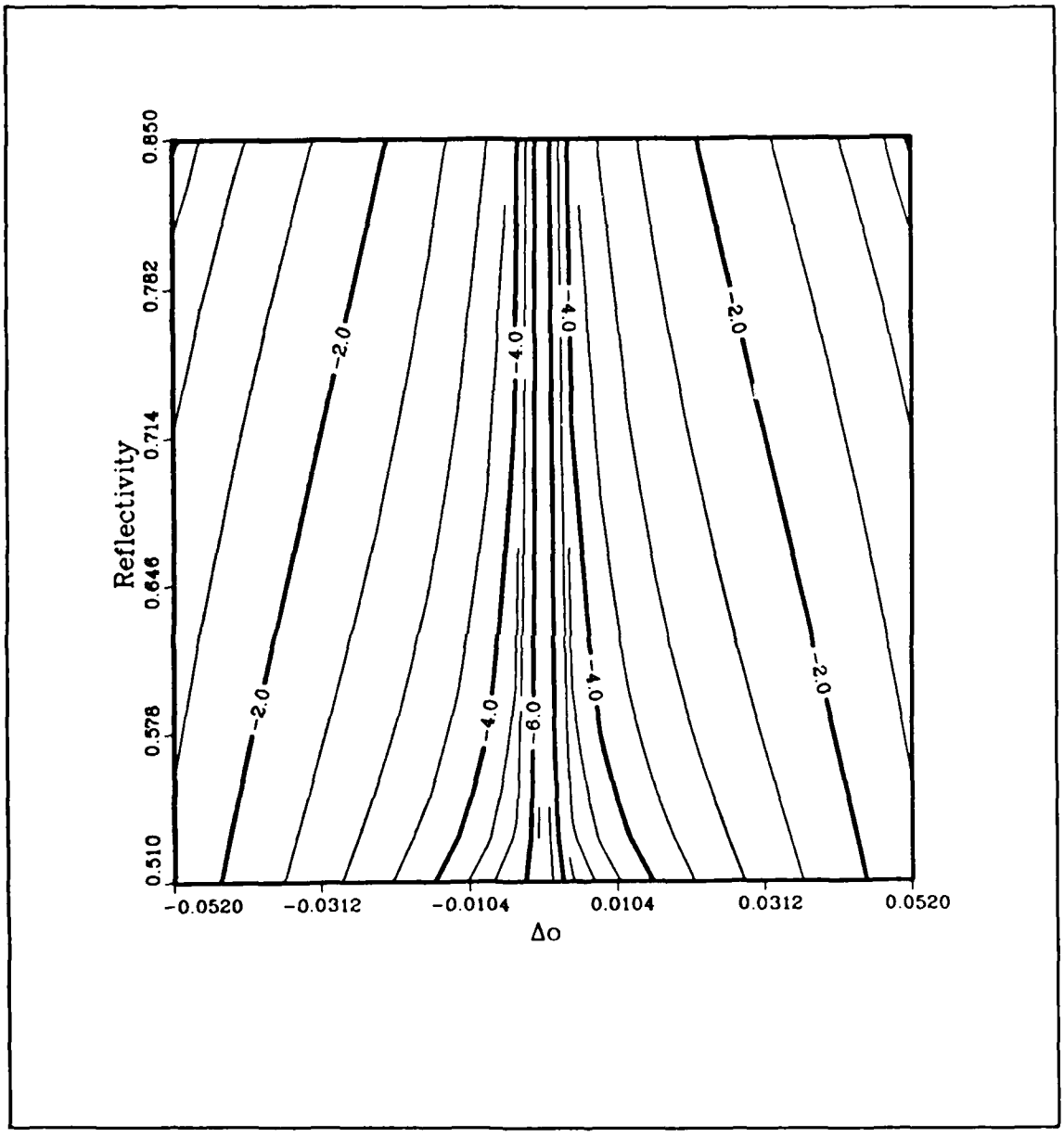

Figure C.24. $\log_{10} I_I$ contours at the MG2 point (data set 27). The data is from as large a rectangular region in the $(\Delta\hat{o}, r_D)$ plane as possible.

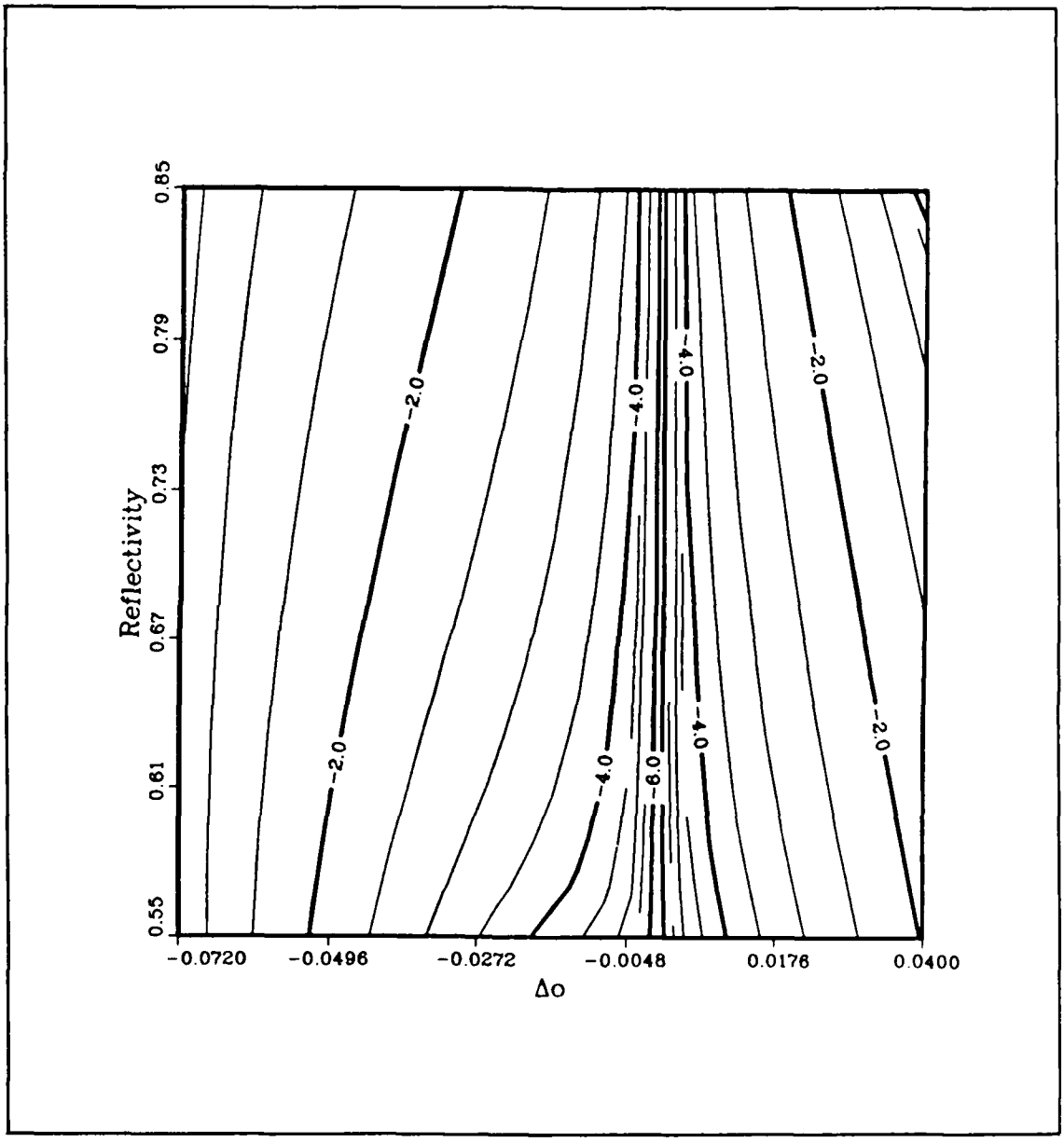

Figure C.25. $\log_{10} I_I$ contours at the MG2 point (data set 36). The data is from as large a rectangular region in the $(\Delta\hat{o}, r_B)$ plane as possible.

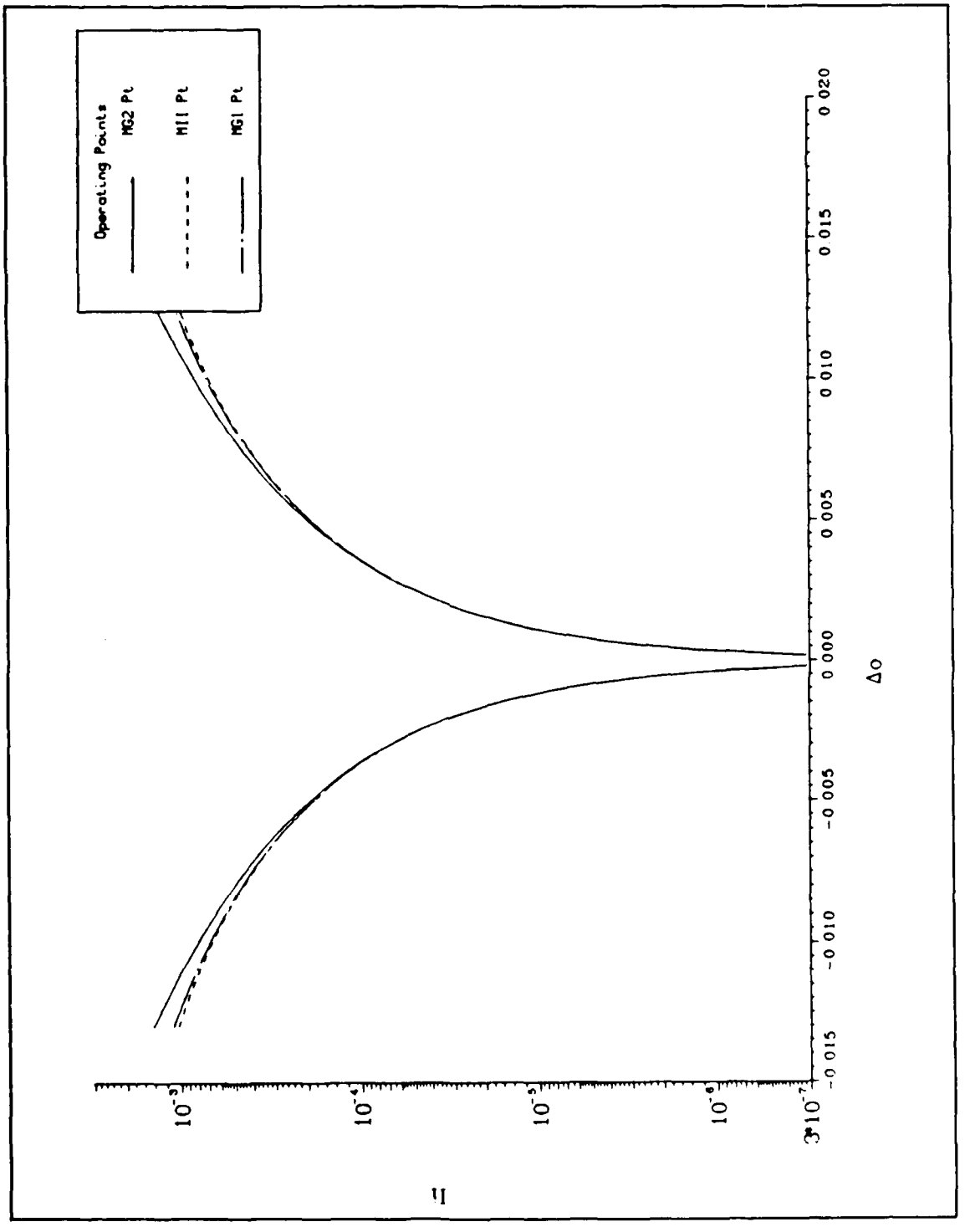

Figure C.26. I_I vs $\Delta\hat{o}$ (data set 27). $r_B = 0.75$. Curves for the three operating points are displayed in the figure.

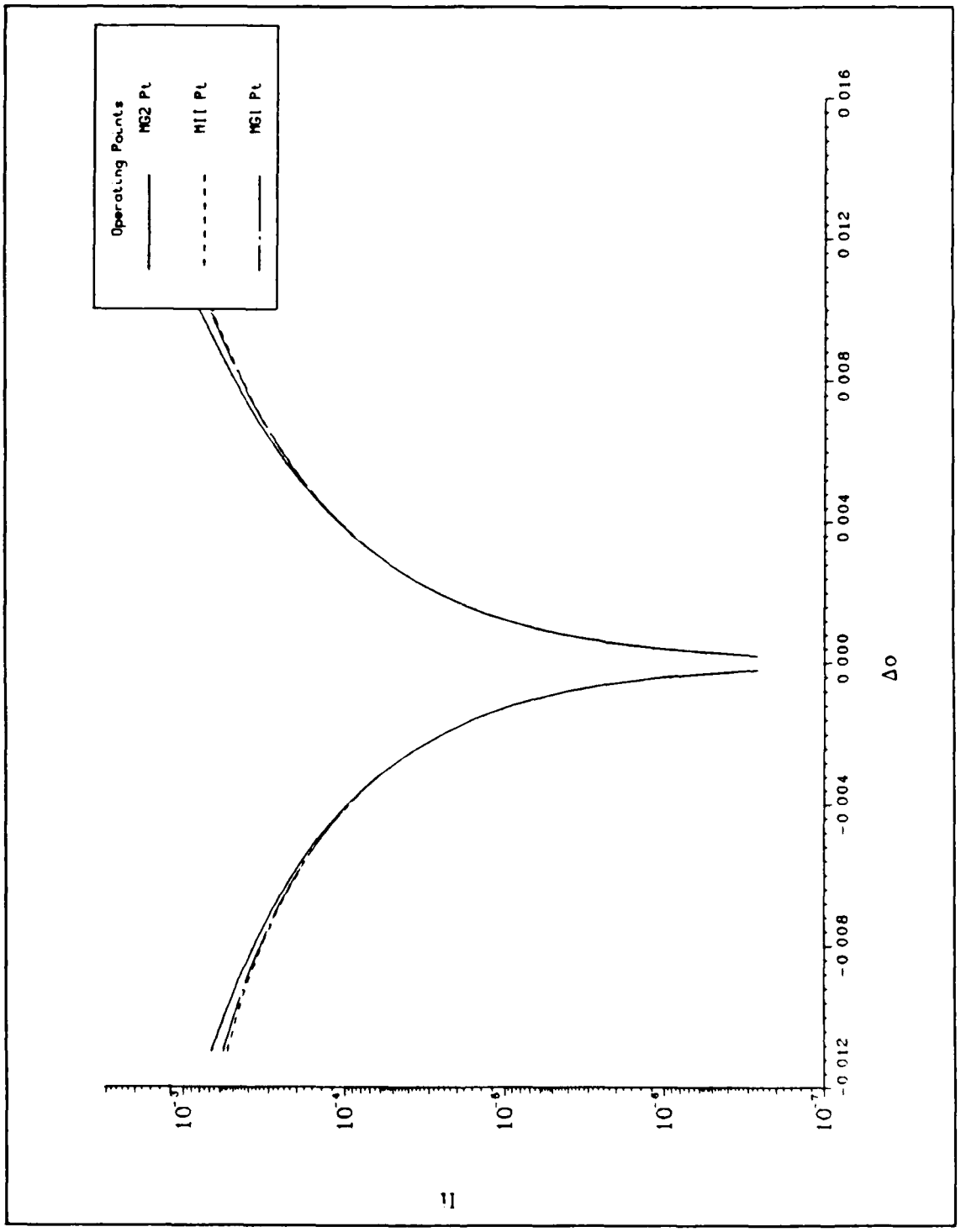

Figure C.27. I_J vs $\Delta\hat{o}$ (data set 36). $r_B = 0.75$. Curves for the three operating points are displayed in the figure.

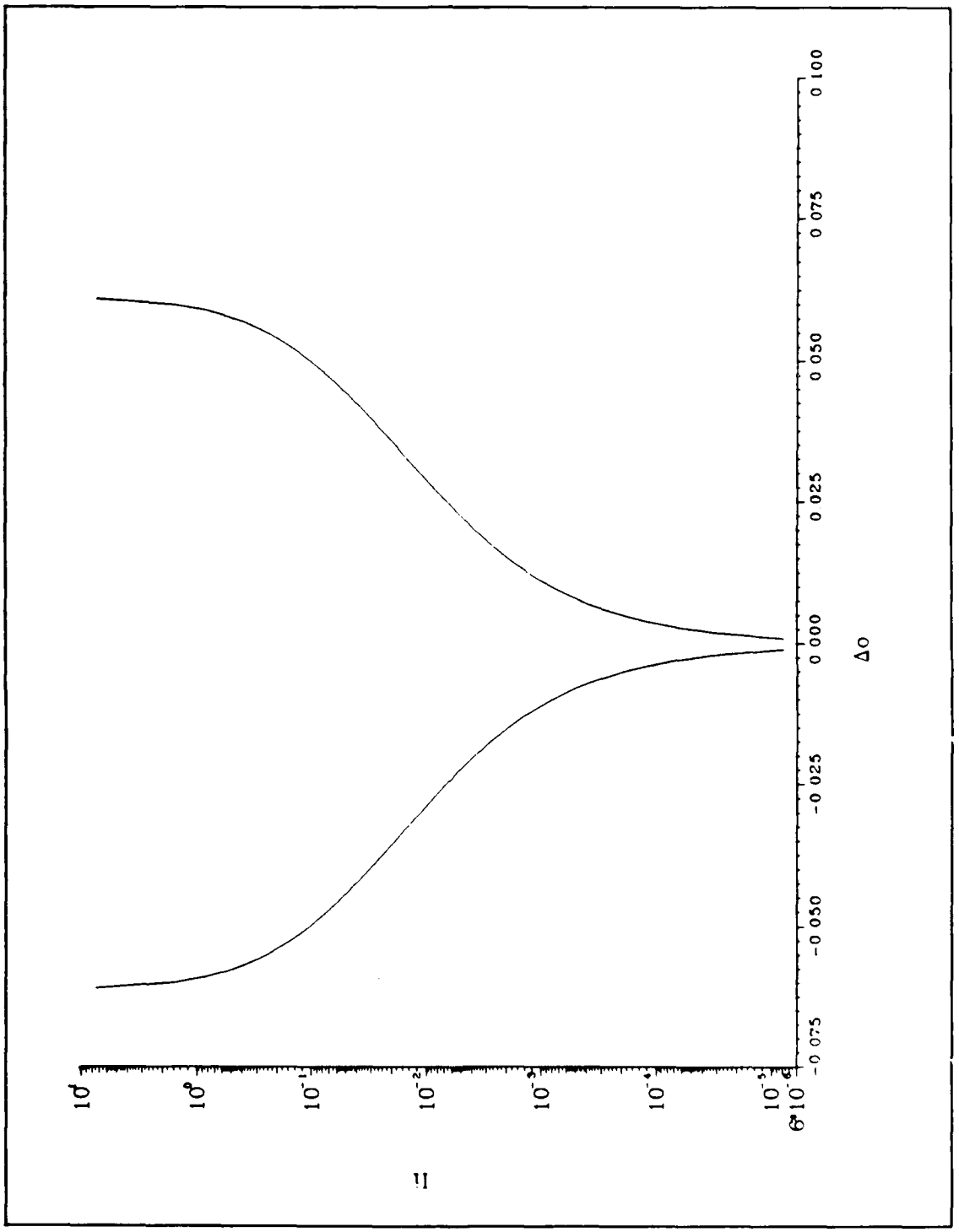

Figure C.28. I_I vs $\Delta\delta$ (data set 27). $r_B = 0.75$. The curve is taken from the MG2 operating point data.

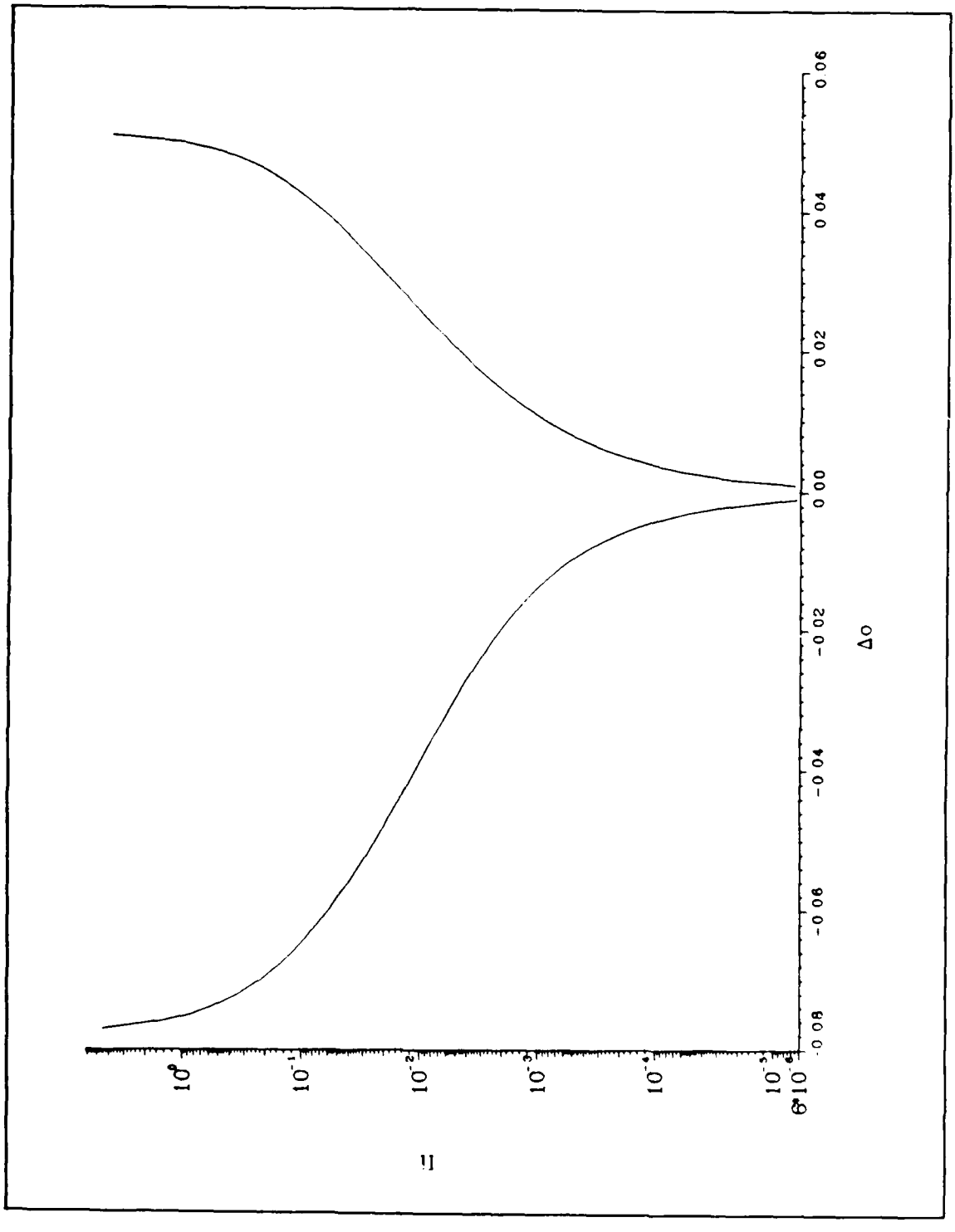

Figure C 29. I_I vs $\Delta\hat{o}$ (data set 36). $r_B = 0.75$. The curve is taken from the MG2 operating point data.

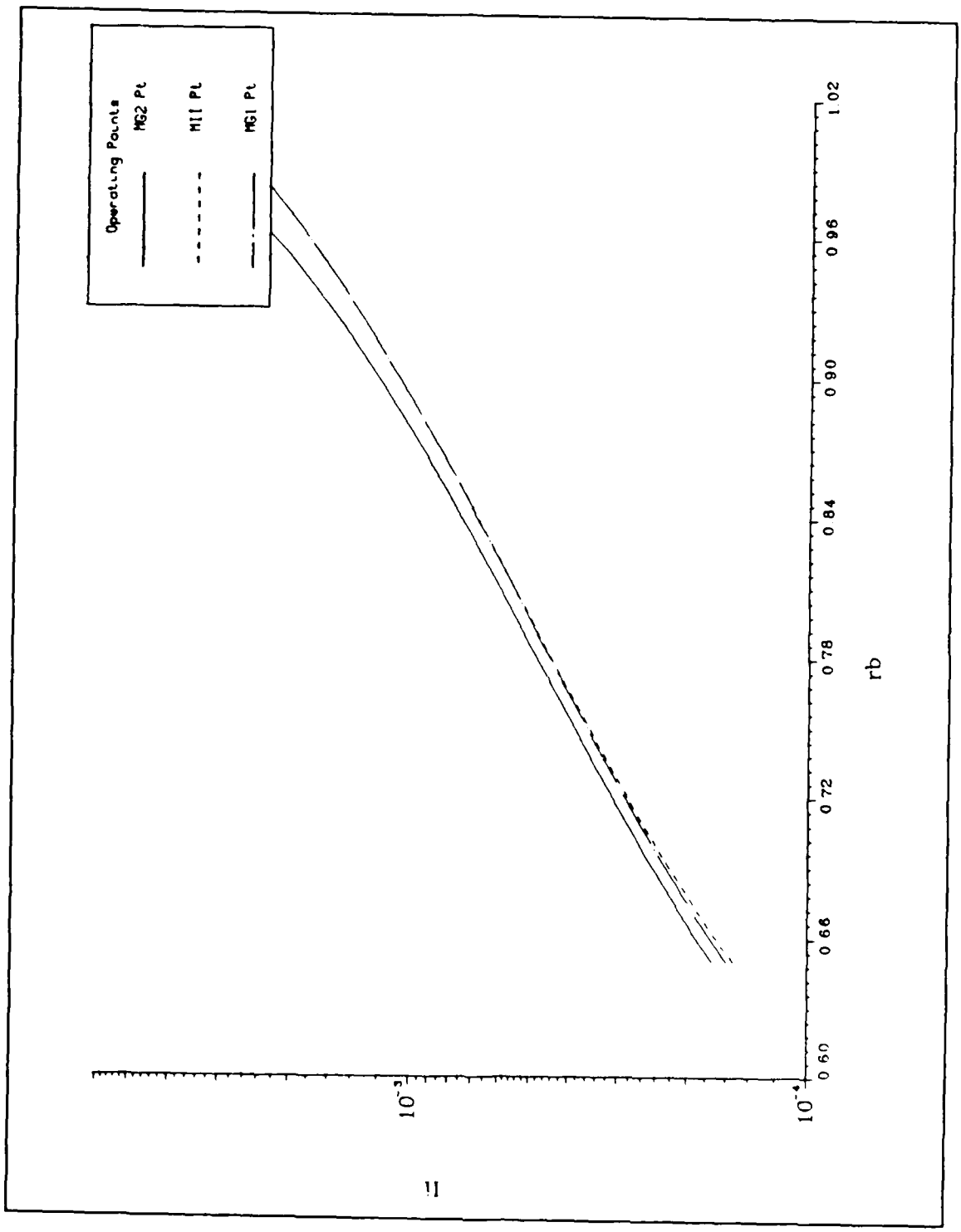

Figure C.30. I_I vs r_B (data set 27). $\Delta\delta$ 0.007. Curves for the three operating points are displayed in the figure.

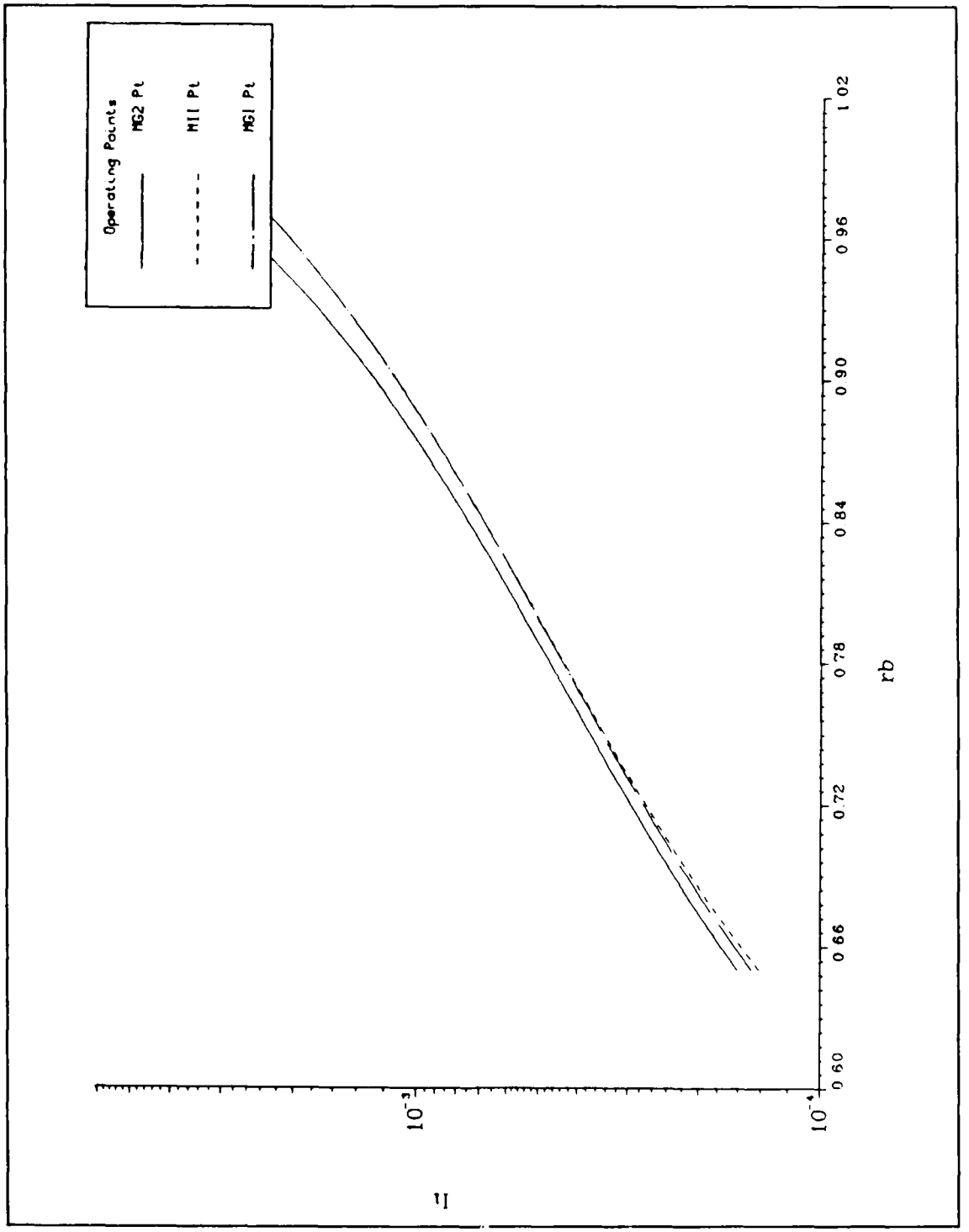

Figure C.31. I_I vs r_B (data set 36). $\Delta\hat{o} = 0.007$. Curves for the three operating points are displayed in the figure.

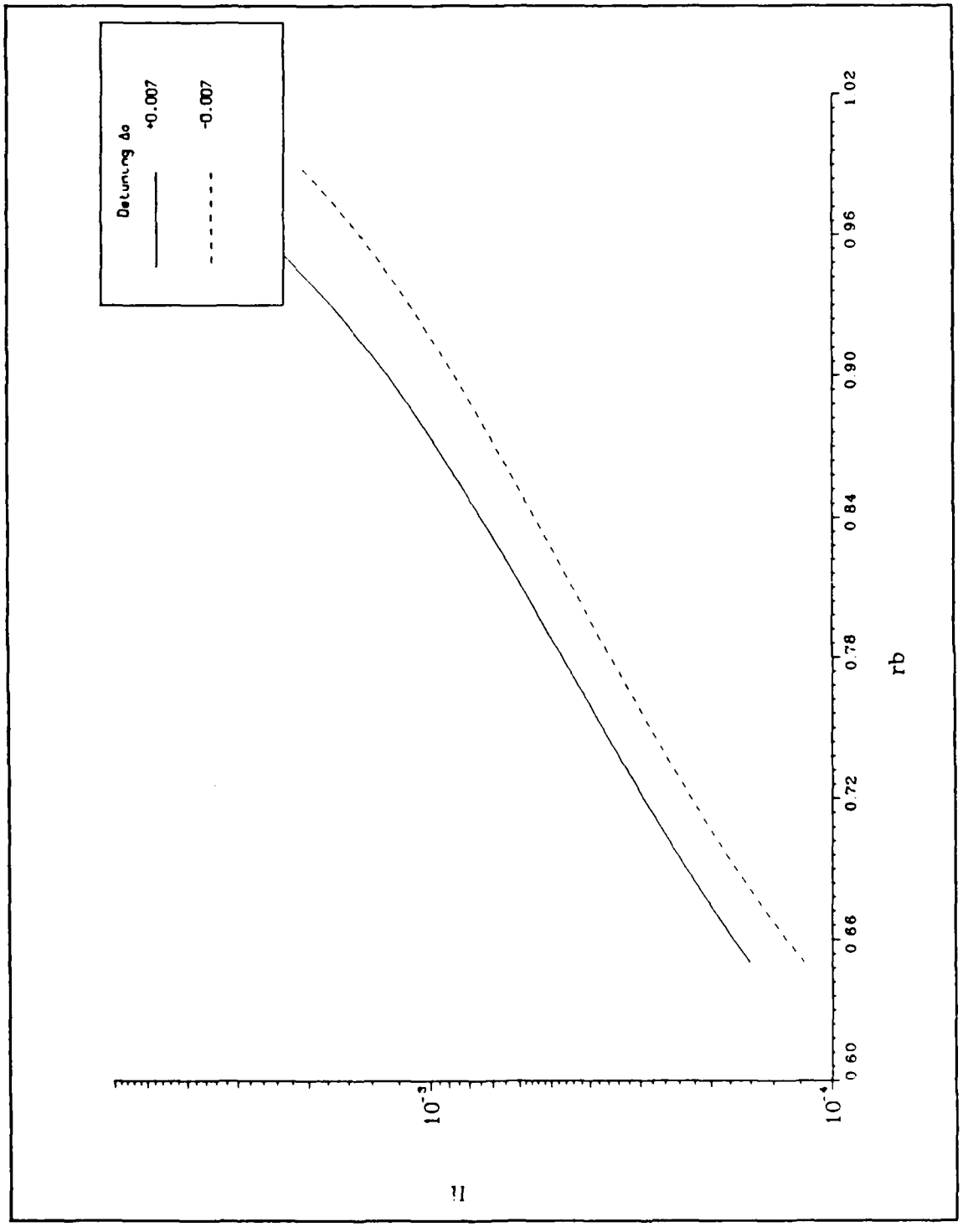

Figure C.32. I_I vs r_B (data set 36). $\Delta\hat{o} = \pm 0.007$. The curves are taken from the MG2 operating point data.

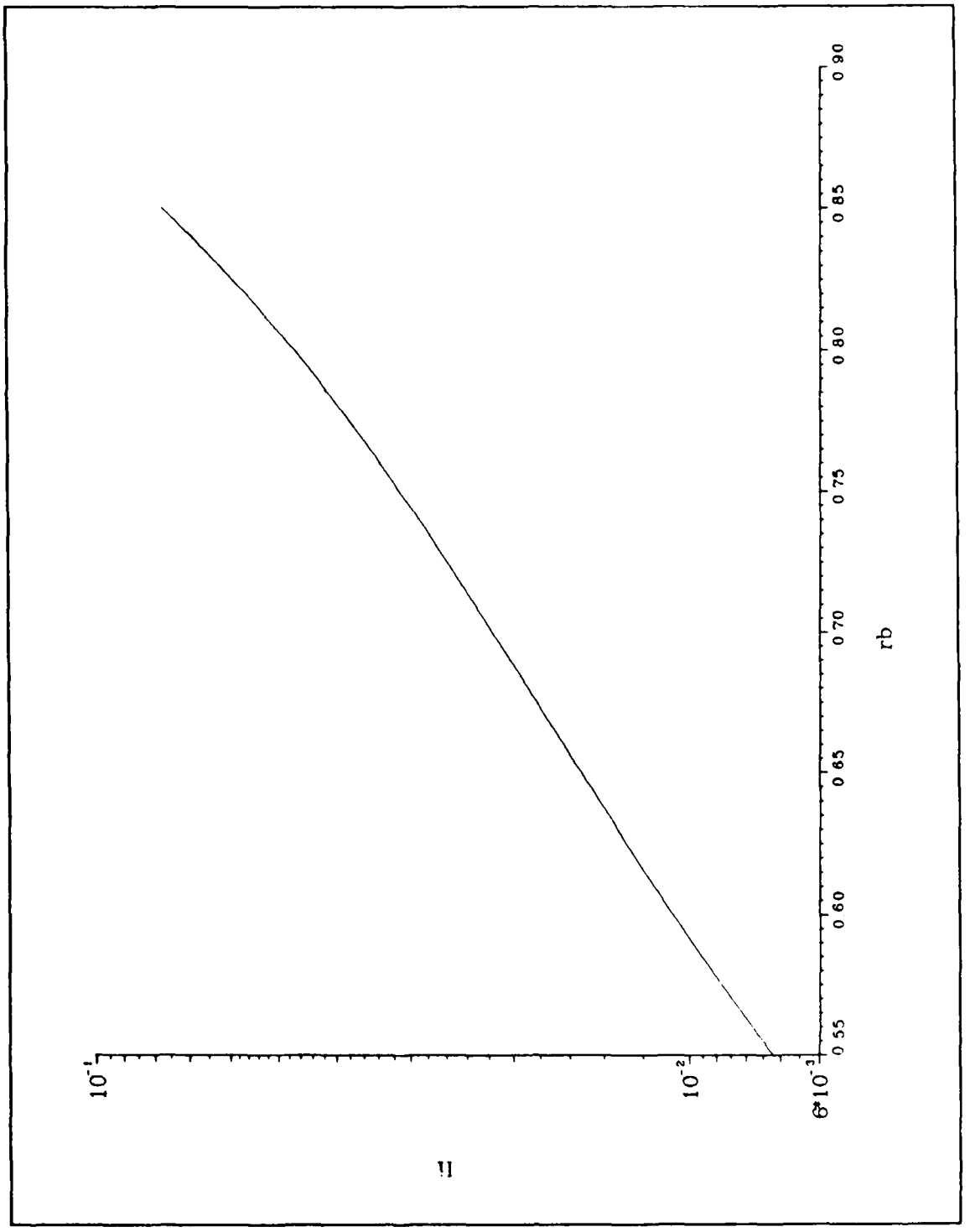

Figure C.33. I_I vs r_B (data set 27). $\Delta\hat{o} = 0.040$. The curve is taken from the MG2 operating point data.

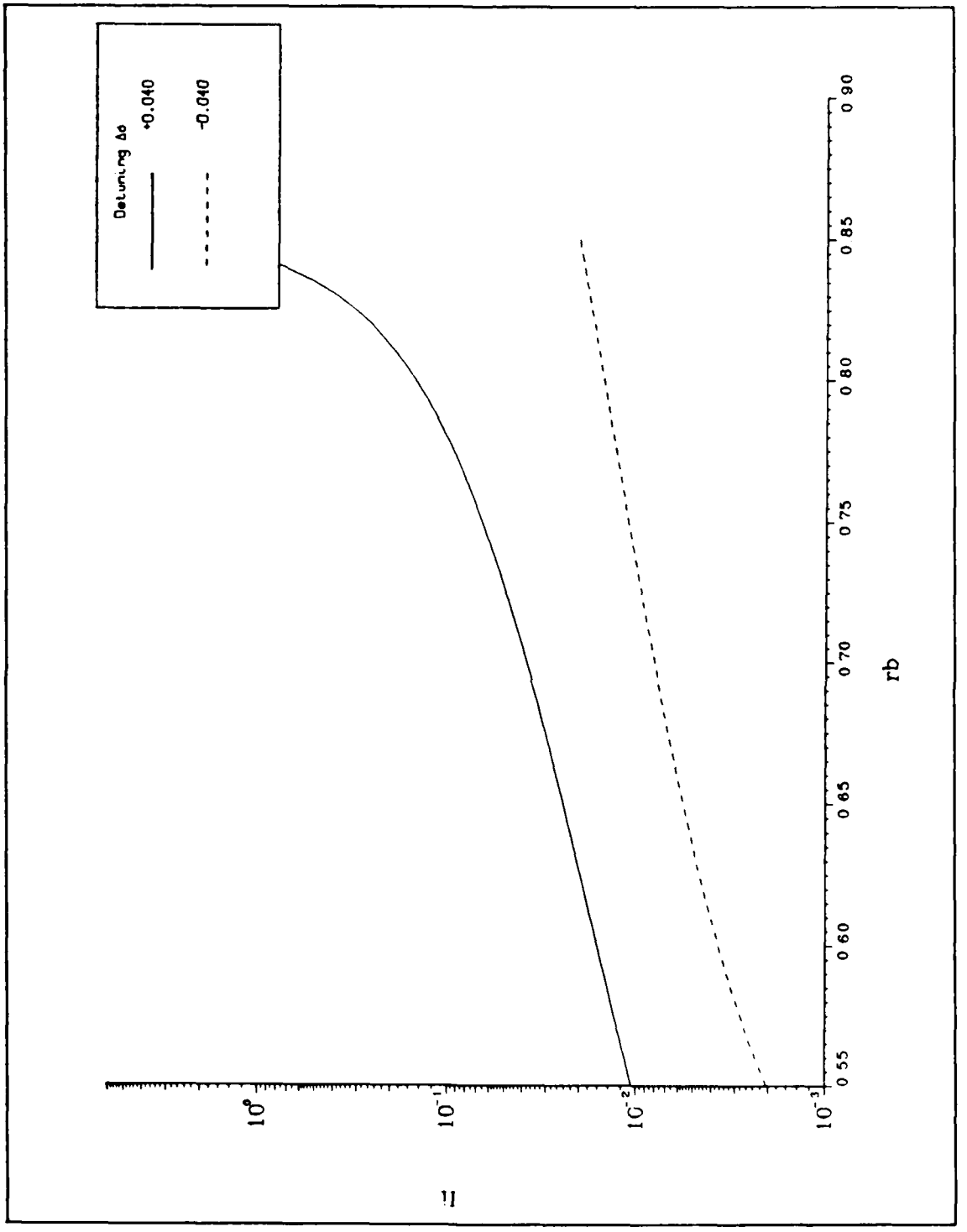

Figure C.34. I_I vs r_B (data set 36). $\Delta\hat{o} = \pm 0.040$. The curves are taken from the MG2 operating point data.

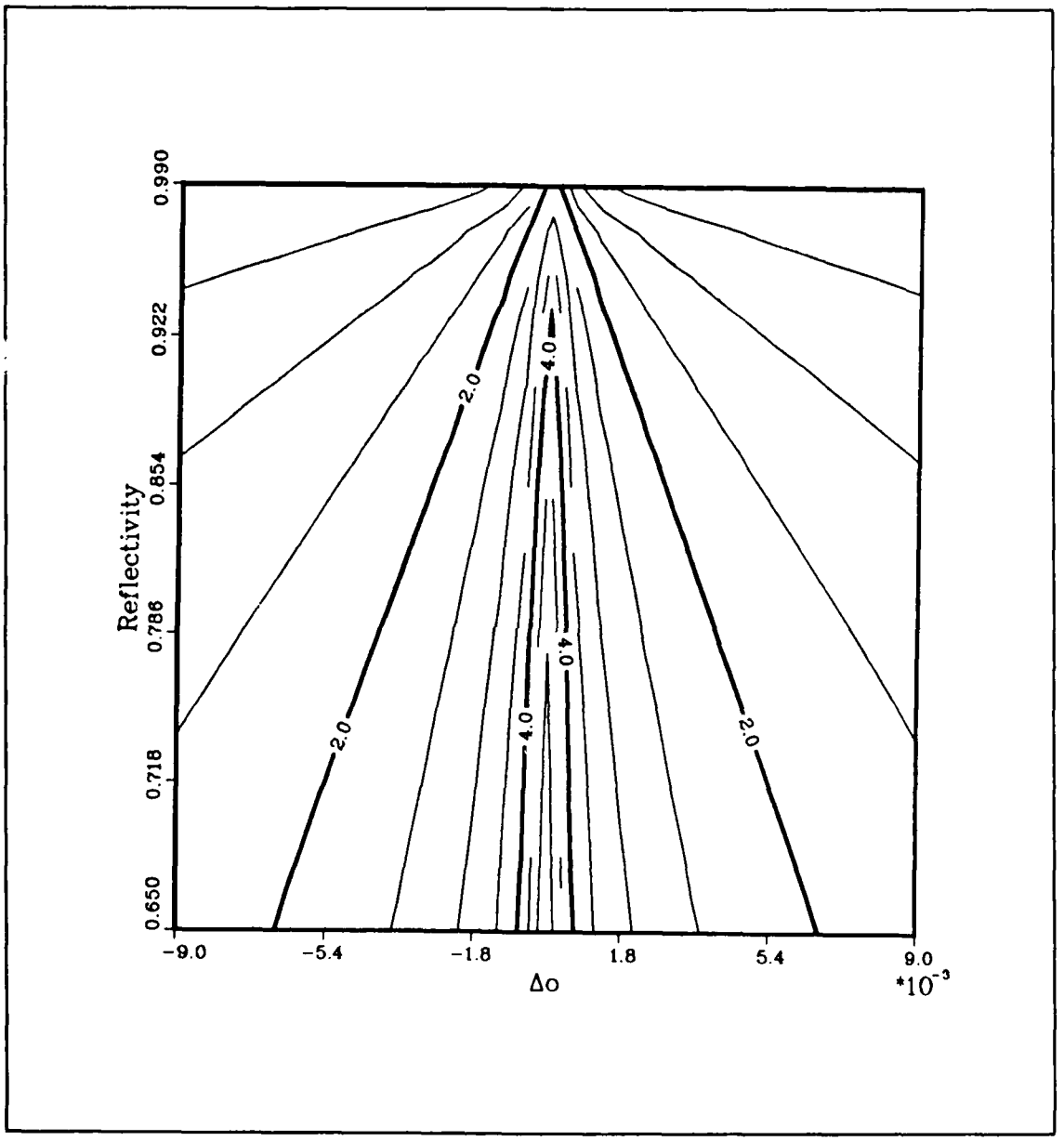

Figure C.35. $\log_{10} G_1$ contours at the MII point (data set 27).

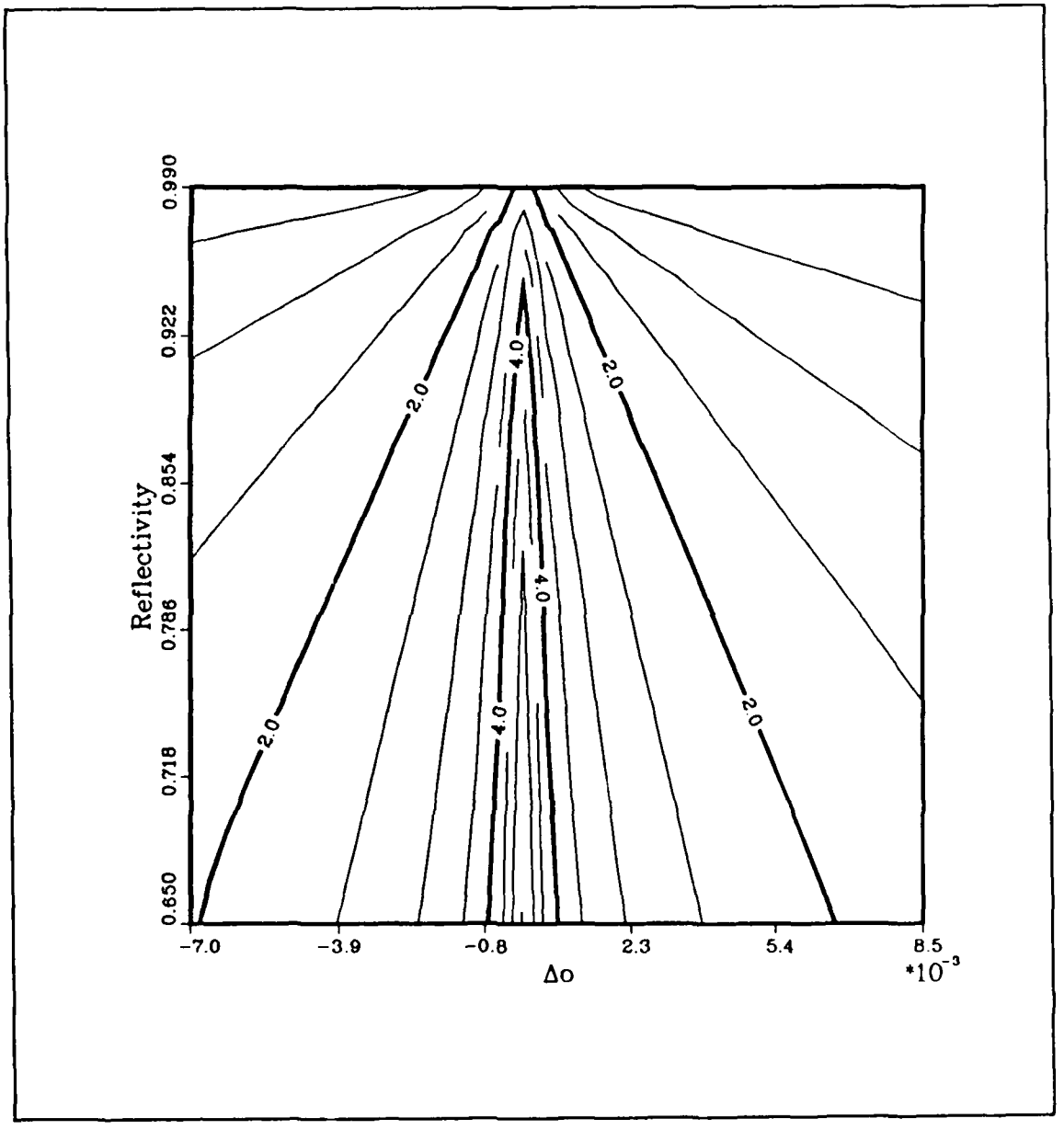

Figure C.36. $\log_{10} G_1$ contours at the MII point (data set 36).

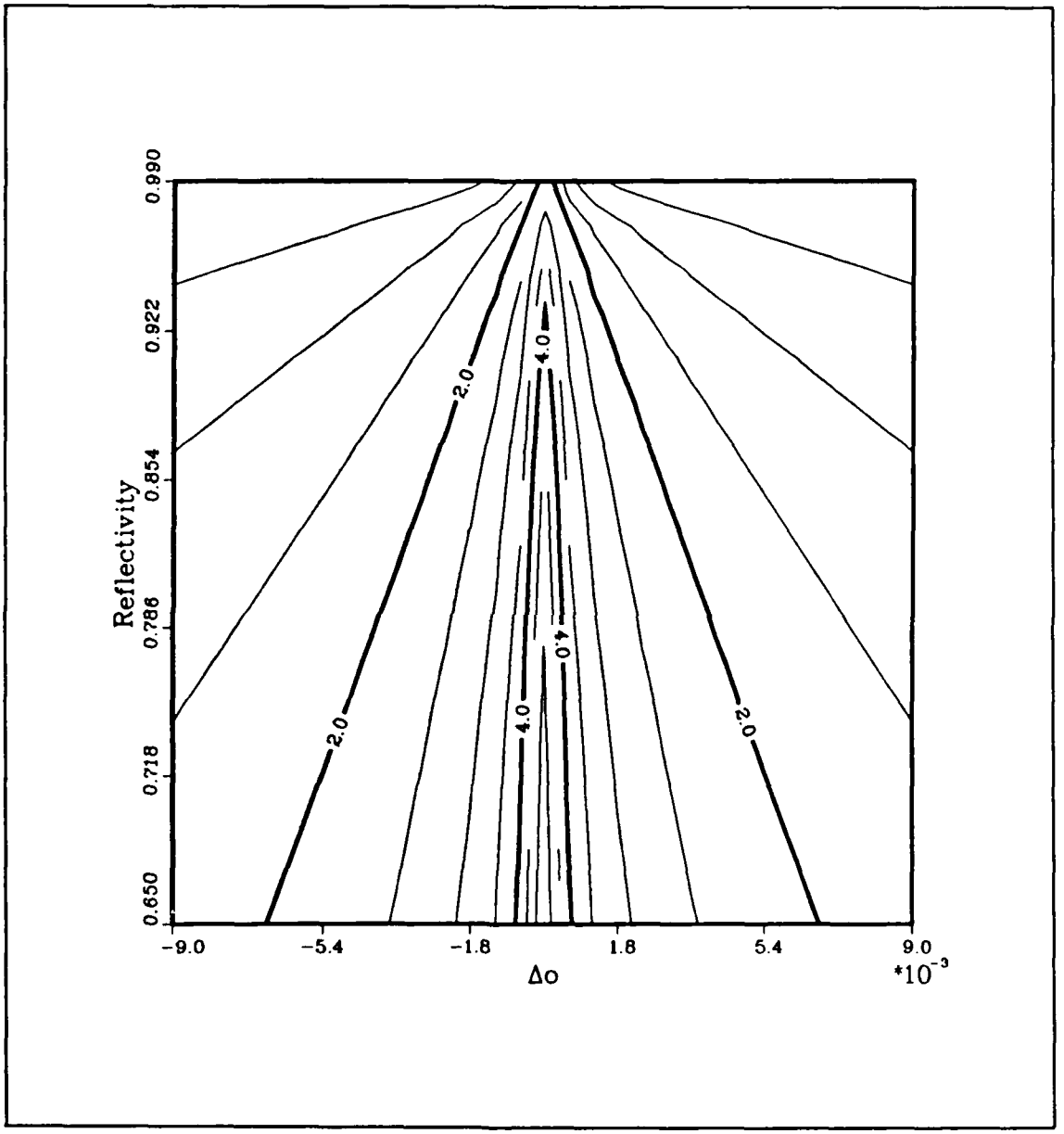

Figure C.37. $\log_{10} G_1$ contours at the MG1 point (data set 27).

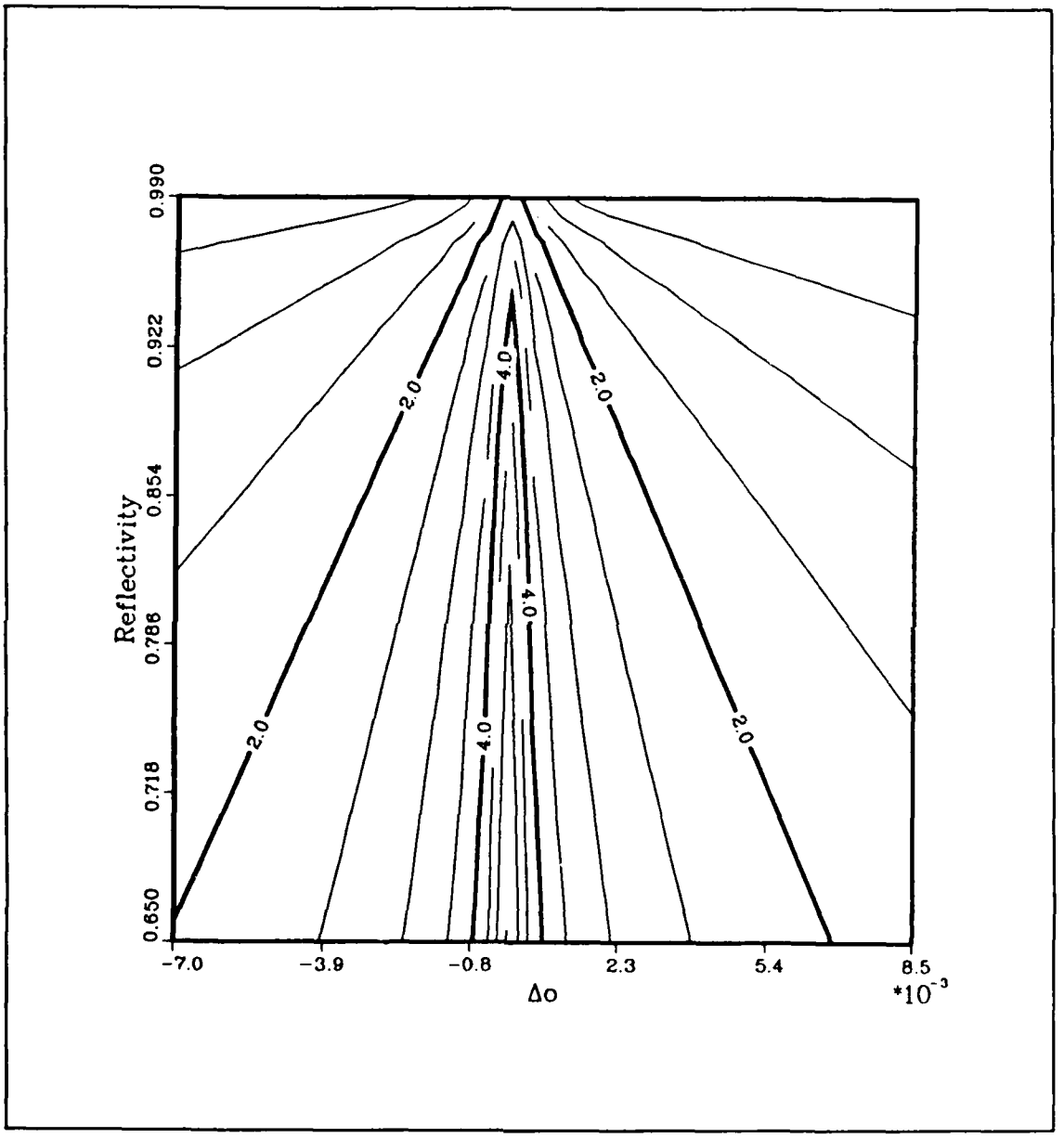

Figure C.38. $\log_{10} G_1$ contours at the MG1 point (data set 36).

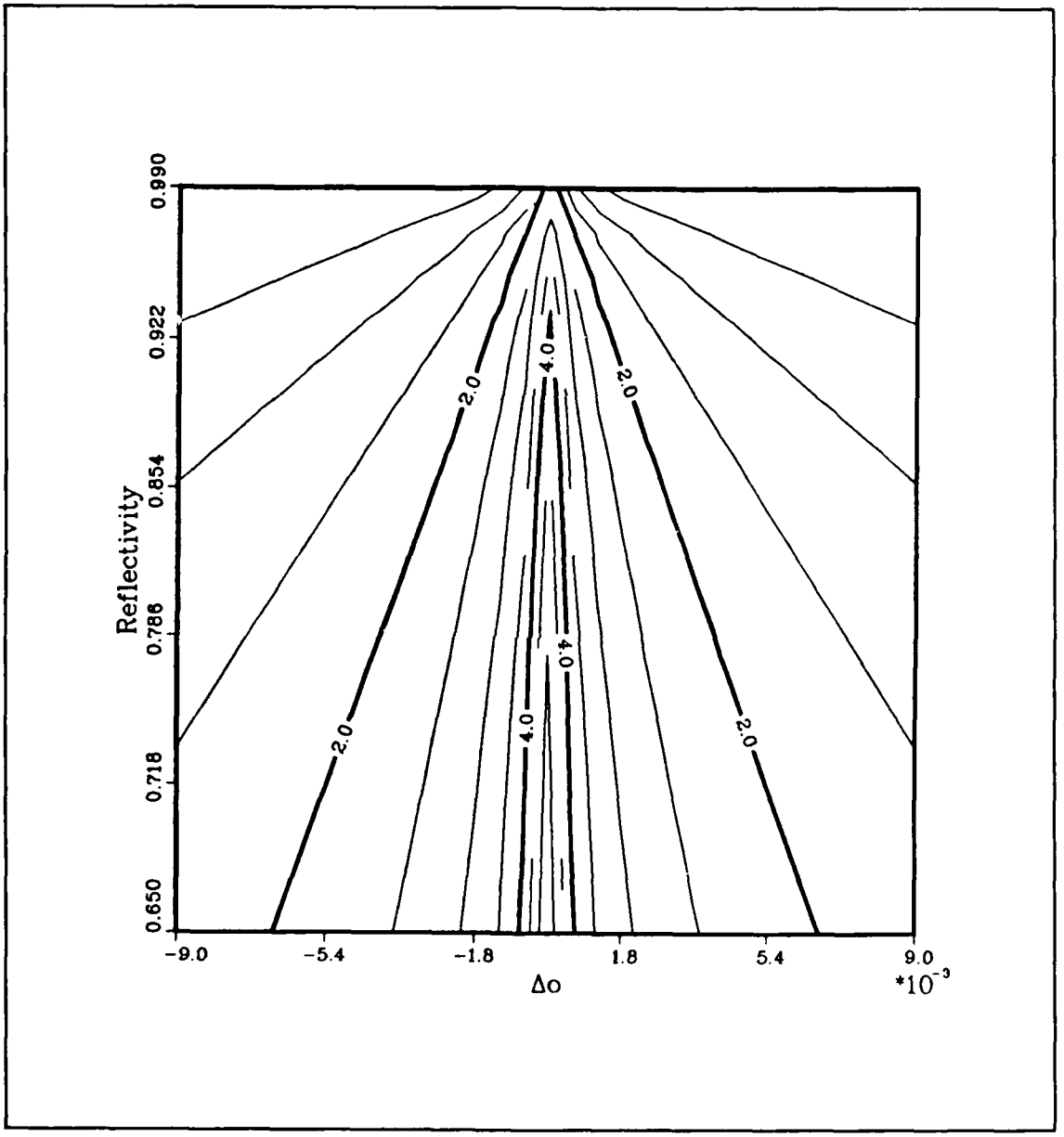

Figure C.39. $\log_{10} G_1$ contours at the MG2 point (data set 27). The data is from the region in the $(\Delta\delta, r_B)$ plane where the cubic curves retain the s-shape.

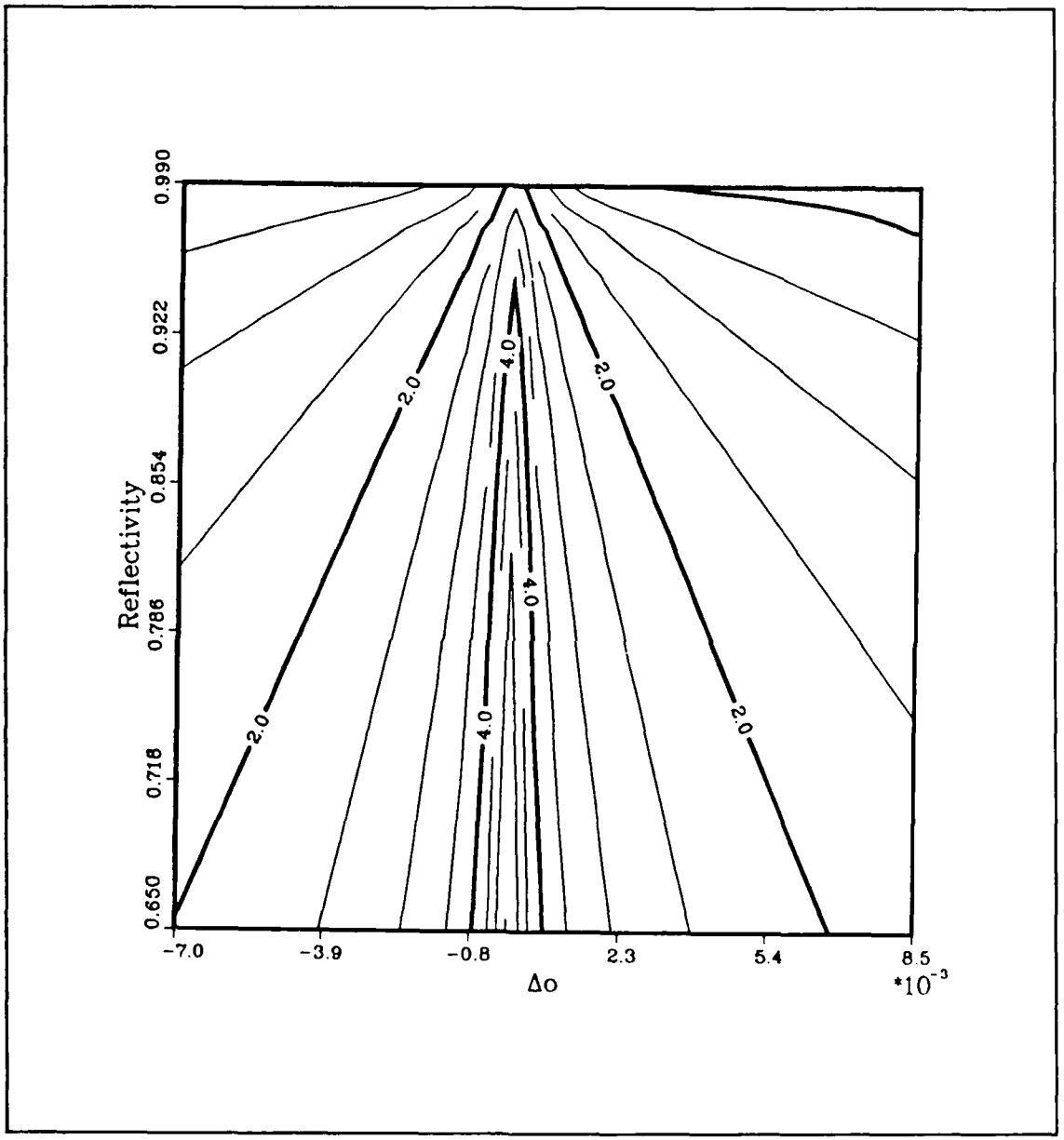

Figure C.40. $\log_{10} G_1$ contours at the MG2 point (data set 36). The data is from the region in the $(\Delta\hat{o}, r_B)$ plane where the cubic curves retain the s-shape.

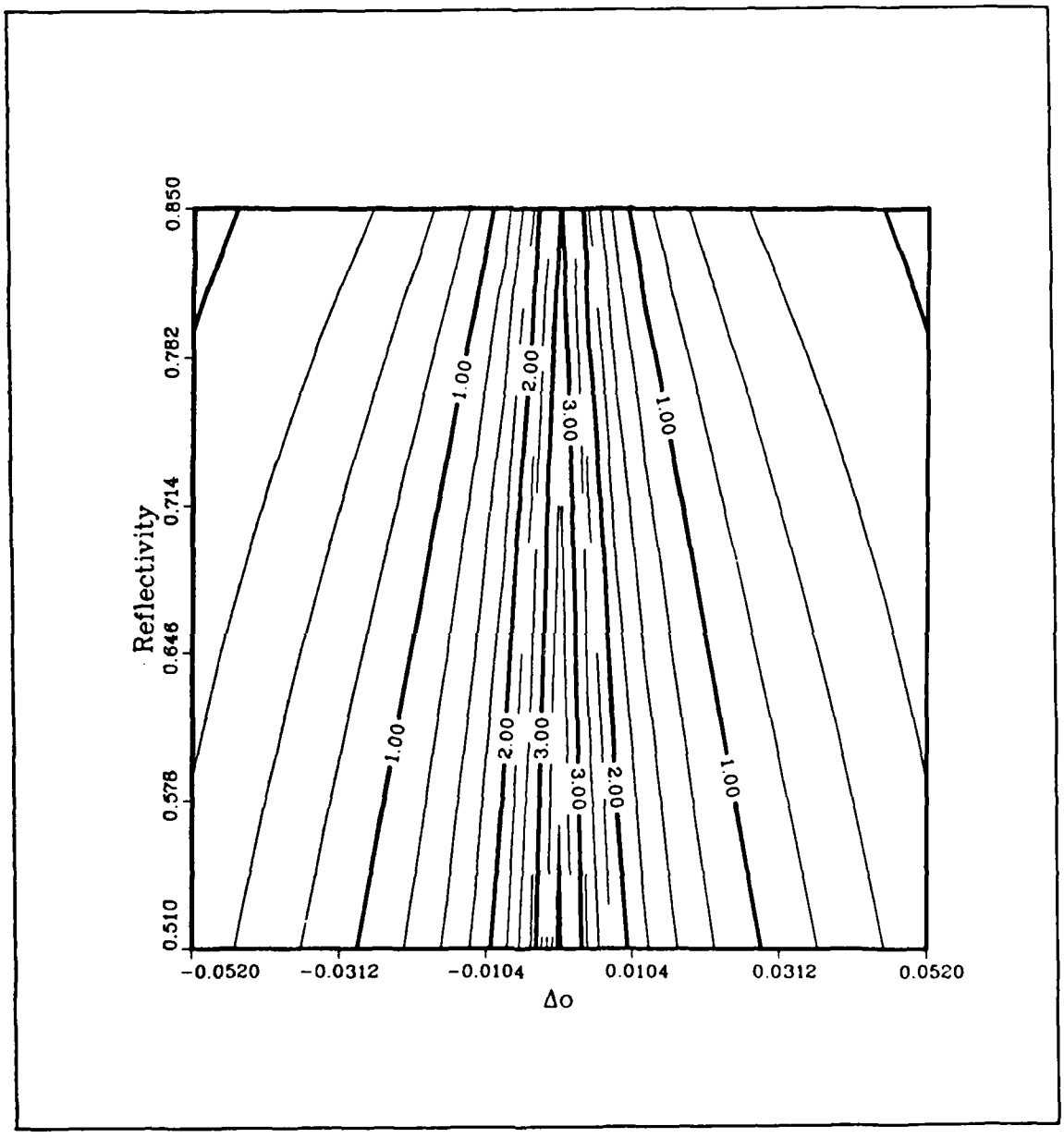

Figure C.41. $\log_{10} G_1$ contours at the MG2 point (data set 27). The data is from as large a rectangular region in the $(\Delta\hat{o}, r_B)$ plane as possible.

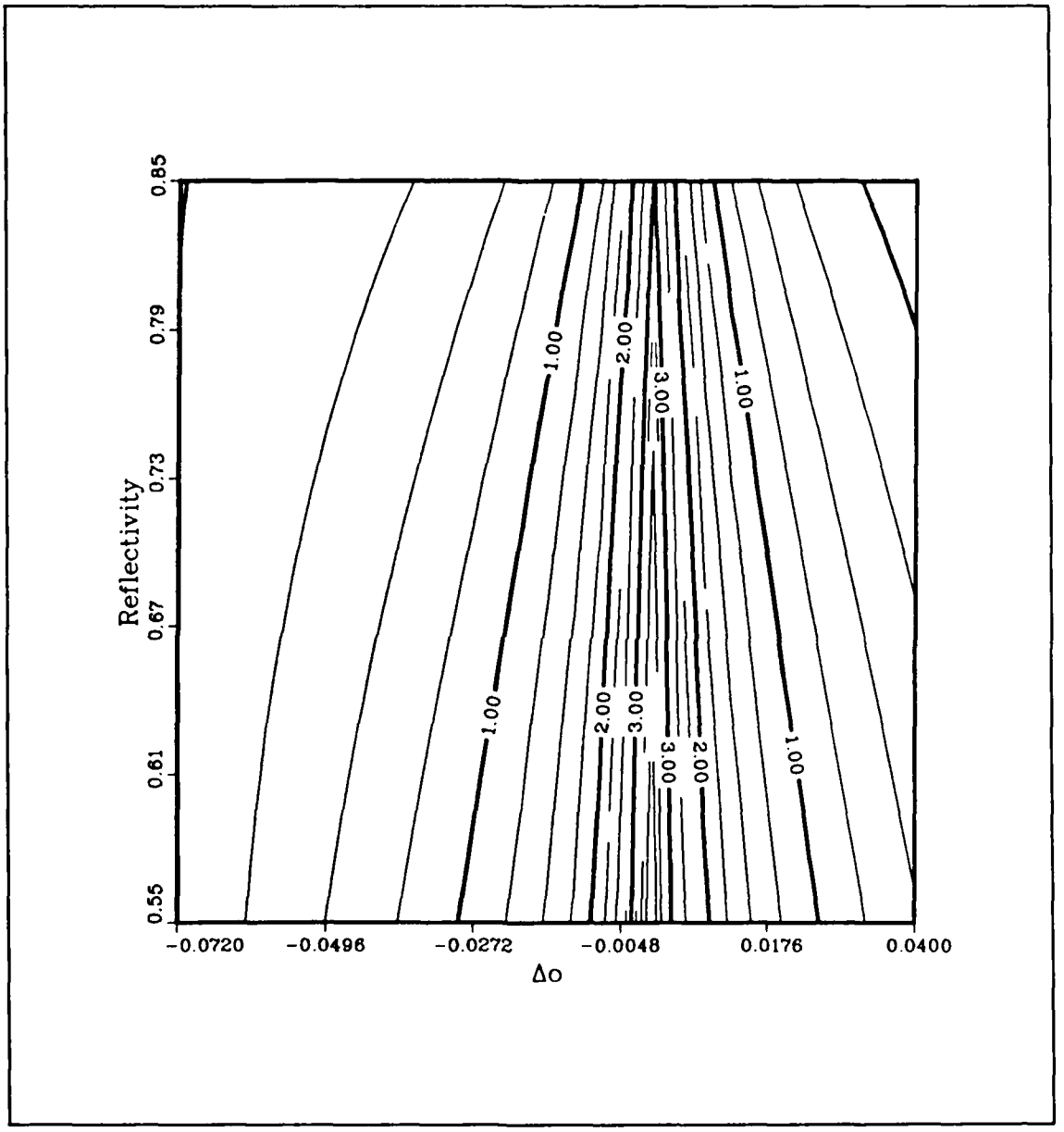

Figure C.42. $\log_{10} G_1$ contours at the MG2 point (data set 36). The data is from as large a rectangular region in the $(\Delta\delta, r_B)$ plane as possible.

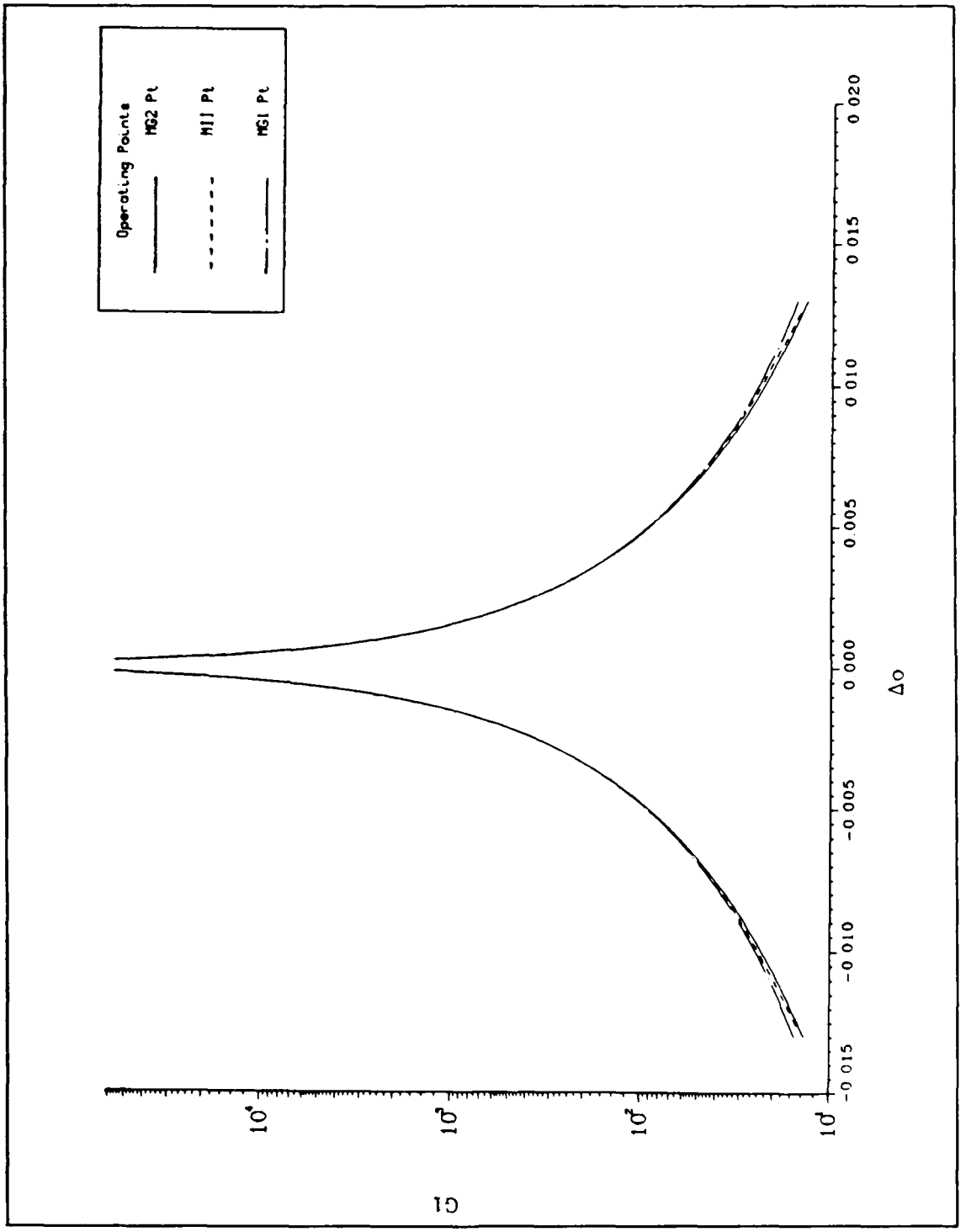

Figure C.43. G_1 vs $\Delta\hat{o}$ (data set 27). $r_B = 0.75$. Curves for the three operating points are displayed in the figure.

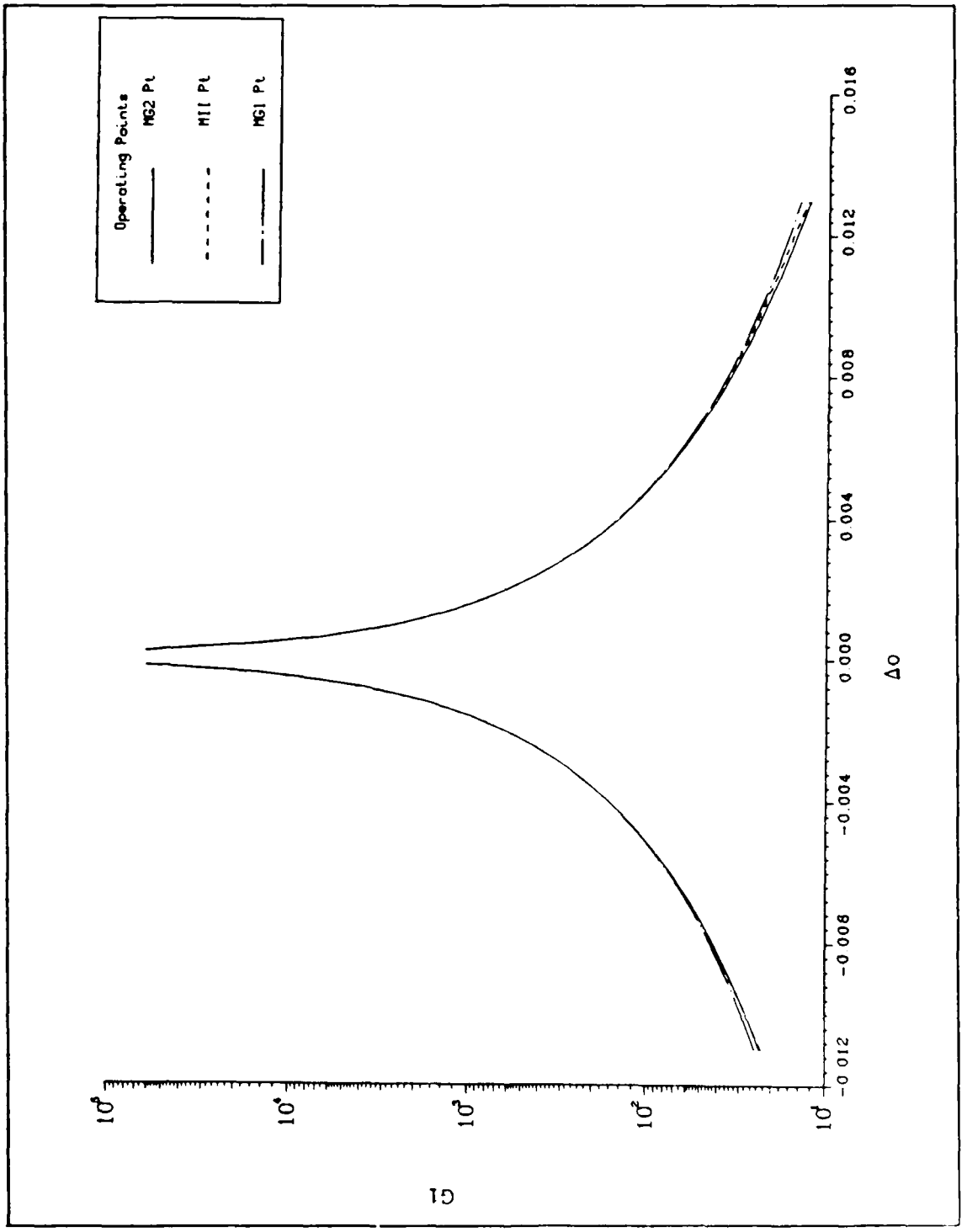

Figure C.44. G_1 vs $\Delta\hat{\delta}$ (data set 36). $r_B = 0.75$. Curves for the three operating points displayed in the figure.

AD-A109 514 SEMICLASSICAL THEORY OF INJECTED LASERS WITH ARBITRARY STABLE AND UNSTABLE RESONATORS(U) AIR FORCE INST OF TECH WRIGHT-PATTERSON AFB OH SCHOOL OF ENGI.. 4/4

UNCLASSIFIED S M RINALDI DEC 87 AFIT/DS/PH/76-3 F/G 9/3 NL

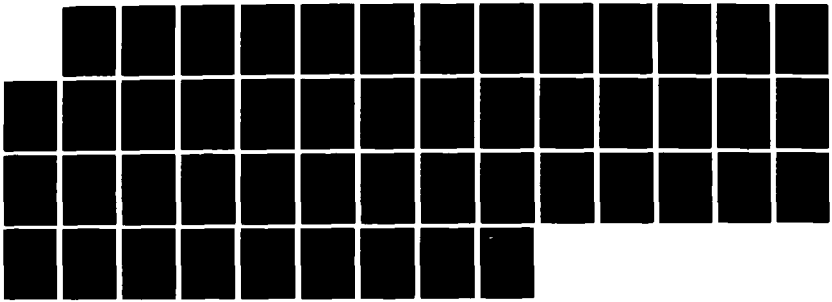

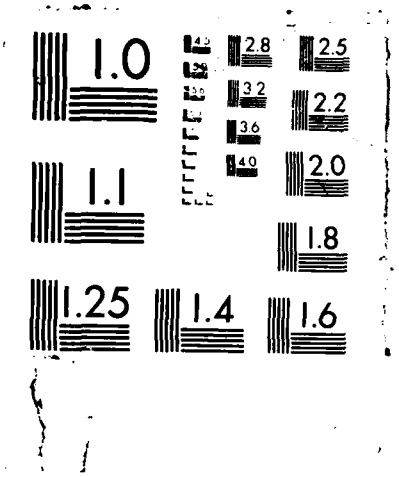
1.0
1.1
1.25
1.4
1.6
1.8
2.0
2.2
2.5
2.8
3.2
3.6
4.0

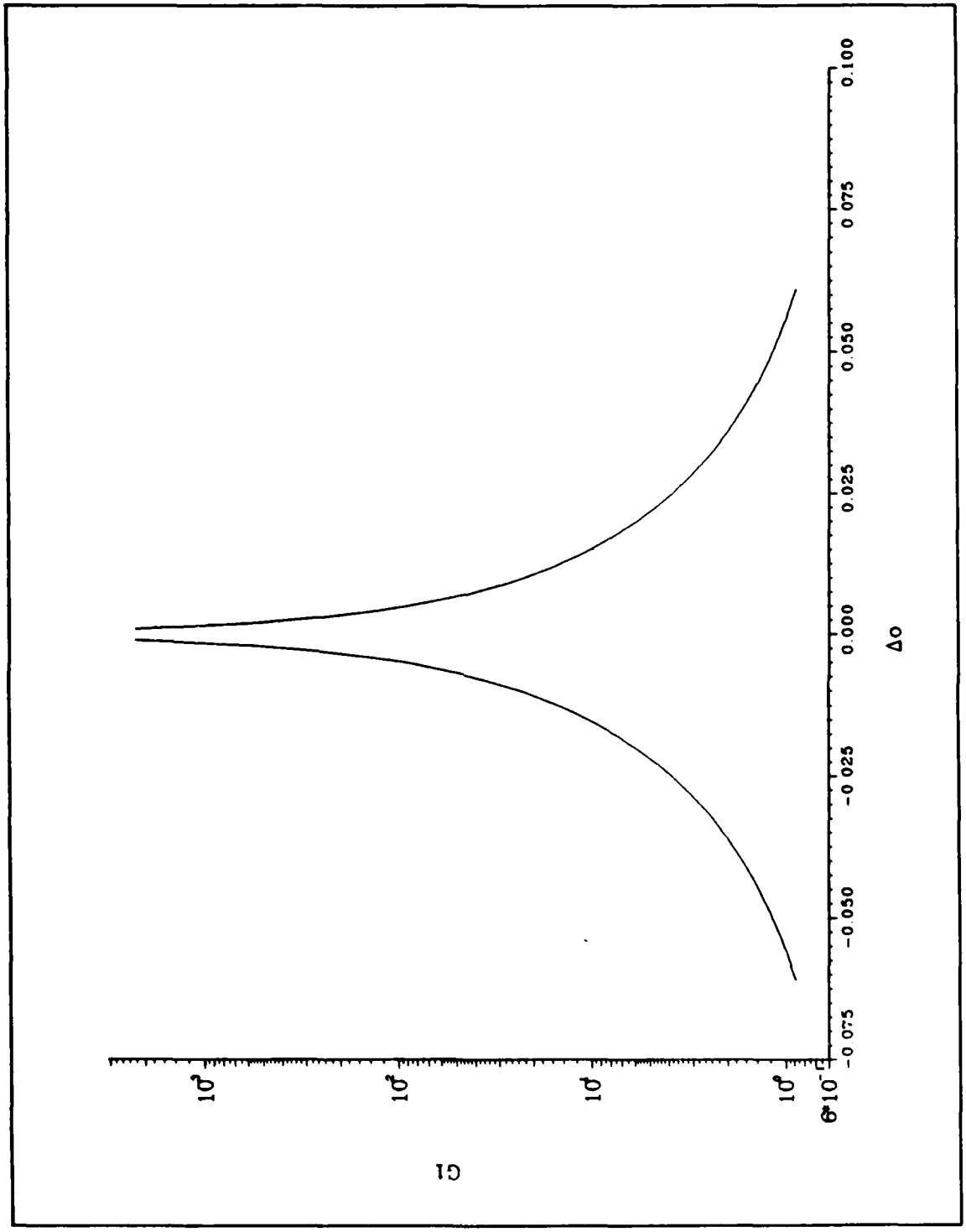

Figure C.45. G_1 vs $\Delta\delta$ (data set 27). $r_B = 0.75$. The curve is taken from the MG2 operating point data.

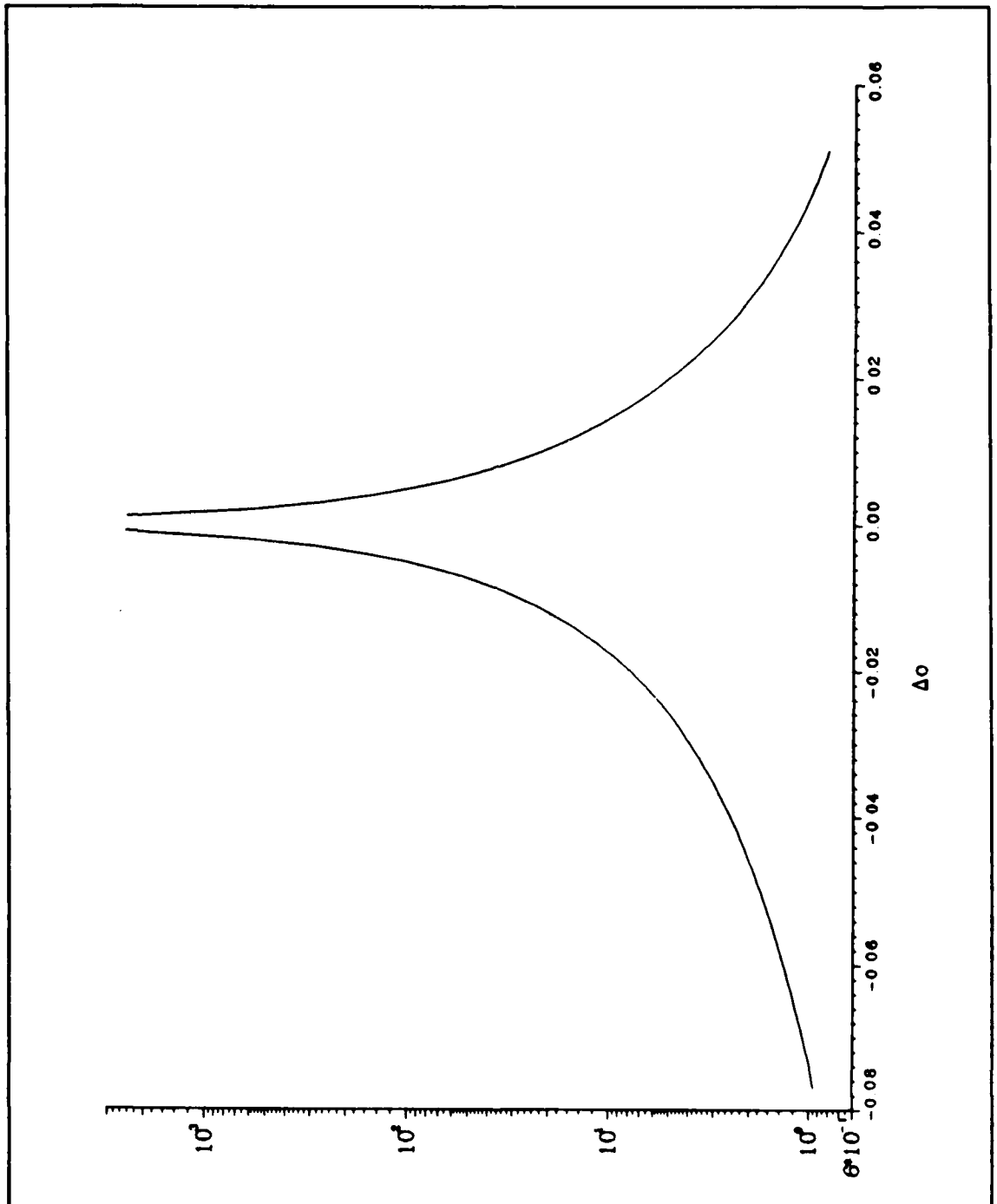

Figure C.46. G_1 vs $\Delta\hat{\delta}$ (data set 36). $r_B = 0.75$. The curve is taken from the MG2 operating point data.

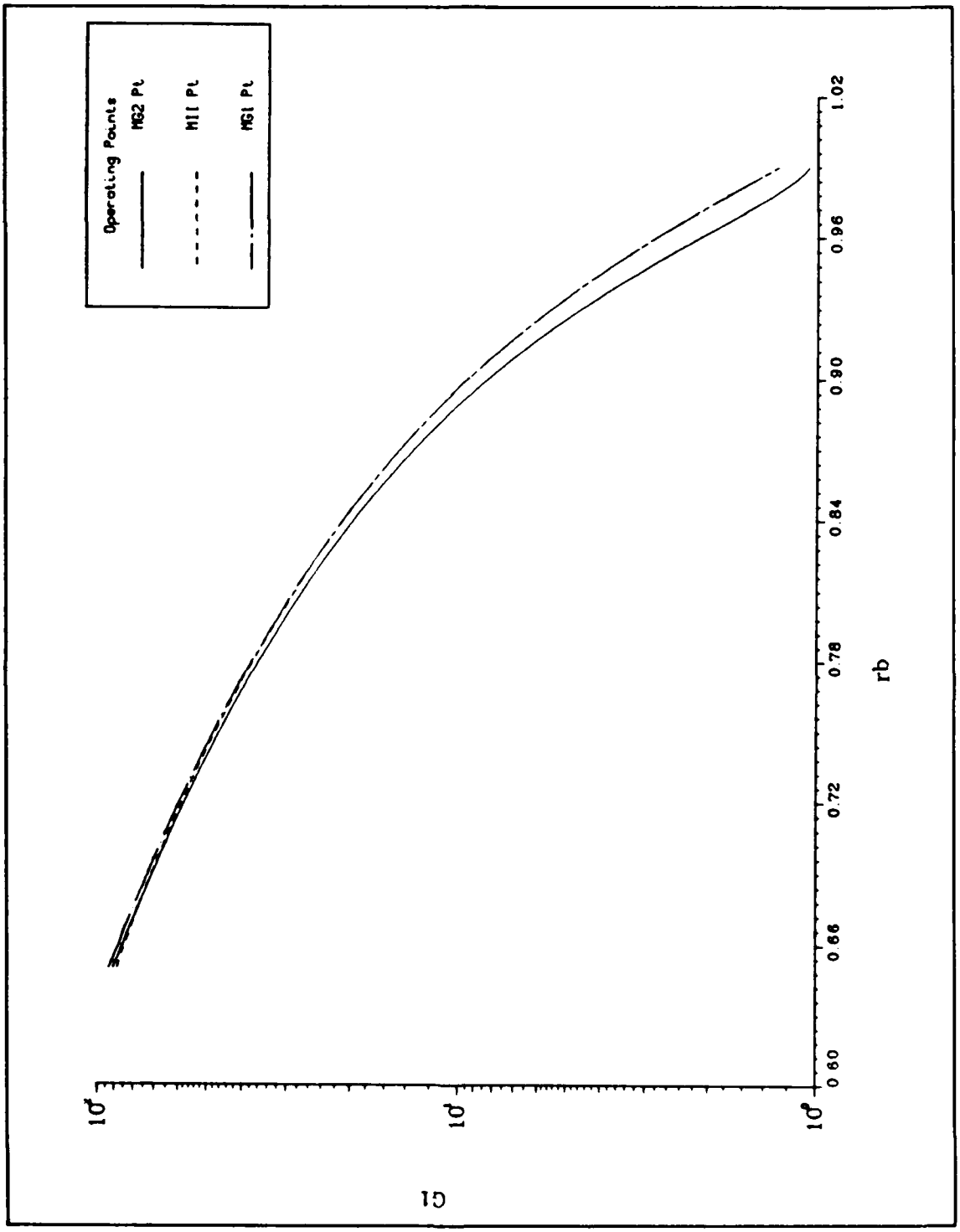

Figure C.47. G_1 vs r_B (data set 27). $\Delta\hat{\delta} = 0.007$. Curves for the three operating points are displayed in the figure.

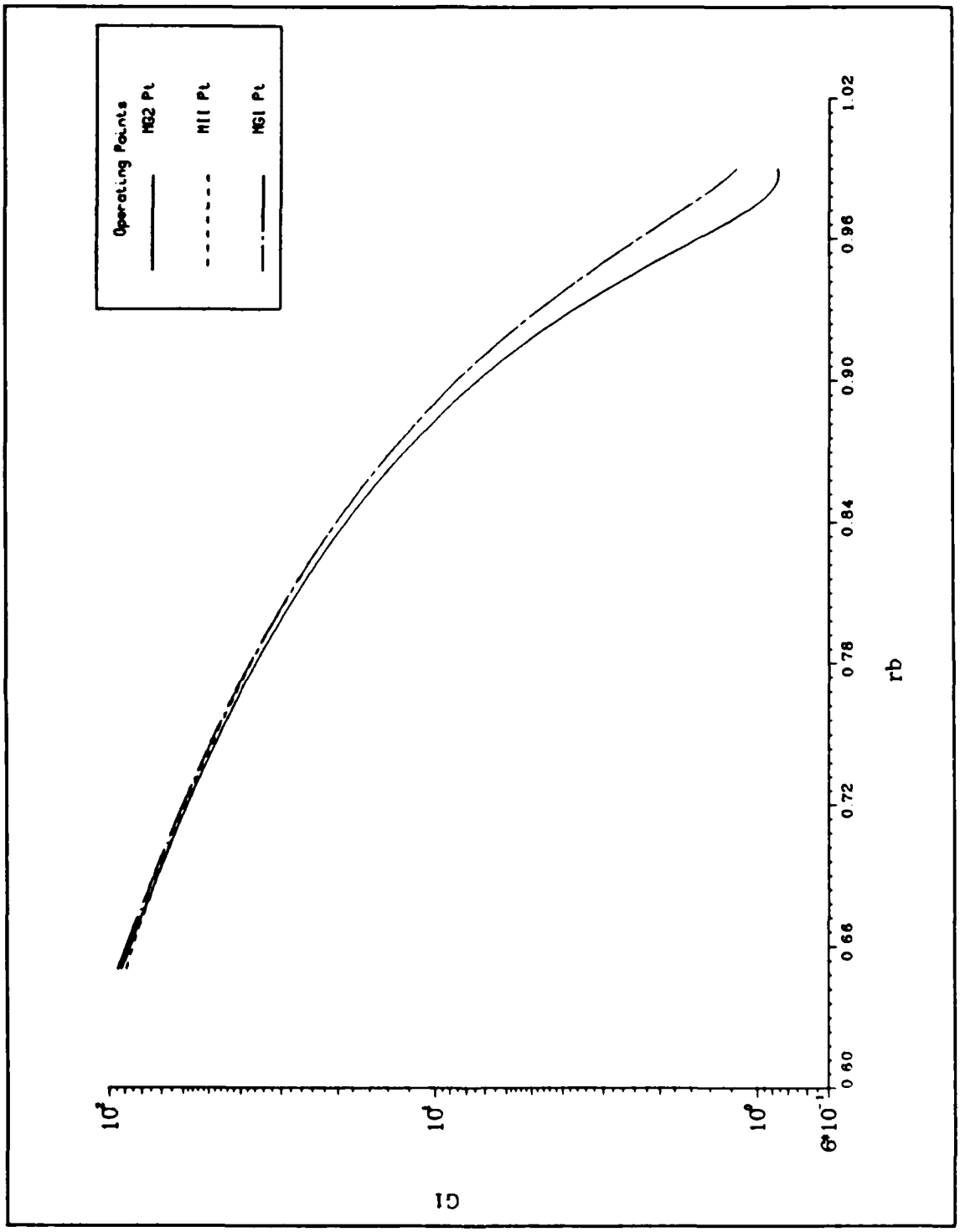

Figure C.48. G_1 vs r_B (data set 36). $\Delta\hat{o} = 0.007$. Curves for the three operating points are displayed in the figure.

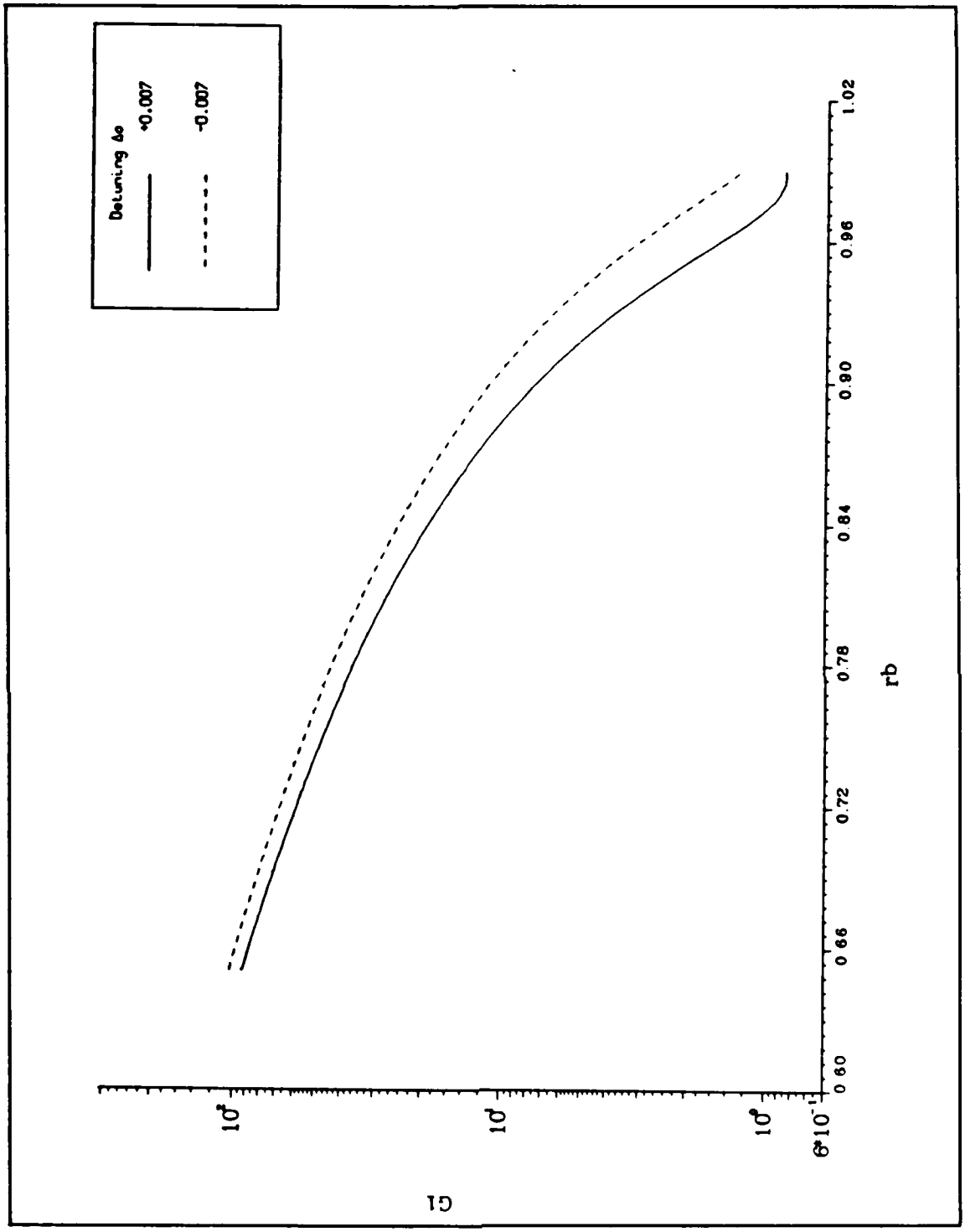

Figure C.49. G_1 vs r_B (data set 36). $\Delta\hat{\delta} = \pm 0.007$. The curves are taken from the MG2 operating point data.

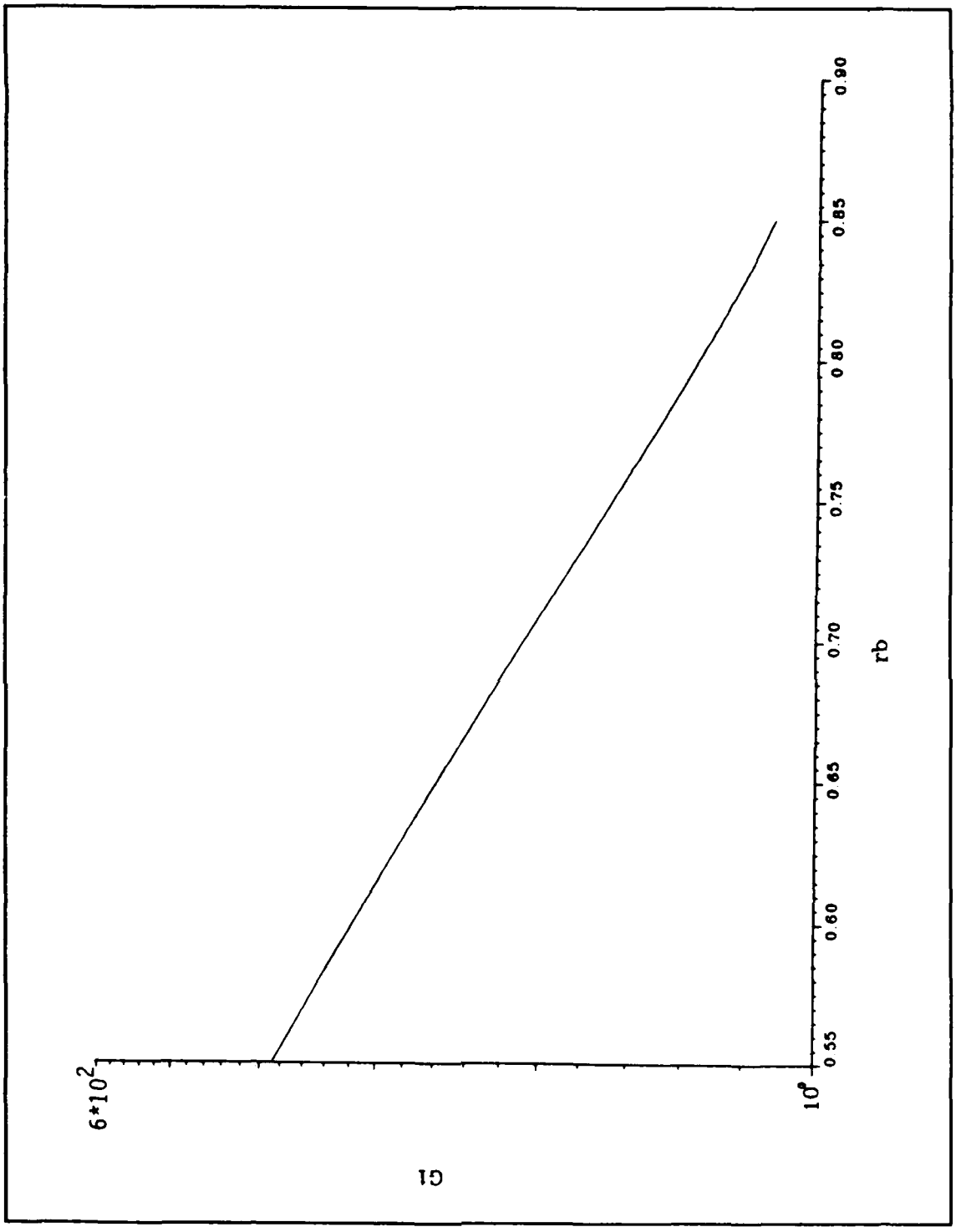

Figure C.50. G_1 vs r_B (data set 27). $\Delta\delta = 0.040$. The curve is taken from the MG2 operating point data.

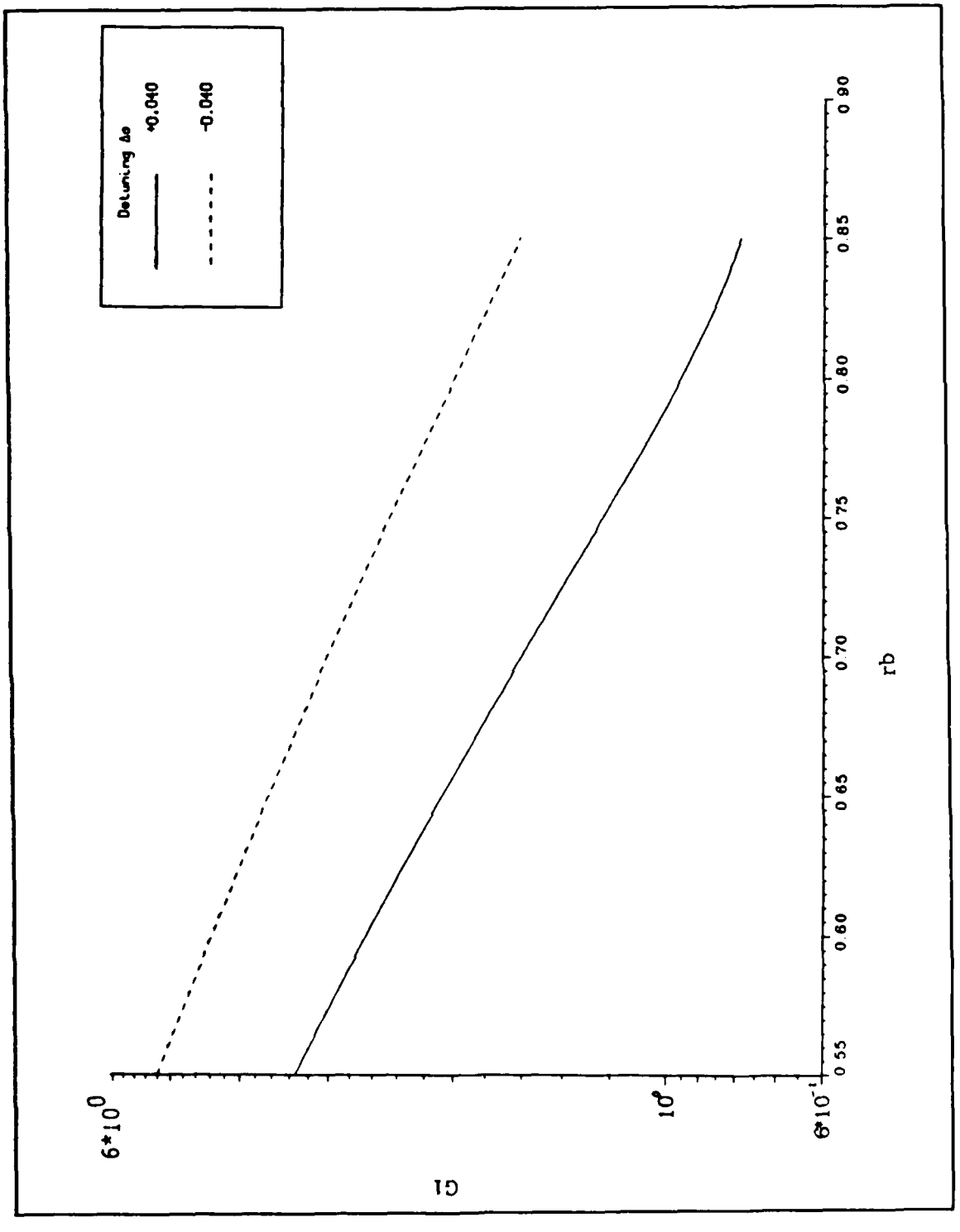

Figure C.51. G_1 vs r_B (data set 36). $\Delta\hat{o} = \pm 0.040$. The curves are taken from the MG2 operating point data.

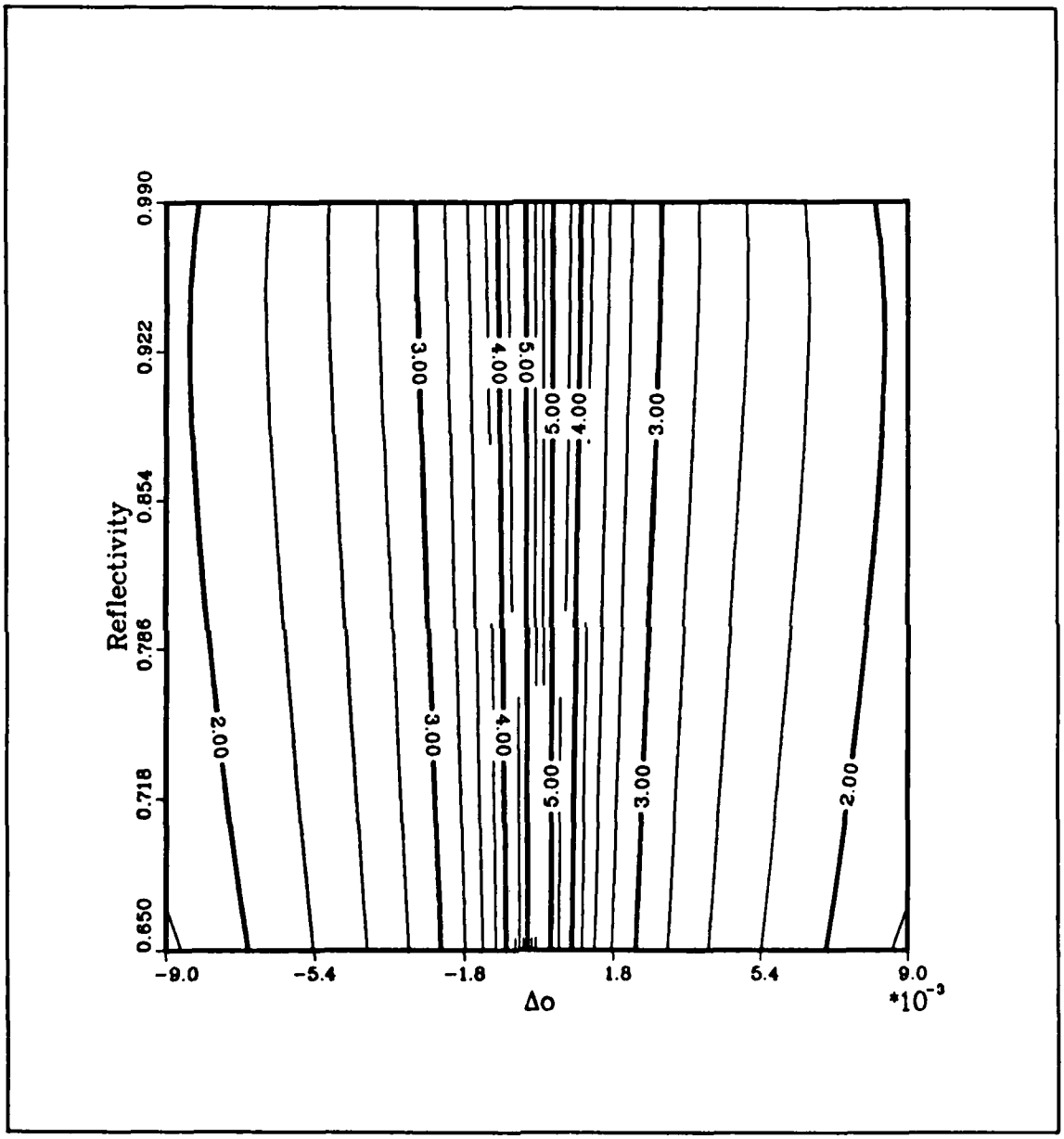

Figure C.52. $\log_{10} G_2$ contours at the MII point (data set 27).

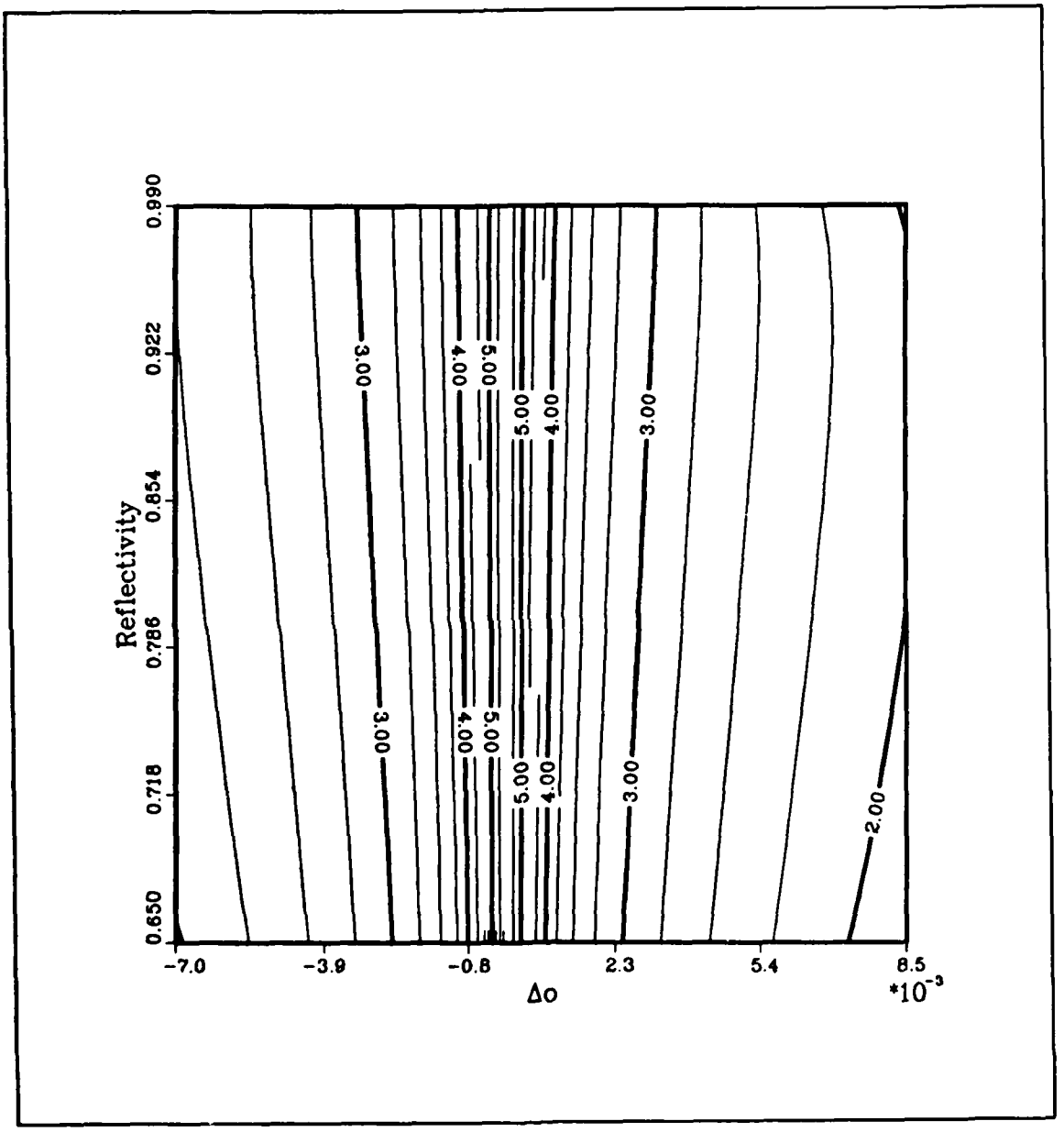

Figure C.53. $\log_{10} G_2$ contours at the MII point (data set 36).

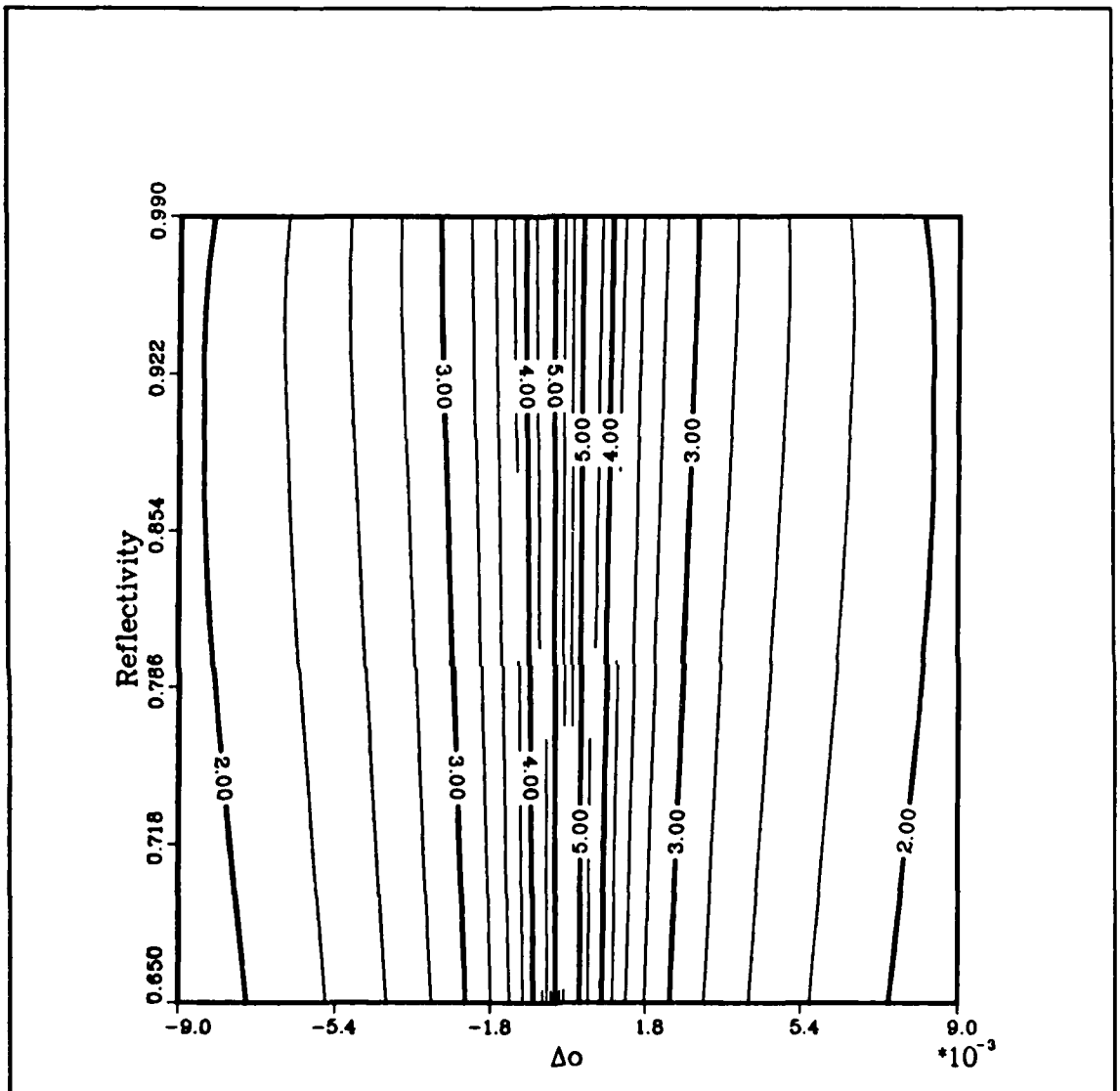

Figure C.54. $\log_{10} G_2$ contours at the MG1 point (data set 27).

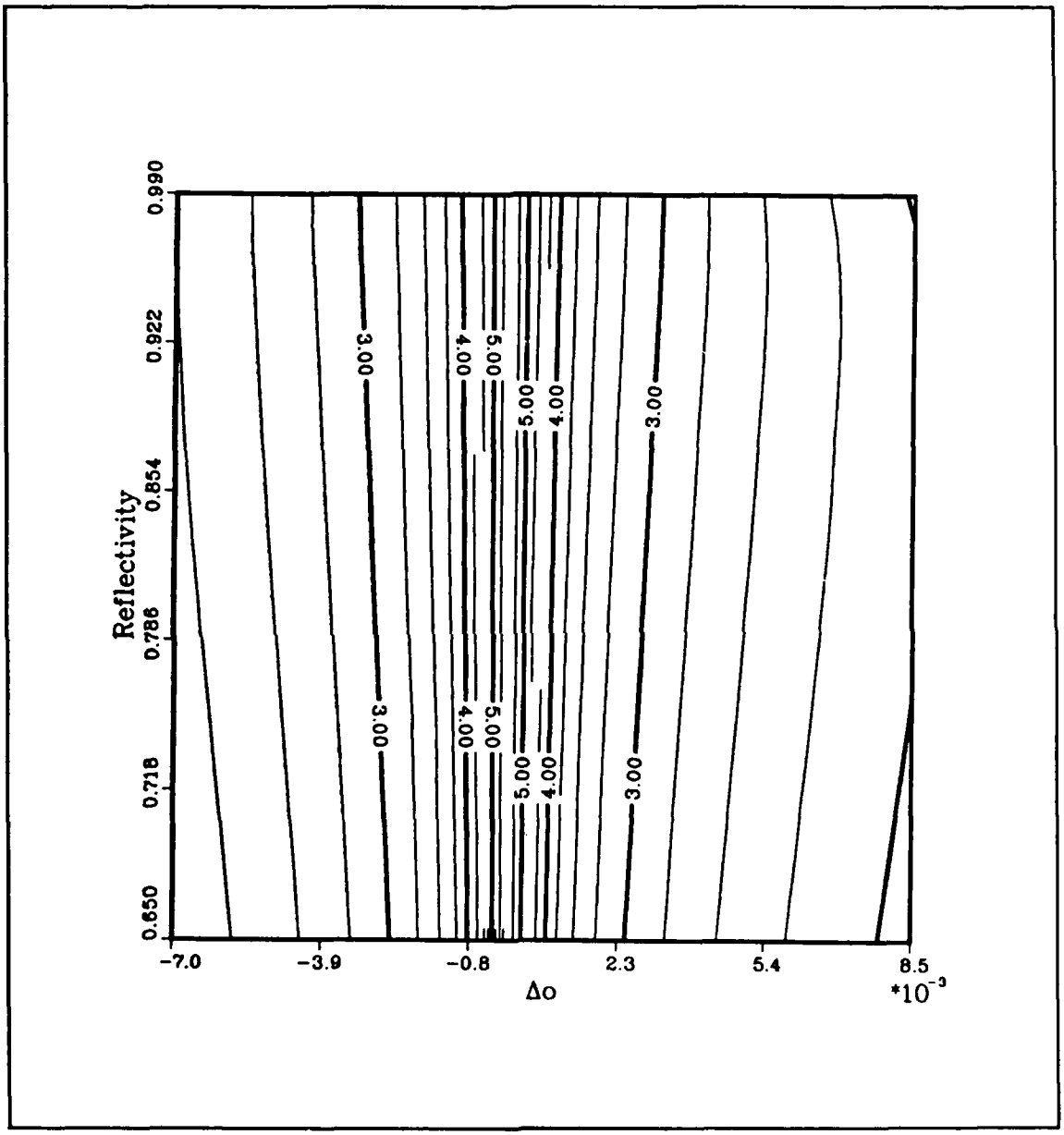

Figure C.55. $\log_{10} G_2$ contours at the MG1 point (data set 36).

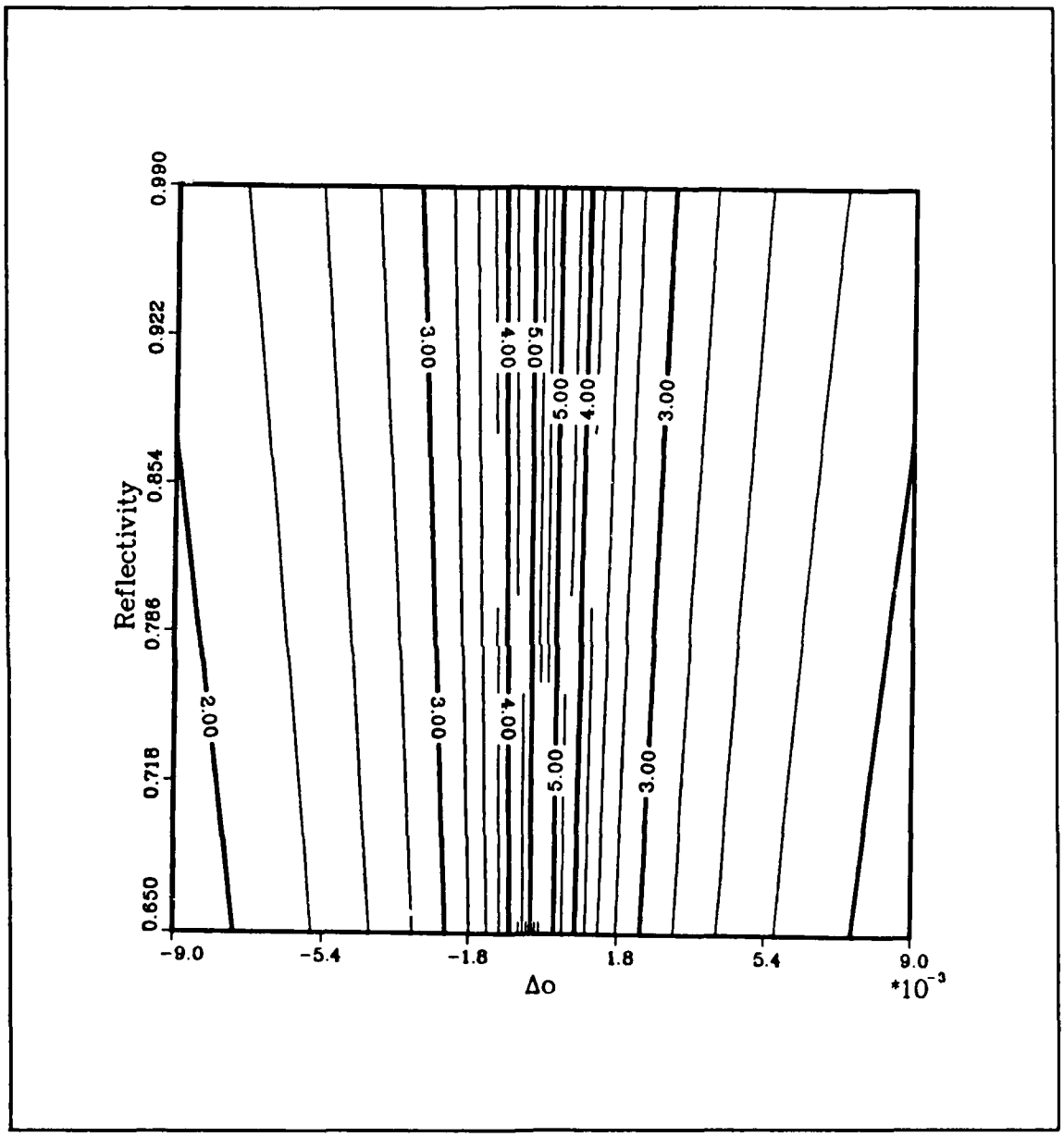

Figure C.56. $\log_{10} G_2$ contours at the MG2 point (data set 27). The data is from the region in the $(\Delta\hat{o}, r_B)$ plane where the cubic curves retain the s-shape.

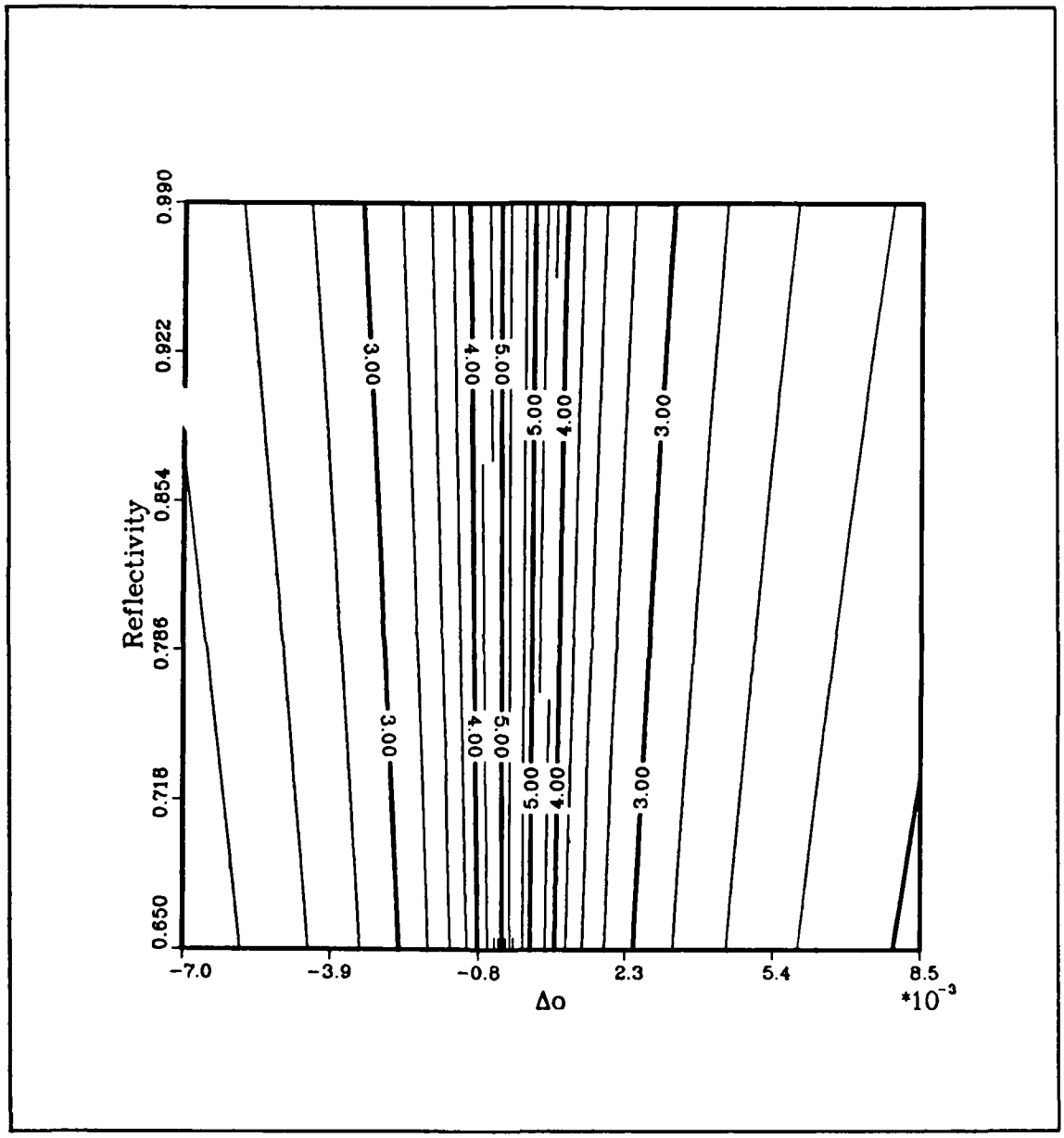

Figure C.57. $\log_{10} G_2$ contours at the MG2 point (data set 36). The data is from the region in the $(\Delta\hat{o}, r_B)$ plane where the cubic curves retain the s-shape.

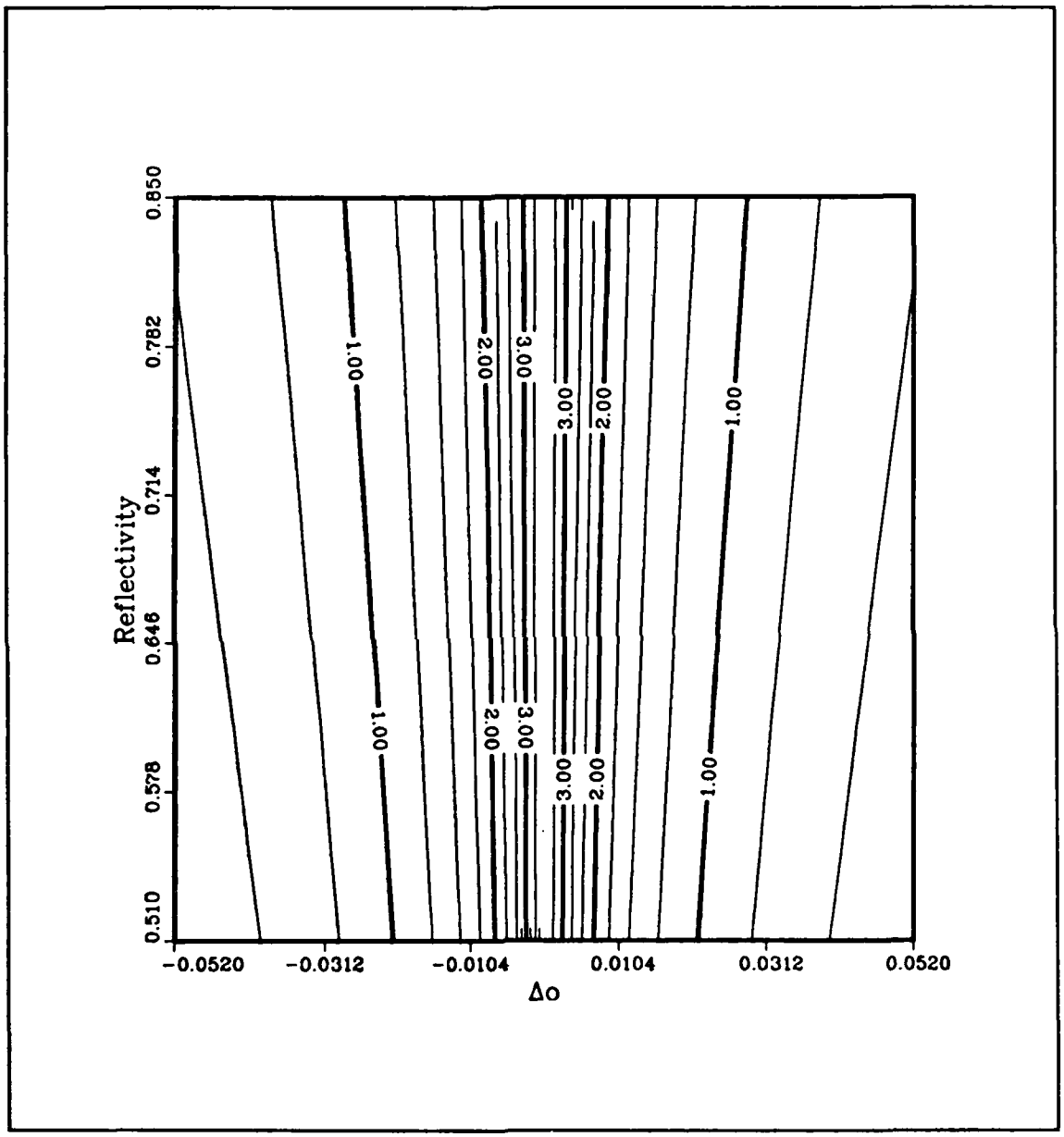

Figure C.58. $\log_{10} G_2$ contours at the MG2 point (data set 27). The data is from as large a rectangular region in the $(\Delta\hat{o}, r_B)$ plane as possible.

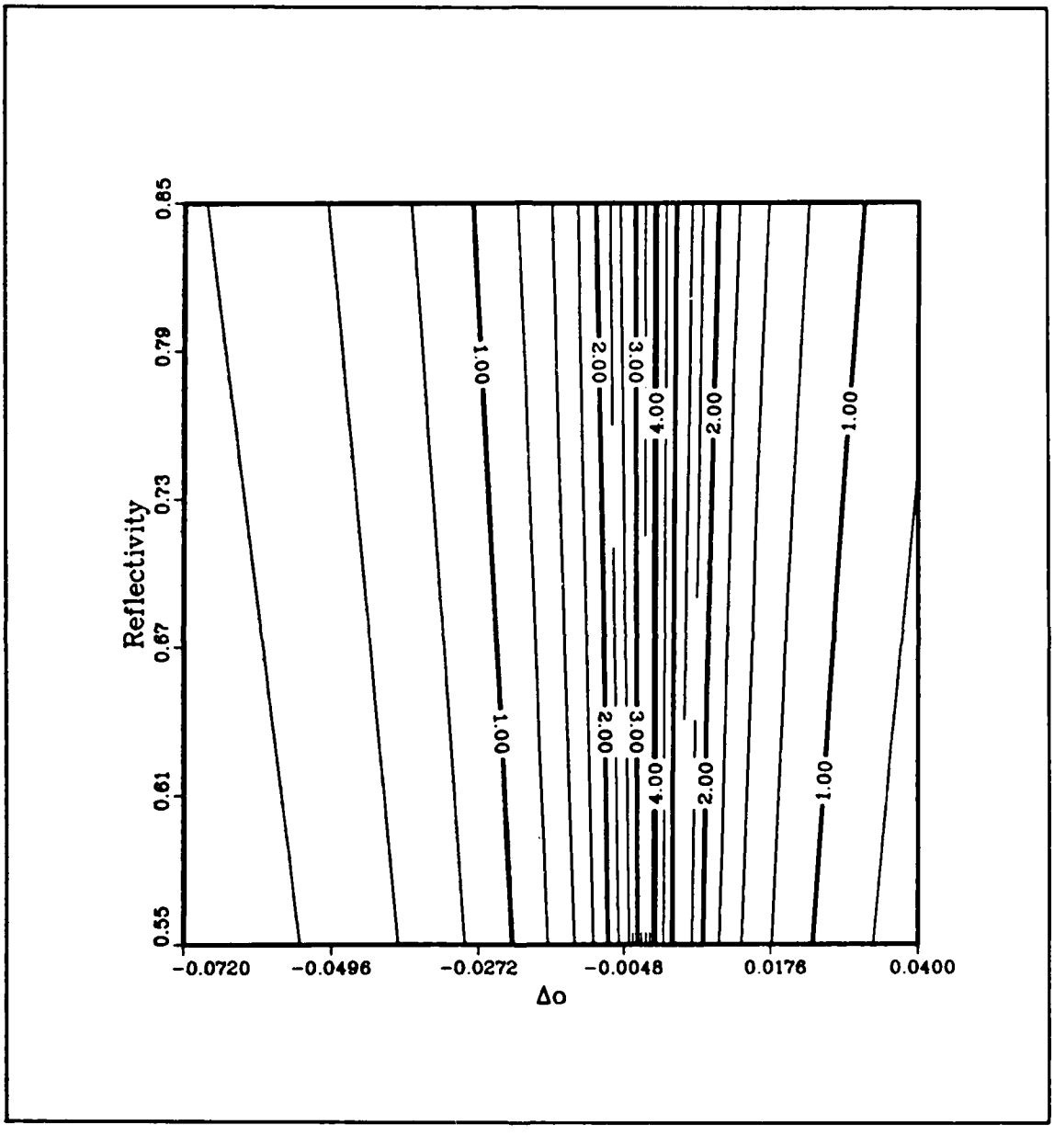

Figure C.59. $\log_{10} G_2$ contours at the MG2 point (data set 36). The data is from as large a rectangular region in the $(\Delta\hat{o}, r_B)$ plane as possible.

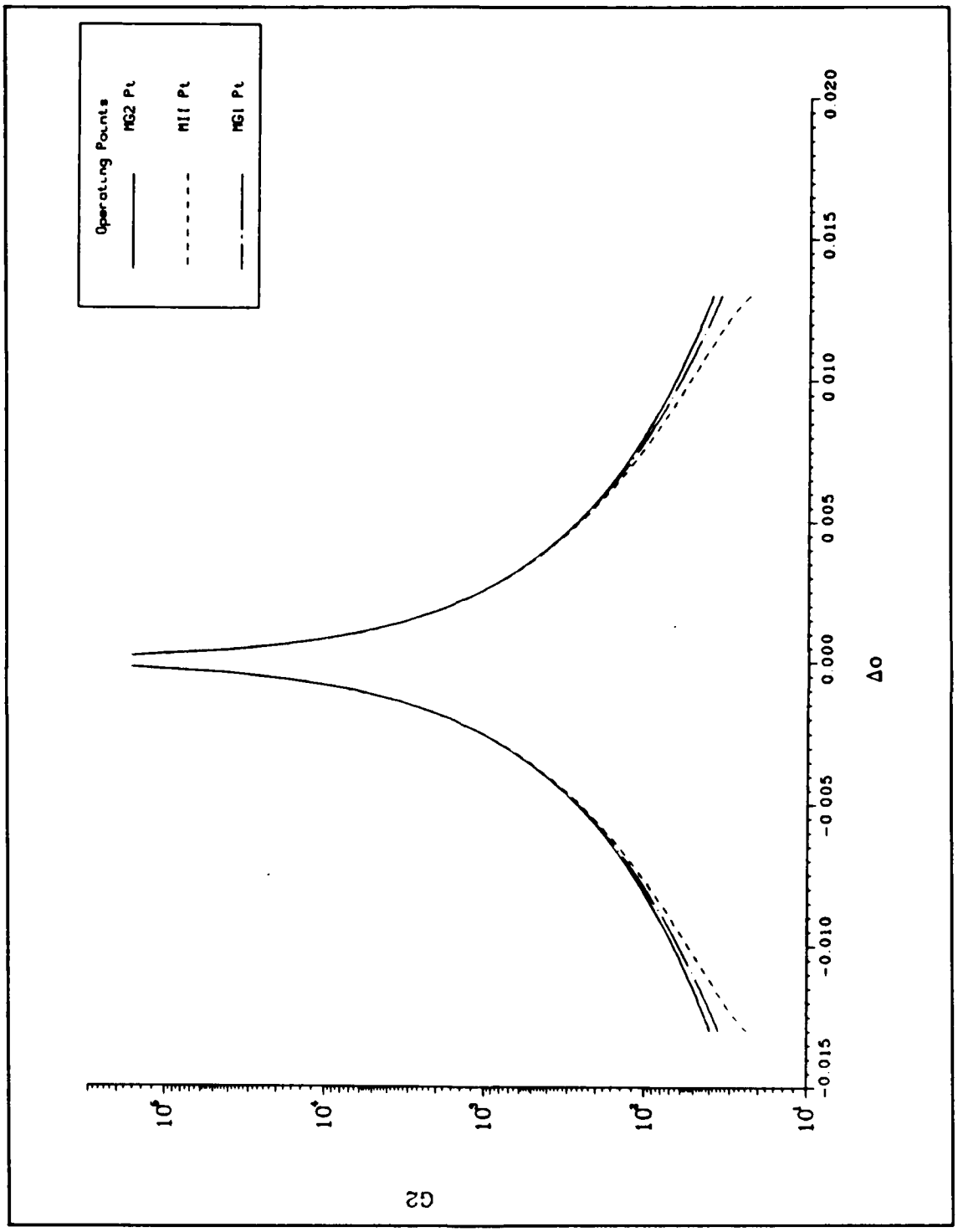

Figure C.60. G_2 vs $\Delta\hat{o}$ (data set 27). $r_B = 0.75$. Curves for the three operating points are displayed in the figure.

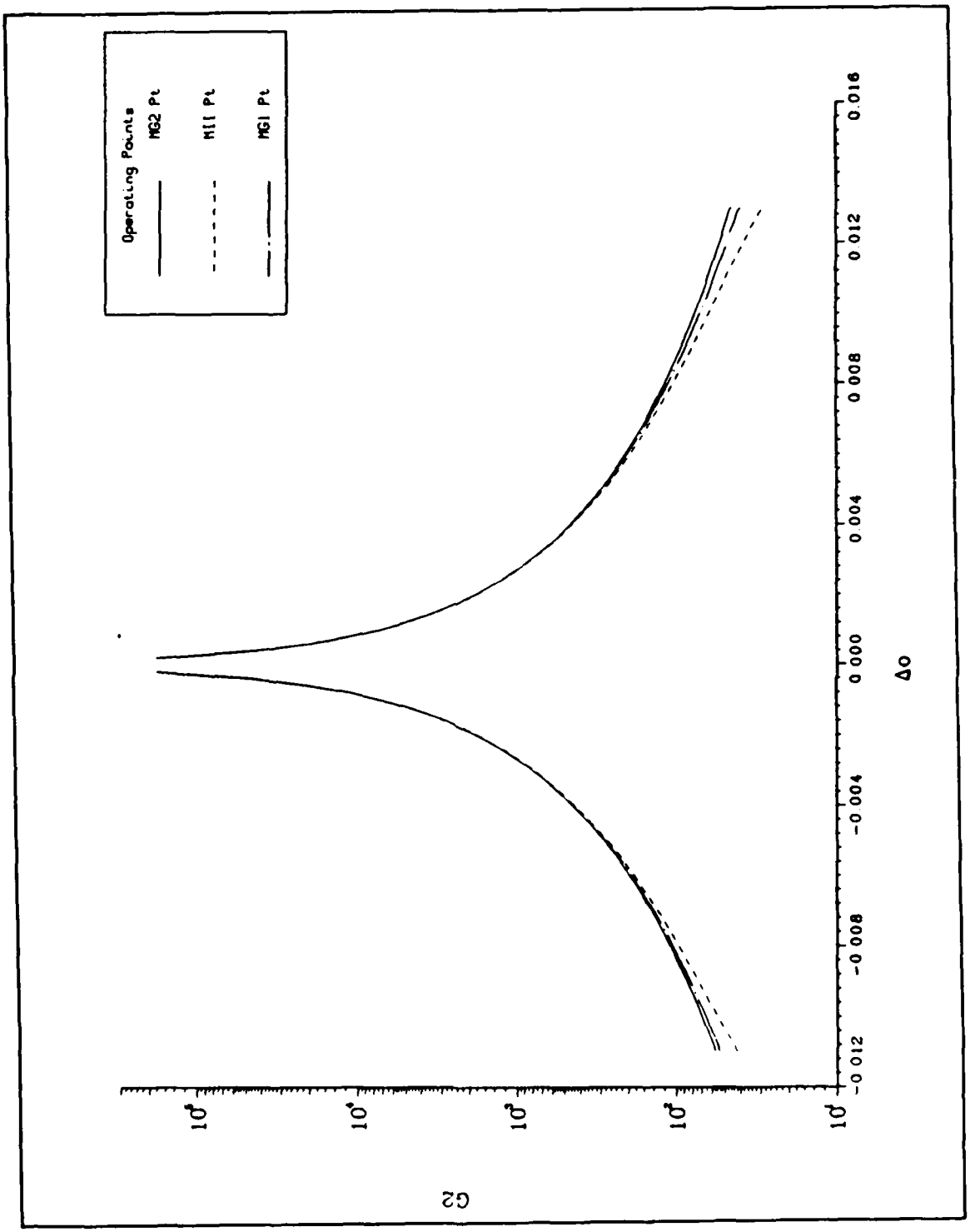

Figure C.61. G_2 vs $\Delta\hat{\delta}$ (data set 36). $r_B = 0.75$. Curves for the three operating points are displayed in the figure.

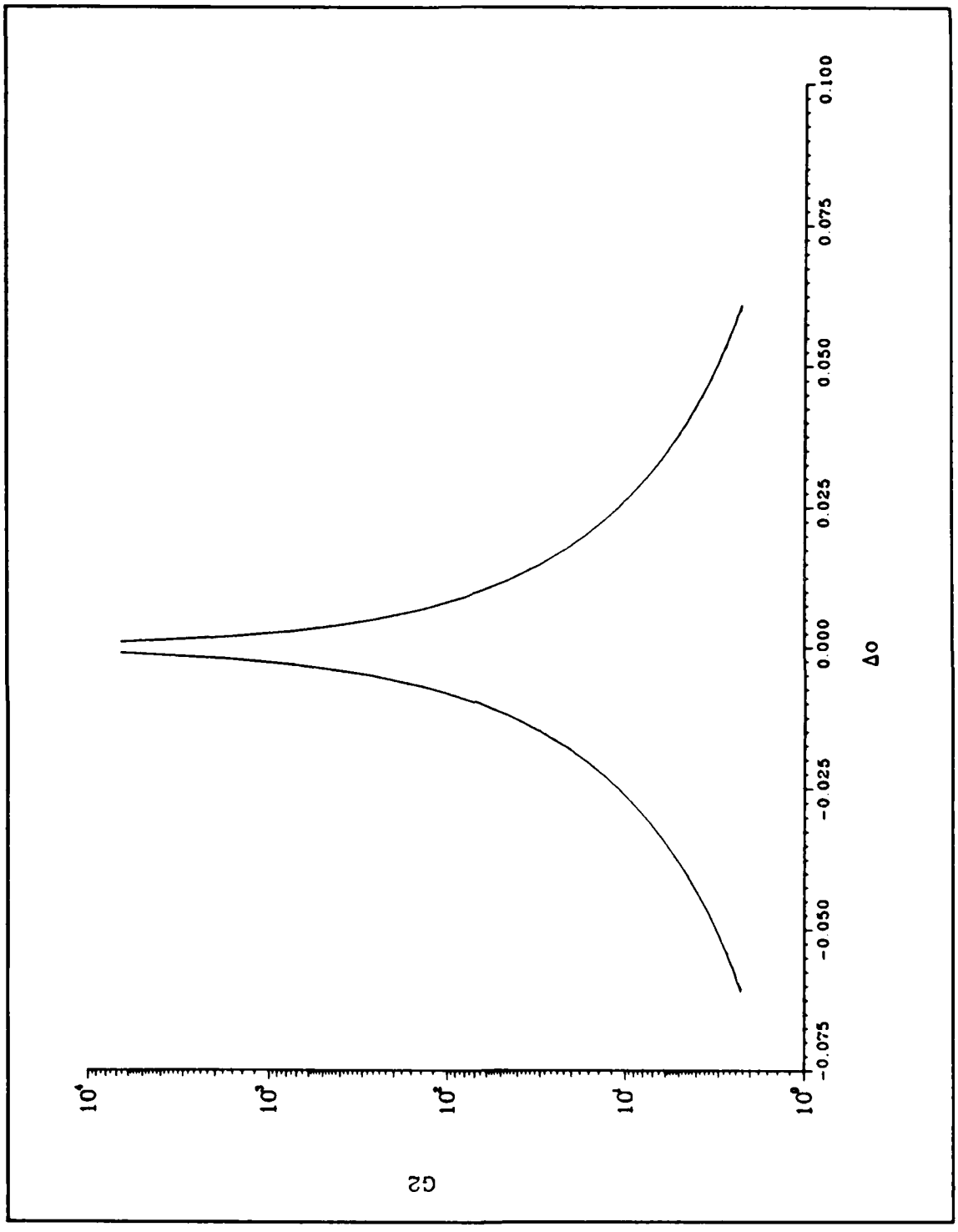

Figure C.62. G_2 vs $\Delta\hat{o}$ (data set 27). $r_B = 0.75$. The curve is taken from the MG2 operating point data.

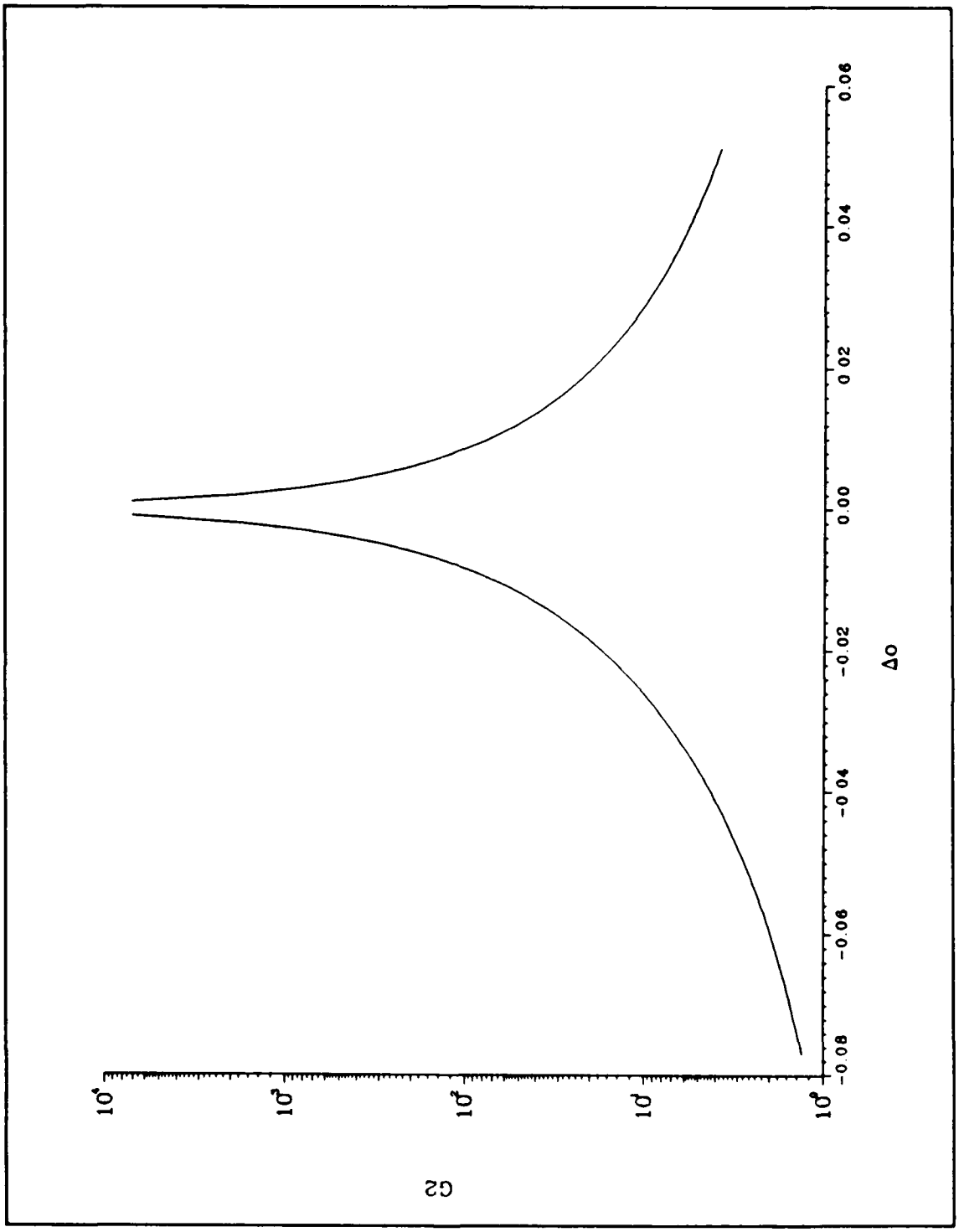

Figure C.63. G_2 vs $\Delta\hat{o}$ (data set 36). $r_B = 0.75$. The curve is taken from the MG2 operating point data.

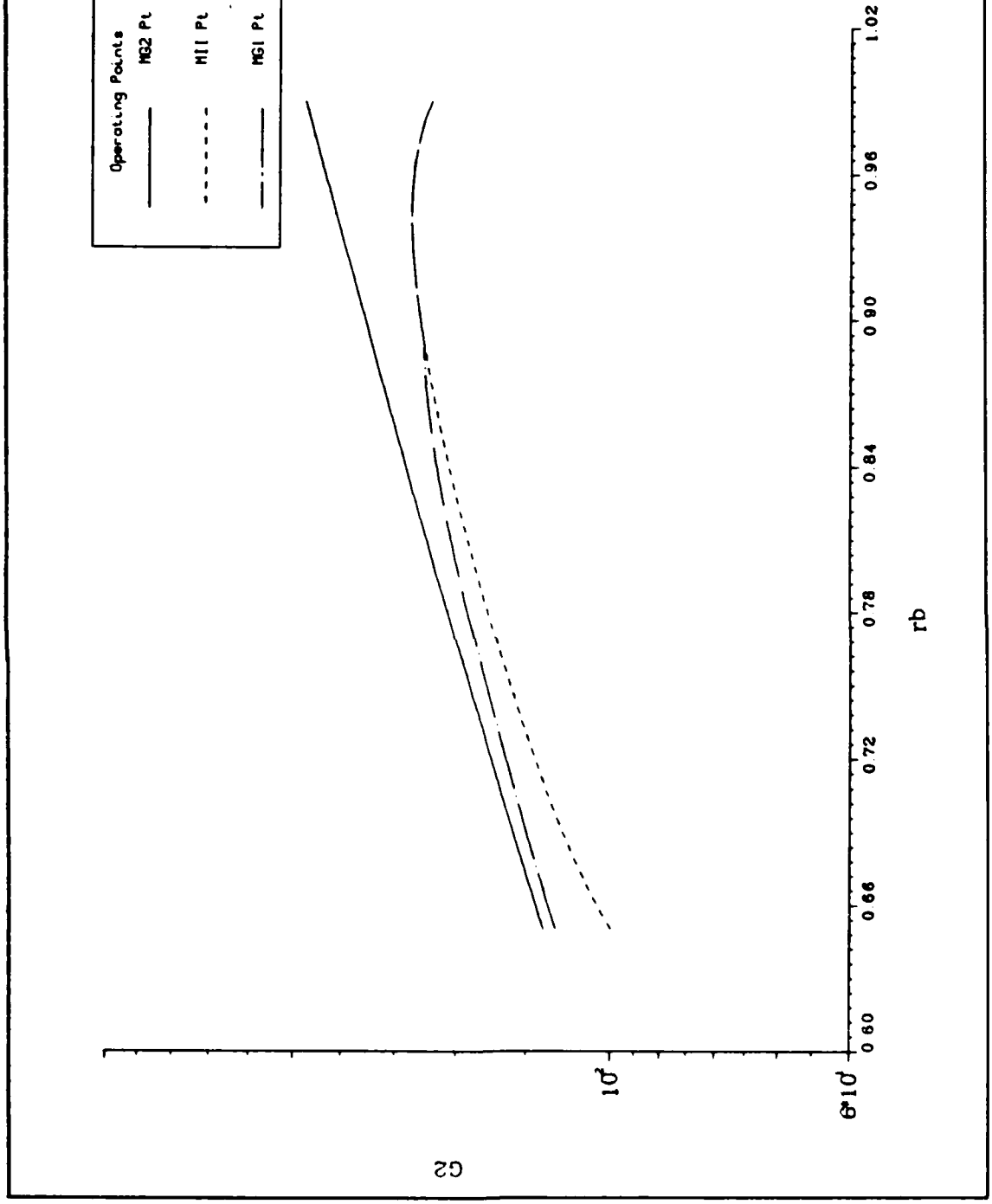

Figure C.64. G_2 vs r_B (data set 27). $\Delta\hat{o} = 0.007$. Curves for the three operating points are displayed in the figure.

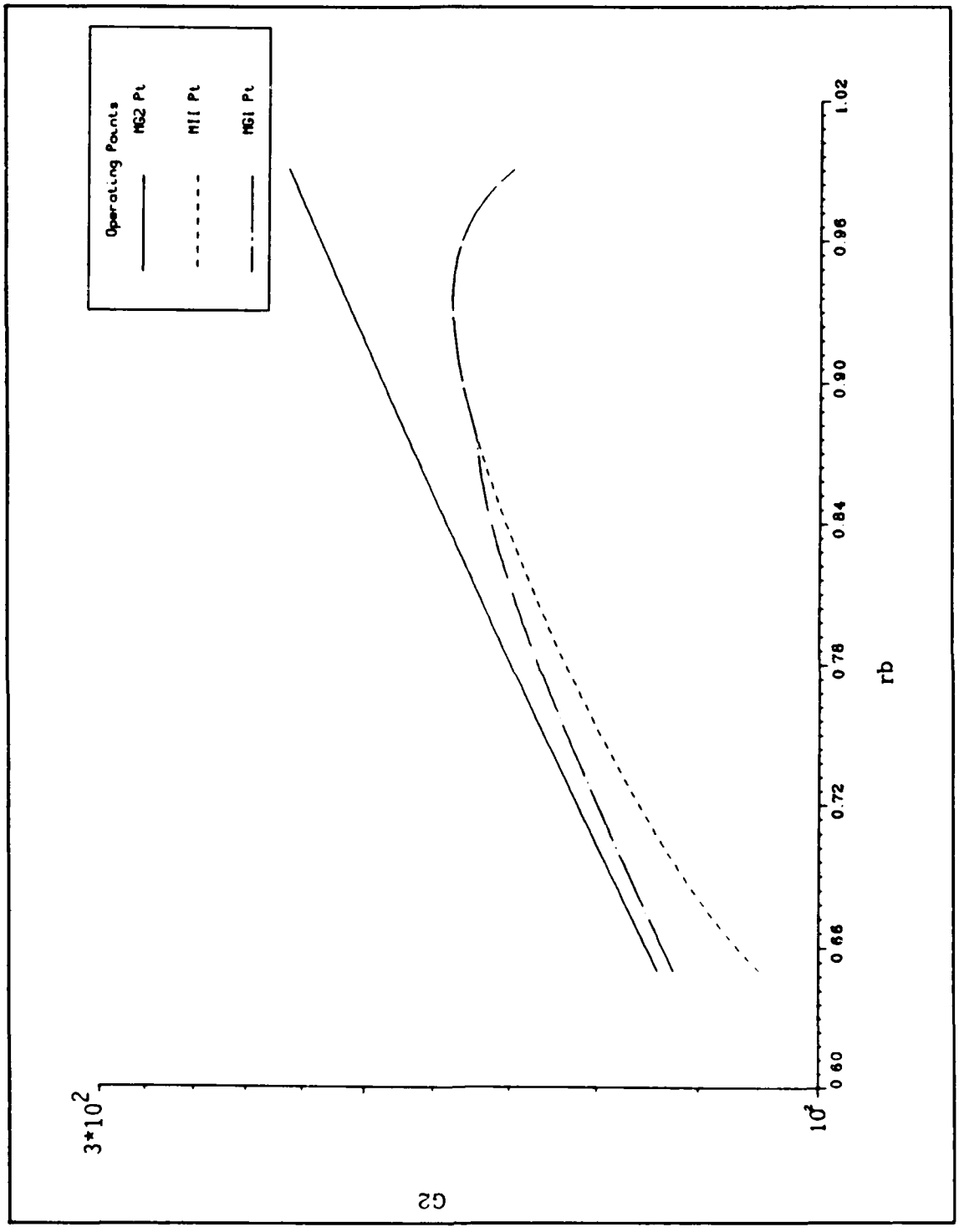

Figure C.65. G_2 vs r_B (data set 36). $\Delta\delta$ = 0.007. Curves for the three operating points are displayed in the figure.

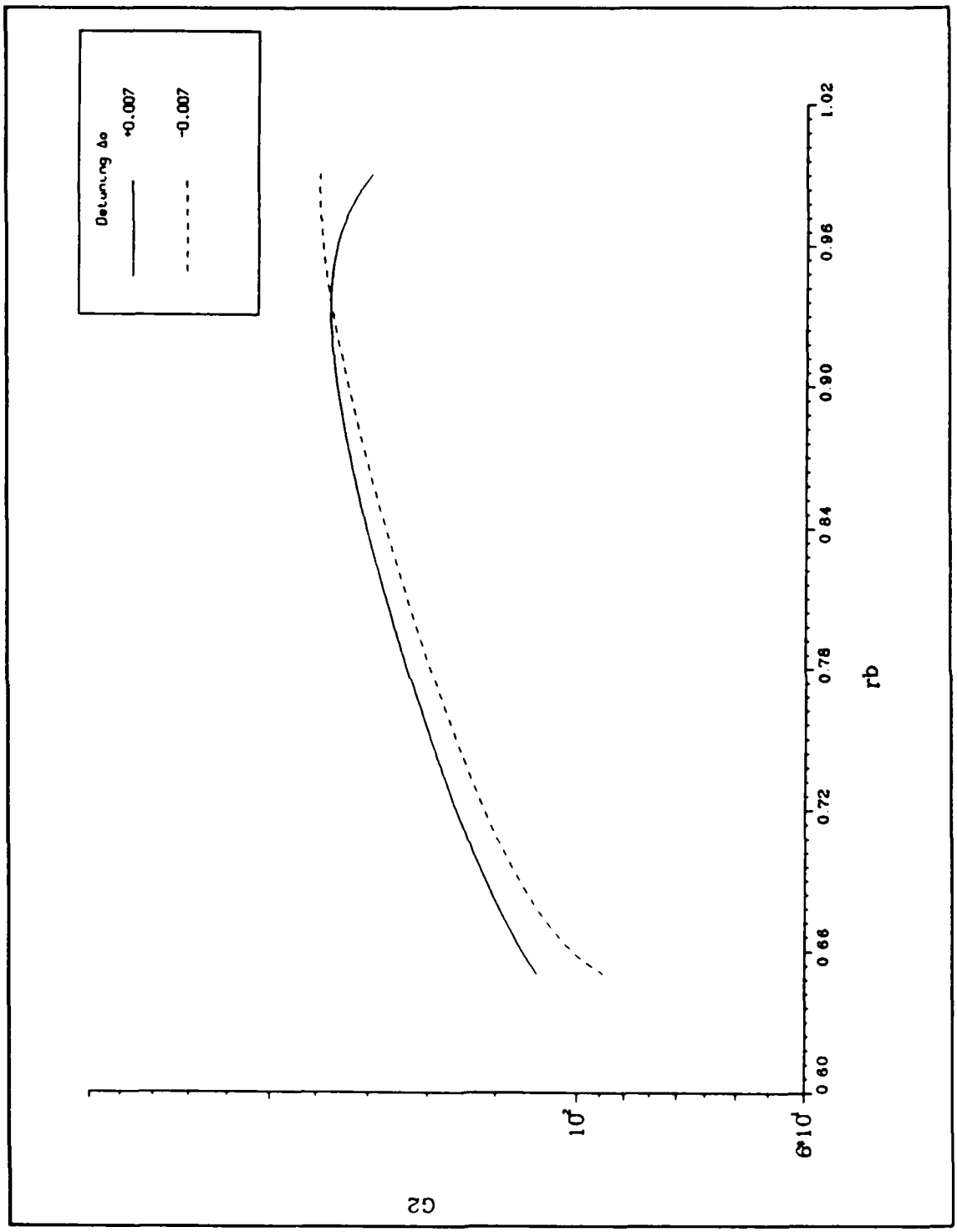

Figure C.66. G_2 vs r_B (data set 36). $\Delta\hat{\sigma} = \pm 0.007$. The curves are taken from the MII operating point data.

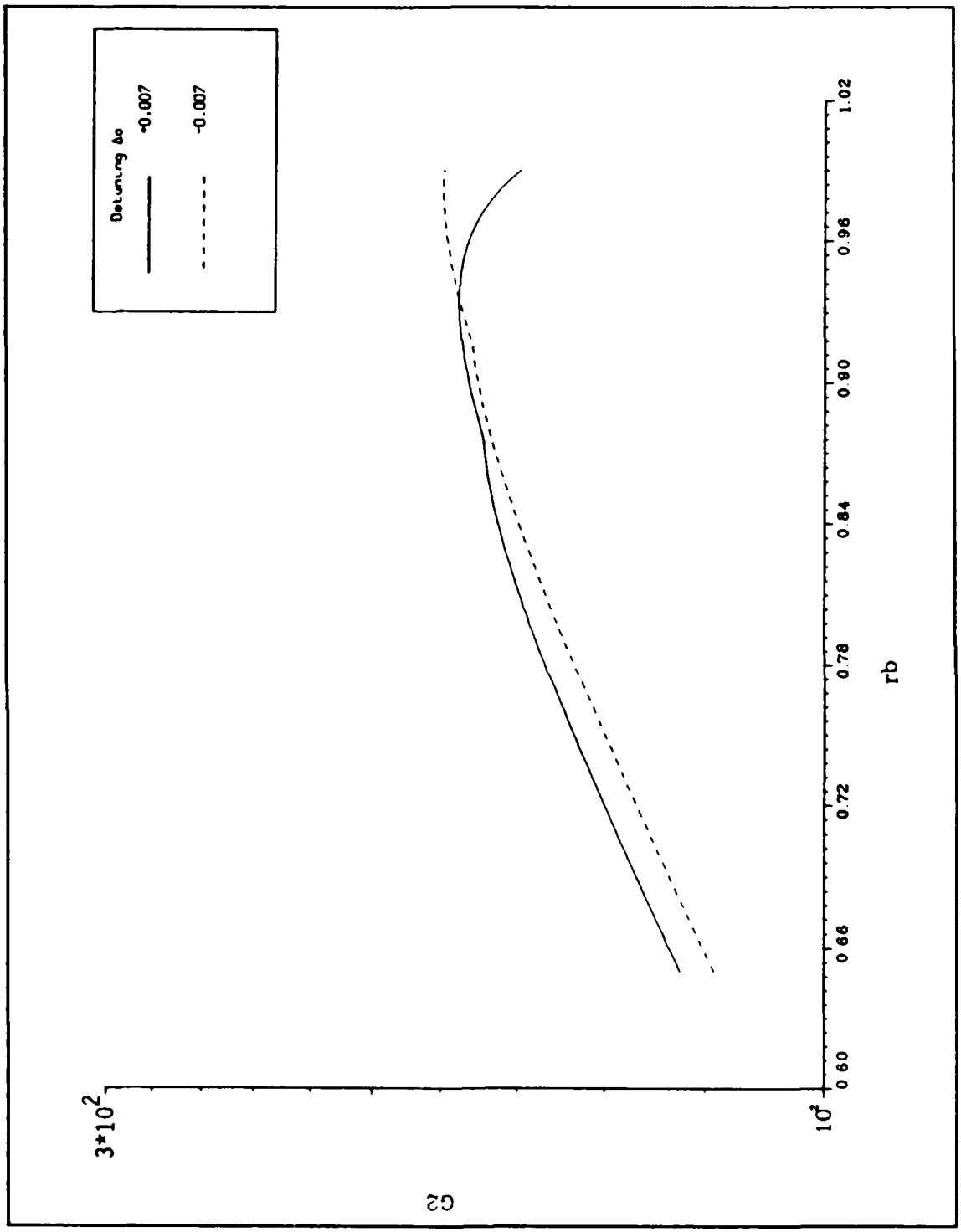

Figure C.67. G_2 vs r_B (data set 36). $\Delta\hat{o} = \pm 0.007$. The curves are taken from the MG1 operating point data.

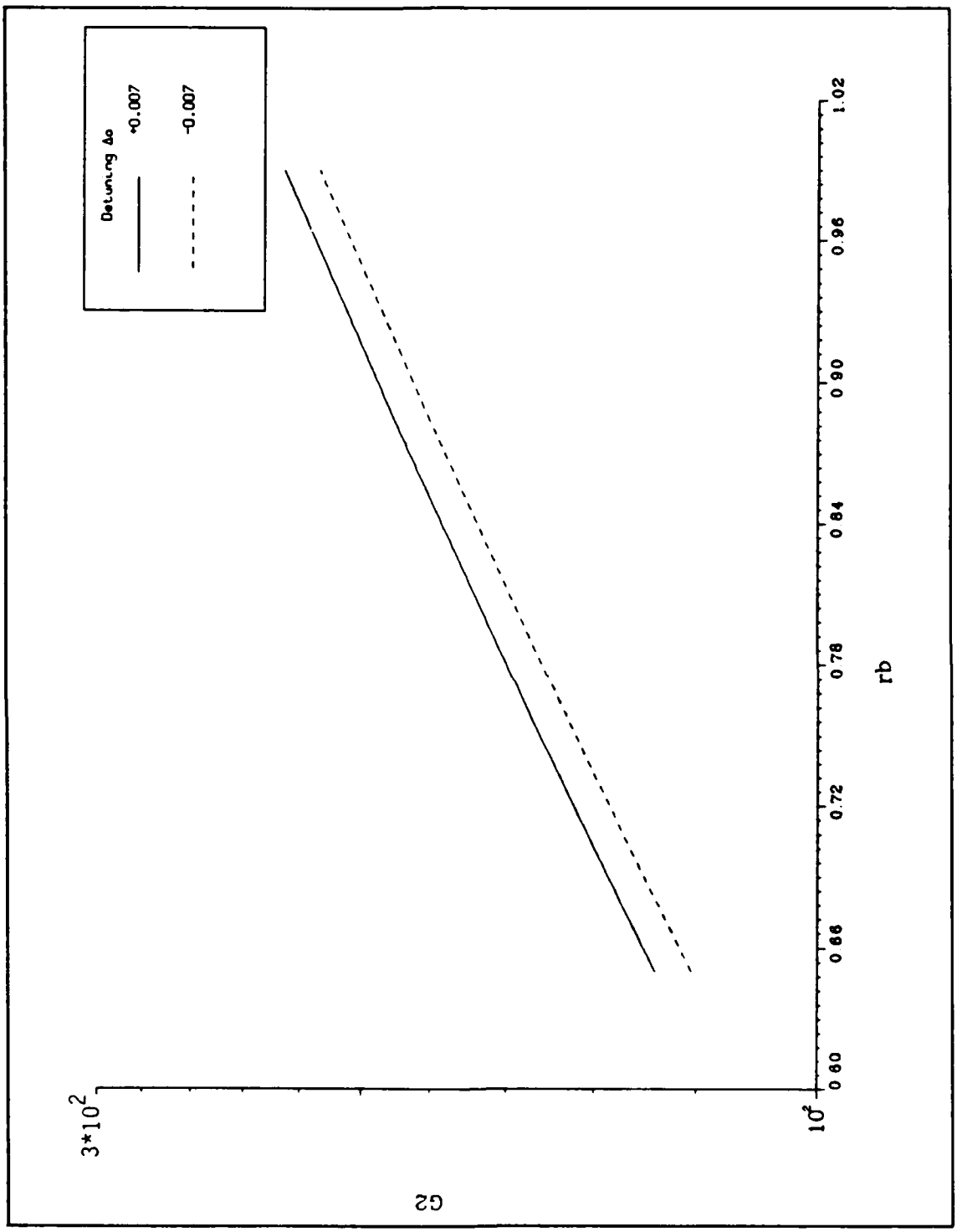

Figure C.68. G_2 vs r_B (data set 36). $\Delta\hat{\delta} = \pm 0.007$. The curves are taken from the MG2 operating point data.

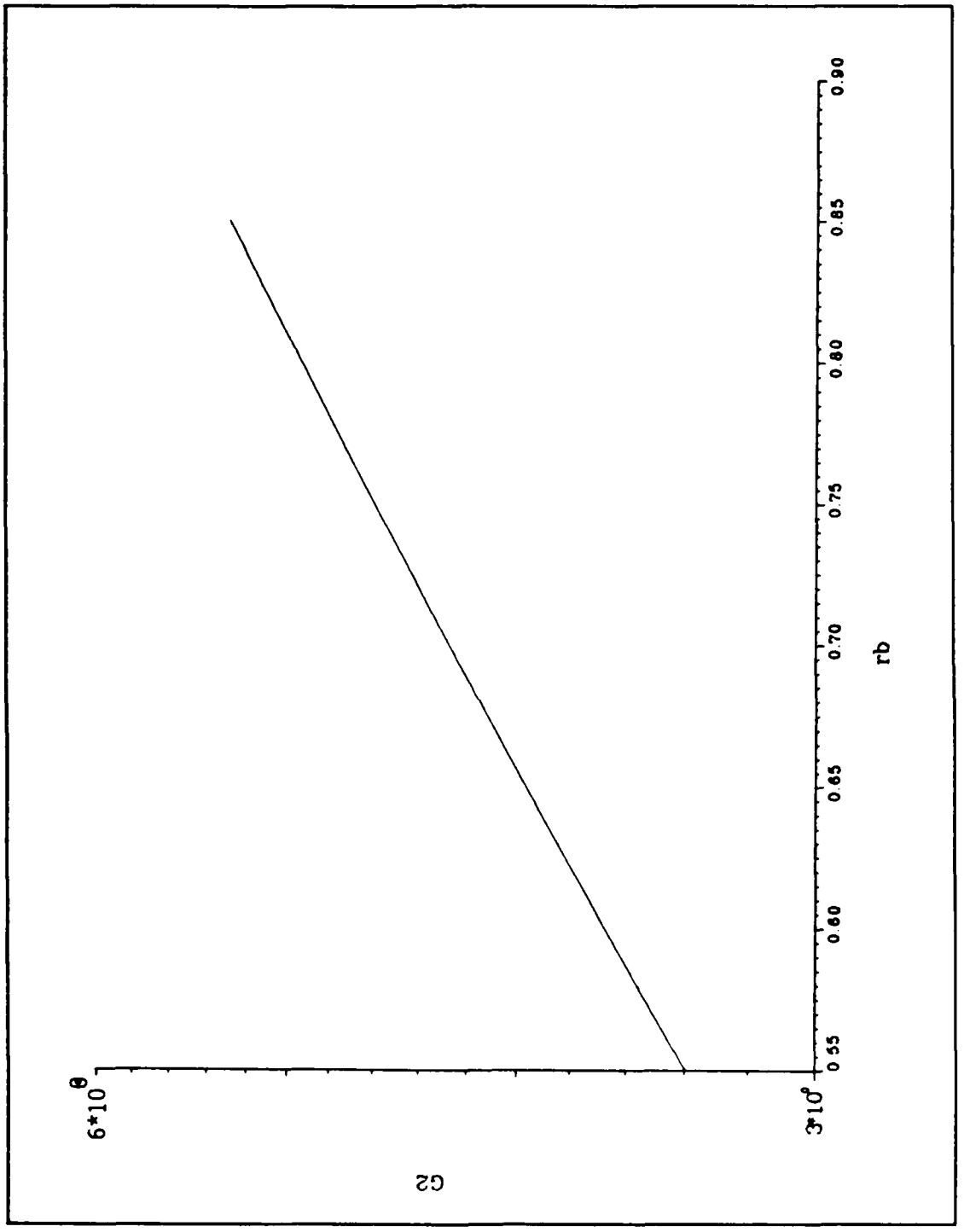

Figure C.69. G_2 vs r_B (data set 27). $\Delta\hat{o} = 0.040$. The curve is taken from the MG2 operating point data.

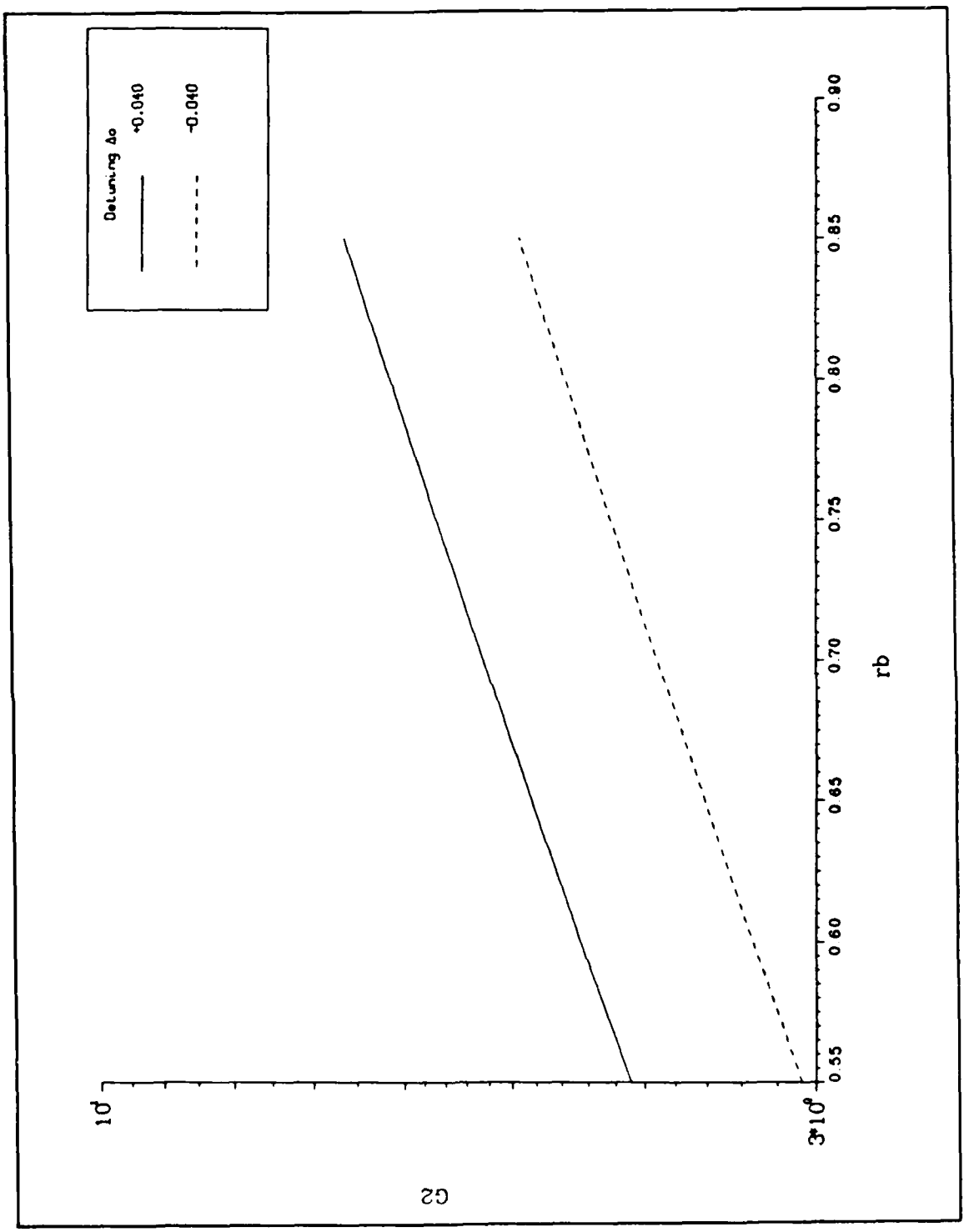

Figure C.70. G_2 vs r_B (data set 36). $\Delta\delta = \pm 0.040$. The curves are taken from the MG2 operating point data.

Glossary

A large number of symbols were used in the previous text. The following glossary lists each symbol, presents a short explanation of the symbol, and references the pages on which the symbol is defined and first used. The definition and first use pages are listed following the explanations, in the form (definition:first use). The caret or "hat" accent denoting a normalized variable is not used, as many of the variables exist in both normalized and unnormalized form. Some symbols have multiple definitions; the applicable meanings are clear from the text in which such symbols are used. Boldface symbols are generally complex quantities; the corresponding amplitudes are in a math italics typeface. For example, $\mathbf{E}_R$ represents a complex electric field with amplitude E_R.

$\|_{th}$	Denotes the threshold value of the preceding variable (70:70)
a	Incoherent intensity summation term, Agrawal-Lax model (71:71)
$\|a\rangle$	Upper lasing level in the two-level atom model (18:18)
$\|\mathrm{a}\rangle$	General atomic energy level or state (18:18)
$a(t)$	Time-dependent coefficient of the atomic eigenfunction ψ_a (20:20)
A	Mirror intensity absorption coefficient (7:7)
A	Incoherent intensity summation term, traveling wave semiclassical laser models (41:41)
A_f	Incoherent intensity summation term in the amplifier region of the PBCUR laser (99:99)
A_{ap}	Area of the output coupler or aperture (170:170)
b	Intensity interference term for the counterpropagating traveling waves, Agrawal-Lax model (17:71)
$\|b\rangle$	Lower lasing level in the two-level atom model (18:18)
$b(t)$	Time-dependent coefficient of the atomic eigenfunction ψ_b (20:20)
B	Intensity interference term for the counterpropagating traveling waves, traveling wave semiclassical models (41:41)
B	Lower turning point on the cubic curves (121:121)
B	Shorthand notation for the electric field amplitude or phase functional variables in the numerical methods sections (209:209)
$\vec{\mathbf{B}}$	Magnetic field flux density vector (29:29)
B_f	Intensity interference term for the counterpropagating traveling waves in the amplifier section of the PBCUR laser (= 0), (99:99)
B_i^j	Functional variable B at mesh point (z_i, t_j); used in the numerical routines (209:209)
$B(\nu)$	Stimulated emission coefficient in the gain medium rate equation models (6:6)
c	Speed of light (31:31)
c.c.	Denotes the complex conjugate (17:16)
C	Intensity interference term for the counterpropagating traveling waves, traveling wave semiclassical models (41:41)

C	Upper turning point on the cubic curves; corresponds to the locking (minimum injected intensity) point (120:120)
C_f	Intensity interference term for the counterpropagating traveling waves in the amplifier section of the PBCUR laser (= 0), (99:99)
C-I-R	Courant-Isaac-Rees numerical technique (210:210)
$\vec{\mathbf{D}}$	Electric field flux density vector (29:29)
D_1	Total loss term for the electric fields, Lamb model (76:76)
D_2	Constant, Lamb model (76:76)
e	Central core region of the PBCUR laser (91:91)
e	Charge of an electron (19:19)
$\vec{\mathbf{e}}$	Unit vector in the direction of the electric field (19:19)
E_a	Energy of eigenstate $\|a\rangle$ (18:18)
E_{a}	Energy of the general eigenstate $\|\mathrm{a}\rangle$ (18:18)
E_b	Energy of eigenstate $\|b\rangle$ (18:18)
E_{HI}	High guess at the electric field, used in some of the numerical methods (199:199)
$\mathbf{E}_I$	Complex total injected electric field, inside the resonator (60:60)
E_I	Amplitude of $\mathbf{E}_I$ (60:60)
$\mathbf{E}_{IN}$	Complex total injected electric field, outside the resonator (60:60)
E_{IN}	Amplitude of $\mathbf{E}_{IN}$ (80:80)
E_{LO}	Low guess at the electric field, used in some of the numerical methods (199:199)
$\mathbf{E}_L(z,t)$	Total complex leftward traveling electric field inside the resonator (16:16)
$E_L(z,t)$	Amplitude of $\mathbf{E}_L(z,t)$, (16:16)
$E_n(z,t)$	Amplitude of the n^{th} electric field longitudinal mode (71:71)
$\mathbf{E}_{out}$	Total complex outcoupled electric field (58:58)
E_{out}	Amplitude of $\mathbf{E}_{out}$ (129:129)
$\vec{\mathbf{E}}(\vec{\mathbf{r}},t)$	Total complex electric field inside the resonator, including all transverse and longitudinal variations (14:14)
$\vec{\mathbf{E}}'(\vec{\mathbf{r}},t)$	Atomic reaction field (14:14)
$\mathbf{E}_R(z,t)$	Total complex rightward traveling electric field inside the resonator (16:16)
$E_R(z,t)$	Amplitude of $\mathbf{E}_R(z,t)$ (16:16)
$\mathbf{E}(z,t)$	Total complex electric field inside the resonator (17:17)
E_1	Initially launched phasor electric field from mirror B, Chow model (83:83)
E_2	Electric field phasor after a round trip through the resonator, Chow model (83:83)
f	Single pass amplifier region of the PBCUR laser (91:91)
f_n	n^{th} function in the general (vector) differential equation set (196:196)
$f_1(\hat{E}_n)$	Saturated gain function, Spencer-Lamb model (82:82)
$\mathrm{F_L}$	Focus of the leftward traveling wave (cylindrical or spherical), (15:15)
$\mathrm{F_R}$	Focus of the rightward traveling wave (cylindrical or spherical), (15:15)
F	General atomic property or observable (22:22)
$F\|_{\mathrm{Mxx}}$	Value of observable F at the MII, MG1, or MG2 operating point (151:151)
g	Conical boundary between regions e and f in the PBCUR laser (91:91)
$g(B)$	Shorthand notation for the driving function of B, used in the numerical methods sections (209:209)
g_0	Intensity small signal gain (68:7)
g_1	Complex laser system gain (electric field amplitude) for injected lasers (62:62)
g_1	Degeneracy of atomic level 1 in the gain medium rate equation models (6:6)

g_2	Degeneracy of atomic level 2 in the gain medium rate equation models (6:6)
g_3	Intensity small signal gain, Agrawal-Lax model (71:71)
G_0	Saturated laser gain, small signal gain models (8:8)
G_1	Laser system gain (electric field intensity) for injected lasers systems (63:63)
G_2	Internal laser intensity gain for injected lasers (63:63)
G_4	Laser system gain (electric field intensity) for injected lasers, Spencer-Lamb model (82:82)
h	Numerical step size between adjacent mesh points along the x axis (198:198)
h	Numerical step size between adjacent mesh points along the z axis (209:209)
$\hbar$	Planck's constant (18:18)
H	Total Hamiltonian applied to an atomic system (19:19)
$\vec{\mathbf{H}}$	Magnetic field vector (29:29)
$\hat{\mathbf{H}}$	Hamiltonian matrix (21:21)
H_{atom}	Atomic Hamiltonian (18:18)
i	Complex operator ($=\sqrt{-1}$), (15:15)
$I_{ap}(x,y,t)$	Intensity in the output aperture of the resonator (102:102)
I_I	Injected intensity inside the laser resonator (85:85)
I_{IN}	Injected intensity external to the laser resonator (3:3)
I_L	Intensity of the leftward traveling wave (68:7)
$\tilde{I}_L$	Intensity of the leftward traveling wave normalized by I_{sat} (137:137)
I'_L	Intensity of the leftward traveling wave, Agrawal-Lax model (72:71)
I_n	Intensity of the n^{th} longitudinal electric field mode of the laser
I_{out}	Intensity of the outcoupled laser electric field (3:3)
I_R	Intensity of the rightward traveling wave (68:7)
$\tilde{I}_R$	Intensity of the rightward traveling wave normalized by I_{sat} (137:137)
I'_R	Intensity of the rightward traveling wave, Agrawal-Lax model (72:71)
I_{sat}	Saturation intensity (69:8)
$\vec{\mathbf{J}}$	Current density vector (29:29)
k	Wavenumber of the electric field (16:16)
k	Numerical step size between adjacent mesh points along the t axis (209:209)
k_l	Linear dielectric constant (71:71)
k_n	Wavenumber of the n^{th} longitudinal electric field mode (73:73)
ℓ	Variable location on the z axis (120:120)
ℓ_L	z axis location of focus F_L (16:16)
ℓ_R	z axis location of focus F_R (16:16)
L	Resonator length (16:16)
L_D	Loss in the electric field equation due to the dielectric bump, Spencer-Lamb model (191:191)
L_g	Length of the laser gain medium (70:62)
L_L	Loss in the electric field equation due to outcoupling through mirror B, Lamb model (191:191)
m	Integer variable (58:58)
m	Atomic mass (18:18)
M	Geometric resonator magnification (89:89)
MG1	Maximum G_1 operating point (148:148)
MG2	Maximum G_2 operating point (148:148)
MII	Minimum injected intensity operating point (148:148)
n	Integer variable (54:54)

n	Atomic density, Agrawal-Lax model (71:71)
n	Index of refraction (143:143)
$n(z,t)$	Photon density, Franz-Nodvik model (208:208)
NLO	Nonlinear optical material (178:178)
$n_0(z,t)$	Initial condition for the photon density, Franz-Nodvik model (308:208)
N_1	Population density of atomic level 1, gain medium rate equation models (6:6)
N_1	Electric field loss term, Spencer-Lamb model (82:82)
N_2	Population density of atomic level 2, gain medium rate equation models (6:6)
N_2	Frequency shift term, Spencer-Lamb model (82:82)
PBCUR	Positive branch, confocal unstable resonator (12:12)
PDE	Partial differential equation (207:207)
$\langle \vec{P}_i \rangle$	Induced polarization in a single atom (14:14)
$\mathbf{P}_L(z,t)$	Complex leftward traveling polarization wave (17:17)
$P_L(z,t)$	Slowly (spatially) varying complex amplitude of $\mathbf{P}_L(z,t)$ (17:17)
$P'_L(z,t)$	Complex amplitude of $\mathbf{P}_L(z,t)$, including the rapidly varying spatial terms (order of e^{-ikz}), (18:18)
P_{out}	Output power from the laser (102:102)
$\vec{\mathbf{P}}(\vec{\mathbf{r}},t)$	Total macroscopic polarization of an atomic medium, including transverse and longitudinal variations (14:14)
$\mathbf{P}_R(z,t)$	Complex rightward traveling polarization wave (17:17)
$P_R(z,t)$	Slowly (spatially) varying complex amplitude of $\mathbf{P}_R(z,t)$ (17:17)
$P'_R(z,t)$	Complex amplitude of $\mathbf{P}_R(z,t)$, including the rapidly varying spatial terms (order of e^{ikz}), (18:18)
$\mathbf{P}(z,t)$	Total complex medium polarization (17:17)
q	Unsaturated complex laser gain (226:226)
$\vec{\mathbf{r}}$	Spatial coordinate (14:14)
$\mathbf{r}_A$	Complex amplitude reflection coefficient of mirror A (15:15)
r_A	Amplitude of $\mathbf{r}_A$ (15:15)
$\mathbf{r}_B$	Complex amplitude reflection coefficient of mirror B (15:15)
r_B	Amplitude of $\mathbf{r}_B$ (15:15)
$\mathbf{r}_D$	Complex amplitude reflection coefficient of the dielectric bump (78:78)
r_D	Amplitude of $\mathbf{r}_D$ (78:78)
R	General mirror intensity reflection coefficient (7:7)
R	Rate variable containing the spatial holeburning terms (40:40)
REA	Rate equation approximation (11:11)
R_s	Rate constant (40:40)
R_1	Pump rate to atomic level 1, gain medium rate equation models (6:6)
R_1	Mirror reference plane (184:184)
$\mathbf{r}_{11}$	General mirror amplitude reflection coefficient, left side (184:184)
R_2	Pump rate to atomic level 2, gain medium rate equation models (6:6)
R_2	Mirror reference plane (184:184)
$\mathbf{r}_{22}$	General mirror amplitude reflection coefficient, right side (184:184)
SL1	Unmodified Spencer-Lamb model (139:139)
SL2	Modified Spencer-Lamb model (139:139)
SSG	Simple saturable gain model (136:136)
SWL	Standing wave laser model (139:139)
t	General mirror amplitude transmission coefficient (185:185)
t	Time variable (6:6)

$\mathbf{t}_A$	Complex amplitude transmission coefficient of mirror A (15:15)
t_A	Amplitude of $\mathbf{t}_A$ (15:15)
$\mathbf{t}_B$	Complex amplitude transmission coefficient of mirror B (15:15)
t_B	Amplitude of $\mathbf{t}_B$ (15:15)
t_c	Photon cavity lifetime, gain medium rate equation models (6:6)
$\mathbf{t}_D$	Complex amplitude transmission coefficient of the dielectric bump (78:78)
t_D	Amplitude of $\mathbf{t}_D$ (78:78)
t_i	Mesh point along the time axis (209:209)
t_{nr}	Nonradiative decay time constant from atomic level 2 to 1, gain medium rate equation models (6:6)
t_{sp}	Spontaneous decay time constant from atomic level 2 to 1, gain medium rate equation models (6:6)
T	Pseudo-transmission coefficient of the dielectric bump (81:81)
TWL	Traveling wave laser model (54:54)
TWURL	Traveling wave unstable resonator laser model (97:97)
t_0	Initial time value (22:22)
t_{10}	Overall decay time constant from atomic level 1 to 0, gain medium rate equation models (6:6)
$\mathbf{t}_{12}$	General mirror amplitude transmission coefficient (184:184)
t_{20}	Overall decay time constant from atomic level 2 to 0, gain medium rate equation models (6:6)
$\mathbf{t}_{21}$	General mirror amplitude transmission coefficient (184:184)
$u_L(z,t)$	Real part of the leftward traveling polarization wave (26:26)
$u_R(z,t)$	Real part of the rightward traveling polarization wave (26:26)
$v_L(z,t)$	Negative imaginary part of the leftward traveling polarization wave (26:26)
$v_R(z,t)$	Negative imaginary part of the rightward traveling polarization wave (26:26)
V	Perturbing Hamiltonian (19:19)
$V_{atom}(\vec{r})$	Potential energy function of the atomic species (18:18)
V_g	Volume of the gain region (103:103)
w	Bloch vector term proportional to the population inversion density (25:25)
w_{eq}	Term proportional to the zero field population inversion density (27:27)
$w_{ew}\|_{cr}$	Critical w_{eq} value at which the Spencer-Lamb laser model is above threshold regardless of the outcoupling (192:192)
x	Independent variable; used in the explanation of the Runge-Kutta numerical routine (196:196)
$\hat{x}$	Transverse coordinate axis to the optical (z) axis; orthogonal to the $\hat{y}$ axis (29:29)
XeF	Xenon fluoride excimer laser (135:135)
x_k	k^{th} mesh point in the x direction; used in the numerical routines (198:198)
$\hat{y}$	Transverse coordinate axis to the optical (z) axis; orthogonal to the $\hat{x}$ axis (29:29)
$\vec{y}$	General vector differential equation system; used in the explanation of the Runge-Kutta numerical routine (196:196)
$\vec{y}_0$	Initial condition for the vector differential equation system $\vec{y}$; used in the Runge-Kutta numerical routine (196:196)
$\vec{y}_k$	Functional evaluation of the vector differential equation system $\vec{y}$ at the k^{th} step; used in the Runge-Kutta numerical routine (198:198)
$\vec{y}(x_0)$	Initial condition for the vector differential equation system $\vec{y}$; same as $\vec{y}$ (196:196)
z	Spatial coordinate along the optical axis; also refers to the optical axis (8:8)
z_i	Mesh point along the z or optical axis; used in the numerical routines (209:209)

z_0	Arbitrary position along the optical axis (25:25)
$\|0\rangle$	Atomic level 0 (ground state) in the gain medium rate equation models (6:6)
$\|1\rangle$	Atomic level 1 (lower lasing level) in the gain medium rate equation models (6:6)
$\|2\rangle$	Atomic level 2 (upper lasing level) in the gain medium rate equation models (6:6)
α	Exponent describing the cylindrical or spherical nature of a traveling wave field (16:16)
α_0	Nonsaturable gain medium losses (68:8)
β	Spatially dependent phase term (40:40)
β_0	Spatially constant phase term (43:43)
β_1	Spatially constant phase term (43:43)
γ	Atomic lifetime; inverse of the atomic linewidth (24:24)
γ_a	Mean lifetime of the upper lasing level, semiclassical theory (17:17)
γ_a	Mean lifetime of the general eigenstate $\|a\rangle$ (18:18)
γ_{ab}	Average of the mean lifetimes γ_a and γ_b (28:28)
γ_b	Mean lifetime of the lower lasing level, semiclassical theory (17:17)
γ_{ph}	Atomic collisional dephasing time (24:24)
Γ	Loss matrix (21:21)
$\delta(z)$	Dirac delta function (78:78)
$\delta\nu$	Longitudinal mode spacing in a loaded resonator (includes the gain medium pulling and pushing effects), (143:143)
$\delta\nu$	Frequency error in the numerical routines (204:204)
$\delta\phi$	Change in phase between adjacent mesh points; used in the initial phase conditions in the time-dependent laser codes (218:218)
$\vec{\Delta}_k$	Incremental change in the vector differential equation system $\vec{y}$ from one step to the next, Runge-Kutta method (198:198)
$\vec{\Delta}_k^{(i)}$	Runge-Kutta numerical routine terms (198:198)
ΔE_1	Fractional electric field amplitude change in a round trip in an injected laser, Chow model (84:83)
$\Delta f_{1/2}$	Full width at half maximum of the Fabry-Perot resonator response curve, in Hz (143:143)
Δm	Detuning of the barecavity mode frequency from the atomic linecenter frequency (54:54)
Δo	Detuning of the injected signal frequency from the free-running laser frequency (120:120)
$\pm\Delta o_{max}$	Detuning Δo at which turning points B and C merge on the cubic curves (125:125)
Δt	Detuning of the free-running laser frequency from the atomic linecenter frequency (54:54)
Δy	"Depth" of a strip PBCUR in the transverse $\hat{y}$ direction (102:102)
$\Delta(z,t)$	Population inversion density, Franz-Nodvik model (208:208)
$\Delta_0(z,t)$	Initial condition for the population inversion density in the laser amplifier, Franz-Nodvik model (208:208)
$\Delta\omega$	Detuning of the injected or reference signal frequency from the atomic linecenter frequency (26:26)
$\Delta\omega_{1/2}$	Full width at half maximum of the Fabry-Perot resonator response curve, in radian frequency (143:143)
ϵ	Exponent used used in the simple saturable gain model; value is dependent on whether the broadening mechanism is homogeneous or inhomogeneous (64:64)
ϵ	Material permittivity (183:183)

ϵ	Fractional phase change in a round trip in an injected laser, Chow model (83:83)
ϵ_{DB}	Permittivity of the dielectric bump (78:78)
ϵ_i	Phase term (219:219)
ϵ_0	Vacuum permittivity (29:29)
ϵ_ϕ	Maximum allowable phase error in the numerical routines (203:203)
ς	Binomial expansion term (67:67)
ς	Spatial variable in the initial conditions, time-dependent laser codes (222:222)
η	Scaled dielectric bump "height" (78:78)
η_L	Laser power extraction efficiency (103:103)
θ	Integration (angular) variable (35:35)
ϑ	Fractional phase "error" in a round trip, TWL and TWURL models (62:62)
θ_0	Integration (angular) limit (35:35)
λ	Optical field wavelength (25:25)
λ_a	Excitation rate to the upper laser level, semiclassical models (23:23)
$\lambda_a(t)$	Excitation rate to the general atomic level $\|a\rangle$, semiclassical models (22:22)
λ_b	Excitation rate to the lower laser level, semiclassical models (23:23)
Λ	"Height" of the dielectric bump (78:78)
$\bar{\Lambda}$	Excitation matrix (23:23)
μ	Dipole moment matrix element (20:20)
μ	Material permeability (183:183)
μ_0	Vacuum permeability (29:29)
ν	Free-running or instantaneous laser frequency (30:30)
ν_{ave}	Average of ν_{HI} and ν_{LO} (203:203)
ν_{HI}	High initial frequency guess; used in the numerical routines (202:202)
ν_I	Injected signal or reference frequency (16:16)
ν_L	Frequency of the leftward traveling wave electric field (38:38)
ν_{LO}	Low initial frequency guess; used in the numerical routines (202:202)
ν_n	Frequency of the n^{th} longitudinal laser mode (73:73)
ν_R	Frequency of the rightward traveling wave electric field (38:38)
ξ_L	Phase term for a leftward traveling cylindrical or spherical wave (35:35)
ξ_R	Phase term for a rightward traveling cylindrical or spherical wave (35:35)
ρ	Density matrix for a single atom (21:21)
ρ_{ij}	ij^{th} element of the single atom density matrix (21:21)
ϱ_{ij}	ij^{th} element of the statistical average (population) density matrix (24:24)
ρ_L	Radial field coordinate, leftward traveling cylindrical or spherical wave (16:16)
ρ_R	Radial field coordinate, rightward traveling cylindrical or spherical wave (16:16)
$\varrho(t)$	Statistical average (population) density matrix (23:23)
σ	Electric field loss term in a medium; also called "pseudo-conductivity" (29:29)
σ	Material absorption coefficient (183:183)
σ	Resonance absorption cross section, Franz-Nodvik model (208:208)
σ_a	Stimulated emission cross section (70:70)
τ	Zero field population inversion density lifetime, unnormalized units, semiclassical models (28:28)
τ_{cav}	Unnormalized electric field decay constant, due to miscellaneous medium losses (photon lifetime), (34:34)
τ_1	Zero field population inversion density lifetime, normalized units, semiclassical models (34:34)

τ_2	Normalized electric field decay constant, due to miscellaneous medium losses (photon lifetime), (34:34)
τ_3	Normalized round trip time inside the laser resonator (62:62)
ϕ	Photon density, gain medium rate equation models (6:6)
ϕ	General electric field phase variable (33:33)
$\dot{\varphi}$	General electric field phase time derivative (41:41)
ϕ_E	Phase error, used in the numerical routines (203:203)
ϕ_I	Phase of $\mathbf{E}_I$ (60:60)
$\dot{\varphi}_L$	Time derivative of $\phi_L(z,t)$ (41:41)
$\phi_L(z,t)$	Phase of $\mathbf{E}_L(z,t)$ (16:16)
ϕ'_L	Constant term in a Taylor series expansion about t of $\phi_L(z,t)$ (38:38)
$\phi_n(t)$	Phase of the n^{th} longitudinal laser mode (74:74)
$\dot{\varphi}_n$	Time derivative of $\phi_n(t)$ (74:74)
$\dot{\varphi}_R$	Time derivative of $\phi_R(z,t)$ (41:41)
ϕ_{RA}	Phase of $\mathbf{r}_A$ (15:15)
ϕ_{RB}	Phase of $\mathbf{r}_B$ (15:15)
ϕ_{RD}	Phase of $\mathbf{r}_D$ (78:78)
$\phi_R(z,t)$	Phase of $\mathbf{E}_R(z,t)$ (16:16)
ϕ'_R	Constant term in a Taylor series expansion about t of $\phi_R(z,t)$ (38:38)
ϕ_{TA}	Phase of $\mathbf{t}_A$ (15:15)
ϕ_{TB}	Phase of $\mathbf{t}_B$ (15:15)
ϕ_{TD}	Phase of $\mathbf{t}_D$ (78:78)
ψ	Normalized speed of light ($= c/\gamma L$), (35:35)
$\psi_a(\vec{\mathbf{r}})$	Eigenfunction of atomic eigenstate $\|a\rangle$ (20:20)
$\psi_a(\vec{\mathbf{r}})$	Eigenfunction of the general atomic state $\|a\rangle$ (18:18)
$\psi_b(\vec{\mathbf{r}})$	Eigenfunction of atomic eigenstate $\|b\rangle$ (20:20)
ψ_{DB}	Pseudo transmission coefficient phase of the dielectric bump (81:81)
ψ_L	Modified ψ (220:220)
ψ_{L1}	Modified ψ (224:223)
ψ_{L2}	Modified ψ (224:223)
ψ_R	Modified ψ (220:220)
ψ_{R1}	Modified ψ (223:223)
ψ_{R2}	Modified ψ (223:223)
$\Psi_a(\vec{\mathbf{r}},t)$	Eigenfunction for the general eigenstate $\|a\rangle$ (18:18)
$\Psi(\vec{\mathbf{r}},t)$	Total atomic eigenfunction (20:20)
ω	Atomic linecenter frequency (18:18)
ω_a	Frequency of eigenstate $\|a\rangle$ (18:18)
ω_b	Frequency of eigenstate $\|b\rangle$ (18:18)
Ω	Barecavity longitudinal mode frequency (31:31)
Ω'	Shifted barecavity longitudinal mode frequency; shifting is due to the frequency effects of the dielectric bump (188:188)

Bibliography

1. Bernard, Jay M. *et al.* "Coupled Multiline CW HF Lasers: Preliminary Experiments," to be published in Optics Letters (November 1987).

2. -----. "Coupled Multiline CW HF Lasers: Experimental Performance," unpublished technical report (20 March 1987).

3. Calahan, Ken R. *et al.* "Coupled CW Atomic Iodine Lasers at 1.315 Microns," unpublished technical report, AFWL/ARBM, Kirtland AFB, New Mexico, 87117-6008.

4. Chandra, S. "Radiation Exchange and Oscillations in a Pair of Cavities Sharing a Partial Reflector," IEEE Journal of Quantum Electronics, QE-19: 261–263 (March 1983).

5. Chow, Weng W. "Frequency Locking in Coupled Lasers," unpublished technical report.

6. Fader, W. J. "Theory of Two Coupled Lasers," unpublished technical note.

7. Fontana, J. R. "Modes in Coupled Optical Resonators with Active Media," IEEE Transactions on Microwave Theory and Techniques: 400–405 (July 1964).

8. Mirels, Harold. "Performance of Two Coupled Lasers," Applied Optics, 25: 2130–2137 (1 July 1986).

9. Palma, G. E. *et al.* Coupled Resonator Mode Analysis Investigation. AFWL-TR-85-98. Kirtland AFB, New Mexico: Air Force Weapons Laboratory, August 1986.

10. -----. Coupled Resonator Beam Combining Investigation. AFWL-TR-84-95. Kirtland AFB, New Mexico: Air Force Weapons Laboratory, June 1984.

11. Rigova, I. V. "Coupled Lasers," Soviet Physics-Technical Physics, 13: 1525–1528 (May 1969).

12. Rinaldi, Steven M. "Coupled Device Technology Program," AIAA/SDIO High Energy Laser Conference, 3-4 March 1987.

13. Rogers, Mark E. "A White Paper on the Coupled Device Technology Program," unpublished technical report, AFWL/ARBL, Kirtland AFB, New Mexico, 87117-6008.

14. Shakir, Sami A. and Weng W. Chow. "The Semiclassical Theory of Coupled Lasers," Optics Letters, 9: 202 (June 1984).

15. Shakir, Sami A. and John H. Erkkila. "Mode Discrimination in Adjoint-Coupled Lasers," unpublished technical report.

16. -----. Modeling and Analysis of Coupled Resonators and Amplifiers. Final task report. Kirtland AFB, New Mexico: Air Force Weapons Laboratory, 22 May 1987.

17. Spencer, Martin B. and Willis E. Lamb, Jr. "Theory of Two Coupled Lasers," Physical Review A, 5: 893–898 (February 1972).

18. Stevens, Charles B. "Air Force Demonstrates Phased-Array Laser," Fusion: 24-26 (July-August 1986).

19. Walsh, Dwight M. "Longitudinal Supermode Analysis of Two Coupled CO_2 Lasers," Proceedings of the SPIE, SE Conference on Optics and Optoelectronics (April 1986).

20. Coffer, J. G. *et al.* "Experiments with Active Phase Matching of Parallel-Amplified Multiline HF Laser Beams by a Phase-Locked Mach-Zehnder Interferometer," Applied Optics, 22: 142-148 (1 January 1983).

21. Jacoby, J. L. *et al.* Multiline CW Coupled Devices. AFWL-TR-87-85. Kirtland AFB, New Mexico: Air Force Weapons Laboratory, June 1987.

22. Sentman, L. H. Temporal Variations in a CW HF MOPA. Technical Report AAE 86-2. Arlington, VA: Defense Advanced Research Projects Agency, April 1986.

23. Hayes, C. L. *et al.* High Power Phase Locked Laser Oscillators. NASA CR-159630. Washington, D.C.: National Aeronautics and Space Administration, May 1979.

24. -----. "High-Power-Laser Adaptive Phased Arrays," Applied Optics, 18: 4106-4111 (15 December 1979).

25. -----. "Experimental Test of an Infrared Phase Conjugate Adaptive Array," Journal of the Optical Society of America, 67: 269-277 (March 1977).

26. Mevers, G. E. *et al.* "Ground-to-Space Optical Power Transfer," Proceedings of the SPIE, Adaptive Optical Components, 141: 108-117 (30-31 March 1978).

27. SooHoo, J. and C. L. Hayes. "Phase Locking of a Multimode to a Single-Mode He-Ne Laser," Optics Letters, 4: 202-204 (July 1979).

28. Brown, Wilbur P. *et al.* Coupled Resonator Modeling Techniques. AFWL-TR-87-68. Kirtland AFB, New Mexico: Air Force Weapons Laboratory, April 1987.

29. White, Jeffrey O. *et al.* "Coherent Combining of Pulsed Dye Oscillators Using Nonlinear Phase Conjugation," unpublished technical report.

30. Dee, Diana *et al.* Coupled Amplifiers. AFWL-TR-86-93. Kirtland AFB, New Mexico: Air Force Weapons Laboratory, July 1986.

31. Rockwell, D. A. and C. R. Giuliano. "Coherent Coupling of Laser Gain Media Using Phase Conjugation," Optics Letters, 11: 147-149 (March 1986).

32. Stephens, R. R. *et al.* "Phase Conjugate Master Oscillator-Power Amplifier Using $BaTiO_3$ and AlGaAs Semiconductor Diode Lasers," unpublished technical report.

33. Leger, James R. *et al.* "Coherent Beam Addition of GaAlAs Lasers by Binary Phase Gratings," Applied Physics Letters, 48: 888-890 (7 April 1986).

34. Veldkamp, Wilfrid B. *et al.* "Coherent Summation of Laser Beams Using Binary Phase Gratings," Optics Letters, 11: 303-305 (May 1986).

35. Akins, Robert and Sing Lee. "Coherent Optical Image Amplification by an Injection-Locked Dye Amplifier at 632.8 nm," Applied Physics Letters, 35: 660–662 (1 November 1979).

36. Angelbeck, A. W. *et al.* Novel Concepts for High Power Chemical Lasers, Phase II. R81-914756-21. Washington, D. C.: Naval Research Laboratory, 15 September 1981.

37. Bava, E. *et al.* "Feasibility of FIR Laser Stabilization by Injection of a Synthesized Signal," IEEE Transactions on Instrumentation and Measurement, IM-29: 273-276 (December 1980).

38. Bigio, Irving J. and Michael Slatkine. "Injection-Locking Unstable Resonator Excimer Lasers," IEEE Journal of Quantum Electronics, QE-19: 1426–1436 (September 1983).

39. -----. "Transform-Limited-Bandwidth Injection Locking of an XeF Laser with an AR-Ion Laser at 3511Å," Optics Letters, 7: 19–21 (January 1982).

40. -----. "Attainment of the Theoretical Minimum Input Power for Injection Locking of an Unstable-Resonator KrF Laser," Optics Letters, 6: 336–338 (July 1981).

41. Bjorkholm, J. E. and H. G. Danielmeyer. "Frequency Control of a Pulsed Optical Parametric Oscillator by Radiation Injection," Applied Physics Letters, 6: 171–173 (15 September 1969).

42. Boulnois, J. L. *et al.* "Self Pulsing in a CO_2 Ring Laser with an Injected Signal," Optics Communications, 58: 124–129 (15 May 1986).

43. Buczek, Carl J. and Robert J. Freiberg. "Hybrid Injection Locking of Higher Power CO_2 Lasers," IEEE Journal of Quantum Electronics, QE-8: 641–650 (July 1972).

44. Burlamacchi, P. and R. Salimbeni. "Spectral Narrowing of a Flashlamp-Pumped, Waveguide Dye Laser by Amplification of Tunable Narrow-Band CW Radiation," Optics Communications, 17: 6–9 (April 1976).

45. Carney, E. R. *et al.* "Injection-Locked Dye Laser Pumped by a Xenon-Ion Laser," IEEE Journal of Quantum Electronics, QE-16: 9–10 (January 1980).

46. Caro, R. G. *et al.* "A Simple Tunable KrF Laser System with Narrow Bandwidth and Diffraction-Limited Divergence," Journal of Physics D: Applied Physics, 15: 767–773 (1982).

47. Corkum, P. B. and H. A. Baldis. "Extra-Cavity Feedback into Unstable Resonators," Applied Optics, 18: 1346–1349 (1 May 1979).

48. Dunn, Robert W. *et al.* "Single-Mode Operation of Doppler-Broadened Lasers by Injection Locking," Optics Letters, 8: 319–321 (June 1983).

49. Erickson, L. E. and A. Szabo. "Spectral Narrowing of Dye Laser Output by Injection of Monochromatic Radiation into the Laser Cavity," Applied Physics Letters, 18: 433–435 (15 May 1971).

50. Flamant, Pierre and Gérard Mégie. "Frequency Locking by Injection in Dye Lasers: Analysis of the CW and Delta Pulse Regimes," IEEE Journal of Quantum Electronics, QE-16: 653–660 (June 1980).

51. Gallion, P. *et al.* "Output Spectrum of an Unlocked Optically Driven Semiconductor Laser," Optics Letters, 11: 294–296 (May 1986).

52. Gibson, A. J. and L. Thomas. "Injection-Locking of a Flashlamp-Pumped Dye Laser Without Longitudinal Mode Matching," Journal of Physics D: Applied Physics, 11: L59–L61 (1978).

53. Goldhar, Julius *et al.* "An Injection-Locked Unstable Resonator Rare-Gas Halide Discharge Laser of Narrow Linewidth and High Spatial Quality," IEEE Journal of Quantum Electronics, QE-16: 235–241 (February 1980).

54. -----. "Injection-Locked, Narrow-Band KrF Discharge Laser Using an Unstable Resonator Cavity," Optics Letters, 1: 199–201 (December 1977).

55. -----. "Injection Locking of a Xenon Fluoride Laser," Applied Physics Letters, 31: 677–679 (15 November 1977).

56. Lowdermilk, W. H. and J. E. Murray. "Injection Locked Nd:YAG Oscillator," IEEE Journal of Quantum Electronics, QE-13: 66D (September 1977).

57. Magyar, G. and H.-J. Schneider-Muntau. "Dye Laser Forced Oscillator," Applied Physics Letters, 20: 406–408 (15 May 1972).

58. Man, C. N. and A. Brillet. "Injection Locking of Argon-Ion Lasers," Optics Letters, 9: 783–784 (August 1984).

59. Megie, G. and R. T. Menzies. "Tunable Single-Longitudinal-Mode Operation of an Injection-Locked TEA CO_2 Laser," Applied Physics Letters, 35: 835–838 (1 December 1979).

60. Mogensen, Finn *et al.* "Locking Conditions and Stability Properties for a Semiconductor Laser with External Light Injection," IEEE Journal of Quantum Electronics, QE-21: 784–793 (July 1985).

61. Moody, S. E. and Thomas N. Carlstrom. "Simple Coupling Method for Injection Locking of Unstable Resonators," Applied Optics, 21: 4401–4403 (15 December 1982).

62. Moses, E. I. *et al.* "Mode Locking of Laser Oscillators by Injection Locking," Applied Physics Letters, 28: 258–260 (1 March 1976).

63. Munch, Jesper and Barbara Saur. Injection Locking of Multiline Chemical Lasers. Final report. Washington, D.C.: Naval Research Laboratory, 31 January 1982.

64. Okada, Tatsuo *et al.* "Spectral Narrowing of a Flashlamp-Pumped High-Energy Dye Laser by Two-Stage Injection Locking," IEEE Journal of Quantum Electronics, QE-15: 616–623 (July 1979).

65. Pacala, Thomas J. and C. P. Christensen. "Control of XeF Laser Output by Pulse Injection," Applied Physics Letters, 36: 620–623 (15 April 1980).

66. Park, Y. K. *et al.* "Stable Single-Axial-Mode Operation of an Unstable-Resonator Nd:YAG Oscillator by Injection Locking," Optics Letters, 5: 96–98 (March 1980).

67. Pease, A. A. *et al.* "An Injection Locked Ring Amplifier," IEEE Journal of Quantum Electronics, QE-13: 28D–29D (September 1977).

68. Product List: Excimer Lasers, Dye Lasers, and Accessories. Lambda Physik, Lasertechnik, Acton, Massachusetts (1987).

69. Shay, T. *et al.* "Line Narrowing and Enhanced Efficiency of an HgBr Laser by Injection Locking," Applied Physics Letters, 39: 783–785 (15 November 1981).

70. Sheffield, R. L. *et al.* "An Independently Controllable Multiline Laser Resonator and Its Use in Multifrequency Injection Locking," Applied Physics Letters, 29: 588–590 (1 November 1976).

71. Stover, H. L. and W. H. Steier. "Locking of Laser Oscillators by Light Injection," Applied Physics Letters, 8: 91–93 (15 February 1966).

72. Turner, J. J. *et al.* "Spectral Narrowing and Electro-Optical Tuning of a Pulsed Dye Laser by Injection-Locking to a CW Dye Laser," Applied Physics Letters, 27: 441–443 (15 October 1975).

73. Urisu, Tsuneo *et al.* "Stabilized Injection Locking Light Amplification of a 1.15 μm He-Ne Laser," Journal of Applied Physics, 52: 3154–3158 (May 1981).

74. Vrehen, Q. H. F. and A. J. Breimer. "Spectral Properties of a Pulsed Dye Laser with Monochromatic Injection," Optics Communications, 4: 416–420 (February/March 1972).

75. Weiss, C. O. *et al.* "Injection Locking of an Optically Pumped FIR Laser," IEEE Journal of Quantum Electronics, QE-16: 498–499 (May 1980).

76. West, John B. *et al.* "Efficient Injection-Locking of an e-Beam-Excited XeF Laser," Journal of Applied Physics, 52: 5383–5385 (August 1981).

77. Bandy, Donna K. *et al.* "Coexisting Attractors in a Laser with an Injected Signal," Journal of the Optical Society of America, B, 2 (January 1985).

78. ----. "Self-Pulsing and the Approach to Chaos in a Laser with Injected Signal," Coherence and Quantum Optics, V, edited by Leonard Mandel and Emil Wolf. Plenum Publishing Corporation, 585–592, 1984.

79. Behling, H. H. "Computer Simulation of Adler's Generalized Equation for the Interaction of Oscillators with Injected Signals," Proceedings of the IEEE, 63: 1522–1523 (October 1975).

80. Buczek, Carl J. *et al.* "Laser Injection Locking," Proceedings of the IEEE, 61: 1411–1431 (October 1973).

81. Calandra, Enrico F. and Antonino M. Sommariva. "Stability Analysis of Injection-Locked Oscillators in Their Fundamental Mode of Operation," IEEE Transactions on Microwave Theory and Techniques, MTT-29: 1137–1144 (November 1981).

82. Chow, Weng W. "Theory of Line Narrowing and Frequency Selection in an Injection Locked Laser," IEEE Journal of Quantum Electronics, QE-19: 243–249 (February 1983).

83. -----. "Phase Locking of Lasers by an Injected Signal," Optics Letters, 7: 417–419 (September 1982).

84. Davies, A. R. *et al.* "INJLOK—A CO_2 Laser Injection Locking Code," Computer Physics Communications, 20: 413–420 (1980).

85. Eimerl, D. "Transient Laser Dynamics," *Laser Program* Annual Report-1979, Volume 3, edited by John R. Strack. UCRL-50021-79. Lawrence Livermore National Laboratory, University of California, Livermore, California, 7-78 – 7-83 (March 1980).

86. -----. "Injection Locking and Amplified Spontaneous Emission (ASE)," *Laser Program* Annual Report-edited by Brian D. Jarman. UCRL-50021-78. Lawrence Livermore National Laboratory, University of California, Livermore, California, 8- 14 – 8-22 (March 1979).

87. Ferguson, Thomas R. "Intensity Extrema in Optically Injected Fabry-Perot Cavities with Saturable Gain," unpublished technical report, AFWL/ARBL, Kirtland AFB, New Mexico, 87117-6008.

88. -----. Private communications. AFWL/ARBM, Kirtland AFB, New Mexico, 87117-6008, January-October 1987.

89. -----. "Inherently Injected Unstable Resonators," Applied Optics, 25: 581–584 (15 February 1986).

90. Ganiel, U. *et al.* "Analysis of Injection Locking in Pulsed Dye Laser Systems," IEEE Journal of Quantum Electronics, QE-12: 704–716 (November 1976).

91. Ibrahim, Magdy M. "On Injection Locking of Homogeneously Broadened Lasers," IEEE Journal of Quantum Electronics, 14: 145–147 (March 1978).

92. Juramy, Pierre *et al.* "Spectral Properties of Pulsed Dye Lasers," IEEE Journal of Quantum Electronics, QE-13: 855–865 (October 1977).

93. Kedmi, J. and D. Treves. "Injection-Locking Optimization in Unstable Resonators," Applied Optics, 20: 2108–2112 (15 June 1981).

94. Kurnosov, V. D. and A. T. Semenov. "Injection Laser with Two Strongly Coupled Resonators," Soviet Journal of Quantum Electronics, 4: 17–20 (July 1974).

95. Lachambre, Jean-Louis *et al.* "Injection Locking and Mode Selection in TEA-CO_2 Laser Oscillators," IEEE Journal of Quantum Electronics, QE-12: 756–764 (December 1976).

96. Lugiato, L. A. and L. M. Narducci. "Self-Pulsing, Breathing and Chaos in Optical Bistability and in a Laser with Injected Signal," Coherence and Quantum Optics, V, edited by Leonard Mandel and Emil Wolf. Plenum Publishing Corporation, 941–955, 1984.

97. Lugiato, L. A. *et al.* "Breathing, Spiking and Chaos in a Laser with Injected Signal," Optics Communications, 46: 64–68 (1 June 1983).

98. Munch, J. *et al.* Theoretical Study of Injection Locking in Chemical Lasers. Final Report. Washington, D.C: Naval Research Laboratory, 15 July 1980.

99. Okada, T. *et al.* "Off-Line Center Operation of an Injection-Locked Single-Mode TEA CO_2 Laser," Applied Optics, 20: 2176–2178 (1 July 1981).

100. Pantell, R. H. "The Laser Oscillator with an External Signal," Proceedings of the IEEE, 53: 474–477 (May 1965).

101. Spencer, Martin B. and Willis E. Lamb, Jr. "Laser with a Transmitting Window," Physical Review A, 5: 884–892 (February 1972).

102. Tang, C. L. and H. Statz. "Phase-Locking of Laser Oscillators by Injected Signal," Journal of Applied Physics, 38: 323–324 (January 1967).

103. Wang, C. P. and P. L. Smith. "Phase Control of HF Chemical Lasers for Coherent Optical Recombination," Applied Optics, 18: 1322–1327 (1 May 1979).

104. Wang, C. P. "Master and Slave Oscillator Array System for Very Large Multiline Lasers," Applied Optics, 17: 83–86 (1 January 1978).

105. Willis, C. R. "Phase Transition Analogy for a Laser with an Injected Signal," Coherence and Quantum Optics, V, edited by Leonard Mandel and Emil Wolf. Plenum Publishing Corporation, 225–232, 1984.

106. Sargent III, Murray. *et al.* Laser Physics. Reading, Massachusetts: Addison-Wesley Publishing Company, 1974.

107. van der Pol, Balth. "The Nonlinear Theory of Electric Oscillations," Proceedings of the Institute of Radio Engineers, 22: 1051–1086 (September 1934).

108. Adler, Robert. "A Study of Locking Phenomena in Oscillators," Proceedings of the I.R.E. and Waves and Electrons, 34: 351–357 (June 1946).

109. Atkinson, J. B. and Frank P. Pace. "The Spectral Linewidth of a Flashlamp-Pumped Dye Laser," IEEE Journal of Quantum Electronics, QE-9: 569–574 (June 1973).

110. Casperson, Lee W. "Spectral Narrowing in Double-Pass Superradiant Lasers," Optics Communications, 8: 85–87 (May 1973).

111. -----. "Saturation and Power in a High-Gain Gas Laser," IEEE Journal of Quantum Electronics, QE-9: 250–252 (February 1973).

112. Chernin, David P. "Optical Extraction Efficiency in Lasers with High Fresnel Number Confocal Unstable Resonators," Applied Optics, 18: 562–566 (1 November 1979).

113. Eimerl, D. "Optical Extraction Characteristics of Homogeneously Broadened CW Lasers with Nonsaturating Lasers," Journal of Applied Physics, 51: 3008–3016 (June 1980).

114. Frantz, Lee M. and John S. Nodvik. "Theory of Pulse Propagation in a Laser Amplifier," Journal of Applied Physics, 34: 2346–2349 (August 1963).

115. Ganiel, U. *et al.* "Amplified Spontaneous Emission and Signal Amplification in Dye-Laser Systems," IEEE Journal of Quantum Electronics, QE-11: 881–892 (November 1975).

116. Hunter, Allen M. and Robert O. Hunter, Jr. "Bidirectional Amplification with Nonsaturable Absorption and Amplified Spontaneous Emission," IEEE Journal of Quantum Electronics, QE-17: 1879–1887 (September 1981).

117. Keller, Richard A. "Effect of Quenching of Molecular Triplet States in Organic Dye Lasers," IEEE Journal of Quantum Electronics, QE-6: 411–416 (July 1970).

118. Marlow, W. C. "Approximate Lasing Condition," Journal of Applied Physics, 41: 4019–4022 (September 1970).

119. Moore, G. T. and R. J. McCarthy. "Lasers with Unstable Resonators in the Geometrical Optics Limit," Journal of the Optical Society of America, 67: 221–227 (February 1977).

120. Moreno, J. B. *et al.* "Amplified Spontaneous Emission and Gain-Saturation Nonlinearity in High-Gain Optical Amplifiers: The Biased Amplifier," Journal of Applied Physics, 48: 238–242 (January 1977).

121. Rigrod, William W. "Homogeneously Broadened CW Lasers with Uniform Distributed Loss," IEEE Journal of Quantum Electronics, QE-14: 377–381 (May 1978).

122. -----. "Saturation Effects in High-Gain Lasers," Journal of Applied Physics, 36: 2487-2490 (August 1965).

123. -----. "Gain Saturation and Output Power of Optical Masers," Journal of Applied Physics, 34: 2602–2609 (September 1963).

124. Schulz-DuBois, E. O. "Pulse Sharpening and Gain Saturation in Traveling-Wave Masers," The Bell System Technical Journal, 43: 625–658 (March 1964).

125. Sorokin, P. P. *et al.* "Flashlamp-Pumped Organic-Dye Lasers," Journal of Chemical Physics, 48: 4726–4741 (15 May 1968).

126. Aronowitz, Frederick. "Theory of a Traveling-Wave Optical Maser," Physical Review, 139: A635–A646 (2 August 1965).

127. O'Bryan III, C. L. and Murray Sargent, III. "Theory of Multimode Laser Operation," Physical Review A, 8: 3071–3092 (December 1973).

128. Casperson, Lee W. "Stability Criteria for High-Intensity Lasers," Physical Review A, 21: 911–923 (March 1980).

129. Close, Donald H. "Strong-Field Saturation Effects in Laser Media," Physical Review, 153: 360–371 (10 January 1967).

130. Davis, L. W. "Semiclassical Treatment of the Optical Maser," Proceedings of the IEEE: 76–80 (January 1963).

131. Feldman, B. J. and M. S. Feld "Theory of a High-Intensity Gas Laser," Physical Review A, 1: 1375–1396 (May 1970).

132. Grasiuk, A. Z. and A. N. Oraevskij. "The Dynamics of Quantum Oscillators," Proceedings of the International School of Physics, "Enrico Fermi". Course XXXI, Quantum Electronics and Coherent Light, edited by P. A. Miles. New York: Academic Press, 192–197, 1964.

133. Haken, H. Light, Volume I: Waves, Photons, Atoms. Amsterdam: North-Holland Publishing Company, 1981.

134. Lamb, Jr., Willis E. "Theory of an Optical Maser," Physical Review, 134: A1429–1450 (15 June 1964).

135. ----. "Theory of Optical Maser Oscillators," Proceedings of the International School of Physics, "Enrico Fermi". Course XXXI, Quantum Electronics and Coherent Light, edited by P. A. Miles. New York: Academic Press, 78–109, 1964.

136. Shirley, Jon H. "Dynamics of a Simple Maser Model," American Journal of Physics, 36: 949–963 (November 1968).

137. Stenholm, Stig. "The Semiclassical Theory of the Gas Laser," Progress in Quantum Electronics, Volume I, edited by J. H. Sanders and K. W. H. Stevens. Oxford: Pergamon Press, 187–270, 1971.

138. Stenholm, Stig and Willis E. Lamb. "Semiclassical Theory of a High-Intensity Laser," Physical Review, 181: 618–635 (10 May 1969).

139. Stroud, Jr., C. R. and E. T. Janynes. "Long-Term Solutions in Semiclassical Radiation Theory," Physical Review A, 1: 106–121 (January 1970).

140. Uchida, Teiji. "Dynamic Behavior of Gas Lasers," IEEE Journal of Quantum Electronics, QE-3: 7–16 (January 1967).

141. Yariv, Amnon. Quantum Electronics (2nd Edition). New York: John Wiley & Sons, 1975.

142. Agrawal, G. P. and M. Lax. "Analytic Evaluation of Interference Effects on Laser Output in a Fabry-Perot Resonator," Journal of the Optical Society of America, 71: 515–519 (May 1981).

143. ----. "Effects of Interference on Gain Saturation in Laser Resonators," Journal of the Optical Society of America, 69: 1717–1719 (December 1979).

144. Kogelnik, H. and T. Li. "Laser Beams and Resonators," Proceedings of the IEEE, 54: 1312-1329 (October 1966).

145. Svelto, Orazio. Principles of Lasers. New York: Plenum Press, 1982.

146. Yariv, Amnon. Introduction to Optical Electronics (Second Edition). New York: Holt, Rinehart and Winston, 1971.

147. Erkkila, John H. "The Dielectric Bump," lecture materials distributed in PH9.99. School of Engineering, Air Force Institute of Technology (AU), Wright-Patterson AFB, Ohio, 1984.

148. Anan'ev, Y. U. "Establishment of Oscillations in Unstable Resonators," Soviet Journal of Quantum Electronics, 5: 615–617 (December 1975).

149. Isaev, A. A. *et al.* "Shaping of the Output Beam in a Pulsed Gas Laser with an Unstable Resonator," Soviet Journal of Quantum Electronics, 7: 746-752 (December 1977).

150. -----. "Evolution of Gaussian Beams and Pulse Stimulated Emission from Lasers with Unstable Resonators," Soviet Journal of Quantum Electronics, 5: 607–614 (December 1975).

151. -----. "Converging Beams in Unstable Telescopic Resonators," Soviet Journal of Quantum Electronics, 4: 761-766 (December 1974).

152. Zemskov, K. I. *et al.* "Use of Unstable Resonators in Achieving the Diffraction Divergence of the Radiation Emitted from High-Gain Pulsed Gas Lasers," Soviet Journal of Quantum Electronics, 4: 474-477 (October 1974).

153. Erkkila, John H. Analyses performed under Contract F29601-85-C-0025. Kirtland AFB, New Mexico: Air Force Weapons Laboratory, 1987.

154. -----. Lecture materials distributed in PH8.99, Laser Resonators. School of Engineering, Air Force Institute of Technology (AU), Wright-Patterson AFB, Ohio, 1983.

155. Rogers, Mark E. Private communications. USAFA/DFP, United States Air Force Academy, Colorado, June 1987.

156. Glessner, John. Private communications. AFWL/ARBM, Kirtland AFB, New Mexico, 87117-6008, June 1987.

157. Rinaldi, Steven M. "Phasing Issues for Coupled Devices," unpublished technical note, AFWL/ARBL, Kirtland AFB, New Mexico, 87117-6008, 30 January 1987.

158. Siegman, A. E. "Unstable Optical Resonators for Laser Applications," Proceedings of the IEEE, 53: 277–287 (March 1965).

159. Gradshteyn, I. S. and I. M. Ryzhik. Table of Integrals, Series, and Products (Corrected and Enlarged Edition). Edited by Alan Jeffrey. New York: Academic Press, 1980.

160. Seigman, A. E. An Introduction to Lasers and Masers. New York: McGraw-Hill Book Company, 1971.

161. Young, David M. and Robert Todd Gregory. A Survey of Numerical Mathematics (Volume I). Reading, Massachusetts: Addison- Wesley Publishing Company, 1972.

162. -----. A Survey of Numerical Mathematics (Volume II). Reading, Massachusetts: Addison-Wesley Publishing Company, 1972.

163. Szidarovszky, F. and S. Yakowitz. Principles and Procedures of Numerical Analysis. New York: Plenum Press, 1978.

164. Wendroff, Burton. Theoretical Numerical Analysis. New York: Academic Press, 179–194, 1966.

165. Courant, Richard *et al.* "On the Solution of Nonlinear Hyperbolic Differential Equations by Finite Differences," Communications on Pure and Applied Mathematics, V: 243–355 (1952).

VITA

Capt Steven M. Rinaldi was born on 28 November 1958 in Passaic, New Jersey. He graduated from Jenks High School, Jenks, Oklahoma, in May 1976. He attended the University of Oklahoma from August 1976 to May 1981. He graduated with a B.S. degree in Electrical Engineering and was commissioned on 20 December 1980. His initial active duty assignment was to the Air Force Institute of Technology, Wright-Patterson Air Force Base, Ohio. Upon completion of an M.S. degree in Electrical Engineering in December 1982, he was extended to the Doctoral Program at the Air Force Institute of Technology. In December 1985, he was reassigned to the Air Force Weapons Laboratory, Kirtland Air Force Base, New Mexico. He is currently the Chief of the Theoretical Section, Quantum Optics Branch, Advanced Radiation Technology Office, Air Force Weapons Laboratory.

Permanent Address: 360 Merrick Dr.
Xenia, Ohio 45385

UNCLASSIFIED
SECURITY CLASSIFICATION OF THIS PAGE

REPORT DOCUMENTATION PAGE

1a. REPORT SECURITY CLASSIFICATION UNCLASSIFIED	1b. RESTRICTIVE MARKINGS
2a. SECURITY CLASSIFICATION AUTHORITY	3. DISTRIBUTION/AVAILABILITY OF REPORT Approved for public release; distribution unlimited.
2b. DECLASSIFICATION/DOWNGRADING SCHEDULE	
4. PERFORMING ORGANIZATION REPORT NUMBER(S) AFIT/DS/PH/87-3	5. MONITORING ORGANIZATION REPORT NUMBER(S)
6a. NAME OF PERFORMING ORGANIZATION School of Engineering Air Force Institute of Tech. — 6b. OFFICE SYMBOL (*If applicable*): AFIT/ENP	7a. NAME OF MONITORING ORGANIZATION
6c. ADDRESS (*City, State, and ZIP Code*) Wright-Patterson AFB, Ohio 45433	7b. ADDRESS (*City, State, and ZIP Code*)
8a. NAME OF FUNDING/SPONSORING ORGANIZATION Air Force Weapons Laboratory — 8b. OFFICE SYMBOL (*If applicable*): ARDF	9. PROCUREMENT INSTRUMENT IDENTIFICATION NUMBER
8c. ADDRESS (*City, State, and ZIP Code*) Kirtland AFB, NM 87117-6008	10. SOURCE OF FUNDING NUMBERS PROGRAM ELEMENT NO. — PROJECT NO. — TASK NO. — WORK UNIT ACCESSION NO.

11. TITLE (*Include Security Classification*)

SEMICLASSICAL THEORY OF INJECTED LASERS WITH ARBITRARY STABLE AND UNSTABLE RESONATORS

12. PERSONAL AUTHOR(S)
Steven M. Rinaldi, Capt, USAF

13a. TYPE OF REPORT	13b. TIME COVERED	14. DATE OF REPORT (*Year, Month, Day*)	15. PAGE COUNT
PhD Dissertation	FROM _____ TO _____	December 1987	334

16. SUPPLEMENTARY NOTATION

17 COSATI CODES			18. SUBJECT TERMS (*Continue on reverse if necessary and identify by block number*)
FIELD	GROUP	SUB-GROUP	Semiclassical Laser Theory Injected Lasers Coupled Lasers

19. ABSTRACT (*Continue on reverse if necessary and identify by block number*)

Dr John H. Erkkila, Chairman, Advisory Committee

Approved for public release: IAW AFR 190-1
LYNN E. WOLAVER
31 Dec 87
Dean for Research and Professional Development
Air Force Institute of Technology
Wright-Patterson AFB OH 45433

20. DISTRIBUTION/AVAILABILITY OF ABSTRACT	21. ABSTRACT SECURITY CLASSIFICATION
☒ UNCLASSIFIED/UNLIMITED ☐ SAME AS RPT ☐ DTIC USERS	UNCLASSIFIED
22a. NAME OF RESPONSIBLE INDIVIDUAL Dr John H. Erkkila, Adjunct Professor	22b. TELEPHONE (*Include Area Code*) 505-844-3013 — 22c. OFFICE SYMBOL RDA/Logicon

DD FORM 1473, 84 MAR — 83 APR edition may be used until exhausted. All other editions are obsolete.

SECURITY CLASSIFICATION OF THIS PAGE
UNCLASSIFIED

Block No. 18:

Locking Range
Resonators

Block No. 19:

A semiclassical analysis of injected lasers with stable and unstable resonators and arbitrary outcoupling fractions was performed. Homogeneously broadened lasers with Fabry-Perot and with positive branch, confocal unstable resonators were modeled. Both time-dependent and steady-state analyses of free-running and injected lasers were performed.

Because of deficiencies in the standing wave semiclassical and the simple saturable gain models, a new semiclassical theory of homogeneously broadened lasers was developed. The theory is predicated upon the following assumptions: the atoms are two-level, a single longitudinal mode exists in the cavity, the transverse mode structure can be adequately modeled by the geometric optics mode, and the laser electric fields can be described by a pair of counterpropagating planar, cylindrical, or spherical traveling waves with different amplitudes. A general semiclassical theory was first developed, and then specialized to the Fabry-Perot and positive branch, confocal unstable resonator cases. Both the Maxwell-Bloch and rate equation approximation forms of the theory were derived. The general theory is sufficiently broad to allow the modeling of the geometric optics mode of any standing wave resonator configuration. The theory was shown to reduce to the simple saturable gain and standing wave semiclassical models in the appropriate limits.

The analyses of the injected lasers were performed with the new semiclassical theory. Both time-dependent and steady-state analyses were performed. The parameter space explored allowed the outcoupling fractions to be varied and the injected signal frequencies to be detuned from the free-running laser frequencies. Observables of interest included the threshold injected intensities, the locking ranges, and the injected laser system gains. Comparisons to three alternate models of injected lasers were performed. In the appropriate limits, the present model was shown to reduce to the other models.

END

DATE

FILMED

MARCH

1988

DTIC